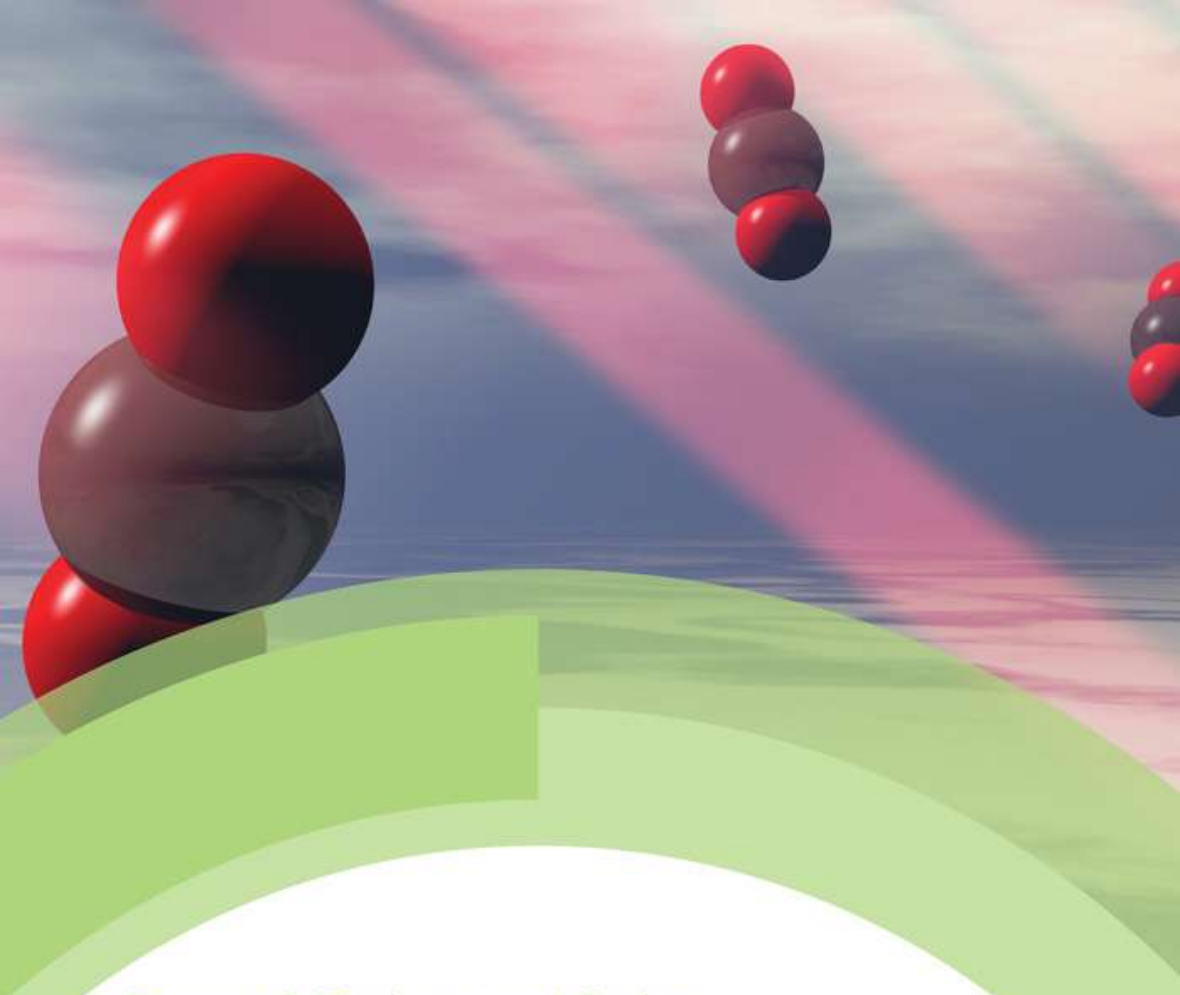

Energy & Environment Series

Carbon Dioxide Electrochemistry

Homogeneous and Heterogeneous Catalysis

Edited by Marc Robert, Cyrille Costentin
and Kim Daasbjerg

ROYAL SOCIETY
OF CHEMISTRY

Carbon Dioxide Electrochemistry
Homogeneous and Heterogeneous Catalysis

Energy and Environment Series

Editor-in-chief:
Heinz Frei, *Lawrence Berkeley National Laboratory, USA*

Series editors:
Nigel Brandon OBE FREng, *Imperial College London, UK*
Roberto Rinaldi, *Imperial College London, UK*
Vivian Wing-Wah Yam, *University of Hong Kong, Hong Kong*

Titles in the series:
1: Thermochemical Conversion of Biomass to Liquid Fuels and Chemicals
2: Innovations in Fuel Cell Technologies
3: Energy Crops
4: Chemical and Biochemical Catalysis for Next Generation Biofuels
5: Molecular Solar Fuels
6: Catalysts for Alcohol-Fuelled Direct Oxidation Fuel Cells
7: Solid Oxide Fuel Cells: From Materials to System Modeling
8: Solar Energy Conversion: Dynamics of Interfacial Electron and Excitation Transfer
9: Photoelectrochemical Water Splitting: Materials, Processes and Architectures
10: Biological Conversion of Biomass for Fuels and Chemicals: Explorations from Natural Utilization Systems
11: Advanced Concepts in Photovoltaics
12: Materials Challenges: Inorganic Photovoltaic Solar Energy
13: Catalytic Hydrogenation for Biomass Valorization
14: Photocatalysis: Fundamentals and Perspectives
15: Photocatalysis: Applications
16: Unconventional Thin Film Photovoltaics
17: Thermoelectric Materials and Devices
18: X-Ray Free Electron Lasers: Applications in Materials, Chemistry and Biology
19: Lignin Valorization: Emerging Approaches
20: Advances in Photoelectrochemical Water Splitting: Theory, Experiment and Systems Analysis
21: Electrochemical Reduction of Carbon Dioxide: Overcoming the Limitations of Photosynthesis
22: Integrated Solar Fuel Generators
23: Magnesium Batteries: Research and Applications
24: Organic Thermoelectric Materials
25: Electrochemical Methods for Hydrogen Production

26: Carbon Capture and Storage
27: Heterogeneous Catalysis for Energy Applications
28: Carbon Dioxide Electrochemistry: Homogeneous and Heterogeneous Catalysis

How to obtain future titles on publication:
A standing order plan is available for this series. A standing order will bring delivery of each new volume immediately on publication.

For further information please contact:
Book Sales Department, Royal Society of Chemistry, Thomas Graham House, Science Park, Milton Road, Cambridge, CB4 0WF, UK
Telephone: +44 (0)1223 420066, Fax: +44 (0)1223 420247
Email: booksales@rsc.org
Visit our website at www.rsc.org/books

Carbon Dioxide Electrochemistry
Homogeneous and Heterogeneous Catalysis

Edited by

Marc Robert
Université de Paris, France
Email: robert@u-paris.fr

Cyrille Costentin
Université de Paris and Université Grenoble-Alpes, France
Email: cyrille.costentin@univ-grenoble-alpes.fr

and

Kim Daasbjerg
Aarhus University, Denmark
Email: kdaa@chem.au.dk

Energy and Environment Series No. 28

Print ISBN: 978-1-78801-546-2
PDF ISBN: 978-1-78801-584-4
EPUB ISBN: 978-1-78801-940-8
Print ISSN: 2044-0774
Electronic ISSN: 2044-0782

A catalogue record for this book is available from the British Library

The Royal Society of Chemistry is a charity, registered in England and Wales, Number 207890, and a company incorporated in England by Royal Charter (Registered No. RC000524), registered office: Burlington House, Piccadilly, London W1J 0BA, UK, Telephone: +44 (0) 20 7437 8656.

For further information see our web site at www.rsc.org

Printed in the United Kingdom by CPI Group (UK) Ltd, Croydon, CR0 4YY, UK

Preface

The increasing energy demand over the past century has been mostly fulfilled *via* fossil fuel burning with tremendous economic, social, and environmental impacts. The first energy crisis in the mid-seventies led to a wave of intensive research to find alternatives to fossil fuels and ways to promote CO_2 reduction to produce fuels. After this initial productive period however, research on CO_2 reduction reverted to a steady, low level, until, over the last decade, we have witnessed a vibrant revival. This was certainly triggered by the progressive awareness to reach sustainability in all areas of our life, notably regarding energy consumption and chemical feedstock origin. In this context, a key and challenging task is to develop technologies that use CO_2 as a carbon source, heading towards a circular economy. In this endeavour, CO_2 electroreduction is a cornerstone, and tremendous progress has been made in recent years in this field. It thus seemed timely and appropriate to gather in this book the current state-of-the-art on CO_2 electrochemistry, covering various aspects from fundamentals to applications, from molecular catalysis to nanostructured materials, from bio-hybrid devices to integrated photoelectrochemical approaches. The goal in producing this book is to provide an overview of the current trends in CO_2 electrochemistry. To that aim we have gathered ten chapters, written by leading experts in the field, covering all domains to show how fundamental knowledge can provide stimulating tools for technological developments, and vice versa.

The first chapter by Kubiak and co-workers gives a complete overview of homogeneous molecular catalysts for CO_2 electroreduction with details on the progress in mechanism deciphering that may lead to rational design of new catalysts, with emphasis on the role of proton donor, electronic effects, and multi-metallic center cooperativity. They also report on advances in methodology for catalyst benchmarking. This chapter is complemented by a

Energy and Environment Series No. 28
Carbon Dioxide Electrochemistry: Homogeneous and Heterogeneous Catalysis
Edited by Marc Robert, Cyrille Costentin and Kim Daasbjerg

Published by the Royal Society of Chemistry, www.rsc.org

contribution in Chapter 2 on heterogenization of molecular catalysts by Costentin, Daasbjerg, and Robert, exposing immobilization strategies, the activity and durability of such supported molecular catalysts and specific mechanistic aspects.

Chapters 3 and 4 present heterogeneous metallic catalysts for CO_2 electroreduction. Interrelated phenomena including catalyst composition and environment are first described by Clark and Bell, discussing effects on activity and selectivity. Then, Roosmeisl, Strasser, and co-workers focus on the design of heterogeneous catalysts at the nanoscale with a rational approach fed by theoretical insights.

The quantum calculation approach is further developed for homogeneous catalysis of CO_2 reduction in Chapter 5 by Neese, Ye, and co-workers. They emphasize how mechanistic insights obtained by computational investigations could provide important guidelines to design tailored CO_2 reduction catalysts with higher efficiency and enhanced product selectivity.

New concepts have recently emerged in the field of electrocatalysis and, in particular, those regarding single-atom catalysts. This approach bridges homogeneous and heterogeneous systems and provides an exciting new area of research. It is introduced by Nam and co-workers in Chapter 6. Integrating a molecular catalyst moiety in a conductive electrode provides future directions to achieve efficient and selective catalytic systems and further integration of combined functionalities that can be used to develop photoelectrochemical devices, as described by Wang in Chapter 7.

An additional step of complexity can be reached by designing biological–inorganic hybrid systems, such as those detailed by Nocera and co-workers in Chapter 8, to achieve CO_2 conversion to fuels *via* exploitation of the biological machinery for CO_2 dark fixation associated with the efficiency of artificial light harvesting and water splitting.

All this new progress is only achievable thanks to new analytical tools such as the *in situ* spectroscopic techniques reviewed by Urakawa and co-workers in Chapter 9.

In the last chapter, Smith, Berlinguette, and co-workers open the door to large scale applications of CO_2 electroreduction *via* a description of electrolyzers capable of converting CO_2 into carbon-based fuels and chemicals at high current densities.

Finally, we would like to thank all the chapter authors for their efforts and contributions, which we believe form a remarkable account of the state-of-the-art of CO_2 electrochemistry, and a perfect entry for scientists willing to join this vibrant and exciting field. We would also like to express our gratitude to Connor Sheppard, Editorial Assistant at the Royal Society of Chemistry, for his continuous enthusiasm and patience during the preparation of this book.

Marc Robert, Cyrille Costentin and Kim Daasbjerg

Contents

Energy and Environment Series No. 28
Carbon Dioxide Electrochemistry: Homogeneous and Heterogeneous Catalysis
Edited by Marc Robert, Cyrille Costentin and Kim Daasbjerg

Published by the Royal Society of Chemistry, www.rsc.org

CHAPTER 1

Approaches to Controlling Homogeneous Electrochemical Reduction of Carbon Dioxide

A. JACOB A. BARRETT,*[a] B. FELIX M. BRUNNER,[a]
C. PO LING CHEUNG,[a] D. CLIFFORD P. KUBIAK,*[a]
E. GWENDOLYENNE L. LEE,[a] F. CHRISTOPHER J. MILLER,[a]
G. KATE M. WALDIE[b] AND H. ALMAGUL ZHANAIDAROVA[a]

[a] Department of Chemistry and Biochemistry, University of California, San Diego 9500 Gilman Drive, Mail Code 0358, La Jolla, California 92093, USA; [b] Department of Chemistry and Chemical Biology, Rutgers, The State University of New Jersey, New Brunswick, New Jersey 08903, United States
*Emails: j1barrett@ucsd.edu; ckubiak@ucsd.edu

1.1 Introduction

Carbon dioxide is the end product of combustion and respiration, and its reduction back to energy-rich products has challenged chemists for well over a hundred years. The first reports of the direct electrochemical reduction of CO_2 appeared in the early 1900s.[1,2] As the field of homogeneous catalysis grew during the 1960s and 1970s, chemists recognized that molecular electrocatalysis was also feasible. The first reports of homogeneous electrochemical reduction of CO_2 by molecular catalysts appeared in the 1970s and 1980s. These included metal phthalocyanine complexes,[3,4] metal tetraaza-macrocycles,[5,6] late metal phosphine complexes,[7] and Re (I) bipyridyl carbonyl complexes.[8] A molecular electrocatalyst both participates in an

Energy and Environment Series No. 28
Carbon Dioxide Electrochemistry: Homogeneous and Heterogeneous Catalysis
Edited by Marc Robert, Cyrille Costentin and Kim Daasbjerg

Published by the Royal Society of Chemistry, www.rsc.org

electron transfer reaction (at an electrode) and increases the rate of a chemical reaction. In organic electrochemistry, *mediators* are often used to mediate the flow of charge between an electrode and a chemical substrate, thus acting as an outer sphere electron donor or acceptor toward the substrate.[9] An electrocatalyst both supplies charge and performs inner sphere reduction or oxidation of an otherwise kinetically stable substrate. Both the electron transfer and chemical kinetics must be fast for an electrocatalyst to be efficient. Additionally, the electrocatalyst must display a good thermodynamic match between the redox potential (E^0) for its electron transfer reaction and the chemical potential difference between the products and reactants (*i.e.* thermodynamic driving force) for the reaction that is being catalyzed (*e.g.* reduction of CO_2). A significant advantage of molecular electrocatalysis is that these factors can be optimized by chemical tuning of the metal centers *via* appropriate ligand design.

Over the past ten years, several comprehensive reviews of the homogeneous electrochemical reduction of CO_2 have appeared.[10–15] In addition to the effects of metal type, *d*-electron configuration, and ligand type, new dimensions in the performance of molecular catalysts have been identified. Many breakthroughs in our understanding of how molecular catalysts respond to their local environment in the electrochemical cell, *e.g.* solvent, electrolyte, and applied bias have occurred over the last decade. One example of innovative catalyst design is the use of pendent proton relays, as well as charged and hydrogen bonding groups attached to the catalysts have been reported. This chapter presents much of the new knowledge that has been gained over the past ten years in the homogeneous electrochemical reduction of CO_2, with the aim of identifying areas where new research may produce further breakthroughs in our understanding and control of the reduction of CO_2 for its conversion to high-value chemicals like CO, formate, methanol, and methane.

1.2 Overview of Parameters for Evaluating Electrocatalysts

This section will give a brief introduction to the parameters commonly used to describe molecular electrochemical catalysis. A more in-depth discussion of these parameters can be found in the 'Catalyst Comparisons' section of this text.

Catalytic Tafel plots are used to visualize catalyst performance using the overpotential (η) and turnover frequency (TOF). The overpotential is the additional potential applied beyond the thermodynamically determined potential (E^0) required for the electrochemical reaction to transpire. The reaction conditions, such as solvent and pK_a of all present proton sources (*i.e.* water, phenol, or acetic acid), must be considered to appropriately determine E^0 of the redox reaction. Furthermore, the products formed (*i.e.* CO, $MgCO_3$, HCO_3^-) are considered in the determination of E^0_{cat}. Thus, the calculation of overpotential is not trivial but enables the comparison of electrocatalysts under different reaction conditions. The TOF is the number of chemical conversions of the substrate per unit of time (typically in

seconds). Catalysts that have a high TOF for a selective transformation with minimal overpotential are ideal.

The catalytic potential for the electron transfer event is reported in several ways. The potential value at the peak catalytic current (E^0_{cat}) is typically reported *versus* a standard electrode potential such as saturated calomel electrode (SCE), silver chloride electrode (Ag/AgCl), or normal hydrogen electrode (NHE). Additionally, this potential may be adjusted based on the redox couple of an internal standard like ferrocene/ferrocenium ($Fc^{+/0}$). The potential at half the catalytic current ($E^0_{cat/2}$) is normally found at the steepest part of the catalytic wave and may also be reported. The Faradaic efficiency (FE) describes the amount of product produced per number of electrons transferred to facilitate the electrochemical reaction. The following sections will provide many of these parameters for an assortment of electrocatalysts.

1.3 Overview of Metals Utilized in Electrochemical CO_2 Reduction

Molecular catalysts can typically be divided into classes based on ligand architecture. Our research group previously described five main classes of catalysts in a 2009 tutorial review published in *Chem. Soc. Rev.*: metals ligated by porphyrins, cyclams, bipyridyls, polypyridyls, and phosphines.[10] This section will briefly recount the molecular catalysts used for electrocatalytic CO_2 reduction by Periodic Group in the literature to date.[10–15] Improvements in catalytic activity *via* changes to the metal identity and/or ligand structure, including tuning of the steric and electronic properties, are discussed. The discussion will also describe new strategies for improving catalytic selectivity (*i.e.* pendent proton relays, Lewis acid additives, hydrogen bonding, and others).

1.3.1 Group 6

The Kubiak and Cowan groups have examined electrocatalytic CO_2 reduction with bipyridine complexes of Group 6 metals. The metal tetracarbonyl bipyridyl, $[M(R\text{-bpy})(CO)_4]$ (M = Mo, W; R = H, *t*Bu), complexes are active for CO_2 reduction with quantitative Faradaic efficiency (FE) for CO at −2.3 V *vs.* saturated calomel electrode (SCE) [*ca.* −2.7 V *vs.* ferrocenium/ferrocene ($Fc^{+/0}$)] in MeCN.[16] The reaction rates are significantly slower than their Group 7 counterparts. Density functional theory (DFT) calculations revealed stronger π-back bonding into the CO ligands with Group 6 metals compared to Re, suggesting that CO release from $[M(R\text{-bpy})(CO)_4]^{2-}$ limits the CO_2 reduction rates of these complexes. The catalytic onset potential of $[M(bpy)(CO)_4]$ (M = Mo, W, Cr) was anodically shifted at Au electrodes compared to glassy carbon (GC) electrodes.[17] Cowan and co-workers used vibrational sum-frequency generation spectroscopy to show that CO loss is enabled by strong interactions with the Au surface, providing access to a lower-energy pathway for generation of the active species $[M(bpy)(CO)_3]^{2-}$.[18]

This is an example of chemically relevant interactions that the electrode materials may have in ''homogenous'' molecular electrocatalysis.

Other Group 6 complexes with modified bidentate ligands[19] or $[Mo(CO)_2(\eta^3\text{-allyl})(\alpha\text{-diamine})(NCS)]$[20] also showed modest catalytic current increases under CO_2. The former systems had low FEs for CO and reduction products were not quantified in the latter. Pyridine monoimine (PMI) analogues $[(PMI)Mo(CO)_4]$ exhibited catalytic behavior under CO_2 on the first voltammogram sweep, but diminished substantially on the second scan.[21] Chemical reduction studies implicated the formation of a CO_2 adduct that interacts across the metal and imine carbon. This irreversible ligand-based reactivity is responsible for the inability of the catalyst to turnover. Grice and co-workers showed that Group 6 carbonyl complexes without other ancillary ligands are capable of CO_2 electroreduction.[22] $[Mo(CO)_6]$ was the most active in this series, producing CO at -2.8 V *vs.* $Fc^{+/0}$ (up to 95% FE_{CO}) while Group 7 analogues $Re_2(CO)_{10}$ and $Mn_2(CO)_{10}$ were not active. The reactivity of related Group $4-6$ metallocenes $[Cp_2MCl_2]$ with CO_2 were also studied by the same group.[23] The niobium, molybdenum, and tungsten complexes reduce CO_2 to CO, albeit at very negative potentials (-3 V *vs.* $Fc^{+/0}$) with low current efficiencies. Cleary, while bipyridine or other redox-active ligands are not required for CO_2 reduction here, the presence of such ancillary ligands enables significantly milder operating potentials. A radically different approach was demonstrated by Jayarathne *et al.* utilizing labile phosphine ligands and chloride ions on a tungsten complex. This complex was able to reduce CO_2 to CO *via* a mechanism involving a tungsten oxo intermediate.[24]

1.3.2 Group 7

Lehn and co-workers first described the activity of $[Re(bpy)(CO)_3Cl]$ (Re-bpy, **1**) for electrocatalytic CO_2 reduction in 1984.[8] This system, sometimes referred to as the Lehn catalyst, reduced CO_2 to CO at -1.49 V *vs.* SCE (*ca.* -1.9 V *vs.* $Fc^{+/0}$) in 9 : 1 *N*,*N*-dimethylformamide (DMF)/H_2O with very high selectivity for CO over H_2 evolution ($FE_{CO} = 98\%$). However, the rate of catalysis, defined by the turnover frequency (TOF), was reported to be relatively slow ($TOF = 21.4\ h^{-1}$).

Infrared-spectroelectrochemistry (IR-SEC) studies indicate that significant Re–Re dimer formation occurs following one-electron reduction of **1**, which was later confirmed by comparison to the independently prepared dimer.[25] Additional reduction is then required to break the Re–Re bond to generate the proposed active catalyst, $[Re(bpy)(CO)_3]^-$. Introduction of *t*-butyl groups in the 4,4′ positions (denoted as $[Re(t\text{Bu-bpy})(CO)_3Cl]$, **2**) dramatically increased the rate of CO_2 reduction.[26] The steric bulk of these substituents largely prevents dimerization as shown by IR-SEC (Figure 1.1) and stopped-flow IR studies.[27] Furthermore, the reduced species, $[Re(R\text{-bpy})(CO)_3]^-$, reacts with CO_2 approximately ten times faster when R = *t*Bu *versus* H, suggesting an additional effect of the *t*-butyl groups (see Section 1.9). Replacement of the halide ligand with a chelating phosphazane (PNP) ligand in $[Re(bpy)(PNP)(CO)_2]OTf$ is another effective strategy to prevent dimerization as the ligand does not fully dissociate upon reduction.[28]

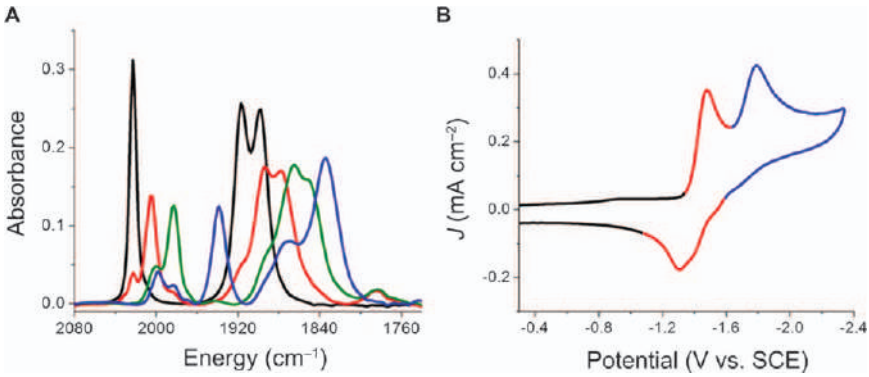

Figure 1.1 IR-SEC of [Re(*t*Bu-bpy)$(CO)_3$Cl] (black, **2**) under N_2 in 0.1 M Bu_4NPF_6/MeCN, showing three major species as the potential is increased cathodically: Re^{I}(*t*Bu-$bpy^{\bullet -}$)$(CO)_3$Cl (red), Re^0(*t*Bu-bpy)$(CO)_3$ (green), Re^0 (*t*Bu-$bpy^{\bullet -}$)$(CO)^3$ (blue). IR-SEC cell: Pt working electrode, Pt counter electrode, Ag pseudo-reference electrode. (B) Cyclic voltammogram of **2** under N_2 in 0.1 M Bu_4NPF_6/MeCN (GC WE, Pt wire CE, Ag/AgCl pseudo-RE, with Fc added as an internal standard), showing correlation to species seen in IR-SEC. *Y*-axis is current density (J) and the *x*-axis is potential (V) *vs.* saturated calomel electrode (SCE).
Reproduced from ref. 29 with permission from American Chemical Society, Copyright 2014.

DFT calculations predict that the HOMO of the two-electron reduced form of the Re(bpy)$(CO)_3$Cl catalyst has a mixed metal–ligand character.[30] It has been proposed that the delocalized electronic structure of $[Re(bpy)(CO)_3]^-$ contributes to the high selectivity of CO_2 reduction over H_2 evolution in the presence of a proton source as formation of a metal hydride requires the electron density to be localized in the Re dz^2 orbital. This proposal was further supported by X-ray absorption studies[31] and Raman spectroscopy[32] which indicated that the active doubly-reduced species $[Re(bpy)(CO)_3]^-$ is best described as $[Re(0)(bpy^{\bullet})(CO)_3]^-$ where one electron has been added to the bpy π^* orbital and the other to the Re $d_z{}^2$ orbital. This electronic configuration was posited to enable reaction with CO_2 through σ and π interactions with a lower reorganization energy near the transition state than for the reaction with a proton, resulting in CO_2 reduction being kinetically favored over H_2 evolution.[31] This was further corroborated *via* DFT calculations by the Carter group that showed that protonation of the anion to produce the Re–hydride has a higher activation energy than formation of the Re–COOH complex.[33] Manganese bipyridine catalysts have been studied as more Earth-abundant and less expensive alternatives to the Re–bpy systems.[34,35] Johnson *et al.* originally reported that the doubly reduced $[Mn(bpy)(CO)_3]^-$ anion (analogous to the active Re catalyst) does not react with CO_2.[36] Bourrez *et al.* discovered that these Mn-bpy compounds are catalytic in the presence of water, and have lower overpotentials (around 0.40 V) when compared to Re-bpy analogues.[35] The overpotential (η) in this

case is the potential difference between the thermodynamically determined reduction potential for aqueous CO_2 reduction and the experimentally observed reduction potential for Mn-bpy compounds under CO_2.

1.3.3 Group 8

Fe porphyrins have been extensively studied for electrocatalytic CO_2 reduction for the past three decades, in particular by Savéant and co-workers.[37,38] Fe(III) tetraphenyl porphyrin (FeTPP, **3**) undergoes three sequential one-electron reductions in DMF under Ar. The current increases at the third reduction (*ca.* −1.6 V *vs.* SCE) under CO_2, corresponding to electrocatalytic CO_2 reduction to CO (Figure 1.2a). However, electrolysis at −1.8 V *vs.* SCE (*ca.* −2.2 V *vs.* $Fc^{+/0}$) revealed that the catalyst rapidly degrades under catalytic conditions, perhaps from carboxylation and/or hydrogenation of the porphyrin.[39]

Ru and Os complexes of the form $[M(bpy)(CO)_2Cl_2]$ undergo polymerization on the electrode upon reduction to form heterogeneous polymer films that are active for CO_2 reduction to CO and formate.[41,42] Following earlier reports of using bulky substituents on the bipyridine ligand to prevent metal–metal dimerization, it was demonstrated that installation of mesityl (mes) groups in 6,6′ positions prevent polymerization, and this system is an active homogeneous catalyst for CO_2 reduction to CO (95% FE) at −2.2 V *vs.* $Fc^{+/0}$ in the presence of phenol.[43] Interestingly, the yield of CO is potential-dependent: at −1.7 V *vs.* $Fc^{+/0}$, FE_{CO} decreased to 63% and formate was detected using NMR. IR-SEC studies support an electron transfer-chemical reaction-electron transfer (ECE) mechanism where one-electron reduction of $Ru(mes\text{-}bpy)(CO)_2Cl_2$ (**4**) leads to chloride loss, followed by protonation and another one-electron reduction to form a Ru(II)–hydride complex (**4b**). Complex **4b** can react with CO_2 to generate a formate complex [Ru-η^1-OCHO] (**4c**) (Scheme 1.1). Dissociation of formate from **4c** may occur, closing the catalytic cycle for CO_2 reduction to formate. However, additional one-electron reduction of **4c** appears to increase

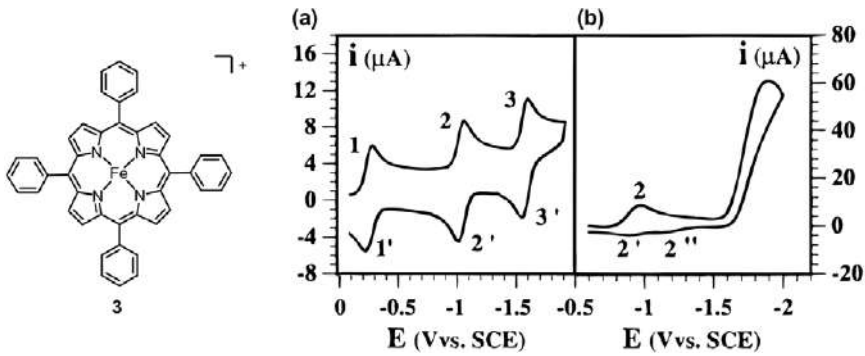

Figure 1.2 (a) Structure of FeTPP (3) and cyclic voltammograms of 3 in 0.1 M Et_4NClO_4 dissolved in DMF (b) under Ar, and (c) under CO_2 with 7.9 mM Mg^{2+}. Reproduced from ref. 40 with permission from American Chemical Society, Copyright 1996.

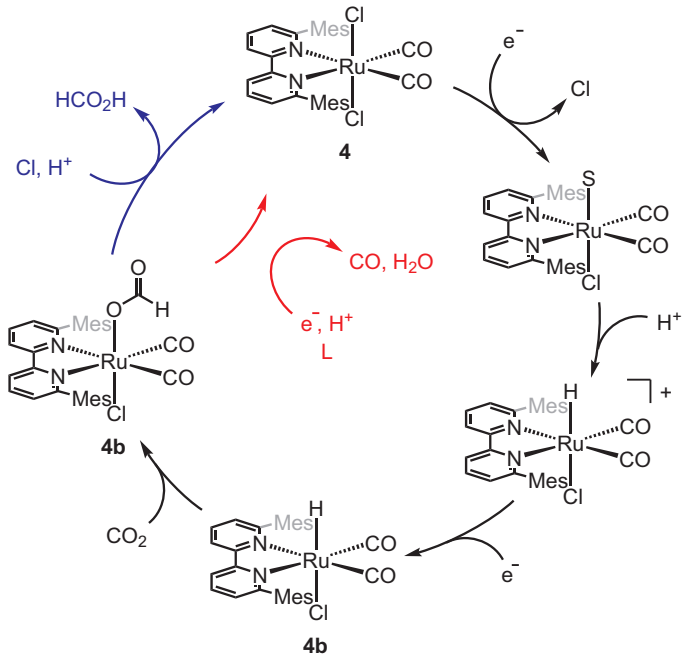

Scheme 1.1 Proposed mechanism for CO_2 reduction to formate (blue path) or CO (red path) with [Ru(mes-bpy)(CO)Cl_2] (4).[43]

the rate of thermal dehydration of Ru-η^1-OCHO, generating CO and water and shifting the product ratio to favor CO. Min and co-workers made a Ru pincer compound using bipyridine with an aminophosphine substituent at the 6 position. An increase in current was observed under CO_2.[44] The current further increased under CO_2 when 3% H_2O was added. Like the M(bpy)$(CO)_2Cl_2$, controlled potential electrolysis (CPE) showed that the compound made both CO (FE = 60.7%) and formate (FE = 37.3%) with trace H_2 in 3% H_2O/MeCN. The compound also showed stability over 24 h, yet the catalyst only achieved 11.2 turnovers during that time.

Meyer and co-workers performed detailed studies of $[Ru(tpy)(bpy)X]^{2+}$ (X = MeCN, Cl^-) to elucidate the pathway for CO_2 reduction in MeCN.[45] $[Ru(tpy)(bpy)(MeCN)]^{2+}$ (**5**) and $[Ru(tpy)(MebImpy)(MeCN)]^{2+}$ (**6**) exhibit two reversible reductive features in cyclic voltammetry under Ar, corresponding to the reduction of terpyridine (tpy) and bipyridine (bpy) or 3-methyl-1-pyridylbenzimidazol-2-ylidene (MebImpy), respectively. Current enhancement is observed at the second reduction in the presence of CO_2, as well as at more negative potentials (Figure 1.3a). The catalytic peak current is scan rate dependent and the wave does not show the typical plateau shape for a rate-limiting catalytic reaction. The rate of catalysis also exhibits saturation behavior with respect to CO_2 concentration. When considered together, these observations are consistent with the rate-limiting step being substitution of the

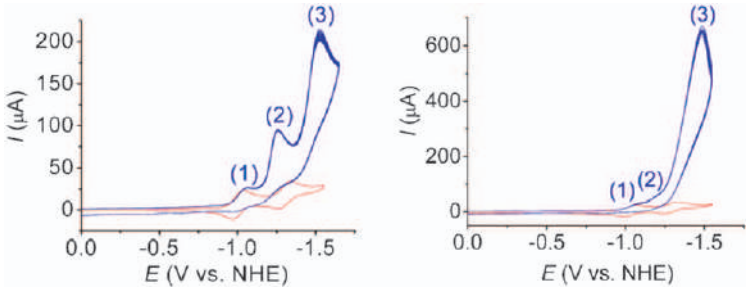

Figure 1.3 Cyclic voltammograms of (a) $[Ru(tpy)(bpy)(MeCN)]^{2+}$ (5), and (b) $[Ru(tpy)(MebImpy)(MeCN)]^{2+}$ (6) under Ar (red trace) or CO_2 (blue trace) in 0.1 M Bu_4NPF_6 in MeCN. The *x*-axis is potential *vs.* Normal Hydrogen Electrode (NHE).
Adapted from ref. 45 with permission from the Royal Society of Chemistry.

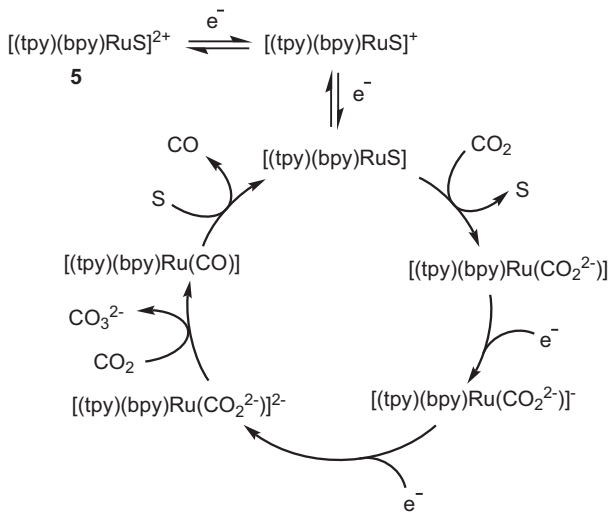

Scheme 1.2 Proposed mechanism for electrocatalytic CO_2 reduction to CO with $[Ru(tpy)(bpy)S]^{2+}$, where S = solvent, in this case MeCN.

MeCN ligand by CO_2 in the doubly-reduced species $[Ru(tpy^{-})(bpy^{-})(MeCN)]^{0}$. This substitution generates $[Ru(tpy^{-})(bpy^{-})(CO_2^{2-})]^{0}$ which undergoes further reduction leading to overall CO_2 reduction and disproportionation to CO and CO_3^{2-} (Scheme 1.2).

Substitution of MeCN by CO_2 in **5** proceeds *via* a dissociative mechanism; therefore, modifications that increase the rate of MeCN dissociation should increase the rate of catalysis. Meyer and co-workers[45] developed the benzimidazolylidene analogue **6**, where the carbene ligand is more donating than bipyridine (Figure 1.4). The increased electron density at the metal increases the lability of MeCN and increases the rate of catalysis from 5.5 to 19 s^{-1}

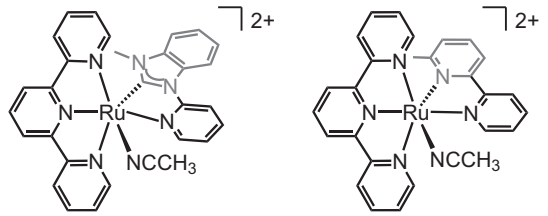

6 **7**

Figure 1.4 Structures of $[Ru(tpy)(Mebim\text{-}py)(MeCN)]^{2+}$ (6) and $[Ru(tpy)(R\text{-}bpy)(MeCN)]^{2+}$ (7).

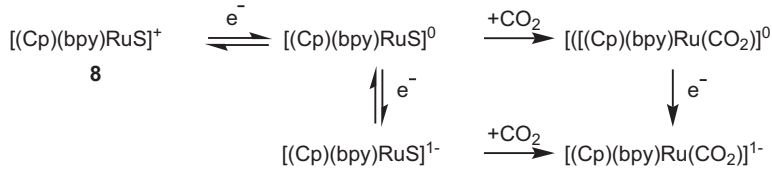

Scheme 1.3 Accessible EEC and ECE pathways to generate the $[Ru\text{-}CO_2]$ adduct with 8, where S = solvent, in this case MeCN.

(Figure 1.3b). Notably, **5** is also active for the hydrogen evolution reaction (HER) and the oxygen evolution reaction (OER). These reactions have been coupled with CO_2 reduction to develop single-catalyst systems capable of producing pure CO or controlled syngas ratios (CO/H_2) at the cathode and O_2 at the anode.[46–48] Additional studies by Ott and co-workers[49] found a correlation between the rate of CO_2 reduction and the rate of monodentate ligand dissociation, which was varied by systematically changing the electron-donating character of the bidentate ligand in **5**. Increasing the ligand donating ability promotes MeCN loss and increases the catalytic rate. Other variations to the original catalysts, $[Ru(tpy)(bpy)Cl]^+$ and $[Ru(bpy)_2(CO)Cl]^+$, have been explored.[50–52] However, in these reports, the new complexes exhibit similar catalytic behavior as the parent systems and are proposed to proceed *via* an analogous mechanism for CO production involving a key $[Ru(tpy)(bpy)(CO_2^{2-})]^0$ intermediate.

A related Ru complex $[CpRu(bpy)(MeCN)]^+$ (**8**), (Cp = cyclopentadiene), was recently reported to facilitate rapid electrochemical CO_2 reduction and disproportionation to CO and CO_3^{2-} triggered by initial one-electron reduction at −1.9 V *vs.* $Fc^{+/0}$.[53] An ECE pathway for initial CO_2 activation analogous to that shown in Scheme 1.3 for **5** was proposed. Substitution of the MeCN ligand by CO_2 occurs with one-electron reduction, after which addition of the second electron occurs at a more positive potential than the first reduction to generate a $[CpRu(bpy)(CO_2)]^-$ complex. However, this system is not catalytic at this potential due to the high stability of the resulting $[CpRu(bpy)(CO)]^+$ species.

1.3.4 Group 9

Co porphyrins have also been shown to exhibit excellent activity for electrocatalytic CO_2 reduction.[54–56] Carbon monoxide is the main CO_2 reduction product using Co porphyrins but the selectivity over H_2 evolution varies depending on the solution pH. Hydrogen dominates at pH 1 while up to 60% CO is produced at pH 3.[54] DFT calculations by the Koper group[55] and by Leung and co-workers[54] supported a mechanism in which a reduced Co(I) complex reacts with CO_2 to generate a $[Co(I)Por–CO_2]^-$ adduct (Por = porphyrin).

The electrochemical conversion of CO_2 to CO by Co(II) catalysts bearing N_4-tetradentate ligands at a glassy carbon electrode (GCE) was investigated by Wang and co-workers.[57] The most effective catalyst *cis*-$[Co(PDP)Cl_2]$ (PDP = 1,1′-bis(2-pyridinylmethyl)-2,2′-bipyrrolidine) exhibited $FE_{CO} = 96\%$ at −1.7 V *vs.* SCE (*ca.* −2.1 V *vs.* $Fc^{+/0}$) with no concomitant H_2 evolution.

While phosphine ligands are commonly used for other catalytic processes, they are rarely utilized in electrocatalytic CO_2 reduction catalysts. Early examples for CO_2 reduction with group 9 metal phosphine complexes date back to the 1980s. Slater *et al.* reported electrochemical CO_2 reduction with $Rh(diphos)_2$, (diphos = 1,2-Bis(diphenylphosphino)ethane) and trinuclear Ni clusters with phosphine ligands have also been reported as electrocatalysts of modest activity.[7,58] $CpCo(P_2N_2)$ was found to catalyze the reduction of CO_2 to formate and is discussed in detail in Section 1.5.[59]

1.3.5 Group 10

The first report demonstrating electrocatalytic CO_2 reduction with molecular Ni and Co catalysts was published by Eisenberg and co-workers in 1980.[5] Reasonable FE_{CO} (up to 65%) using Ni(II) cyclam derivatives were achieved in water/MeCN (2 : 1) between −1.5 V and −1.6 V *vs.* SCE (*ca.* −1.9 to −2.0 V *vs.* $Fc^{+/0}$) at a Hg electrode. Hydrogen made up the remainder of the charge balance. Furthermore, Sauvage and co-workers showed that $[Ni(cyclam)]^{2+}$ (**9**) is exceptionally selective for CO (96%) in pure water at −1.05 V *vs.* NHE at a Hg electrode.[6,60] As shown in Figure 1.5, a large catalytic wave is observed by cyclic voltammetry in water under CO_2, corresponding to TOF = 32 h^{-1} and making **9** one of the more active molecular catalysts for electrocatalytic CO_2 reduction to CO. Ni(II) cyclams substituted with *C*-alkyl groups were shown to have higher TOF than **9** in 20% $MeCN/H_2O$.[61] Schiff bases have been widely explored as planar, tetradentate ligands for catalysis, but have only recently been investigated for CO_2 reduction. A series of Ni(II) and Cu(II) Schiff base complexes exhibited current enhancement under CO_2, but further studies are needed to quantify their activity.[62,63] Mukherjee and co-workers[64] prepared cathode materials of related Ni(II) and Cu(II) salen complexes, which reduced CO_2 to CO and C1+ hydrocarbons. The activity of these materials differed from that of pure metals but since production of hydrocarbons with molecular catalysts is exceedingly rare, further studies to identify the true active species are warranted.

Moving beyond cyclam and related macrocycles, several research groups have made efforts to develop new CO_2 reduction catalysts based on other tetradentate

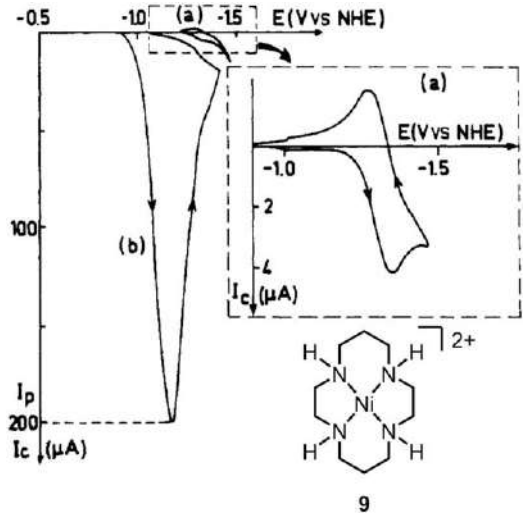

Figure 1.5 Cyclic voltammograms of $[Ni(cyclam)]^{2+}$ (9) at a Hg electrode in water (pH 4.5) under N_2 (curve a) or CO_2 (curve b).
Adapted from ref. 60 with permission from American Chemical Society, Copyright 1986.

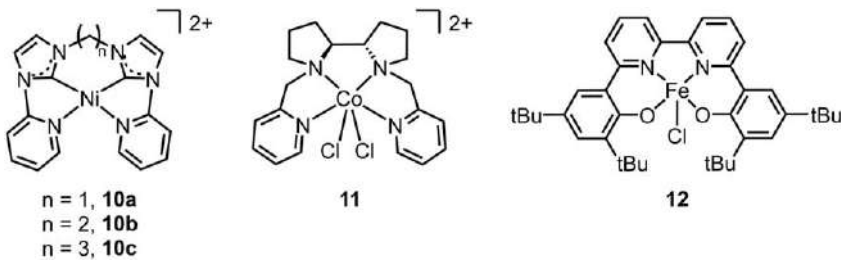

Figure 1.6 Structures of other first-row transition metal catalysts containing tetradentate ligands denoted as complexes 10 – 12.

nitrogen ligands (Figure 1.6). A series of Ni(II) complexes (**10a-c**) with an N-heterocyclic carbene–pyridine ligand yielded CO as the major product of CO_2 reduction at −1.5 V *vs.* SCE (*ca.* −1.9 V *vs.* $Fc^{+/0}$) at GC in MeCN.[65,66] Unfortunately, Faradaic efficiencies were not reported and the catalysts decomposed over extended times. Further optimization of this ligand architecture led to improved stability and up to 0.2 V decrease in operating potential for CO_2 reduction, but the catalytic rates remained far slower than for **9**.[66]

Group 10 metal phosphines were studied primarily by the Dubois group in the 1990s and 2000s.[11,58,67] A library of $[Pd(triphosphine)(S)](BF_4)_2$ complexes were screened as CO_2 reduction catalysts.[67] It was found that triphosphine complexes with an additional labile ligand produce CO. In contrast, later studies with tetraphosphine ligands show that the reactions proceed through a hydride intermediate to produce formate. Substitution of one or more

phosphines with heteroatoms resulted in complete loss of activity. One of the main degradation pathways is the formation of dimers by the reduced state. Several new derivatives were synthesized, including dimeric catalysts that showed extraordinary enhancement in catalytic performance.[68] The bimetallic bridged $[Pd_2(CH_3CN)_2(eHTP)](BF_4)_4$ (eHTP = bis(bis((diethylphosphino)ethyl)-phosphino)methane) complex has a very similar structure to the [NiFe] CO dehydrogenase enzyme and di-metallic cooperativity is proposed to play a crucial role in catalysis.[11] The flexible modular synthetic pathways to those ligands gave rise to a large variety of similar ligands with different functional groups attached to enhance cooperative catalysis; those catalysts are discussed in further detail in Section 1.5.[69]

In recent years, carbene pincer complexes of group 10 metals were shown to reduce CO_2 selectively in the presence of acids. In 2014 Wolf *et al.* reported the use of tridentate N-heterocyclic carbene (NHC) ligands with Pd to produce CO with moderate efficiency and selectivity.[70] The NHC ligands bind to the metal in a CNC configuration (two NHC carbon atoms and 1 pyridine nitrogen atom). Sheng *et al.* showed that Pd can be substituted by the more abundant Ni.[71] Independently, Cope *et al.* reported a CCC-NHC pincer Ni complex that exhibited similar behavior.[69] "CCC-NHC" denotes the binding of the metal by 3 C atoms of the ligand. In both cases, the main product was CO with water present as a proton source. Notably, systematic studies comparing Ni, Pd, and Pt by Wolf *et al.* found that a very similar catalyst mainly produces hydrogen in the presence of CO_2 and added TFA, and only the Pd catalyst is active for CO production.[72] These findings emphasize the influence of the proton source on the performance of CO_2 reduction catalysts. The performance of these catalysts was only slightly improved, FE_{CO} increased to 28% from 23%, by tuning the electronic properties of the ligand.[11,70]

While the appropriate combination of metal and ligand is crucial for the design of an active catalyst for CO_2 reduction, tuning the electronic and/or steric properties of the ligands often only leads to an incremental increase in catalytic performance. Furthermore, simultaneously improving the catalytic rate and decreasing the overpotential is very challenging with simple ligand optimization. In evaluating the comprehensive body of work in this field, we conclude that other factors can have just as much of an effect on improving catalysis, if not more, than basic changes to the metal and/or ligand. These other factors include: selection of the appropriate Brønsted acid source (although water is preferred), addition of stoichiometric or co-catalytic additives, introduction of pendent functional groups, and multinuclear metal ensembles. Here, we highlight the recent literature where these parameters are considered to control the performance of many of the catalysts presented in Section 1.3.

1.4 Brønsted Acid Source

Savéant and co-workers demonstrated that the rate of CO_2 reduction and FeTPP catalyst lifetime are increased by the addition of weak Brønsted acids (Figure 1.7).[73,74] Notably, the product distribution depends on the strength of

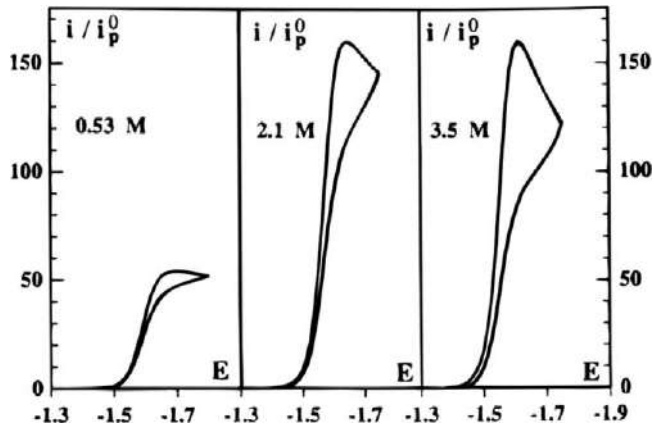

Figure 1.7 Cyclic voltammograms of FeTPP (**3**) under CO_2 in DMF with 0.1 M Et_4NClO_4 and increasing concentrations of TFE. *Y*-axis is the measured current normalized against the peak current for the $Fe(I)^-/Fe(0)^{2-}$ redox couple. Adapted from ref. 74 with permission from American Chemical Society, Copyright 1996.

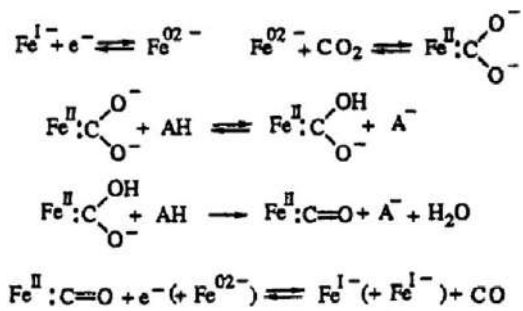

Scheme 1.4 Proposed mechanism for CO_2 reduction by FeTPP (**3**) in the presence of a Brønsted acid.
Reproduced from ref. 73 with permission from American Chemical Society, Copyright 1994.

the Brønsted acid. Specifically, the formic acid (HCOOH) yield is inversely correlated with the Brønsted acid strength. For example, the addition of 1-propanol resulted in both CO and formate (FE ≈ 60% and 35%, respectively), while the stronger acid trifluoroethanol (TFE) yielded only CO (FE > 96%). This counterintuitive behavior arises from the greater hydrogen bonding stabilization of catalytic intermediates with stronger acids. In the presence of Brønsted acid, water is formed as a co-product as shown in Scheme 1.4, thereby eliminating the issue of precipitation of carbonate salts on the electrode.

A more robust ligand, bis-hydroxyphenyl bipyridine, was recently explored for CO_2 reduction by Machan and co-workers (Figure 1.8).[75] In the absence of Brønsted acid, the Fe complex, Fe(*t*Budhbpy)Cl (**12**) (*t*Budhbpy = 6,6′-di(3,5-di-*tert*-butyl-2-hydroxybenzene)-2,2′-bipyridine) facilitated CO_2 reduction

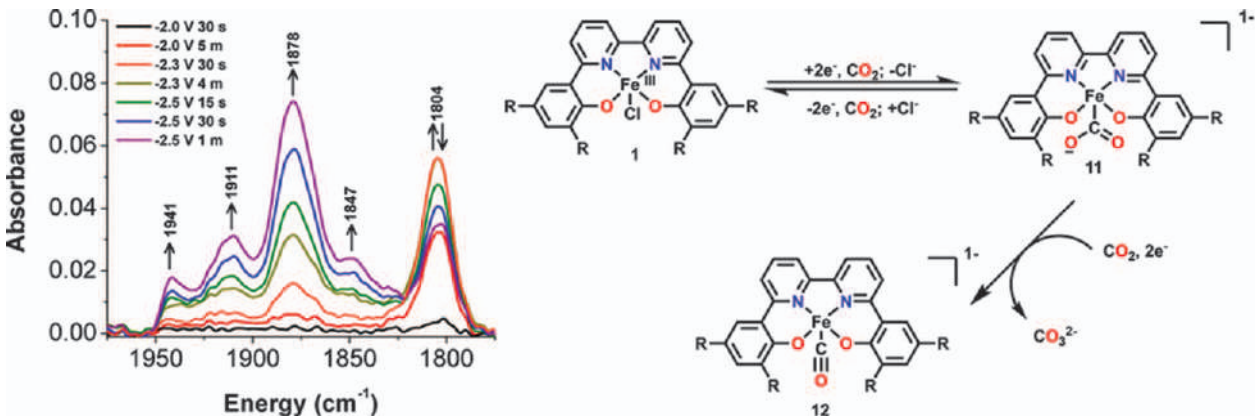

Figure 1.8 IR-SEC experiment (left) with 3 mM Fe(*t*Budhbpy)Cl (**12**) in 0.1 M $TBAPF_6$/DMF with CO_2 which was sparged through the solution for approximately 20 s. GC working electrode, Ag metal pseudo-reference electrode, GC counter electrode, and Fc internal standard. Proposed reaction mechanism of Fe(*t*Budhbpy)Cl with CO_2 at reducing potentials (right). Adapted from ref. 75 with permission from American Chemical Society, Copyright 2018.

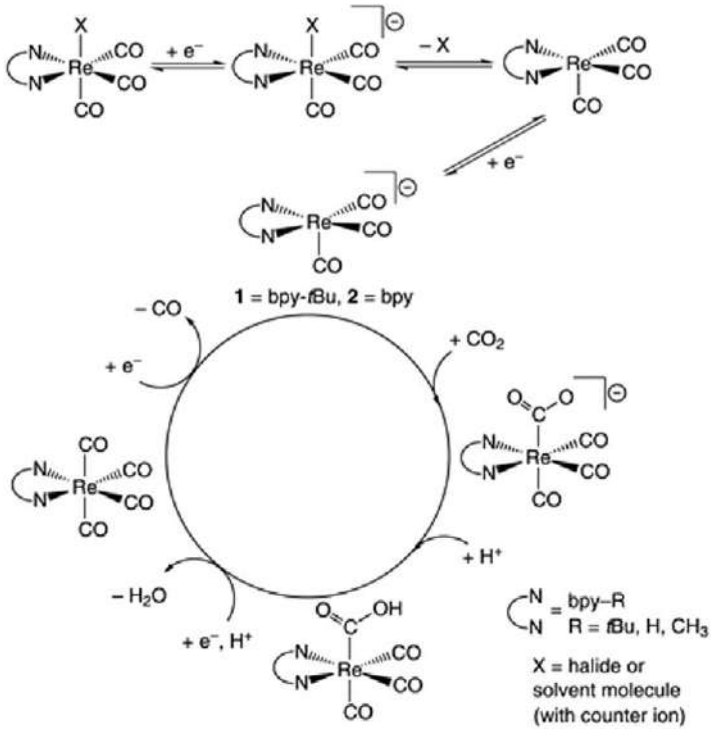

Scheme 1.5 Proposed mechanism for the electrocatalytic reduction of CO_2 by Re(R-bpy)$(CO)_3$X catalysts.
Reproduced from ref. 27 with permission from the Royal Society of Chemistry.

and disproportionation to CO and CO_3^{2-} at −2.5 V *vs.* $Fc^{+/0}$ in DMF at GC; however, only a FE_{CO} of 1.1% is observed due to strong binding of CO to the Fe center. This behavior is similar to that of FeTPP (**3**) at GC electrodes: CO dissociation from the metal is rate limiting and the high CO binding affinity eventually leads to catalyst decomposition. However, upon addition of phenol to **12**, an increase in current is seen, and formate is observed as the main CO_2 reduction product (FE = 68%). IR-SEC supports a mechanism involving a Fe(III)-hydride species, which upon further reduction is capable of hydride transfer to CO_2 to generate formate.

The proposed mechanism for CO_2 reduction with the Re-bpy catalysts is shown in Scheme 1.5. Following CO_2 binding at the active catalyst $[Re(bpy)(CO)_3]^-$, protonation yields a hydroxycarbonyl species that undergoes further reduction and protonation to generate $[Re(bpy)(CO)_4]$ *via* rate-limiting C-O cleavage.[76] The Re(COOH)(bpy)$(CO)_3$Cl intermediate for **1** and the *t*-butyl analogue **2** have been observed by stopped-flow IR spectroscopy.[77] This proposed mechanism was also supported by DFT calculations from Carter and co-workers.[78] In the absence of Brønsted acid, ligand-bound carboxylate is produced.[79] DFT calculations on the Re centered radical

[·Re(bpy)$(CO)_3$] purported the insertion of CO_2 into a Re carboxylate dimer [Re(Me-bpy)$(CO)_3]_2(\mu\text{-}CO_2)$.[79]

To better understand the mechanism of catalyst regeneration, the tetracarbonyl species, $[Re(bpy)(CO)_4]^+$ and $[Re(t\text{Bu-bpy})(CO)_4]^+$, were synthesized.[79] IR-SEC and chemical reduction studies revealed that these complexes undergo substitution at reducing potentials, releasing CO and generating $[Re(R\text{-bpy})(CO)_3(CH_3CN)]^+$ in an electron-transfer catalyzed process. This reaction occurs at potentials almost 0.5 V more positive than the catalytic operating potential for **1**, which implies that CO elimination and regeneration of the active catalyst is facile and not rate-limiting in electrocatalytic CO_2 reduction.[36]

Mn-bpy compounds have important mechanistic differences from their Re-bpy counterparts. Detailed mechanistic studies of Mn(*t*Bu-bpy)$(CO)_3$Br revealed that one-electron metal-based reduction is followed by immediate loss of bromide to give a five-coordinate Mn-based radical.[80] DFT calculations indicate that the Mn-based radical is more stable than the six-coordinate MeCN-coordinated complex, contrary to the Re-bpy analogue.[33] The dimer [Mn(*t*Bu-bpy)$(CO)_3]_2$ is rapidly formed, at a rate 10^9 times faster than the analogous Re–Re dimer.[33,81,82] The doubly reduced anionic species $[Mn(R\text{-bpy})(CO)_3]^-$ is formed after reductive cleavage of the dimer, and this is the chemical process that ensues the second reduction observed by cyclic voltammetry.[35,81,83] A CO_2 molecule is then added to the nucleophilic metal center of the anionic species, and subsequent protonation of the bound CO_2 ligand leads to a hydroxycarbonyl $[Mn(R\text{-bpy})(CO)_3(C(O)OH]^0$ complex. The mechanism can proceed *via* two different pathways: reduction-first or protonation-first (Scheme 1.6). In the reduction-first pathway, the hydroxycarbonyl complex is reduced to give $[Mn(bpy\text{-}R)(CO)_3(C(O)OH]^-$, which undergoes C–OH bond cleavage initiated by protonation of the OH to form water and CO. In the protonation-first pathway, the hydroxycarbonyl complex is protonated, leading to C–OH bond cleavage and formation of water and the tetracarbonyl cationic complex $[Mn(bpy\text{-}R)(CO)_4]^+$. The tetracarbonyl complex generates CO upon further reduction. There was a considerable discourse about whether the Mn–Mn dimer or the anionic species is the active species for CO_2 reduction. While the $Mn^0 - Mn^0$ dimer has been shown to be catalytically active, photochemically and electrochemically reducing CO_2 to formic acid or CO,[33,81,82] the rates for these catalytic reactions are much slower than the electrocatalytic reduction of CO_2 to CO by the anionic $[Mn(R\text{-bpy})(CO)_3]^-$ species.[33,82] Furthermore, the experimental catalytic reaction order is first-order in catalyst, suggesting the catalytic intermediate should be mononuclear, *i.e.* not dimers.[33,84,85]

Electrocatalytic reduction of CO_2 to CO and water necessarily means a proton source must be present in the reaction medium, according to eqn (1.1). While select catalysts are capable of the reduction and disproportionation of CO_2 to CO and CO_3^{2-} under aprotic conditions (eqn (1.2)), the vast majority of CO_2 electrocatalysts require a Brønsted acid such as water, phenol, or TFE in order to drive the catalytic cycle to generate CO and water. In the absence of added

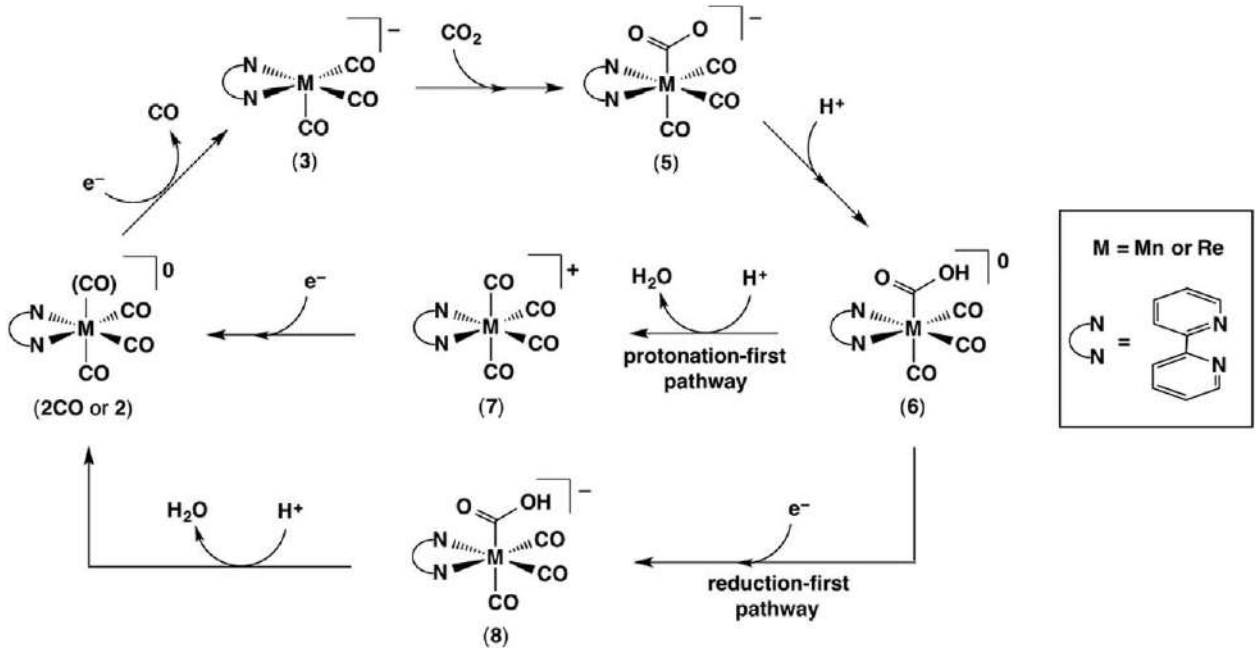

Scheme 1.6 Proposed catalytic reaction mechanism of CO_2 reduction by $Mn(bpy)(CO)_3Br$ and $Re(bpy)(CO)_3Br$ catalysts. Reproduced from ref. 33 with permission from American Chemical Society, Copyright 2014.

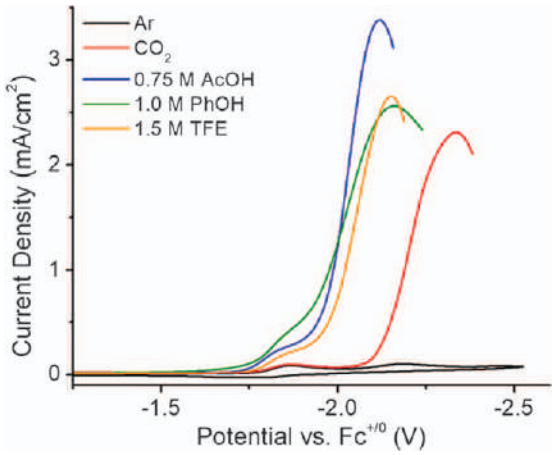

Figure 1.9 Linear sweep voltammograms of [Re(*t*Bu-bpy)(CO)$_3$Cl] (**2**) under Ar (black) or CO_2 (red), and under CO_2 in the presence of different Brønsted acids: acetic acid (blue), phenol (green), and TFE (orange). The return sweep is omitted.
Adapted from ref. 86 with permission from American Chemical Society, Copyright 2018.

acid, some catalysts are still active for CO_2 reduction according to eqn (1.1) and must therefore scavenge protons from the bulk solution.[8,86] Tetraalkylammonium electrolyte salts, MeCN (solvent), and/or trace water have been proposed as possible proton sources in these cases, however, the actual proton source when none is deliberately added remains poorly investigated.

$$CO_2 + 2H^+ + 2e^- \rightarrow CO + H_2O \quad (1.1)$$

$$2CO_2 + 2e^- \rightarrow CO + {CO_3}^{2-} \quad (1.2)$$

The selectivity and activity of CO_2 reduction typically depend on the strength of the acid source. For example, while Re tricarbonyl catalysts such as [Re(*t*Bu-bpy)(CO)$_3$Cl] (**2**) are capable of CO_2 reduction to CO in the absence of added proton source, it has been well established that weak Brønsted acids such as water increase the rate of catalysis due to more facile formation of the Re-COOH intermediate, the most stable species in the catalytic cycle.[76,86,87] CO_2 reduction is observed with quantitative FE_{CO} with no H_2 production upon addition of phenol or TFE ($pK_a = 29.1$ and 35.4 in MeCN, respectively). The rate of CO_2 reduction is comparable to that in the absence of added proton source, but the catalytic potential is shifted positive by nearly 0.2 V. In the presence of acetic acid ($pK_a = 23.5$ in MeCN[88,89]), the selectivity decreased to $FE_{CO} = 35\%$ with increased H_2 evolution (35%). As shown in Figure 1.9, a larger maximal current enhancement is observed for **2** with acetic acid compared to the weaker Brønsted acids; likely due to the additional contributions of competitive H_2 evolution to the current. Thus, it is critical to strike a balance between a Brønsted acid that is sufficiently

acidic to rapidly generate stable hydroxycarbonyl species, but not too strong as to increase the favorability of H_2 evolution.

The acid pK_a dependence on selectivity can also vary with the electronic structure of the ligands: increasing the donating ability of the ligands leads to a more basic metal center, which will be more susceptible to protonation by weaker Brønsted acids. This trend is exemplified by comparing the reactivity of **2** to that of a related Re complex bearing a bidentate pyridyl-N-heterocyclic carbene ligand.[90] This carbene complex is active for electrocatalytic CO_2 reduction to CO at high $FE_{CO} > 90\%$ with water present, similar to the behavior of **2**. However, FE_{CO} with the carbene catalysts drops to 43% and 21% for TFE and phenol, respectively, and a significant amount of H_2 was also generated with phenol. CO selectivity remained high for [Re(*t*Bu-bpy)$(CO)_3$Cl] under the same conditions with TFE and phenol.[86] The difference in CO selectivity is attributed to the increased donating ability of the carbene ligand compared to bipyridine and highlights the importance of optimizing the relative pK_as of the chosen acid and the reduced form of the electrocatalyst.

Decreased selectivity for CO_2 reduction has been observed for the Fe porphyrin catalyst FeTPP (**3**) with increasingly stronger acids. Increased H_2 evolution is observed for FeTPP when using stronger Brønsted acids such as triethylammonium which is well established.[91] The Mn-bpy catalysts required the addition of weak Brønsted acids in order to achieve CO_2 reduction to CO, and also shows an increase in current density with increasing acid strength, but no selectivity change.[82] Additionally, it was found that [Mn(*t*Bu-bpy)$(CO)_3$(MeCN)] (**13**) is more active than the Re version when using water as the proton source, but is less active when using methanol or TFE.

One aspect of proton source selection that is rarely considered is the resulting conjugate base generated upon deprotonation of the Brønsted acid. For the weak O-H acids typically used for electrocatalytic CO_2 reduction, the conjugate bases are alkoxide species, themselves capable of reacting with CO_2 to form alkyl carbonates. The trifluoroethoxide (generated from deprotonation of TFE) was proposed by Gray and co-workers to assist $[Mn(t\text{Bu-bpy})(CO)_3]^-$ in electrocatalytic CO_2 reduction by providing an additional driving force for protonation of the $[Mn\text{-}CO_2]^-$ intermediate and facilitating the dehydroxylation of the hydroxycarbonyl intermediate. DFT calculations suggest that this activity is due to the homoconjugation (trifluoroethoxide H-bonding dimer) and/or carboxylation of the conjugate base of this dimer.[92] While the formation of these alkoxide species from weak Brønsted acids may be unavoidable, the consequences of their presence in solution and their effects on the reaction thermodynamics must be considered. This is especially important in discussions of overpotential, as the thermodynamics of CO_2 reduction coupled to alkyl carbonate formation is clearly different than for an aqueous system.

Many of the literature reports state that water was chosen as a very weak Brønsted acid source for CO_2 reduction, having a $pK_a(H_2O) \approx 38\text{-}40$ in MeCN. However, upon saturation of the reaction solution with CO_2, carbonic acid

will be formed to some degree according to eqn (1.3). Carbonic acid is relatively acidic in organic solvent ($pK_a = 7.37$ in DMF), and therefore will very likely be the strongest Brønsted acid present in solution. This should be considered when evaluating the thermodynamics of CO_2 reduction in mixed organic/aqueous systems, as described by Savéant and co-workers.[93]

$$CO_2 + H_2O \rightleftharpoons H_2CO_3 \tag{1.3}$$

Fe and Ru catalysts containing the redox- and proton-active cyclopentadienone ligand have been widely utilized for hydrogenation of various organic substrates, including CO_2. The tricarbonyl Fe complex, tricarbonyl(η^4-2,5-bistrimethylsilylcyclopentadienone)iron (**14**), originally reported by Knölker,[94] exhibited an irreversible reduction at −1.4 V *vs.* NHE (*ca.* −2.0 V *vs.* $Fc^{+/0}$) followed by a smaller reversible feature at −1.5 V *vs.* NHE in MeCN under Ar.[95] The introduction of CO_2 resulted in a dramatic current enhancement at lower potentials in the absence of added Brønsted or Lewis acid sources (Figure 1.10). By CPE, CO is selectively produced ($FE_{CO} = 96\%$) with no H_2 evolution. Under these conditions, the overpotential for CO_2 reduction to CO is 0.85 V.

Water was produced during CPE in roughly equimolar quantities to CO. The formation of water suggests that catalysis does not proceed *via* CO_2 reduction and disproportionation, as is often observed in the absence of added acid. In order to generate water with no added Brønsted acid, the catalyst must scavenge protons from the solvent, residual water, or supporting electrolyte. However, as the catalyst turns over, more water will be generated which will be a better proton source for CO_2 reduction. The reaction will thus become catalytic in water and a continual increase in water production is not expected.

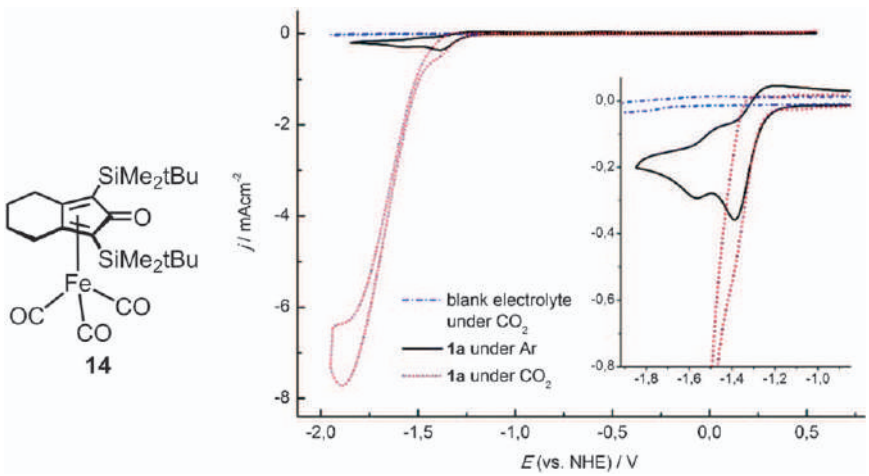

Figure 1.10 Cyclic voltammograms of tricarbonyl(η^4-2,5-bistrimethylsilylcyclopentadienone)iron (**14**) in MeCN under Ar (black) or CO_2 (red dashed). Adapted from ref. 95 with permission from the Royal Society of Chemistry.

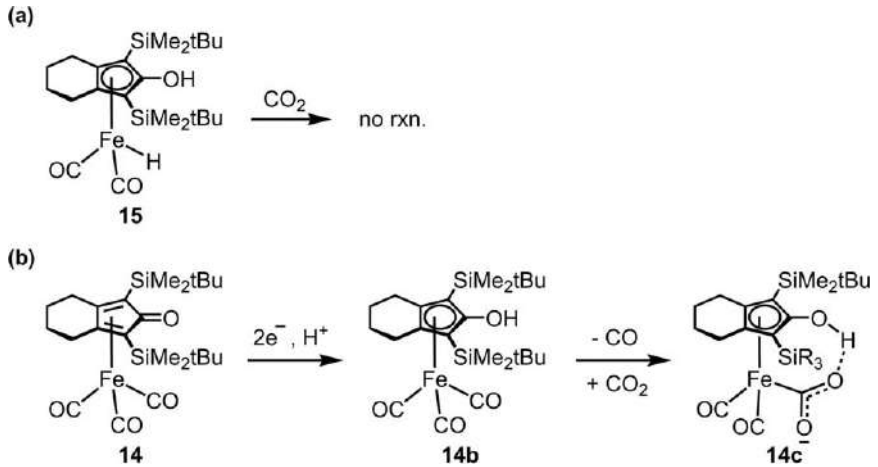

Scheme 1.7 Reaction pathways of CO_2 with tricarbonyl(η^4-2,5-bistrimethylsilylcyclopentadienone)iron. (a) No reaction is observed between Fe-hydride **15** and CO_2. (b) Proposed initial steps for CO_2 activation with **14**.[95]

Further studies into the proton source during catalysis may be warranted. An additional avenue of exploration is the influence of weak Brønsted acids on the rate and selectivity of CO_2 reduction which were not reported. The important role of the added proton source on CO_2 reduction with [Re(R-bpy)(CO)$_3$X] catalysts is discussed elsewhere in this section.[86]

The hydride complex of tricarbonyl(η^4-2,5-bistrimethylsilylcyclopentadienone)iron (**15**) is a key intermediate in the catalytic hydrogenation of other substrates. Surprisingly, exposure of **15** to CO_2 does not result in any reaction (Scheme 1.7a), indicating that this species is not involved in electrocatalytic CO_2 reduction. DFT calculations predict that CO_2 reduction proceeds *via* two-electron-one-proton reduction of **14** to the hydroxycyclopentadienyl complex (**14b**), from which loss of a CO ligand occurs readily followed by association of CO_2 (Scheme 1.7b). The Fe-CO_2 adduct of tricarbonyl(η^4-2,5-bistrimethylsilylcyclopentadienone)iron (**14c**) is stabilized by hydrogen bonding between the carboxylate and hydroxyl group. Similar behavior was noted for FeTPP catalysts bearing O–H groups on the ligand.[93] This hydrogen bond also facilitates cleavage of the carboxylate C–O bond and lowers the barrier for water loss. Thus, the ability to reduce the cyclopentadienone ligand and the optimal positioning of the resulting hydroxyl group are both critical for the electrocatalytic activity of **14**.

Electrocatalytic reduction of CO_2 has been extensively explored over the past three decades with Ru(II) complexes bearing polypyridyl ligands. Since reduction of Ru(II) is generally inaccessible at potentials relevant to CO_2 reduction, the polypyridyl ligands play a critical role in catalysis by storing reducing equivalents. In a seminal report, Tanaka and co-workers[96] showed that $[Ru(bpy)_2(CO)_2]^{2+}$ (**16**) is an active electrocatalyst for CO_2 reduction. In 1 : 1 DMF : H_2O, CO_2 reduction is observed at -1.40 V *vs.* SCE (*ca.* -1.78 V *vs.* $Fc^{+/0}$),

producing CO and formate with only trace H_2. Notably, a Brønsted acid such as water is required for catalysis, and the solution pH dictates the major product. Following two-electron reduction of **16** and loss of one CO ligand, a $[Ru(bpy)_2(CO_2^-)]^+$ adduct is generated under CO_2 that either favors CO or formate production under acidic or basic conditions, respectively.

A closely related catalyst $[Ru(tpy)(bpy)(CO)]^{2+}$ (**17**) was later reported by Tanaka and co-workers to also perform electrocatalytic CO_2 reduction.[97] In 20% DMF/H_2O, CO and formate are both produced *via* CPE at −1.6 V *vs.* Ag/Ag^+ (*ca.* −1.73 V *vs.* $Fc^{+/0}$), along with trace methanol. Varying the solvent and temperature has a significant effect on the products, demonstrating the importance of solvent effects. In 80% EtOH/H_2O at −20 °C, a range of products were detected including formaldehyde, glyoxylic acid, glycolic acid, and methanol.[97]

1.5 Pendent Proton Shuttles

Considering the importance of the proton source for electrocatalytic CO_2 reduction, it is not surprising that significant efforts have been undertaken to incorporate pendent acid or base groups as proton shuttles into known molecular catalysts. Enzyme active sites are highly optimized to shuttle multiple protons and electrons to and from the substrate as well as shuttle the product away from the active site; hence, many bio-inspired molecular catalysts have been developed with pendent proton shuttles to mimic enzymatic behavior and enhance catalytic performance.[98] This has been especially well utilized for H_2 evolution catalysts but is also becoming more commonly integrated into CO_2 reduction catalysts.

A particularly successful example of using pendent acid groups to improve CO_2 reduction was reported by Savéant and co-workers.[93,99] As discussed in Section 1.4, the addition of weak Brønsted acids such as phenol to the reaction solution enhances the rate of CO_2 reduction by Fe porphyrin catalysts including FeTPP (**3**).[40,73] The installation of phenol substituents at each *ortho* position on the phenyl rings in iron 5,10,15,20-tetrakis(2′,6′-dihydroxylphenyl)porphyrin (FeTDHPP) (**18**) resulted in an extremely fast rate of CO_2 reduction in DMF with 2 M water, TOF = 1.6×10^6 s^{-1} (Figure 1.11).[93] This rate is equivalent to the activity expected for the binary catalyst system (*i.e.* **3** and phenol) at a phenol concentration of 150 M.[93] Notably, it is not physically possible to run this reaction at this phenol concentration. Later studies revealed that this rate enhancement is not only due to the high local proton concentration near the reacting center but also due to stabilization of the $[Fe\text{-}CO_2]^{2-}$ intermediate by intramolecular hydrogen bonding between the carboxylate and the pendent O–H groups (Figure 1.11).[99,100]

Since this report, the activities of other CO_2 reduction catalysts have been enhanced in a similar fashion. Marinescu and co-workers investigated Co aminopyridine macrocycles for electrocatalytic CO_2 reduction.[101,102] Complexes containing alkyl substitutions on the pendent amine groups were compared to cobalt(II) 2,4,6,8-tetraaza-1,3,5,7(2,6)-tetrapyridinacyclooctaphane

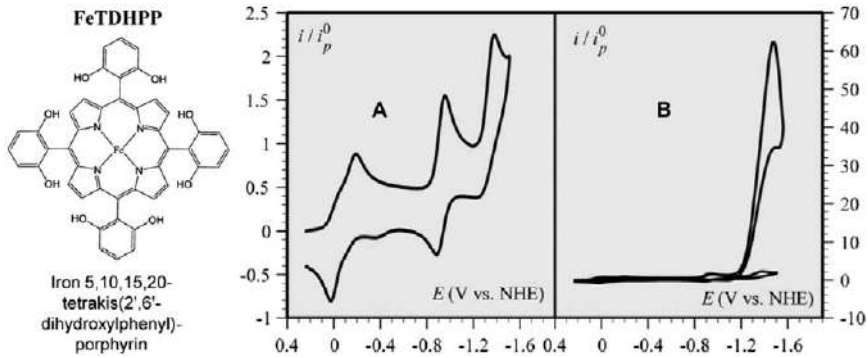

Figure 1.11 Cyclic voltammograms of 0.1 mM FeTDHPP (**18**) in 0.1 M Bu_4NPF_6/DMF with 2 M H_2O under (A) an inert atmosphere and (B) CO_2. *Y*-axis is the measured current normalized against the peak current for the $Fe(I)^-/Fe(0)^{2-}$ redox couple.
Adapted from ref. 93 with permission from AAAS, Copyright 2012.

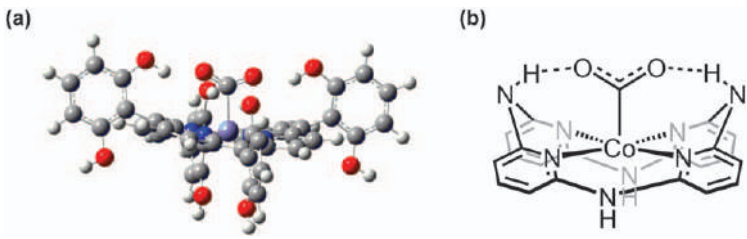

Figure 1.12 Structure of the (a) DFT-calculated [Fe-CO_2] adduct for FeTDHPP (**18**),[99] and (b) proposed [Co-CO_2] adduct of cobalt(II) 2,4,6,8-tetraaza-1,3,5,7(2,6)-tetrapyridinacyclooctaphane (**19**).[101]
Adapted from ref. 99 and ref. 101 with permission from American Chemical Society, Copyright 2014 and 2016.

19 (Figure 1.12). The TON for **19** was 300 times higher than that for the methyl or allyl substituted analogous Co macrocycles. Furthermore, **19** was highly selective for CO ($FE_{CO} = 98\%$), and the presence of the N–H moieties positively shifted the reduction potential. In a computational study of Co porphyrin, Koper and co-workers[103] found that the mechanism of the formation of the neutral hydroxycarbonyl adduct [Co–CO_2H] changes from concerted proton-coupled electron transfer (CPET) to mixed CPET and sequential proton-electron transfer (SPET) around pH 3.5, the pK_a of this intermediate. This transition mirrors the observed increase in CO production upon increasing the pH from $1-3$, indicating the importance of accessing the $[Co\text{-}CO_2]^-$ adduct *via* an SPET pathway in order to favor CO_2 reduction over proton reduction. For [Mn(R-bpy)$(CO)_3$Br]-type complexes, the introduction of a phenol substituent in close proximity to the metal center provided a local Brønsted acid source for enhanced proton transfer to the $[Mn\text{-}CO_2]^-$ adduct intermediate, which

enabled electrocatalytic CO_2 reduction to CO to proceed even in anhydrous MeCN.[104,105] Analogous complexes without the pendent acid group showed no catalytic response by cyclic voltammetry under identical aprotic conditions. Furthermore, a seven-fold increase in the rate of CO_2 reduction was observed upon addition of water as a proton source, as compared to the activity of the parent complex.[106] A series of detailed investigations into hydrogen bonding interactions for [Re(R-bpy)$(CO)_3$X] catalysts containing 4,4′-substituted bipyridine ligands with methylacetamidomethyl (dacbpy)[107] or tyrosine groups (Tyrdac-*t*Bu) have also been reported.[108,109] It was found that dacbpy promotes the formation of a hydrogen-bonded dimer, enabling access to an alternate bimolecular mechanism for CO_2 reduction (see Section 1.8).[107] The phenol group of Tyrdac-*t*Bu similarly participates in the structural assembly of a bimetallic active species, and can additionally function as a local proton source for catalysis.[108,109]

While the rather weakly acidic phenol group seems to be the pendent acid of choice for early transition metal catalysts that primarily produce CO, a stronger protic substituent is required for later transition metal complexes that produce formate. The prototypical example is the bidentate phosphine P_2N_2 ligands containing pendent amine groups, which have already been widely exploited as ligands for H_2 evolution catalysts.[11] Hydride complexes of $[M(P_2N_2)_2]^{2+}$ systems, where M = Group 10 transition metals, are generally not sufficiently hydridic to react with CO_2.[110,111] Artero and co-workers recently demonstrated that a series of complexes $[CpCo(P^R{}_2N^{R'}{}_2)I]^+$ (**20**) are active electrocatalysts for CO_2 reduction to formate.[59] These complexes undergo two sequential one-electron reductions to Co(I) near −0.9 and −1.2 V *vs.* $Fc^{+/0}$ in DMF under Ar. A large current enhancement is observed around −2 V *vs.* $Fc^{+/0}$, upon addition of CO_2 and various concentrations of water, which is significantly more negative than the Co(II)/Co(I) couple. While all three complexes were active catalysts, an impressive maximum TOF was calculated for the fastest system $[CpCo(P^{Cy}{}_2N^{Bn}{}_2)I]^+$, where TOF > 1000 s^{-1}. CPE studies confirmed that formate is produced with excellent FE (up to 98%) at −2.05 to −2.25 V *vs.* $Fc^{+/0}$, corresponding to an overpotential of approximately 0.4 − 0.6 V. Notably, the related complex [CpCo(dppp)I]I (dppp = diphenylphosphinopropane) exhibited a very small current increase under identical conditions. The proposed catalytic mechanism involves a net three-electron-one-proton reduction of the Co(III) starting complex to generate a Co(II)-hydride intermediate, which is a strong hydride donor and is thermodynamically capable of hydride transfer to CO_2 (Scheme 1.8). Although some questions regarding the exact details of the mechanism remain unanswered at this stage, it is evident that the pendent amine plays a crucial role, not only as a proton shuttle but also to stabilize the hydride transfer intermediates. However, we note that the pendent amine group as well as the identity of the amine substituent both have a significant influence on the electronic properties of the catalyst, which makes it difficult to independently parse out the influence of the protic functionality of the amine group on catalysis.

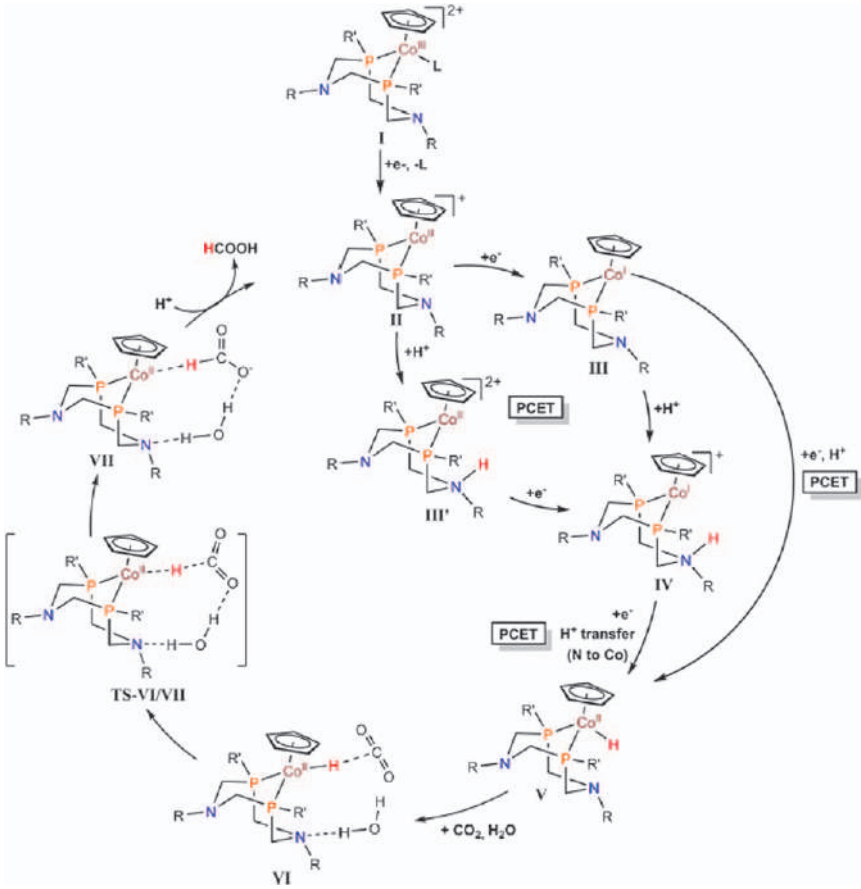

Scheme 1.8 Proposed mechanism for electrocatalytic CO_2 reduction by $[CpCo(P^R{}_2N^{R'}{}_2)I]^+$ (**20**).
Reproduced from ref. 59 with permission from American Chemical Society, Copyright 2017.

A tetradentate Co complex with an N-H group directly bound to the Co center was examined for CO_2 reduction by the Peters' group.[112] In MeCN with water as a proton source, CO_2 reduction to CO was observed at -1.88 V *vs.* $Fc^{+/0}$ with an FE of 45%. Simultaneously, H_2 evolution (30%) was observed under these conditions. The CO_2 adduct is stabilized through hydrogen bonding to one of the protons of a coordinated amine, significantly lowering the energy of the transition state.[113] The identity of the metal was shown to affect selectivity with a similar pentadentate macrocylic ligand. When Co(II) was used in electrochemical CO_2 reduction, CO production dominated, but when Fe(II) was used, formic acid selectivity was observed at low overpotentials. It is unclear if the N-H group's interaction with the metal plays a role in this selectivity difference and further mechanistic studies are required.[114]

Inspired by Savéant, the Nocera and Chang groups have recently examined so-called Fe hangman porphyrins.[115–117] Fe hangman porphyrins containing phenol, guanidine, and sulfonic acid groups electrocatalytically reduced CO_2 to CO between -2.1 and -2.2 V *vs.* $Fc^{+/0}$ with $FE_{CO} > 93\%$. DFT calculations suggest that the CO_2 adduct is stabilized by the intramolecular binding with the pendent group. In this series of results, the complex with the strongest CO_2 interaction (*i.e.* phenol hangman) exhibited the highest apparent rate constant for CO_2 reduction. Notably, phenol was the only Brønsted acid source used in this study. The effect of varying acid strength with the different pendent groups may be worth exploring. The proximity of the proton shuttle to the metal center was examined by the Chang group. The activity of FeTPP catalysts with an amide at different positions was compared.[116] The *ortho*-amide pendent groups both significantly enhanced the rate of catalysis, with the distally placed amide exhibiting greater enhancement (Figure 1.13).

The nature of the pendent acid must be carefully selected for the particular catalyst system of interest. If the pK_a of the pendent group and the metal center are not appropriately matched, the activity and/or selectivity for CO_2 reduction over H_2 evolution can decrease substantially.[110] This consideration is especially important for catalysts that produce formate since a metal hydride species is typically the branching point between CO_2 reduction to formate *versus* H^+ reduction to H_2.[111] The stability of pendent groups should also be considered. Fujita and co-workers attempted to use redox-active phenol ligands and observed a tendency to deprotonate upon reduction and react with CO_2.[118,119] Das and co-workers used the redox activity of a pendent carboxylate to their advantage. The labile pendent carboxylate acts to stabilize the metal center, provides a local proton source, and provides a binding site for CO_2.[120]

There are other consequential factors to consider when pendent proton shuttles are installed close to the catalytic site. These substituents can significantly alter the electronic properties of the ligand and can exert significant electronic and Coulombic influence on the metal center. Thus, the presence of these groups can dramatically change the catalyst activity due to these other second coordination sphere effects, either in addition to or instead of their protic functionality. Therefore, control experiments with complexes bearing inactive substituents having similar electronic and steric properties are highly advised in order to confirm that no other competing effects from the second coordination sphere functional groups are operative. For example, addition of a carboxylic acid group to the cyclam ligand in $[Ni(cyclam)]^{2+}$ (**9**) resulted in an increased reaction rate and improved selectivity for aqueous CO_2 reduction at low pH (2–5).[121] The authors propose that these improvements may be due to the availability of a local proton source; however, electronic effects from the electron-withdrawing carboxylic acid were not specifically ruled out with control experiments.

The pendent group may also have other functions, such as facilitation of CO dissociation.[80] Compain and co-workers synthesized dicarbonyl and tricarbonyl Mn-terpyridine (tpy) complexes and examined their CO-releasing properties. The tpy ligand exhibits bidentate binding in the tricarbonyl Mn

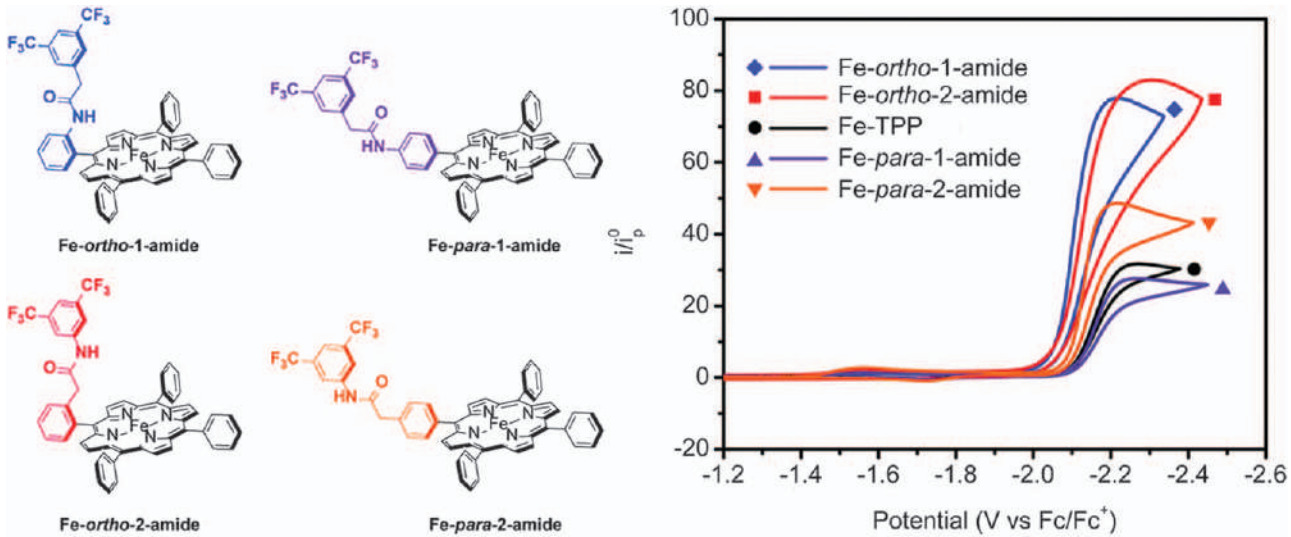

Figure 1.13 Structures of amide-modified FeTPP catalysts (left) and cyclic voltammograms (right) of amide-functionalized porphyrins and unfunctionalized FeTPP with 100 mM phenol in 0.1 M Bu_4NPF_6/DMF, saturated with CO_2.
Adapted from ref. 116 with permission from the Royal Society of Chemistry.

complex and switches to tridentate upon externally triggered CO-release to generate the dicarbonyl Mn complex. It has also been shown that the tridentate tpy coordinated dicarbonyl Mn complex was active for CO_2 reduction but degrades faster than the Mn-bpy catalysts.[122] A bipyridine with a pendent NAD-like structure (Nicotinamide adenine dinucleotide) was proposed to facilitate hydride transfer to metal-bound CO_2 to explain the observed enhanced selectivity for formate.[123] The pendent groups function as more than proton shuttles in each of these cases and further studies should critically analyze the chemical behavior of these systems. A pendent thiourea group in the second coordination sphere of the Re-bpy catalyst acts as a hydrogen bond promoter and proton donor.[124] DFT calculations indicated an N–H bond of the thiourea group stabilizes the Re–carboxylate and acts as a proton source to form the hydroxycarbonyl species. Pendent groups act as more than local proton sources and their influence on the CO_2 reduction reaction mechanism should be evaluated holistically.

1.6 Through Space Effects

A very different trend is observed using charged substituents to effect through-space Coulombic interactions, as demonstrated by Savéant and coworkers.[125] The incorporation of trimethylammonium groups at the *para* positions in iron tetraphenylporphyrin (**21**) shifted the reduction potentials in a more positive direction, decreasing the overpotential from 0.6 V for FeTPP (**3**) to 0.4 V (Figure 1.14). Most notably, however, the catalytic rate was not diminished compared to **3**. The reduced basicity of the Fe center in **21** is now counterbalanced by increased stabilization of the $[Fe\text{-}CO_2]^{2-}$ adduct through coulombic interactions between the positively-charged trimethylammonium groups and the negatively-charged oxygens of the carboxylate. This effect was even more pronounced in the *ortho* derivative (**22**): closer proximity of the charged substituents led to stronger coulombic attraction and greater stabilization of $[Fe\text{-}CO_2]^{2-}$ resulting in a nearly two-fold increase in rate and decrease in overpotential to 0.2 V (Figure 1.14). As expected, the opposite behavior was observed for the sulfonate-substituted version (**23**): the anionic substituents shifted the catalytic operating potential to a more negative value and decreased the rate of CO_2 reduction. This approach of using through-space coulombic effects to move beyond typical through-bond scaling relationships could be applied to other catalyst systems involving intermediates with a localized charge similar to the $[Fe\text{-}CO_2]^{2-}$ adduct.

The *para*-substituted catalyst **21** was originally developed as a water-soluble catalyst. Electrocatalytic CO_2 reduction to CO in neutral water (pH 6.7) was achieved using **21**, where the cationic trimethylammonium groups enable aqueous solubility.[127] Under these conditions, an extremely large maximum TOF of 10^7 s^{-1} was estimated, corresponding to a second-order rate constant of $k = 2.5 \times 10^8$ M^{-1} s^{-1}. Only trace amounts of H_2 were detected by CPE at -0.97 V *vs.* NHE, indicating a significant preference of CO_2 reduction over H_2 evolution. One explanation is that the $[Fe\text{-}CO_2]^{2-}$

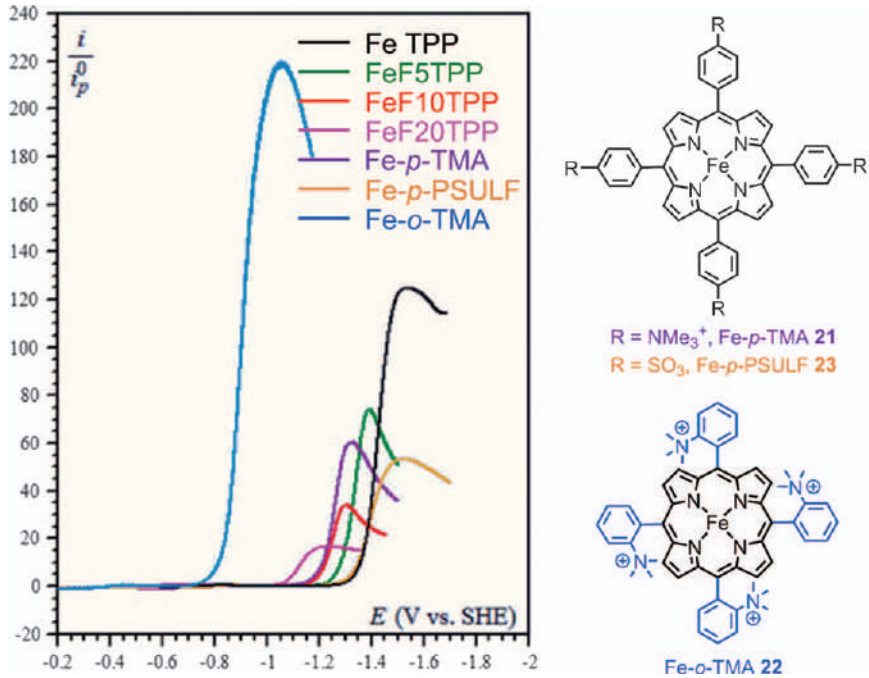

Figure 1.14 Linear scan voltammograms of Fe porphyrin catalysts (1 mM) under CO_2 in DMF with 0.1 M H_2O and 3 M phenol.
Adapted from ref. 126 with permission from American Chemical Society, Copyright 2016.

intermediate is stabilized *via* hydrogen bonding with water and *via* Coulombic attractions with the cationic trimethylammonium groups. Further mechanistic studies are required to confirm the origins of the impressive rate and selectivity of **21** for CO_2 reduction in water.

The mechanism of CO_2 reduction with $[Ni(cyclam)]^{2+}$ (**9**) was initially proposed by Sauvage and co-workers (Scheme 1.9).[60] DFT calculations on the homogeneous activity of **9** by Ye and co-workers[128] further supported this proposal: following reduction to Ni(I), generation of a Ni-η^1-CO_2 carboxylate adduct that leads to CO formation is energetically favored by 14 kcal mol^{-1} over the Ni-η^1-OCO complex, which leads to formate production. Thus, this initial binding event determines the observed product selectivity. Further reduction of $[Ni(III)\text{-}CO_2]^+$ to the Ni-hydroxycarbonyl likely occurs *via* a PCET pathway, followed by C–O cleavage and loss of CO.

The rate of CO_2 reduction with $[Ni(cyclam)]^{2+}$ does not exhibit a linear increase with catalyst concentration and catalysis occurs approximately 0.3 V more positive than the reversible Ni(II/I) couple, both suggesting the involvement of adsorbed species.[60] Anson and co-workers later showed that **9** is only weakly adsorbed at potentials relevant to catalysis, but the one-electron reduced species $[Ni(cyclam)]^+$ is strongly adsorbed and plays a

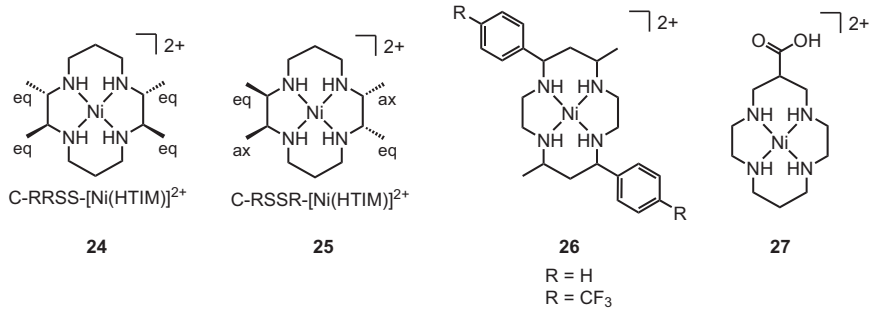

Scheme 1.9 Proposed mechanism for the electrocatalytic reduction of CO_2 to CO by $[Ni(cyclam)]^{2+}$ (**9**).[60,128]

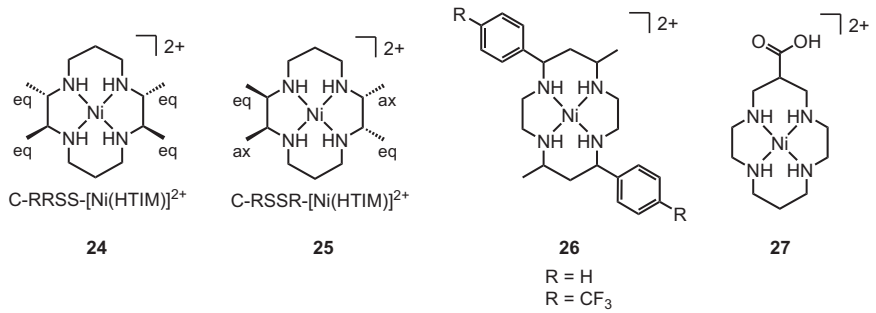

Figure 1.15 Structures of modified Ni cyclam catalysts.

crucial role in CO_2 reduction.[129] Computational studies support the role of the Hg as a promoter by maintaining noncovalent dispersive interactions with the cyclam N-H groups.[130] These interactions favor flattening of the cyclam ring and destabilize the Ni(I)–CO form of the catalyst, enabling CO release and suppressing catalyst degradation to Ni(0) carbonyl species. Further investigations by Fujita and co-workers highlighted the important role of the cyclam conformation. For example, C-*RRSS*-$[Ni(HTIM)]^{2+}$ (2,3,9,10-tetramethyl-1,4,8,11-tetraazacyclotetradecane) (**24**) is a better catalyst than **9** due to the nearly flat geometry of the ligand enforced by the methyl substituents, which enables closer approach of the catalyst to the Hg surface (Figure 1.15).[131] The C-*RSSR*-isomer **25**, on the other hand, exhibited significantly diminished catalytic activity due to the steric bulk of the axial methyl groups that prohibited close surface interactions.

While **9** is one of the best catalysts for CO_2 reduction at Hg electrodes, it is also active at GC and other electrode materials, albeit at much lower rates.[130,132,133] The Kubiak group[132] demonstrated that **9** is highly selective for CO ($FE_{CO} = 90\%$) with no H_2 evolution at GC at -1.30 V *vs.* NHE, but the TON (=4) and TOF (=90 s^{-1}) were both significantly lower than at Hg. DFT calculations predict that CO_2 binding to the metal is more favorable in the

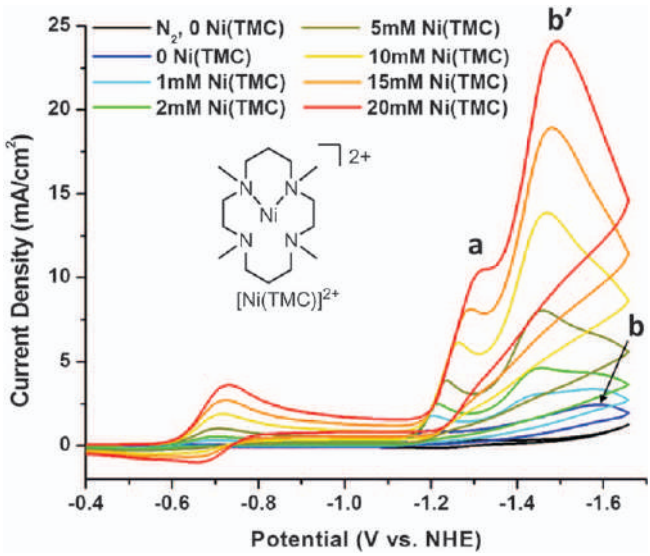

Figure 1.16 Cyclic voltammograms of $[Ni(cyclam)]^{2+}$ (**9**) (1 mM) under CO_2 with increasing concentrations of $[Ni(TMC)]^{2+}$ in 20% H_2O/MeCN. Adapted from ref. 133 with permission from American Chemical Society, Copyright 2015.

SSSS-isomer of the freely-diffusing catalyst, perhaps due to hydrogen bonding with the N–H groups. In the absence of surface interactions with Hg to stimulate the loss of CO, $[Ni(cyclam)(CO)]^{+}$ accumulates in solution and undergoes decomposition to $[Ni(CO)_4]$, limiting the catalyst lifetime at the GCE. The addition of $[Ni(TMC)]^{2+}$ (TMC = 1,4,8,11-tetramethyl-1,4,8,11-tetraazacyclotetradecane), which itself is not a CO_2 reduction catalyst at GC but has a strong affinity for CO after reduction to $[Ni(TMC)]^{+}$, dramatically increases the rate of CO_2 reduction with **9** by scavenging CO and inhibiting catalyst deactivation.[133] As shown in Figure 1.16, the catalytic current density is increased by nearly 40 times in the presence of 20 equivalents of $[Ni(TMC)]^{2+}$.

In the Mn-bpy class of electrocatalysts, Mn–Mn dimer formation negatively shifts the reduction potential of the second reduction, and different strategies have been adopted to avoid dimerization. Steric bulkiness is a proven way to avoid dimerization.[84,134,135] A bulky 6,6′-dimesityl-2,2′-bipyridine (mesbpy) ligand was used to make $Mn(mesbpy)(CO)_3Br$ (**28**) and $[Mn(mesbpy)(CO)_3(MeCN)](OTf)$ (**29**).[33] These Mn complexes exhibit a single, two-electron reduction wave under a nitrogen atmosphere with no dimerization (Figure 1.17). IR-SEC and chemical reductions with KC_8 further confirmed the formation of both the singly reduced and doubly reduced Mn complexes at the same potential, suggesting that elimination of dimerization lowers the second reduction potential. The active species $[Mn(mesbpy)(CO)_3]^{-}$ binds CO_2 at −1.6 V *vs* $Fc^{+/0}$, but catalysis does not

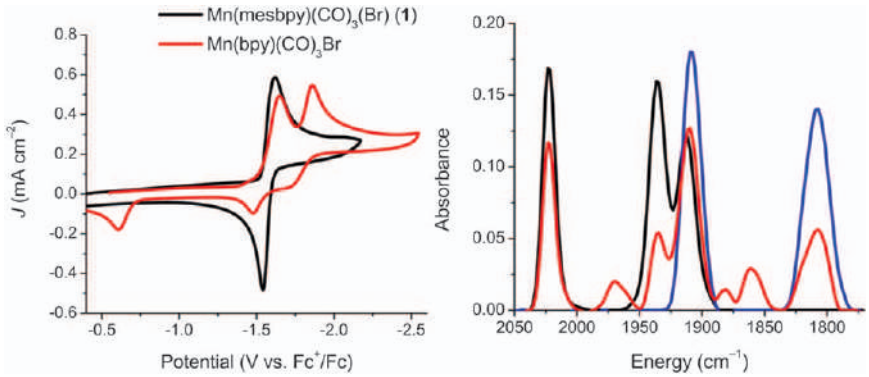

Figure 1.17 Comparison of cyclic voltammograms of Mn(mesbpy)-$(CO)_3$Br (**28**) and Mn(bpy)$(CO)_3$Br (**29**) under identical conditions and IR-SEC spectrum of Mn(mesbpy)-$(CO)_3$Br showing no dimerization upon first and second reduction. The resting species (black), at approximately −1.6 V *vs.* $Fc^{+/0}$ (red) singly reduced species and doubly reduced species are present. When the voltage of the cell is held at approximately −1.6 V for more than 1 min, all species are doubly reduced (blue). The reference electrode used was Ag/AgCl.
Adapted from ref. 84 with permission from American Chemical Society, Copyright 2014.

occur until more negative potentials are applied. IR-SEC experiments under CO_2/H^+ indicate that reduction of a Mn(I) − C(O)OH catalytic intermediate may determine the unusual ''over-reduction'' required to initiate catalysis. Moreover, replacing the axial bromide for a pseudohalogen (CN) in Mn(bpy)$(CO)_3$(CN) can also avoid dimerization.[136] IR-SEC and cyclic voltammetry indicate a disproportionation mechanism of two one-electron-reduced species, generating the catalytically active species.

Similar to the modifications to the Re catalyst, many nitrogen-containing aromatic ligands can be used to replace bipyridines. N-heterocyclic carbene (NHC) ligands are popular choices since they are versatile for different kinds of modifications.[136–138] However, their enhanced σ-donor character compared to bipyridines results in an increased HOMO–LUMO gap and hence a cathodic shift (more negative) of the one- and two-electron reduction potentials.[137] Replacing the Br^- ligand with NCS^- and CN^- in Mn-NHC compounds shows similar negative impacts on reduction potentials.[136] On the other hand, the increased π acidity of pyrimidine shifts the two-electron reduction to −1.77 V *vs* $Fc^{+/0}$, 70 mV more positive than that for the Mn-bpy catalyst.[138] Similar positive shifts can be achieved by extending the π network of imidazole ligands.[136] Extension of the bipyridine ligand to a phenylazopyridine positively shifts the reduction potential to −0.93 V *vs.* $Fc^{+/0}$.[139] Nonetheless, when bipyridines are replaced with other nitrogen-containing ligands, the catalytic performance is usually lower than the bulky Mn(mesbpy)$(CO)_3$Br catalysts, because these catalysts do not solve the problem of dimerization and may exhibit stability issues during catalysis.[80,122,135,140,141]

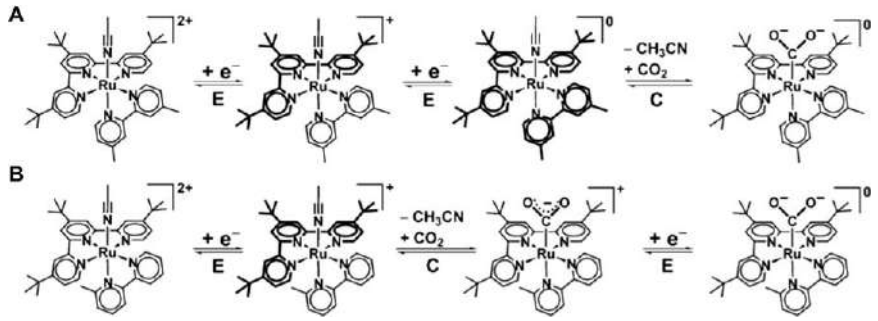

Scheme 1.10 Proposed reaction pathway for electrocatalytic CO_2 reduction by $[Ru(tpy)(bpy)X]^{n+}$ catalysts (A) **31** and (B) (**30**) highlighting the differences in the order of steps.
Reproduced from ref. 142 with permission from John Wiley and Sons, Copyright © 2016 Wiley-VCH Verlag GmbH & Co. KGaA, Weinheim.

The lability of the monodentate ligand in $[Ru(tpy)(bpy)X]^{n+}$ (**5**) can also be increased by altering the steric properties of bipyridine. Ott and co-workers[142] found that introducing an *ortho*-methyl on bipyridine significantly improves the rate of MeCN dissociation in (**30**) compared to the 4,4′-dimethyl version (**31**) (Scheme 1.10). The steric bulk of the methyl group causes bipyridine to tilt towards the MeCN ligand and promotes dissociation.[40] Both **30** and **31** are active for CO_2 reduction to CO below -2 V *vs.* $Fc^{+/0}$ by the typical ECE pathway. However, for **24**, catalysis is also observed at the first reduction potential (-1.82 V *vs.* $Fc^{+/0}$). The increased lability of MeCN enables substitution by CO_2 to occur after only one-electron reduction, forming $[Ru(tpy)(mbpy)(CO_2^{\bullet-})]^+$ to which the addition of the second electron is facile and generates the key $[Ru(II)\text{-}CO_2^{2-}]$ species (Scheme 1.10). While the TOF at the first potential is low (1.14 s^{-1}), the ability to access this ECE mechanism with **30** lowers the overpotential by 0.4 V without any loss in FE_{CO}.

1.7 Lewis Acid and Base Additives

The stability and reaction rates of Fe(III) tetraphenyl porphyrin FeTPP (**3**) are improved by the addition of Lewis acidic cations such as Mg^{2+} (Figure 1.18), with CO and formate produced in FE's of 60% and 30%, respectively.[39,40] Although the addition of Lewis acid cations dramatically improved the catalysis, carbonate is also formed, which precipitates as $MgCO_3$, and quickly passivates the electrode.

The mechanism of CO_2 reduction by Fe porphyrins has been studied in detail by Savéant and others and is shown in Scheme 1.11.[40] Following reductions of FeTPP (**3**), nucleophilic attack of CO_2 by $[FeTPP]^{2-}$ generates an $[Fe-CO_2]^{2-}$ adduct. This adduct can be stabilized by ion pairing between the carboxylate group and Mg^{2+}, which weakens the C–O bonds by "pulling" an electron pair out of CO_2 and facilitates formation of an [Fe(II)–CO]

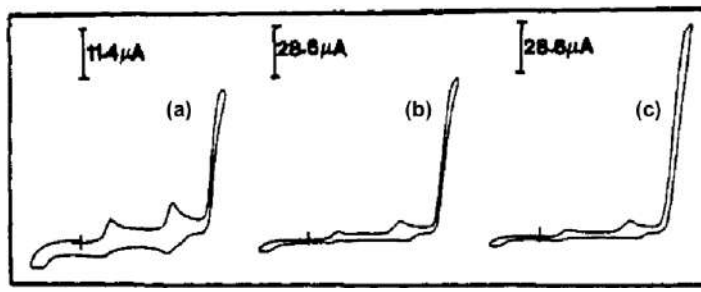

Figure 1.18 Cyclic voltammograms of FeTPP (**3**) in 0.1 M Et_4NClO_4/DMF under CO_2 with increasing amounts of Mg^{2+} (a < b < c, 3, 24, and 68 mM) showing the increase in catalytic current.
Reproduced from ref. 39 with permission from American Chemical Society, Copyright 1991.

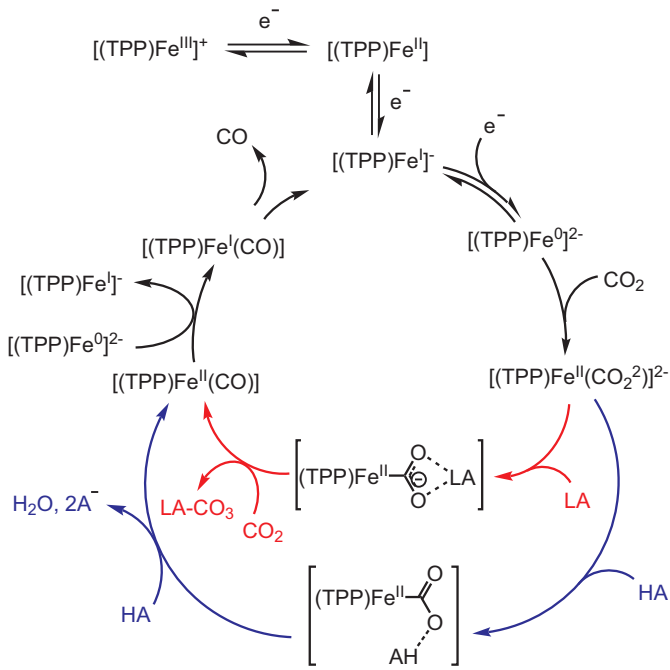

Scheme 1.11 Proposed mechanism of electrocatalytic CO_2 reduction to CO with FeTPP (**3**) in the presence of Lewis acidic cation (LA, red path) or weak Brønsted acid (HA, blue path).[40,91]

species. Alternatively, weak Brønsted acids can stabilize the carboxylate adduct *via* hydrogen bonding and similarly enable C–O cleavage. This behavior is termed as a two-electron ''push-pull'' mechanism, where an electron pair is pushed from the catalyst ($[FeTPP]^{2-}$) into the substrate (CO_2) and then pulled out of $[Fe-CO_2]^{-}$ with the help of an electrophile (Brønsted or Lewis

acid). The electronic structure of $[FeTPP]^{2-}$ remains under debate. A recent study by Neese and co-workers[143] suggested that $[FeTPP]^{2-}$ is an intermediate-spin Fe(II) center antiferromagnetically coupled to a porphyrin diradical dianion. Savéant and co-workers proposed an Fe(0) description due to its reactivity toward alkyl halides.[144] This question of non-innocent ligand contributions often arises in electrocatalysis. Highly reduced catalytic intermediates containing redox-active ligands such as $[FeTPP]^{2-}$ can have the charge distributed over both metal-based and ligand-based orbitals.

Despite this important advance being initially reported in 1991, it would be more than two decades later before the use of Lewis acids to promote CO_2 electroreduction with a different catalyst system was published. Inspired by this early publication, the authors' group examined the CO_2 reduction activity of $[Mn(mesbpy)(CO)_3(MeCN)]$ (**29**) in the presence of Lewis acids.[134] Generation of the [Mn(I)-COOH] hydroxycarbonyl species occurs at the two-electron reduction of **29**, under CO_2 with weak Brønsted acids such as TFE. The [Mn(I)-hydroxycarbonyl] species must be further reduced in order to access the "fast catalysis" regime (Figure 1.19).[134] However, an alternate mechanism for CO_2 reduction is likely operative in the "slow catalysis" regime. DFT calculations suggest that additional protonation of [Mn(I)-hydroxycarbonyl] leads to C–O bond cleavage, analogous to the Brønsted acid-assisted catalysis with FeTPP (**3**) (Scheme 1.11). Clearly this route with **29** is comparatively slow, and using stronger acids to increase the rate resulted in H_2 evolution.[145] It was shown that the Lewis acidic Mg^{2+} could be used in place of a Brønsted acid, triggering CO_2 reduction at a significantly lower overpotential (roughly $0.3 - 0.45$ V) with high selectivity for CO generation ($FE_{CO} = 96\%$).[134] However, similar to FeTPP (**3**) in the presence of Mg^{2+},[5] the stoichiometric use of Mg^{2+} and the formation of insoluble $MgCO_3$ that quickly blocks the electrode are major drawbacks of this

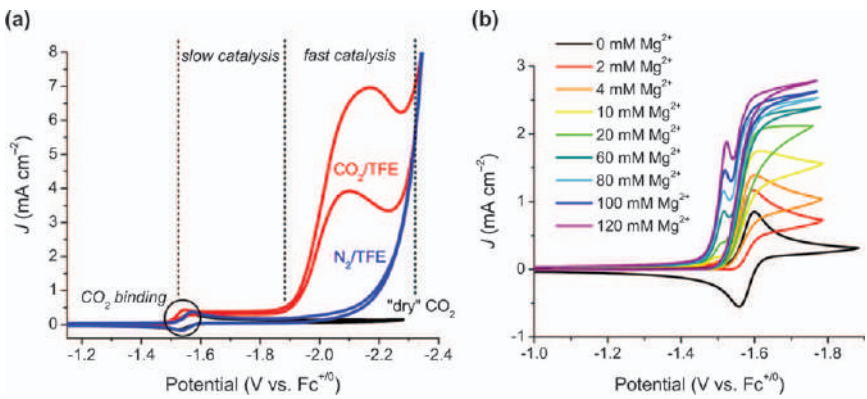

Figure 1.19 (a) Cyclic voltammograms of $[Mn(mesbpy)(CO)_3(MeCN)]^+$ (**29**) under CO_2 in 0.1 M Bu_4NPF_6/MeCN with TFE (1.3 M) and (b) (**29**) (1 mM) under CO_2 with the addition of Mg^{2+}.
Adapted from ref. 134 with permission from American Chemical Society, Copyright 2016.

approach. To overcome this issue, the Kubiak group later developed an improved catalytic system using $[Zn(cyclam)]^{2+}$ as a soluble Lewis acid cation in conjunction with **29**.[146] Here, the equatorial coordination of the ligand did not block the Lewis acid functionality of the Zn^{2+} center but the cyclam ligand prevents precipitation of Zn carbonate during catalysis. Thus, $[Zn(cyclam)]^{2+}$ could be used in co-catalytic amounts as opposed to a sacrificial additive like Mg^{2+}. The TOF for **29** in the presence of $[Zn(cyclam)]^{2+}$ (30 mM) was estimated to be 105 s^{-1}, five times greater than that observed in the presence of Mg^{2+} (120 mM, TOF = 20 s^{-1}) suggesting that $[Zn(cyclam)]^{2+}$ is indeed functioning as a co-catalyst. Importantly, high selectivity for CO was maintained with $[Zn(cyclam)]^{2+}$ ($FE_{CO} = 82\%$ at -1.6 V *vs.* $Fc^{+/0}$).

Several studies have appeared in recent years exploring the influence of ionic liquids as additives or as the reaction medium for CO_2 reduction with molecular catalysts. The addition of an ionic liquid, 1-butyl-3-methylimidazolium tetrafluoroborate ($BMImBF_4$), as an additive (0.3 M) to FeTPP (**3**) with trifluoroethanol (1 M) in DMF solution resulted in a lower overpotential (η) for electrocatalytic CO_2 reduction, $\eta = 0.67$ V compared to 0.82 V for **3** in the absence of the ionic liquid additive.[147] In this case, the positively charged ionic liquid interacts with negatively charged reduced porphyrin, acting as a co-catalyst in the CO_2 reduction to CO by FeTPP. These interactions lead to the positive shift in the reduction potential of Fe^{I} to Fe^{0} and an overall decreased overpotential leading to increased current densities. Notably, a four-fold increase in TOF was observed under these conditions, compared to the parent catalyst without an ionic liquid. Furthermore, the selectivity for CO production over H_2 evolution remained high ($FE_{CO} = 93\%$). Electrocatalytic reduction of CO_2 to CO by Re-bpy in the presence of the ionic liquid 1-ethyl-3-methylimidazolium tetracyanoborate ([emim][TCB]) was described by Grills and co-workers.[148] The [emim][TCB] was used as a solvent and an electrolyte and decreased the overpotential for CO_2 reduction to CO by 0.45 V, with much faster catalytic rates than in MeCN. The rapid dissociation of a chloride ligand occurred at the second electron-reduction potential of *fac*(Re-(bpy)$(CO)_3$Cl in the presence of $[emim]^+$ in comparison to neat MeCN. This resulted in a lower activation energy and an order of magnitude increased apparent catalytic rate constant for CO_2 reduction to CO. Notably, CO_2 is less soluble in [emim][TCB] than MeCN/H_2O (0.13 M atm^{-1} *vs.* 0.26 M atm^{-1}). Thermodynamic and mechanistic studies of CO_2 reduction by *fac*(Re-(bpy)$(CO)_3$Cl in the presence of imidazolium-based ionic liquids were reported by the same group.[149] The proposed mechanism was supported by DFT calculations, as depicted in Scheme 1.12. The imidazolium cation interacts with doubly reduced $[Re(bpy)(CO)_3]^-$, followed by protonation and CO_2 binding to the reduced metal center to form a metal–carboxylic acid that possesses more positive reduction potential of the species than in conventional electrolytes. Similarly, the effect of positively charged ammonium groups of a norbornenyl polymer with attached Re(bpy)$(CO)_3$Cl was demonstrated by Kubiak and Gianneschi.[150] The authors found that positively charged polymers with

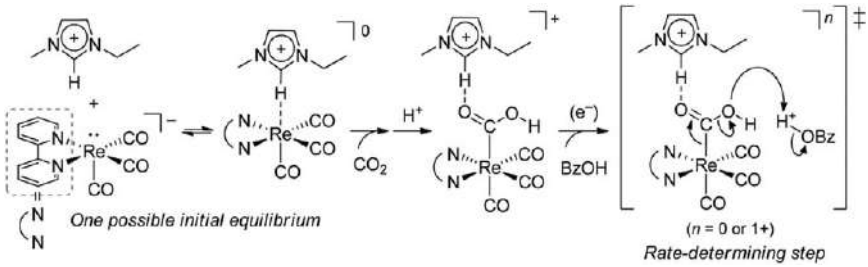

Scheme 1.12 Proposed reaction scheme for *fac*[Re-(bpy)$(CO)_3$Cl with $[emim]^+$. Reproduced from ref. 149 with permission from American Chemical Society, Copyright 2015.

quaternary ammonium salts exhibit a 300 mV more positive shift in comparison to the neutral polymers, while the negatively charged polymers displayed a negative shift in potential with no reactivity towards CO_2. This observation is analogous to FeTPP catalysts with charged NMe_3 groups.[125]

In a slightly different approach, Grubbs, Gray, and co-workers developed brush polymer ion gels for electrocatalytic CO_2 reduction to CO.[151] High selectivity for CO ($FE_{CO} = 90\%$) and a potential shift of 450 mV was observed in this case in comparison to the conventional organic solvents, which can also be attributed to the cation effect of a charged ionic liquid as described in a previous paper. Nippe and co-workers developed and studied pendent imidazolium Re-bpy catalysts.[152,153] The synthetic design for these catalysts was inspired by nature. The protonated imidazolium and amine groups of histidine and lysine residues of Ni, Fe-carbon monoxide dehydrogenases stabilize metal carboxylate and hydroxycarbonyl intermediates through hydrogen bonding interactions. The installation of an imidazolium functional group to the Mn-bpy catalyst sought to mimic the hydrogen bonding behavior of amino acid residues in enzymes. The Mn–Me($ImMe_x$)bpy catalysts reduce CO_2 at -1.5 V *vs.* $Fc^{+/0}$ with $FE_{CO} = 77\%$. This corresponds to reduction potentials that are 100 mV more positive than the Mn-mesbpy.[153] Electrochemical CO_2 reduction by similar imidazolium functionalized Re-bpy complexes also occurs at significantly more positive potentials (~200 mV) compared to the Re-bpy catalyst.[152]

1.8 Cooperativity in Multinuclear Metal Systems

Nature uses multinuclear ensembles to enable multi-electron transfer processes. In one example, the metalloenzyme carbon monoxide dehydrogenase (CODH) contains a key dinuclear Ni-Fe complex in the active site that cooperatively facilitates electrochemical CO_2 reduction to CO at a low overpotential ($\eta < 0.1$ V).[154] Thus, the bio-inspired incorporation of multiple reactive metal centers into a single molecular catalyst has attracted some attention in recent years in the context of electrocatalytic CO_2 reduction.

A series of co-facial Fe porphyrin dimers have been developed by Naruta and co-workers.[155,156] In their first report, two Fe triphenylporphyrin fragments were connected *via* an *ortho*- or *meta*-substituted benzene ring (**32** and **33** in Figure 1.20, respectively).[155] The *ortho* version **32** outperformed **33**, as well as the mononuclear catalyst FeTPP (**3**), displaying high FE_{CO} (=95%) and an impressive turnover frequency (TOF = 4300 s^{-1}) at a moderate overpotential ($\eta = 0.66$ V) in 10% H_2O/DMF. For the related Mn–Mn analogue, the two metals are held apart by a distance of approximately 3.7–6.2 Å.[157–159] The authors propose that a similar Fe–Fe distance exists in **27**, which creates a molecular pocket that may be occupied by CO_2. The arrangement of the two Fe centers appears to enable an intramolecular ''push-pull'' mechanism to occur. In the reduced state, one Fe center may act as a Lewis base to push an electron pair onto CO_2, while the second Fe center may act as a Lewis acid to promote C–O bond cleavage. The same group later studied the effects of electron-withdrawing or donating substituents on the phenyl rings of these bis-porphyrin structures.[156] As observed with mononuclear Fe porphyrins, electron-withdrawing groups lowered the catalytic overpotential by positively shifting the reduction potentials of the complex; however, the decreased electron density at the Fe center resulted in a lower TOF for CO production. Electron-donating groups had the opposite effects. Further investigations should explore tuning of hetero-dinuclear complexes to overcome this conflicting scaling relationship between overpotential and rate.

Machan *et al.* used two hydrogen bonding acetoamido (dac) functionalized Re and Mn-bpy electrocatalysts (Re(dacbpy)$(CO)_3$Cl (**34**) and Mn(dacbpy)-$(CO)_3$Br (**35**)) to make a supramolecular assembly to study the mechanism of CO_2 reduction in a heterobimetallic system.[160] Electrochemical studies showed that the redox features of the co-catalyst system are different from the overlay of redox features of the individual catalysts (Figure 1.21). Additional cyclic voltammetric experiments in DMF indicated that metal–metal bond formation occurs for the co-catalyst mixture under conditions where the respective homobimetallic analogues (either **34** or **35**) are not generated, which is suggestive of a favorable heterobimetallic interaction at reducing potentials (Scheme 1.13). The increased catalytic current response of the co-catalyst mixture is also consistent with a cooperative effect. Control experiments with

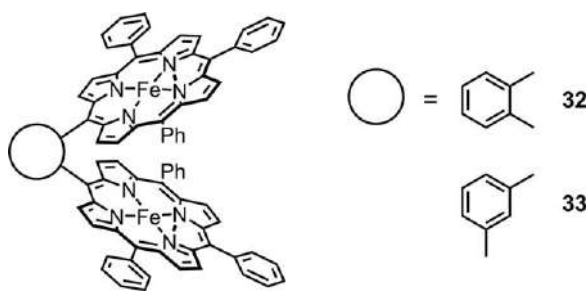

Figure 1.20 Structure of Fe porphyrin dimers **32** and **33**.

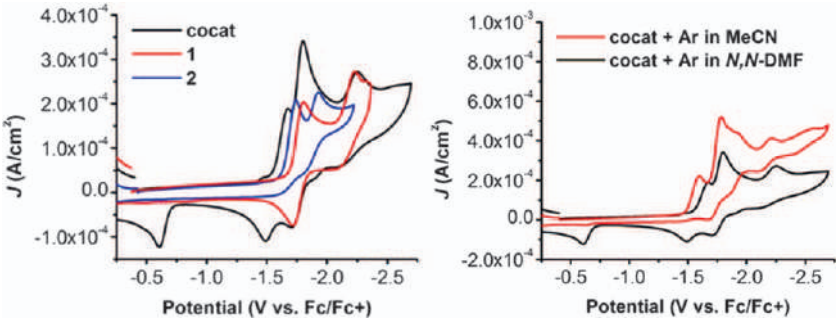

Figure 1.21 Left: Cyclic voltammograms of the co-catalyst mixture (black), Re(dacbpy)$(CO)_3$Cl (red), and Mn(dacbpy)$(CO)_3$Br (blue) taken in DMF under Ar saturation. Right: responses of Re(dacbpy)$(CO)_3$Cl and Mn(dacbpy)$(CO)_3$Br as a co-catalyst mixture under Ar in MeCN (red) and DMF (black).
Reproduced from ref. 160 with permission from the Royal Society of Chemistry.

the co-catalyst mixture in DMF and with an equimolar mixture of Re(CH_3-bpy) and Mn(CH_3-bpy) in MeCN did not show an increased current response. It was concluded that Re(dacbpy)$(CO)_3$Cl operates *via* a similar bimolecular mechanism based on DFT calculations and IR-SEC observations.[108] A cooperative effect was also observed for a peptide modified Re-bpy catalyst which was designed to promote hydrogen bonding between complexes, and homo-dimer formation.[109]

Homogeneous transition metal catalysts for electrochemical CO_2 reduction primarily produce CO and/or formate, and only in very rare cases are further reduction products observed. Bouwman and co-workers reported a Cu(I) thiolate catalyst, inspired by Ni-containing superoxide dismutase, that exists as a dinuclear dimer (**36**) bridging through a disulfide bond in the solid state and in solution.[161] Upon exposure to air, **36** preferentially captures CO_2 rather than O_2, resulting in oxidation of Cu(I) to Cu(II) and concomitant formation of oxalate (Scheme 1.14). A tetranuclear species (**36b**) is formed from this reaction, where the Cu(II) centers are bridged by oxalate anions. Elimination of the product oxalate was achieved chemically by treatment with hydrochloric acid to generate oxalic acid, or electrochemically by CPE in MeCN at −0.03 V *vs.* NHE (*ca.* −0.66 V *vs.* $Fc^{+/0}$). Under a CO_2 atmosphere, oxalate is formed in a near quantitative FE (96%), demonstrating a successful electrocatalytic system for CO_2 reduction to oxalate. However, the addition of lithium perchlorate is critical to the activity of this system. Precipitation of lithium oxalate drives product elimination from **36b** and enables catalyst turnover. At the same time, the crystallization of lithium oxalate at the electrode gradually passivates the electrode. Maverick and co-workers[162] later used a similar approach to generate oxalate from CO_2 with a dinuclear Cu(I) complex (**37**) (Figure 1.22), but no electrocatalytic studies with this system have been reported. The reactivity of **36** and **37**

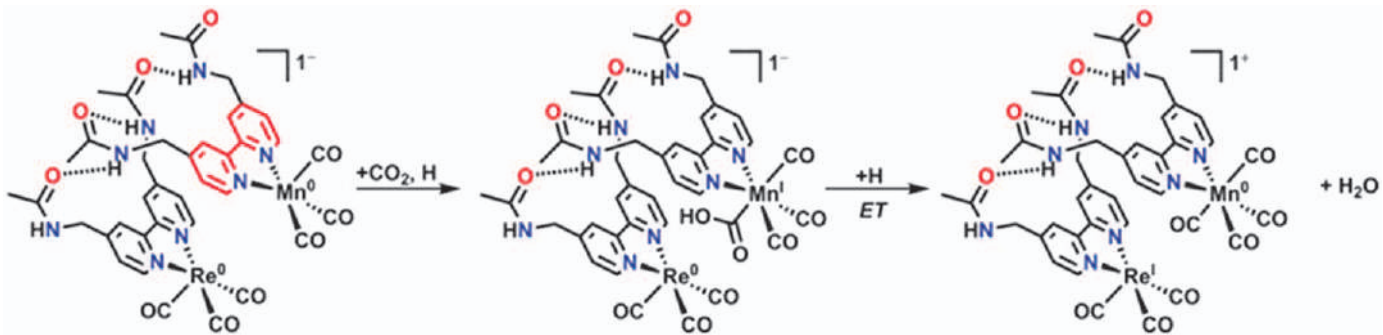

Scheme 1.13 Proposed mechanism of CO_2 reduction by the hydrogen-bonded heterobimetallic active species. Reproduced from ref. 160 with permission from the Royal Society of Chemistry.

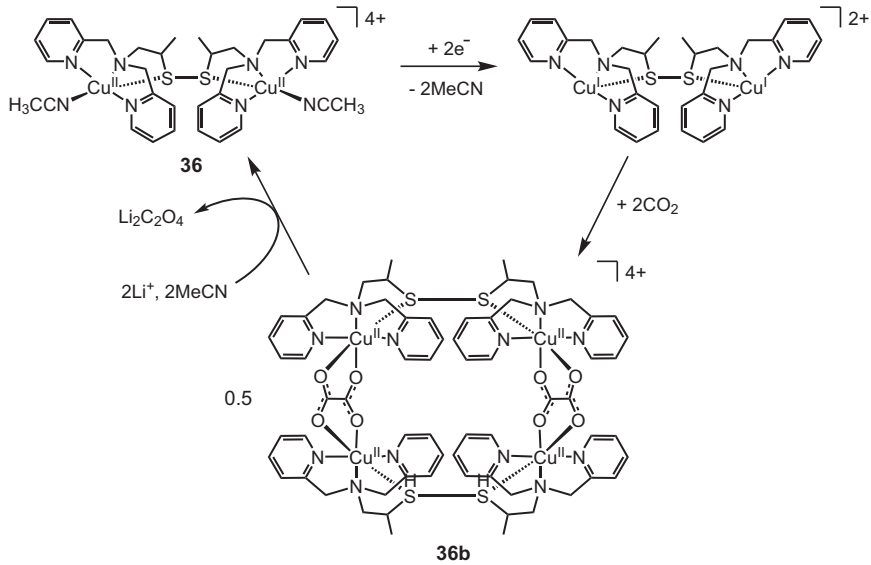

Scheme 1.14 Proposed mechanism for electrocatalytic CO_2 reduction to lithium oxalate using dimer (**36**).[161]

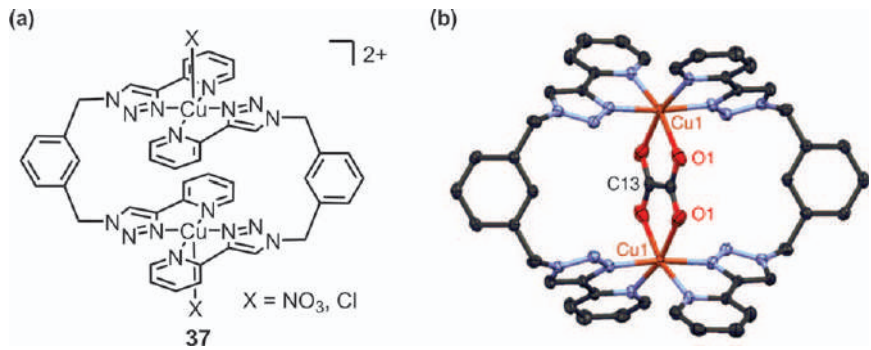

Figure 1.22 (a) Structure of Cu(I) dinuclear complex (**37**). (b) Crystal structure of the resulting oxalate-bridged species. 50% probability level.
Adapted from ref. 162 with permission from Springer Nature, Copyright 2014.

differs from that of previously reported dinuclear Cu complexes, which favor CO_2 reductive disproportionation to CO and CO_3^{2-}.[163]

It should be noted that the use of a binuclear complex does not guarantee cooperative behavior between metal centers. For example, a dinuclear version of $[Ru(tpy)(bpy)(MeCN)]^{2+}$ (**5**) was developed by Oshio and co-workers, where two Ru complexes were connected *via* a long alkyl bridge.[164] Due to the flexibility of the bridging ligand, the catalytic behavior of the dinuclear species was essentially identical to that of the parent mononuclear

complex (**5**). Indeed, careful design of the ligand structure is critical in order to promote close approach between the metal centers in the correct geometry for catalysis, either through rigid bridging structures, as in the co-facial Fe porphyrin dimer (**32**), or through soft hydrogen bonding interactions as in Re(dacbpy)$(CO)_3$Cl (**34**). Jurss and co-workers used rigid anthracene bridged Re(bpy)$(CO)_3$Cl to show that the orientation of the active Re sites dictates the reaction mechanism.[165] When the Re active sites adopt a *cis* confirmation a cooperative bimetallic reaction pathway is observed in the electrochemical studies. When the Re active sites adopt a *trans* confirmation a predominantly monometallic reaction pathway is observed. Constrictive ligand structures have also been utilized in the design of bimetallic Ni and Co complexes.[166,167]

1.9 Overpotential – Activity Relationship

The introduction of different ligand substituents in FeTPP provides a means to tune the catalyst properties in order to improve the overpotential and rate of CO_2 reduction. Aromatic substituents (biphenyl, pyrene, and phenyl–pyrene) on the porphyrin periphery had a negligible effect on the three reduction potentials of the complexes under Ar, but resulted in enhanced catalytic rates for CO production compared to (**3**).[168] The authors suggested that this rate improvement may be due to local accumulation of CO_2 in the hydrophobic space created by the π-conjugated groups; however, no evidence was presented to support this proposal, and this hypothesis seems unlikely given the known properties of CO_2. Savéant and co-workers showed that replacement of the phenyl groups in **3** with electron-withdrawing perfluorophenyl groups in FeF5TPP, FeF10TPP, and FeF20TPP (**38** – **40**, Figure 1.23) successively shifts the catalytic operating potential to a more positive value, thereby decreasing the overpotential.[127] However, these electron-deficient ligands also decrease the basicity of the reduced forms of the catalyst, which negatively affects formation of the $[Fe\text{-}CO_2]^{2-}$ adduct and cleavage of the C–O bond and therefore decreases the catalytic rate. This is a general trend observed for many electrocatalytic systems: improving the overpotential often comes at the cost of reduced catalytic rates, and *vice versa*. For **38** – **40**, the substituent inductive effects follow the linear free energy relationship shown in Figure 1.23 between the maximum turnover frequency TOF_{max} and the catalytic operating potential E°_{cat}.

The electronic influence of ligand substituents also depends on the position of the functional group, as shown by Duan, Sun, and co-workers.[169] In this report, a methoxy group was installed at the *ortho*, *meta*, or *para* position on each phenyl ring in FeTPP (**3**). The potential of the Fe(I/0) couple shifted positively in the order Fe-*ortho*-$COOCH_3$ < FeTPP < Fe-*meta*-$COOCH_3$ < Fe-*para*-$COOCH_3$, indicating that the *ortho* complex is the most electron-rich system, likely due to the dipole effect. Thus, Fe-*ortho*-$COOCH_3$ is expected to be the fastest CO_2 reduction catalyst with the largest overpotential in this series, which was confirmed experimentally in DMF.[169] Again, tuning the

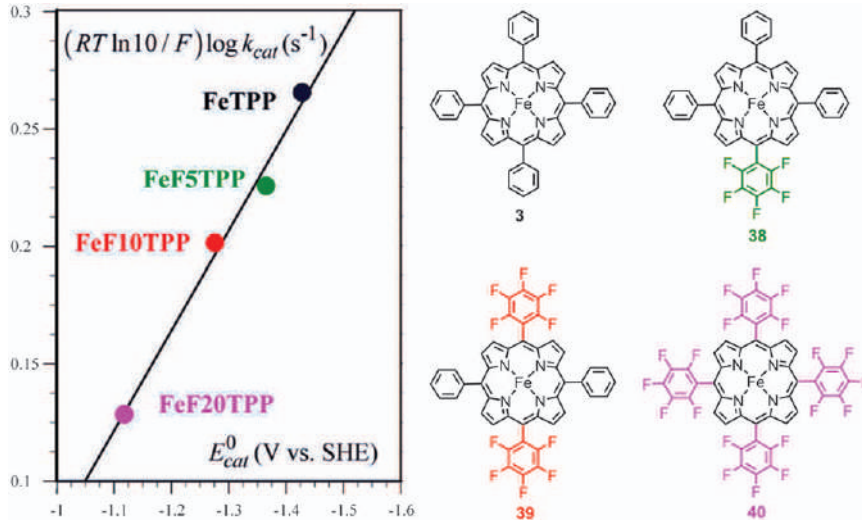

Figure 1.23 Linear correlation between TOF_{max} (given by k_{cat}) and E°_{cat} for electrocatalytic CO_2 reduction with Fe porphyrin catalysts (**38**–**40**) in 0.1 M Bu_4NPF_6/DMF and phenol (3 M).
Adapted from ref. 127 with permission from American Chemical Society, Copyright 2016.

electronic properties of the ligand led to an improvement in one parameter (*i.e.* rate) at the expense of the other (*i.e.* overpotential). The linear correlation in Figure 1.23 clearly depicts the limitations of using through-bond inductive effects to improve catalysis.

Several substituent changes on the original Re-bpy catalyst have been made in attempts to increase the catalytic activity.[86] The introduction of various electron-donating or withdrawing substituents on bipyridine has been systematically studied by the Kubiak group.[170,171] A series of 4,4′-substituted [Re(R-bpy)$(CO)_3$Cl] complexes were prepared (where R = OCH_3, CH_3, *t*Bu, CF_3, CN) and compared to the parent catalyst **2**.[86,170] The first reduction potentials of these complexes range from −1.2 V to −1.9 V *vs.* $Fc^{+/0}$ and exhibit an almost linear correlation with the *para*-substituted Hammett parameter, consistent with this reduction occurring at the bpy ligand (Figure 1.24). While *t*Bu and CH_3 have appropriate electron-donating powers for better catalytic performance than the unsubstituted catalyst, stronger donors like OCH_3 not only have higher overpotentials, but have unstable reduced states that lead to degradation of the catalyst over time. The electron-withdrawing groups CF_3 and CN were substituted onto the bipyridine to lower the overpotential. However, these groups change the electronic structure of the catalyst, shifting the site of the second reduction from the metal to the ligand, and thus making them only active at the third reduction. A similar study[171] showed that the 5,5′- substituted catalysts have higher catalytic activity ($i_{cat}/i_p = 29.6$) than the 3,3′-substituted catalysts ($i_{cat}/i_p = 17.0$), where i_{cat} is the catalytic current and i_p is the

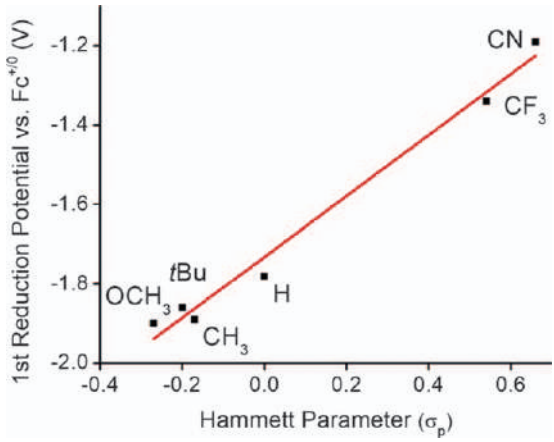

Figure 1.24 Trend between the electron-donating character of the 4,4′-bpy substituent and the first reduction potential of the corresponding Re complex. Reproduced from ref. 86 with permission from American Chemical Society, Copyright 2018.

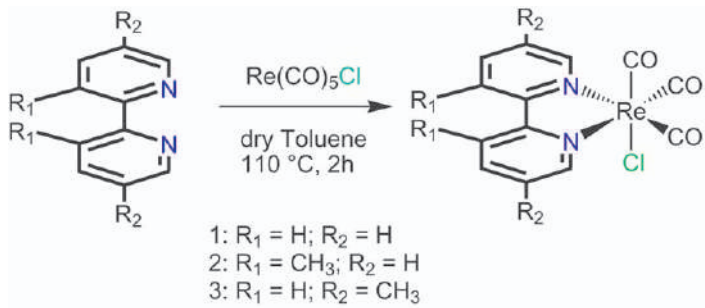

Complex	1st reduction (V vs. Ag/AgCl)	2nd reduction (V vs. Ag/AgCl)	i_{cat}/i_p	i_{cat}/i_p with 1 M TFE
1	−1.40	−1.78	4.5 ± 0.3	20.3 ± 0.4
2	−1.52	−1.81	4.8 ± 1.0	17.0 ± 1.1
3	−1.54	−1.85	4.9 ± 1.8	29.6 ± 2.0

Figure 1.25 Summary of cyclic voltammetry data obtained from 5,5′- and 3,3′-substituted catalysts.
Adapted from ref. 171 with permission from American Chemical Society, Copyright 2014.

peak current for the redox couple of the catalyst (Figure 1.25). The authors suggested that the steric hindrance from the 3,3′-substituents distorts the planarity of the bipyridines thus destabilizing the reduced intermediate.

Several π-delocalizing groups have been added to the bipyridines to improve electrocatalysis or photocatalysis. In general, the withdrawing nature

of these ligands caused a positive shift in the reduction potentials of the complexes when compared to Re-bpy but they also tended to have lower Faradaic efficiencies. For example, Qiao and co-workers[172] reported that nanographene Re catalysts have up to an 800 mV positive shift of onset potential for CO_2 reduction compared to Re-bpy in a tetrahydrofuran (THF)/methanol mixture. DFT calculations by Franco and co-workers[173] suggested that this trend comes from the fact that π-conjugation lowers the SOMO-LUMO gap as compared to the Re-bpy catalyst and moves the LUMO + 1 onto the ligand. When the extended π system is not co-planar, as shown in the Re(bis-pyridine anthracene)$(CO)_3Cl$ catalyst,[174] the system shows a negative shift of reduction potential as well as lower $FE_{CO} = 20\%$.

Ligands with similar electronic structures are used as a substitute for bipyridines to lower the overpotential of catalysis. There are detailed studies of Re catalysts with imines which show a similar mechanism to the Re(bpy) compound but generally have lower FE_{CO}.[36,175–177] For example, Re with diazabutadiene (DAB) ligands show a similar mechanism to bpy-based compounds under CO_2 in electron paramagnetic resonance (EPR) and IR-SEC studies. Under CO_2 they undergo a two-electron disproportionation reaction during catalysis to form CO ($FE_{CO} < 10\%$) and CO_3^{2-}.[176] The authors used IR-SEC data to propose that product inhibition was due to the weaker electron donation by DAB ligands to the metal center in the reduced state. Additionally, the CO_3^{2-} formed during disproportionation requires a more negative potential for dissociation.[177] When more donating diamine compounds are used, like Re-pytacompounds (pyta = 2-pyridyl-1,2,3-triazole),[178] the selectivity for CO production increases. Despite the high selectivity for CO production, they have a higher overpotential and lower TON than the Re-bpy catalyst under the same conditions. Nganga and coworkers found that Re(pyridine-oxazoline)$(CO)_3Cl$ complexes have faster catalysis than the Re-bpy catalyst. The authors argue that this is due to the superior σ donation of the oxazoline ligand compared with bipyridine.[179] Dinuclear Re α-diimine complexes,[180] and Re imidazole complexes[181] with extended π networks have positive shifts of reductions but lower FE or turnovers for CO than Re-bpy catalysts. Overall, diimine and other di-nitrogen ligands are less selective or slower than the Re-bpy catalyst.

NHC containing ligands provide an accommodating framework for electronic and steric tuning. The Agarwal group[182] focused on tuning Re-NHC complexes. They substituted the atoms next to the carbene with sulfur or oxygen for steric and electronic tuning. While tuning changed the product distribution slightly, the trend is that these catalysts have significant H_2 production and minor formate formation in addition to CO formation ($FE_{CO} = 60\%$). Liyanage and co-workers studied the electronic factors with four electron-deficient Re-pyNHC complexes. The best catalyst Re(PyNHC-$PhCF_3$)$(CO)_3Br$ shows 4.5 times higher TON_{CO} than Re(bpy)$(CO)_3Br$ while maintaining a high $FE_{CO} > 90\%$ over 1 h in a 2 M H_2O/MeCN mixture. Importantly, this catalyst also showed a lower FE_{CO} when weaker acids, such as TFE and PhOH, were used.[90] Their stability was not tested for longer than an hour. Re-Pyridyl-NHCs catalysts undergo the reductive disproportionation

reaction with two equivalents of CO_2 to give CO and CO_3^{2-}. Overall, NHC ligands tend to shift the product distribution compared to the Re-bpy system and have yet to show efficient, long term stability.

To summarize, catalytic rates and selectivity of Re-bpy complexes can be improved by adding moderately electron-donating groups, but at the cost of increasing the overpotential for catalysis. Modifications to lower the overpotential by using a π-conjugated network to bipyridines, replacing bipyridines with imines, NHCs, diazine and pyridine-oxazoline usually lead to a lower FE_{CO}.

1.10 Selective Formate Production

The reaction of CO_2 with Ir(III)-hydrides such as iridium(III) 2,6-bis((diisopropylphosphaneyl)methyl)pyridine trihydride[Ir(PNP)$(H)_3$] (**41**) was initially explored for CO_2 hydrogenation. Nozaki and co-workers[183] demonstrated that CO_2 insertion into one of the hydride bonds in **41** occurs readily under ambient conditions in THF, yielding an equilibrium mixture of the hydride and formate complexes (Figure 1.26a). Similar reactivity was later shown by Meyer, Brookhart and co-workers[184] with the five-coordinate [Ir(PCP)$(H)_2$] (**42**), where the favorability of CO_2 insertion is increased by κ^2-formate coordination.[185] This result was applied to develop the first example of selective electrocatalytic CO_2 reduction to formate.

The cyclic voltammogram of [Ir(PCP)$(H)_2$] (**42**) in 5% H_2O/MeCN under Ar does not exhibit any reduction features within the solvent window, but current enhancement is observed under CO_2 at −1.4 V *vs.* NHE (*ca.* −2.0 V *vs.* $Fc^{+/0}$), as shown in Figure 1.26b.[184] The origin of this current increase was

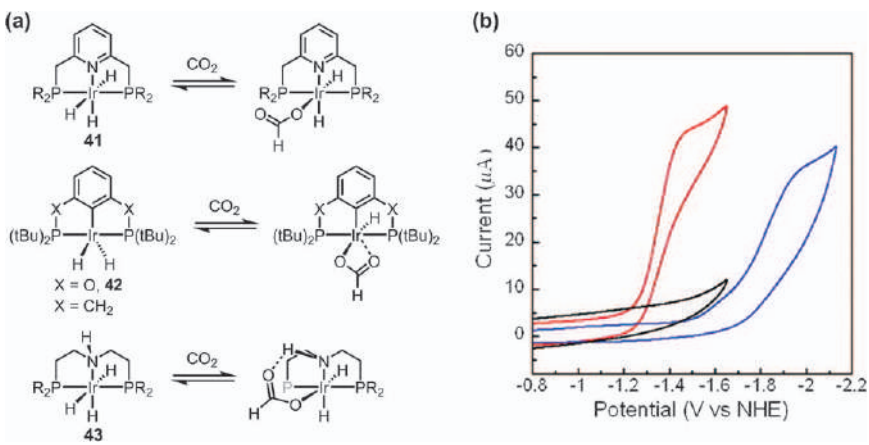

Figure 1.26 (a) Reactions of CO_2 with Ir hydride complexes **41**, **42**, and **43** in 5% H_2O/THF. (b) Cyclic voltammograms of **42** under Ar (black trace) or CO_2 (red) in 5% H_2O/MeCN, and under CO_2 in 5% H_2O/THF (blue). Supporting electrolyte was 0.1 M Bu_4NPF_6.
Adapted from ref. 184 with permission from American Chemical Society, Copyright 2012.

confirmed by CPE where formate was generated with 85% FE. The methylene version is also an active catalyst for formate production but requires more negative potentials (-1.8 V *vs.* NHE, *ca.* -2.4 V *vs.* $Fc^{+/0}$). Additionally, Bernskoetter, Hazari, Palmore and co-workers[186] demonstrated that a related complex $[Ir(PN^{H}P)(H)_2]$ (**43**) can catalyze CO_2 reduction to formate. While the operating potential is less negative than that of **42**, lower current densities are achieved due to a slow loss of formate which interacts with the ligand N–H group through hydrogen bonding (Figure 1.26a). Addition of $NaPF_6$ increases the catalytic current perhaps by facilitating formate release.[187] However, precipitation of a solid on the electrode rapidly shuts down catalysis.

The oxidized form of $[Ir(PCP)(H)_2]$, $[Ir(PCP)(MeCN)_2H]^+$ (**44**), displays a similar current enhancement to that of **42** under CO_2 in 5% H_2O/MeCN with a catalytic TOF of $\sim$20 s^{-1}. The rate of catalysis increases upon addition of water up to *ca.* 4%, indicating the important role of water in the mechanism. Furthermore, NMR studies show that MeCN coordinates $[Ir(PCP)(H)_2]$ to give $[Ir(PCP)(MeCN)(H)_2]$ (**45**) in anhydrous MeCN and does not react with CO_2, but the addition of 5% water triggers CO_2 insertion and release of formate. Water is proposed to stabilize the formate anion *via* hydrogen bonding, increasing the favorability of the CO_2 insertion equilibrium and facilitating CO_2 reduction. The reactivity of **45** is consistent with the proposed mechanism (Scheme 1.15) which is supported by DFT studies.[188] The rate-limiting CO_2 insertion step involves direct hydride transfer *via* an $[Ir-H\cdots CO_2]$ intermediate, and this step has a lower calculated transition state barrier in water than MeCN. DFT calculations also support that formate release is promoted by hydrogen bonding between formate and water.

While the original catalyst $[Ir(PCP)(H)_2]$ (**42**) is insoluble in aqueous solution, introduction of quaternary amine groups on the ligand renders these complexes water soluble.[189] The electrochemical behavior of **46** in water is

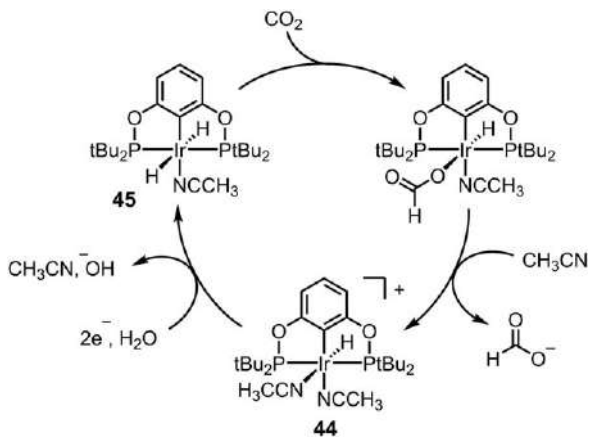

Scheme 1.15 Proposed mechanism for electrocatalytic CO_2 reduction to formate with $[Ir(PCP)(MeCN)_2H]^+$ (**44**).[188]

directly analogous to that of **44** in 5% H_2O/MeCN. The TOF under these conditions is 7.3 s^{-1}, corresponding to a second-order rate constant of $k_{CO2} = 220\ M^{-1}\ s^{-1}$ for the reaction of **46** with CO_2. The relationship between TOF and k_{CO2} is discussed in the 'Catalyst Comparisons' section. This rate constant is ~3.5 times faster compared to [Ir(PCP)$(H)_2$] in 5% H_2O/MeCN. However, the observed TOF, also denoted k_{cat} by the authors, is nearly three-fold slower due to the poor solubility of CO_2 in water (0.033 M). CPE confirms formate production with FE_{HCOO^-} of up to 93% in 0.1 M $NaHCO_3$ with 1% MeCN (pH 7). Notably, 1% MeCN is critical for sustaining catalysis by facilitating loss of a κ^2-formate ligand from Ir and regenerating the starting complex (**46**) to close the catalytic cycle (Scheme 1.15, Figure 1.27).

Further DFT calculations by Ahlquist and co-workers[190] confirmed that the mechanism shown in Scheme 1.15 is feasible in water, with an activation barrier of 16.6 kcal mol^{-1}. However, an alternate pathway was found involving a square-planar Ir(I)-hydride, which likely forms *via* reduction of $[Ir(PCP)(MeCN)_2H]^+$ (**44**). The calculated barrier for CO_2 insertion into $[Ir(PCP)H]^-$ (only 12.3 kcal mol^{-1}) is less than that for **45**, suggesting that an Ir(I) mechanism is more energetically accessible than an Ir(III) pathway. Computational studies from Nielsen and co-workers corroborate that both pathways may be operative.[191]

Nielsen and co-workers calculated the energetics of H_2 evolution *via* protonation of an Ir(III) or Ir(I) hydride.[191] In all cases, the activation barrier for HER is prohibitively large, consistent with the high selectivities for CO_2 reduction. Notably, both H_2 evolution from water and CO_2 insertion to formate are thermodynamically favorable reactions based on the calculated hydricities of the Ir hydrides. While not a kinetic parameter, hydricity (ΔG_H^-) does provide some useful guidance in catalyst design. Hydricity is the hydride donor ability of a molecule. From their computational results, the authors conclude that using metal hydride catalysts just sufficiently hydridic to reduce CO_2 coupled with weak Brønsted acids is critical for achieving selective formate production. This conclusion is in line with a recent report from the Kubiak lab,[111] where similar limitations are outlined for the reaction conditions as a function of catalyst hydricity that are necessary for selective CO_2 reduction to formate.

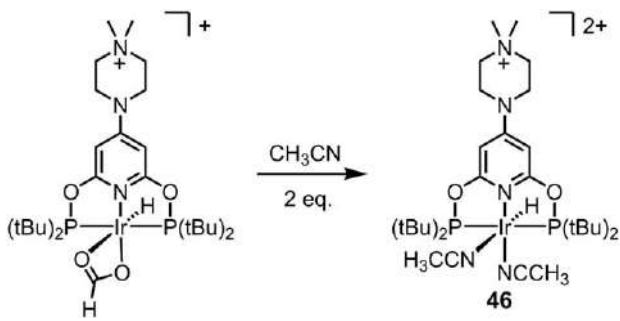

Figure 1.27 Loss of κ^2-formate ligand to generate $[Ir(qaPCP)(MeCN)_2H]^{2+}$ (**46**) in the presence of MeCN.[189]

A series of Fe carbonyl clusters have been explored by Berben and co-workers[192] for electrocatalytic CO_2 reduction in the presence of weak acids. The butterfly-shaped monoanionic cluster (Bu_4N)-$[Fe_4N(CO)_{12}]$ (**47**), exhibits a reversible one-electron reduction at −1.23 V *vs.* SCE (*ca.* −1.61 V *vs.* $Fc^{+/0}$) in MeCN (Figure 1.28). The addition of acids such as tosylic acid leads to H_2 evolution at this potential. Further electrochemical studies revealed that the rate of H_2 evolution depends on the acid strength, and the use of weaker organic acids enables the electrochemical generation of the hydride cluster $[HFe_4N(CO)_{12}]^-$ (**47b**) by one-electron-one-proton reduction of **47** without subsequent protonation to H_2. These observations were used to select conditions where the reaction of $[HFe_4N(CO)_{12}]^-$ with CO_2 was favored over H_2 evolution. Indeed, CO_2 reduction to formate is observed at the $[HFe_4N(CO)_{12}]^{-/0}$ couple in the presence of benzoic acid (Figure 1.24), albeit only in trace quantities.

The $[(diglyme)_2Na]^+$ salt of $[Fe_4N(CO)_{12}]^-$ is water soluble and allowed for electrochemical studies in aqueous solution. In the absence of CO_2, **47** is an active catalyst for H_2 evolution at −1.25 V *vs.* SCE (−1.01 V *vs.* NHE, pH 5).[193] Introduction of CO_2 results in a complete change in selectivity at this potential, with formate generated at high FE (up to 96%) between pH 5–13.[193] The best results were obtained at pH 7, which corresponds to an overpotential of 0.44 V for CO_2 reduction to formate. This work represents a remarkable advance for homogeneous CO_2 reduction catalysis: selective generation of formate is achieved with a first-row transition metal catalyst in water near-neutral pH at mild overpotentials.

Further studies by cyclic voltammetry and IR-SEC were performed to gain insight into the operative mechanism in MeCN or water. In both solvents, the reaction is first order in $[Fe_4N(CO)_{12}]^-$ and CO_2. One-electron reduction of $Fe_4N(CO)_{12}]^-$ in 5% H_2O/MeCN under N_2 leads to quantitative generation of the hydride (**42b**) as seen using IR-SEC. A crystal structure of

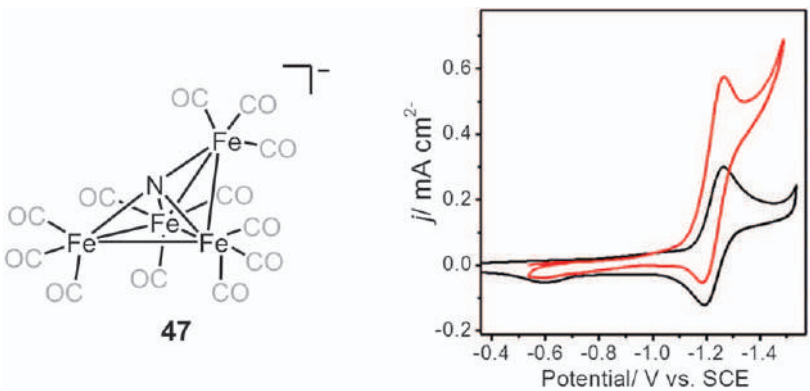

Figure 1.28 Cyclic voltammograms of $[Fe_4N(CO)_{12}]^-$ (**47**) in 0.1 M Bu_4NPF_6/MeCN with one equivalent of benzoic acid under N_2 (black trace) or CO_2 (red trace).
Adapted from ref. 194 with permission from American Chemical Society, Copyright 2015.

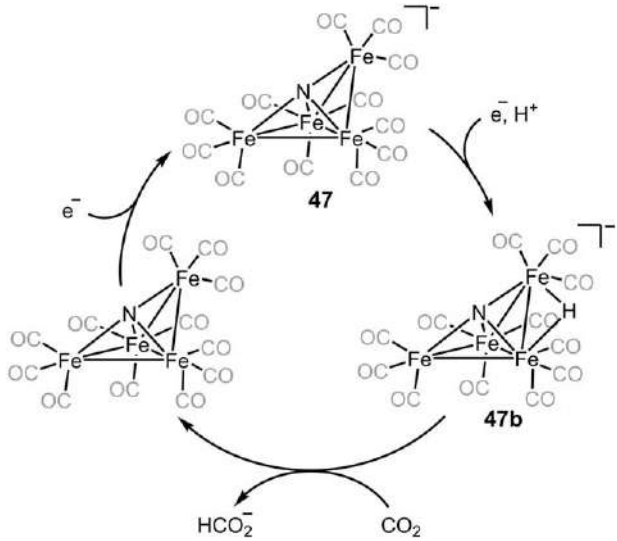

Scheme 1.16 Proposed mechanism for electrocatalytic CO_2 reduction to formate with the iron cluster **47**.[194]

$[HFe_4N(CO)_{12}]^-$ was also obtained, indicating that the hydride is bridged across an edge of the butterfly cluster. Exposure of $[HFe_4N(CO)_{12}]^-$, prepared independently or generated *in situ* by IR-SEC, to CO_2 results in formate production, suggesting that (**42b**) is the key species that reacts with CO_2. These results are consistent with the mechanism shown in Scheme 1.16.

The high selectivity of $[Fe_4N(CO)_{12}]^-$ for CO_2 reduction over H_2 evolution in aqueous solution is notable. Additionally, the reaction rate and formate selectivity in MeCN is greatly improved by addition of 5% water.[194] Here, it is important to recognize how the solvent affects the properties of (**47b**). The hydricity of this complex in MeCN is 49 kcal mol^{-1} and 15.5 kcal mol^{-1} in aqueous solution.[195] The hydricity of formate decreases significantly less, going from 44 kcal mol^{-1} in MeCN to 24.1 kcal mol^{-1} in water. Therefore, hydride transfer from **47b** to CO_2 is unfavorable by 5 kcal mol^{-1} in MeCN, but favorable in water by 8.6 kcal mol^{-1}. These energies are consistent with the improvement in catalytic rate and formate selectivity observed with increasing water concentration. Furthermore, it is a general trend that the hydricities of metal hydrides decrease much more in aqueous solution than that of formate due to the greater stabilization of the formate anion from hydrogen bonding with water.[196] This suggests that the development of new metal hydride catalysts capable of hydride transfer to CO_2 should be easier in water than in organic solvents.

The related carbide cluster $[Fe_4C(CO)_{12}]^-$ (**48**) is a better hydride donor than **47** (Figure 1.29) with hydricities of 44 and $<$15 kcal mol^{-1} in MeCN and water, respectively.[195] These stronger hydricities increase the favorability of hydride transfer to CO_2 but also increase the driving force for HER, and the rate of H_2 evolution is greater than C–H bond formation. Berben concludes

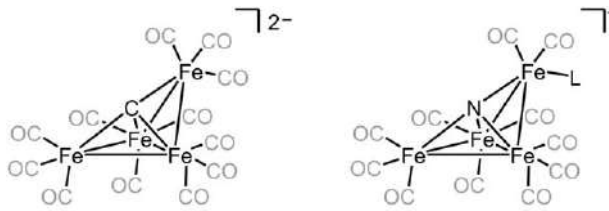

Figure 1.29 Structures of related Fe clusters **48** – **50**.

that catalysts with modest hydricities within a narrow range (the ''formate window'') are critical to favoring CO_2 reduction over competitive hydrogen evolution, which is in agreement with the findings of Nielsen and co-workers[191] and Kubiak and co-workers.[111,195]

Inspired by previous reports on the beneficial role of proton relays (Section 1.5), one carbonyl in $[Fe_4N(CO)_{12}]^-$ was replaced with a phosphine bearing a pendent hydroxyl group (Figure 1.29).[197] Reduction of **50** occurred at more negative potentials compared to **49** due to the greater donating nature of phosphine. Notably, no current increase is observed at the $[HFe_4N(CO)_{12}]^{-/0}$ couple under CO_2, and CPE at −1.4 V *vs.* SCE (*ca.* −1.78 V *vs.* $Fc^{+/0}$) confirmed that only H_2 is produced (FE = 97%). On the other hand, when L = PPh_3, electrocatalytic CO_2 reduction occurs under otherwise identical conditions, generating formate with 61% FE (background reduction of water produces 36% H_2). This sharp change in selectivity arises from the close proximity of the hydroxyl group to the metal hydride, which facilitates rapid H_2 evolution. This report highlights the potential pitfalls of installing pendent acidic groups for CO_2 reduction, and emphasizes the need to balance the kinetics and thermodynamics of CO_2 reduction *versus* HER to obtain selective formate production from metal hydride catalysts.

1.11 Catalyst Comparison

This section offers a brief description of the best practices when comparing electrocatalysts. Savéant and co-workers pioneered the development of these techniques and we direct the reader to several references which describe them more comprehensively.[198–200] The text, *Elements of Molecular and Biomolecular Electrochemistry: An Electrochemical Approach to Electron Transfer Chemistry*, serves as a thorough guide to electrochemical catalysis.[201]

Catalytic Tafel plots are an effective way to visualize the difference between catalysts in the context of turnover frequency (TOF) and overpotential (η). An optimal electrocatalyst undergoes many selective molecular reactions per second, *i.e.* has a high TOF. An ideal electrocatalytic system also operates with minimal additional potential exceeding the thermodynamically determined reduction potential (E^0_{cat}) for the redox event. The calculated E^0_{cat} for proton-coupled electron transfer CO_2 reduction to CO in MeCN (eqn (1.1)) is

−0.54 V *vs.* $Fc^{+/0}$ considering standard states for CO_2 and CO as 1 M. The calculated E^0_{cat} for CO_2 disproportionation to CO and CO_3^{2-} (eqn (1.2)) was estimated to be −1.15 V to −1.3 V *vs.* $Fc^{+/0}$ based on the standard reduction potential for aqueous CO_2 disproportionation and the free energy of formation for $MgCO_3$ by Sampson *et al.*[134] It is important to bear in mind that these calculated standard potentials are sensitive to the proton source used (*i.e.* water *vs.* phenol) and the products made (*i.e.* $MgCO_3$ *vs.* HCO_3^-). Determination of the overpotential is not trivial and reaction conditions should be considered when calculating E^0_{cat}. Nonetheless, Tafel plots can enable catalyst benchmarking for different experimental conditions. The most optimal catalyst will have an "elbow" in the top left corner of the plot (low overpotential and high TOF).

Kinetically limited conditions are steady-state conditions in catalyst consumption. A cyclic voltammogram of a kinetically limited process, where the substrate consumption in the diffusion layer is negligible, yields an S-shaped wave that is independent of scan rate where the forward scan (to more negative potential) is overlaid with the backward scan (to less negative potential). The catalytic rate constant (k_{cat}) is calculated using the plateau current obtained from the S-shaped wave (i_{cat}) and the peak current for the reversible redox potential of the wave (i_p). The equations shown are for purposes of illustration and refer specifically for the catalytic reduction of CO_2 by Re-bpy. The relationship between the peak catalytic current observed and the catalytic rate constant for a reversible electron transfer-fast catalytic reaction (EC') mechanism is shown in eqn (1.4). All electron transfers are assumed to occur at the electrode surface.

$$i_{cat} = n_{cat} F \mathrm{A}[\mathrm{cat}] \sqrt{(D k_{cat} [\mathrm{CO_2}]^y)} \tag{1.4}$$

In this equation, the number of electrons transferred (n_{cat}) in the reaction (2 e^- for CO_2 reduction of CO), the amount of charge carried by one mole of electrons (F, Faraday's constant), the electrode surface area (A), the catalyst concentration ([cat]), the diffusion coefficient for the catalytically-active species (D), the rate constant of the catalytic reaction (k_{cat}), and the substrate concentration ([CO_2]) is related to the peak catalytic current (i_{cat}). This relationship assumes the reaction is first order in the catalyst and substrate (y = 1) and the substrate is in large excess of the catalyst (pseudo-first-order conditions).

The Randles–Sevcik equation (eqn (1.5)) describes the relationship between the peak current for a reversible electron transfer event and the potential scan rate. In this equation, the universal gas constant (R), temperature (T), Faraday's constant (F), the diffusion coefficient for the catalytically-active species (D), the electrode surface area (A), and the scan rate (υ) are related to peak current (i_p).

$$i_p = 0.446 F \mathrm{A}[\mathrm{cat}] \sqrt{\frac{FD\nu}{RT}} \tag{1.5}$$

Normalization of the observed catalytic current to the peak current for the reversible wave (i_{cat}/i_p) circumvents the need to accurately determine the

electrode surface area and catalyst diffusion coefficient (eqn (1.6)). This derivation of the equation is for a 2 e^- CO_2 reduction and a 1 e^- reversible redox couple. The catalyst diffusion coefficient can change between resting and activated states. For example, the Re-bpy catalyst is anionic after reduction and could be better solvated than its neutral resting state. This difference is assumed to be negligible under ideal conditions. The k_{cat} also represents the theoretical maximum number of catalyst turnovers per unit time (TOF_{max}).

$$\frac{i_{cat}}{i_p} = 2.24\sqrt{\frac{2RTk_{cat}}{F\nu}} \tag{1.6}$$

The catalytic Tafel plot is created by determining TOF at each η value using eqn (1.7). For this relationship the standard potential for the reduction of CO_2 ($E^0_{CO_2}$) under the specific catalytic conditions must be known. A plot of log (TOF) *vs.* overpotential generates the elbow plots shown below and enables catalyst benchmarking independent of reaction conditions.

$$TOF = \frac{TOF_{max}}{1 + \exp\left[\frac{F}{RT}\left(E^0_{CO_2} - E^0_{cat}\right)\right]\exp\left(-\frac{F}{RT}\eta\right)} \tag{1.7}$$

While catalytic Tafel plots are critical quantitative benchmarks, accurate determination of catalytic values (TOF and η) requires catalysts that are well behaved. Many catalyst systems are not ideal, and side phenomena such as product inhibition of the catalyst or catalyst degradation occur. These side-phenomena greatly influence the quality of the catalytic kinetic data as they can affect the shape of the wave and the observed peak potential of catalysis. When the scan rate is increased, the amount of charge passed is decreased and the influence of side-phenomena on wave shape are diminished. Typical S-shaped curves are not obtained, and the catalytic wave may exhibit scan-rate dependence. A scan-rate dependent catalytic current cannot be reliably used to calculate a catalytic rate constant. Savéant and co-workers developed the foot-of-the-wave analysis (FOWA) to derive catalytic rates from non-ideal catalytic waves where a plateau current is not achieved.[198–200] The onset potential of a catalytic wave is an approximation for the least negative electrode potential required for a reductive catalytic process. FOWA is an examination of the current response observed for the voltammetric wave at this onset potential (halfway up the wave), where side-phenomena have only minor contributions. Eqn (1.8) is applied to determine the observed rate constant (k) which is the slope of the linear region of the plot of i/i_p *vs.* $1/(1 + \exp[(F/RT)(E - E^0{}_{cat})]$. This is the relationship between the current (i) that corresponds to the potential (E) and the reaction rate constant (k_{cat}).

$$\frac{i}{i_p} = \frac{2.24\sqrt{\frac{RT}{F\nu}2k[CO_2]}}{1 + \exp\left[\frac{F}{RT}\left(E - E^0_{cat}\right)\right]} \tag{1.8}$$

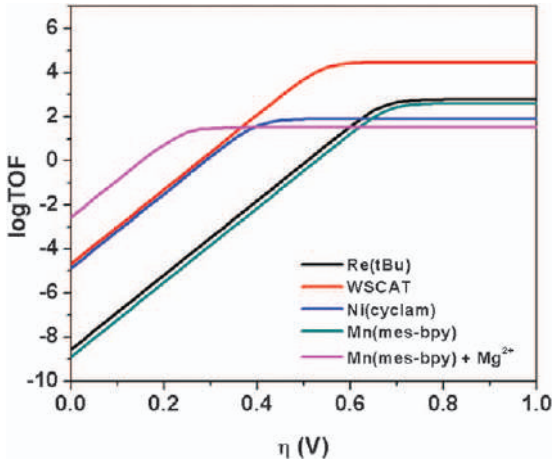

Figure 1.30 Catalytic Tafel plot for the catalyst with Brønsted acid added. WSCAT (**21**) with 1 M PhOH in 0.1 M Bu_4NPF_6/DMF. Re(*t*Bu-bpy)$(CO)_3Cl$ (**2**), $[Ni(cyclam)]^{2+}$ (**9**), and Mn(mesbpy)$(CO)_3Br$ (**28**) with 1 M PhOH in 0.1 M Bu_4NPF_6/MeCN. Mn(mesbpy)$(CO)_3Br$ with 0.1 M Mg^{2+} in 0.1 M Bu_4NPF_6/MeCN.

Figure 1.30 shows a comparison of the log TOF *vs.* η for Re(*t*Bu-bpy)$(CO)_3Cl$, FeTPP with four paraphenyl trimetylammonium groups (WSCAT; **21**), $[Ni(cyclam)]^{2+}$; **9**, Mn(mes-bpy)$(CO)_3Br$; **28**, and **28** with Mg^{2+} added. The addition of Mg^{2+}, as $Mg(OTf)_2$, significantly increases the reaction rate for CO_2 reduction by the Mn(mes-bpy)$(CO)_3Br$ catalyst at low overpotentials. The Mg^{2+} enhances catalysis at the CO_2 binding potential (-1.5 V *vs.* $Fc^{+/0}$) for Mn(mes-bpy)$(CO)_3Br$ by enabling a reduction and the reductive disproportionation mechanism. The beneficial effects of Lewis acids added to FeTPP were previously reported by Savéant and co-workers (as described in Section 1.7). The addition of Lewis acids to catalytic systems which show CO_2 binding and ''slow catalysis'' at lower overpotentials is currently an underutilized strategy for improving catalysis.

Rhenium is less abundant in the Earth's crust than platinum, thus catalysts which use manganese are more attractive from a sustainability perspective. This has stimulated research in the development of Mn-based catalysts with catalytic performance on par with their 2nd row counterparts. Figure 1.31 shows a comparison of the log TOF *vs.* η for Group 7 metal catalysts. Notably, Mn-*t*Bubpy operates at a lower overpotential compared to Re-*t*Bubpy. The Re-bpy can operate without an added acid since the CO_2 adduct is so strongly basic it can deprotonate MeCN.[76]

Fontecave and co-workers recently prepared a series of bis-terpyridine complexes of first-row transition metals.[202] Of the metals examined, Co, Ni, and Zn exhibit CO_2 reduction behavior by cyclic voltammetry in 5% H_2O/DMF. However, low Faradaic efficiencies are observed for $[Co(tpy)_2]^{2+}$ and $[Ni(tpy)_2]^{2+}$ (12% CO and 5% H_2 for Co at -2.03 V *vs.* $Fc^{+/0}$, and 20% CO

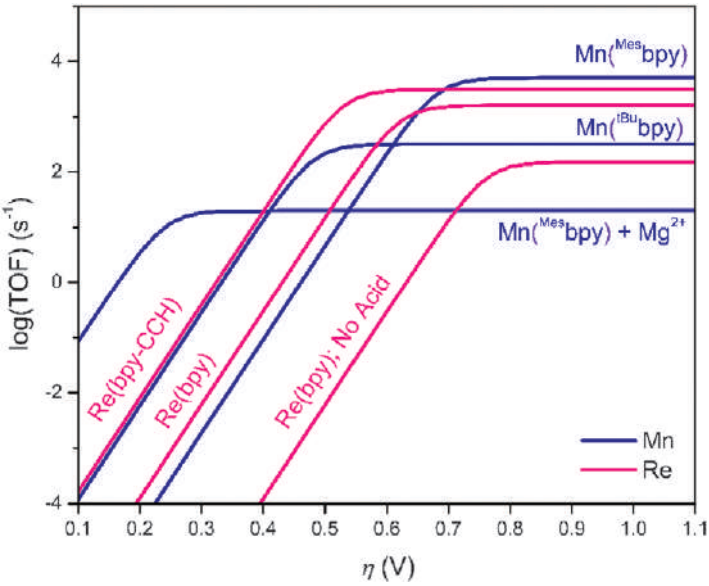

Figure 1.31 Catalytic Tafel plot for various Re-bpy and Mn-bpy catalysts in 0.1 M Bu_4NPF_6/MeCN with added Brønsted acid. Re(bpy-CCH) and Re(bpy) with 1.5 M TFE. Mn(*t*Bubpy) with 1.4 M TFE. Mn(mesbpy) with 0.3 M TFE.

for Ni at −1.72 V) and no productive catalysis is seen with $[Zn(tpy)_2]^{2+}$, which is likely due to reductive degradation of the terpyridine ligands. Using mixtures of terpyridine and $CoCl_2$ led to improved activity, with a 76% Faradaic efficiency for CO obtained using a 1 : 1 Co : ligand ratio, suggesting that only one terpyridine is present in the active species. Further studies with $[Co(R\text{-}tpy)_2]^{2+}$ showed that by tuning the ligand substituents the rate of competitive H_2 evolution could be significantly decreased, effectively ''turning off'' H_2 production while still enabling CO_2 reduction.[203] This approach of tuning the catalyst to disfavor competing reactions in order to indirectly improve CO_2 selectivity may be a useful approach for other catalysts.

1.12 Future Outlook and Recommendations

To provide a useful guide for further improvement of different catalysts, we compared catalytic performances of different catalysts with their turnover numbers and frequencies, Faradaic efficiencies, i_{cat}/i_p, k_{cat} and other properties. Tafel plots, which are less commonly reported, are recommended as they give direct visual measurement of catalytic performances, while eliminating the unfairness brought by different experimental conditions. Bearing in mind the significance of direct and fair comparisons among different catalysts, we have several recommendations as protocols for optimization of catalytic conditions.

Different acids with a range of pK_a should be tested in addition to anhydrous conditions under catalytic conditions. Many catalysts, such as porphyrins and Mn bipyridine compounds, are highly catalytic only in the presence of weak Brønsted acids or Lewis acids. In the case of Re bipyridine catalysts, while much effort has been devoted to new ligand designs to enhance catalysis, the use of appropriate weak Brønsted acids or Lewis acid for the best performance has been underestimated, and often provides more leverage. The acidity also affects the selectivity towards CO_2 reduction over hydrogen evolution. Generally, TFE, PhOH, MeOH, and water are common choices of weak acids in MeCN and DMF, and stronger acids such as acetic acid often result in significant hydrogen production.

Careful CPE studies are the most important evaluation of long-term catalytic performance. Although i_{cat}/i_p and k_{cat} obtained in cyclic voltammetry are convenient measurements of catalytic performance, the calculated efficiencies are usually higher than those obtained in CPE due to the imperfect curve shape in cyclic voltammetry, and catalyst degradation over time. Since the long term stability of a catalyst is vital for applications on an industrial scale, CPE studies with different weak acids should be done with at least $3-4$ turnovers for catalysis. These results can reveal the selectivity for CO_2 reduction, which is not measurable by cyclic voltammetry. In addition, gas leakage is one of the biggest concerns in CPE studies with gaseous products, therefore, standard conditions, *e.g.* Re(*t*Bu-bpy) with 1 M TFE in MeCN, should be tested and reported for fair comparison of catalytic performance of new catalytic systems. Turnover numbers or turnover frequencies should be reported together with Faradaic efficiencies for clearer understanding of catalysts.

Mechanistic investigations are the key to understanding catalytic cycles and effects of catalyst modifications. Apart from electrochemistry, common tools like DFT calculations, IR and UV–vis measurements, NMR and EPR studies, and laser investigations have been used frequently for many catalysts. For example, IR-SEC has been used to great advantage the in Re-bpy and Mn-bpy systems as their three carbonyl groups show significant shifts in the IR over the range of ~2100 and 1800 cm^{-1}, reflecting electron density on metal centers by back-bonding in different redox states. One point in DFT computations that must be included in the model is the role of solvent molecules.

Design strategies for obtaining higher catalytic rates at a lower overpotential need to address more than the electronic structural changes that attend various ligand modifications. Through space substituent effects may play an equally important role in the continued development of homogeneous electrochemical CO_2 reduction catalysts. The design strategies discussed in this chapter were selected to provide some examples of real solutions to the challenges at hand, but also to stimulate further thinking on how to move off the trade-offs of linear scaling relationships. By now, it is quite clear that the secondary coordination sphere can be tuned in much the same way that the primary coordination sphere has been tuned over the last forty years.

Acknowledgements

JAB gratefully acknowledges funding from the UCSD Chancellor's Postdoctoral Fellowship Program (CPFP/PPFP). CPK gratefully acknowledges funding from the Air Force Office of Scientific Research (AFOSR), U. S. Department of Energy (DOE) through the Joint Center for Artificial Photosynthesis (JCAP), and DARPA and the many graduate students and postdocs who contributed to our group's efforts on the electrochemical reduction of CO_2.

References

1. A. Coehn and S. Jahn, *Ber. Dtsch. Chem. Ges.*, 1904, **37**, 2836–2842.
2. F. Fischer and O. Prziza, *Ber. Dtsch. Chem. Ges.*, 1914, **47**, 256–260.
3. S. Meshitsuka, M. Ichikawa and K. Tamaru, *J. Chem. Soc., Chem. Commun.*, 1974, **5**, 158–159.
4. H. Kazuya, T. Katsuhiro, S. Hideo and T. Shinobu, *Chem. Lett.*, 1977, **6**, 1137–1140.
5. B. J. Fisher and R. Eisenberg, *J. Am. Chem. Soc.*, 1980, **102**, 7361–7363.
6. M. Beley, J. P. Collin, R. Ruppert and J. P. Sauvage, *J. Chem. Soc., Chem. Commun.*, 1984, 1315–1316.
7. S. Slater and J. H. Wagenknecht, *J. Am. Chem. Soc.*, 1984, **106**, 5367–5368.
8. J. Hawecker, J.-M. Lehn and R. Ziessel, *J. Chem. Soc., Chem. Commun.*, 1984, 328–330.
9. R. Francke and R. D. Little, *Chem. Soc. Rev.*, 2014, **43**, 2492–2521.
10. E. E. Benson, C. P. Kubiak, A. J. Sathrum and J. M. Smieja, *Chem. Soc. Rev.*, 2009, **38**, 89–99.
11. M. R. Dubois and D. L. Dubois, *Acc. Chem. Res.*, 2009, **42**, 1974–1982.
12. A. J. Morris, G. J. Meyer and E. Fujita, *Acc. Chem. Res.*, 2009, **42**, 1983–1994.
13. A. M. Appel, J. E. Bercaw, A. B. Bocarsly, H. Dobbek, D. L. DuBois, M. Dupuis, J. G. Ferry, E. Fujita, R. Hille, P. J. A. Kenis, C. A. Kerfeld, R. H. Morris, C. H. F. Peden, A. R. Portis, S. W. Ragsdale, T. B. Rauchfuss, J. N. H. Reek, L. C. Seefeldt, R. K. Thauer and G. L. Waldrop, *Chem. Rev.*, 2013, **113**, 6621–6658.
14. C. Costentin, M. Robert and J.-M. Savéant, *Chem. Soc. Rev.*, 2013, **42**, 2423–2436.
15. J. Qiao, Y. Liu, F. Hong and J. Zhang, *Chem. Soc. Rev.*, 2014, **43**, 631–675.
16. M. L. Clark, K. A. Grice, C. E. Moore, A. L. Rheingold and C. P. Kubiak, *Chem. Sci.*, 2014, **5**, 1894–1900.
17. J. Tory, B. Setterfield-Price, R. A. W. Dryfe and F. Hartl, *ChemElectroChem*, 2015, **2**, 213–217.

18. G. Neri, P. M. Donaldson and A. J. Cowan, *J. Am. Chem. Soc.*, 2017, **139**, 13791–13797.
19. F. Franco, C. Cometto, F. Sordello, C. Minero, L. Nencini, J. Fiedler, R. Gobetto and C. Nervi, *ChemElectroChem*, 2015, **2**, 1372–1379.
20. J. Tory, G. Gobaille-Shaw, A. M. Chippindale and F. Hartl, *J. Organomet. Chem.*, 2014, **760**, 30–41.
21. D. Sieh, D. C. Lacy, J. C. Peters and C. P. Kubiak, *Chem. – Eur. J.*, 2015, **21**, 8497–8503.
22. K. A. Grice and C. Saucedo, *Inorg. Chem.*, 2016, **55**, 6240–6246.
23. K. A. Grice, C. Saucedo, M. A. Sovereign and A. P. Cho, *Electrochim. Acta*, 2016, **218**, 110–118.
24. U. Jayarathne, P. Chandrasekaran, H. Jacobsen, J. T. Mague and J. P. Donahue, *Dalton Trans.*, 2010, **39**, 9662–9671.
25. E. E. Benson and C. P. Kubiak, *Chem. Commun.*, 2012, **48**, 7374–7376.
26. J. M. Smieja and C. P. Kubiak, *Inorg. Chem.*, 2010, **49**, 9283–9289.
27. M. D. Sampson, J. D. Froehlich, J. M. Smieja, E. E. Benson, I. D. Sharp and C. P. Kubiak, *Energy Environ. Sci.*, 2013, **6**, 3748–3755.
28. M. R. Crawley, K. J. Kadassery, A. N. Oldacre, A. E. Friedman, D. C. Lacy and T. R. Cook, *Organometallics*, 2019, **38**, 1664–1676.
29. C. W. Machan, M. D. Sampson, S. A. Chabolla, T. Dang and C. P. Kubiak, *Organometallics*, 2014, **33**, 4550–4559.
30. E. E. Benson, K. A. Grice, J. M. Smieja and C. P. Kubiak, *Polyhedron*, 2013, **58**, 229–234.
31. E. E. Benson, M. D. Sampson, K. A. Grice, J. M. Smieja, J. D. Froehlich, D. Friebel, J. A. Keith, E. A. Carter, A. Nilsson and C. P. Kubiak, *Angew. Chem., Int. Ed.*, 2013, **52**, 4841–4844.
32. S. I. Kallane and M. van Gastel, *J. Phys. Chem. A*, 2016, **120**, 7465–7474.
33. C. Riplinger, M. D. Sampson, A. M. Ritzmann, C. P. Kubiak and E. A. Carter, *J. Am. Chem. Soc.*, 2014, **136**, 16285–16298.
34. J. Emsley, *The Elements*, Oxford University Press, Oxford, 1989.
35. M. Bourrez, F. Molton, S. Chardon-Noblat and A. Deronzier, *Angew. Chem., Int. Ed.*, 2011, **50**, 9903–9906.
36. F. P. A. G. Johnson, M. W. Hartl and F. Turner, J. J, *Organometallics*, 1996, **15**, 3374–3387.
37. M. Hammouche, D. Lexa, J. M. Savéant and M. Momenteau, *J. Electroanal. Chem.*, 1988, **249**, 347–351.
38. C. Costentin, S. Drouet, G. Passard, M. Robert and J.-M. Savéant, *J. Am. Chem. Soc.*, 2013, **135**, 9023–9031.
39. M. Hammouche, D. Lexa, M. Momenteau and J. M. Savéant, *J. Am. Chem. Soc.*, 1991, **113**, 8455–8466.
40. I. Bhugun, D. Lexa and J. M. Savéant, *J. Phys. Chem.*, 1996, **100**, 19981–19985.
41. C. E. Castillo, J. Armstrong, E. Laurila, L. Oresmaa, M. Haukka, J. Chauvin, S. Chardon-Noblat and A. Deronzier, *ChemCatChem*, 2016, **8**, 2667–2677.

42. J. Tory, L. King, A. Maroulis, M. Haukka, M. J. Calhorda and F. Hartl, *Inorg. Chem.*, 2014, **53**, 1382–1396.
43. C. W. Machan, M. D. Sampson and C. P. Kubiak, *J. Am. Chem. Soc.*, 2015, **137**, 8564–8571.
44. S. Min, S. Rasul, H. Li, D. C. Grills, K. Takanabe, L.-J. Li and K.-W. Huang, *ChemPlusChem*, 2016, **81**, 166–171.
45. Z. Chen, C. Chen, D. R. Weinberg, P. Kang, J. J. Concepcion, D. P. Harrison, M. S. Brookhart and T. J. Meyer, *Chem. Commun.*, 2011, **47**, 12607–12609.
46. Z. Chen, J. J. Concepcion, M. K. Brennaman, P. Kang, M. R. Norris, P. G. Hoertz and T. J. Meyer, *Proc. Natl. Acad. Sci. U. S. A.*, 2012, **109**, 15606–15611.
47. Z. Chen, P. Kang, M.-T. Zhang and T. J. Meyer, *Chem. Commun.*, 2014, **50**, 335–337.
48. P. Kang, Z. Chen, A. Nayak, S. Zhang and T. J. Meyer, *Energy Environ. Sci.*, 2014, **7**, 4007–4012.
49. T. A. White, S. Maji and S. Ott, *Dalton Trans.*, 2014, **43**, 15028–15037.
50. F. H. Haghighi, H. Hadadzadeh, H. Farrokhpour, N. Serri, K. Abdi and H. A. Rudbari, *Dalton Trans.*, 2014, **43**, 11317–11332.
51. H. Hadadzadeh, H. Farrokhpour, J. Simpson, J. Shakeri, M. Daryanavard and M. Shokrollahi, *New J. Chem.*, 2016, **40**, 6347–6357.
52. M. Daryanavard, H. Hadadzadeh, M. Weil and H. Farrokhpour, *J. CO_2 Util.*, 2017, **17**, 80–89.
53. S. Ramakrishnan and C. E. D. Chidsey, *Inorg. Chem.*, 2017, **56**, 8326–8333.
54. K. Leung, I. M. B. Nielsen, N. Sai, C. Medforth and J. A. Shelnutt, *J. Phys. Chem. A*, 2010, **114**, 10174–10184.
55. J. Shen, M. J. Kolb, A. J. Gottle and M. T. M. Koper, *J. Phys. Chem. C*, 2016, **120**, 15714–15721.
56. Y. Y. Birdja, J. Shen and M. T. M. Koper, *Catal. Today*, 2017, **288**, 37–47.
57. F. Wang, B. Cao, W.-P. To, C.-W. Tse, K. Li, X.-Y. Chang, C. Zang, S. L.-F. Chan and C.-M. Che, *Catal. Sci. Technol.*, 2016, **6**, 7408–7420.
58. D. L. DeLaet, R. Del Rosario, P. E. Fanwick and C. P. Kubiak, *J. Am. Chem. Soc.*, 1987, **109**, 754–758.
59. S. Roy, B. Sharma, J. Pecaut, P. Simon, M. Fontecave, P. D. Tran, E. Derat and V. Artero, *J. Am. Chem. Soc.*, 2017, **139**, 3685–3696.
60. M. Beley, J. P. Collin, R. Ruppert and J. P. Sauvage, *J. Am. Chem. Soc.*, 1986, **108**, 7461–7467.
61. B. L. Mash, A. Raghavan and T. Ren, *Eur. J. Inorg. Chem.*, 2019, **2019**, 2065–2070.
62. M. Y. Udugala-Ganehenege, Y. Liu, C. Forsyth, A. M. Bond and J. Zhang, *Transition Met. Chem.*, 2014, **39**, 883–891.
63. M. Y. Udugala-Ganehenege, N. M. Dissanayake, Y. Liu, A. M. Bond and J. Zhang, *Transition Met. Chem.*, 2014, **39**, 819–830.

64. S. Singh, B. Phukan, C. Mukherjee and A. Verma, *RSC Adv.*, 2015, **5**, 3581–3589.
65. V. S. Thoi and C. J. Chang, *Chem. Commun.*, 2011, **47**, 6578–6580.
66. V. S. Thoi, N. Kornienko, C. G. Margarit, P. Yang and C. J. Chang, *J. Am. Chem. Soc.*, 2013, **135**, 14413–14424.
67. D. L. Dubois, *Comments Inorg. Chem.*, 1997, **19**, 307–325.
68. J. W. Raebiger, J. W. Turner, B. C. Noll, C. J. Curtis, A. Miedaner, B. Cox and D. L. DuBois, *Organometallics*, 2006, **25**, 3345–3351.
69. J. D. Cope, N. P. Liyanage, P. J. Kelley, J. A. Denny, E. J. Valente, C. E. Webster, J. H. Delcamp and T. K. Hollis, *Chem. Commun.*, 2017, **53**, 9442–9445.
70. J. A. Therrien, M. O. Wolf and B. O. Patrick, *Inorg. Chem.*, 2014, **53**, 12962–12972.
71. M. L. Sheng, N. Jiang, S. Gustafson, B. You, D. H. Ess and Y. J. Sun, *Dalton Trans.*, 2015, **44**, 16247–16250.
72. J. A. Therrien, M. O. Wolf and B. O. Patrick, *Dalton Trans.*, 2018, **47**, 1827–1840.
73. I. Bhugun, D. Lexa and J. M. Savéant, *J. Am. Chem. Soc.*, 1994, **116**, 5015–5016.
74. I. Bhugun, D. Lexa and J.-M. Savéant, *J. Am. Chem. Soc.*, 1996, **118**, 1769–1776.
75. A. W. Nichols, S. Chatterjee, M. Sabat and C. W. Machan, *Inorg. Chem.*, 2018, **57**, 211–2121.
76. J. A. Keith, K. A. Grice, C. P. Kubiak and E. A. Carter, *J. Am. Chem. Soc.*, 2013, **135**, 15823–15829.
77. B. P. Sullivan, C. M. Bolinger, D. Conrad, W. J. Vining and T. J. Meyer, *J. Chem. Soc., Chem. Commun.*, 1985, 1414–1416.
78. J. Agarwal, E. Fujita, H. F. Schaefer and J. T. Muckerman, *J. Am. Chem. Soc.*, 2012, **134**, 5180–5186.
79. K. A. Grice, N. X. Gu, M. D. Sampson and C. P. Kubiak, *Dalton Trans.*, 2013, **42**, 8498–8503.
80. J. D. Compain, M. Bourrez, M. Haukka, A. Deronzier and S. Chardon-Noblat, *Chem. Commun.*, 2014, **50**, 2539–2542.
81. D. C. Grills, J. A. Farrington, B. H. Layne, S. V. Lymar, B. A. Mello, J. M. Preses and J. F. Wishart, *J. Am. Chem. Soc.*, 2014, **136**, 5563–5566.
82. J. M. Smieja, M. D. Sampson, K. A. Grice, E. E. Benson, J. D. Froehlich and C. P. Kubiak, *Inorg. Chem.*, 2013, **52**, 2484–2491.
83. H. K. Takeda, H. Koizumi, K. Okamotoa and O. Ishitani, *Chem. Commun.*, 2014, **50**, 1491–1493.
84. M. D. Sampson, A. D. Nguyen, K. A. Grice, C. E. Moore, A. L. Rheingold and C. P. Kubiak, *J. Am. Chem. Soc.*, 2014, **136**, 5460–5471.
85. E. S. Rountree, B. D. McCarthy, T. T. Eisenhart and J. L. Dempsey, *Inorg. Chem.*, 2014, **53**, 9983–10002.
86. M. L. Clark, P. L. Cheung, M. Lessio, E. A. Carter and C. P. Kubiak, *ACS Catal.*, 2018, **8**, 2021–2029.

87. C. Riplinger and E. A. Carter, *ACS Catal.*, 2015, **5**, 900–908.
88. B. D. McCarthy, D. J. Martin, E. S. Rountree, A. C. Ullman and J. L. Dempsey, *Inorg. Chem.*, 2014, **53**, 8350–8361.
89. A. Kütt, I. Leito, I. Kaljurand, L. Sooväli, V. M. Vlasov, L. M. Yagupolskii and I. A. Koppel, *J. Org. Chem.*, 2006, **71**, 2829–2838.
90. N. P. Liyanage, H. A. Dulaney, A. J. Huckaba, J. W. Jurss and J. H. Delcamp, *Inorg. Chem.*, 2016, **55**, 6085–6094.
91. I. Bhugun, D. Lexa and J.-M. Savéant, *J. Am. Chem. Soc.*, 1996, **118**, 3982–3983.
92. Y. C. Lam, R. J. Nielsen, H. B. Gray and W. A. Goddard, *ACS Catal.*, 2015, **5**, 2521–2528.
93. C. Costentin, S. Drouet, M. Robert and J.-M. Savéant, *Science*, 2012, **338**, 90–94.
94. H.-J. Knölker, J. Heber and C. H. Mahler, *Synlett*, 1992, 1002–1004.
95. A. Rosas-Hernandez, H. Junge, M. Beller, M. Roemelt and R. Francke, *Catal. Sci. Technol.*, 2017, **7**, 459–465.
96. H. Ishida, K. Tanaka and T. Tanaka, *Organometallics*, 1987, **6**, 181–186.
97. H. Nagao, T. Mizukawa and K. Tanaka, *Inorg. Chem.*, 1994, **33**, 3415–3420.
98. M. R. DuBois and D. L. DuBois, *Chem. Soc. Rev.*, 2009, **38**, 62–72.
99. C. Costentin, G. Passard, M. Robert and J.-M. Savéant, *J. Am. Chem. Soc.*, 2014, **136**, 11821–11829.
100. C. Costentin, G. Passard, M. Robert and J. M. Savéant, *Proc. Natl. Acad. Sci. U. S. A.*, 2014, **111**, 14990–14994.
101. A. Chapovetsky, T. H. Do, R. Haiges, M. K. Takase and S. C. Marinescu, *J. Am. Chem. Soc.*, 2016, **138**, 5765–5768.
102. A. Chapovetsky, M. Welborn, J. M. Luna, R. Haiges, T. F. Miller and S. C. Marinescu, *ACS Cent. Sci.*, 2018, **4**, 397–404.
103. A. J. Gottle and M. T. M. Koper, *Chem. Sci.*, 2017, **8**, 458–465.
104. F. Franco, C. Cometto, F. F. Vallana, F. Sordello, E. Priola, C. Minero, C. Nervi and R. Gobetto, *Chem. Commun.*, 2014, **50**, 14670–14673.
105. F. Franco, C. Cometto, L. Nencini, C. Barolo, F. Sordello, C. Minero, J. Fiedler, M. Robert, R. Gobetto and C. Nervi, *Chem. – Eur. J.*, 2017, **23**, 4782–4793.
106. J. Agarwal, T. W. Shaw, H. F. Schaefer, III and A. B. Bocarsly, *Inorg. Chem.*, 2015, **54**, 5285–5294.
107. C. W. Machan, S. A. Chabolla, J. Yin, M. K. Gilson, F. A. Tezcan and C. P. Kubiak, *J. Am. Chem. Soc.*, 2014, **136**, 14598–14607.
108. C. W. Machan, J. Yin, S. A. Chabolla, M. K. Gilson and C. P. Kubiak, *J. Am. Chem. Soc.*, 2016, **138**, 8184–8193.
109. S. A. Chabolla, C. W. Machan, J. Yin, E. A. Dellamary, S. Sahu, N. C. Gianneschi, M. K. Gilson, F. A. Tezcan and C. P. Kubiak, *Faraday Discuss.*, 2017, **198**, 279–300.
110. C. S. Seu, D. Ung, M. D. Doud, C. E. Moore, A. L. Rheingold and C. P. Kubiak, *Organometallics*, 2013, **32**, 4556–4563.

111. K. M. Waldie, A. L. Ostericher, M. H. Reineke, A. F. Sasayama and C. P. Kubiak, *ACS Catal.*, 2018, **8**, 1313–1324.
112. D. C. Lacy, C. C. L. McCrory and J. C. Peters, *Inorg. Chem.*, 2014, **53**, 4980–4988.
113. M. Zhang, M. El-Roz, H. Frei, J. L. Mendoza-Cortes, M. Head-Gordon, D. C. Lacy and J. C. Peters, *J. Phys. Chem. C*, 2015, **119**, 4645–4654.
114. L. Chen, Z. Guo, X.-G. Wei, C. Gallenkamp, J. Bonin, E. Anxolabéhère-Mallart, K.-C. Lau, T.-C. Lau and M. Robert, *J. Am. Chem. Soc.*, 2015, **137**, 10918–10921.
115. C. G. Margarit, C. Schnedermann, N. G. Asimow and D. G. Nocera, *Organometallics*, 2019, **38**, 1219–1223.
116. E. M. Nichols, J. S. Derrick, S. K. Nistanaki, P. T. Smith and C. J. Chang, *Chem. Sci.*, 2018, **9**, 2952–2960.
117. P. Sen, B. Mondal, D. Saha, A. Rana and A. Dey, *Dalton Trans.*, 2019, **48**, 5965–5977.
118. G. F. Manbeck, J. T. Muckerman, D. J. Szalda, Y. Himeda and E. Fujita, *J. Phys. Chem. B*, 2015, **119**, 7457–7466.
119. L. Duan, G. F. Manbeck, M. Kowalczyk, D. J. Szalda, J. T. Muckerman, Y. Himeda and E. Fujita, *Inorg. Chem.*, 2016, **55**, 4582–4594.
120. B. Das, L. Ezzedinloo, M. Bhadbhade, M. P. Bucknall and S. B. Colbran, *Chem. Commun.*, 2017, **53**, 10006–10009.
121. G. Neri, I. M. Aldous, J. J. Walsh, L. J. Hardwick and A. J. Cowan, *Chem. Sci.*, 2016, **7**, 1521–1526.
122. C. W. Machan and C. P. Kubiak, *Dalton Trans.*, 2016, **45**, 17179–17186.
123. D. Ghosh, K. Kobayashi, T. Kajiwara, S. Kitagawa and K. Tanaka, *Inorg. Chem.*, 2017, **56**, 11066–11073.
124. E. Haviv, D. Azaiza-Dabbah, R. Carmieli, L. Avram, J. M. L. Martin and R. Neumann, *J. Am. Chem. Soc.*, 2018, **140**, 12451–12456.
125. C. Costentin, M. Robert, J.-M. Savéant and A. Tatin, *Proc. Natl. Acad. Sci. U. S. A.*, 2015, **112**, 6882–6886.
126. I. Azcarate, C. Costentin, M. Robert and J.-M. Savéant, *J. Am. Chem. Soc.*, 2016, **138**, 16639–16644.
127. I. Azcarate, C. Costentin, M. Robert and J. M. Savéant, *J. Phys. Chem. C*, 2016, **120**, 28951–28960.
128. J. Song, E. L. Klein, F. Neese and S. Ye, *Inorg. Chem.*, 2014, **53**, 7500–7507.
129. G. B. Balazs and F. C. Anson, *J. Electroanal. Chem.*, 1992, **322**, 325–345.
130. Y. Wu, B. Rudshteyn, A. Zhanaidarova, J. D. Froehlich, W. Ding, C. P. Kubiak and V. S. Batista, *ACS Catal.*, 2017, **7**, 5282–5288.
131. J. Schneider, H. F. Jia, K. Kobiro, D. E. Cabelli, J. T. Muckerman and E. Fujita, *Energy Environ. Sci.*, 2012, **5**, 9502–9510.
132. J. D. Froehlich and C. P. Kubiak, *Inorg. Chem.*, 2012, **51**, 3932–3934.
133. J. D. Froehlich and C. P. Kubiak, *J. Am. Chem. Soc.*, 2015, **137**, 3565–3573.
134. M. D. Sampson and C. P. Kubiak, *J. Am. Chem. Soc.*, 2016, **138**, 1386–1393.

135. S. J. P. Spall, T. Keane, J. Tory, D. C. Cooker, H. Adams, H. Fowler, A. Meijer, F. Hartl and J. A. Weinstein, *Inorg. Chem.*, 2016, **55**, 12568–12582.
136. J. Agarwal, C. J. Stanton, T. W. Shaw, J. E. Vandezande, G. F. Majetich, A. B. Bocarsly and H. F. Schaefer, *Dalton Trans.*, 2015, **44**, 2122–2131.
137. J. Agarwal, T. W. Shaw, C. J. Stanton, G. F. Majetich, A. B. Bocarsly and H. F. Schaefer, *Angew. Chem., Int. Ed.*, 2014, **53**, 5152–5155.
138. C. J. Stanton, J. E. Vandezande, G. F. Majetich, H. F. Schaefer and J. Agarwal, *Inorg. Chem.*, 2016, **55**, 9509–9512.
139. B. D. Matson, E. A. McLoughlin, K. C. Armstrong, R. M. Waymouth and R. Sarangi, *Inorg. Chem.*, 2019, **58**, 7453–7465.
140. Q. Zeng, J. Tory and F. Hartl, *Organometallics*, 2014, **33**, 5002–5008.
141. M. Stanbury, J. D. Compain, M. Trejo, P. Smith, E. Goure and S. Chardon-Noblat, *Electrochim. Acta*, 2017, **240**, 288–299.
142. B. A. Johnson, S. Maji, H. Agarwala, T. A. White, E. Mijangos and S. Ott, *Angew. Chem., Int. Ed.*, 2016, **55**, 1825–1829.
143. C. Romelt, J. S. Song, M. Tarrago, J. A. Rees, M. van Gastel, T. Weyhermuller, S. DeBeer, E. Bill, F. Neese and S. F. Ye, *Inorg. Chem.*, 2017, **56**, 4745–4750.
144. D. Lexa, J. M. Saveant and D. L. Wang, *Organometallics*, 1986, **5**, 1428–1434.
145. M. D. Sampson and C. P. Kubiak, *Inorg. Chem.*, 2015, **54**, 6674–6676.
146. A. Zhanaidarova, H. Steger, M. H. Reineke and C. P. Kubiak, *Dalton Trans.*, 2017, **46**, 12413–12416.
147. J. Choi, T. M. Benedetti, R. Jalili, A. Walker, G. G. Wallace and D. L. Officer, *Chem. – Eur. J.*, 2016, **22**, 14158–14161.
148. D. C. Grills, Y. Matsubara, Y. Kuwahara, S. R. Golisz, D. A. Kurtz and B. A. Mello, *J. Phys. Chem. Lett.*, 2014, **5**, 2033–2038.
149. Y. Matsubara, D. C. Grills and Y. Kuwahara, *ACS Catal.*, 2015, **5**, 6440–6452.
150. S. Sahu, P. L. Cheung, C. W. Machan, S. A. Chabolla, C. P. Kubiak and N. C. Gianneschi, *Chem. – Eur. J.*, 2017, **23**, 8619–8622.
151. B. J. McNicholas, J. D. Blakemore, A. B. Chang, C. M. Bates, W. W. Kramer, R. H. Grubbs and H. B. Gray, *J. Am. Chem. Soc.*, 2016, **138**, 11160–11163.
152. S. Sung, D. Kumar, M. Gil-Sepulcre and M. Nippe, *J. Am. Chem. Soc.*, 2017, **139**, 13993–13996.
153. S. Sung, X. Li, L. M. Wolf, J. R. Meeder, N. S. Bhuvanesh, K. A. Grice, J. A. Panetier and M. Nippe, *J. Am. Chem. Soc.*, 2019, **141**, 6569–6582.
154. W. Shin, S. H. Lee, J. W. Shin, S. P. Lee and Y. Kim, *J. Am. Chem. Soc.*, 2003, **125**, 14688–14689.
155. E. A. Mohamed, Z. N. Zahran and Y. Naruta, *Chem. Commun.*, 2015, **51**, 16900–16903.
156. Z. N. Zahran, E. A. Mohamed and Y. Naruta, *Sci. Rep.*, 2016, **6**, 24533.

157. Y. Naruta and M.-a. Sasayama, *J. Chem. Soc., Chem. Commun.*, 1994, 2667–2668.
158. Y. Naruta, M.-a. Sasayamab and T. Sasaki, *Angew. Chem., Int. Ed.*, 1994, **33**, 1839–1841.
159. Y. Shimazaki, T. Nagano, H. Takesue, B.-H. Ye, F. Tani and Y. Naruta, *Angew. Chem., Int. Ed.*, 2004, **43**, 98–100.
160. C. W. Machan and C. P. Kubiak, *Dalton Trans.*, 2016, **45**, 15942–15950.
161. R. Angamuthu, P. Byers, M. Lutz, A. L. Spek and E. Bouwman, *Science*, 2010, **327**, 313–315.
162. U. R. Pokharel, F. R. Fronczek and A. W. Maverick, *Nat. Commun.*, 2014, **5**, 5883.
163. R. J. Haines, R. E. Wittrig and C. P. Kubiak, *Inorg. Chem.*, 1994, **33**, 4723–4728.
164. S. Kuramochi, G. N. Newton, T. Shiga and H. Oshio, *Chem. Lett.*, 2014, **43**, 1222–1225.
165. W. Yang, S. Sinha Roy, W. C. Pitts, R. L. Nelson, F. R. Fronczek and J. W. Jurss, *Inorg. Chem.*, 2018, **57**, 9564–9575.
166. T. Ouyang, H.-H. Huang, J.-W. Wang, D.-C. Zhong and T.-B. Lu, *Angew. Chem., Int. Ed.*, 2017, **56**, 738–743.
167. L.-M. Cao, H.-H. Huang, J.-W. Wang, D.-C. Zhong and T.-B. Lu, *Green Chem.*, 2018, **20**, 798–803.
168. Y. Okabe, S. K. Lee, M. Kondo and S. Masaoka, *J. Biol. Inorg. Chem.*, 2017, **22**, 713–725.
169. R. B. Ambre, Q. Daniel, T. Fan, H. Chen, B. B. Zhang, L. Wang, M. S. G. Ahlquist, L. L. Duan and L. C. Sun, *Chem. Commun.*, 2016, **52**, 14478–14481.
170. M. L. Clark, B. Rudshteyn, A. Ge, S. A. Chabolla, C. W. Machan, B. T. Psciuk, J. Song, G. Canzi, T. Lian, V. S. Batista and C. P. Kubiak, *J. Phys. Chem. C*, 2016, **120**, 1657–1665.
171. S. A. Chabolla, E. A. Dellamary, C. W. Machan, F. A. Tezcan and C. P. Kubiak, *Inorg. Chim. Acta*, 2014, **422**, 109–113.
172. X. Qiao, Q. Li, R. N. Schaugaard, B. W. Noffke, Y. Liu, D. Li, L. Liu, K. Raghavachari and L.-s. Li, *J. Am. Chem. Soc.*, 2017, **139**, 3934–3937.
173. F. Franco, C. Cometto, C. Garino, C. Minero, F. Sordello, C. Nervi and R. Gobetto, *Eur. J. Inorg. Chem.*, 2015, **2015**, 296–304.
174. T. A. Manes and M. J. Rose, *Inorg. Chem. Commun.*, 2015, **61**, 221–224.
175. E. Portenkirchner, E. Kianfar, N. S. Sariciftci and G. Knor, *ChemSusChem*, 2014, **7**, 1347–1351.
176. M. V. Vollmer, C. W. Machan, M. L. Clark, W. E. Antholine, J. Agarwal, H. F. Schaefer, C. P. Kubiak and J. R. Walensky, *Organometallics*, 2015, **34**, 3–12.
177. C. W. Machan, S. A. Chabolla and C. P. Kubiak, *Organometallics*, 2015, **34**, 4678–4683.

178. H. Y. V. Ching, X. Wang, M. He, N. P. Holland, R. Guillot, C. Slim, S. Griveau, H. C. Bertrand, C. Policar, F. Bedioui and M. Fontecave, *Inorg. Chem.*, 2017, **56**, 2966–2976.
179. J. K. Nganga, C. R. Samanamu, J. M. Tanski, C. Pacheco, C. Saucedo, V. S. Batista, K. A. Grice, M. Z. Ertem and A. M. Angeles-Boza, *Inorg. Chem.*, 2017, **56**, 3214–3226.
180. A. Wilting, T. Stolper, R. A. Mata and I. Siewert, *Inorg. Chem.*, 2017, **56**, 4176–4185.
181. S. Sinha, E. K. Berdichevsky and J. J. Warren, *Inorg. Chim. Acta*, 2017, **460**, 63–68.
182. C. J. Stanton, C. W. Machan, J. E. Vandezande, T. Jin, G. F. Majetich, H. F. Schaefer, C. P. Kubiak, G. H. Li and J. Agarwal, *Inorg. Chem.*, 2016, **55**, 3136–3144.
183. R. Tanaka, M. Yamashita and K. Nozaki, *J. Am. Chem. Soc.*, 2009, **131**, 14168–14169.
184. P. Kang, C. Cheng, Z. F. Chen, C. K. Schauer, T. J. Meyer and M. Brookhart, *J. Am. Chem. Soc.*, 2012, **134**, 5500–5503.
185. P. Kang, Z. F. Chen, M. Brookhart and T. J. Meyer, *Top. Catal.*, 2015, **58**, 30–45.
186. S. T. Ahn, E. A. Bielinski, E. M. Lane, Y. Q. Chen, W. H. Bernskoetter, N. Hazari and G. T. R. Palmore, *Chem. Commun.*, 2015, **51**, 5947–5950.
187. E. A. Bielinski, P. O. Lagaditis, Y. Zhang, B. Q. Mercado, C. Würtele, W. H. Bernskoetter, N. Hazari and S. Schneider, *J. Am. Chem. Soc.*, 2014, **136**, 10234–10237.
188. L. Cao, C. Sun, N. Sun, L. Meng and D. Chen, *Dalton Trans.*, 2013, **42**, 5755–5763.
189. P. Kang, T. J. Meyer and M. Brookhart, *Chem. Sci.*, 2013, **4**, 3497–3502.
190. I. Osadchuk, T. Tamm and M. S. G. Ahlquist, *ACS Catal.*, 2016, **6**, 3834–3839.
191. S. I. Johnson, R. J. Nielsen and W. A. Goddard, *ACS Catal.*, 2016, **6**, 6362–6371.
192. M. D. Rail and L. A. Berben, *J. Am. Chem. Soc.*, 2011, **133**, 18577–18579.
193. A. D. Nguyen, M. D. Rail, M. Shanmugam, J. C. Fettinger and L. A. Berben, *Inorg. Chem.*, 2013, **52**, 12847–12854.
194. A. Taheri, E. J. Thompson, J. C. Fettinger and L. A. Berben, *ACS Catal.*, 2015, **5**, 7140–7151.
195. A. Taheri and L. A. Berben, *Chem. Commun.*, 2016, **52**, 1768–1777.
196. Y. Matsubara, E. Fujita, M. D. Doherty, J. T. Muckerman and C. Creutz, *J. Am. Chem. Soc.*, 2012, **134**, 15743–15757.
197. N. D. Loewen, E. J. Thompson, M. Kagan, C. L. Banales, T. W. Myers, J. C. Fettinger and L. A. Berben, *Chem. Sci.*, 2016, **7**, 2728–2735.
198. C. Costentin and J.-M. Savéant, *ChemElectroChem*, 2014, **1**, 1226–1236.

199. C. Costentin, G. Passard and J.-M. Savéant, *J. Am. Chem. Soc.*, 2015, **137**, 5461–5467.
200. C. Costentin, S. Drouet, M. Robert and J.-M. Savéant, *J. Am. Chem. Soc.*, 2012, **134**, 11235–11242.
201. J.-M. Savéant and C. Costentin, in *Elements of Molecular and Biomolecular Electrochemistry*, John Wiley & Sons, Inc., 2019.
202. N. Elgrishi, M. B. Chambers, V. Artero and M. Fontecave, *Phys. Chem. Chem. Phys.*, 2014, **16**, 13635–13644.
203. N. Elgrishi, M. B. Chambers and M. Fontecave, *Chem. Sci.*, 2015, **6**, 2522–2531.

CHAPTER 2

Homogeneous Electrochemical Reduction of CO_2. From Homogeneous to Supported Systems

CYRILLE COSTENTIN,*[a,b] KIM DAASBJERG*[c] AND MARC ROBERT*[d,e]

[a] Département de Chimie Moléculaire, Université Grenoble-Alpes, CNRS, UMR 5250, 38000 Grenoble, France; [b] Université de Paris, France; [c] Department of Chemistry, Aarhus University, Langelandsgade 140, DK-8000 Aarhus C, Denmark; [d] Université de Paris, Laboratoire d'Electrochimie Moléculaire, CNRS, F-75013 Paris, France; [e] Institut Universitaire de France (IUF), F-75005 Paris, France
*Emails: cyrille.costentin@univ-grenoble-alpes.fr; kdaa@chem.au.dk; robert@u-paris.fr

2.1 Introduction

The electrochemical CO_2 reduction reaction (CO_2RR) represents an important process with prospective applications in the storage of renewable electricity,[1] as well as in the chemical industry.[2,3] The most common reduction products are CO, HCOOH, CH_3OH, C_2H_5OH, CH_4, and C_2H_4. Unfortunately, the activation barrier associated with CO_2RR is high, because bonds are broken and geometries changed along the reaction pathway. This brings challenges for the CO_2RR at an electrode due to the necessity of applying a

Energy and Environment Series No. 28
Carbon Dioxide Electrochemistry: Homogeneous and Heterogeneous Catalysis
Edited by Marc Robert, Cyrille Costentin and Kim Daasbjerg

Published by the Royal Society of Chemistry, www.rsc.org

high overpotential. To overcome the activation barrier and reduce the applied overpotential, various molecular catalysts have been considered. The most studied include metal–porphyrin[4–8] and metal–polypyridine[9–12] complexes because of their well-defined structure and the tunable coordination environment making it relatively straightforward to improve the catalyst performance through functionalizations.[4,7,10]

Homogeneous electrocatalysis involving molecular catalysts constitutes an indirect pathway by which CO_2RR can be accomplished efficiently (Figure 2.1).[13] At the same time, it offers an opportunity of gaining valuable insight into the reaction mechanism. In recent years, tremendous efforts have been dedicated to benchmarking the catalytic performance of numerous electrocatalysts.[14–16] Nevertheless, distinct challenges persist for the homogeneous approach.[13] Firstly, the catalyst stability and recyclability are, in general, not sufficiently good enough for long-term use and scale-up. Secondly, for fast catalytic reactions only a small fraction of catalyst molecules in the reaction layer participates, with the remaining ones being inactive bystanders. Thirdly, low solubility of the catalyst can put severe limitations on the choice of electrolyte. Fourthly, product separation is often not straightforward. To solve these issues, considerable efforts have been directed towards the immobilization of molecular catalysts on electrode surfaces for supported catalysis (Figure 2.1).[17]

From an electrochemical point of view, the catalytic activity relies on a number of important metrics, *i.e.* the overpotential (η) featuring the cell's voltage efficiency, the current density featuring the rate constant of the overall electrochemical reaction, the faradaic efficiency (FE) featuring the process selectivity, the turnover frequency (TOF) featuring the catalytic efficiency, and the maximal turnover number (TON_{max}) featuring the catalyst stability. The performance of the supported CO_2RR involving molecular electrocatalysts is, in addition to the intrinsic activity of the catalysts, highly dependent on the exact way they are immobilized on the electrode surface.[18]

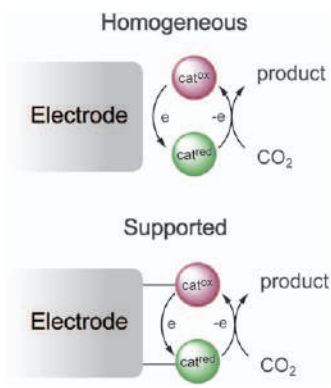

Figure 2.1 The principle of homogeneous and supported catalysis for the electrochemical CO_2RR, where cat^{ox} and cat^{red} denote the oxidized and reduced form of the mediator couple, respectively.

Key parameters to consider when designing the electrochemical process for the supported case are catalyst loading and accessibility, conductivity, electron transfer kinetics, mass transport effects, and catalyst/electrode stability. In this context, it becomes of paramount importance to consider carefully both the nature of the support and the immobilization mode. In fact, the different results obtained when using different supports are attributed to specific support–catalyst interactions.[19] An unresolved issue pertains to the substantial solvation energy changes coming from introducing a porous support material, which to a high extent may impact the catalyst activity.[20] Below we cover various modes of immobilization of molecular catalysts and give a description of single metal atoms dispersed in carbon materials.

2.2 Immobilization of Molecular Catalysts and Creation of Single-atom Catalysts

2.2.1 Support Material

Before describing the various immobilization modes, a discussion of the support material seems appropriate. Along with metal oxides, carbon supports such as carbon powder, carbon nanotubes (CNTs), graphene, or graphene oxides are the most popular, usually used in combination with a binder such as Nafion.[21,22] In general, the high porosity of the support will allow increased loading and improved mass transport. Likewise, high electrical conductivity of the support will facilitate electron transfer processes. This means that the use of more porous[23] and conductive[24] materials is greatly advantageous for CO_2RR, although the exact location and configuration of the immobilized catalyst (in the strong interfacial electric field close to the electrode surface) will still exert a strong impact on catalyst performance.[25] The supported catalyst systems are complex and still not fully understood (*i.e.* how the catalyst molecule resides on the surface of a support), but from an experimental point of view it is, nevertheless, encouraging that the CO_2RR activity can be tuned using specific functional group modification of the support.[23,26,27]

2.2.2 Methods for Immobilization of Molecular Catalysts

Three main strategies are widely applied for the immobilization of catalysts on electrode surfaces, *i.e.* physical adsorption (which is non-covalent), chemical bonding, and integration into three-dimensional (3-D) porous frameworks as described below.

Physical adsorption. By exploiting π–π (Figure 2.2a) and/or other electrostatic interactions (Figure 2.2b) molecular catalysts can be physisorbed on electrodes with[19,24,28,29] or without[30–32] additional support. A profound advantage of using this approach is its simplicity; it can be carried out using simple dipping procedures. In addition, it requires no special

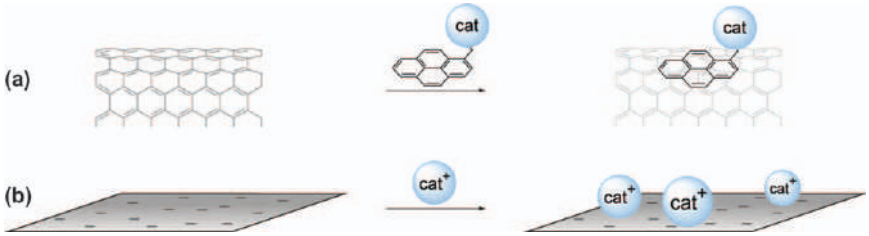

Figure 2.2 (a) Physisorption of a catalyst exploiting π–π stacking between a pyrene-appended catalyst and a CNT support. (b) Physisorption of a catalyst exploiting the electroctrostatic interaction between a positively charged catalyst [*e.g.* a pendant $-N(CH_3)_3^+$ group] and a negatively charged support material consisting of *e.g.* graphene or graphite.

functionalization of either the catalyst or electrode, while giving, in general, a good electronic communication between the catalyst and conductive support. On the other hand, physically adsorbed molecular catalysts easily suffer from electrode surface detachment due to the weakness of the interaction forces.[23]

The selectivity observed for homogeneous catalysts is usually retained once heterogenized[33,34] but exemptions are found. For example, among a series of metal porphyrin (MTPP) and metal phthalocyanine (MPc) catalysts (see Figure 2.5 in Section 2.3), the activity was observed to be strongly influenced by the identity of the metal (M = Fe, Ni, or Co). While in the homogeneous case, Fe-centered catalysts were better reductants than their Ni and Co counterparts,[35,36] the order was reversed once the catalysts were immobilized in the supported case with the Co complexes being the better ones.[30,37] This finding of opposite activity orders for the same catalyst series suggests that the interaction between the immobilized catalyst and its support may override the intrinsic activity order. In fact, it may even change the mechanism as seen in a study of CoTPP (**Co4**, Figure 2.5) where the active species changed from Co^0 in the homogeneous CO_2RR to Co^I in the supported case.[35]

A great advantage of using the physisorption approach is the ease by which catalyst loading can be tuned to span a range from a few to hundreds of nmol cm^{-2}.[28] Furthermore, its effect on catalysis metrics can be tentatively rationalized.[19,38] Yet, a precise control of the catalyst dispersion is difficult to accomplish due to the non-covalent nature of electrostatic interactions which certainly are less specific than chemical bonding would be. In particular, catalyst stacking can become a serious issue by hindering the mass transport of CO_2 to the covered catalysts. As such, this compromises the performance of the immobilized catalysts for CO_2RR, in that high catalyst loadings can give a high current density with a low TOF and low loadings can give a low current density with a high TOF.[32,34,35] Furthermore, the description of the reaction system becomes much more complicated, especially at high catalyst loadings, making it difficult to extract reliable

kinetic parameters.[32] In some instances, it may even affect the product selectivity as seen for physically adsorbed Mn–bipyridine complexes.[38] While CO was found to be the dominant product at high catalyst loading because of the formation of dimeric Mn^0 species, formate became the primary product at low loading due to a preferential generation of the monomeric Mn–hydride (see the further discussion of this example in Section 2.4).

Cyclic voltammetry is an excellent technique for determining the surface concentration of immobilized molecular catalysts, at least if the voltammetric response is easily discernible from the background signal. In one such example, a pyrene-appended iron triphenyl porphyrin bearing six pendant OH groups on the phenyl rings (**Fe3**, Figure 2.5) was immobilized on CNTs and further deposited on a glassy carbon electrode.[39] In voltammetric experiments, the amount of electroactive surface catalyst was assessed by integrating the charge at the level of the Fe^{III}/Fe^{II} wave. Electroactive surface concentration varied from $\sim 2.5 \times 10^{-8}$ to $\sim 10^{-9}$ mol cm^{-2}, depending on the initial concentration of the porphyrin solution used when preparing the electrode. The film remained active over a long electrolysis time, *i.e.* after 12 h, and TON = 813 was obtained (TOF = 0.02 s^{-1}) with a catalytic selectivity of 85% for the CO_2-to-CO conversion.

In another work, a simple and facile self-assembly method was demonstrated by π–π stacking/electrostatic interaction for the fabrication of a porphyrin/graphene framework (FePGF) composed of iron 5,10,15,20-tetra(4′-*N,N,N*-trimethylanilinium)porphyrin (**Fe2**, Figure 2.5) and reduced liquid crystalline graphene oxide. This framework was utilized for the electrocatalytic reduction of CO_2 to CO on a glassy carbon electrode in an aqueous electrolyte.[24] In addition, a high surface area carbon fiber paper was used as the substrate for the FePGF catalyst, resulting in an enhanced current density of 1.68 mA cm^{-2} with 98.7% CO faradaic efficiency at $\eta = 430$ mV for 10 h, corresponding to TOF = 2.9 s^{-1} and TON = 104 400. In this case, the redox peaks were somewhat ill-defined and accompanied by large capacitive currents. Moreover, the TOF and TON numbers were derived on the basis that only 3.5% of the catalyst molecules were assessed to be active. Nevertheless, the huge difference in TOFs of the above two systems using a similar molecular catalyst underlines the crucial role of the immobilization strategy. Note also in this context that the electrochemically active surface area, *i.e.* the area accessible to the electrolyte, can be obtained from a measurement of the capacitive current as a function of scan rate.[30]

Chemical bonding. Molecular catalysts can be covalently bonded to electrodes if the catalyst and/or the electrode are modified with specific functional groups, such as aryldiazonium,[40,41] amine,[41] alkynyl,[42,43] sulfonyl fluoride,[44,45] phosphonic acid,[46,47] or thiol (Figure 2.3).[25] A profound advantage of the direct chemical bonding created in surface reactions is the robust linkage that it imparts between the catalyst and the electrode.[34,40] Unfortunately, the catalyst loading on the surface usually becomes low (0.005–0.5 nmol cm^{-2}) because most surface modifications provide a monolayer of catalyst.[40,42,43,46] However, the aryldiazonium electrografting

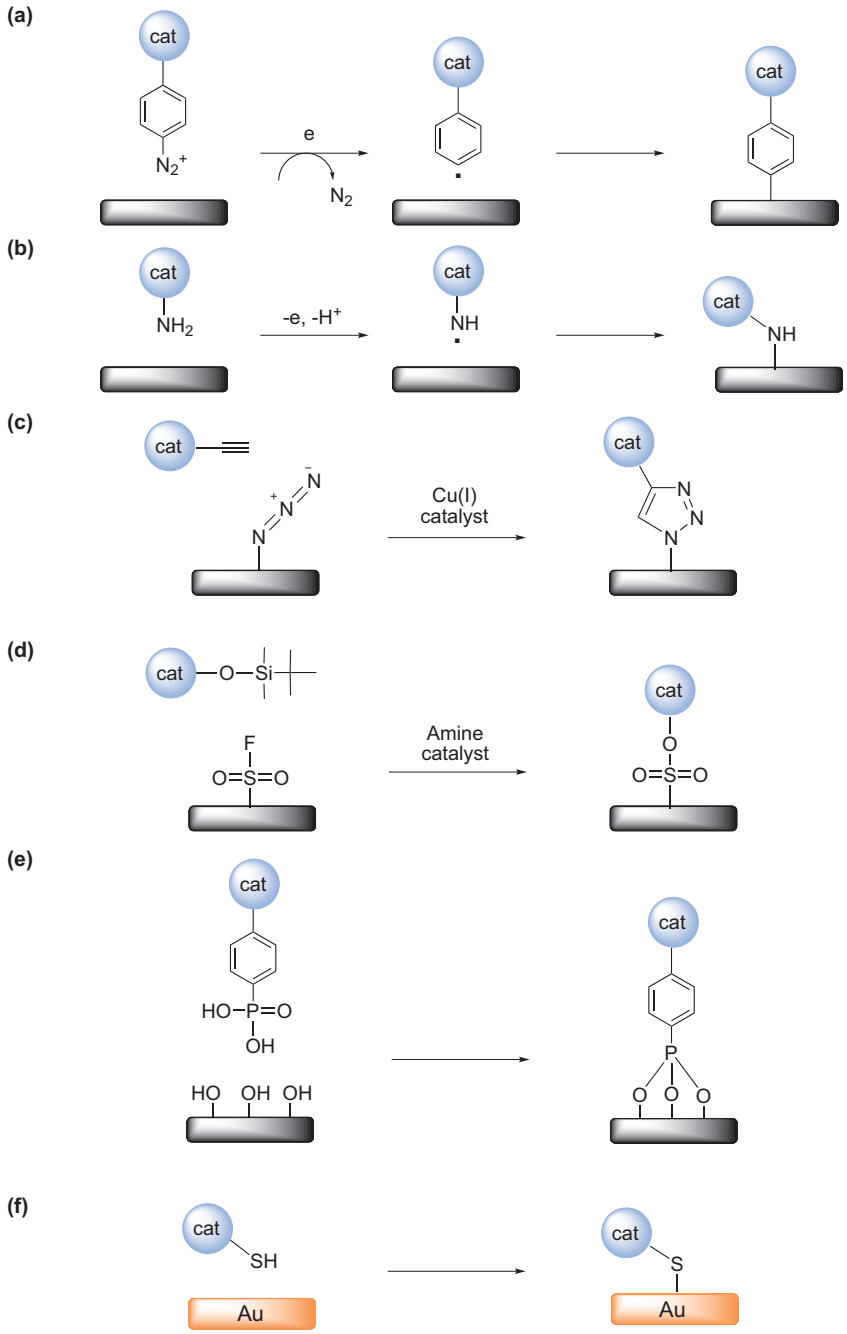

Figure 2.3 Various ways of functionalizing surfaces using (a) aryldiazonium salts, (b) alkyl amines, (c) click chemistry involving alkynes on already azide-modified surfaces, (d) sulfur–fluoride exchange reaction, (e) phosphonic acid in a hydrolysis process, and (f) self-assembly of thiols on gold.

approach can be used to generate a multilayered catalyst film (>10 nmol cm^{-2}),[41] although a substantial fraction of the catalyst molecules will appear electrochemically inactive because of the insulating character of the obtained film. For these reasons, directly bonded catalysts usually show low activity,[40,42,46] low selectivity,[40,42] and/or poor stability[40] for CO_2RR.

A valuable approach to significantly increase the current density and the selectivity for CO_2RR is to use a high-surface (porous) conductive material to bind the molecular catalyst.[17] In this way, catalyst loading can be increased by as much as 10–100 times, while facilitating the transport of both CO_2 and electrolyte to the catalytic sites to enhance the overall electron transfer rate. Similarly to what is observed for physically adsorbed catalysts, catalyst stacking may occur at high loading to make some of the immobilized catalysts electrochemically inactive for CO_2RR.[46] Thus, a too high catalyst loading can result in a lower TOF, even if the current density becomes larger (*e.g.* FeTPP/SnO_2 *vs.* FeTPP).[46] One solution to alleviate catalyst stacking is to adhere the molecular catalysts to the electrode through the metal center *via* chemical bonds,[34] instead of the usual ligand site.[46–48] In this way, a loading of CoTPP as high as 84.8 nmol cm^{-2} with good dispersion could be accomplished, while seeing an increase in both the current density and TOF.[34] Obviously, the electron transfer process is facilitated by the shortened distance from the support to the metal center. In addition, both the catalyst stability and product selectivity were improved compared with the ligand-bound[42] and physically adsorbed CoTPP.[35] A good catalyst stability is imperative for long-term electrolyses and for accomplishing a successful scale-up at a later point. One particularly interesting idea in this respect is to exploit catalyst self-healing to achieve high TONs.[49]

Along these lines, transparent porous conductive or semi-conductive supports have been developed to build up devices with photoelectrodes, or to couple electrochemical measurements to spectroscopy. Meso-nanoporous indium–tin oxide (ITO) is the most used material. Anchoring molecular catalysts relies on physisorption[50] or chemisorption taking advantage of phosphoryl groups[51,52] but may also be obtained *via* covalent attachment through diazonium chemistry.[53] *In situ* IR has been used in homogeneous CO_2 reduction to reveal the nature of the intermediates. Until now, *in situ* Raman spectroscopy was not considered for immobilized molecular catalysts, although it has been used for other heterogeneous catalysts.[54]

3-D frameworks. Electropolymerisation has proven to be a useful strategy to deposit polymer films of high surface densities.[55,56] The fact that the film is directly grown on the electrode surface ensures, at the same time, a close electrochemical contact between the film and electrode.[57] Electropolymerization of metal porphyrins and phthalocyanines from their amine-containing analogues are thought to be formed *via* an oxidative, polyaniline-type mechanism.[58,59] Heterogenized CuPc monomers and polymers were found to produce methyl formate and CO when using methanol as the solvent.[60] It is unknown to what extent demetallation of CuPc to form Cu nanoparticles[61] has occurred. Electropolymerized films of cobalt

tetrakis(4-aminophenyl)porphyrin were reported to reduce CO_2 to CO with 65% FE in ionic liquids.[62] Similarly, electropolymerized films of cobalt tetraaminophthalocyanine produced exclusively formic acid in perchloric acid electrolytes.[63]

In another study, an iron-porphyrin catalyst was immobilised inside a 3D microporous CO_2 absorbing material.[64] Specifically, this was done by carrying out an oxidative electropolymerisation on glassy carbon or ITO electrodes of pendant carbazole substituents chemically linked to the iron porphyrin. The iron–porphyrin unit served as the electrocatalyst as well as the mediator for the electron hopping process occurring across the polymer film. The prepared films showed electrocatalytic activity for CO_2RR, but the stability of the as-anchored electrocatalyst was not sufficiently good enough for long-term use.

Other important members of 3-D structured frameworks include covalent organic and metal-organic frameworks (COFs or MOFs, respectively).[65–71] Beneficial features of these systems include the lack of requirement for an additional support material, the excellent exposure of active sites to the electrolyte and CO_2 (because of the high porosity), and the possibility of structurally modifying the catalyst and/or the organic linker to tune the electronic character of the active sites. In general, COF materials exhibit relatively high activity for CO_2RR with improved electron transfer and mass transport characteristics. This is due to the fact that catalyst molecules are integrated into an extended porous conjugated lattice,[57,65] although the rather low conductivity measured in the case of a CoTPP based COF ($\sim 10^{-6}$ S cm^{-1}) should be noted.[57] In comparison, the FeTPP and CoTPP based MOF materials show moderate catalytic activity and selectivity[65,66] due to the poor efficiency of the electron hopping between neighboring metal sites of the non-conjugated material.[66] Most MOFs have a conductivity as low as that of the COFs, unless specifically designed chemical structures are used to alleviate this shortcoming.[72] An alternative approach to achieve a better catalytic performance consists of mixing the MOF-based catalysts with conductive carbon materials.[72,73] For regular polymers the conditions are very much the same.[74,75] A promising strategy to improve conductivity consists of post-synthetic carbonization of COFs.[76] However, the integrity of the molecular catalyst moiety and its electronic coupling with the conductive phase may be questioned and in this sense the obtained material is not a true molecularly supported film.

Finally, from an analysis point of view, it may be noted that fluorine-doped tin oxide (FTO) is a widely used substrate to deposit electrocatalyst-containing frameworks on top to record *in situ* UV–vis spectra while varying the applied potential.[65,66] In this manner, it was possible to observe the reduction of Co^{II} to Co^{I} under reductive polarization to substantiate that Co^{I} is the active species during CO_2RR. *In situ* X-ray absorption measurements could also probe the oxidation state change of Co^{II} to Co^{I}.[57] More generally, coupling X-ray absorption techniques to electrochemical catalytic systems, including supported molecular catalysts, holds great promise for *in situ* and

in operando studies. This not only achieves insight into the catalytic processes but also insight into the degradation processes. In fact, this is an overlooked, yet essential aspect of mechanistic studies, and there is little doubt that such studies will attain much more focus in upcoming years.

2.2.3 Single-atom Catalysts: Bridging Molecular Supported Catalysis and Electrocatalysis

An emerging topic related to supported molecular catalysis is single-atom catalysts (SACs), with the catalysis originating from single metal atoms dispersed in usually carbon materials (Figure 2.4).[77] SACs are able to show maximum atom-utilization efficiency (ideally 100%)[77] with an enhanced activity[78] compared to their bulk or nanoscale counterparts. These typically mimic the metal porphyrin structure and exhibit distinct activity and improved stability for CO_2RR due to the specific interaction between the metal center and a conductive porous material.[37,79,80] In principle, these atoms are expected to behave as single catalytic sites with a well-defined coordination environment, yet the strong electronic coupling of the dispersed atoms with the material electronic states prevents defining a standard potential. At least, this is so, unless a charge can be localized on the SAC thanks to strong interaction of the resulting species with an ion crossing the double layer for charge neutralization.[81] Thus, exploring the links (similarities, differences, borderline cases) between supported molecular catalysts and SACs would be beneficial for the progress of both fields.[82]

The enormous potential of using SACs, supported on nitrogen-doped carbon materials, for electrochemical CO_2RR has sparked a huge interest in this area.[79,83,84] From a product selectivity point of view, the SACs[37,79,83,84] all mainly show high selectivity for the conversion of CO_2 to CO. In spite of the progress, many challenges exist in the study of SACs for CO_2 reduction.

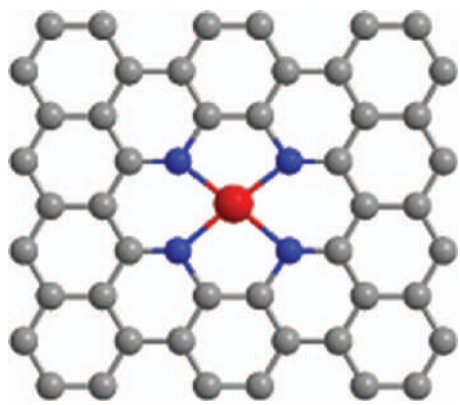

Figure 2.4 SAC with M–N_4 structure in a carbon scaffold achievable from high-temperature synthesis (M, N, and C shown as red, blue and grey balls, respectively).

From a synthesis and structural point of view, the SACs supported on carbon materials have all been prepared by high-temperature synthesis (800–1000 °C), featuring structures with the metal atom coordinated with varying numbers of nitrogen/carbon atoms.[85] The high-temperature synthesis makes it possible to modify the structure of the SACs, by introducing dopants to improve the catalytic activity. However, the precise control of the coordination environment of the central metal atoms is highly challenging,[86] as little knowledge has been acquired on how the atoms of the carbon scaffold are reorganized at high temperature. Furthermore, the complexity of the SAC structures (no selectivity to a specific type of structure during high-temperature synthesis) makes the understanding of the real active sites and the catalytic process for CO_2 reduction challenging. In that regard, investigation of model systems such as graphite–phenazine modified electrodes is useful.[81,87] A further discussion of several aspects regarding both supported molecular catalysts and SACs is given in Section 2.3.

2.3 Characterization and Performance of Assemblies

Most of these supported systems have been characterized from electrolysis experiments in H-cell configuration with CO_2 simply dissolved in the electrolyte solution, and very few detailed analyses of the current responses using cyclic voltammetry or rotating ring disk voltammetry techniques have been done. Such detailed mechanistic analyses that would lead to intrinsic properties of the supported catalysts are thoroughly described in Section 2.4. Therefore, and in that sense, the reported performances are empirical, and even the most active systems are typically limited by diffusion of the substrate and not by intrinsic catalytic activity, with recent exceptions related to the insertion of supported molecular catalysts in flow cells.[88–91]

An additional difficulty lies in the fact that determining the exact electrocatalytically active fraction of the molecules in the film is a difficult task, leading to underestimated values of turnover numbers and turnover frequencies in many cases (in favorable practical cases, a non-catalytic redox wave of the catalyst allows one to determine the electrochemically active concentration which is often significantly smaller than the total catalyst concentration added in the film).[28] Moreover, very few analyses of the degradation over time of the catalytic systems have been performed, leaving unanswered the question of rationally tuning the catalyst structure to improve performances. Even in the most stable systems reported to date, stability does not last for more than one day. It should also be noted that a last pitfall arises from possible structural change of the supported catalysts, which then turns out to be a pre-catalyst leading, for example, to nanoparticle formation in the deposited film, as is the case with Cu porphyrin deposited at carbon paper. Upon electrolysis, copper particles are formed and convert CO_2 to various products including methane and ethylene, a degradation process that was not identified in the original publication.[92] These limits being identified, many interesting systems have since been

characterized, with the use of the classical metrics described in Section 2.1, including current densities j (relatively to the geometric surface of the supporting electrode), TON and TOF at a given overpotential η, and the apparent energy efficiency [faradaic efficiency $\times$ ($\Delta E^{\circ\prime}/\Delta E_{cell}$), where $\Delta E^{\circ\prime}$ is the apparent standard potential difference between the anodic and cathodic reactions and ΔE_{cell} is the actual cell overall voltage]. These data allow for some comparison between systems even if meaningful benchmarking would require detailed mechanistic studies.

An exhaustive description of the recent catalyst performances is beyond the scope of this chapter; reviews may be consulted for further information.[93] Among the emblematic examples that have been alluded to in Section 2.2 and that will be discussed in detail in Section 2.4, Co phthalocyanines (**Co1**-**Co3**, Figure 2.5) have been thoroughly investigated since the 70s,[94] and immobilized at carbon surfaces for CO_2RR in water since the 80s.[95] These catalysts can efficiently convert CO_2 to CO in close to neutral aqueous solutions, with selectivity ranging from 90–98%. Immobilization strategies at carbon materials such as nanotubes or particles, and based on either non-covalent (electrostatic, π–π interactions) linkage, covalent or periodic immobilization (porous organic polymers, metal–organic frameworks) have been investigated for variously substituted catalysts (*e.g.* **Co1**–**Co3**, Figure 2.5). Partial current density j_{CO} up to 18 mA cm^{-2} (maximum TOF 6.8 s^{-1}) was obtained with typical electrolysis potentials ranging from -0.61 to -0.68 *vs.* RHE (which corresponds to overpotential values ranging from 475 to 540 mV, respectively), where E (V *vs.* RHE) = E (V *vs.* SCE) + 0.244 + 0.059×pH, and the pH value is between 6.8 and 7.3. The most efficient system was obtained with **Co3** simply absorbed to carbon nanotubes at a low loading of 14.4 nmol cm^{-2}.[90] Once deposited at a gas diffusion electrode (GDE, carbon paper) inserted into a flow cell, this catalyst led to a j_{CO} up to 165 mA cm^{-2} (94% FE) at η = 810 mV in basic conditions (pH 14).[90] Note that post-electrolysis examination of the GDE upon X-ray absorption technique [Co K-edge XANES (X-ray Absorption Near Edge Structure) spectroscopy] showed no degradation of the catalyst.

This later example illustrates that results obtained in H-cell configuration, even with the most efficient molecular catalysts, are limited by mass transport phenomena. But it also opens a broad range of opportunities to use molecular catalysts at an industrially relevant rate for CO production. Other typical cobalt catalysts include porphyrins (*e.g.* **Co4** and **Co5**, Figure 2.5). Protoporphyrin **Co5** showed particularly interesting features once covalently grafted to carbon nanotubes by a substitution reaction at the metal center, leading to j_{CO} = 25 mA cm^{-2} (FE 98.3%) at an overpotential of 490 mV (pH 7.3) with TOF = 1.9 s^{-1}.[96] Another state-of-the art cobalt catalyst is the quaterpyridine complex **Co6** (Figure 2.6) which, in similar pH conditions than **Co5**, gave j_{CO} = 20 mA cm^{-2} (FE 100%) at an overpotential of 440 mV and a TOF = 12 s^{-1}.[28] Regarding iron catalysts, 5,10,15,20-tetra(4′-*N,N,N*-trimethylanilinium)porphyrin **Fe2** (Figure 2.5) immobilized at a graphene-based hydrogel electrode led to a partial current density *ca.* 2 mA cm^{-2} for

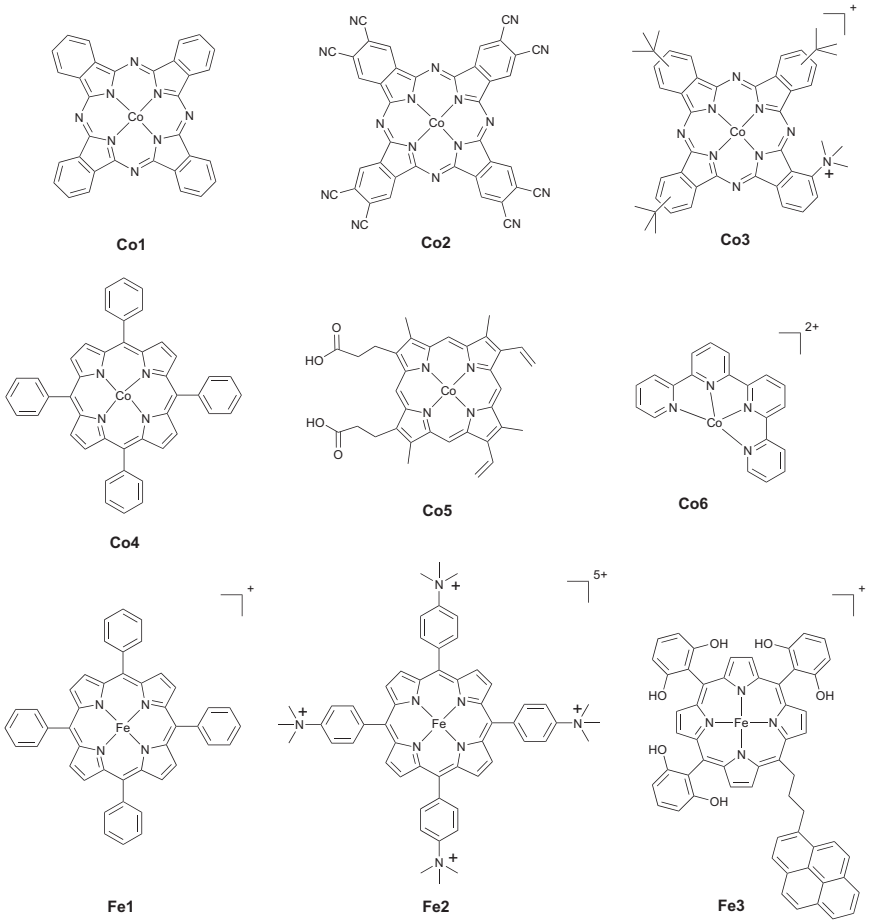

Figure 2.5 Typical Co and Fe substituted phthalocyanines, porphyrins, and quaterpyridine complexes that have been inserted into thin films as molecular supported catalysts for CO_2RR in water.

CO production (FE 95%) at $\eta = 430$ mV, with a TOF of 2.5 s^{-1}.[29] When the catalyst was mixed with carbon black, deposited at a carbon paper electrode (GDE) and further included in a flow cell, the performances significantly increased providing $j_{CO} = 152$ mA cm^{-2} (>98% selectivity) at an overpotential of 470 mV in basic solution (pH 14).[91] In the same conditions, a current density of 27 mA cm^{-2} could be sustained for 24 h at an overpotential of only 50 mV and with close to perfect 99.7% selectivity. At close to neutral pH (7.3), a maximum current density of 83.7 mA cm^{-2} was obtained (FE 98%).

All these examples exclusively gave CO as a reaction product. Very few examples led to the formation of formate with high selectivity. An Ir based pincer complex has been recently reported with FE 93% and a relatively large current density of 3.3 mA cm^{-2} (TOF = 7.4 s^{-1}), although at a large overpotential (790 mV) in a 0.1 M $NaHCO_3$ solution (pH 6.8).[97]

Finally, there is only a rare example where CO_2 could be reduced with more than 2 electrons and 2 protons with convincing evidence that the product indeed originates from carbon dioxide. A recent example concerns the simple phthalocyanine **Co4** which was absorbed in multi-wall carbon nanotubes (MWCNT) and then deposited onto carbon paper.[98] The electrochemical reduction of both CO_2 and CO affords MeOH with a maximum FE efficiency of 14% (pH 13) and $j_{MeOH} = 0.68$ mA cm^{-2} ($E = -0.64$ V *vs.* RHE). Formaldehyde was clearly identified as an intermediate in this process, and labeled experiments showed that both CO, formaldehyde and CH_3OH originate from CO_2.[98,99] The molecular nature of the catalysis was further demonstrated by XANES (X-ray Absorption Near-Edge Structure) spectroscopy. Shortly after, the use of highly dispersed **Co4** at MWCNT was shown to improve the catalytic activity for methanol, with FE up to 44% at -0.94 V *vs.* RHE (pH 6.8).[100] These remarkable examples clearly indicate that molecular catalysts are not restricted to the formation of either CO or formate. Therefore, it calls for thorough mechanistic investigation to understand the observed reactivity and improve the structure of the catalyst on a rational basis. The fact that no such reactivity has been observed with any of the numerous homogeneous catalysts transforming CO_2 into CO suggests an important role of the support as already mentioned in Section 2.2.

2.4 Toward Kinetic and Mechanistic Characterization of Supported Systems

2.4.1 Introduction

The mechanistic information on molecular catalysis of CO_2 electroreduction has been so far mainly obtained in organic solvents with the catalyst dissolved in the solution (homogeneous systems, see Chapter 1). This information has been gathered from electrochemical measurements in well-defined hydrodynamics conditions as well as *via* spectro-electrochemical measurements and sometimes with the help of theoretical calculations or spectroscopic studies (including the use of Raman, IR, and X-ray techniques). Moving to supported systems, extraction of mechanistic information from kinetic measurements (current densities, FE as a function of electrode potential, electron transfer, mass transport, *etc.*) may become more difficult because various situations can be met depending on the catalyst immobilization mode, on the support structure as well as on the cell configuration (H-cell *vs.* flow cell). It is obviously not tractable to provide an exhaustive description of actual experimental systems which would result in multiple unknown adjustable parameters. The strategy to gain insights into mechanism and kinetic control of the systems is to consider a simplified description enabling one to pull out the main factors controlling the catalytic response. An H-cell configuration where the substrate (CO_2) is dissolved in the bulk solution is considered as it is the most common set-up

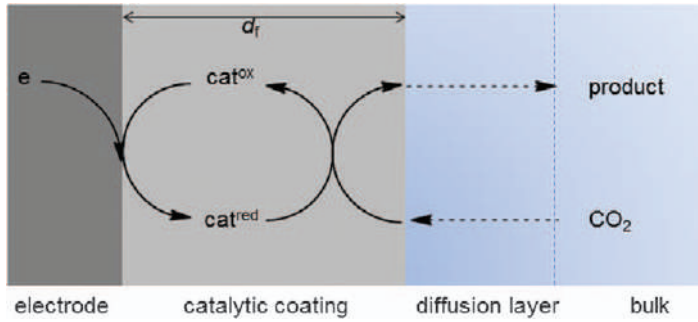

Figure 2.6 Coated electrode scheme showing the bulk solution, the diffusion layer and the coating layer where catalysis takes place.

in reported studies so far.[101] Specificities related to flow cell reactors more suitable for practical applications are discussed in Section 2.4.4. Prior to the review of the existing CO_2 electroreduction systems in Section 2.4.3, we present some general considerations regarding kinetic control of catalysis of electrochemical reactions by a supported molecular catalyst (Section 2.4.2).

2.4.2 General Considerations for Kinetic Analysis of Supported Systems

We consider the electrode configuration depicted in Figure 2.6, *i.e.* an underlying conductive electrode coated by a porous support with a molecular catalyst attached to it, and a solution with a dissolved substrate (CO_2) of which the concentration in the bulk is constant. Putting aside selectivity and assuming a monomolecular catalytic mechanism, which is likely for a supported catalyst, the reactivity of the system is characterized by an apparent limiting rate constant k_{cat} (s^{-1}) for the reduction of CO_2 by the reduced catalyst. It includes the effects of possible co-substrates assumed to be in large excess so that k_{cat} is a function of substrate concentration $[CO_2]_{bulk}$ and co-substrate concentrations. Mechanistic investigations seem to be only relevant if the molecular catalyst is "good" enough so that the corresponding apparent limiting rate constant is large, meaning that, in the context of cyclic voltammetry, $k_{cat}/(FV/RT) \gg 1$. The maximal current density at a large overpotential is given by eqn (2.1)

$$I_{max} = \frac{i}{S_{geom}} = nF\Gamma_{cat}k_{cat} \tag{2.1}$$

where n is the stoichiometric factor of transferred electrons ($n = 2$ for CO_2 conversion to CO or formate) and $\Gamma_{cat} = d_f \times C_{cat}$ is the surface concentration of catalyst (d_f is the film thickness and C_{cat} is the volumic concentration of catalyst in the electrode coating). Measurement of this maximal current

while knowing Γ_{cat} and n should, in principle, be a way to get access to k_{cat} and to extract mechanistic information *via* evaluation of co-substrate reaction orders. Note that we have assumed the reaction to be first-order in CO_2.

However, reaching this maximal current density is not an easy task due to several possible limitations. Among those we do not discuss here are electrode inhibition and catalyst deactivation although these are important issues in practice. As already mentioned, we also do not consider in this general discussion limitation by co-substrates, although it has to be kept in mind that co-substrates can play an important role.[102] Hence the remaining reasons for the maximal current not to be reached are (i) a catalyst standard potential being too negative so that, according to Nernst law, all catalyst molecules cannot be activated within the accessible potential window, (ii) slow charge transport within the support, (iii) substrate (CO_2) mass transport limitation within the coated catalytic film and/or within the solution. We will now successively discuss these various effects.

(i) It is trivial but important to recall that molecular catalysts are characterized by a standard potential E° that pins the onset of the catalytic current. The value of this standard potential may be different from the homogeneous counterpart and hence should be determined to enable mechanistic investigation.[35] In the absence of concurrent reactions (hydrogen evolution reaction for example), running cyclic voltammetry in the absence of CO_2 allows one to obtain several pieces of key information: the total catalyst loading Γ_{cat}, the catalyst standard potential and the kinetics for electron transfer between the catalyst and the conductive support.[39,57] If the latter is fast, then according to Nernst law, the active (reduced) form of the catalyst is given by eqn (2.2):

$$\Gamma_{red} = \Gamma_{cat} \Big/ \left(1 + \exp\left(\frac{F(E - E^\circ)}{RT}\right)\right) \tag{2.2}$$

The maximal activity can only be reached when $\Gamma_{red} \approx \Gamma_{cat}$ at $E \ll E^\circ$. At lower overpotential, extraction of the apparent rate constant from the measured current requires deconvolution from the applied potential effect.

(ii) The main difference between homogeneous catalysis and supported catalysis is that in the latter case, molecular catalysts are immobile. Hence, activation of the catalyst *via* its reduction enabling its reaction with CO_2 requires either the catalyst to be in direct contact with the conductive support, or a hopping electron transfer process to be at work to transport charges. This hopping process can occur between catalyst molecules themselves or *via* an additional redox species.

Two limiting behaviors depicted in Figure 2.7 can be delineated to appreciate the effect of charge transport on the catalytic response, noting that in real systems an intermediate situation can be encountered. The first case corresponds to a non-conductive film support, *e.g.* a porous polymeric

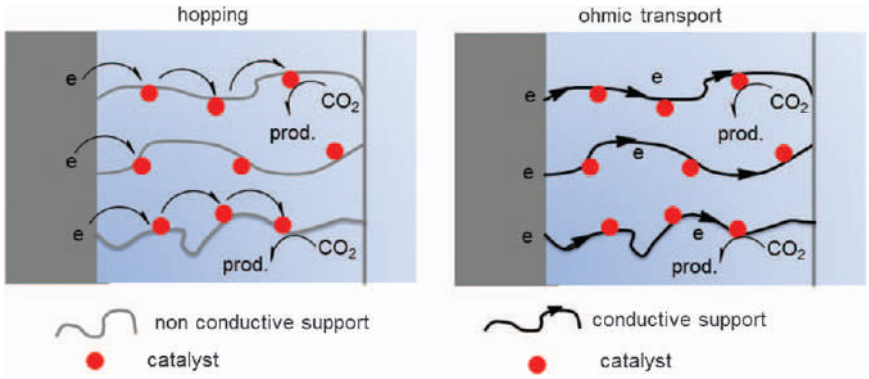

Figure 2.7 Charge transport in catalytic films. Left: electron transport *via* hopping between molecular catalytic sites. Right: ohmic electron transport *via* a conductive support.

framework permeated by the electrolyte, where charge transport is carried out *via* hopping between adjacent catalytic redox sites.[66] It has been shown that it is equivalent to a diffusional transport of charges characterized by an apparent diffusion coefficient D_e. Therefore, in the framework of fast catalysis and no substrate or co-substrate mass transport limitation, the current-potential response of the catalytic system is governed by the dimensionless parameter $d_f/\sqrt{D_e/k_{cat}}$.[103] For small values of this parameter, charge transport has no effect and all molecular catalysts are active at a large overpotential leading to the maximal current density. Alternatively, for large values of this parameter, thick films, and/or a slow hopping process, a diffusion-reaction thickness develops in the film and only a fraction of the catalyst molecules can be activated. This leads to a maximal current density which is jointly controlled by the catalytic rate and charge transport. In such a situation, the current density is independent of film thickness. Knowing D_e is required to extract the catalytic rate constant from electrochemical measurements and gain mechanistic information.

The second limiting situation corresponds to an electronically conductive support with all molecular catalysts in electronic connection with that support *via* chemical or physical immobilization.[39] Although conductive, the film support may present a substantial resistivity and therefore all catalysts do not experience the same electrical potential. Such a situation may be modeled as a transmission line with molecular catalysts distributed along the pores.[104] This leads to an ohmic drop effect on the rising (potential dependent) part of the catalytic response (no effect on the plateau current). It has been shown that it ultimately corresponds to an apparent slow electron transfer kinetic control (Tafel plot slope of 120 mV per decade). Unfortunately, ohmic drop correction is not an easy task due to the transmission line type configuration. Consequently, to avoid misinterpretation of current-potential data, a careful characterization of conduction properties of the

film, both electronic conduction in the support and ionic conduction in the pores is thus a safe precaution prior to any mechanistic investigation of catalytic films.

(iii) As CO_2 solubility in solvent is limited, in particular in water, substrate mass transport interference in the kinetic control of the current density is difficult to avoid experimentally as the apparent rate constant might be in most cases first-order in substrate, *i.e.* $k_{cat} = k[CO_2]_{bulk}$. Due to the cell configuration considered here, usually referred to as H-cell configuration (Figure 2.6), mass transport in both the film pores and the solution have to be envisioned. Therefore, current-potential data have to be gathered in well-defined hydrodynamics conditions. This is readily achieved in cyclic voltammetry or rotating disk electrode voltammetry. Steady-state measurements can also be obtained *via* constant stirring of the solution and kinetic information can be extracted if the corresponding constant diffusion layer thickness has been duly determined. In the framework of fast electron transport in the catalytic film, fast catalysis and no mass transport limitation by co-substrates, the influence of substrate mass transport can be analyzed in cyclic voltammetry by considering two dimensionless parameters according to eqn (2.3)

$$d_f \sqrt{D_{out} F v / RT / D_{in}} \quad \text{and} \quad D_{in} / \left(d_f^2 \, k \, C_{cat} \right) \tag{2.3}$$

where $C_{cat} = \Gamma_{cat} \times d_f$ and D_{out} and D_{in} are the substrate diffusion coefficients in the solution and in the film respectively.[105] A zone diagram can thus be drawn (Figure 2.8) showing that in the right part [zones R^{canon}, $(R+S)^{can}$ and SR^{can}] S-shaped cyclic voltammograms (CVs) are expected due to the absence of mass transport in the solution. The distinct characteristics of the three zones [R, (R + S) and SR] arise from interference of mass transport in the film or not as sketched by representation of substrate concentration profiles in Figure 2.8. Slow mass transport in the film induces a thin diffusion-reaction layer (SR zones) making only the catalysts close to the film/solution interface active. Maximal solution mass transport limitation is observed in the left lower part of the diagram [zones R^{tot}, $(R+S)^{tot}$ and SR^{tot}] where peaked CVs are expected corresponding to total catalysis situations. Kinetic information can thus be gathered from the peak position rather than from the peak current. Similar analysis has been provided in the framework of steady-state techniques but interference of solution mass transport is less eye-catching as S-shaped CVs are expected in all situations.

The development of a diffusion-reaction layer in the right side of the film (close to the film/solution interface) due to mass transport limitation in the film is symmetrical from the development of a diffusion-reaction layer in the left side of the film (close to the underlying electrode/film interface) in the case of slow charge transport *via* a hooping process. In both cases increasing the film thickness does not improve catalysis as additional molecular catalysts are not activated. If both phenomena occur, then an

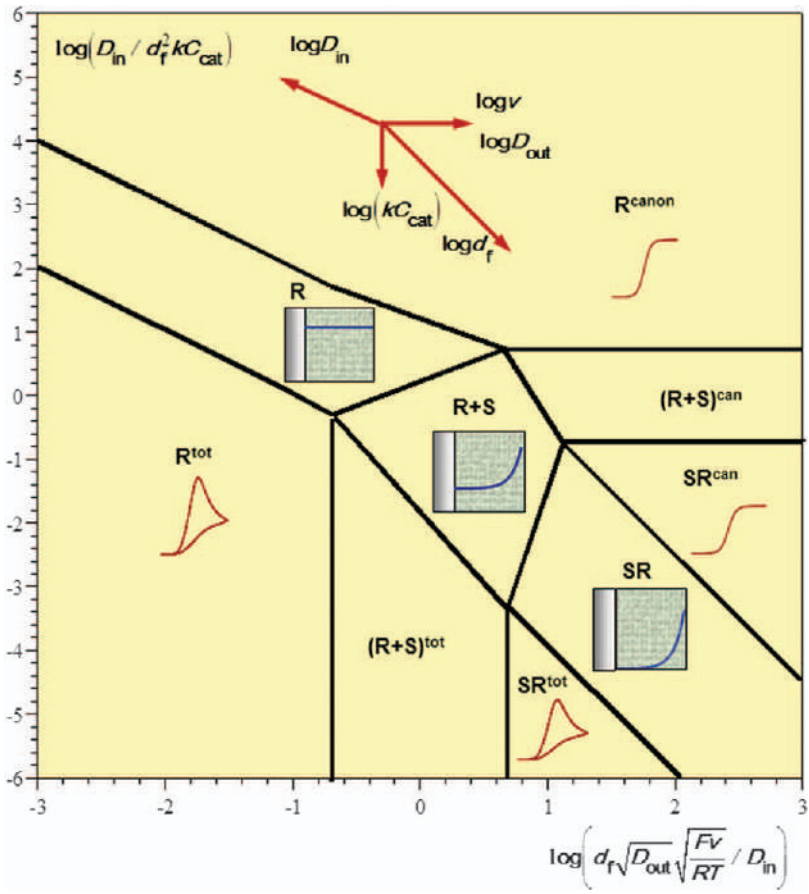

Figure 2.8 Zone diagram showing the various cyclic voltammetry behaviors for a heterogeneous catalytic system in pure kinetics conditions and fast electron transport. In the transition zones (R, R + S and SR), the concentration profile of the substrate (CO_2) is sketched in blue.

increase of the film thickness can be counterproductive as shown in a formal description.[106]

Finally, the above description considers that heterogenized catalysts behave as *molecular catalysts* meaning that they are characterized by a well-defined standard potential, *i.e.* they have orbitals not conjugated with the electronic states of the conductive material (Figure 2.9, right). Another situation might be encountered when the catalyst orbitals are part of the conductive material electronic states[107] and hence the *hybrid* catalyst behaves as a *catalytic site* (such as the SACs described in Section 2.2) as on a metallic electrocatalytic electrode. Redox features can then only be observed in the presence of a species (*e.g.* CO_2) able to bind to the site in concert with electron localization (Figure 2.9, left). As a consequence, in this situation the

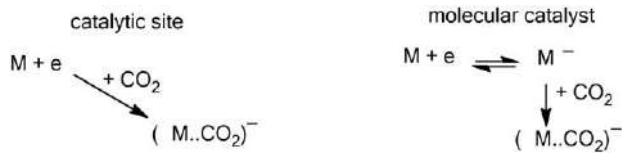

Figure 2.9 CO_2 initial reduction on a surface catalytic site (M) (left) or by a molecular reduced catalyst (M^-) (right).

initial steps of the catalytic process cannot be an EC type sequence as considered for a molecular catalyst and the relevant standard potential includes the substrate chemical potential.

2.4.3 Insights into Mechanisms for CO_2 Reduction

The general considerations discussed in the previous section are the important physico-chemical phenomena to consider when analyzing current-potential data for CO_2 electroreduction with supported molecular catalysts. However, these considerations do not take into account specific characteristics of CO_2 reduction. First of all, CO_2 electroreduction can lead to several products and be in competition with other reactions such as hydrogen evolution. As a consequence, the current density does not necessarily represent CO_2 reduction and product analysis is an indispensable complement to current-potential measurements. Besides it has to be kept in mind that product selectivity may be partially governed by mass transport. Hence the hydrodynamic regime used in quantitative product detection experiments should match the hydrodynamic regime used in the mechanistic analysis unless the FE toward a single product is very high which is a common situation for molecular catalysts.

Among the reasons to move from homogeneous molecular catalysts to supported catalysis is that practical applications are best envisioned in an aqueous environment, either *via* an aqueous catholyte or humidified gaseous CO_2, where solubility of molecular catalysts is problematic. As a consequence of running CO_2 electroreduction in an aqueous environment some specific characteristics of CO_2 aqueous system have to be considered when extracting kinetic data and obtaining mechanistic insight. We first note that, although solubility of CO_2 in water is limited (~34 mM), it does not govern the position of the system in the zone diagram (Figure 2.8). However, it sets the maximal current density reachable for a given cell hydrodynamic configuration. Apparition of a peak shaped CV is probably indicative of current limitation by CO_2 mass transport as observed with a hybrid Co quaterpyridine (**Co6**, Figure 2.5) complex/carbon nanotube assembly.[28] Nonetheless, the framework used for the establishment of the zone diagram in Figure 2.8 corresponds to a simplified situation that does not take into account homogeneous reactions involving CO_2. A thorough

description should include the various reactions at play summarized in Table 2.1. CO_2 hydration produces quite a strong acid H_2CO_3 ($pK_a = 3.6$) which may serve as a substrate for a competitive HER reaction as most molecular catalysts are competent for both CO_2RR and HER.[110] However, this hydration reaction is kinetically slow, hence limiting this deleterious competing reaction. More importantly, CO_2 electroreduction requires protons, except for oxalate formation, therefore producing conjugated bases (H_2O, HCO_3^-, CO_3^{2-} or HO^-) which eventually makes the local environment more basic and favors homogeneous CO_2 consumption in a non-productive way: the more so the higher the current density.[111] This phenomenon can be described as a weak buffering effect of the CO_2/carbonic acid/bicarbonate/carbonate system. Introduction of an additional buffer, typically phosphate at pH ~ 7, to moderate local pH increase may unfortunately trigger competitive HER. This was shown *via* the investigation of one of the scarce molecular catalyst soluble in water, namely iron 5,10,15,20-tetra(4′-*N,N,N*-trimethylanilinium)porphyrin[112] (**Fe2**, Figure 2.5) that was subsequently physically immobilized in a Nafion film in the presence of carbon powder.[113]

Only a handful of molecular catalysts has been studied in the framework of supported catalysis for CO_2 reduction. We will review here the mechanistic information gathered on a few of them, namely cobalt porphyrin (CoTPP: **Co4**, Figure 2.5), iron porphyrin (FeTPP: **Fe1**, Figure 2.5), cobalt phthalocyanine (CoPc: **Co1**, Figure 2.5), manganese bipyridine (Mnbpy, Figure 2.10) and cobalt quaterpyridine (Coqpy: **Co6**, Figure 2.5), and we will try to obtain information from existing experimental data.

In the early studies of immobilization of cobalt porphyrin on electrodes in the 90s to convert CO_2 into CO[114,115] it was recognized that aggregation of

Table 2.1 CO_2 aqueous system homogeneous reactions.

Reaction	K	k_f
hydration reactions[a]		
$CO_2 + H_2O \rightleftharpoons H_2CO_3$	1.7×10^{-3}	$0.03^{b,c}$
$CO_2 + HO^- \rightleftharpoons HCO_3^-$	4.27×10^{7}	2.2×10^{3} [d,e]
acid-base reactions[c]		
$H_2CO_3 + H_2O \rightleftharpoons H_3O^+ + HCO_3^-$	2.51×10^{-4}	2.51×10^{6} [b]
$HCO_3^- + H_2O \rightleftharpoons H_3O^+ + CO_3^{2-}$	4.8×10^{-11}	0.48^{b}
$HCO_3^- + HCO_3^- \rightleftharpoons H_2CO_3 + CO_3^{2-}$	1.9×10^{-7}	1.9×10^{3} [d]
$H_2CO_3 + OH^- \rightleftharpoons HCO_3^- + H_2O$	2.5×10^{10}	10^{10} [d]
$HCO_3^- + OH^- \rightleftharpoons CO_3^{2-} + H_2O$	4.8×10^{3}	10^{8} [d]
$2\ H_2O \rightleftharpoons H_3O^+ + OH^-$	10^{-14}	10^{-4} [d]

[a]Bulk concentrations of species in 0.1 M $NaHCO_3$ solution under a CO_2 atmosphere: $[CO_2] = 0.038$ M; $[H_2CO_3] = 6.5\times10^{-5}$ M; $[HCO_3^-] = 0.1$ M; $[CO_3^{2-}] = 2.9\times10^{-5}$ M.
[b]In s^{-1}.
[c]Ref. 108.
[d]In $M^{-1}\,s^{-1}$.
[e]Ref. 109.

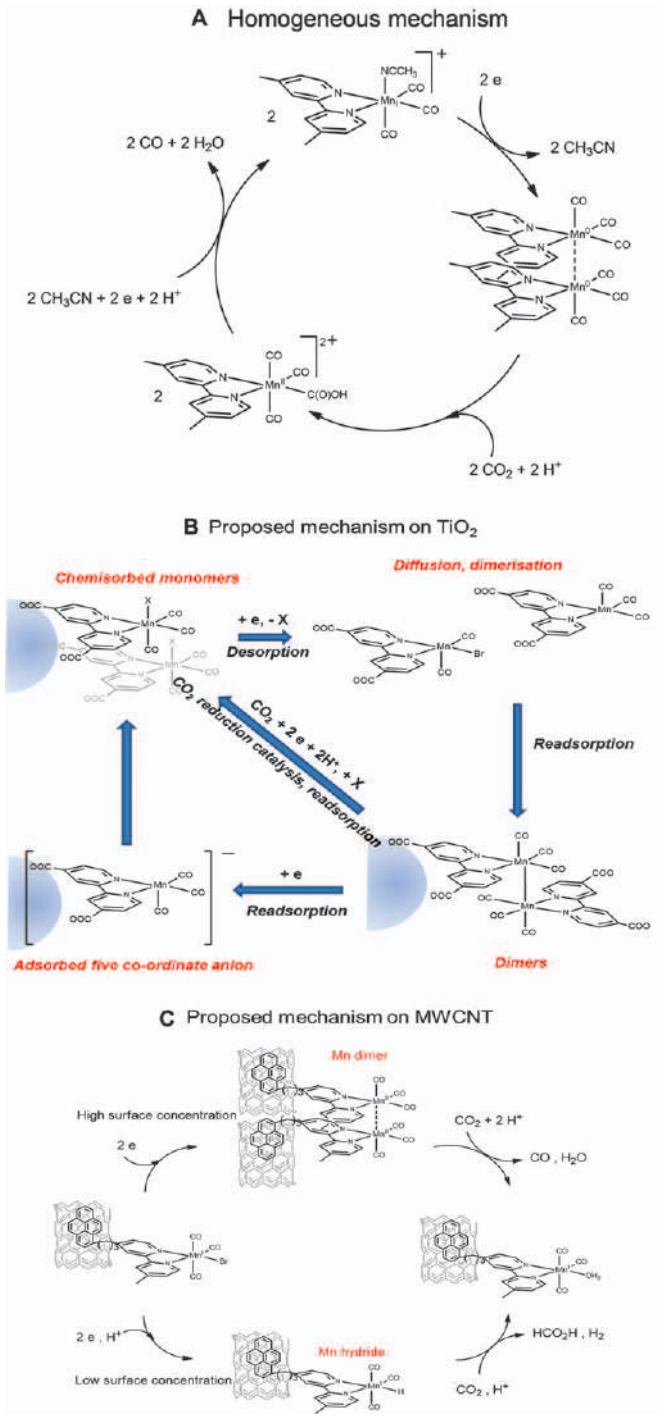

Figure 2.10 Mechanisms of CO_2 reduction by a $Mn(bpy)(CO)_3Br$ catalyst. Adapted from ref. 125, 127 and 128.

the catalyst *via* π–π stacking was an issue maybe limiting transport of CO_2 within the catalyst film (*i.e.* very small D_{in} in the framework of the zone diagram in Figure 2.8).[116] It is thus suggested that isolation of catalyst centers is required to get insights into intrinsic reactivity. This drawback of physically adsorbed catalyst aggregation is confirmed by the saturation of CO production rate upon increasing surface coverage Γ_{cat} of CoTPP on carbon material.[35] Nonetheless, it is shown that physically adsorbed CoTPP seems to exhibit a different reactivity than CoTPP in solution as it is proposed that the active form of the catalyst is Co(I)TPP rather than Co(0)TPP. The very highly reported Tafel plot slope (255 mV per decade) is difficult to interpret. In another study,[26] it is postulated that the peculiar reactivity of physically adsorbed CoTPP is due to specific interactions with the conductive support. This hypothesis is supported by experimental results showing that nitrogen atoms embedded in graphene increase the activity of a deposited CoTPP *via* an increase of the electron density of cobalt atoms. This strong electronic interaction between the catalyst and the conductive support then opens the question on whether this type of assembly should be viewed as molecular catalysis or electrocatalysis, *i.e.* description of the catalytic process *via* molecular catalyst *vs.* catalytic site (Figure 2.9). A more detailed mechanistic investigation of similar assemblies (CoTPP physically adsorbed on carbon) reveals at low overpotential and low loading (to avoid aggregation) a 120 mV per decade Tafel plot slope together with a first kinetic order in CO_2 and zero order in bicarbonate.[117] Taken together these results suggest that the rate determining step is a reduction of the catalyst (Co(II)TPP/Co(I)TPP couple) concerted with adsorption of the substrate (CO_2) on the catalyst. It is an indication that physically adsorbed CoTPP behaves as a catalyst site electronically embedded in the support conductive material and not as a molecular catalyst (Figure 2.9; concerted pathway as the rate determining step). However, we note that the ohmic drop due to uncompensated resistance in the film porosity might also result in a 120 mV per decade Tafel slope and a first order in CO_2.[104] Such an ambiguity does not exist when the same molecular catalyst, CoTPP, is chemically bound to the conductive support *via* a linker breaking the electronic communication between the catalyst orbitals and the support electronic states. With a phenylene linker, a peak is clearly observed in cyclic voltammetry suggesting interference of mass transport, presumably of CO_2; in steady state conditions a large Tafel plot slope (455 mV per decade) is measured and interpreted as a chemical step kinetic limitation while interference of mass transport cannot be excluded as hydrodynamic conditions are unknown.[118] Using a different bonding strategy, *via* oxygen atoms on carbon nanotubes (CNTs) allowing binding a cobalt protoporphyrin (**Co5**, Figure 2.5), a monolayer of catalyst is obtained and interestingly results similar to physically adsorbed catalysts are obtained (127 mV per decade Tafel slope, first order in CO_2, zero order in bicarbonate).[96] The same conclusion can thus be made: kinetic control is either due to a concerted inner-sphere electron transfer or due to ohmic drop convoluted molecular type

catalysis. This reveals that in depth knowledge of both charge transport in the film and electronic communication between CNT and the catalyst are required to get a definitive conclusion on the mechanism at work for CoTPP catalysts supported on conductive materials.

The same molecular catalyst has also been immobilized as part of three-dimensional assemblies: COF,[57] MOF,[65] or polyoxometalate-metal organic framework (PMOF).[73] These assemblies allow one to avoid slow diffusion in the film. However, small electronic conductivity ($D_e = 2\times10^{-12}$ cm^2 s^{-1}) is a serious limitation probably as the source of the large Tafel plot slope with COF and MOF and even the linear current density-potential plot with PMOF. The same observation was made when iron porphyrins are part of three-dimensional assemblies: $D_e = 5\times10^{-13}$ cm^2 s^{-1} and 188 or 175 mV per decade Tafel plot slope (from ref. 66, 119 and 75, respectively). Iron porphyrins have also been immobilized on carbon supports either *via* covalent bonding[34] or physical adsorption *via* an appended pyrene group[39] but so far no mechanistic information is available, except that catalysis seems to be triggered at the Fe(I)TPP/Fe(0)TPP couple as in homogeneous catalysis. It is interesting to note that it is at variance with CoTPP where physically adsorbed CoTPP behaves differently from homogeneous CoTPP. As described above, such a discrepancy might be due to the specific electronic interaction between the catalyst and the conductive support when the catalyst is physically adsorbed *via* the orbitals of the reactive site and thus induce a behavior similar to M-N-C SACs.[37,83]

Whereas homogeneous CoPc is a poor molecular catalyst for CO_2 electroreduction, it was shown that deposited onto pyrolytic graphite or carbon cloth it can produce CO upon electrode polarization together with a large amount of hydrogen.[120] With no surprise, as in the case of cobalt porphyrins, the nature of the support and its interaction with the catalyst molecule has to be considered to discuss and categorize catalytic properties of CoPc in the CO_2-to-CO conversion. When immobilized on a poly-vinylpyridine polymeric film, CoPc behaves as a molecular catalyst but it is observed that the selectivity (CO *vs.* H_2) is improved.[121] The polymeric structure prevents aggregation of the CoPc catalyst and electron transport, presumably *via* hopping, which appears to be fast as a surface wave is observed for the $CoPc^+$/CoPc couple. The presence of pyridine is proposed to bolster the nucleophilic properties of the cobalt atom and the polymeric environment was shown to influence proton transport which occurs through proton relays rather than *via* diffusion in the film.[122]

CoPc has also been dispersed on oxygen-functionalized carbon paper and produces almost exclusively CO.[32] Upon increasing the catalyst loading (from $5\times10^{-12} - 10^{-7}$ mol cm^{-2}), the TOF calculated assuming a canonical behavior (*i.e.* no interference of electron transport or substrate/cosubstrate transport, R^{canon} zone in Figure 2.8) is decreasing. It might be a consequence of catalyst aggregation equivalent to decreasing D_{in}. However, focusing on low catalyst coverage, it is reported that the current density is first order in CO_2, zero order in bicarbonate and exhibits a Tafel plot slope of 120 mV per

decade. Hence, we can question the molecular behavior and rather consider it to be site behavior. The reaction orders change at high bicarbonate concentrations (from 1 to 0.6 for CO_2 and from zero to 1.4 for bicarbonate). Interpretation of these effects requires carefully taking into account homogeneous equilibria (Table 2.1) that set the concentrations in solution. As an illustration, electrolysis of a highly concentrated bicarbonate solution under a nitrogen atmosphere can produce CO, as equilibrium allows a substantial CO_2 concentration to be reached.[123]

A quasi-hybrid system was designed by making a conformal polymerized CoPc layer on CNT while avoiding catalyst aggregation.[74] The measured 120 mV per decade Tafel plot slope suggests an electron transfer rate-determining step but the hybrid character of the system cannot be formally confirmed as the CO_2 reaction order was not determined. Direct sonication of CoPc in the presence of CNT leads to a hybrid system *via* presumably strong π–π interaction between catalyst molecules and CNT.[19] The hybrid character of the system is in part revealed *via* modification of either the support (carbon black or reduced graphene oxide instead of CNT) or the catalyst (cobalt cyanophthalocyanine instead of cobalt phthalocyanine) inducing a change in reactivity. Using a similar architecture a steric modification of the catalyst macrocycle was shown to reduce aggregation and enhance catalytic activity *via* a decrease of substrate limitation through the catalytic film.[124] It is important to note here that aggregation of the molecular catalyst might induce a change of a site-type catalyst (only catalyst molecules hybridized with the conductive support) to a mixed situation where both site-type and molecular catalysts are operating, the latter being activated *via* a hopping charge transport.

Aside from macrocycle ligand type, other transition metal complexes have been investigated as the catalyst for CO_2 electroreduction and immobilized at the electrode. One of the most studied is a manganese bypiridine complex, $Mn(bpy)(CO)_3Br$ which selectively reduces CO_2 into CO *via* a well-established mechanism when used homogeneously in an organic solvent (Figure 2.10A).[125] Upon immobilization on a TiO_2 electrode *via* phosphonate groups, the mechanism *via* a dimer was first proposed to be retained for CO_2 electroreduction in acetonitrile based on spectroscopic evidence.[126] Later on, the mechanism was further investigated and this dimer mechanism was confirmed (Figure 2.10B) but was shown not to be the sole catalytic pathway.[127] $Mn(bpy)(CO)_3Br$ was also immobilized on CNT either *via* direct physical adsorption of the complex[128] or through an appended pyrene moiety[38] and studied as the catalyst for CO_2 electroreduction in water. Interestingly it was shown that the surface loading changes the selectivity from CO, being the product at high loading *via* a dimeric mechanism involving a desorption/re-adsorption process, to formate being the product *via* formation of a hybrid at low loading (Figure 2.10C). It is, however, puzzling to observe that, once covalently immobilized *via* diazonium reduction-type grafting the selected product is CO, and not formate, although a mechanism involving a desorption/re-adsorption process is not possible.[129]

As with other catalysts, the role of the interaction of molecular catalyst and the support is questionable and it has been reported that surface adsorbed K^+ ions provide a favorable environment when a Mn-complex catalyst was physically adsorbed on MWCNTs.[130] This emphasizes that mechanistic investigation of CO_2 electroreduction with supported catalysts should also include the role of the supporting electrolyte which sets the double-layer structure within which catalysis may take place if the system behaves as a site-type catalyst.

Cobalt polypyridine complexes have also been immobilized on electrode surfaces. Whereas cobalt terpyridine covalently attached to carbon surfaces leading to poor reactivity toward CO_2 reduction,[40] cobalt quaterpyridine immobilized in a Nafion film together with MWCNT is a selective and durable catalyst.[28] A 120 mV per decade Tafel plot slope indicates an electron transfer rate-limiting step at low overpotentials with the caveat that it is not known whether the catalyst is of molecular-type or site-type. At larger overpotentials a peak is observed in a cyclic voltammogram at a low scan rate indicating interference of mass transport but at a high scan rate an S-shaped type voltammogram is obtained indicating a limitation by a chemical step and/or a mixed control by a chemical step and substrate mass transport within the catalytic film.

2.4.4 Toward Improved Efficiency

From the above short overview of current data on CO_2 reduction with immobilized molecular catalysts, it appears that several parameters are critical in governing the current density, the overpotential and the faradaic efficiency. The first parameter is probably the control of the interaction between the conductive support and the catalyst, *i.e.* molecular catalysis *vs.* catalytic sites. The second one is the control of catalyst aggregation or dispersion which might induce mass transport limitation or change of selectivity.[100] Another parameter is the electronic conductivity of the catalytic coating (hopping *vs.* ohmic) which can be analyzed *via* deposition of the coating on interdigitated electrodes arrays[131,132] or using cyclic voltammetry.[104] Finally, mass transport and homogeneous reactions are prime factors in H-cell configuration if high current densities are targeted.[133] We note, however, that HER *vs.* CO_2RR competition is less critical with molecular catalysts as compared to metallic electrocatalysts as molecular catalysts are often intrinsically selective toward CO_2RR.

In an effort to circumvent mass transport limitation in H-cell configuration inherent to low CO_2 solubility in water, gas diffusion electrodes have been proposed for a long time[134] and have recently been reinvestigated[135,136] together with flow cell configurations,[137] as briefly described in Section 2.2. Nonetheless it has to be noted that increasing the CO_2 reduction rate induces increased production of hydroxide ions and hence sequestration of CO_2 *via* bicarbonate and carbonate formation (Table 2.1), thus decreasing the efficiency of CO_2 conversion.[138]

References

1. D. T. Whipple and P. J. A. Kenis, *J. Phys. Chem. Lett.*, 2010, **1**, 3451.
2. E. E. Benson, C. P. Kubiak, A. J. Sathrum and J. M. Smieja, *Chem. Soc. Rev.*, 2009, **38**, 89.
3. C. Costentin, M. Robert and J.-M. Savéant, *Chem. Soc. Rev.*, 2013, **42**, 2423.
4. C. Costentin, S. Drouet, M. Robert and J.-M. Savéant, *Science*, 2012, **338**, 90.
5. I. Azcarate, C. Costentin, M. Robert and J.-M. Savéant, *J. Phys. Chem. C*, 2016, **120**, 28951.
6. C. Costentin, M. Robert, J.-M. Savéant and A. Tatin, *Proc. Natl. Acad. Sci. U. S. A.*, 2015, **112**, 6882.
7. I. Azcarate, C. Costentin, M. Robert and J.-M. Savéant, *J. Am. Chem. Soc.*, 2016, **138**, 16639.
8. A. Khadhraoui, P. Gotico, B. Boitrel, W. Leibl, Z. Halime and A. Aukauloo, *Chem. Commun.*, 2018, **54**, 11630.
9. J. A. Keith, K. A. Grice, C. P. Kubiak and E. A. Carter, *J. Am. Chem. Soc.*, 2013, **135**, 15823.
10. K. T. Ngo, M. McKinnon, B. Mahanti, R. Narayanan, D. C. Grills, M. Z. Ertem and J. Rochford, *J. Am. Chem. Soc.*, 2017, **139**, 2604.
11. N. Elgrishi, M. B. Chambers and M. Fontecave, *Chem. Sci.*, 2015, **6**, 2522.
12. C. Cometto, L. J. Chen, P. K. Lo, Z. G. Guo, K. C. Lau, E. Anxolabehere-Mallart, C. Fave, T. C. Lau and M. Robert, *ACS Catal.*, 2018, **8**, 3411.
13. R. Francke, B. Schille and M. Roemelt, *Chem. Rev.*, 2018, **118**, 4631.
14. C. Costentin and J.-M. Savéant, *Nat. Chem. Rev.*, 2017, **1**, 0087.
15. C. Costentin, S. Drouet, G. Passard, M. Robert and J.-M. Savéant, *J. Am. Chem. Soc.*, 2013, **135**, 9023.
16. C. Costentin, S. Drouet, M. Robert and J.-M. Savéant, *J. Am. Chem. Soc.*, 2012, **134**, 11235.
17. X.-M. Hu, S. U. Pedersen and K. Daasbjerg, *Curr. Opin. Electrochem.*, 2019, **15**, 148.
18. R. M. Bullock, A. K. Das and A. M. Appel, *Chem. – Eur. J.*, 2017, **23**, 7626.
19. X. Zhang, Z. Wu, X. Zhang, L. Li, Y. Li, H. Xu, X. Li, X. Yu, Z. Zhang, Y. Liang and H. Wang, *Nat. Commun.*, 2017, **8**, 14675.
20. Q. Sun, S. Wang, B. Aguila, X. J. Meng, S. Q. Ma and F. S. Xiao, *Nat. Commun.*, 2018, **9**, 3236.
21. P. Kang, C. Cheng, Z. Chen, C. K. Schauer, T. J. Meyer and M. Brookhart, *J. Am. Chem. Soc.*, 2012, **134**, 5500.
22. S. Aoi, K. Mase, K. Ohkubo and S. Fukuzumi, *Chem. Commun.*, 2015, **51**, 10226.
23. Y. Y. Birdja, R. E. Vos, T. A. Wezendonk, L. Jiang, F. Kapteijn and M. T. M. Koper, *ACS Catal.*, 2018, **8**, 4420.

24. J. Choi, P. Wagner, R. Jalili, J. Kim, D. R. MacFarlane, G. G. Wallace and D. L. Officer, *Adv. Energy Mater.*, 2018, **8**, 1801280.
25. M. L. Clark, A. Ge, P. E. Videla, B. Rudshteyn, C. J. Miller, J. Song, V. S. Batista, T. Lian and C. P. Kubiak, *J. Am. Chem. Soc.*, 2018, **140**, 17643.
26. M. Zhu, C. Cao, J. Chen, Y. Sun, R. Ye, J. Xu and Y.-F. Han, *ACS Appl. Energy Mater.*, 2019, **2**, 2435.
27. J. Wang, X. Huang, S. Xi, J.-M. Lee, C. Wang, Y. Du and X. Wang, *Angew. Chem., Int. Ed.*, 2019, **58**, 13532.
28. M. Wang, L. Chen, T.-C. Lau and M. Robert, *Angew. Chem., Int. Ed.*, 2018, **57**, 7769.
29. J. Choi, J. Kim, P. Wagner, S. Gambhir, R. Jalili, S. Byun, S. Sayyar, Y. M. Lee, D. R. MacFarlane, G. G. Wallace and D. L. Officer, *Energy Environ. Sci.*, 2019, **12**, 747.
30. Z. Zhang, J. Xiao, X.-J. Chen, S. Yu, L. Yu, R. Si, Y. Wang, S. Wang, X. Meng, Y. Wang, Z.-Q. Tian and D. Deng, *Angew. Chem., Int. Ed.*, 2018, **57**, 16339.
31. N. Morlanés, K. Takanabe and V. Rodionov, *ACS Catal.*, 2016, **6**, 3092.
32. M. Zhu, R. Ye, K. Jin, N. Lazouski and K. Manthiram, *ACS Energy Lett.*, 2018, **3**, 1381.
33. N. Coutard, N. Kaeffer and V. Artero, *Chem. Commun.*, 2016, **52**, 13728.
34. A. Maurin and M. Robert, *Chem. Commun.*, 2016, **52**, 12084.
35. X.-M. Hu, M. H. Rønne, S. U. Pedersen, T. Skrydstrup and K. Daasbjerg, *Angew. Chem., Int. Ed.*, 2017, **56**, 6468.
36. I. Bhugun, D. Lexa and J.-M. Savéant, *J. Am. Chem. Soc.*, 1994, **116**, 5015.
37. X.-M. Hu, H. H. Hval, E. T. Bjerglund, K. J. Dalgaard, M. R. Madsen, M.-M. Pohl, E. Welter, P. Lamagni, K. B. Buhl, M. Bremholm, M. Beller, S. U. Pedersen, T. Skrydstrup and K. Daasbjerg, *ACS Catal.*, 2018, **8**, 6255.
38. B. Reuillard, K. H. Ly, T. E. Rosser, M. F. Kuehnel, I. Zebger and E. Reisner, *J. Am. Chem. Soc.*, 2017, **139**, 14425.
39. A. Maurin and M. Robert, *J. Am. Chem. Soc.*, 2016, **138**, 2492.
40. N. Elgrishi, S. Griveau, M. B. Chambers, F. Bedioui and M. Fontecave, *Chem. Commun.*, 2015, **51**, 2995.
41. C. F. Sun, L. Rotundo, C. Garino, L. Nencini, S. S. Yoon, R. Gobetto and C. Nervi, *ChemPhysChem*, 2017, **18**, 3219.
42. S. A. Yao, R. E. Ruther, L. Zhang, R. A. Franking, R. J. Hamers and J. F. Berry, *J. Am. Chem. Soc.*, 2012, **134**, 15632.
43. A. Zhanaidarova, C. E. Moore, M. Gembicky and C. P. Kubiak, *Chem. Commun.*, 2018, **54**, 4116.
44. J. Yatvin, K. Brooks and J. Locklin, *Angew. Chem., Int. Ed.*, 2015, **54**, 13370.
45. K. Brooks, J. Yatvin, M. Kovaliov, G. H. Crane, J. Horn, S. Averick and J. Locklin, *Macromolecules*, 2018, **51**, 297.
46. E. A. Mohamed, Z. N. Zahran and Y. Naruta, *Chem. Mater.*, 2017, **29**, 7140.

47. Y. Wang, S. L. Marquard, D. Wang, C. Dares and T. J. Meyer, *ACS Energy Lett.*, 2017, **2**, 1395.
48. M. Zhu, J. Chen, L. Huang, R. Ye, J. Xu and Y.-F. Han, *Angew. Chem., Int. Ed.*, 2019, **58**, 6595.
49. C. Costentin and D. G. Nocera, *Proc. Natl. Acad. Sci. U. S. A.*, 2017, **114**, 13380.
50. C. Renault, K. D. Harris, M. J. Brett, V. Balland and B. Limoges, *Chem. Commun.*, 2011, **47**, 1863.
51. Z. Chen, J. J. Concepcion, J. F. Hull, P. G. Hoertz and T. J. Meyer, *Dalton Trans.*, 2010, **39**, 6950.
52. A. Forget, B. Limoges and V. Balland, *Langmuir*, 2015, **31**, 1931.
53. Y. S. Kim, S. Fournier, S. Lau-Truong, P. Decorse, C. H. Devilliers, D. Lucas, K. D. Harris, B. Limoges and V. Balland, *ChemElectroChem*, 2018, **5**, 1625.
54. Y. C. Li, Z. Wang, T. Yuan, D.-H. Nam, M. Luo, J. Wicks, B. Chen, J. Li, F. Li, F. P. G. de Arquer, Y. Wang, C.-T. Dinh, O. Voznyy, D. Sinton and E. H. Sargent, *J. Am. Chem. Soc.*, 2019, **141**, 8584.
55. H. C. Hurrell, A. L. Mogstad, D. A. Usifer, K. T. Potts and H. D. Abruña, *Inorg. Chem.*, 1989, **28**, 1080.
56. D. L. Ashford, A. M. Lapides, A. K. Vannucci, K. Hanson, D. A. Torelli, D. P. Harrison, J. L. Templeton and T. J. Meyer, *J. Am. Chem. Soc.*, 2014, **136**, 6578.
57. S. Lin, C. S. Diercks, Y.-B. Zhang, N. Kornienko, E. M. Nichols, Y. Zhao, A. R. Paris, D. Kim, P. Yang, O. M. Yaghi and C. J. Chang, *Science*, 2015, **349**, 1208.
58. H. W. Li and T. F. Guarr, *J. Chem. Soc., Chem. Commun.*, 1989, 832.
59. A. Bettelheim, B. A. White and R. W. Murray, *J. Electroanal. Chem.*, 1987, **217**, 271.
60. T. V. Magdesieva, I. V. Zhukov, D. N. Kravchuk, O. A. Semenikhin, L. G. Tomilova and K. P. Butin, *Russ. Chem. Bull.*, 2002, **51**, 805.
61. Z. Weng, Y. S. Wu, M. Y. Wang, J. B. Jiang, K. Yang, S. J. Huo, X. F. Wang, Q. Ma, G. W. Brudvig, V. S. Batista, Y. Liang, Z. Feng and H. Wang, *Nat. Commun.*, 2018, **9**, 415.
62. D. Quezada, J. Honores, M. J. Aguirre and M. Isaacs, *J. Coord. Chem.*, 2014, **67**, 4090.
63. M. Isaacs, F. Armijo, G. Ramírez, E. Trollund, S. R. Biaggio, J. Costamagna and M. J. Aguirre, *J. Mol. Catal. A: Chem.*, 2005, **229**, 249.
64. X.-M. Hu, Z. Salmi, M. Lillethorup, E. B. Pedersen, M. Robert, S. U. Pedersen, T. Skrydstrup and K. Daasbjerg, *Chem. Commun.*, 2016, **52**, 5864.
65. N. Kornienko, Y. Zhao, C. S. Kley, C. Zhu, D. Kim, S. Lin, C. J. Chang, O. M. Yaghi and P. Yang, *J. Am. Chem. Soc.*, 2015, **137**, 14129.
66. J. E. Pander, III, A. Fogg and A. B. Bocarsly, *ChemCatChem*, 2016, **8**, 3536.
67. I. Hod, M. D. Sampson, P. Deria, C. P. Kubiak, O. K. Farha and J. T. Hupp, *ACS Catal.*, 2015, **5**, 6302.

68. C. S. Diercks, S. Lin, N. Kornienko, E. A. Kapustin, E. M. Nichols, C. Zhu, Y. Zhao, C. J. Chang and O. M. Yaghi, *J. Am. Chem. Soc.*, 2018, **140**, 1116.
69. H. Wu, M. Zeng, X. Zhu, C. Tian, B. Mei, Y. Song, X.-L. Du, Z. Jiang, L. He, C. Xia and S. Dai, *ChemElectroChem*, 2018, **5**, 2717.
70. C.-L. Yao, J.-C. Li, W. Gao and Q. Jiang, *Chem. – Eur. J.*, 2018, **24**, 11051.
71. X.-D. Zhang, S.-Z. Hou, J.-X. Wu and Z.-Y. Gu, *Chem. – Eur. J.*, 2020, **26**, 1604.
72. M. Ko, L. Mendecki and K. A. Mirica, *Chem. Commun.*, 2018, **54**, 7873.
73. Y.-R. Wang, Q. Huang, C.-T. He, Y. Chen, J. Liu, F.-C. Shen and Y.-Q. Lan, *Nat. Commun.*, 2018, **9**, 4466.
74. N. Han, Y. Wang, L. Ma, J. G. Wen, J. Li, H. C. Zheng, K. Q. Nie, X. X. Wang, F. P. Zhao, Y. F. Li, J. Fan, J. Zhong, T. P. Wu, D. J. Miller, J. Lu, S. T. Lee and Y. G. Li, *Chem*, 2017, **3**, 652.
75. P. T. Smith, B. P. Benke, Z. Cao, Y. Kim, E. M. Nichols, K. Kim and C. J. Chang, *Angew. Chem., Int. Ed.*, 2018, **57**, 9684.
76. P. Yin, T. Yao, Y. Wu, L. Zheng, Y. Lin, W. Liu, H. Ju, J. Zhu, X. Hong, Z. Deng, G. Zhou, S. Wei and Y. Li, *Angew. Chem., Int. Ed.*, 2016, **55**, 10800.
77. A. Q. Wang, J. Li and T. Zhang, *Nat. Rev. Chem.*, 2018, **2**, 65.
78. Z. Chen, E. Vorobyeva, S. Mitchell, E. Fako, M. A. Ortuño, N. López, S. M. Collins, P. A. Midgley, S. Richard, G. Vilé and J. Pérez-Ramírez, *Nat. Nanotechnol.*, 2018, **13**, 702.
79. H. B. Yang, S.-F. Hung, S. Liu, K. Yuan, S. Miao, L. Zhang, X. Huang, H.-Y. Wang, W. Cai, R. Chen, J. Gao, X. Yang, W. Chen, Y. Huang, H. M. Chen, C. M. Li, T. Zhang and B. Liu, *Nat. Energy*, 2018, **3**, 140.
80. J. Su, R. Ge, Y. Dong, F. Hao and L. Chen, *J. Mater. Chem. A*, 2018, **6**, 14025.
81. M. N. Jackson, S. Oh, C. J. Kaminsky, S. B. Chu, G. Zhang, J. T. Miller and Y. Surendranath, *J. Am. Chem. Soc.*, 2018, **140**, 1004.
82. X. Cui, W. Li, P. Ryabchuk, K. Junge and M. Beller, *Nat. Catal.*, 2018, **1**, 385.
83. T. N. Huan, N. Ranjbar, G. Rousse, M. Sougrati, A. Zitolo, V. Mougel, F. Jaouen and M. Fontecave, *ACS Catal.*, 2017, **7**, 1520.
84. Y. Pan, R. Lin, Y. Chen, S. Liu, W. Zhu, X. Cao, W. Chen, K. Wu, W.-C. Cheong, Y. Wang, L. Zheng, J. Luo, Y. Lin, Y. Liu, C. Liu, J. Li, Q. Lu, X. Chen, D. Wang, Q. Peng, C. Chen and Y. Li, *J. Am. Chem. Soc.*, 2018, **140**, 4218.
85. T. Wang, Q. Zhao, Y. Fu, C. Lei, B. Yang, Z. Li, L. Lei, G. Wu and Y. Hou, *Small Methods*, 2019, **3**, 1900210.
86. Y.-N. Gong, L. Jiao, Y. Qian, C.-Y. Pan, L. Zheng, X. Cai, B. Liu, S.-H. Yu and H.-L. Jiang, *Angew. Chem., Int. Ed.*, 2020, **59**, 2705.
87. N. D. Ricke, A. T. Murray, J. J. Shepherd, M. G. Welborn, T. Fukushima, T. Van Voorhis and Y. Surendranath, *ACS Catal.*, 2017, **7**, 7680.
88. X. Lu, Y. Wu, X. Yuan, L. Huang, Z. Wu, J. Xuan, Y. Wang and H. Wang, *ACS Energy Lett.*, 2018, **3**, 2527.

89. S. Ren, D. Joulié, D. Salvatore, K. Torbensen, M. Wang, M. Robert and C. Berlinguette, *Science*, 2019, **365**, 367.
90. M. Wang, K. Torbensen, D. Salvatore, S. Ren, D. Joulie, F. Dumoulin, D. Mendoza, B. Lassalle-Kaiser, U. Isci, C. P. Berlinguette and M. Robert, *Nat. Commun.*, 2019, **10**, 3602.
91. K. Torbensen, C. Han, B. Boudy, N. Von Wolff, C. Bertail, W. Braun and M. Robert, *Chem. – Eur. J.*, 2020, **26**, 3034.
92. Z. Weng, J. Jiang, Y. Wu, Z. Wu, X. Guo, K. L. Materna, W. Liu, V. S. Batista, G. W. Brudvig and H. Wang, *J. Am. Chem. Soc.*, 2016, **138**, 8076.
93. L. Sun, V. Reddu, A. C. Fisher and X. Wang, *Energy Environ. Sci.*, 2020, **13**, 374.
94. S. Meshitsuka, M. Ichikawa and K. Tamaru, *J. Chem. Soc., Chem. Commun.*, 1974, 158.
95. M. N. Mahmood, D. Massheder and C. J. Harty, *J. Appl. Electrochem.*, 1987, **17**, 1223.
96. M. Zhu, J. Chen, L. Huang, R. Ye, J. Xu and Y.-F. Han, *Angew. Chem., Int. Ed.*, 2019, **58**, 6595.
97. P. Kang, S. Zhang, T. J. Meyer and M. Brookhart, *Angew. Chem., Int. Ed.*, 2014, **53**, 8709.
98. E. Boutin, M. Wang, J. C. Lin, M. Mesnage, D. Mendoza, B. Lassalle-Kaiser, C. Hahn, T. Jaramillo and M. Robert, *Angew. Chem., Int. Ed.*, 2019, **58**, 16172.
99. T. Chatterjee, E. Boutin and M. Robert, *Dalton Trans.*, 2020, **49**, 4257.
100. Y. Wu, Z. Jiang, Y. Liang and H. Wang, *Nature*, 2019, **575**, 639.
101. N. Corbin, J. Zheng, K. Williams and K. Manthiram, *Nano Res.*, 2019, **12**, 2093.
102. J. S. Zheng, N. Corbin, K. Williams and K. Manthiram, *ACS Catal.*, 2020, **10**, 4326.
103. C. Costentin and J.-M. Savéant, *J. Phys. Chem. C*, 2015, **119**, 12174.
104. C. P. Andrieux, C. Costentin, C. Di Giovanni, J.-M. Savéant and C. Tard, *J. Phys. Chem. C*, 2016, **120**, 21263.
105. C. Costentin and J.-M. Savéant, *Phys. Chem. Chem. Phys.*, 2015, **17**, 19350.
106. C. Costentin and J.-M. Savéant, *ChemElectroChem*, 2015, **2**, 1774.
107. M. N. Jackson, S. Oh, C. J. Kaminsky, S. B. Chu, G. Zhang, J. T. Miller and Y. Surendranath, *J. Am. Chem. Soc.*, 2018, **140**, 1004.
108. C. Ho and J. M. Sturtevant, *J. Biol. Chem.*, 1963, **238**, 3499.
109. R. Pohorecki and W. Moniuk, *Chem. Eng. Sci.*, 1988, **43**, 1677.
110. T. Agarwal and S. Kaur-Ghumaan, *Coord. Chem. Rev.*, 2019, **397**, 188.
111. F. Zhang and A. C. Co, *Angew. Chem., Int. Ed.*, 2020, **59**, 1674.
112. C. Costentin, M. Robert, J.-M. Savéant and A. Tatin, *Proc. Natl. Acad. Sci. U. S. A.*, 2015, **112**, 6882.
113. A. Tatin, C. Comminges, B. Kokoh, C. Costentin, M. Robert and J.-M. Savéant, *Proc. Natl. Acad. Sci. U. S. A.*, 2016, **113**, 5526.

114. T. Atoguchi, A. Aramata, A. Kazusaka and M. Enyo, *J. Electroanal. Chem.*, 1991, **318**, 309.
115. (a) We note that CO is the commonly obtained production for CO_2 reduction with cobalt porphyrins whereas other products have been detected (e.g. methane) with a cobalt protoporphyrin; (b) J. Shen, R. Kortlever, R. Kas, Y. Y. Birdja, O. Diaz-Morales, Y. Kwon, I. Ledezma-Yanez, K. J. P. Schouten, G. Mul and M. T. M. Koper, *Nat. Commun.*, 2015, **6**, 8177.
116. H. Tanaka and A. Aramata, *J. Electroanal. Chem.*, 1997, **437**, 29.
117. M. Zhu, D.-T. Yang, R. Ye, J. Zeng, N. Corbin and K. Manthiram, *Catal. Sci. Technol.*, 2019, **9**, 974.
118. A. N. Marianov and Y. Jiang, *Appl. Catal. B*, 2019, **244**, 881.
119. B.-X. Dong, S.-L. Qian, F.-Y. Bu, Y.-C. Wu, L.-G. Feng, Y.-L. Teng, W.-L. Liu and Z.-W. Li, *ACS Appl. Energy Mater.*, 2018, **1**, 4662.
120. C. M. Lieber and N. S. Lewis, *J. Am. Chem. Soc.*, 1984, **106**, 5033.
121. W. W. Kramer and C. C. L. McCrory, *Chem. Sci.*, 2016, **7**, 2506.
122. Y. Liu and C. C. L. McCrory, *Nat. Commun.*, 2019, **10**, 1683.
123. T. Li, E. W. Lees, M. Goldman, D. A. Salvatore, D. M. Weekes and C. P. Berlinguette, *Joule*, 2019, **3**, 1487.
124. N. J. Choi, P. Wagner, S. Gambhir, R. Jalili, D. R. MacFarlane, G. G. Wallace and D. L. Officer, *ACS Energy Lett.*, 2019, **4**, 666.
125. M. Bourrez, M. Orio, F. Molton, H. Vezin, C. Duboc, A. Deronzier and S. Chardon-Noblat, *Angew. Chem., Int. Ed.*, 2014, **53**, 240.
126. T. E. Rosser, C. D. Windle and E. Reisner, *Angew. Chem., Int. Ed.*, 2016, **55**, 7388.
127. J. J. Walsh, M. Forster, C. L. Smith, G. Neri, R. J. Potter and A. Cowan, *Phys. Chem. Chem. Phys.*, 2018, **20**, 6811.
128. J. J. Walsh, G. Neri, C. L. Smith and A. Cowan, *Chem. Commun.*, 2014, **50**, 12698.
129. L. Rotundo, J. Filippi, R. Gobetto, H. A. Miller, R. Rocca, C. Nervi and F. Vizza, *Chem. Commun.*, 2019, **55**, 775.
130. S. Sato, K. Saita, K. Sekizawa, S. Maeda and T. Morikawa, *ACS Catal.*, 2018, **8**, 4452.
131. C. Costentin and D. G. Nocera, *J. Phys. Chem. C*, 2019, **123**, 1966.
132. C. E. D. Chidsey and R. W. Murray, *J. Phys. Chem.*, 1986, **90**, 1479.
133. B. A. Zhang, T. Ozel, J. S. Elias, C. Costentin and D. G. Nocera, *ACS Cent. Sci.*, 2019, **5**, 1097.
134. D. W. Dewulf and A. J. Bard, *Catal. Lett.*, 1988, **1**, 73.
135. L.-C. Weng, A. T. Bell and A. Z. Weber, *Energy Environ. Sci.*, 2019, **12**, 1950.
136. T. Burdyny and W. A. Smith, *Energy Environ. Sci.*, 2019, **12**, 1442.
137. D. M. Weekes, D. A. Salvatore, A. Reyes, A. Huang and C. P. Berlinguette, *Acc. Chem. Res.*, 2018, **51**, 910.
138. B. A. Zhang, C. Costentin and D. G. Nocera, *Joule*, 2019, **3**, 1565.

CHAPTER 3

Heterogeneous Electrochemical CO_2 Reduction

EZRA L. CLARK[a] AND ALEXIS T. BELL*[b]

[a] Surface Science and Catalysis (SurfCat), Department of Physics, Technical University of Denmark, 2800 Kgs. Lyngby, Denmark; [b] Department of Chemical and Biomolecular Engineering, University of California at Berkeley, Berkeley, CA 94720, United States
*Email: alexbell@berkeley.edu

3.1 Introduction

Extensive use of fossil fuels over the past century has led to the progressive accumulation of carbon dioxide (CO_2) in the atmosphere with significant consequences for the environment.[1,2] This situation can be mitigated by developing technologies that utilize renewable energy sources, such as wind and solar energies, to produce chemicals and fuels by recycling CO_2.[3,4] One approach to do this is the electrochemical reduction of CO_2. However, the amount of renewable electricity required to replace all carbon-based fossil fuels would significantly exceed that currently used for the production of grid power. Therefore, it is more reasonable to think that the electrochemical reduction of CO_2 would most likely be used first for the production of chemicals and subsequently for the production of carbon-based fuels for transportation modes that cannot be electrified, such as aviation and marine transport. However, the first step towards commercializing the electrochemical reduction of CO_2 is to understand the fundamentals of the process.

CO_2 reduction electrolyzers consist of an anode, a cathode, and an electrolyte, as shown in Figure 3.1. The oxygen (O_2) evolution reaction

Energy and Environment Series No. 28
Carbon Dioxide Electrochemistry: Homogeneous and Heterogeneous Catalysis
Edited by Marc Robert, Cyrille Costentin and Kim Daasbjerg

Published by the Royal Society of Chemistry, www.rsc.org

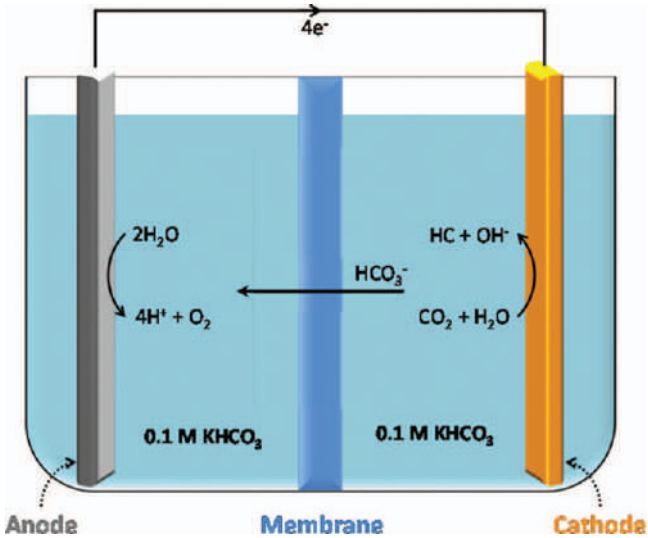

Figure 3.1 Simplified schematic of a CO_2 reduction electrolyzer.

($E^\circ = 1.23$ V *vs.* SHE) is typically performed over the anode electrocatalyst (eqn (3.1) and (3.2))

$$\text{Acid:} \quad 2H_2O \rightarrow O_2 + 4H^+ + 4e^- \tag{3.1}$$

$$\text{Base:} \quad 4OH^- \rightarrow O_2 + 2H_2O + 4e^- \tag{3.2}$$

Other oxidation reactions can also be conducted, such as chloride oxidation as shown in eqn (3.3) ($E^\circ = 1.36$ V *vs.* SHE) or wastewater (glucose) oxidation ($E^\circ = -0.01$ V *vs.* SHE) as shown in eqn (3.4)

$$2Cl^- \rightarrow Cl_2 + 2e^- \tag{3.3}$$

$$C_6H_{12}O_6 + 6H_2O \rightarrow 6CO_2 + 24H^+ + 24e^- \tag{3.4}$$

The advantage of these alternative oxidation processes is that they produce more economically valuable products and require lower oxidizing potentials than the O_2 evolution reaction. An external power supply, such as a photovoltaic device, is used to increase the electrochemical potential of the electrons liberated from the reducing agent so that they are sufficiently energetic to reduce CO_2 over the cathode electrocatalyst. A myriad of CO_2 reduction reactions can occur over the cathode electrocatalyst according to eqn (3.5)–(3.14).

$$\text{Acid:} \quad CO_2 + H^+ + 2e^- \rightarrow HCOO^- \tag{3.5}$$

$$CO_2 + 2H^+ + 2e^- \rightarrow CO + H_2O \tag{3.6}$$

$$CO_2 + 8H^+ + 8e^- \rightarrow CH_4 + 2H_2O \tag{3.7}$$

$$2CO_2 + 12H^+ + 12e^- \rightarrow C_2H_5OH + 3H_2O \tag{3.8}$$

$$2CO_2 + 12H^+ + 12e^- \rightarrow C_2H_4 + 4H_2O \tag{3.9}$$

$$\text{Base:}\quad CO_2 + H_2O + 2e^- \rightarrow HCOO^- + OH^- \tag{3.10}$$

$$CO_2 + H_2O + 2e^- \rightarrow CO + 2OH^- \tag{3.11}$$

$$CO_2 + 6H_2O + 8e^- \rightarrow CH_4 + 8OH^- \tag{3.12}$$

$$2CO_2 + 9H_2O + 12e^- \rightarrow C_2H_5OH + 12OH^- \tag{3.13}$$

$$2CO_2 + 8H_2O + 12e^- \rightarrow C_2H_4 + 12OH^- \tag{3.14}$$

To be effective, CO_2 reduction must also compete with the relatively facile H_2 evolution reaction (eqn (3.15) and (3.16)).

$$\text{Acid:}\quad 2H^+ + 2e^- \rightarrow H_2 \tag{3.15}$$

$$\text{Base:}\quad 2H_2O + 2e^- \rightarrow H_2 + 2OH^- \tag{3.16}$$

Aqueous electrolytes are used in most contemporary studies of CO_2 reduction. The pH of the aqueous electrolyte determines whether protons derived from water or water itself acts as the H source for CO_2 reduction over the cathode. As discussed below, there are also instances in which protons may derive from buffering anions (*e.g.*, HCO_3^-). If O_2 and CH_4 are evolved at the anode and cathode, respectively, the overall reaction can be written according to eqn (3.17).

$$CO_2 + 2H_2O \rightleftharpoons CH_4 + 2O_2 \tag{3.17}$$

The free energy of this reaction is 800.6 kJ mol^{-1}, which corresponds to a thermodynamic voltage requirement of 1.037 V.

Heterogeneously catalyzed CO_2 reduction involves both the cathode electrocatalyst and the electrolyte in the immediate vicinity of its surface. As a result, the properties of both the electrocatalyst and the electrolyte contribute to the activity and selectivity of heterogeneously catalyzed CO_2 reduction. This chapter illustrates how electrocatalyst composition and structure, electrolyte composition, and reaction conditions influence the activity and selectivity of heterogeneously catalyzed CO_2 reduction. We also discuss how these factors can be used to achieve optimal activity and product selectivity. Since a comprehensive review of the literature is not one of our objectives, we refer the reader to recent reviews and the references cited therein.[5–18]

3.2 Electrocatalyst

3.2.1 Aqueous CO_2 Chemistry

An electrolyte in equilibrium with dissolved CO_2 contains bicarbonate (HCO_3^-) and carbonate (CO_3^{2-}) anions produced by the reactions given in eqn (3.18) and (3.19).

$$CO_2 + H_2O \rightarrow HCO_3^- + H^+ \tag{3.18}$$

$$HCO_3^- \rightarrow CO_3^{2-} + H^+ \tag{3.19}$$

The acid-dissociation constants and the rate coefficients for these reactions are summarized in Table 3.1. While the conversion of CO_2 to HCO_3^-

Table 3.1 Acid-dissociation and kinetic rate constants for the formation of bicarbonate and carbonate anions.

Reaction	p*K*a	k (s^{-1})
$CO_2 + H_2O \rightarrow HCO_3^- + H^+$	6.37	0.0371
$HCO_3^- \rightarrow CO_3^{2-} + H^+$	10.25	59.44

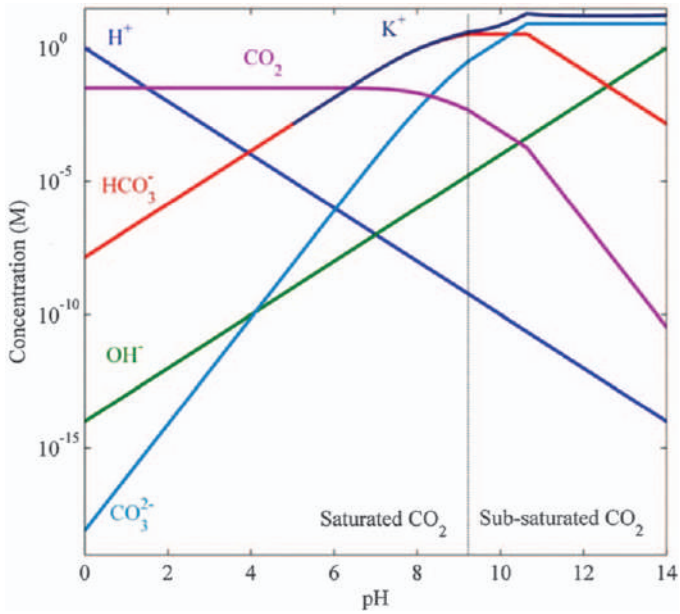

Figure 3.2 Speciation of an aqueous solution in equilibrium with 1 atm of CO_2 at 25 °C with an unbounded cation concentration.
Reproduced from ref. 19 with permission from the PCCP Owner Societies.

is a relatively slow reaction, the conversion of HCO_3^- into CO_3^{2-} rapidly equilibrates. Due to these reactions, the speciation of an aqueous solution in equilibrium with CO_2 depends on the bulk pH, as shown in Figure 3.2.[19] As the bulk pH of the solution increases, it becomes increasingly saline since a greater fraction of the dissolved carbon is present as HCO_3^- and CO_3^{2-} anions. The increased salinity of the solution reduces the concentration of dissolved CO_2 due to the "salting out" effect.[19] Furthermore, the bulk CO_2 concentration decreases precipitously above pH = 10.6 due to the precipitation of alkali carbonates. However, since the conversion of CO_2 into HCO_3^- is relatively slow, dissolved CO_2 can momentarily exist in relatively alkaline conditions.

Since an electrolyte in equilibrium with CO_2 contains several forms of dissolved carbon it is important to identify which of these species serves as the reactant during electrochemical CO_2 reduction. Experimental studies have concluded that only H_2 is evolved in carbonate and bicarbonate-based electrolytes saturated with an inert gas.[20,21] Conversely, a myriad of

"carbon"-containing products are evolved when the same electrolytes are saturated with CO_2. Thus, dissolved CO_2 serves as the reactant during electrochemical CO_2 reduction. Since CO_2 will react with hydroxide ions to form electrochemically inert HCO_3^- and CO_3^{2-}, CO_2 reduction cannot be performed continuously in highly alkaline electrolytes. Despite their irreducibility, HCO_3^- and CO_3^{2-} play critical roles during CO_2 reduction as both charge carriers and buffering species, as discussed later in the chapter.

3.2.2 Selectivity Trends

The CO_2 reduction activity of many transition and post-transition metals have been measured experimentally.[22–24] The selectivity trends observed in these studies are summarized in Figure 3.3. The majority of transition metals exhibit negligible activity for CO_2 reduction and only evolve hydrogen (H_2) in the presence of CO_2. However, H_2 evolution over these transition metals is significantly inhibited by the presence of CO_2, suggesting that they are poisoned by irreversibly bound CO_2-derived species. Late- and post-transition metals have exceptionally low H binding energies, which make them among the worst monometallic electrocatalysts for H_2 evolution.[25] As a result, most contemporary studies of CO_2 reduction have investigated electrocatalysts consisting of these elements. Several late-transition metals exhibit high selectivity for CO evolution while the post-transition metals exhibit high selectivity for $HCOO^-$ evolution. Most notably, Cu is the only

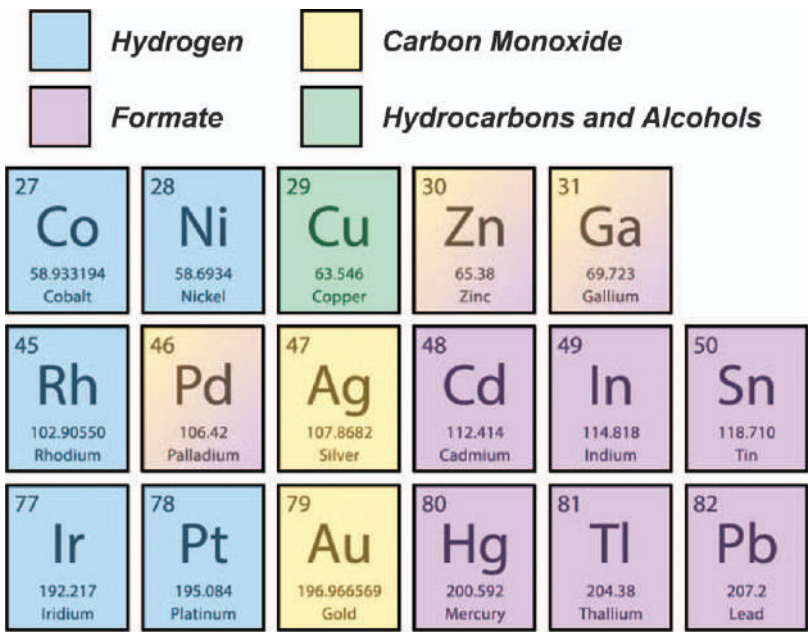

Figure 3.3 Periodic selectivity trends observed during CO_2 reduction over late- and post-transition monometallic electrocatalysts.

monometallic electrocatalyst that exhibits significant selectivity for hydrocarbon and alcohol evolution. The material properties that dictate these selectivity trends will be examined in the following sections.

3.2.3 Activating Carbon Dioxide

The simplest products of electrochemical CO_2 reduction are $HCOO^-$ and CO. As shown in Figure 3.4A, the CO evolution activity observed over monometallic electrocatalysts exhibits a volcano relationship when the *COOH adsorption energy is utilized as the activity descriptor.[26] *COOH binds to the electrocatalyst surface through the C atom. The plot exhibits a maximum since the formation energy of all reaction intermediates that bind to the electrocatalyst surface through the C atom will scale with the *COOH adsorption energy. At low *COOH adsorption energies the activation of CO_2 through the C atom is the rate-determining step (RDS), whereas at high *COOH adsorption energies the desorption of CO is the RDS. This relationship suggests that the relative carbophobicity of late-transition metals is responsible for their CO evolution activity. Interestingly, vibrational modes attributed to *COOH have been observed spectroscopically during CO_2 reduction over Ag,[27] giving credence to the validity of this empirical relationship. In contrast, Figure 3.4B demonstrates that the $HCOO^-$ evolution activity observed over the same monometallic electrocatalysts exhibits a volcano relationship when the *OCHO binding energy is utilized as the activity descriptor. *OCHO binds to the electrocatalyst surface in a bidentate fashion through the O atoms. The plot exhibits a maximum because the formation energy of all reaction intermediates that bind to the electrocatalyst surface through the O atom scale with the *OCHO adsorption energy. At low *OCHO adsorption energies, the activation of CO_2 through the O atoms is the RDS, whereas at high *OCHO adsorption energies the desorption of $HCOO^-$ is the RDS. This relationship suggests that the oxophillicity of the post-transition metals is responsible for their $HCOO^-$ evolution activity. Thus, the carbo- and oxophillicity of a transition metal electrocatalyst determines the orientation in which CO_2 interacts with the catalyst surface, which in turn determines the initial reaction pathways of CO_2 reduction.

3.2.4 Carbon Monoxide Evolution Over Silver and Gold

Polycrystalline Ag and Au are the most widely studied monometallic electrocatalysts for CO evolution. Both metals exhibit an exponential increase in CO partial current density at low overpotentials, as shown in Figure 3.5.[28,29] Furthermore, their low intrinsic activity for H_2 evolution enables them to achieve a faradaic efficiency (FE) for CO production approaching 100%. However, Au exhibits superior CO evolution activity than Ag due to its slightly higher carbophillicity, as shown in Figure 3.4. At more cathodic potentials, the FE for H_2 observed over both metals begins to increase at the expense of the FE for CO. This phenomenon is accompanied by a suppression of the CO evolution activity that would be expected based on an extrapolation of the initial Tafel

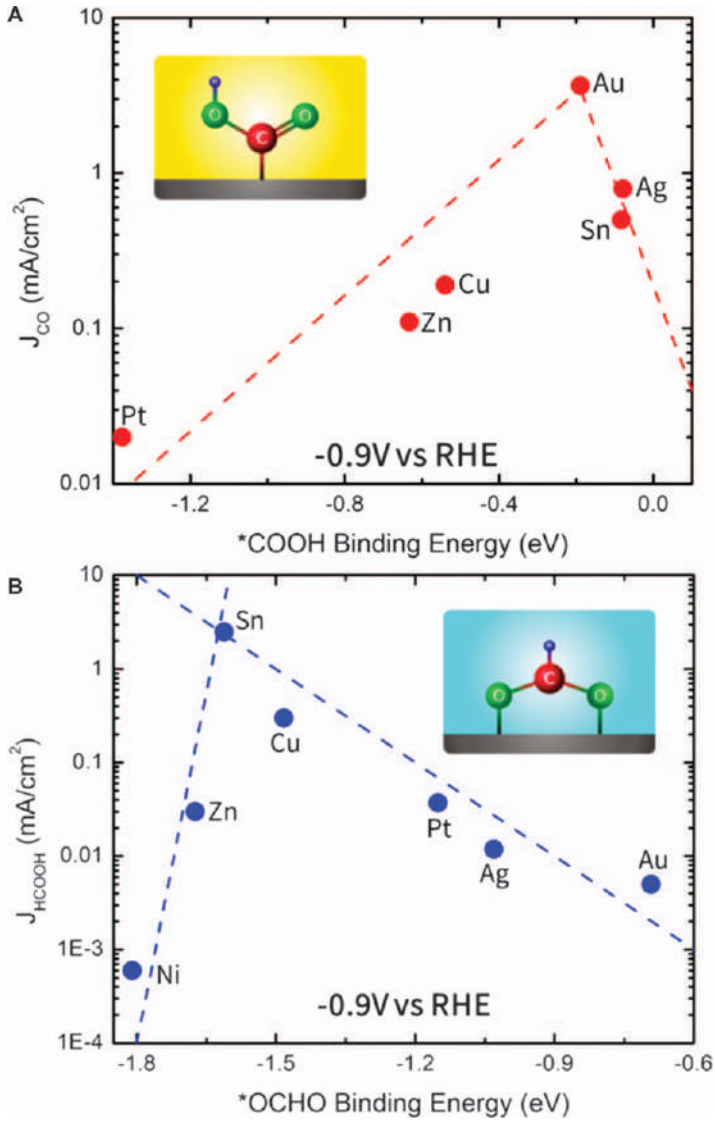

Figure 3.4 Activity volcano plots for (A) CO evolution using *COOH as the activity descriptor and (B) $HCOO^-$ evolution using *OCHO as the activity descriptor. Electrocatalytic activity data was measured over planar metal foils at −0.9 V *vs.* RHE in 0.1 M $KHCO_3$ (pH = 6.8).
Reproduced from ref. 26 with permission from American Chemical Society, Copyright 2017.

kinetics. The suppression of the CO partial current density occurs due to CO_2 mass transfer limitations, as discussed later in this chapter.

The surface atomic structure of Ag and Au has a significant influence on their activity and selectivity for CO evolution. The dependence of the CO

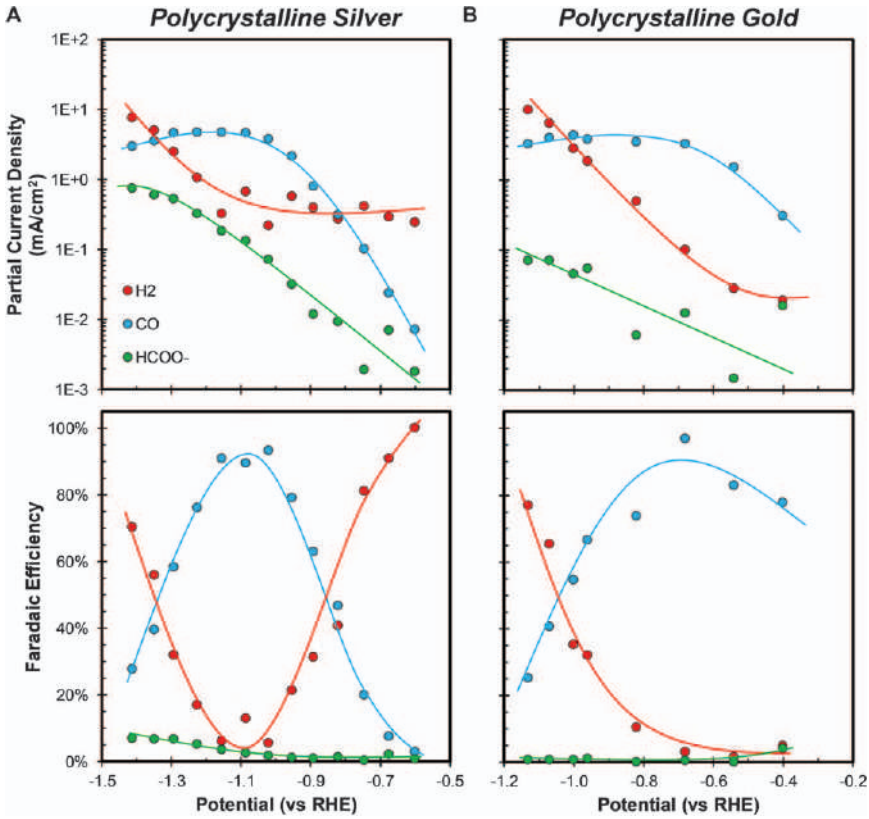

Figure 3.5 Partial current densities and product Faradaic efficiencies observed during CO_2 reduction over (A) polycrystalline Ag foil and (B) polycrystalline Au foil in 0.1 M $KHCO_3$ (pH = 6.8).
Adapted from ref. 28 and 29 with permission from the PCCP Owner Societies.

evolution activity of these metals on their surface atomic structure has been established through investigations of both single crystal and epitaxial thin film electrocatalysts. In the case of Ag, the (111) and (100) basal planes exhibit roughly equivalent CO evolution activity, whereas stepped (110) surfaces exhibit superior activity, as shown in Figure 3.6A.[30,31] In the case of Au, (111) basal planes exhibit superior activity to (100) basal planes.[32,33] However, stepped (110) and (211) surfaces exhibit nearly equivalent activities that are roughly an order of magnitude higher than that observed over (111) basal planes, as shown in Figure 3.6B. These activity differences are attributed to variations in the *COOH binding energy, which is stabilized over more undercoordinated surface sites.[30,31] Interestingly, the H_2 evolution activity observed over both Ag and Au is independent of surface atomic structure, since the H binding energy does not exhibit a significant facet dependance.[31]

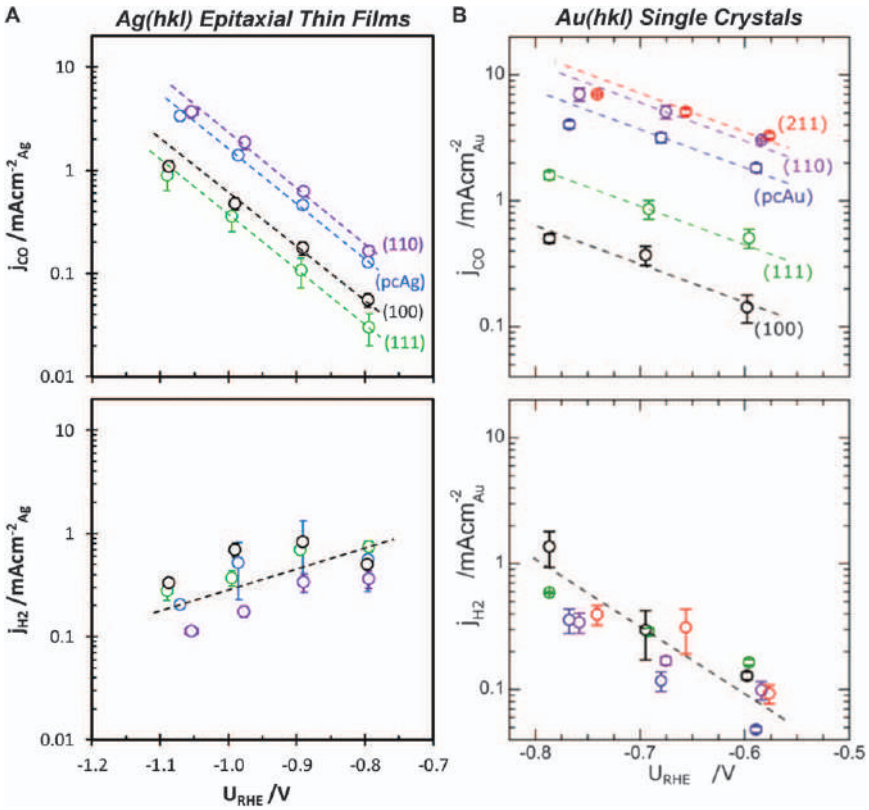

Figure 3.6 Partial current densities observed during CO_2 reduction over (A) epitaxial Ag thin films and (B) Au single crystal electrodes in 0.1 M $KHCO_3$ (pH = 6.8).
Epitaxial Ag thin film data adapted from ref. 31 with permission from American Chemical Society, Copyright 2019. Au single crystal data reproduced from ref. 33 with permission from John Wiley and Sons, Copyright © 2019 WILEY-VCH Verlag GmbH & Co. KGaA, Weinheim.

Single crystal electrodes cannot be assumed to be free of surface defects since they are typically miscut by ~0.5°, which corresponds to a step edge defect density of ~1%.[34] As a result, the activity observed over single crystal electrodes is a convolution of the activities of both the predominate facet and these surface defects. Underpotential deposition preferentially occurs at undercoordinated surface atoms, such as those found at step edge defects.[35] As a result, selective titration of undercoordinated surface sites (defects) can be accomplished by underpotential deposition, as shown in Figure 3.7.[33] The true activity of a basal plane surface can be measured after titrating these surface sites, which is accomplished by depositing a fraction of a monolayer corresponding to the surface defect density. Interestingly, titrating only 3% of the most undercoordinated surface sites on a Au(111) single-crystal reduces the CO evolution activity by >50%.[33] Furthermore, titrating 15% of the surface sites

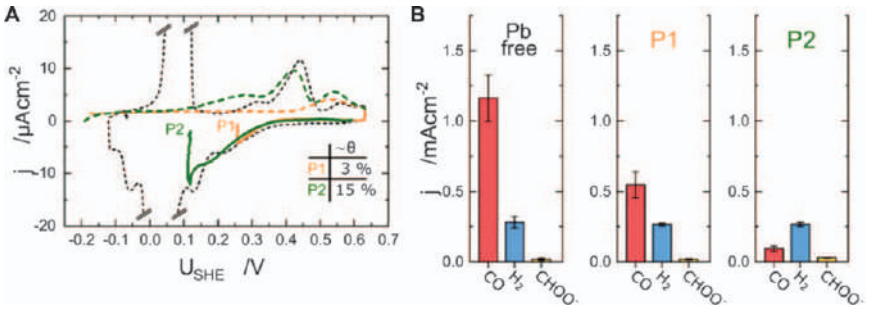

Figure 3.7 (A) Cyclic voltammetry of Pb underpotential deposition onto Au(111) in 0.1 M $KClO_4 + 1$ mM $Pb(ClO_4)_2$. (B) Partial current densities observed over Au(111) with 0%, 3% and 15% Pb coverage at −0.7 V *vs.* RHE in 0.1 M $KHCO_3$ (pH = 6.8).
Reproduced from ref. 33 with permission from John Wiley and Sons, Copyright © 2019 WILEY-VCH Verlag GmbH & Co. KGaA, Weinheim.

reduces the CO evolution activity by an order of magnitude. These observations suggest that a small fraction of surface defects is responsible for the majority of the CO evolution activity observed over basal plane single crystal electrodes. In support of this conclusion, a theoretical study has shown that the CO evolution activity of stepped Ag surfaces is superior to that of more fully coordinated basal planes.[31] Furthermore, the CO evolution activity of these step surfaces was found to be independent of the atomic structure of the step, suggesting that the CO evolution activity of all undercoordinated sites is roughly equivalent. By comparing the reaction thermodynamics over different surface sites it was concluded that step edge defects dominate the activity observed over single-crystal electrodes, in agreement with experimental observations.[31]

3.2.5 Enhancing Carbon Monoxide Evolution Activity

Many experimental studies have sought to improve the intrinsic CO evolution activity of Ag and Au-based electrocatalysts by increasing the abundance of undercoordinated surface atoms. This has typically been accomplished by nanostructuring induced by thermal oxidation,[36,37] dealloying,[38] electrochemical cycling,[39,40] or plasma oxidation.[41] Unfortunately, many of these studies do not report surface area normalized activity data, which makes it difficult to determine whether the observed activity enhancements are a result of intrinsically superior electrocatalytic activity or merely an increased number of active sites.[42] However, in the cases where the surface area normalized activity has been measured, it has been found to be roughly an order of magnitude higher than the corresponding planar surfaces.[38] Perhaps the most straightforward method of synthesizing defective Ag electrocatalysts involves electrochemical oxidation and reduction in the presence of chloride ions, as shown in Figure 3.8A.[39] Oxidation of Ag in the presence of chloride ions produces a AgCl precursor phase, which yields nanostructured Ag upon electrochemical reduction, as shown in Figure 3.8B. This highly nanostructured Ag

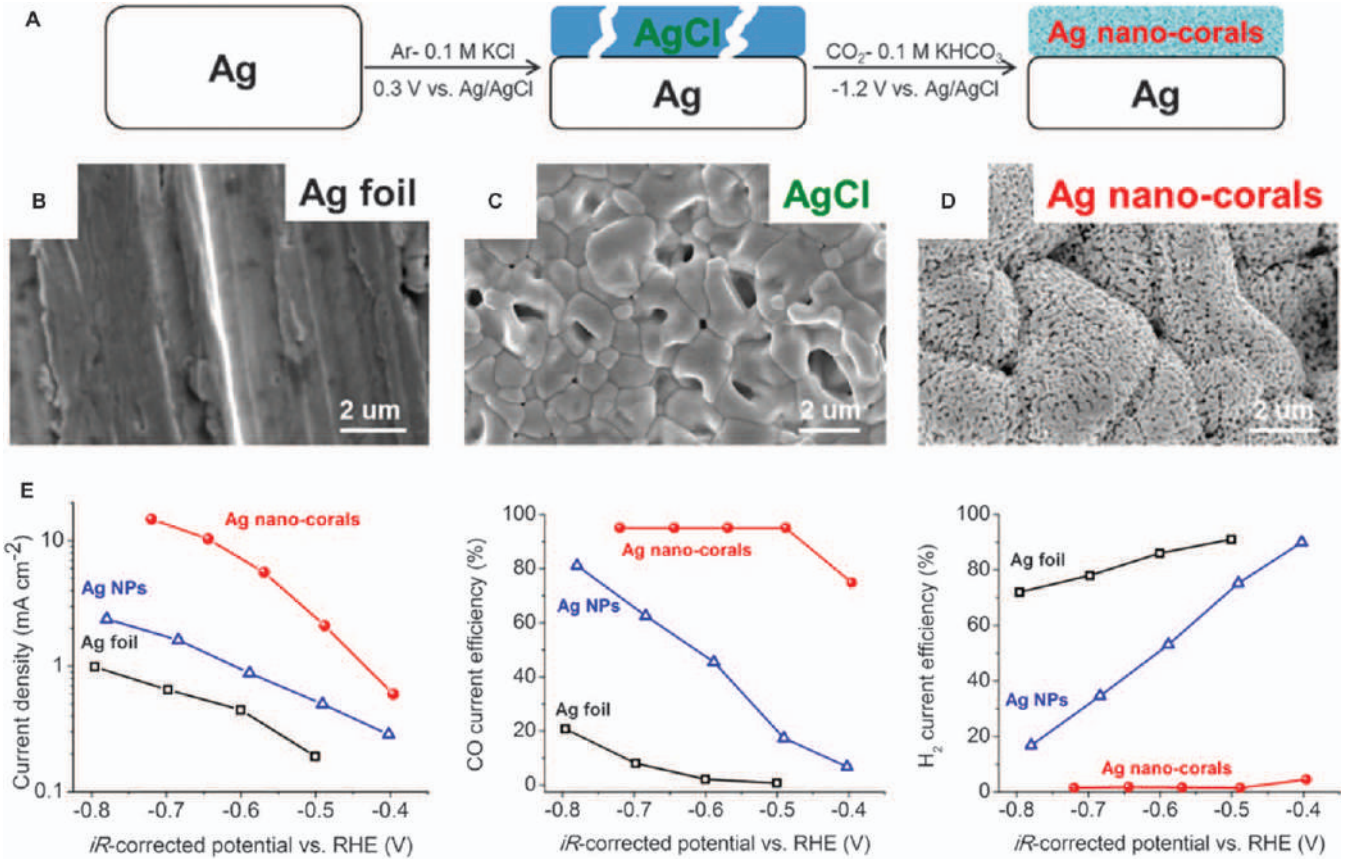

Figure 3.8 (A) Schematic depicting the electrochemical synthesis of nanostructured Ag by electrochemical oxidation and reduction in the presence of chloride anions. Scanning electron micrographs of (B) Ag foil, (C) AgCl, and (D) nanostructured Ag. (E) Electrocatalytic activity and product Faradaic efficiencies observed over Ag foil, Ag nanoparticles, and nanostructured Ag. Reproduced from ref. 39 with permission from American Chemical Society, Copyright 2015.

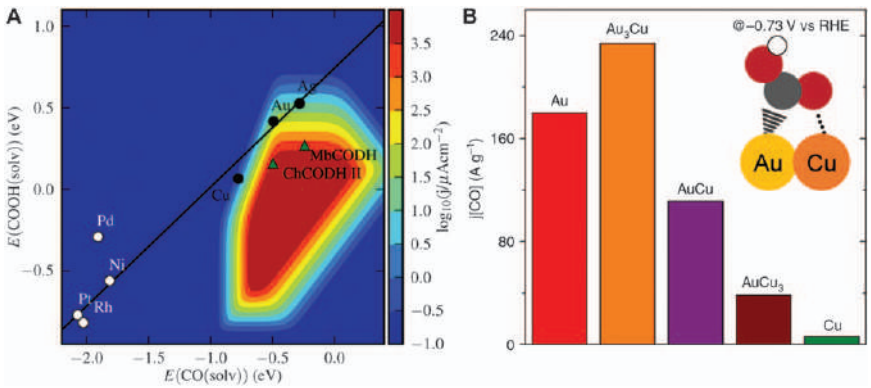

Figure 3.9 (A) Activity volcano plot for CO evolution over (211) metal surfaces. Reproduced from ref. 44 with permission from American Chemical Society, Copyright 2013. (B) CO evolution activity observed over Au_xCu_{1-x} nanoparticles in 0.1 M $KHCO_3$ (pH = 6.8). Reproduced from ref. 49 with permission from Springer Nature, Copyright 2014.

exhibits both enhanced electrocatalytic activity and superior FE for CO compared to planar polycrystalline Ag foil, as shown in Figure 3.7C.

Theoretical studies have concluded that the reduction of CO_2 to *COOH is the last elementary step in the mechanism of CO evolution to become exergonic as the applied potential is reduced over Ag and Au.[43–46] This suggests that the formation of *COOH is the RDS of CO evolution over Ag and Au electrocatalysts. Thus, enhancing the stability of *COOH should yield superior CO evolution activity over these metals. However, since *COOH and *CO both bind to the electrode surface through the C atom, increasing the stability of *COOH also increases the stability of *CO.[44] As a result of this linear scaling relationship, metals that bind *COOH more strongly than Au exhibit inferior CO evolution activity since the desorption of *CO becomes the RDS. Therefore, the linear scaling relation between the adsorption energies of *COOH and *CO needs to be broken to obtain electrocatalysts with significantly superior CO evolution activity, as shown in Figure 3.9A.[44] Interestingly, some enzymes exhibit almost reversible CO evolution activity since their active sites break the linear scaling relationship through bidentate bonding to both the C and O atoms of *COOH.[44,47] A similar effect can be accomplished by introducing a small concentration of an oxophillic element, such as Cu, into the Au surface, as shown in Figure 3.9B.[48–50] The superior CO evolution activity observed over Cu-promoted Au has been hypothesized to be the result of bidentate bonding of *COOH through both the C and O atoms to co-located Au and Cu atoms, respectively.[49]

3.2.6 Distribution of Products Formed Over Polycrystalline Copper

Polycrystalline Cu can produce up to 16 different reaction products during CO_2 reduction, as shown in Figure 3.10A.[51] Besides $HCOO^-$ and CO, Cu

A

Product	# e⁻	E	Product	# e⁻	E
Formate	2	−0.02	Acetaldehyde	10	0.05
Carbon monoxide	2	−0.10	Ethanol	12	0.09
Methanol	6	0.03	Ethylene	12	0.08
Glyoxal	6	−0.16	Hydroxyacetone	14	0.46
Methane	8	0.17	Acetone	16	−0.14
Acetate	8	−0.26	Allyl alcohol	16	0.11
Glycolaldehyde	8	−0.03	Propionaldehyde	16	0.14
Ethylene glycol	10	0.20	1-Propanol	18	0.21

B

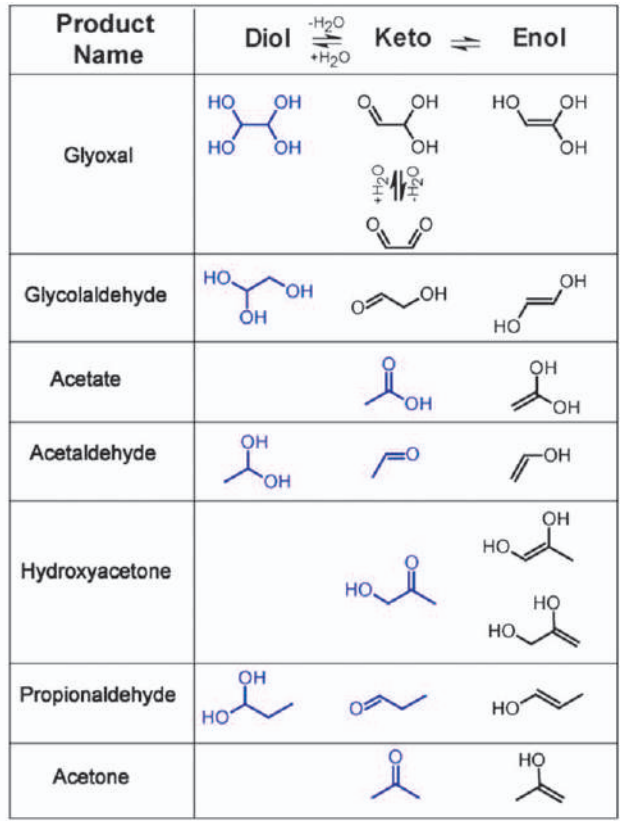

Figure 3.10 (A) CO_2 reduction products observed over polycrystalline Cu and their standard reduction potentials on a RHE scale at pH = 6.8. (B) Aqueous equilibria of the carbonyl-containing CO_2 reduction products observed over polycrystalline Cu. Blue indicates the most stable structure under typical reaction conditions.
Reproduced from ref. 51 with permission from the Royal Society of Chemistry.

produces a mixture of more reduced products: CH_4, C_2H_4, C_{2-3} primary alcohols, and C_{2-3} carbonyl-containing species (aldehydes and the conjugate bases of carboxylic acids). It is important to recognize that the carbonyl-containing products can be present in the electrolyte in several different forms, as shown in Figure 3.10B.[51] While all carbonyl-containing products will be present in aqueous solutions in either their keto or hydrated diol form, they may exist in their enol form when adsorbed to the electrocatalyst. Such adsorption-induced tautomerization may have important mechanistic ramifications.

The partial current densities and product FEs observed over polycrystalline Cu during CO_2 reduction are shown in Figure 3.11.[51] The product distribution varies substantially with the applied potential.[51–53] A mixture of H_2, $HCOO^-$, and CO is produced at a low overpotential. However, at more cathodic potentials (roughly −0.75 V *vs.* RHE) the evolution of CH_4, C_2H_4, and a myriad of liquid-phase products are also observed. It is important to realize that the onset potential of hydrocarbon and alcohol detection is not a meaningful metric of electrocatalytic activity since it is more significantly influenced by the design of the experimental setup utilized to study the electrocatalyst than the intrinsic properties of the electrocatalyst itself.[42] While a wide distribution of reduced products is observed over polycrystalline Cu, only CH_4, C_2H_4, and ethanol (EtOH) are produced with FEs exceeding 10%. As the FEs of the hydrocarbons and alcohols increase, the FEs of $HCOO^-$ and CO decrease. This observation suggests that either $HCOO^-$ or CO is an intermediate to more reduced products. Interestingly, the multicarbon product partial current densities all plateau and decline simultaneously as the applied overpotential increases, suggesting that these products all share a common intermediate. The plateau and decline of the multi-carbon product partial current densities is accompanied by an increase in the H_2 and CH_4 partial current densities. This behavior is the result of insufficient CO_2 mass transfer and is not intrinsic to polycrystalline Cu, as discussed later in this chapter.[42]

3.2.7 CO as the Intermediate to Hydrocarbons and Alcohols

$HCOO^-$ is cathodically inert since its negative charge results in Coulombic repulsion from the Helmholtz layer of the negatively charged cathode.[54] Conversely, the reduction of CO over Cu produces an identical mixture of reaction products to those in the reduction of CO_2, as shown in Figure 3.12.[52,55–58] Thus, CO is an intermediate in the reduction of CO_2 to hydrocarbons and alcohols over Cu. CO reduction is often conducted in alkaline electrolytes since it does not react chemically with OH^- to produce electrochemically inert HCO_3^- and CO_3^{2-}, as is the case for CO_2. It would appear that CO reduction requires a lower overpotential than CO_2 reduction when comparing the activity data in Figures 3.11 and 3.12. However, this discrepancy is the result of a Nernstian potential shift arising from the difference in the bulk pH of the electrolytes utilized to measure the activity

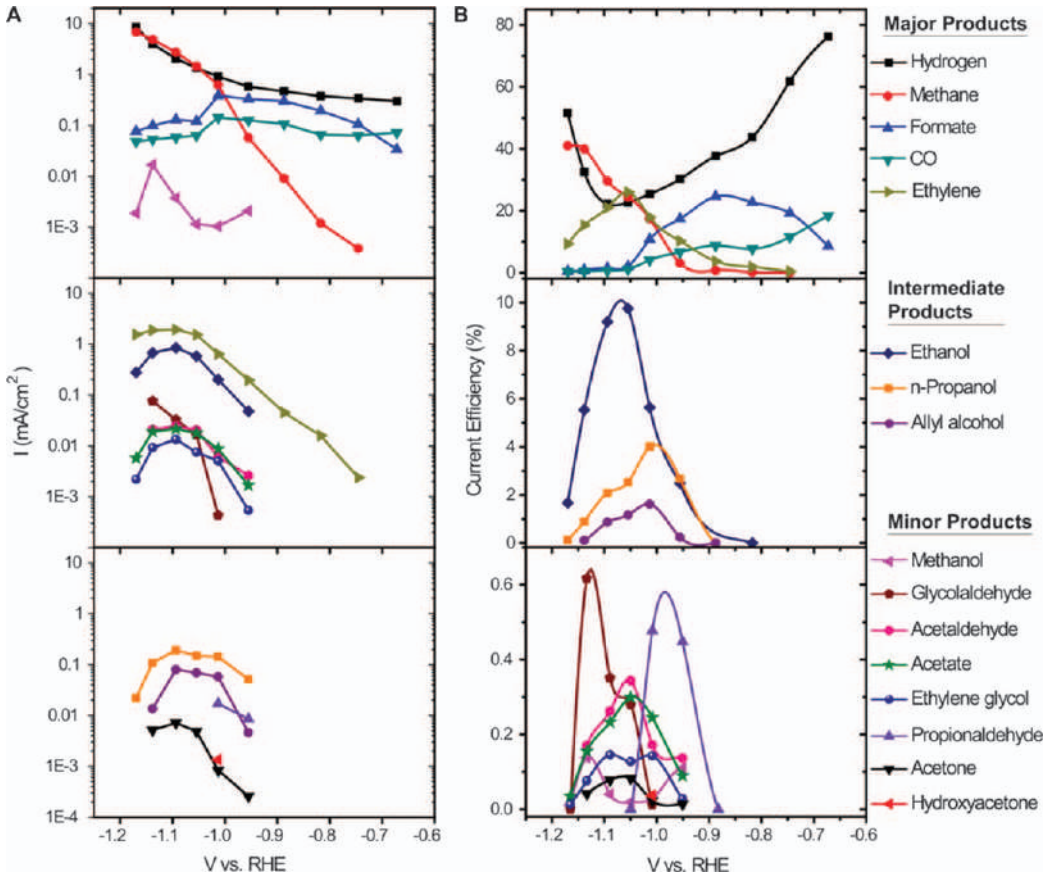

Figure 3.11 (A) Partial current densities and (B) product Faradaic efficiencies observed during CO_2 reduction over polycrystalline Cu foil in 0.1 M $KHCO_3$ (pH = 6.8).
Reproduced from ref. 51 with permission from the Royal Society of Chemistry.

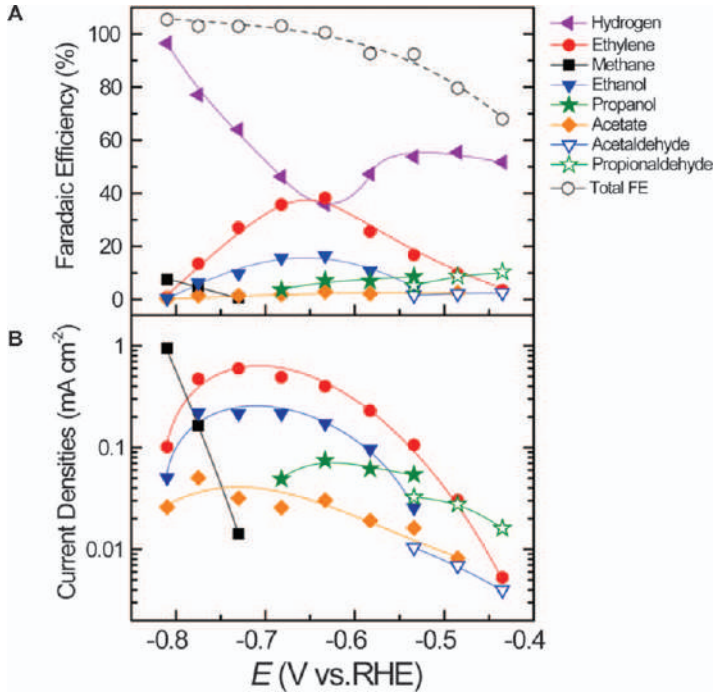

Figure 3.12 (A) Partial current densities and (B) product Faradaic efficiencies observed during CO reduction over polycrystalline Cu foil in 0.1 M KOH (pH = 13).
Reproduced from ref. 58 with permission from American Chemical Society, Copyright 2018.

Table 3.2 Comparison of the CO and CO_2 reduction activities observed over polycrystalline Cu during chronopotentiometry at -5 mA cm^{-2} in a phosphate buffer solution (pH = 6 – 6.5). Adapted from ref. 52 with permission from the Royal Society of Chemistry.

Reactant	Potential (V *vs.* RHE)	H_2	CH_4	C_2H_4	EtOH
CO	– 0.86	75.4%	16.8%	1.7%	0.0%
CO_2	– 0.85	72.4%	17.0%	1.8%	0.7%

data, as explained later in the chapter. In fact, the production of hydrocarbons and alcohols requires the same overpotential when both reactions are reduced in electrolytes with the same bulk pH, as shown in Table 3.2.[52,59] The overpotentials required to drive CO and CO_2 reduction can only be accurately compared in a phosphate buffer since it is the only electrolyte in which both species can be reduced at the same bulk pH, albeit with different buffering capacities. The observation that CO and CO_2 reduction requires the same overpotential to produce hydrocarbons and alcohols supports the hypothesis that the RDS in the reduction of CO_2 to hydrocarbons and alcohols over Cu occurs after the formation of an adsorbed CO intermediate.

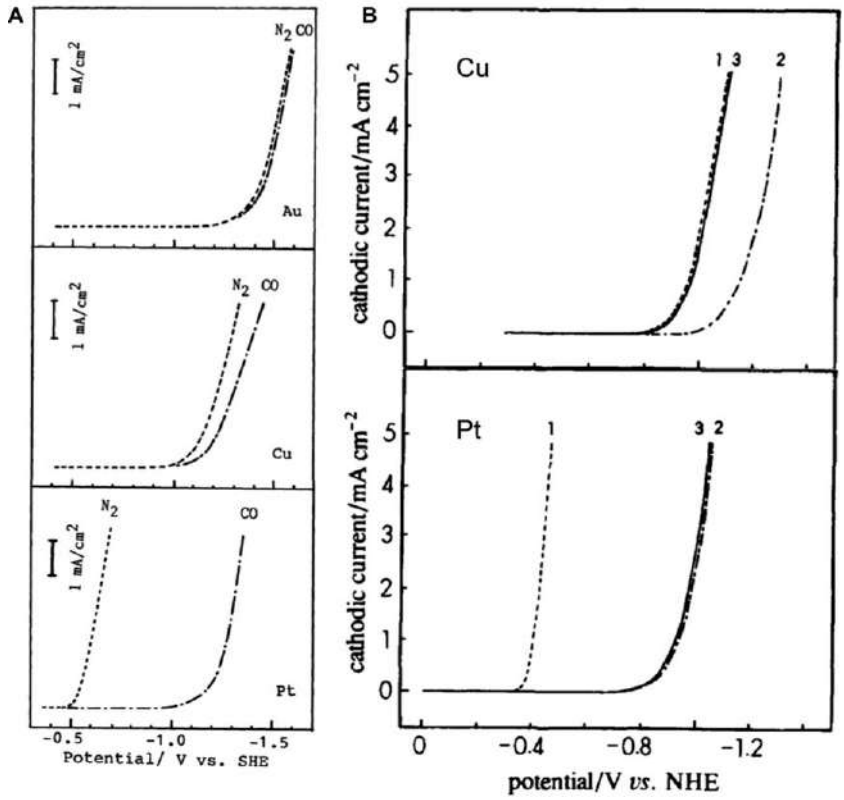

Figure 3.13 (A) Impact of the presence of CO on the H_2 evolution activity of transition metal electrocatalysts in 0.1 M $KHCO_3$ (pH = 10). Reproduced from ref. 67 with permission from the Chemical Society of Japan. (B) Reversibility of the CO poisoning observed over Cu and Pt in a phosphate buffer (pH = 6.8). Numbers denote measurements conducted in electrolytes saturated with: (1) Ar, (2) CO, and (3) CO and then Ar sequentially. Reproduced from ref. 52 with permission from the Royal Society of Chemistry.

In agreement with this conclusion, several *in situ* spectroscopic investigations have observed adsorbed CO during CO_2 reduction over Cu.[60–66]

3.2.8 Reversibly Adsorbed CO

Since adsorbed CO is an intermediate in the reduction of CO_2 to hydrocarbons and alcohols over Cu, it is likely that the CO adsorption energy of Cu is responsible for its unique reactivity. Indeed, Cu has an intermediate CO binding energy compared to other transition metals. The importance of the CO binding energy can be illustrated by comparing the impact that CO has on the H_2 evolution activity of transition metal electrocatalysts. The presence of CO does not inhibit the H_2 evolution activity of transition metals that evolve

CO during CO_2 reduction, such as Au, because they bind CO weakly enough to prevent significant surface poisoning, as shown in Figure 3.13A.[67] Since these metals are also exceptionally poor electrocatalysts for H_2 evolution,[25] they can achieve high CO FEs during CO_2 reduction. Conversely, the presence of CO significantly inhibits the H_2 evolution activity of transition metals that strongly bind CO, such as platinum. This occurs because CO is irreversibly bound to such transition metals and does not desorb from their surface even if CO is stripped from the electrolyte, as shown in Figure 3.13B.[52] As a result, these metals quickly deactivate during CO_2 reduction due to the formation of irreversibly bound CO and only evolve H_2 at a steady state.[68–72] Interestingly, Cu is the only transition metal with an intermediate CO adsorption, which enables a significant coverage of reversibly adsorbed CO to populate the Cu surface during CO_2 reduction.[52,63,73] The ability of Cu to catalyze the reduction of CO has been attributed to this unique CO adsorption energy.[22,43,67]

3.2.9 Dependence of Methane and Ethene Evolution Activity on Surface Atomic Structure

The surface atomic structure of Cu significantly influences its activity and selectivity for hydrocarbon and alcohol evolution. Systematic studies over Cu single crystal electrodes have been conducted in order to establish relationships between the surface atomic structure of the Cu electrocatalyst and its activity and selectivity for CO reduction.[34,74–78] Cu single crystal electrodes are known to be susceptible to surface reconstruction under electrochemical conditions.[79,80] However, Cu(111) and Cu(100) have been verified to be stable under CO reduction conditions.[81] Cu(100) exhibits superior activity and multi-carbon product selectivity compared to Cu(111) during both CO and CO_2 reduction, as shown in Table 3.3.[74] The higher multi-carbon product selectivity observed over Cu(100) is hypothesized to be the result of a superior CO adsorption energy,[82] which increases the probability of C–C coupling by elevating the coverage of adsorbed CO at a steady state.

The CH_4 and C_2H_4 evolution activities observed over Cu(111) and (100) single-crystal electrodes during CO reduction has been monitored qualitatively during linear sweep voltammetry, as shown in Figure 3.14.[83] Both CH_4 and C_2H_4 were evolved over Cu(111) at a relatively high overpotential (-0.75 V *vs.* RHE). However, C_2H_4 was exclusively evolved over Cu(100) at a

Table 3.3 Comparison of the CO and CO_2 reduction activities observed over Cu(111) and Cu(100) single crystal electrodes during chronopotentiometry at -5 mA cm^{-2} in 0.1 M $KHCO_3$ (pH = 6.8 for CO_2 and 10 for CO). Adapted from ref. 74 with permission from Elsevier, Copyright 1995.

Cu(hkl)	Reactant	Potential (V *vs.* RHE)	H_2	CH_4	C_2H_4	EtOH
(111)	CO_2	-1.16	56.5%	38.9%	4.7%	0.9%
	CO	-0.82	67.3%	21.8%	10.2%	2.0%
(100)	CO_2	-1.02	23.3%	25.0%	31.7%	9.8%
	CO	-0.76	69.8%	8.6%	23.3%	0.8%

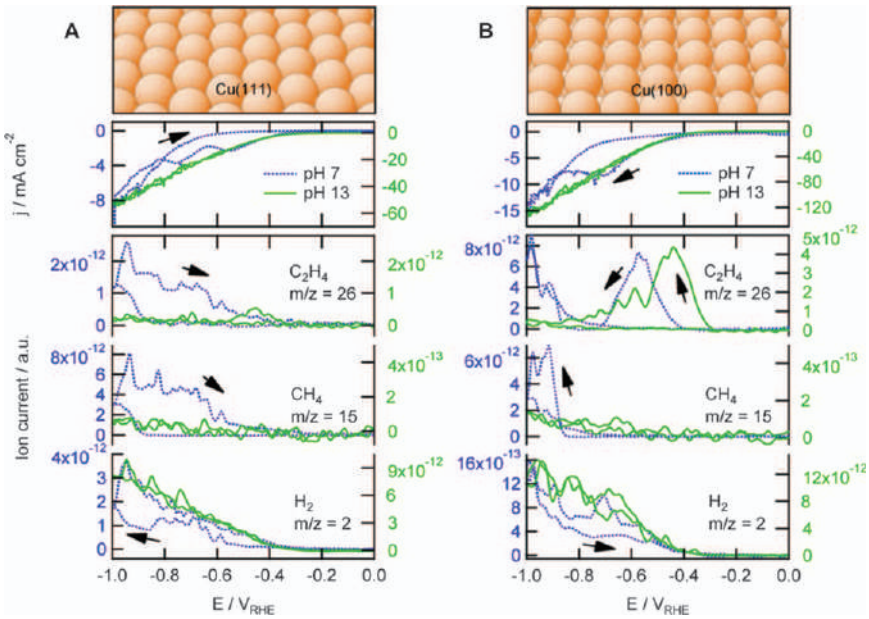

Figure 3.14 Mass-ion currents associated with H_2, CH_4, and C_2H_4 evolved during CO reduction over (A) Cu(111) and (B) Cu(100) single crystal electrodes in both a phosphate buffer (pH = 7) and 0.1 M NaOH (pH = 13). Reproduced from ref. 83 with permission from American Chemical Society, Copyright 2012.

relatively low overpotential (−0.5 V *vs.* RHE). As the overpotential was increased, the rate of C_2H_4 evolution over Cu(100) deceased before increasing again at more cathodic potentials with concomitant CH_4 evolution (−0.75 V *vs.* RHE). The complex C_2H_4 partial current potential dependence observed over Cu(100) led to the hypothesis that there are two distinct mechanisms of C–C bond formation: a low overpotential mechanism that bypasses the reduction of CO, and a higher overpotential mechanism in which a CO-derived intermediate shared with the CH_4 evolution pathway undergoes C–C coupling. Since the low overpotential pathway bypasses the reduction of CO it was hypothesized to occur *via* the dimerization of neighboring CO molecules.[84]

The impact of adding step sites with different orientations on the electrocatalytic activity and selectivity of Cu(111) and Cu(100) single crystal electrodes has also been investigated.[34,75,76] The activity and selectivity observed over these surfaces vary systematically with the step site density, as shown in Figure 3.15. Interestingly, Cu surfaces with higher activity also exhibit superior selectivity for C_2H_4 relative to CH_4. The optimal Cu surfaces were found to be those with an angle of ∼10° relative to the (100) plane, which corresponds to a (100) surface with a step site density of ∼20%. Interestingly, the activity of these stepped surfaces was dependent only on the step site density and were independent of the atomic structure of the step site. This observation suggests that the morphology of the step site does

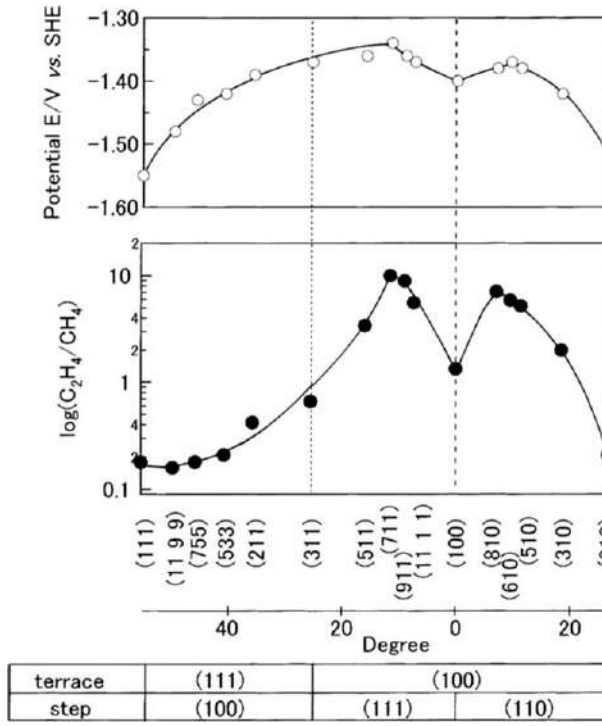

Figure 3.15 Potential required to maintain a current density of -5 mA cm^{-2} and the Faradaic efficiency for C_2H_4 relative to CH_4 observed during CO_2 reduction over Cu single crystal electrodes as a function of the angle of the surface plane relative to the (100) plane.
Reproduced from ref. 76 with permission from Elsevier, Copyright 2003.

not significantly alter its intrinsic activity, as is the case for the monometallic electrocatalysts that are active for CO evolution. In agreement with these conclusions, the integrated band intensity of adsorbed CO observed using IR spectroscopy was found to scale linearly with the step site density regardless of the atomic structure of the step site.[62] However, a theoretical understanding of why a step site density of ~20% yields optimal activity and multicarbon product selectivity is currently lacking.

3.2.10 Dependence of Methane and Ethene Evolution Activity on Electrolyte pH

The CH_4 and C_2H_4 evolution activities observed over Cu exhibit different dependences on the electrolyte pH, as shown in Figure 3.16.[56,58,77] Specifically, the CH_4 partial current density decreases, whereas the C_2H_4 partial current density remains constant, as the electrolyte pH is increased when comparing activity data on the pH-independent SHE scale.[56,58,77] Conversely, the CH_4 partial current density remains constant, whereas the C_2H_4 partial current density increases, as the electrolyte pH increases when comparing

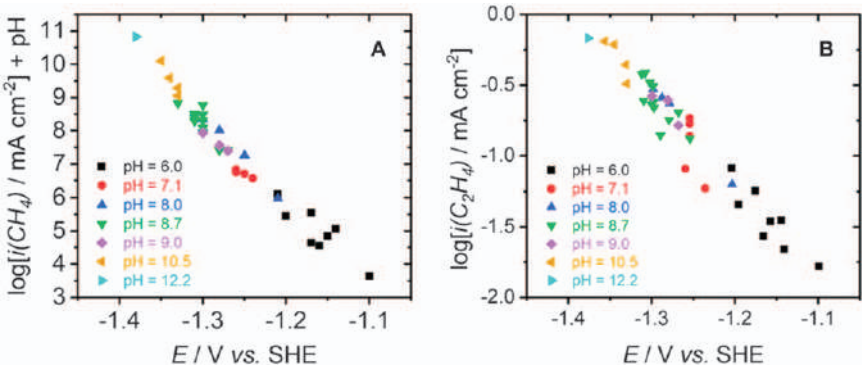

Figure 3.16 (A) $\log(i_{CH_4}) + \text{pH}$ and (B) $\log(i_{C_2H_4})$ correlated with the electrode potential on a SHE scale observed during CO reduction over polycrystalline Cu in a variety of electrolytes with different bulk pH values.
Adapted from ref. 56 with permission from American Chemical Society, Copyright 1997.

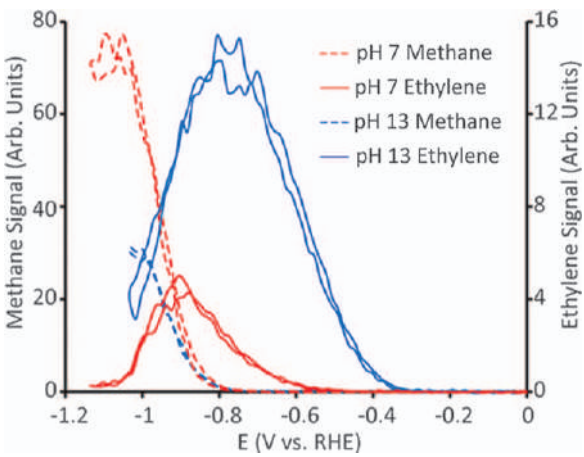

Figure 3.17 Mass-ion currents associated with CH_4 and C_2H_4 evolved during CO reduction over Cu(100) at pH = 7 and 13.
Reproduced from ref. 77 with permission from John Wiley and Sons, Copyright © 2016 WILEY-VCH Verlag GmbH & Co. KGaA, Weinheim.

activity data on the pH-dependent RHE scale, as shown in Figure 3.17. Thus, conducting CO reduction at high pH improves both the activity and multi-carbon product selectivity observed over Cu. These observations suggest that the RDS of CH_4 formation is the electrochemical hydrogenation of CO or a CO-derived intermediate due to the independence of the CH_4 evolution activity on pH when comparing activity data on the RHE scale. Conversely, observations suggest that the RDS of multi-carbon product formation does not involve the hydrogenation of CO or a CO-derived intermediate due to the independence of the C_2H_4 evolution activity on pH when comparing activity

data on the SHE scale. The subsequent sections will explore these reaction mechanisms in further detail.

3.2.11 Mechanism of CO Methanation

Almost all theoretical investigations have concluded that the last elementary step to become exergonic in the mechanism of CO_2 methanation over Cu as the applied potential is reduced is the reduction of CO.[85–87] This suggests that the reduction of CO is the RDS for CH_4 evolution over Cu. The reduction of CO *via* proton coupled electron transfer (PCET) can produce either *COH or *CHO. However, the reduction of CO to *CHO has been found to be energetically favored, as shown in Figure 3.18.[87,88] Early studies concluded that formaldehyde was an intermediate in the reduction of *CHO to CH_4.[85] However, this hypothesis was inconsistent with the experimental observation that formaldehyde reduction over Cu produces methanol, which is not a product of CO_2 reduction over Cu.[56] This discrepancy between theory and experiment was later rectified by recognizing that formaldehyde is entirely present as methane-1,1-diol in aqueous solutions. Subsequent theoretical analysis demonstrated that the reduction of this hydrated form of formaldehyde to methanol over Cu is energetically favored.[89] Despite this, most contemporary studies have concluded that the reduction of *CHO yields *CHOH and ultimately *CH.[87,88]

The reduction of *CO to *CHO is the RDS in the reduction of CO_2 to CH_4 since it has the highest activation barrier of any PCET step in the reaction mechanism, as shown in Figure 3.18.[88] Thus, this activation barrier must be reduced to enhance the CH_4 evolution activity. The activation barrier for *CHO formation scales with the CO adsorption energy since both species

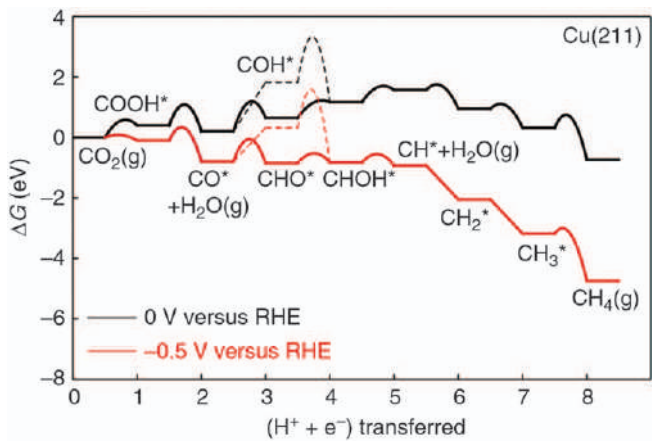

Figure 3.18 Free energy diagram for the reduction of CO_2 to CH_4 over Cu(211) at 0 and −0.5 V *vs.* RHE.
Reproduced from ref. 88, https://doi.org/10.1038/ncomms15438, under the terms of the CC BY 4.0 license, http://creativecommons.org/licenses/by/4.0/.

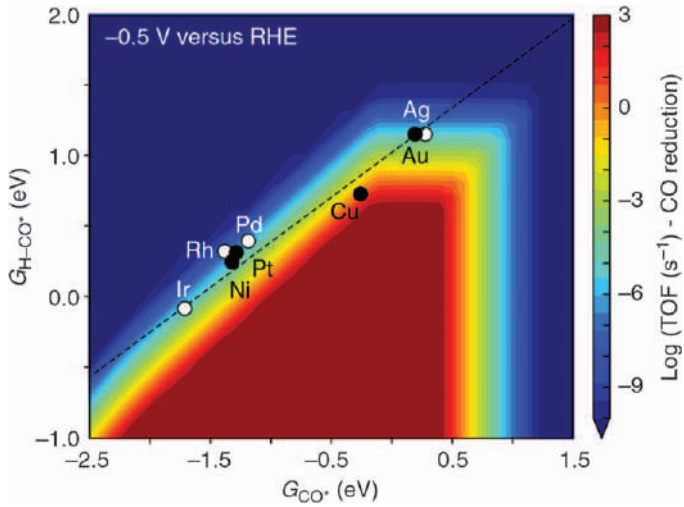

Figure 3.19 Activity volcano plot for CO reduction over (211) metal surfaces. Reproduced from ref. 88, https://doi.org/10.1038/ncomms15438, under the terms of the CC BY 4.0 license, http://creativecommons.org/licenses/by/4.0/.

bind to the electrode surface through the C atom.[88] As a result, the stability of the *CHO intermediate cannot be increased relative to *CO. Thus, a method of decoupling the binding energies of *CO and *CHO must be discovered in order to develop superior electrocatalysts for CH_4 evolution, as shown in Figure 3.19.[88] One method of accomplishing this goal is to stabilize the *CHO intermediate though bidentate bonding to the electrocatalyst surface through both the C and O atoms.[43] However, this approach has yet to be demonstrated experimentally.

3.2.12 Mechanisms of C–C Coupling

Potential routes for C–C coupling over Cu(100) have been explored using periodic Kohn-Sham density functional theory (DFT) in which the solvent was included as a continuum dielectric and the electrolyte was described using a linearized Poisson–Boltzmann model.[90] The authors concluded that the mechanism of C–C coupling over Cu(100) depends on the applied potential, as shown in Figure 3.20.[90] At low overpotentials, C–C coupling occuring *via* CO dimerization is favored, in agreement with the conclusions drawn from experimental studies.[83,90] However, as the applied overpotential increases, the surface dipole of adsorbed CO increases, due to the enhanced electron back donation from the Cu surface into the $2\pi^*$ orbitals of the adsorbed CO. As a result, this pathway becomes increasingly unfavorable as the applied overpotential increases due to elevated dipole–dipole repulsion between neighboring CO molecules. Instead, C–C coupling between *CHO and *CO becomes more favorable. As discussed previously, *CHO is also envisioned to be an

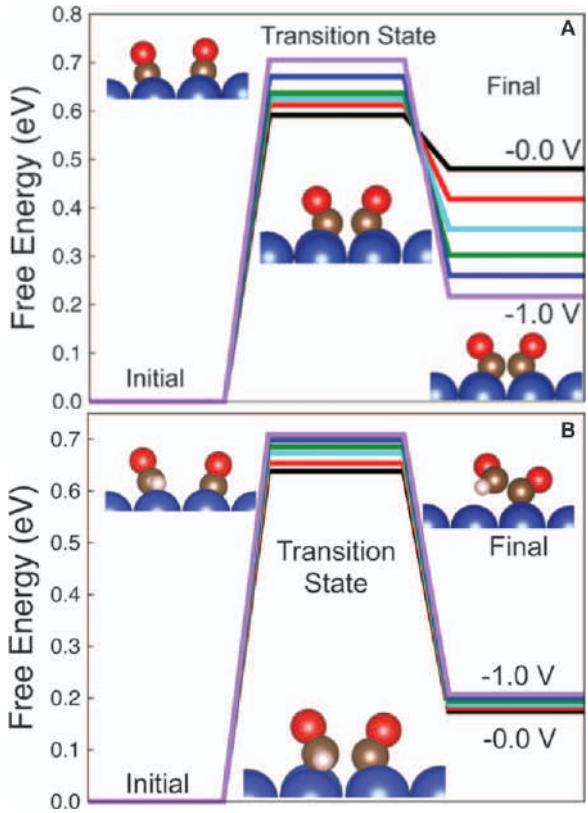

Figure 3.20 Free energy diagram for (A) CO dimerization and (B) CO-CHO coupling over Cu(100) at potentials ranging from 0 to −1.0 V *vs.* RHE at pH = 7. Reproduced from ref. 90 with permission from American Chemical Society, Copyright 2016.

intermediate in the mechanism of CH_4 evolution. Thus, the theoretical study concluded that there are two mechanisms of C–C coupling: a low overpotential mechanism that bypasses the direct reduction of CO and a higher overpotential mechanism in which an intermediate that is shared with the mechanism of CH_4 evolution undergoes C–C coupling. Thus, the conclusions drawn are in agreement with the experimental observations.

The electric field across the electrochemical double layer significantly influences the stability of many potential CO_2 reduction intermediates, as shown in Figure 3.21.[91,92] However, the stability of the critical intermediates involved in C–C coupling (*CO–CO and *CO–CHO) are significantly more sensitive to the magnitude of the double layer field than other potential intermediates of CO_2 reduction due to their large dipole moments. The surface charge density of the cathode determines the strength of the double layer field. Furthermore, the difference between the applied potential on a SHE scale and the potential of zero charge of the cathode determines the surface charge. As a result, the

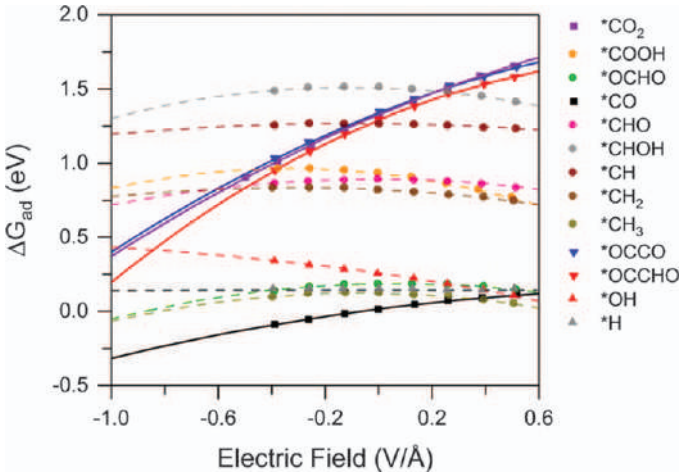

Figure 3.21 Adsorption energies of potential CO_2 reduction intermediates to Cu(111) as a function of the magnitude of a uniform electric field oriented perpendicular to the surface. Solid lines denote adsorbates that experience significant field stabilization due to their high dipole moment. Reproduced from ref. 92 with permission from American Chemical Society, Copyright 2017.

applied potential on the pH-independent SHE scale determines the stability of the critical intermediates involved in C–C coupling.[93] This is why the partial current densities of C_2H_4 and the other multi-carbon products remain constant on a SHE scale, as previously discussed.

The coverage of adsorbed CO should increase systematically with the applied potential on the pH-independent SHE scale since it is also field stabilized. To illustrate this, Figure 3.22 shows a plot of the integrated CO band intensities observed during CO reduction over polycrystalline Cu as a function of the applied potential in electrolytes of varying pH.[63] Interestingly, the normalized CO band intensity is independent of the electrolyte pH at a given potential on the pH-independent SHE scale. This means that the CO adsorption energy increases with the applied potential on the pH-independent SHE scale, or alternatively, the CO adsorption energy increases at a fixed potential on the pH-dependent RHE scale as the electrolyte pH increases.

3.2.13 Aldehydes as Intermediates to Primary Alcohols

A notable feature of the product distribution observed over polycrystalline Cu is that the relative abundance of a given liquid-phase product increases with its extent of reduction. This observation suggests that less reduced liquid-phase products (carbonyl containing species) serve as intermediates to more reduced liquid-phase products (alcohols) and that these intermediate liquid-phase products are relatively easy to reduce. In support of this hypothesis, several studies have demonstrated that acetaldehyde (MeCHO) can be reduced to EtOH over Cu.[56,94,95] Additionally, propionaldehyde (EtCHO) can be reduced to

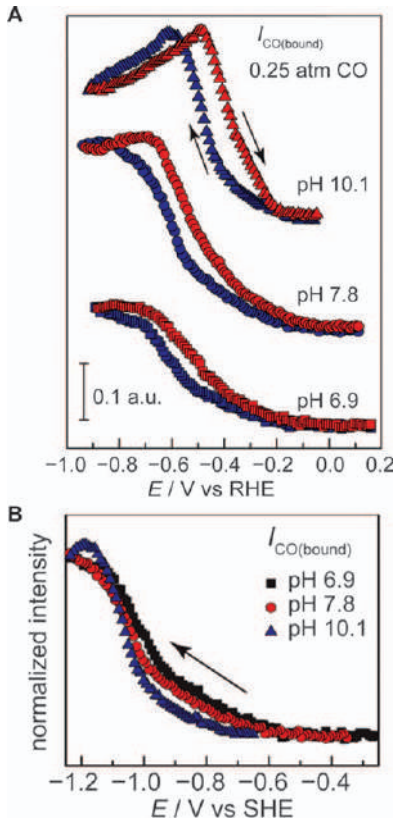

Figure 3.22 (A) Integrated CO band intensities observed during CO reduction over polycrystalline Cu in 0.1 M (bi)carbonate buffers (pH = 6.9, 7.8, and 10.1). Blue points denote the cathodic sweep while red points denote the anodic sweep. (B) Normalized integrated CO band intensities observed during the cathodic sweep as a function of the applied potential on the SHE scale.
Reproduced from ref. 63 with permission from American Chemical Society, Copyright 2016.

n-propanol (*n*-PrOH) over Cu.[56] In another study, the electrochemical reduction of glyoxal and glycolaldehyde were investigated.[59] Glyoxal is a notable species because it is the simplest multi-carbon product of CO and CO_2 reduction over Cu.[51] The reduction of glyoxal over Cu produced MeCHO at low overpotentials and EtOH at higher overpotentials, as shown in Figure 3.23. Glycolaldehyde reduction yielded identical results, suggesting that it is an intermediate in the reduction of glyoxal to MeCHO and ultimately EtOH over Cu. The inability to observe the transiently produced glycolaldehyde during glyoxal reduction is unsurprising since the analytical instruments utilized in the study could only observe volatile reaction products and glycolaldehyde is only present in aqueous solutions as a hydrated germinal diol with a low vapor pressure.

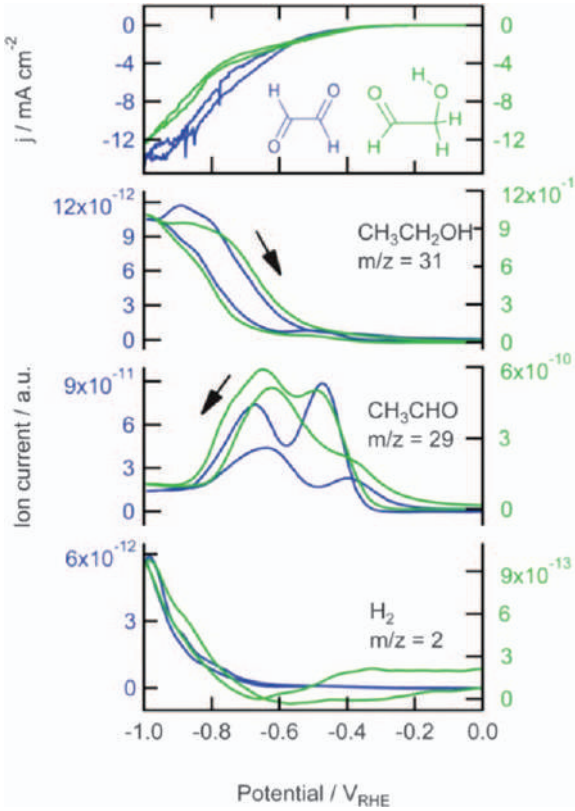

Figure 3.23 Mass-ion currents associated with H_2, acetaldehyde, and ethanol during glyoxal and glycolaldehyde reduction (50 mM) over polycrystalline Cu in a phosphate buffer (pH = 7).
Reproduced from ref. 59 with permission from the Royal Society of Chemistry.

While these studies confirm that primary aldehydes are potential intermediates to the corresponding primary alcohols, they do not preclude the existence of other reaction mechanisms responsible for the generation of these products. However, the existence of alternative mechanisms of primary alcohol formation are unlikely based on the results of several other experimental studies. The first study monitored the transient liquid-phase product generation rates during CO reduction over Cu by repeatedly sampling the catholyte of a closed electrochemical cell.[57] While the MeCHO concentration initially increased more rapidly than EtOH, it quickly plateaued after the first few minutes of electrolysis. This observation suggests that MeCHO is reversibly adsorbed to Cu and can be reduced further to yield more reduced products. In the initial moments of CO_2 reduction, transiently produced MeCHO preferentially desorbs from the cathode surface since it is in equilibrium with an electrolyte that is completely devoid of MeCHO. However, after the MeCHO concentration in the electrolyte increases it remains adsorbed to the Cu surface and it is reduced

to EtOH. In the second study, $C^{16}O$ reduction was conducted in the presence of a $H_2{}^{18}O$-based electrolyte and the isotopic composition of the resulting liquid-phase products were measured using GC–MS.[96] A substantial fraction of the primary alcohols produced were found to contain oxygen derived from solvent water. The incorporation of oxygen derived from solvent water into the primary alcohols produced during CO reduction occurs by isotopic scrambling of aldehyde intermediates with solvent water *via* reversible hydration.[97] In support of this hypothesis, a theoretical study concluded that the reversible hydration of MeCHO ($CH_3CH^{16}O + H_2{}^{18}O \leftrightarrow CH_3CH^{18}O + H_2{}^{16}O$) occurs rapidly at ambient conditions since it is catalyzed by OH^-, which is present in abundance in the vicinity of the cathode.[97] In the final study, the relative abundance of the liquid-phase products in the vicinity of the Cu surface were measured during CO_2 reduction using a DEMS cell with a Cu-coated pervaporation membrane as the cathode, as shown in Figure 3.24.[21] The relative abundance of the multi-carbon aldehydes was found to exceed that of the corresponding primary alcohols near

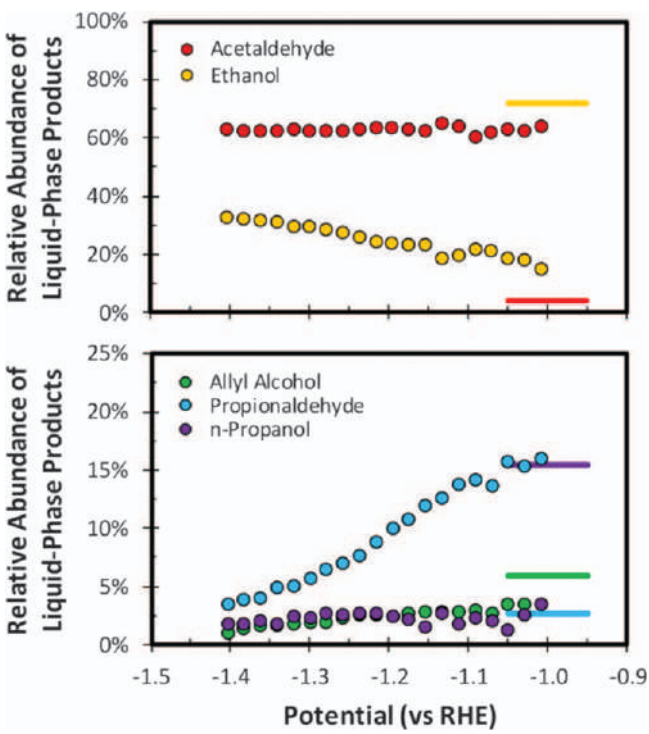

Figure 3.24 Relative abundance of the liquid-phase products in the vicinity of the polycrystalline Cu cathode during CO_2 reduction in 0.1 M $CsHCO_3$ (pH = 6.8). The solid lines represent the relative abundance observed in the bulk electrolyte when conducting CO_2 reduction over polycrystalline Cu at −1 V *vs.* RHE.
Reproduced from ref. 21 with permission from American Chemical Society, Copyright 2018.

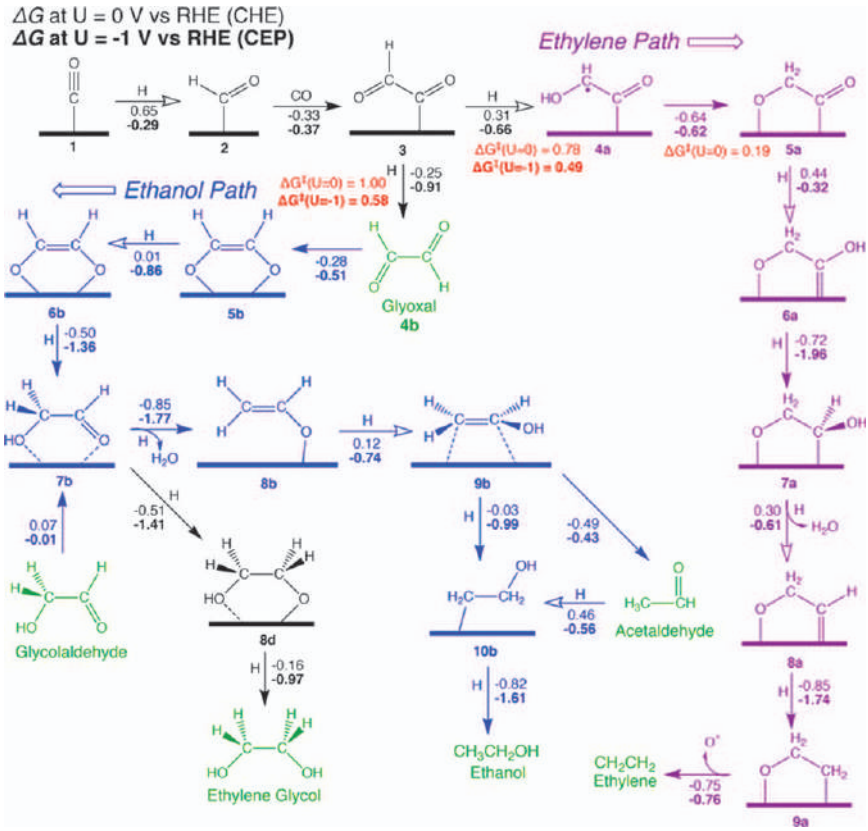

Figure 3.25 Mechanism of C_2 product formation over Cu(100). Calculated free energies of the different reaction steps are written next to the corresponding arrow at both U = 0 and −1 V. Free energy barriers are also included for the critical reaction steps.
Reproduced from ref. 98 with permission from American Chemical Society, Copyright 2018.

the cathode surface, contrary to what is typically observed in the bulk electrolyte. These observations support the notion that carbonyl-containing species are abundantly produced during CO_2 reduction over Cu but are typically reduced further to yield the corresponding primary alcohols.

A theoretical investigation of the reaction pathways responsible for the formation of the C_2 products of CO_2 reduction over Cu concluded that there are two dominate reaction pathways by which *CO–CHO can be reduced to hydrocarbons and alcohols, as shown in Figure 3.25.[98] In the first pathway, *CO–CHO is reduced to *CO–CHOH, which undergoes tautomerization to form CO–CH_2O before being reduced further to C_2H_4O and ultimately C_2H_4. In support of this mechanism, the reduction of C_2H_4O over Cu yields C_2H_4.[59] In the second pathway, *CO–CHO is reduced to glyoxal. Glyoxal can then undergo a series of reduction steps to yield glycolaldehyde, MeCHO, and ultimately

EtOH. Furthermore, the reduction steps beyond *CO–CHO formation were found to be more exergonic than the reduction of CO. Thus, the proposed mechanism is in complete agreement with the experimental observations.

3.2.14 Aldehydes as Intermediates to the Conjugate Bases of Carboxylic Acids

The formation of acetate anions during CO and CO_2 reduction is difficult to explain since few experimental or theoretical studies have investigated the pathways leading to the formation of this product. The formation of acetate anions during CO reduction is particularly interesting since it necessitates the formation of C–O bonds under reducing conditions. Interestingly, the rate of acetate formation scales with that of MeCHO, suggesting that the formation of these products are related.[76] Furthermore, the electrochemical reduction of primary aldehydes yield the conjugate bases of the corresponding carboxylic acids in addition to the corresponding primary alcohols, as shown in Figure 3.26.[99] A ''Cannizzaro-like'' disproportionation of the reacting aldehydes within the relatively alkaline environment present near the cathode surface has been hypothesized to be responsible for the formation of these conjugate bases (eqn (3.20)).

$$2(\text{R–CHO}) + \text{OH}^- \rightarrow \text{R–CH}_2\text{OH} + \text{R–COO}^- \qquad (3.20)$$

In fact, the formate concentration observed during formaldehyde reduction increased as the buffer capacity of the near-neutral electrolyte decreased, validating the role of the alkaline environment near the cathode in the mechanism of formate formation.[99] It is notable, however, that a higher

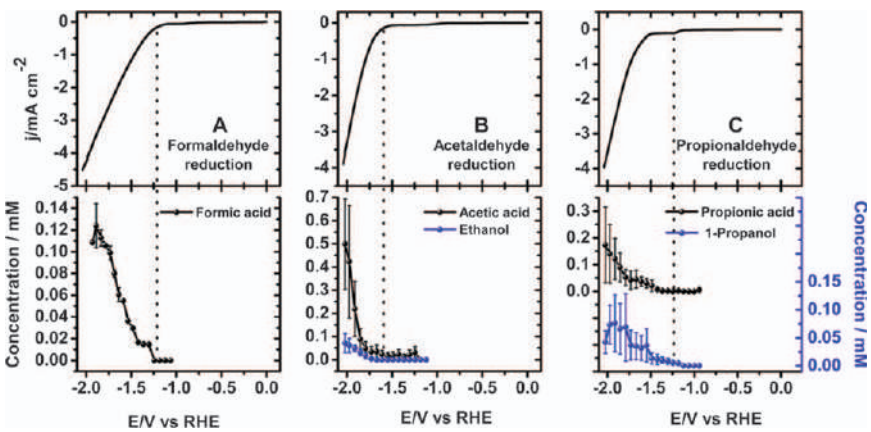

Figure 3.26 Liquid products detected during the electrochemical reduction of (A) formaldehyde, (B) acetaldehyde, and (C) propionaldehyde over boron-doped diamond in 0.001 M $HClO_4$ + 0.099 M $NaClO_4$ (pH = 3). Reproduced from ref. 99 with permission from American Chemical Society, Copyright 2017.

concentration of the conjugate bases of the carboxylic acids than the corresponding primary alcohols was observed in this study, which is inconsistent with a disproportionation mechanism in which the abundance of the two species are equivalent. Furthermore, acetate is the only multi-carbon conjugate base of a carboxylic acid observed during CO or CO_2 reduction despite the fact that both MeCHO and EtCHO are produced in relative abundance.[21] Conversely, quantum mechanical calculations have concluded that acetate anion formation occurs *via* the nucleophilic addition of hydroxide to a surface bound ketene intermediate.[100] The role of hydroxide addition in the mechanism of acetate formation is supported by isotope studies that have revealed that one of the oxygen atoms in acetate is derived from solvent water.[96,101] However, further experimentation and theoretical study is required to validate this mechanism.

3.2.15 Modifying the Selectivity of Copper

Since the Cu(100) surface has been found to exhibit superior activity and multi-carbon product selectivity relative to other non-stepped surfaces, significant efforts have been undertaken to enhance the (100) faceting of Cu electrocatalysts. The simplest way to enhance the fraction of Cu(100) facets is through oxidative and reductive potential cycling in the presence of halides, as shown in Figure 3.27.[77,102–104] Cu electrocatalysts prepared in this way exhibit enhanced activity due largely to the increase in surface roughness. Such roughened surfaces exhibit a significantly enhanced FE for C_2H_4 due to the increased fraction of (100) basal planes at the electrode surface. Through the use of *in situ* Raman spectroscopy it has been revealed that oxidizing Cu in the presence of halides forms a Cu-halide species that rapidly decomposes to form cubic cuprous oxide (Cu_2O).[104] This cubic Cu_2O precursor forms (100) faceted Cu upon electrochemical reduction. With the recognition of Cu_2O as the precursor to (100) faceted Cu, several different methods of preparing Cu_2O by electrodeposition have been developed.[105–108] These Cu_2O-derived Cu electrocatalysts all exhibit an enhanced FE for C_2H_4 relative to planar polycrystalline Cu foil.[105–108]

The recognition that rough Cu surfaces containing an abundance of (100) facets, in addition to numerous surface defects, are both more active and selective for producing multi-carbon products has stimulated a large effort aimed at producing highly roughened Cu surfaces. One approach to this goal has been to prepare metallic Cu from heavily oxidized precursors. The oxidation of Cu has been achieved through many different means, including thermal,[109,110] hydrothermal,[111] and plasma oxidation.[112,113] Such oxide derived Cu (OD-Cu) electrocatalysts exhibit a higher superficial activity and FEs for multi-carbon product evolution compared to planar Cu. It is noted, however, that activity comparisons between Cu electrocatalysts with significantly different degrees of surface roughness must be conducted cautiously, since mass transfer effects occur at lower cathodic overpotentials as the surface roughness increases. In fact, the earlier onset of significant

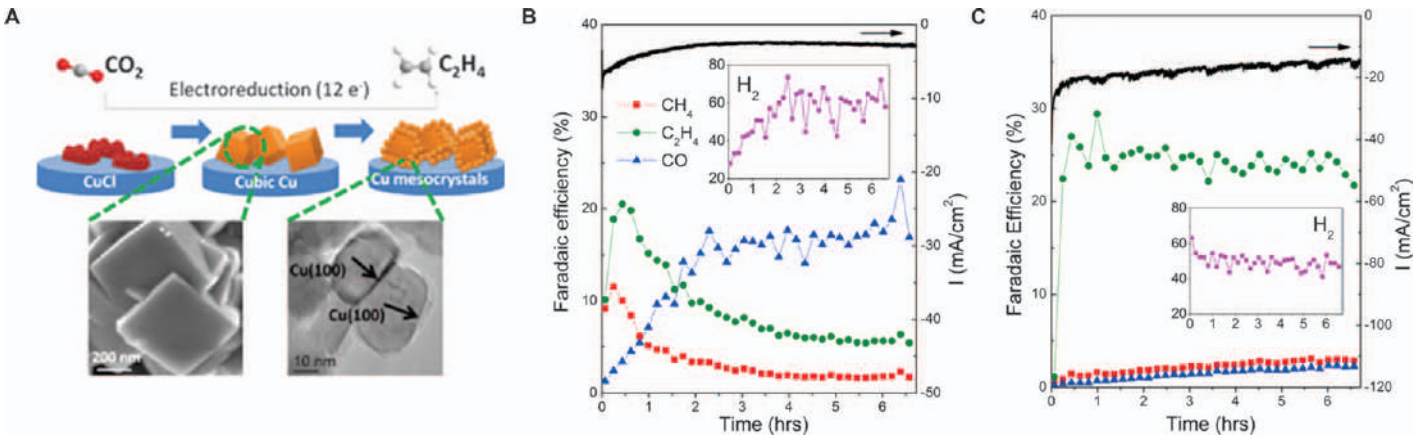

Figure 3.27 (A) Schematic depicting the electrochemical synthesis of (100) faceted Cu by electrochemical cycling in the presence of halides. Electrocatalytic activity observed during CO_2 reduction over (B) electropolished and (C) halide cycled Cu in 0.1 M $KHCO_3$ (pH = 6.8).
Reproduced from ref. 102 with permission from the Royal Society of Chemistry.

concentration polarization over OD-Cu may be partially responsible for the enhanced FE for producing multi-carbon products, since an elevated pH enhances multi-carbon product evolution for the reasons previously discussed in relation to Figures 3.16 and 3.17.

The enhanced selectivity to multi-carbon products observed over OD-Cu has been hypothesized to be the result of unique surface sites that strongly adsorb CO.[114] These strong binding sites are hypothesized to be defective grain boundaries based on the observation that the activity of OD-Cu scales with the surface grain boundary density, as shown in Figure 3.28A.[115,116] Recent theoretical work done on a rough Cu surface created by Monte Carlo simulation has concluded that the formation of multi-carbon products correlates with the stability of *CO–COH, an intermediate hypothesized to be involved in the formation of ethene and ethanol. The binding energy of *CO–COH is found to be highest over (100)-like sites located next to a (111)-like step and twin boundaries.[117,118] Based on this analysis, it was proposed that the selectivity to multi-carbon products should correlate with the grain boundary density.

It has also been proposed that strong CO binding sites arise due to the presence of metastable subsurface oxygen. This hypothesis is largely based on the observation of oxygen on Cu during CO_2 reduction that was detected using *quasi in situ* ambient pressure X-ray photoelectron spectroscopy (APXPS).[119] However, isotope and *operando* XRD studies indicate that the oxygen in the oxidized Cu precursors is completely and immediately eliminated upon cathodic polarization to potentials required to drive CO_2 reduction, as shown in Figure 3.28B.[120,121] In agreement with these experimental observations, theoretical studies have concluded that subsurface oxygen will rapidly diffuse to the electrode surface and be eliminated, as shown in Figure 3.28C.[122,123] Thus, it seems unlikely that subsurface oxygen plays any role in the enhanced C_2H_4 selectivity observed over OD-Cu electrocatalysts.

It has recently been demonstrated that CO reduction in the presence of amines yields products containing C–N bonds.[100] For example, the co-electrolysis of CO and NH_3 yields acetamide with a FE of ~40%. Quantum mechanical calculations concluded that C–N bond formation occurs *via* the nucleophilic addition of the corresponding amine to a surface bound ketene intermediate, which is in direct competition with the acetate formation mechanism previously mentioned. However, the calculations suggest that the nucleophilic addition of the amine is thermodynamically favored over the addition of hydroxide. Further studies may yet identify other nucleophiles capable of reacting with the multi-carbon intermediates of CO and CO_2 reduction.

3.3 Electrolyte

3.3.1 Concentration Polarization

The evolution of hydroxide anions from the cathode during CO_2 reduction significantly alters the alkalinity of the local reaction environment since the reaction is typically conducted in electrolytes with near-neutral pH.[124,125]

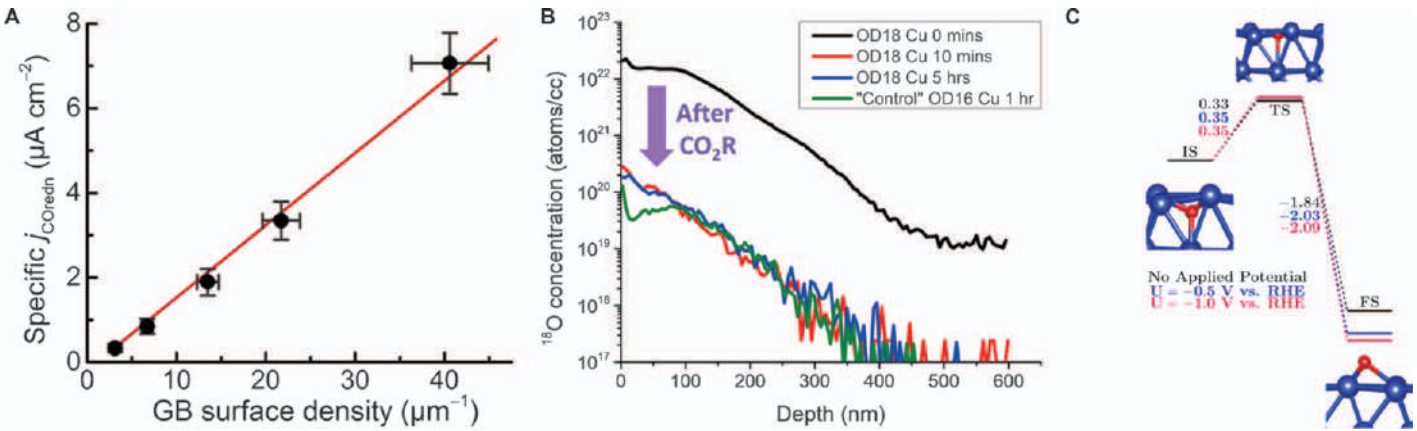

Figure 3.28 (A) Correlation between the CO reduction activity and surface grain boundary density observed over Cu electrocatalysts at −0.3 V *vs.* RHE in 0.1 M KOH (pH = 13). Reproduced from ref. 115 with permission from American Chemical Society, Copyright 2016. (B) ^{18}O content of ^{18}OD-Cu electrocatalysts after conducting $C^{16}O_2$ reduction for different lengths of time. Reproduced from ref. 120 with permission from John Wiley and Sons, Copyright © 2017 WILEY-VCH Verlag GmbH & Co. KGaA, Weinheim. (C) Free energy profile for the migration of a subsurface oxygen atom to the surface at various applied potentials (pH = 7). Reproduced from ref. 122 with permission from American Chemical Society, Copyright 2018.

Furthermore, the rate of CO or CO_2 consumption at the cathode surface can easily outpace the rate of mass transfer through the hydrodynamic boundary layer due to both the low solubility of these species and their low diffusion coefficients in aqueous solutions.[125] The formation of reactant and product concentration gradients is known as concentration polarization. Concentration polarization is problematic for electrochemical cells because it introduces energetic inefficiencies in the form of Nernstian potential losses. Nernstian potential losses arise due to the dependence of the equilibrium potential of an electrochemical reaction on the concentration of reactants and products in the immediate vicinity of the electrocatalyst. However, Nernstian potential losses also introduce uncertainty into electrocatalytic activity measurements.[42] The magnitude of the polarization losses depend primarily on the geometric current density, which determines the flux of reactants and products to and from the cathode surface, respectively.[124–126] The magnitude of the polarization loss has typically been determined using continuum modeling due to the lack of experimental methods to accurately quantify the composition of the local reaction environment.[124–126] The calculated polarization losses in bicarbonate-based electrolytes increase rapidly with current density due to the inability of the buffering species to dissociate until the pH of the electrolyte in the vicinity of the cathode rises from the bulk value (pH = 6.8) to the acid-dissociation constant of HCO_3^- (p*K*a = 10.3). However, the magnitude of the polarization loss continues to increase with current density, albeit at a slower rate, after the near-surface pH reaches the acid-dissociation constant of HCO_3^- due to insufficient mass transfer of HCO_3^- through the hydrodynamic boundary layer. The magnitude of the polarization loss associated with the local pH gradients has recently been determined experimentally by measuring the concentrations of HCO_3^- and CO_3^{2-} near the cathode surface using IR spectroscopy.[127] This method of determining the local pH is accurate since HCO_3^- and CO_3^{2-} are rapidly equilibrated, as previously mentioned. The magnitude of the polarization loss associated with the local pH gradients determined using this approach agree with those calculated using continuum modeling, as shown in Figure 3.29B.

The composition of the local reaction environment during CO_2 reduction over polycrystalline Cu has been determined using continuum modeling.[125] The onset of significant CO_2 depletion occurs at roughly −1 V *vs.* RHE, as shown in Figure 3.30. Interestingly, the rate of multi-carbon product evolution also plateaus and begins to decline at this potential.[51] These observations suggest that the decreasing rate of multi-carbon product evolution observed at −1 V *vs.* RHE is the result of CO_2 depletion and is not intrinsic to polycrystalline Cu. This makes sense given that the steady state coverage of adsorbed CO will decrease as the local CO_2 concentration decreases. The reduced coverage of adsorbed CO inhibits the rate of C–C coupling and results in excessive H_2 evolution. However, it is important to realize that the magnitude of these concentration gradients is primarily dependent on the geometric current density. As a result, nanostructured electrocatalysts with

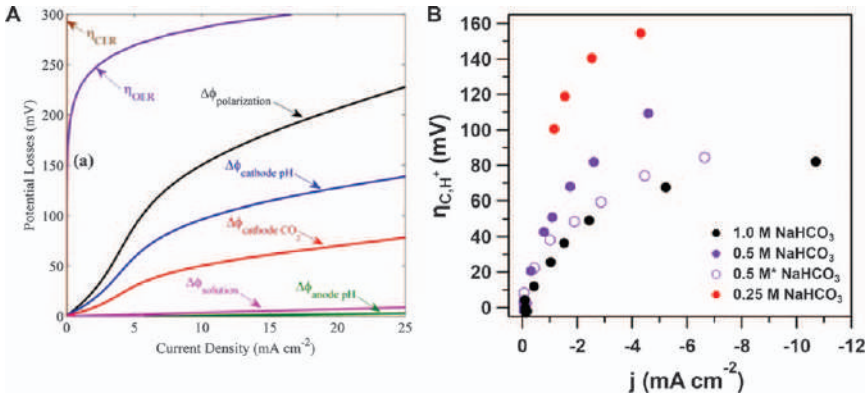

Figure 3.29 (A) Dependence of the calculated polarization losses on the current density in 1 M $KHCO_3$ (pH = 7.8) with a hydrodynamic boundary layer thickness of 100 μm. Reproduced from ref. 19 with permission from the PCCP Owner Societies. (B) Dependence of the cathodic pH polarization losses on the current density determined by measuring the concentrations of HCO_3^- and CO_3^{2-} in the vicinity of the cathode using ATR-FTIR. Reproduced from ref. 127 with permission from American Chemical Society, Copyright 2018.

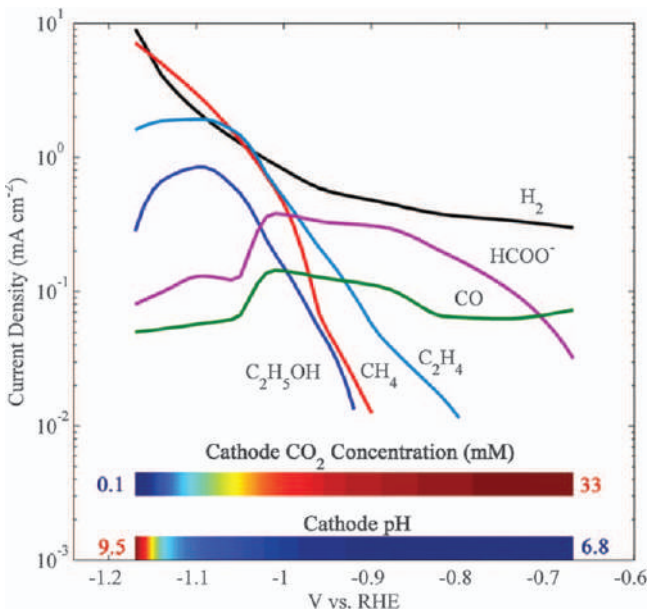

Figure 3.30 Calculated near-surface pH and CO_2 concentration over polycrystalline Cu during CO_2 reduction in 0.1 M $KHCO_3$ (pH = 6.8) with a hydrodynamic boundary layer thickness of 40 μm.
Reproduced from ref. 19 with permission from the PCCP Owner Societies.

high surface roughness are more susceptible to these effects than planar electrocatalysts.[42] This complicates accurate comparison of the intrinsic activities of electrocatalysts with vastly different roughness factors.

3.3.2 Impact of Electrochemical Cell Hydrodynamics

The magnitude of the concentration gradients that form in the vicinity of the cathode also depends on the hydrodynamics of the electrochemical cell, as shown in Figure 3.31.[19,42] As the mixing of the electrolyte in the cell is enhanced, the magnitude of the concentration gradients formed upon polarization is reduced. This is because the diffusional flux to and from the cathode surface depends inversely on the hydrodynamic boundary layer thickness. The hydrodynamic boundary layer thickness of an electrochemical cell can be quantified by measuring the diffusion-limited current density of an electrochemically reversible reaction.[42] An electrochemical reaction is reversible if electron transfer to the reacting species is facile such that the observed rate of the reaction is only limited by the mass transfer of the reacting species to the electrode surface. An example of an electrochemically reversible reaction is ferricyanide reduction (eqn (3.21))

$$Fe(CN)_6^{3-} + e^- \rightleftharpoons Fe(CN)_6^{4-} \tag{3.21}$$

Ferricyanide reduction occurs at a potential where no other Faradaic processes occur over Au, as shown in Figure 3.33. As a result, the Faradaic

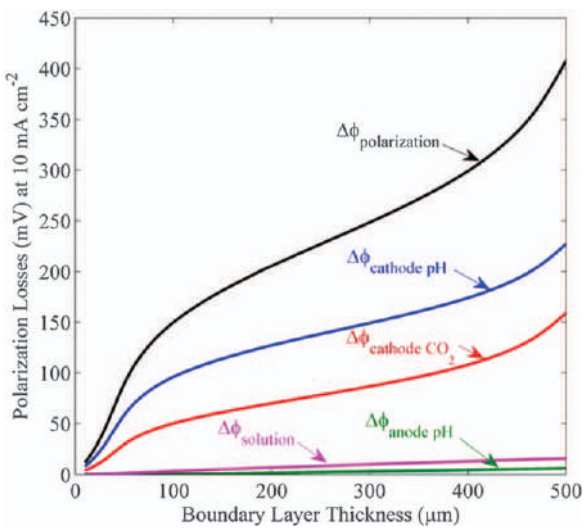

Figure 3.31 Dependence of the calculated polarization losses at a current density of 10 mA cm^{-2} on the hydrodynamic boundary layer thickness in 1 M $KHCO_3$ (pH = 7.8).
Reproduced from ref. 19 with permission from the PCCP Owner Societies.

current observed upon cathodic polarization can be attributed entirely to ferricyanide reduction. The diffusion-limited current density of ferricyanide reduction increases as the flow rate of CO_2 through the electrochemical cell increases due to the enhanced mixing of the electrolyte by the column of CO_2 bubbles, as shown in Figure 3.32B. As shown in Figure 3.32C, the average hydrodynamic boundary layer thickness at the cathode surface can be calculated using Fick's law (eqn (3.22))

$$\delta_{BL} = \frac{F \times D_{Fe(CN)_6^{3-}} \times C^{*}_{Fe(CN)_6^{3-}}}{J_{SS}} \tag{3.22}$$

where F is Faraday's constant, $D_{Fe(CN)63-}$ is the diffusion coefficient of ferricyanide, $C_{Fe(CN)63-}$ is the bulk concentration of ferricyanide, and J_{SS} is the steady state current density of ferricyanide reduction.

The hydrodynamic boundary layer thickness at the cathode surface has a significant influence on the activity observed during CO_2 reduction, as illustrated over polycrystalline Ag in Figure 3.33. The activity and selectivity observed over polycrystalline Ag does not vary substantially with the hydrodynamic boundary layer thickness at anodic potentials of -1 V *vs.* RHE, suggesting that concentration polarization has not occurred in this potential regime. However, substantial variations are observed at more cathodic potentials, suggesting that the onset of concentration polarization occurs at roughly -1 V *vs.* RHE under these experimental conditions. As the hydrodynamic boundary layer thickness decreases, less H_2 and more CO are produced at a given potential, resulting in a CO FE swing of roughly 60% at -1.4 V *vs.* RHE. Furthermore, the maximum attainable CO partial current density scales inversely with the measured hydrodynamic boundary layer thickness, as expected for a diffusion-limited reaction.

3.3.3 Impact of Buffer Concentration and Acidity

The magnitude of the pH and CO_2 gradients that form in the vicinity of the cathode also depend on the buffer capacity of the electrolyte.[125,126,128] The buffer capacity of the electrolyte depends on both the concentration and acidity of the buffering species. Most studies of CO_2 reduction utilize HCO_3^- as the buffering species since it yields the highest CO_2-derived product selectivity.[52,128] However, the relatively low acidity of the HCO_3^- anion ($pKa = 10.3$) enables the near-surface pH to rapidly rise with the current density until the near-surface pH becomes alkaline enough for HCO_3^- dissociation to occur. Nevertheless, the near-surface pH can rise above the acid dissociation constant of HCO_3^- once the rate of hydroxide anion evolution from the cathode surface outpaces the rate of HCO_3^- mass transfer through the hydrodynamic boundary layer. However, this can be mitigated by increasing the concentration of the buffering species.

Many studies have sought to elucidate the influence of HCO_3^- concentration on the activity and selectivity of polycrystalline Cu.[126,128–130] The general

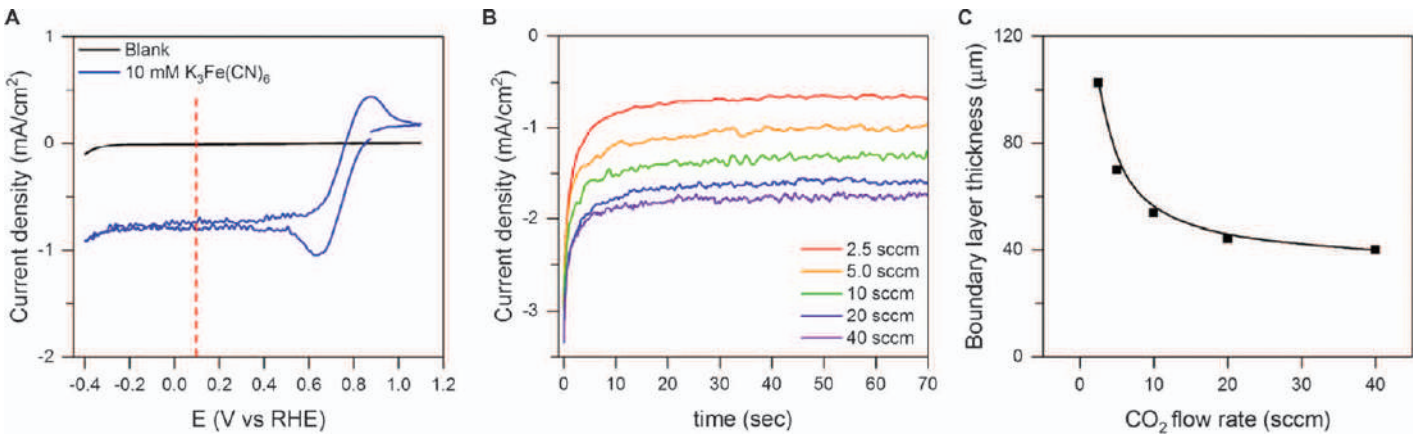

Figure 3.32 (A) Cyclic voltammograms observed over polycrystalline Au in 0.1 M $CsHCO_3$ (pH = 6.8) with and without the addition of 10 mM $K_3Fe(CN)_6$. (B) Transient current densities observed during chronoamerometry at +0.1 V *vs.* RHE over polycrystalline Au under a series of different hydrodynamic conditions. (C) Dependence of the hydrodynamic boundary layer thickness on the CO_2 flow rate utilized to mix the electrolyte as calculated using the chronoamperometry data.
Reproduced from ref. 42 with permission from American Chemical Society, Copyright 2018.

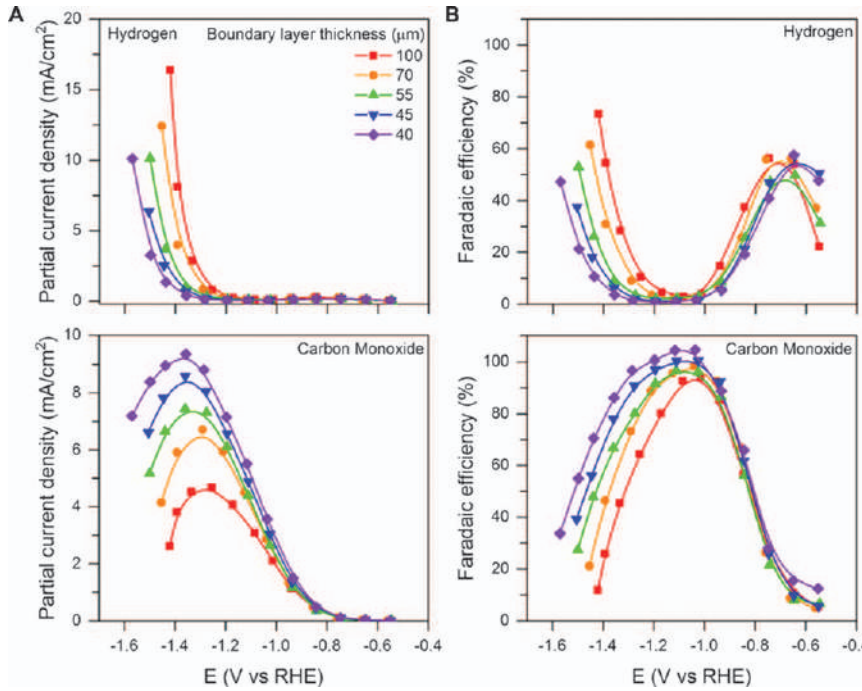

Figure 3.33 (A) Partial current densities and (B) product Faradaic efficiencies observed during CO_2 reduction over polycrystalline Ag foil as a function of the hydrodynamic boundary layer thickness in 0.1 M $CsHCO_3$ (pH = 6.8). Reproduced from ref. 42 with permission from American Chemical Society, Copyright 2018.

conclusion is that the FEs for H_2 and CH_4 increase at the expense of the multi-carbon products as the HCO_3^- concentration increases, as shown in Figure 3.34.[126,128] Continuum modeling has concluded that the near-surface pH decreases as the HCO_3^- concentration increases at a given current density, since the magnitude of the concentration gradients formed during CO_2 reduction decrease with the buffer capacity of the electrolyte.[124,126,130] This variation in the local pH partially explains the activity trends observed in electrolytes of varying buffer concentration. However, the intrinsic activity for H_2 and CH_4 evolution increase with the HCO_3^- concentration,[129,130] even when the applied potentials are corrected to account for the Nernstian potential shifts arising from these local pH gradients.[130] Conversely, the activity for producing C_2H_4 and the other multi-carbon products does not vary with the HCO_3^- concentration when the activity data is plotted on the pH-independent SHE scale, as is appropriate for these products. These observations suggest that HCO_3^- has a direct influence on the intrinsic activity of H_2 and CH_4 evolution beyond the indirect influence of modulating the local pH. Since the RDS in the mechanism of H_2 and CH_4 evolution is an electrochemical hydrogenation step, it has been hypothesized that HCO_3^- can serve as the

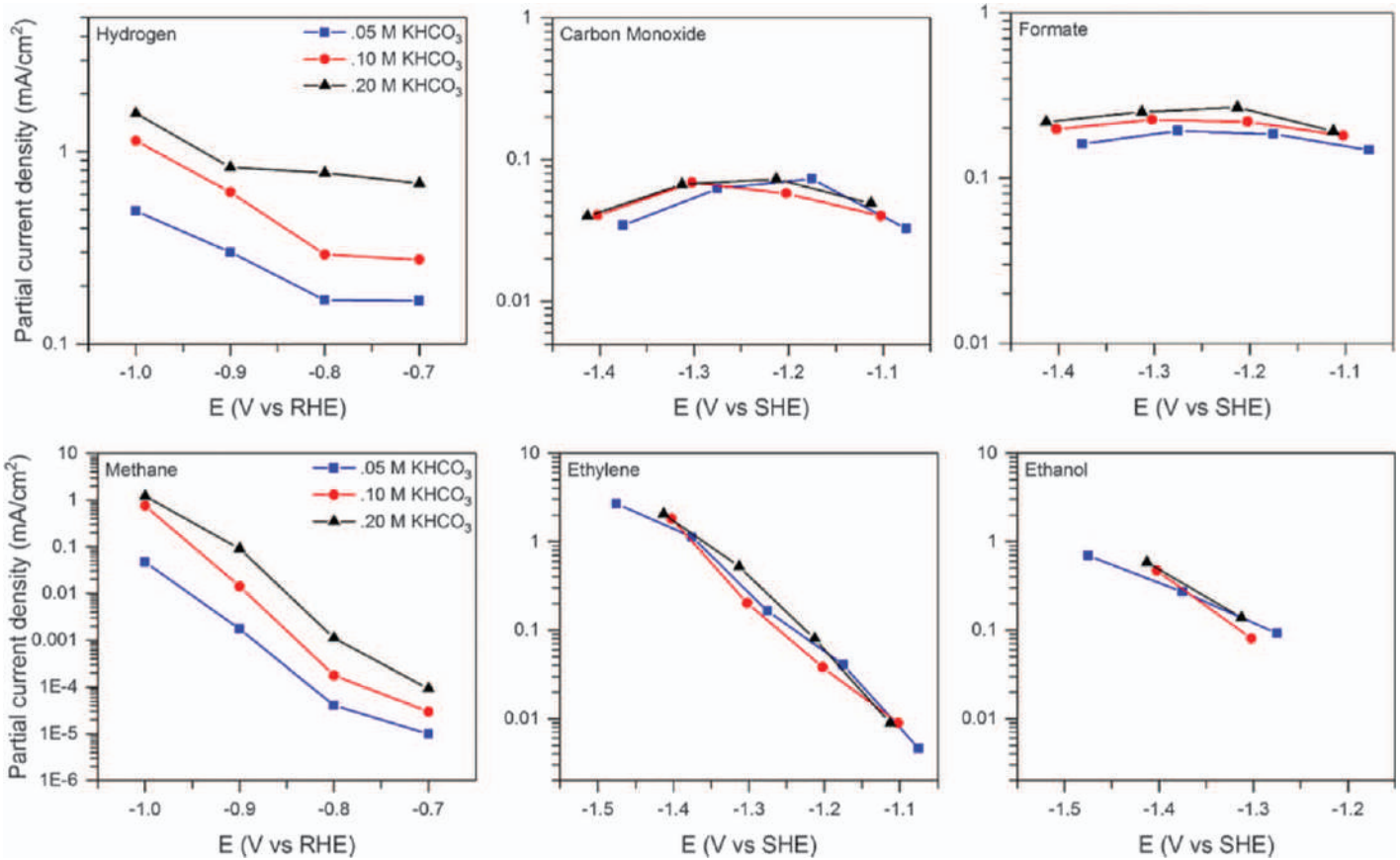

Figure 3.34 Partial current densities observed during CO_2 reduction over Cu(100) thin films as a function of the applied potential and $KHCO_3$ concentration. Note that H_2 and CH_4 are plotted on a RHE scale while other products are plotted on a SHE scale. Reproduced from ref. 130 with permission from John Wiley and Sons, Copyright © 2018 WILEY-VCH Verlag GmbH & Co. KGaA, Weinheim.

H source at the cathode.[130] The reason that HCO_3^- anions are an effective H source is that the p*K*a of HCO_3^- is 3.7 p*K*a units lower than water (10.3 *vs.* 14), which means that despite the lower concentration of HCO_3^- relative to water (0.1 *vs.* 55 M), HCO_3^- is a more effective H donor.

The ability of the buffering species to supply H to the cathode increases with its acidity. Increasing the acidity of the buffering species selectively enhances the rates of H_2 and CH_4 evolution since an electrochemical hydrogenation step is the RDS in the formation mechanism of these products. This can be illustrated by comparing activity data measured in non-buffering electrolytes, such as perchlorate and sulfate, with that measured in buffering electrolytes utilizing phosphate (p*K*a = 7.21), borate (p*K*a = 8.98), and bicarbonate (p*K*a = 10.3) as the buffering species. The H_2 and CH_4 evolution activity observed over Cu increases with the acidity of the buffering species when the data are plotted on the pH-dependent RHE scale, as shown in Figure 3.35. Conversely, the multi-carbon product evolution activity of Cu is not influenced by the acidity of the buffering species, as evidenced by the independence of their partial current densities with buffer acidity when the activity data is plotted on the pH-independent SHE scale.

3.3.4 Impact of Cation Size

The activity and product selectivity observed over Cu is influenced significantly by the identity of the electrolyte cation. As the size of the alkali cation increases the FEs for the multi-carbon products increase at the expense of H_2 and CH_4, as shown in Figure 3.36A.[131–135] Notably, the rates of H_2 and CH_4 evolution are independent of cation identity, whereas the rates of multi-carbon product formation increase by nearly an order of magnitude at a given applied potential upon switching from Li^+ to Cs^+ as the electrolyte cation, as shown in Figure 3.36B. Interestingly, the activity observed over Cu in electrolytes containing multiple alkali metal cations is not a linear combination of the activities observed in electrolytes containing the individual cations.[134] Instead, the activity more closely resembles that observed in an electrolyte containing only the larger alkali cation, as shown in Figure 3.36C. In fact, 80% of the activity observed in an electrolyte that contains only the larger alkali cation is obtained when using an electrolyte that contains only 10% of the larger alkali cation.[134] This observation suggests that larger alkali cations occupy the space within the Helmholtz layer more competitively than the smaller alkali metal cations. This has been hypothesized to be the result of the relatively low hydration energy of large alkali cations, which enables them to more easily become partially desolvated and approach the cathode surface.[134]

Recent theoretical analysis has concluded that the magnitude of the double layer field is substantially elevated in the vicinity of cations present in the Helmholtz layer, as shown in Figure 3.37.[136] The magnitude of these local electric fields is dependent on the surface charge density of the cathode, which is determined by the difference between the applied potential on a SHE scale and the potential of zero charge of the electrocatalyst and the

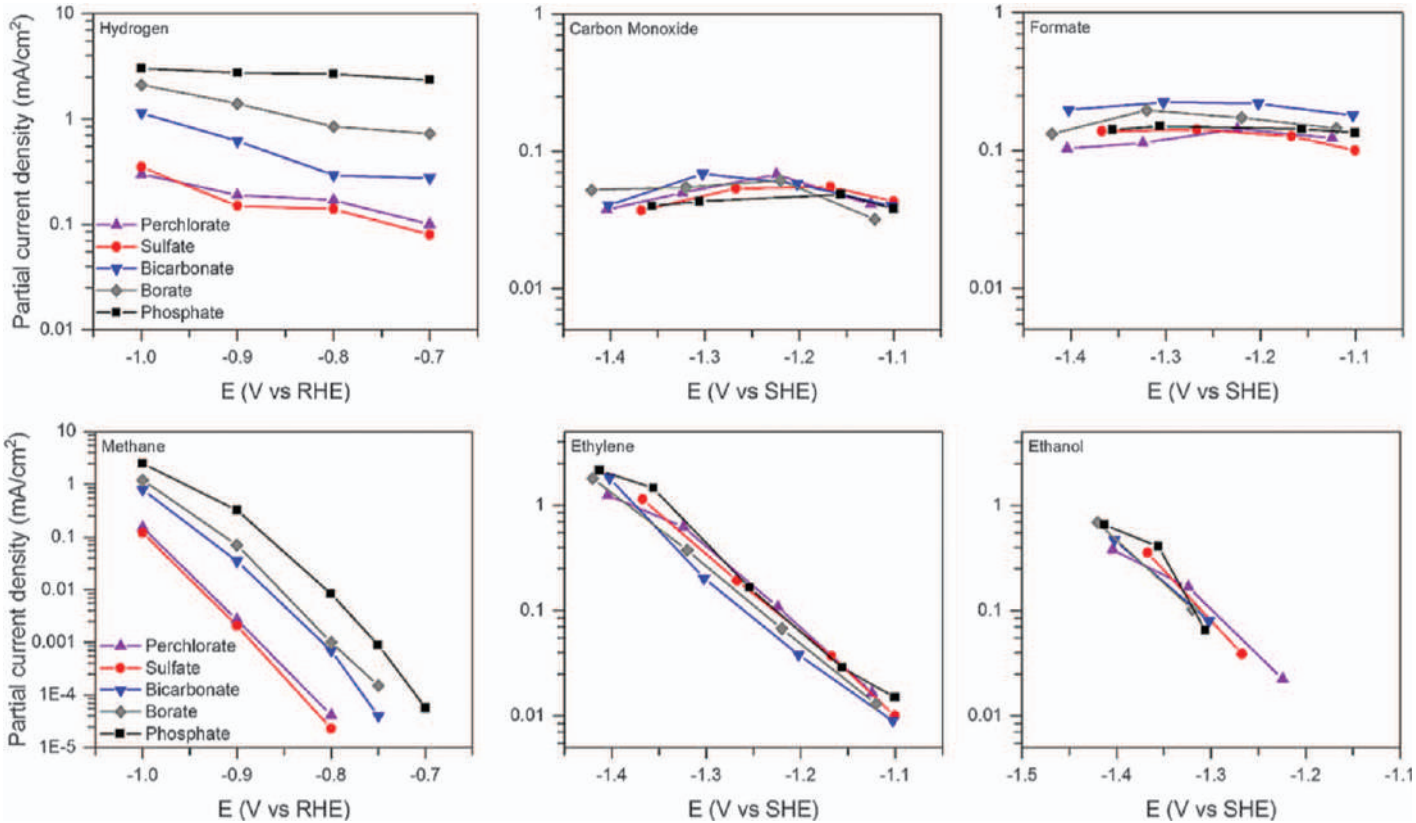

Figure 3.35 Partial current densities observed during CO_2 reduction over Cu(100) thin films as a function of the applied potential and acidity of the buffering species. Note that H_2 and CH_4 are plotted on a RHE scale while other products are plotted on a SHE scale. Reproduced from ref. 130 with permission from John Wiley and Sons, Copyright © 2018 WILEY-VCH Verlag GmbH & Co. KGaA, Weinheim.

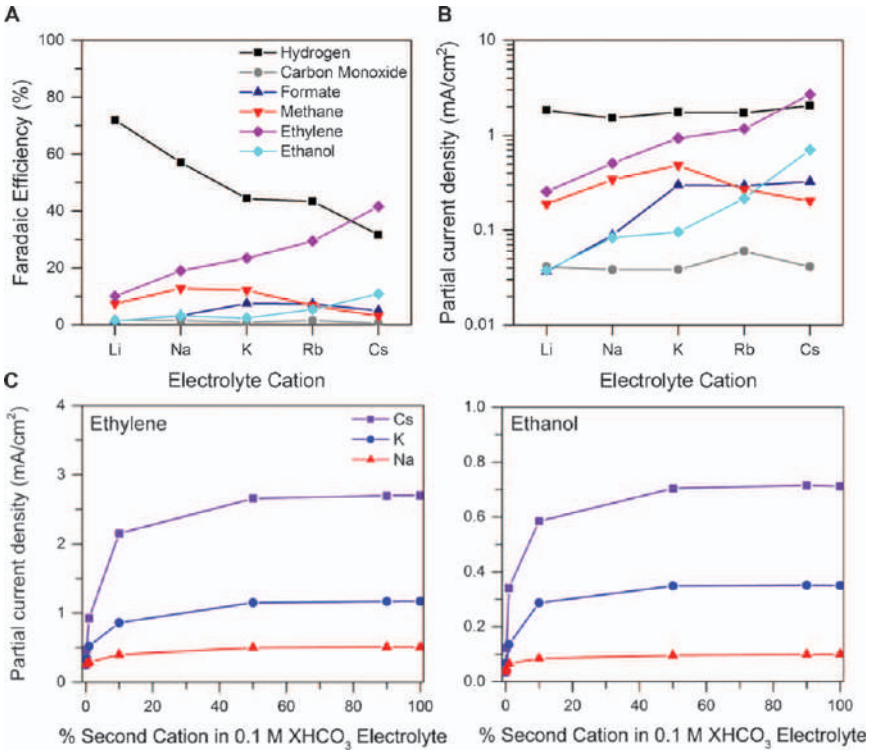

Figure 3.36 (A) Faradaic efficiencies and (B) partial current densities for selected products observed during CO_2 reduction in 0.1 M bicarbonate electrolytes as a function of the identity of the alkali cation. Reproduced from ref. 42 with permission from American Chemical Society, Copyright 2018. (C) Partial current densities for ethene and ethanol observed during CO_2 reduction as a function of the cation composition of a 0.1 M bicarbonate electrolyte (pH = 6.8) balanced with Li^+. All the experiments were conducted over Cu(100) thin films at −1 V *vs.* RHE. Reproduced from ref. 92 with permission from American Chemical Society, Copyright 2017.

concentration of cations in the Helmholtz region, as shown in Figure 3.38A. Hydrated cations can pack more densely into the Helmholtz region as their size decreases. The ionic radius and the number of water molecules present in its hydration shell determine the size of a hydrated cation. The number of water molecules in the hydration shell of a cation is determined by its hydration energy, which scales inversely with the cation radius due to Coulomb's law. Thus, smaller alkali cations have significantly more water molecules in their hydration shell than larger alkali cations, and consequently, the size of a hydrated alkali cation decreases as its cationic size increases.[137] This means that the local electric fields in the vicinity of hydrated Cs^+ present in the Helmholtz layer are stronger than that for hydrated Li^+. In agreement with this interpretation, the double layer

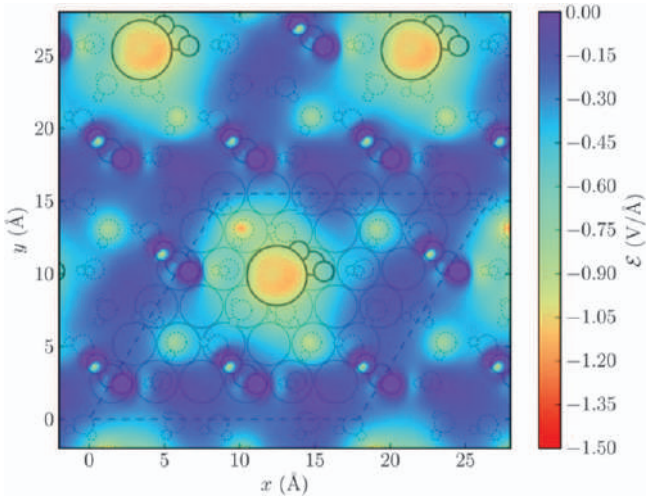

Figure 3.37 Electric field distribution taken at a *z*-slice near the center of *CO_2 in a 6×6 unit cell with a K^+ coverage of 1/36.
Reproduced from ref. 136 with permission from American Chemical Society, Copyright 2016.

capacitance measured over Au single crystal electrodes increases systematically as the hydration energy of the alkali metal cation decreases, as shown in Figure 3.38B.[138] This occurs due to the enhanced double layer capacitance afforded by the increased cation density in the Helmholtz layer. The impact of these effects on the stability of *CO–CO, an intermediate in the formation of C_2 products, is nicely illustrated in a recent theoretical study that combines size-modified Poisson–Boltzmann theory with *ab initio* simulations of the field effects.[139] Figure 3.38C shows that this model provides good quantitative agreement with the experimental activity trends for multi-carbon product evolution over Cu.

3.4 Conclusions

The electrochemical reduction of CO_2 enables a myriad of carbon-neutral chemicals and fuels to be synthesized using renewable electricity. However, commercial implementation of the technology will require superior electrocatalysts to be developed. This can only be accomplished by first understanding the fundamental reaction mechanisms responsible for the evolution of the desired products. Establishing such an understanding is challenging due to the sensitivity of the reaction to concentration polarization, which complicates the characterization of the intrinsic activity of electrocatalysts by modifying the composition of the local reaction environment. However, significant insight into the mechanisms of CO_2 reduction have been established despite these challenges. CO has been identified as a critical intermediate in the formation of hydrocarbons and alcohols. The methanation of CO is enhanced whenever

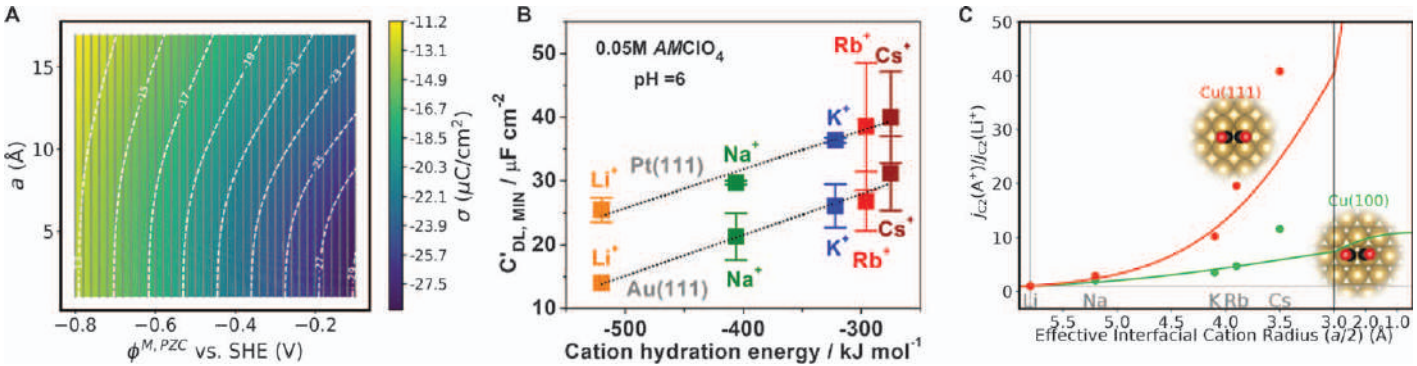

Figure 3.38 (A) Calculated surface charge density at −1 V *vs.* RHE (pH = 7) as a function of the hydrated cation radius and the potential of zero charge of the electrocatalyst. Reproduced from ref. 139 with permission from the Royal Society of Chemistry. (B) Double-layer capacitances of Pt(111) and Au(111) measured by impedance spectroscopy in 0.05 M perchlorate electrolytes (pH = 6) as a function of the hydration energy of the alkali cation. Reproduced from ref. 138 with permission from American Chemical Society, Copyright 2018. (C) Multi-carbon product partial current densities observed over Cu(111) and Cu(100) at −1 V *vs.* RHE as a function of the hydrated size of alkali cations present in the Helmholtz region. Activity data is normalized to that observed in the presence of Li^+. Filled circles represent the experimental data points and solid lines represent the theoretical predictions. Reproduced from ref. 139 with permission from the Royal Society of Chemistry.

elementary hydrogenation steps are promoted, which can be accomplished by applying more cathodic potentials on a RHE scale or by increasing the local concentration and acidity of willing H donors. Conversely, the formation of multi-carbon products is enhanced by stabilizing dipolar C–C coupled intermediates by increasing the local electric field strength. The local electric field strength depends on the surface charge density of the electrocatalyst, which can be increased by applying more cathodic potentials on a SHE scale or by utilizing electrolyte cations that more densely populate the Helmholtz region. While a large variety of multi-carbon products are produced by the reaction, experimental and theoretical studies suggest that the hydrocarbon and liquid-phase product pathways quickly diverge after C–C bond formation and that carbonyl-containing species are intermediates to the corresponding primary alcohols. Future improvements in CO_2 reduction electrocatalysis will require the identification of CO reduction electrocatalysts beyond Cu and the elucidation of C–C coupling mechanisms resulting in the formation of C_{3+} products.

References

1. Intergovernmental Panel on Climate Change. *Climate Change 2014: Synthesis Report*, 2014, https://www.cambridge.org/core/books/climate-change-2014-mitigation-of-climate-change/81F2F8D8D234727D153EC10D428A2E6D.
2. Adoption of the Paris Agreement, 2015.
3. B. Obama, *Science*, 2017, **355**, 126–129.
4. S. Chu, Y. Cui and N. Liu, *Nat. Mater.*, 2017, **16**, 16–22.
5. M. Gattrell, N. Gupta and A. Co, *J. Electroanal. Chem.*, 2006, **594**, 1–19.
6. H. R. M. Jhong, S. Ma and P. J. A. Kenis, *Curr. Opin. Chem. Eng.*, 2013, **2**, 191–199.
7. R. Kortlever, J. Shen, K. J. P. Schouten, F. Calle-Vallejo and M. T. M. Koper, *J. Phys. Chem. Lett.*, 2015, **6**, 4073–4082.
8. D. D. Zhu, J. L. Liu and S. Z. Qiao, *Adv. Mater.*, 2016, **28**, 3423–3452.
9. B. Zhang and J. Zhang, *J. Energy Chem.*, 2017, **26**, 1050–1066.
10. H. Xie, T. Wang, J. Liang, Q. Li and S. Sun, *Nano Today*, 2018, **21**, 41–54.
11. Z. Gu, H. Shen, L. Shang, X. Lu, L. Qian and G. Zheng, *Small Methods*, 2018, **2**, 1800121.
12. A. Rendón-Calle, S. Builes and F. Calle-Vallejo, *Curr. Opin. Electrochem.*, 2018, **9**, 158–165.
13. D. Raciti and C. Wang, *ACS Energy Lett.*, 2018, **3**, 1545–1556.
14. R. M. Arán-Ais, D. Gao and B. Roldan Cuenya, *Acc. Chem. Res.*, 2018, **51**, 2906–2917.
15. S. Xu and E. A. Carter, *Chem. Rev.*, 2019, **119**, 6631–6669.
16. J. E. Pander, D. Ren, Y. Huang, N. W. X. Loo, S. H. L. Hong and B. S. Yeo, *ChemElectroChem*, 2018, **5**, 219–237.
17. S. A. Nitopi, E. Bertheussen, S. B. Scott, X. Liu, A. K. Engstfeld, S. Horch, B. Seger, I. E. L. Stephens, K. Chan, C. Hahn, J. K. Nørskov, T. F. Jaramillo and I. Chorkendorff, *Chem. Rev.*, 2019, **119**, 7610–7672.

18. J. Qiao, Y. Liu, F. Hong and J. Zhang, *Chem. Soc. Rev.*, 2014, **43**, 631–675.
19. M. R. Singh, E. L. Clark and A. T. Bell, *Phys. Chem. Chem. Phys.*, 2015, **17**, 18924–18936.
20. E. L. Clark, M. R. Singh, Y. Kwon and A. T. Bell, *Anal. Chem.*, 2015, **87**, 8013–8020.
21. E. L. Clark and A. T. Bell, *J. Am. Chem. Soc.*, 2018, **140**, 7012–7020.
22. Y. Hori, K. Kikuchi and S. Suzuki, *Chem. Lett.*, 1985, **14**, 1695–1698.
23. H. Noda, S. Ikeda, Y. Oda, K. Imai, M. Maeda and K. Ito, *Bull. Chem. Soc. Jpn.*, 1990, **63**, 2459–2462.
24. K. Hara, A. Kudo and T. Sakata, *J. Electrochem. Soc.*, 1990, **391**, 141–147.
25. J. K. Nørskov, T. Bligaard, A. Logadottir, J. R. Kitchin, J. G. Chen, S. Pandelov and U. Stimming, *J. Electrochem. Soc.*, 2005, **152**, J23–J26.
26. J. T. Feaster, C. Shi, E. R. Cave, T. Hatsukade, D. N. Abram, K. P. Kuhl, C. Hahn, J. K. Nørskov and T. F. Jaramillo, *ACS Catal.*, 2017, **7**, 4822–4827.
27. N. J. Firet and W. A. Smith, *ACS Catal.*, 2017, **7**, 606–612.
28. T. Hatsukade, K. P. Kuhl, E. R. Cave, D. N. Abram and T. F. Jaramillo, *Phys. Chem. Chem. Phys.*, 2014, **16**, 13814–13819.
29. E. R. Cave, J. H. Montoya, K. P. Kuhl, D. N. Abram, T. Hatsukade, C. Shi, C. Hahn, J. K. Nørskov and T. F. Jaramillo, *Phys. Chem. Chem. Phys.*, 2017, **19**, 15856–15863.
30. N. Hoshi, M. Kato and Y. Hori, *J. Electroanal. Chem.*, 1997, **440**, 283–286.
31. E. L. Clark, S. Ringe, M. Tang, A. Walton, C. Hahn, T. F. Jaramillo, K. Chan and A. T. Bell, *ACS Catal.*, 2019, **9**, 4006–4014.
32. N. Todoroki, H. Tei, H. Tsurumaki, T. Miyakawa, T. Inoue and T. Wadayama, *ACS Catal.*, 2019, **9**, 1383–1388.
33. S. Mezzavilla, S. Horch, I. E. L. Stephens, B. Seger and I. Chorkendorff, *Angew. Chem., Int. Ed.*, 2019, **58**, 3774–3778.
34. Y. Hori, I. Takahashi, O. Koga and N. Hoshi, *J. Phys. Chem. B*, 2002, **106**, 15–17.
35. E. Herrero, L. J. Buller and H. D. Abruna, *Chem. Rev.*, 2001, **101**, 1897–1930.
36. Y. Chen, C. W. Li and M. W. Kanan, *J. Am. Chem. Soc.*, 2012, **134**, 19969–19972.
37. M. Ma, B. J. Trześniewski, J. Xie and W. A. Smith, *Angew. Chem., Int. Ed.*, 2016, **55**, 9748–9752.
38. Q. Lu, J. Rosen, Y. Zhou, G. S. Hutchings, Y. C. Kimmel, J. G. Chen and F. Jiao, *Nat. Commun.*, 2014, **5**, 1–6.
39. Y.-C. Hsieh, S. D. Senanayake, Y. Zhang, W. Xu and D. E. Polyansky, *ACS Catal.*, 2015, **5**, 5349–5356.
40. X. Peng, S. G. Karakalos and W. E. Mustain, *ACS Appl. Mater. Interfaces*, 2018, **10**, 1734–1742.
41. H. Mistry, Y. W. Choi, A. Bagger, F. Scholten, C. S. Bonifacio, I. Sinev, N. J. Divins, I. Zegkinoglou, H. S. Jeon, K. Kisslinger, E. A. Stach,

J. C. Yang, J. Rossmeisl and B. Roldan Cuenya, *Angew. Chem., Int. Ed.*, 2017, **56**, 11394–11398.
42. E. L. Clark, J. Resasco, A. Landers, J. Lin, L.-T. Chung, A. Walton, C. Hahn, T. F. Jaramillo and A. T. Bell, *ACS Catal.*, 2018, **8**, 6560–6570.
43. A. Peterson and J. Nørskov, *J. Phys. Chem. Lett.*, 2012, **3**, 251–258.
44. H. A. Hansen, J. B. Varley, A. A. Peterson and J. K. Nørskov, *J. Phys. Chem. Lett.*, 2013, **4**, 388–392.
45. C. Shi, H. A. Hansen, A. C. Lausche and J. K. Nørskov, *Phys. Chem. Chem. Phys.*, 2014, **16**, 4720.
46. J. Rosen, G. S. Hutchings, Q. Lu, S. Rivera, Y. Zhou, D. G. Vlachos and F. Jiao, *ACS Catal.*, 2015, **5**, 4293–4299.
47. A. Parkin, J. Seravalli, K. A. Vincent, S. W. Ragsdale and F. A. Armstrong, *J. Am. Chem. Soc.*, 2007, **129**, 10328–10329.
48. G. Kyriacou and A. Anagnostopoulos, *J. Electroanal. Chem.*, 1992, **328**, 233–243.
49. D. Kim, J. Resasco, Y. Yu, A. M. Asiri and P. Yang, *Nat. Commun.*, 2014, **5**, 1–8.
50. J. Christophe, T. Doneux and C. Buess-Herman, *Electrocatalysis*, 2012, **3**, 139–146.
51. K. P. Kuhl, E. R. Cave, D. N. Abram and T. F. Jaramillo, *Energy Environ. Sci.*, 2012, **5**, 7050–7059.
52. Y. Hori, A. Murata and R. Takahashi, *J. Chem. Soc. Faraday Transations 1*, 1989, **85**, 2309–2326.
53. H. Noda, S. Ikeda, Y. Oda and K. Ito, *Chem. Lett.*, 1989, **18**, 289–292.
54. R. L. Cook, R. C. MacDuff and A. F. Sammells, *J. Electrochem. Soc.*, 1989, **136**, 1982–1984.
55. Y. Hori, A. Murata, R. Takahashi and S. Suzuki, *J. Am. Chem. Soc.*, 1987, **109**, 5022–5023.
56. Y. Hori, R. Takahashi, Y. Yoshinami and A. Murata, *J. Phys. Chem. B*, 1997, **101**, 7075–7081.
57. E. Bertheussen, T. V. Hogg, Y. Abghoui, A. K. Engstfeld, I. Chorkendorff and I. E. L. Stephens, *ACS Energy Lett.*, 2018, **3**, 634–640.
58. L. Wang, S. A. Nitopi, E. Bertheussen, M. Orazov, C. G. Morales-Guio, X. Liu, D. C. Higgins, K. Chan, J. K. Nørskov, C. Hahn and T. F. Jaramillo, *ACS Catal.*, 2018, **8**, 7445–7454.
59. K. J. P. Schouten, Y. Kwon, C. J. M. van der Ham, Z. Qin and M. T. M. Koper, *Chem. Sci.*, 2011, **2**, 1902–1909.
60. Y. Hori, K. Osamu, H. Yamazaki and T. Matsuo, *Electrochim. Acta*, 1995, **40**, 2617–2622.
61. I. Oda, H. Ogasawara and M. Ito, *Langmuir*, 1996, **12**, 1094–1097.
62. O. Koga, S. Teruya, K. Matsuda, M. Minami, N. Hoshi and Y. Hori, *Electrochim. Acta*, 2005, **50**, 2475–2485.
63. A. Wuttig, C. Liu, Q. Peng, M. Yaguchi, C. H. Hendon, K. Motobayashi, S. Ye, M. Osawa and Y. Surendranath, *ACS Cent. Sci.*, 2016, **2**, 522–528.

64. J. Heyes, M. Dunwell and B. Xu, *J. Phys. Chem. C*, 2016, **120**, 17334–17341.
65. C. M. Gunathunge, X. Li, J. Li, R. P. Hicks, V. J. Ovalle and M. M. Waegele, *J. Phys. Chem. C*, 2017, **121**, 12337–12344.
66. C. M. Gunathunge, V. J. Ovalle, Y. Li, M. J. Janik and M. M. Waegele, *ACS Catal.*, 2018, **8**, 7507–7516.
67. Y. Hori, A. Murata, R. Takahashi and S. Suzuki, *Chem. Lett.*, 1987, **16**, 1665–1668.
68. Y. Hori and A. Murata, *Electrochim. Acta*, 1990, **35**, 1777–1780.
69. N. Hoshi and Y. Hori, *Electrochem. Acta*, 2000, **45**, 4263–4270.
70. S. A. Akhade, W. Luo, X. Nie, N. J. Bernstein, A. Asthagiri and M. J. Janik, *Phys. Chem. Chem. Phys.*, 2014, **16**, 20429–20435.
71. Y. J. Zhang, V. Sethuraman, R. Michalsky and A. A. Peterson, *ACS Catal.*, 2014, **4**, 3742–3748.
72. E. R. Cave, C. Shi, K. P. Kuhl, T. Hatsukade, D. N. Abram, C. Hahn, K. Chan and T. F. Jaramillo, *ACS Catal.*, 2018, **8**, 3035–3040.
73. Y. Hori, A. Murata and Y. Yoshinami, *J. Chem. Soc., Faraday Trans.*, 1991, **87**, 125–128.
74. Y. Hori, H. Wakebe, T. Tsukamoto and O. Koga, *Surf. Sci.*, 1995, **335**, 258–263.
75. I. Takahashi, O. Koga, N. Hoshi and Y. Hori, *J. Electroanal. Chem.*, 2002, **533**, 135–143.
76. Y. Hori, I. Takahashi, O. Koga and N. Hoshi, *J. Mol. Catal. A: Chem.*, 2003, **199**, 39–47.
77. F. S. Roberts, K. P. Kuhl and A. Nilsson, *ChemCatChem*, 2016, **8**, 1119–1124.
78. C. Hahn, T. Hatsukade, Y.-G. Kim, A. Vailionis, J. H. Baricuatro, D. C. Higgins, S. A. Nitopi, M. P. Soriaga and T. F. Jaramillo, *Proc. Natl. Acad. Sci. U. S. A.*, 2017, **114**, 5918–5923.
79. H. Matsushima, A. Taranovskyy, C. Haak, Y. Gründer and O. M. Magnussen, *J. Am. Chem. Soc.*, 2009, **131**, 10362–10363.
80. H. Matsushima, C. Haak, A. Taranovskyy, Y. Gründer and O. M. Magnussen, *Phys. Chem. Chem. Phys.*, 2010, **12**, 13992–13998.
81. Y. G. Kim, A. Javier, J. H. Baricuatro, D. Torelli, K. D. Cummins, C. F. Tsang, J. C. Hemminger and M. P. Soriaga, *J. Electroanal. Chem.*, 2016, **780**, 290–295.
82. S. Vollmer, G. Witte and C. Wöll, *Catal. Lett.*, 2001, **77**, 97–101.
83. K. J. P. Schouten, Z. Qin, E. P. Gallent and M. T. M. Koper, *J. Am. Chem. Soc.*, 2012, **134**, 9864–9867.
84. F. Calle-Vallejo and M. T. M. Koper, *Angew. Chem., Int. Ed.*, 2013, **52**, 7282–7285.
85. A. A. Peterson, F. Abild-Pedersen, F. Studt, J. Rossmeisl and J. K. Nørskov, *Energy Environ. Sci.*, 2010, **3**, 1311–1315.
86. X. Nie, M. R. Esopi, M. J. Janik and A. Asthagiri, *Angew. Chem., Int. Ed.*, 2013, **52**, 2459–2462.

87. T. Cheng, H. Xiao and W. A. Goddard, *Proc. Natl. Acad. Sci. U. S. A.*, 2017, **114**, 1795–1800.
88. X. Liu, J. Xiao, H. Peng, X. Hong, K. Chan and J. K. Nørskov, *Nat. Commun.*, 2017, **8**, 1–7.
89. H. A. Hansen, J. H. Montoya, Y. J. Zhang, C. Shi, A. A. Peterson and J. K. Nørskov, *Catal. Lett.*, 2013, **143**, 631–635.
90. J. D. Goodpaster, A. T. Bell and M. Head-Gordon, *J. Phys. Chem. Lett.*, 2016, **7**, 1471–1477.
91. R. B. Sandberg, J. H. Montoya, K. Chan and J. K. Nørskov, *Surf. Sci.*, 2016, **654**, 56–62.
92. J. Resasco, L. D. Chen, E. Clark, C. Tsai, C. Hahn, T. F. Jaramillo, K. Chan and A. T. Bell, *J. Am. Chem. Soc.*, 2017, **139**, 11277–11287.
93. J. H. Montoya, C. Shi, K. Chan and J. K. Nørskov, *J. Phys. Chem. Lett.*, 2015, **6**, 2032–2037.
94. E. Bertheussen, A. Verdaguer-Casadevall, D. Ravasio, J. H. Montoya, D. B. Trimarco, C. Roy, S. Meier, J. Wendland, J. K. Nørskov, I. E. L. Stephens and I. Chorkendorff, *Angew. Chem., Int. Ed.*, 2016, **55**, 1450–1454.
95. I. Ledezma-Yanez, E. P. Gallent, M. T. M. Koper and F. Calle-Vallejo, *Catal. Today*, 2015, **262**, 90–94.
96. Y. Lum, T. Cheng, W. A. Goddard and J. W. Ager, *J. Am. Chem. Soc.*, 2018, **140**, 9337–9340.
97. E. L. Clark, J. Wong, A. J. Garza, Z. Lin, M. Head-Gordon and A. T. Bell, *J. Am. Chem. Soc.*, 2019, **141**, 4191–4193.
98. A. Garza, A. T. Bell and M. Head-Gordon, *ACS Catal.*, 2018, **8**, 1490–1499.
99. Y. Y. Birdja and M. T. M. Koper, *J. Am. Chem. Soc.*, 2017, **139**, 2030–2034.
100. M. Jouny, J. Lv, T. Cheng, B. H. Ko, J. Zhu, W. A. G. Iii and F. Jiao, *Nat. Chem.*, 2019, **11**, 846–851.
101. M. Jouny, W. Luc and F. Jiao, *Nat. Catal.*, 2018, **1**, 748–755.
102. C. S. Chen, A. D. Handoko, J. H. Wan, L. Ma, D. Ren and B. S. Yeo, *Catal. Sci. Technol.*, 2015, **5**, 161–168.
103. F. S. Roberts, K. P. Kuhl and A. Nilsson, *Angew. Chem., Int. Ed.*, 2015, **54**, 5179–5182.
104. A. Y. Kwon, Y. Lum, E. L. Clark, J. W. Ager, A. T. Bell, Y. Kwon, Y. Lum, E. L. Clark, J. W. Ager and A. T. Bell, *ChemElectroChem*, 2016, **3**, 1012–1019.
105. R. Kas, R. Kortlever, A. Milbrat, M. T. M. Koper, G. Mul and J. Baltrusaitis, *Phys. Chem. Chem. Phys.*, 2014, **16**, 12194–12201.
106. D. Kim, S. Lee, J. D. Ocon, B. Jeong, J. K. Lee and J. Lee, *Phys. Chem. Chem. Phys.*, 2015, **17**, 824–830.
107. D. Ren, N. T. Wong, A. D. Handoko, Y. Huang and B. S. Yeo, *J. Phys. Chem. Lett.*, 2016, **7**, 20–24.
108. D. Ren, Y. Deng, A. D. Handoko, C. S. Chen, S. Malkhandi and B. S. Yeo, *ACS Catal.*, 2015, **5**, 2814–2821.

109. C. W. Li and M. W. Kanan, *J. Am. Chem. Soc.*, 2012, **134**, 7231–7234.
110. C. W. Li, J. Ciston and M. W. Kanan, *Nature*, 2014, **508**, 504–507.
111. A. D. Handoko, C. W. Ong, Y. Huang, Z. G. Lee, L. Lin, G. B. Panetti and B. S. Yeo, *J. Phys. Chem. C*, 2016, **120**, 20058–20067.
112. H. Mistry, A. S. Varela, C. S. Bonifacio, I. Zegkinoglou, I. Sinev, Y. W. Choi, K. Kisslinger, E. A. Stach, J. C. Yang, P. Strasser and B. R. Cuenya, *Nat. Commun.*, 2016, **7**, 1–8.
113. D. Gao, I. Zegkinoglou, N. J. Divins, F. Scholten, I. Sinev, P. Grosse and B. Roldan Cuenya, *ACS Nano*, 2017, **11**, 4825–4831.
114. A. Verdaguer-Casadevall, C. W. Li, T. P. Johansson, S. B. Scott, J. T. McKeown, M. Kumar, I. E. L. Stephens, M. W. Kanan and I. Chorkendorff, *J. Am. Chem. Soc.*, 2015, **137**, 9808–9811.
115. X. Feng, K. Jiang, S. Fan and M. W. Kanan, *ACS Cent. Sci.*, 2016, **2**, 169–174.
116. R. G. Mariano, K. McKelvey, H. S. White and M. W. Kanan, *Science*, 2017, **358**, 1187–1192.
117. T. Cheng, H. Xiao and W. A. Goddard, *J. Am. Chem. Soc.*, 2017, **139**, 11642–11645.
118. Y. Huang, Y. Chen, T. Cheng, L. W. Wang and W. A. Goddard, *ACS Energy Lett.*, 2018, **3**, 2983–2988.
119. A. Eilert, F. Cavalca, F. S. Roberts, J. Osterwalder, C. Liu, M. Favaro, E. J. Crumlin, H. Ogasawara, D. Friebel, L. G. M. Pettersson and A. Nilsson, *J. Phys. Chem. Lett.*, 2017, **8**, 285–290.
120. Y. Lum and J. W. Ager, *Angew. Chem., Int. Ed.*, 2018, **57**, 551–554.
121. S. B. Scott, T. V. Hogg, A. T. Landers, T. Maagaard, E. Bertheussen, J. C. Lin, R. C. Davis, J. W. Beeman, D. Higgins, W. S. Drisdell, C. Hahn, A. Mehta, B. Seger, T. F. Jaramillo and I. Chorkendorff, *ACS Energy Lett.*, 2019, **4**, 803–804.
122. A. J. Garza, A. T. Bell and M. Head-Gordon, *J. Phys. Chem. Lett.*, 2018, **9**, 601–606.
123. M. Fields, X. Hong, J. K. Nørskov and K. Chan, *J. Phys. Chem. C*, 2018, **122**, 16209–16215.
124. N. Gupta, M. Gattrell and B. MacDougall, *J. Appl. Electrochem.*, 2006, **36**, 161–172.
125. M. R. Singh, E. L. Clark and A. T. Bell, *Phys. Chem. Chem. Phys.*, 2015, **17**, 18924–18936.
126. R. Kas, R. Kortlever, H. Yilmaz, M. T. M. Koper and G. Mul, *ChemElectroChem*, 2015, **2**, 354–358.
127. M. Dunwell, X. Yang, B. P. Setzler, J. Anibal, Y. Yan and B. Xu, *ACS Catal.*, 2018, **8**, 3999–4008.
128. Y. Hori, A. Murata, R. Takahashi and S. Suzuki, *J. Chem. Soc., Chem. Commun.*, 1988, 17–19.
129. A. S. Varela, M. Kroschel, T. Reier and P. Strasser, *Catal. Today*, 2016, **260**, 8–13.

130. J. Resasco, Y. Lum, E. L. Clark, J. Zeledon and A. T. Bell, *ChemElectroChem*, 2018, **5**, 1–10.
131. A. Murata and Y. Hori, *Bull. Chem. Soc. Jpn.*, 1991, **64**, 123.
132. G. Z. Kyriacou and A. K. Anagnostopoulos, *J. Appl. Electrochem.*, 1993, **23**, 483–486.
133. M. R. Singh, Y. Kwon, Y. Lum, J. W. Ager and A. T. Bell, *J. Am. Chem. Soc.*, 2016, **138**, 13006–13012.
134. J. Resasco, L. D. Chen, E. Clark, C. Tsai, C. Hahn, T. F. Jaramillo, K. Chan and A. T. Bell, *J. Am. Chem. Soc.*, 2017, **139**, 11277–11287.
135. E. Pérez-Gallent, G. Marcandalli, M. C. Figueiredo, F. Calle-Vallejo and M. T. M. Koper, *J. Am. Chem. Soc.*, 2017, **139**, 16412–16419.
136. L. D. Chen, M. Urushihara, K. Chan and J. K. Nørskov, *ACS Catal.*, 2016, **6**, 7133–7139.
137. Y. Marcus, *Biophys. Chem.*, 1994, **51**, 111–127.
138. B. Garlyyev, S. Xue, S. Watzele, D. Scieszka and A. S. Bandarenka, *J. Phys. Chem. Lett.*, 2018, **9**, 1927–1930.
139. S. Ringe, E. L. Clark, J. Resasco, A. Walton, B. Seger, A. T. Bell and K. Chan, *Energy Environ. Sci.*, 2019, **12**, 3001–3014.

CHAPTER 4

Nanostructures for CO_2 Reduction: From Theoretical Insight to Material Design

WEN JU,[a,†] ALEXANDER BAGGER,[b,†] NATHANIEL LEONARD,[a] XINGLI WANG,[a] JAN ROSSMEISL*[b] AND PETER STRASSER*[a]

[a] The Electrochemical Energy, Catalysis, and Materials Science Laboratory, Department of Chemistry, Chemical Engineering Division, Technical University Berlin, 10623, Berlin, Germany; [b] Department of Chemistry, University Copenhagen, Universitetsparken 5, 2100 Copenhagen, Denmark
*Emails: jan.rossmeisl@chem.ku.dk; pstrasser@tu-berlin.de

4.1 Introduction

Consumption of fossil resources is increasing the atmospheric concentration of CO_2, which causes drastic climate change and ocean acidification.[1,2] This threat calls for political and technological attention to close the carbon cycle using carbon capture, storage, and transforming technologies. Therefore, many integrated technologies have been designed and generated, focusing on the CO_2 threat. Among possible strategies, the electrochemical CO_2 reduction reaction (eCO_2RR) arises as a promising alternative to convert waste CO_2 (ideally from the direct CO_2 emission source) into useful value-added products. For this conversion,

[†] These authors contributed equally.

Energy and Environment Series No. 28
Carbon Dioxide Electrochemistry: Homogeneous and Heterogeneous Catalysis
Edited by Marc Robert, Cyrille Costentin and Kim Daasbjerg

Published by the Royal Society of Chemistry, www.rsc.org

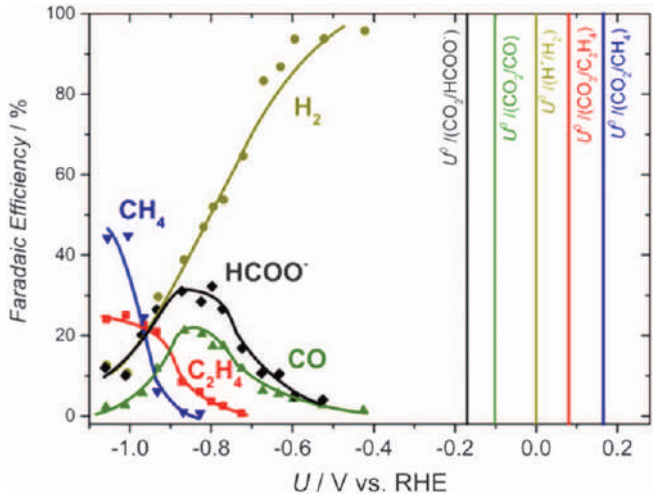

Figure 4.1 The faradaic product distribution on polycrystalline Cu measured with a constant current of -5 mA cm^{-2} *versus* the reversible hydrogen electrode potential (U/V *vs.* RHE).
Adapted from ref. 4 with permission from Elsevier, Copyright 2016, and from ref. 5 with permission from the Royal Society of Chemistry.

water and renewable electricity are the major co-feedstocks. In comparison to other methods for CO_2 reuse, eCO_2RR possesses the advantage of occurring under ambient, mild conditions. However, such electrochemical conversion is not yet industrially viable owing to i) a high overpotential requirement (over 1.0 V); ii) low selectivity to desired valuable products against the competition of H_2 evolution reaction (HER),[3] and iii) limited working current densities (overall reaction activity). To overcome these technical boundaries, selectively and efficiently converting CO_2 into desired products on a large scale, the catalyst material is one of the most essential building blocks.

The most significant example is the eCO_2RR occurring over a polycrystalline Cu surface, which yields a complicated product distribution varying with applied potential (see Figure 4.1). At low overpotentials, the unwanted HER (H_2 product) is activated, while at higher overpotentials, multiple different carbon products occur from the reduction. It should be noted that the carbon product onsets are far from the thermodynamic potentials shown by the vertical lines. Hence, the experimental result on Cu illustrates the selectivity challenge with CO_2 reduction, which is different from the better understood Hydrogen Evolution/Reduction Reactions (HER/HOR) and Oxygen Evolution/Reduction Reactions (OER/ORR).

The amount of recent literature on CO_2RR is overwhelming. However, it can be elucidated by a literature search in the Web of Science (WOS) for CO_2 and the related CO reduction reaction.

Web Of Science (WOS) search Monday 21st January 2019: TI = (electrochemical CO_2 reduction OR CO_2 electroreduction OR Electrochemical Reduction CO OR CO electroreduction OR electroreduction carbon monoxide OR CO_2 reduction overpotential OR CO_2 electrocatalytic OR CO_2 reduction electrodes OR CO_2 reduction catalyst OR CO reduction catalyst OR CO reduction overpotential OR electroreduction carbon dioxide OR CO Reduction copper OR electrochemical carbon dioxide reduction OR electrochemical carbon monoxide reduction OR electrocatalytic carbon monoxide reduction OR electrocatalytic carbon dioxide reduction OR electrocatalytic CO reduction OR electrocatalytic CO_2 reduction) NOT TI = oxygen.

The WOS search is shown in Figure 4.2, revealing the number of research papers published on the topic each year since 1990. Since 1990, the field has evolved with ~50 publications each year, while after 2011 the field has seen an almost exponential growth. We identify the top 7 most cited papers and this analysis should, in principle, lead us to the landmark papers in the field. The works done by Benson *et al.*,[6] Qiao *et al.*,[7] and Gattrell *et al.*[8] are review papers, and Hori's work[3] is a book chapter compiling his previous studies. Kuhl *et al.*[9] provided a better measurement of polycrystalline Cu than Hori,[5] and Li *et al.*[10] completed work concerning oxidized copper (Cu-OD), which could be an effect of having a high surface area catalyst. Finally, Peterson *et al.*[11] wrote a simulation paper on the Cu(211) facet. These are all critical, high-quality papers. However, it illustrates a problem in the scientific currency of "citations", where reviews or reproductions of results get more citations than the original work. The real pioneering studies in the field are the experimental work by Hori,[5] which dates back to 1989. These studies will be the primary source of experimental references for the classification of metal CO_2 electrocatalysts in this

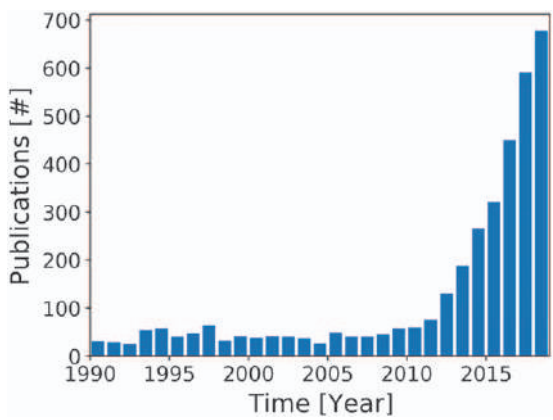

Figure 4.2 Number of publications in electrochemical CO_2 and CO reduction research published per year. The top-cited papers are Benson *et al.*,[6] Qiao *et al.*,[7] Kuhl *et al.*,[9] Peterson *et al.*,[11] Li *et al.*,[10] Gattrell *et al.*,[8] and Hori *et al.*[3] This Web of Science search was carried out on the 10th Jan 2020.

chapter. We strongly encourage the readers to cite the original work and not only the reviews, including this book chapter.

4.2 Theoretical Insights in Electrochemical CO_2 Reduction

In this section, the latest advances within theoretical studies and simulations for electrochemical CO_2 conversion toward different products are discussed. The focus is on how to use state-of-the-art methods to develop schemes and understanding of the electrochemical CO_2 reduction reaction (eCO_2RR). Specifically, this section emphasizes building robust frameworks from simulated density functional theory binding energies and using these as descriptors. The descriptors are then compared with experimental trend studies, and new materials can be predicted.

Before discussing the simulating techniques, simple concepts of catalysis will be outlined and set in context for the eCO_2RR. A concept to explain how the catalyst reactivity affects the performance of a catalyst is given qualitatively by the Sabatier principle:[12]

Sabatier principle: A catalyst's reactivity should be just right, not too weak so that reactants cannot adsorb and not too strong so that products cannot desorb from the catalyst

The volcano plot can illustrate the Sabatier principle in action by the HER and OER volcano in Figure 4.3. Furthermore, the figure shows how to think of different reaction complexities and how to find the related energies and descriptors to create volcano plots. When a two-electron reaction exists, as with HER/HOR, the reaction will have only one intermediate on the surface (eqn (4.1)).

$$2\,(H^+ + e^-) \leftrightarrow (H^+ + e^-) + H^* \leftrightarrow H_2 \tag{4.1}$$

The binding strength of the H* is a good candidate for a simple descriptor, since it is the only intermediate during the overall reaction.[13,14] For increased reaction complexity, the four electron ORR/OER reaction multiple intermediates come into play (eqn (4.2)).

$$2\,(H_2O) \leftrightarrow (H^+ + e^-) + H_2O + OH^* \leftrightarrow 2\,(H^+ + e^-) + H_2O + O^* \leftrightarrow 3\,(H^+ + e^-) + OOH^* \leftrightarrow 4\,(H^+ + e^-) + O_2 \tag{4.2}$$

In this case OH*, O*, and OOH* intermediates require more insights to create the volcano plot. Here the linear scaling relationship helps create a simple describing model.[15] For OER and ORR, specifically, the OOH* and OH* intermediates both bind at the same surface site and the two energies scale with the oxygen.[15–17] This scaling allows construction of the volcano. For eCO_2RR many more electrons may be transferred from the observed products in Figure 4.1 (C_2H_4 requires 12 protons and electrons). This results in a huge number of possible intermediates and reaction pathways, which makes the construction of a valid volcano challenging. Furthermore, the

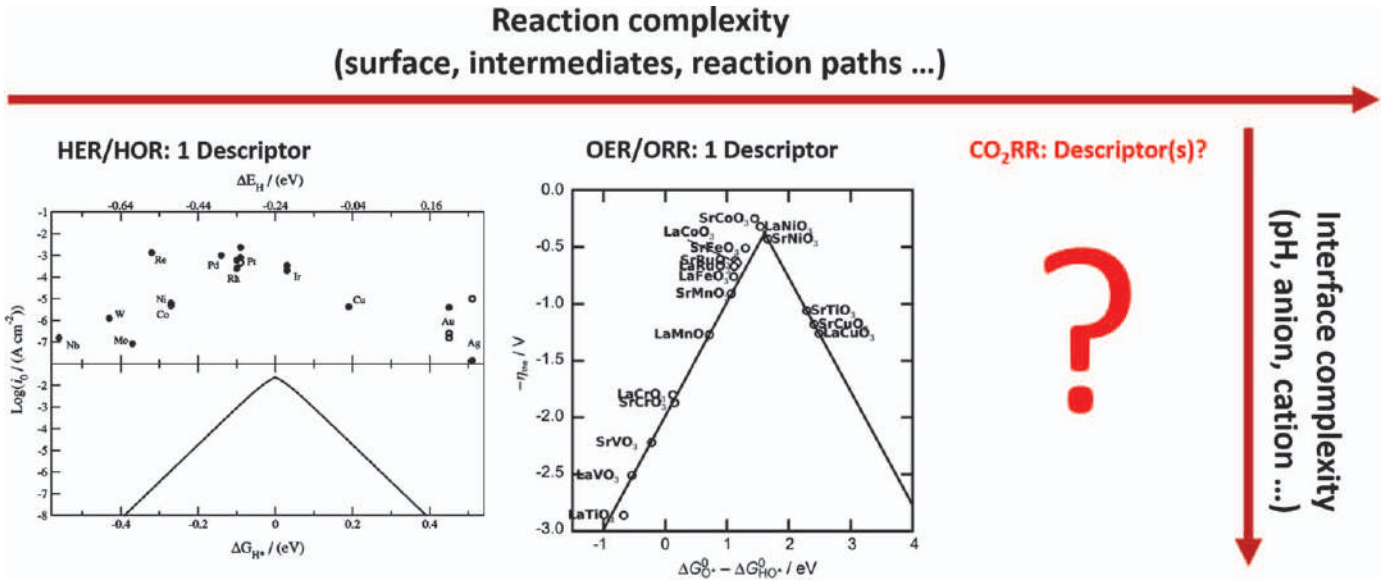

Figure 4.3 The reaction and interface complexity of the CO_2 reduction reaction in the context of HER/HOR and OER/ORR volcano plots. The multi-dimension intermediate space of the CO_2 reduction reaction is difficult to address, and perhaps volcanoes for this reaction do not exist. The HER volcano is from ref. 18 and the OER volcano from ref. 19.

interface complexity involves the bulk/local pH and anion/cation effects. These effects are not included in the volcano analysis but are much more difficult to address from a simulation perspective.

In general, a volcano relates a catalytic parameter (rate or overpotential) to a descriptor. The turnover frequency is used in heterogeneous catalysis and overpotential is used in electrochemistry. The overpotential is determined as the additional potential required to drive a reaction relative to the thermodynamic equilibrium potential. The descriptor can be a simulated parameter, such as the d-band center of transition metals[20] and/or the binding energy of adsorbates to the metal surfaces.[18] However, the descriptor could also be an experimental measurement, such as CO* binding energies obtained from Temperature Programmed Desorption (TPD) experiments[21] or OH* binding energies obtained from Cyclic Voltammetry (CV).[22]

For simple reactions, as with HER, volcanoes rely on the linear concept of optimizing descriptors to maximize performance for a reaction parameter. This method only allows for the optimization of one product. For many electrochemistry challenges, this means minimizing the reaction overpotential. For reactions that have selectivity issues, the tuning of selectivity towards a specific product is preferable and may be more desirable than optimizing the overpotential. For such problems, the descriptor does not need to be a one-dimensional property, and furthermore, the set of descriptors does not need to be linear with the product distribution or overpotential. For these types of problems, a selectivity principle can be loosely defined:

Selectivity is a multidimensional challenge, for which several parameters need to be considered.

This is the case for eCO_2RR and the corresponding electrochemical CO reduction reaction, which are addressed in this chapter.

4.2.1 Reaction Complexity

The reaction complexity of eCO_2RR is different from many other reactions. As shown in Figure 4.1, there is a significant complexity with the reaction selectivity. This selectivity varies on different materials. In Figure 4.4a a periodic table is shown with Hori's experimental results on a series of metal catalysts. The periodic table shows that four types of metal catalysts exist: metals that produce primarily i) H_2, ii) HCOOH (formic acid), iii) CO, and iv) products beyond CO* (a series of alcohols and hydrocarbons produced on Cu). The first three products are only with two proton–electron transfers (eqn (4.3)–(4.5)).

$$2\left(H^+ + e^-\right) \leftrightarrow H_2 \tag{4.3}$$

$$2\left(H^+ + e^-\right) + CO_2 \leftrightarrow CO + H_2O \tag{4.4}$$

$$2\left(H^+ + e^-\right) + CO_2 \leftrightarrow HCOOH + H_2O \tag{4.5}$$

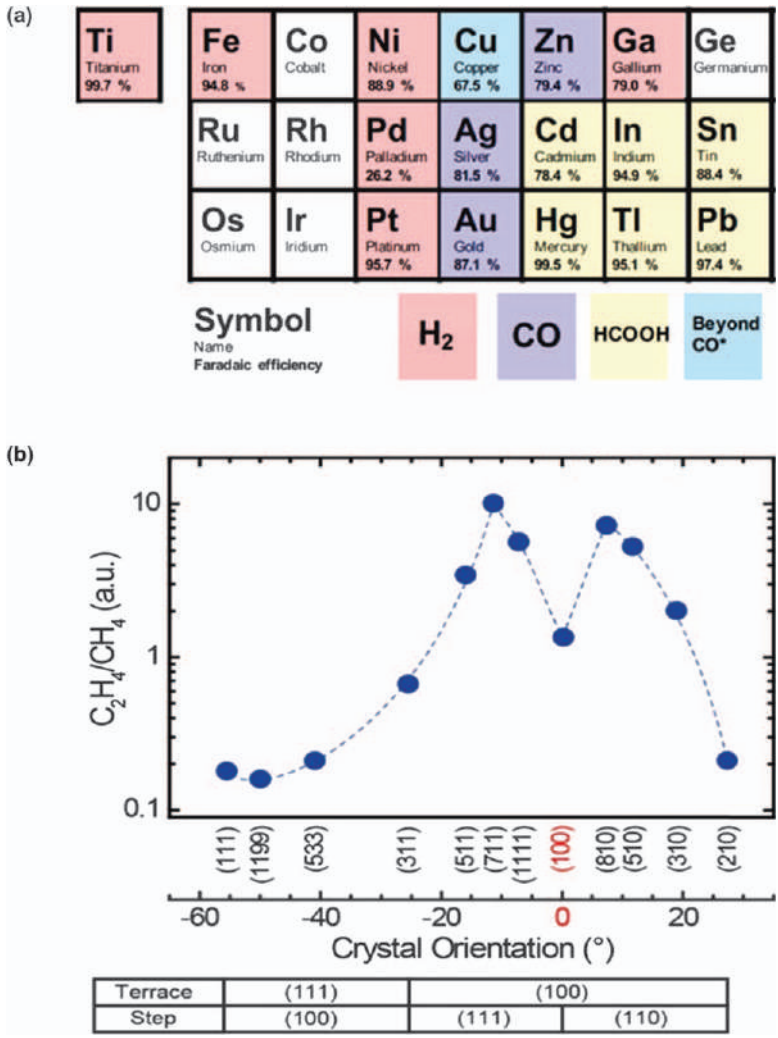

Figure 4.4 (a) Display of experimentally tested metal catalysts from the periodic table and their major product indicated by color. (b) The logarithmic ratio of C_2H_4/CH_4 current densities *versus* the crystal orientation from several tested Cu single-crystal metal facets. The figures show how Cu, and certain facets of Cu, produce highly valuable products.
Reproduced from ref. 23 with permission from John Wiley and Sons, Copyright © 2017 Wiley-VCH Verlag GmbH & Co. KGaA, Weinheim, and from ref. 24 with permission from Elsevier, Copyright 2003.

However, for the products beyond CO* the reaction complexity increases significantly, with many more proton–electron transfers. Ethylene (C_2H_4) and methane (CH_4) are two of the major products, beyond CO*, observed from the Cu catalyst. Figure 4.4b shows the experimental measurement of the logarithmic ratio of C_2H_4/CH_4 partial current densities *versus* the crystal orientation of a series of Cu single-crystals. As seen, the product ratio of these hydrocarbons highly depends on the exact Cu facets. Mainly, facets which have Cu(100) basal planes are good at producing C_2H_4, whereas facets with Cu(111) planes produce more CH_4.

Indeed, the observed selectivity changes with material and crystal orientation cause additional complexity for someone trying to understand the reaction. First, we will discuss some of the work on reaction paths and intermediates. Then we will focus primarily on descriptors independent of the reaction pathway.

4.2.2 Reaction Paths and Intermediates

There are many different reaction mechanisms proposed in the literature. These reaction paths depend on how the modeling was carried out. For the simple two-electron reactions, the proposed mechanistic reaction steps are shown in eqn (4.6)–(4.8).

$$2\left(H^+ + e^-\right) \leftrightarrow H^* \leftrightarrow H_2 \tag{4.6}$$

$$2\left(H^+ + e^-\right) + CO_2 \leftrightarrow COOH^* \leftrightarrow CO^* \leftrightarrow CO + H_2O \tag{4.7}$$

$$2\left(H^+ + e^-\right) + CO_2 \leftrightarrow HCOO^* \leftrightarrow HCOOH + H_2O \tag{4.8}$$

These reaction paths are relatively straightforward, whereas the reaction toward hydrocarbons is more complicated. Peterson *et al.*[11] have shown a simulated reaction pathway toward CH_4 on Cu(211). This simulated reaction path has the protonation of CO* to CHO* as the reaction-limiting step. However, the protonation step of CO* towards either CHO* or COH* depends on the exact simulation method and setup. In Table 4.1, five publications show how water, facets, or barriers of elementary steps all influence and can change the mechanism from CHO* to COH* for Cu. We have investigated the (111), (100) and (110) facets, including *Ab Initio* Molecular Dynamics (AIMD) of water at 300 K, showing that the choice of COH* or CHO* intermediate depends on the specific stabilization by water.[25] This

Table 4.1 Selected publications on the mechanism for CO_2 reduction arriving at different CO* protonation steps.

Author	Facet	Water	Barrier of elementary steps	Mechanism
Andrew A. Peterson *et al.*[11]	(211)	No	No	$CO^* \rightarrow CHO^*$
Xiaowa Nie *et al.*[31]	(111)	Yes	Yes	$CO^* \rightarrow COH^*$
Chuan Shi *et al.*[32]	(211)	No	Yes	$CO^* \rightarrow CHO^*$
Javed Hussain *et al.*[29]	(111)	Yes	Yes	$CO^* \rightarrow COH^*$
Thomas Ludwig *et al.*[33]	(211)	Yes	No	$CO^* \rightarrow CHO^*$

presents a reaction mechanistic problem when trying to investigate reaction paths and intermediates for products beyond CO*. Additionally, the reduction toward C–C products, which is an experimental almost unique observation on facets including the Cu(100) basal plane, is complicated to understand. The work by Federico Calle–Vallejo and Marc T. M. Koper[26] gives insight into the formation of C–C products on the Cu(100) facet. They postulate that a charged OCCO* (dimer) intermediate is stable, and that this is the origin of the early C–C coupling experimentally observed in the study.[27] A problem with researching the C–C coupling theoretically is that it is almost impossible to develop trend scheme analysis when only one experimental point is available [the Cu(100) facet]. Still, several works give different explanations of the C–C coupling on Cu(100).[28–30]

4.2.3 CO_2RR Descriptors

Reaction paths and intermediates are important, however, it is difficult to learn something from them, when they are so method dependent, as shown above. Hence, we leave the idea of finding reaction paths, and instead focus primarily on descriptors, without knowing the reaction path.

The most straightforward approach is to not consider the eCO_2RR descriptors at all, and instead focus on the well-known competitive HER reaction. For HER the H* binding energy is dominating and we may split the experimental data set from the work of Hori *et al.*[34] into faradaic efficiency for HER and CO_2RR. In Figure 4.5 the eCO_2RR faradaic efficiency is then plotted against the H* binding energy. This shows that two regimes exist concerning the H* binding energy,

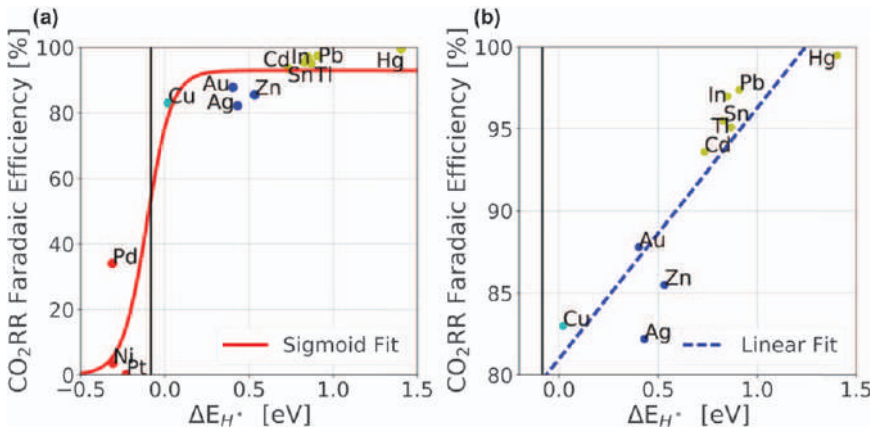

Figure 4.5 Faradaic efficiency of CO_2RR *versus* HER as a function of H* binding energies. (a) The plot includes the H* UPD metals (Pd, Ni, and Pt) that primarily produce H_2 due to H* UPD (on the left side of the black separation line), while (b) plots the studied non-H* UPD metals that are selective for eCO_2RR. The sigmoid function illustrates the importance of using H* UPD as a distinction in the analysis of CO_2 descriptors.
Reproduced from ref. 23 with permission from John Wiley and Sons,

which is directly related to our defined 'selectivity principle'. In Figure 4.5a the sigmoid fit to the data shows that the metals with H under potential deposited (H* UPD) do not reduce CO_2, particularly as HER dominates on these metals. This indicates that to find new eCO_2RR catalysts, they must not be so reactive as to have H* UPD. In Figure 4.5b a linear fit is shown for the metals with the ability to reduce CO_2. In this regime, there are two overall groups, the ones that make formic acid and the ones producing CO, while Cu is unique. By considering only the competitive HER description, H* binding energy, we can already predict something about a new potential catalyst candidate, and it is highly relevant not to activate H* UPD.

However, the descriptor space for eCO_2RR intermediates is more significant than only the H* binding energy, since the reaction cascades go to different products, such as formate, CO, hydrocarbons, and alcohols. In Figure 4.6a, a three-dimensional representation of H*, COOH*, and HCOO* is displayed for the metals (configuration is shown in Figure 4.6a), where COOH* and HCOO* are considered to be the key intermediates for the CO and formic acid products, respectively.[23] In this three-dimensional representation one can observe three groupings indicated by color. In Figure 4.6b–d each of the planes (*i.e.* two-dimensional binding analysis) shows that the COOH* and HCOO* cannot be used to distinguish the CO and formic acid product, which is rather surprising. Instead, it turns out that the H* binding descriptor again seems to be the best descriptor across the metals.

4.2.4 CORR Descriptors

From the eCO_2RR products beyond the CO products, the descriptor space becomes more difficult, as more products are possible on the different Cu facets. To obtain products beyond CO, CO* adsorption is required. Therefore, the binding energy of CO* is a relevant factor.[35] Furthermore, the H* binding energy is an important descriptor as discussed above. Hence, we plot the binding energy of CO* *versus* H* in Figure 4.7a and b for the metals and Cu facets, where the experimental results represented by the colors are from Hori *et al.*[24,34] This gives a visible indication of what is unique about Cu. Cu is selective toward hydrocarbons (products beyond CO), because of the ability to bind CO* without having H* UPD. Thus CO* can be activated without activating H* UPD. This appears to be an either-or property, *i.e.* either a catalyst can bind CO* or it cannot. Hence, eCO_2RR toward hydrocarbons seems not to be a continuous property defined by a simple Sabatier principle.

An investigation of the Cu facets in Figure 4.7b shows that the CO* and H* binding energies for these facets are rather close. The C_{2+} product [*i.e.*, C_2H_4, ethanol (EtOH), acetaldehyde (MeD), propionaldehyde (PrD), allyl alcohol (AlOH), and propanol (PrOH)] faradaic efficiency is indicated by the color code. A weak tendency is observed, namely, that the C_{2+} efficiency increases if the CO* binding becomes stronger, while the H* binding is weakened. However, all Cu facets data points are within ± 0.1 eV for the CO* and the H* binding energies.

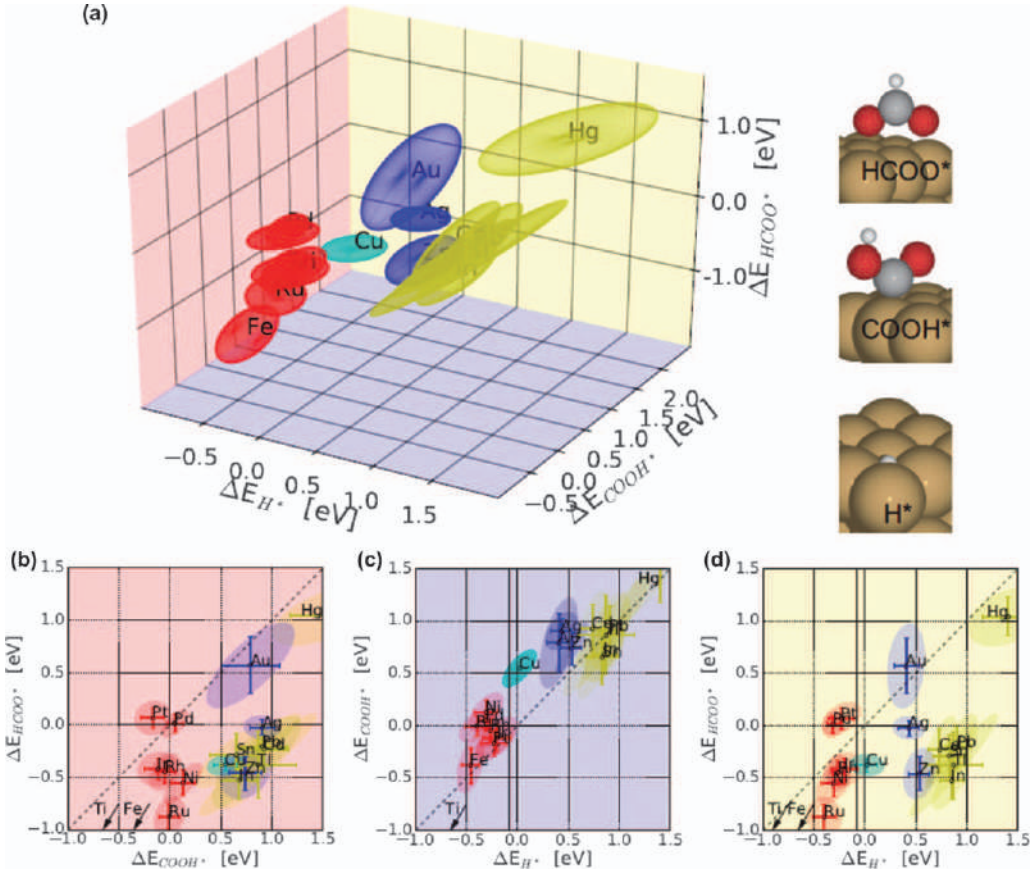

Figure 4.6 (a) A three-dimensional representation of the three suggested intermediates, *i.e.* H*, COOH*, and HCOO*. (b–d) Plots showing each of the colored two-dimensional planes of the intermediate binding energies. The coloring corresponds to the periodic table in Figure 4.4a, with groups of H_2 (red), HCOOH (yellow), and CO (blue)-producing metals.
Reproduced from ref. 23 with permission from John Wiley and Sons, Copyright © 2017 Wiley-VCH Verlag GmbH & Co. KGaA, Weinheim.

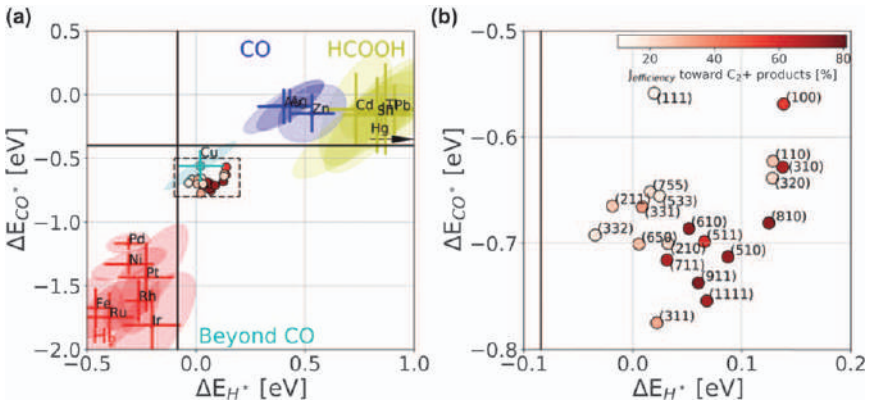

Figure 4.7 (a) A two-dimensional representation of the CO* *versus* H* binding energy for the metals and all Cu facets. (b) The plot shows a zoom of the dashed square to display how close the different facets are in energetics. The C_{2+} product faradaic efficiency is defined as C_2H_4, EtOH, PrD, AlOH, and PrOH. Experimental results are from Hori *et al.*[24,34] Reproduced from ref. 36 with permission from American Chemical Society, Copyright 2019.

The CO* and H* binding energies are certainly important parameters to fulfill, in order to obtain products beyond CO*. However, to understand the products beyond CO*, the scheme of descriptors has been expanded significantly.[36]

Figure 4.8 shows a two-dimensional principal component analysis (PCA) of the correlations within the product distribution, the coordination number, and a set of selected binding energies, respectively. The Cu facets are colored according to the C_{2+} faradaic efficiency, and the original descriptor components are plotted as green lines.

Figure 4.8a shows that close to ~80% of the expressed variation of the data sets is captured by the two components. This confirms that a two-dimensional representation of the Cu facet product distribution is appropriate. The only concern is which two-dimensional description of the products is the best.

Figure 4.8b displays the coordination number principal component analysis. Here the facets with some (100) basal plane are grouped together, with the highest C_{2+} faradaic efficiency. Furthermore, the (110) and (311) are detached moderately from the ones with a partly (111) basal plane. Clearly, this analysis is close to Hori and co-worker's analysis of the logarithmic ratio of C_2H_4/CH_4 partial current densities in Figure 4b. However, this representation may be more intuitive to read off the structural effects in the product distribution.

Figure 4.8c visualizes the series of C*, O*, CO*, OCCOH*, OH*, COOH*, and H* as potential binding energy descriptors in two dimensions. One would expect that the OCCOH* binding energy, a protonated form of the dimer,[26] would stand out as the descriptor for the C_{2+} products. This is not really the case. Instead, the PCA of all the binding energies is very similar to the ΔE_{CO^*} *vs.* ΔE_{H^*} binding energy picture in Figure 4.7b. Which is observed as Figure 4.8c is almost a rotation of Figure 4.7b. This shows that no more

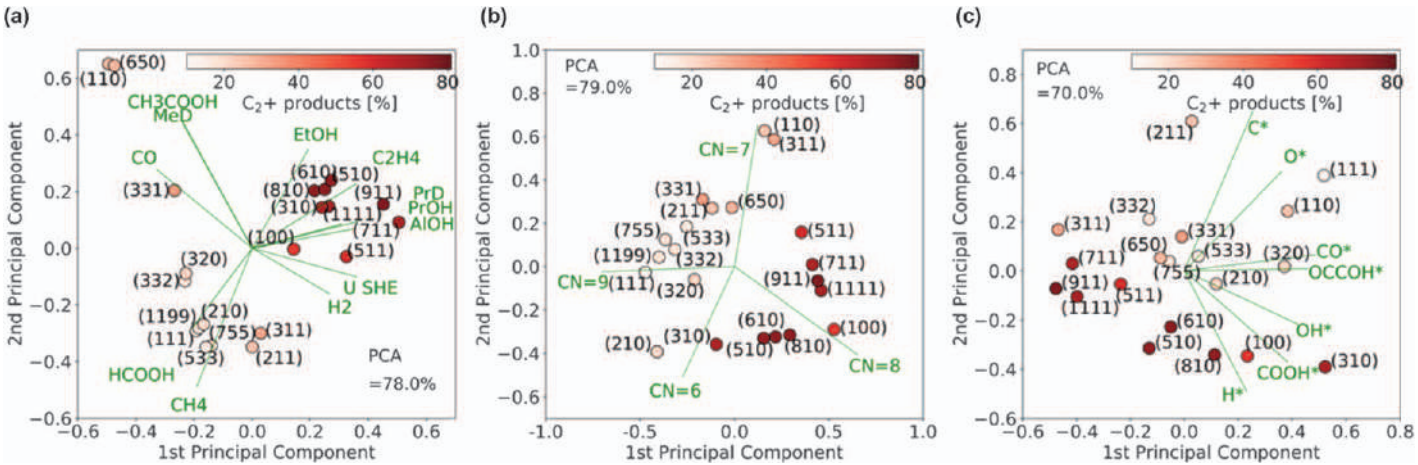

Figure 4.8 Test of the best two-dimensional description of the experimental C_{2+} product results by PCA of (a) the faradaic efficiency, (b) the coordination number, and (c) the binding energies. The PCA explained variance ratio is plotted to show how well two principal components describe the variation. The projection of the original features is co-plotted in green in the PCA plot. Reproduced from ref. 36 with permission from American Chemical Society, Copyright 2019.

information can be gained than from the CO* and H* binding energy analysis. It is quite surprising that the O*/C* and OH*/COOH* binding energies are relatively close. This shows the difference between scaling relations[15–17] and trend scheme analysis over metals and in this case Cu facets. The binding energies for the facets measure the local environment of the binding. Both OH* and COOH* bind on top and hence correlate. The O* and C* binds in the hollow site (preferring the 4-fold hollow of the Cu(100) basal plane), and the H* prefer the 3-fold hollow site of the Cu(111) basal plane.

As shown in the coordination number analysis, investigating the structure of the facet, seems to be a descriptor that could be used as it distinguishes the different facets. From this analysis, it is interesting to focus on the different products, *i.e.* methane, acetaldehyde, ethylene, and ethanol (see Figure 4.9).

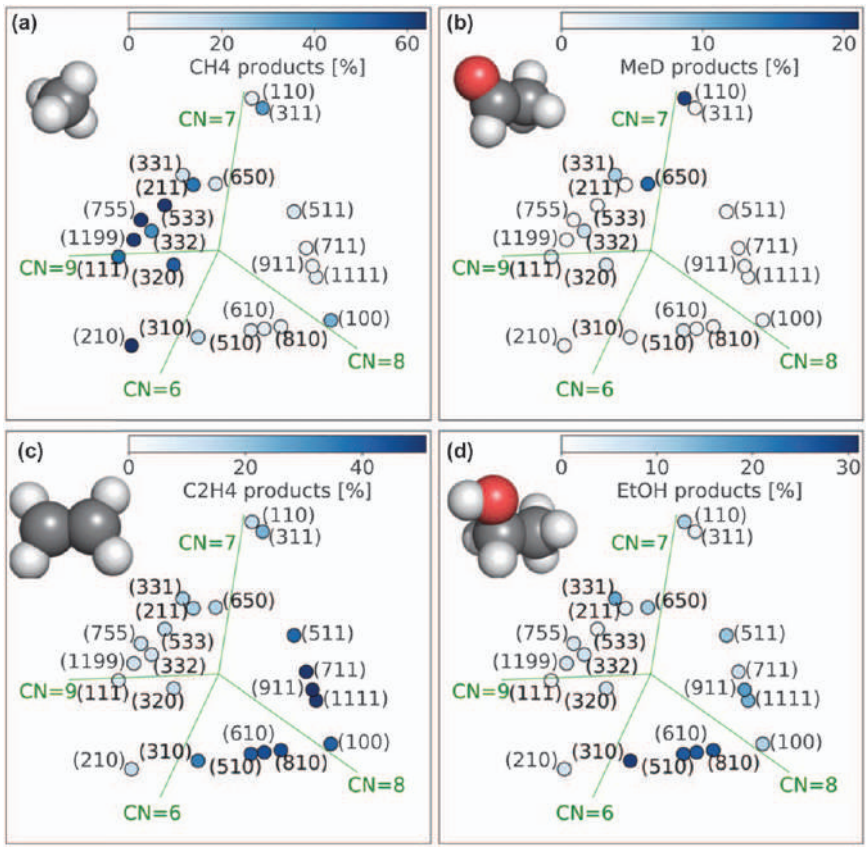

Figure 4.9 The choice of the local structure (coordination number) description displayed as the most important two-dimensional description of the products. This allows for identification of active sites of the Cu catalyst: (a) Cu(111) gives methane, (b) Cu(110) gives acetaldehyde, (c) Cu(100) gives ethylene, and (d) the $n(100)\times(110)$ step produces ethanol.
Reproduced from ref. 36 with permission from American Chemical Society, Copyright 2019.

Figure 4.9a shows that methane is primarily produced on facets with the Cu(111) basal plane. Figure 4.9b shows that special facets Cu(110), Cu(650), and Cu(331) have a high acetaldehyde production, while ethylene is produced on the Cu(100) facets (Figure 4.9c). Finally, Figure 4.9d shows that having the (100) basal plane with the specific (110) step increases ethanol production. Raising the (100)×(110) step density increases the ethanol faradaic efficiency, which uniquely allows for the identification of the (100)×(110) step as a particular ethanol site, while the basal plane of (100) produces C_{2+} products overall. A note should be made for the Cu(210) facets with the highest (100)×(110) step density, which have a decrease in ethanol faradaic efficiency. This shows that an ethanol site needs both the (100)×(110) step and a minor Cu(100) basal plane next to it to produce ethanol.

Previously, acetaldehyde has been proposed as a precursor for ethanol.[37–39] This is, to some extent, correct. However, in this analysis, it is shown that (100)×(110) sites produce ethanol without acetaldehyde production. Only specific facets Cu(110), Cu(650), and Cu(331) have both increased acetaldehyde and ethanol production. This can be interpreted as these facets (sites) primarily produce acetaldehyde, which is then further reduced at another site to ethanol. Hence, acetaldehyde does not need to be on the direct pathway to ethanol but can indeed be reduced to ethanol.

To summarize the results, the work shows that multiple electron–proton transfer reactions involving complex reaction scheme mechanisms are complicated to capture from a theoretical point-of-view because the predicted mechanism will be highly dependent on the methods used. Here a trend-based descriptors scheme has allowed for identification of descriptors for the significant four groups in eCO_2RR (H_2, CO, HCOOH, and products beyond CO) by the ΔE_{CO^*} *vs.* ΔE_{H^*} energetic scheme. These descriptors are straightforward and useful in the screening of new potential catalysts. For CORR, beyond CO products, trend analysis on Cu facets have been carried out to determine descriptors for the product distribution. The study has shown the relation between the products, the structural effect on the products, and a broad set of relevant binding energies relating to the products. As the key results, a two-dimensional PCA is carried out on the variation in outcomes, coordination number, and binding energies. From this it is observed that a two-dimensional analysis captures 70–80% of variation in the product distribution, showing that two orthogonal descriptors provide a reasonable description of the CO* reduction product distribution. Beyond this, we analyze the Cu facet structures for the coordination number allowing for unique identification of active sites (see Figure 4.9).

As an outlook to the trend studies above, it would be highly relevant to simulate and investigate the reaction steps in a detailed manner based on the trend studies. However, we suggest that correlation studies have to come prior to the detailed understanding of reactions mechanisms, when the number of possible reactions is large and when the conclusions of the simulations are so sensitive to the simulation setup. This also shows how vital careful experimental trend studies are for the understanding of catalyst materials and their performance.

4.3 Nanostructured Mono-metallic Catalysts

So, for this chapter we have considered flat metal surfaces, where most of the atoms are underneath, in the bulk phase, and do not participate in the catalytic reaction. Additionally, the surfaces of typical metal foils are usually polycrystalline that involves multiple exposed facets. These effects cause a low utilization of the metal atoms (especially those in the precious group) in terms of catalysis and inefficient composition of facets for the catalytic process. In particular, the catalytic selectivity on specific facets, either HER selective (H* favored) or CO_2RR selective (COOH* favored/H* unfavored), is difficult to control. In light of the recent catalyst investigations, namely, in the development of novel nanostructure catalysts,[40] significant signs of progress have been made to achieve a better eCO_2RR reactivity.

In principle, the nanomaterials deliver excellent catalytic performance due to different reasons. Extrinsically, their enlarged interface allows contributing extended surface area and/or active centers in comparison to the typical bulk ones. Intrinsically, the electronic structure of the active centers could be tuned to adjust the desired catalysis (see Figure 4.10). Both can together influence the catalytic performance in terms of activity, selectivity, and durability. Thus, understanding the structure sensitivity of CO_2 electroreduction over nanostructured catalysts is highly complicated because of the combined effects of the properties mentioned above. For instance, the morphologies (roughness, grain boundaries), coordination environments, and oxidation states play significant roles on the eCO_2RR activity and selectivity. All these will be discussed in detail in this chapter.

4.3.1 Nanostructured Au Catalysts

It is well known that electrochemical CO_2 reduction yields a wide range of carbon-based chemicals. In this section, we focus on Au, which is generally

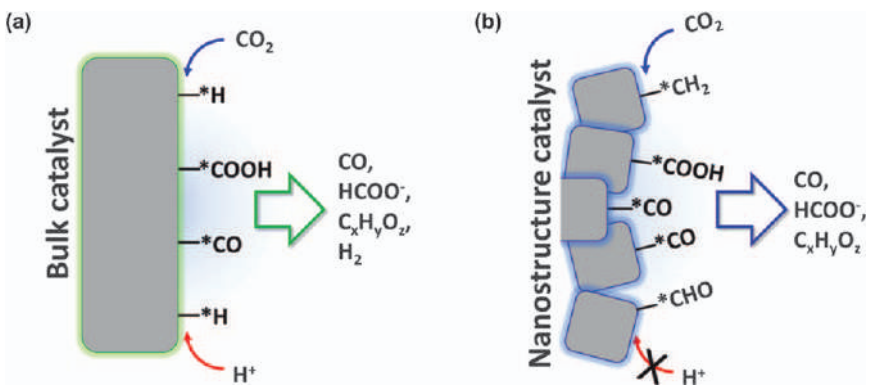

Figure 4.10 Comparison of bulk metal catalyst and nanostructure metal catalyst. (a) Illustration of bulk catalyst accompanied with possible reaction intermediates and products, and (b) illustration of nanostructure metal catalyst with enlarged surface area and modified eCO_2RR selective (H* denied) facets.

associated with the CO_2 to CO process. This reaction involves only two proton-coupled electron-transfer steps resulting in usually lower kinetic limitations than the formation of more complicated hydrocarbons or oxygenates. One crucial characteristic of CO generation is that it is always accompanied by a finite amount of H_2 production. Together, these constitute syngas feedstock for synthetic fuels production *via* the thermal catalytic Fischer–Tropsch process.[41] Other procedures, such as the production of phosgene for polyurethane and/or polycarbonate production, however, require pure CO streams.

Up to now, various materials have been reported as the catalysts for electrochemical CO_2 to CO conversion.[3,42–49] Among all the metallic candidates, Au is the most efficient catalyst for CO production due to its CO selectivity at low overpotentials.[3] Atomic insight suggests that the Au surface falls in the class of CO evolution in Figure 4.7a where the H* adsorption for HER is minimal.[23] However, the large-scale utilization of Au is hindered by its scarcity. Therefore, to deploy Au for massive investments, nanostructured catalysts are of interest due to the enlarged surface area (increased active sites) and minimal material consumption.

To achieve this increased utilization, Nursanto and co-workers investigated the catalytic performance of direct electrocatalytic CO_2 conversion to CO by depositing small Au NPs onto carbon paper using an electron beam. They observed that the morphologies of deposited Au gradually changed from small NPs (particle-size $\sim$ 4 nm) to an aggregated layered film with increased deposition. It is noteworthy that the 4 nm Au NPs (1 nm thick layered) exhibited a remarkable CO formation mass activity value, as high as 166 mA mg^{-1} at -0.59 V *vs.* RHE (see Figure 4.11).[47]

Nursanto's work shows high gravimetric CO evolution activity using 4 nm-sized Au NPs. However, the size effect of such nanostructured catalysts was not systematically studied. To understand the full impact of Au particle size

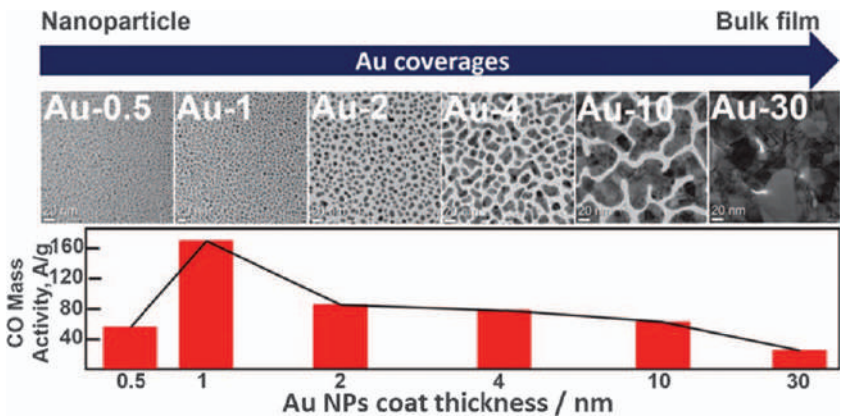

Figure 4.11 CO mass activity on nanostructured Au catalysts with different particle loading (thickness). Electrochemical CO_2 reduction is carried out in CO_2 saturated 0.1 M $KHCO_3$ electrolyte at -0.59 V *vs.* RHE.
Adapted from ref. 47 with permission from Elsevier, Copyright 2016.

Table 4.2 Comparison of different nanostructured Au catalysts for electrochemical CO_2 reduction in terms of small-scale H-cell characterization.

SAMPLE	Electrolyte	pH	η (mV)[a]	j_{CO} (mA cm^{-2})	j_{CO} (mA mg^{-1})	Ref.
Au foil	0.5 M $KHCO_3$	7.2	520	5.5	N/A	51 (Hori)
Au NPs (4 nm)	0.5 M $KHCO_3$	7.03	480	N/A	166.1	47 (Nursanto)
Au NPs (4 nm)	0.5 M $KHCO_3$	7.2	260	N/A	0.33	45 (Zhu)
Au NPs (8 nm)	0.5 M $KHCO_3$	7.2	260	N/A	0.14	
Au NWs (500 nm)	0.5 M $KHCO_3$	7.2	240	0.23	1.84	46 (Zhu)
Au NWs (100 nm)	0.5 M $KHCO_3$	7.2	240	0.12	0.74	

[a]Denotes the overpotential.

for eCO_2RR, Hemma *et al.* conducted the assessments on a series of micelle-synthesized size-controlled Au NPs.[50] Similar to Nursanto's finding, the overall activity is dramatically enhanced with decreasing NP size (see Table 4.2), however, the competitive HER process seemed to be more selective. This relationship is likely due to the increase in low-coordinated sites on the NPs surface resulting in smaller NPs, while the edge-per-surface tends to bind H* strongly. Therefore, the binding to COOH* for eCO_2RR is limited under high H* coverage conditions.

Zhu *et al.* performed an interesting joint theoretical and experimental study by modifying the exposed facet of polycrystalline Au NPs to evolve the CO evolution.[40] Polycrystal Au NPs are controlled to 4, 6, 8, and 10 nm (NP size), respectively, to serve as the model catalysts. In line with the aforementioned studies, the smaller Au NPs (4 nm) show greater mass CO activity (for HER as well). Interestingly, the 8 nm sized particles have optimal FE_{CO} (faradaic efficiency to CO formation) compared to other sized NPs (see Figure 4.12a–c). To explain the selectivity trends with particle size, DFT modeling was done on various Au facets. The simulation indicates that the edge sites (colored orange in Figure 4.12a) favor reducing CO_2, while the corner sites (colored dark orange in Figure 4.12a) prefer to catalyze the unwanted HER. They claimed that the 8 nm-sized Au NPs could provide the optimal ratio of eCO_2RR selective edge sites to HER favoring corner sites.[45] Acting upon this theory, they designed and synthesized longer Au NWs (nanowires, corner sites rich, displayed in Figure 4.12d), which exhibited 94% FE_{CO} with considerable mass activity (1.84 mA mg^{-1}) at -0.35 V *vs.* RHE, and, stayed at this level for 6 hours without any noticeable activity change.[46]

4.3.2 Nanostructured Ag Catalysts

Ag poses as an interesting option for eCO_2RR thanks to its high selectivity to CO, although such conversion demands a relatively higher overpotential to that occurring on Au candidates. Furthermore, minute amounts of formate could also been traced at high potentials (over -1.0 V *vs.* RHE).[42] One advantage of Ag is that it does not cost as much as other precious materials. As a result, Ag NPs are often considered the most promising catalyst for scaled eCO_2RR applications.[43,49,52,53]

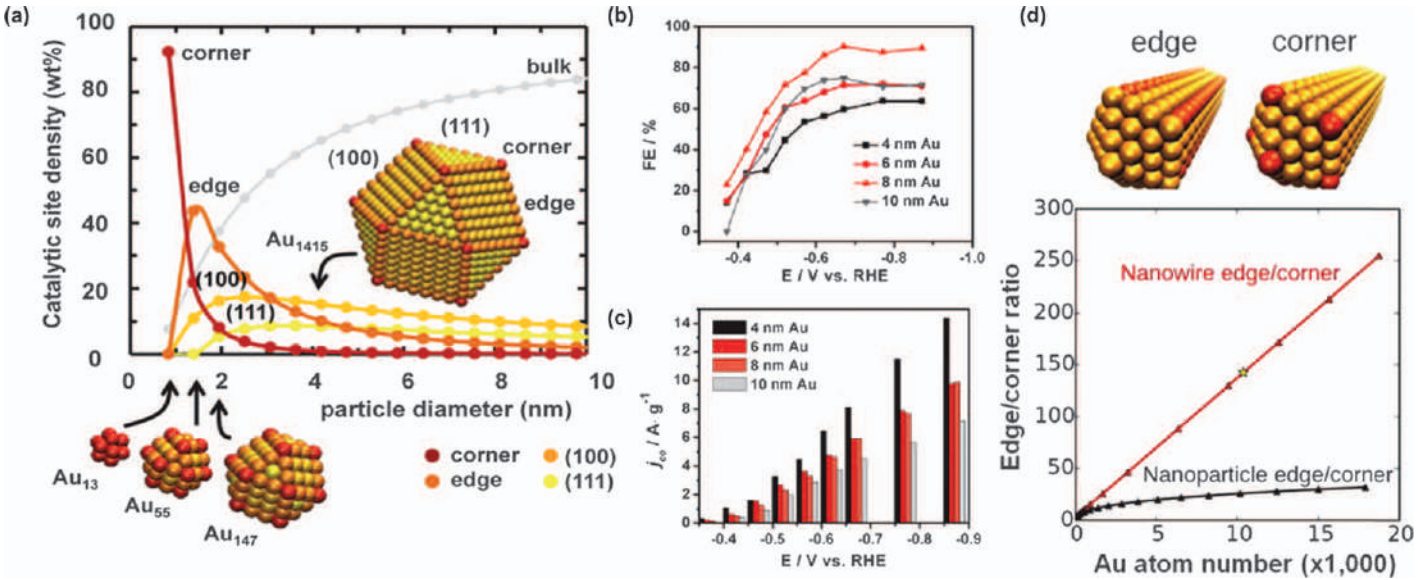

Figure 4.12 (a) Density of adsorption sites [yellow, light orange, dark orange, or red symbols for (111), (001), edge, or corner on-top sites, respectively] on closed-shell cuboctahedral Au clusters *vs.* the cluster diameter. The weight fraction of Au bulk atoms is marked with gray dots. (b) Potential-dependent FEs of the Au NPs on the electrocatalytic reduction of CO_2 to CO. (c) Current densities for CO formation (mass activities) on the Au NPs at various potentials. (d) Atomic illustration and ratio of edge sites/corner sites in nanowires and nanoparticles.
Reproduced from ref. 45 and ref. 46 with permission from American Chemical Society, Copyright 2013 and 2014.

Similar to Au NPs, nanostructured Ag has also been investigated to enhance the eCO_2RR performance. In 2014, Lu and co-workers synthesized nanoporous Ag electrocatalysts by two-step de-alloying a Ag–Al precursor. This process produces a homogeneously distributed porous structure [scanning electron microscopy (SEM) image is presented in Figure 4.13a] compared to Ag NPs (Figure 4.13b). This nanoporous Ag shows an impressive selectivity toward CO of ~92% (comparable to bulk Ag electrodes) with reaction rates over three orders of magnitude higher than for the bulk catalyst at -0.6 V *vs.* RHE. A large portion of the enhanced activity is the result of the enlarged, nanoporous electrochemical surface area (~150 times larger), while the rest can

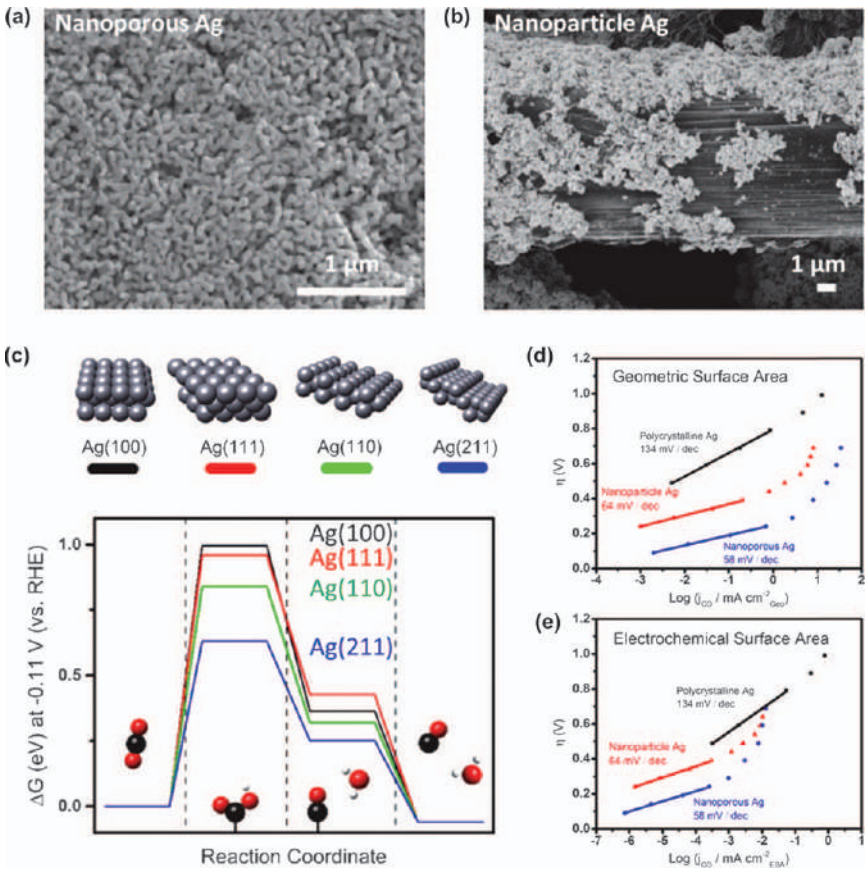

Figure 4.13 SEM images of (a) nanoporous Ag and (b) Ag NP catalysts. (c) Schematic illustration and free-energy diagrams of electrochemical reduction of CO_2 to CO on flat Ag(111), Ag(100) and edge Ag(221), Ag(110) surfaces. Tafel slope plots (overpotential *vs.* logarithm CO production partial current density) on polycrystalline Ag, nanoporous Ag and Ag NP based on (d) geometric area and (e) electrochemical surface area.
Reproduced from ref. 55 with permission from American Chemical Society, Copyright 2015.

likely be attributed to the intrinsic activity of the stepped surface (steps and edges, contributing around 20 times more compared with polycrystalline Ag) (see Figure 4.13c and d).[54]

The increased surface of the nanostructured Ag is not the only reason for the enhanced eCO_2RR activity. In addition, the nanostructure impacts intrinsic activity.[54] Rosen *et al.* analyzed commercial Ag NP (>100 nm) model catalysts and observed a boosted CO production rate compared with the bulk ones (Figure 4.13d). In part, such enhancement should be due to the increased surface area of the NP assemble, which is in line with Lu's conclusion.[55] To further quantify the improvements in the intrinsic catalytic activity of the nanostructured Ag catalyst (both nanoporous[54] and nanoparticle one), the Tafel plots are normalized to the electrochemical surface area (shown in Figure 4.13e). The nanostructured catalysts outperform the bulk Ag even on a per-site basis at low overpotentials where the reaction is kinetically limited. The reason for this difference is made clear by DFT calculations that compare the free-energy diagrams from CO_2 to CO on distinct Ag facets. Steps and edges [Ag(211) and Ag(110)] that provide low coordination Ag sites could adsorb COOH* intermediates on the surface. In contrast, the formation energy of COOH* is relatively higher for closed facets like Ag(100) and Ag(111). This formation energy is a significant barrier for CO evolution. As a result, the steps and edges on the Ag surface created by nanostructuring play a vital role in dynamically lowering the activation barrier for eCO_2RR to CO (*via* the COOH* state) facilitating the overall reaction rate.

Nanostructuring Ag catalysts improve the catalytic activity by expanding the surface area and creating low coordinated surface atoms. However, these effects could simultaneously enhance the turnover frequency of the competitive HER. Therefore, it is necessary to search alternative strategies to control the CO_2 reduction selectivity beyond just structural properties. Kim *et al.* synthesized a series of carbon-supported Ag NPs using a facile one-pot method using a cysteamine anchoring agent. Transmission electron microscope (TEM) images of the NPs (shown in Figure 4.14a–c) reveal that the presence of the cysteamine agent could control the Ag NP size. In the accompanying electrochemical characterization, these supported NPs exhibit significantly improved mass activity over the foil catalyst with the optimal size being 5 nm (see Table 4.3). Additionally, the overpotential requirement, as well as the optimal CO selectivity, is decreased (Figure 4.14d–f).[56]

In an attempt to explain the decreased overpotential for CO evolution on Ag NPs, DFT calculations were carried out to examine the binding energy toward COOH* and CO*. Unfortunately, in Kim *et al.*'s simulation, the modulated size effect does not directly correlate with the overpotential decrease between particle sizes of 3 and 10 nm. Instead, the cysteamine anchoring agent covering the Ag surface likely enhances the activity, although the exact coverage is difficult to quantify. Kim *et al.* postulate that the existence of the cysteamine anchoring agent could provide a more covalent character to the Ag–COOH* bond, effectively stabilizing the COOH* intermediate, which would boost the CO_2 to CO reaction (shown in Figure 4.14g).[56]

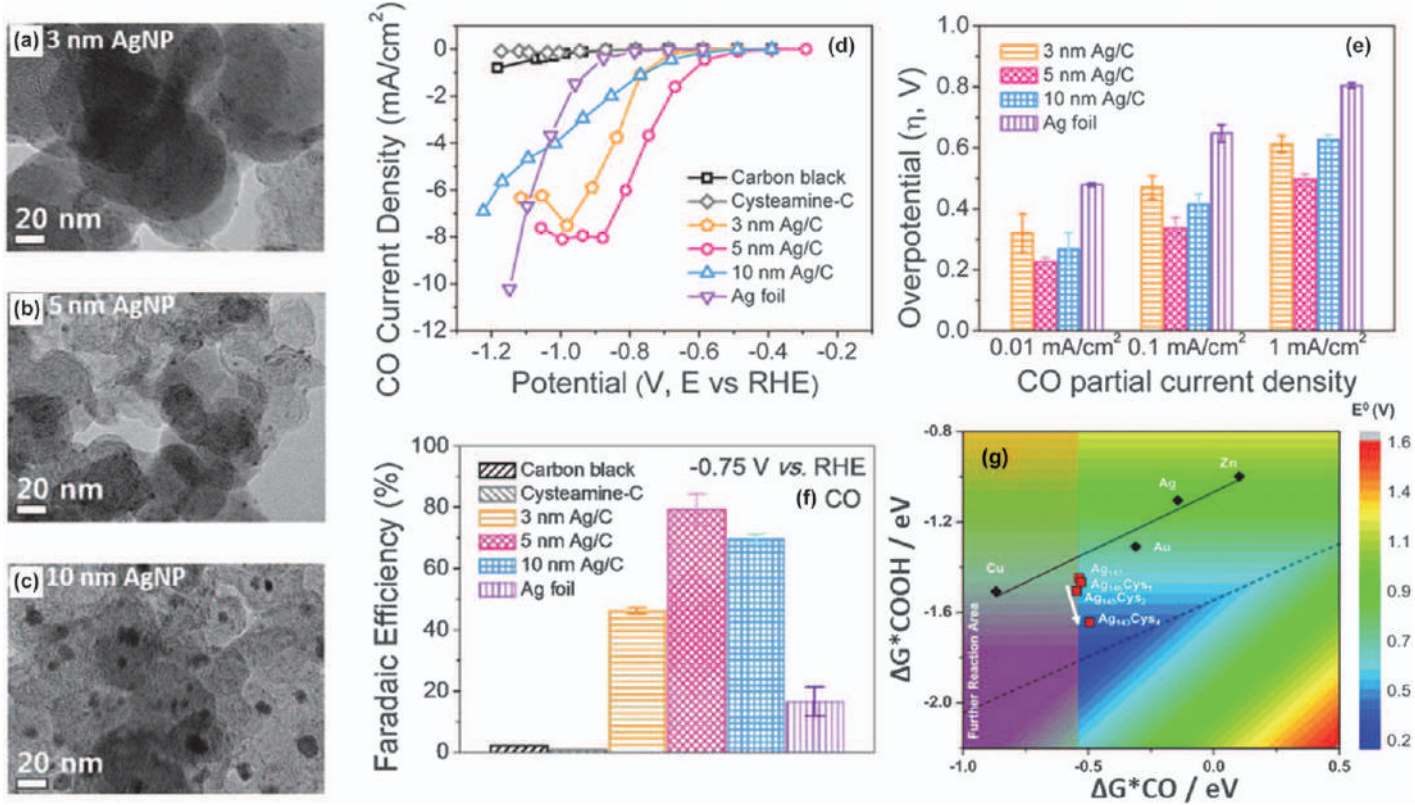

Figure 4.14 TEM images of (a) 3 nm-, (b) 5 nm-, and (c) 10 nm-sized Ag NPs synthesized on the carbon support. (d) Geometric CO partial current density as a function of applied potential, (e) overpotentials at fixed current densities and (f) CO faradaic efficiency at −0.75 V *vs.* RHE. Experiments are performed in CO_2 saturated 0.5 M $KHCO_3$. (g) Effect of anchoring agents on COOH* and CO* binding energies examined using $Ag_{(147-n)}Cys_n$ ($n = 0$, 1, 2, 4) models. The colored map shows the theoretical CO_2 reduction potential (E°) as a function of COOH* and CO* binding free energies (ΔG_{COOH^*} and ΔG_{CO^*}). For comparison, ΔG_{COOH^*} and ΔG_{CO^*} calculated for the (111) slab surface of Cu, Au, Ag, and Zn are also displayed, which corresponds to the typical metal foil. Reproduced from ref. 6 with permission from American Chemical Society, Copyright 2015.

Table 4.3 Comparison of various nanostructured Ag catalysts for the electrochemical CO_2 reduction using small-scale H-cell characterization.

SAMPLE	Ag loading ($mg\,cm^{-2}$)	Electrolyte	pH	η (mV)[a]	j_{CO} ($mA\,cm^{-2}$)	j_{CO} ($mA\,mg^{-1}$)	Ref.
Polycrystal Ag	N/A	0.5 M $KHCO_3$	7.2	390	0	N/A	56 (Kim)
Nanoporous Ag	40	0.5 M $KHCO_3$	7.2	390	8	0.1989	54 (Lu)
Ag NP (100 nm)	1.0	0.5 M $KHCO_3$	7.2	390	0.022	0.022	55 (Rosen)
Ag NP (5 nm)	0.09	0.5 M $KHCO_3$	7.2	390	0.23	2.56	56 (Kim)
Amine mod. Ag/C	0.06	0.5 M $KHCO_3$	7.2	390	0.12	1.85	57 (Kim)
Thiol mod. Ag/C	0.07	0.5 M $KHCO_3$	7.2	390	0.15	2.08	

[a]Denotes the overpotential.

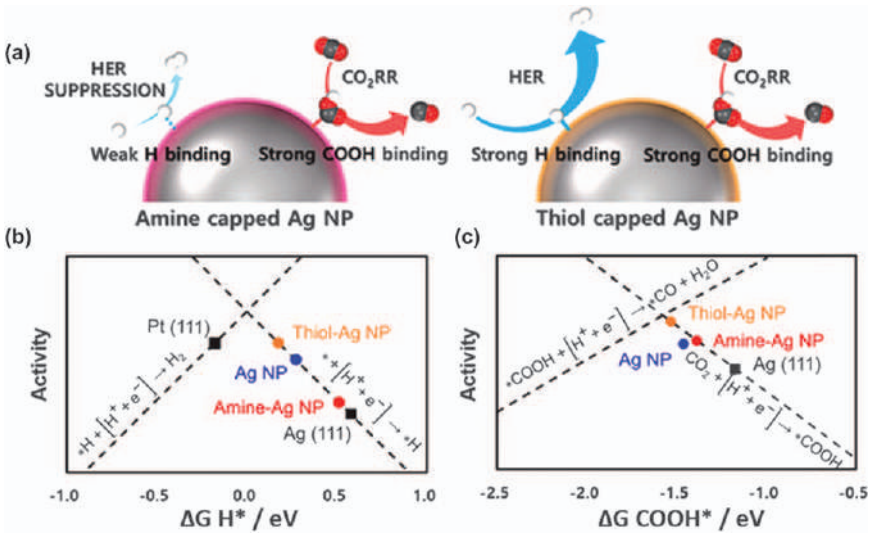

Figure 4.15 (a) Schematic illustration of HER and CO_2RR on amine-capped Ag NPs and thiol-capped NPs. (b) Volcano plots of HER activity as a function of binding energy toward H* on various Ag surfaces. (c) Volcano plots of CO_2RR activity as a function of binding energy toward COOH* on distinct Ag surfaces.
Reproduced from ref. 57 with permission from American Chemical Society, Copyright 2017.

To further understand the role of capping agents, Kim and co-workers systematically investigated the effect of small organic capping molecules on the Ag NP surfaces (see Figure 4.15). These molecules could tune the chemical properties of the surface and modify the catalytic activity for eCO_2RR. It was found that the amine functional group on the Ag surface effectively improved the FE_{CO} to >94% by suppressing unwanted HER. In contrast, the thiol group boosted both CO_2RR and HER rates. This has been explained in DFT simulations, in that, both the H* and COOH* binding energies are strengthened by the thiol ligand, while the H* is inhibited on

the amine-modified Ag. For this reason, the CO_2 to CO reaction is boosted in the presence of amine capping, whereas the HER remains sluggish (the schematic is illustrated in Figure 4.15a).[57]

4.3.3 Nanostructured Cu Catalysts[‡]

Among all metals and regarding oxides catalysts, Cu is uniquely special as it can produce value-added hydrocarbons and alcohols.[5,9] Recently, high selectivities toward C2 and C3 products during eCO_2RR have been reported on specially designed Cu-derived catalysts and/or advanced Cu-based electrodes,[10,59–62] showing a high potential of fabricating the upscaled electrochemical hydrocarbons and oxygenates. Other metals beyond Cu, as well as solid non-metallic carbon-based catalysts, could also produce hydrocarbons, but in exceedingly slow processes.[44,63] The differing selectivity of Cu in comparison to other metals appears to be due to the interaction toward the intermediates during eCO_2RR. First, proper binding energies to H* and COOH* enable a significant production of CO, which is the key intermediate for forming hydrocarbons. Second, the Cu surface could further bind and protonate the adsorbed CO*, thus pushing the further formation of single or multi-carbon products[11,25] without being poisoned.[23] In contrast, on metals such as Pt, that can strongly bind with CO*, the intermediate CO would rather sit and block the surface.[64]

Unlike the metallic Au or Ag catalysts that only yield CO, Cu-based catalysts deliver a complicated product distribution, making it challenging to address the reaction path towards each single one, especially to complicated hydrocarbons and alcohols. To deconvolute all the crucial factors that control the reactivity of hydrocarbons or alcohols, the binding energy of Cu to each possible intermediate, such as CO*, methyl group, and aldehydes group *etc.*, should be taken into account.

First, we focus on the size effect on the reaction dynamics. In a recent study of size-controlled Cu NPs synthesized through reverse micelle encapsulation, it was determined that the activity toward CO_2 electroreduction over Cu NPs significantly increased for <5 nm-sized particles owing to the high surface ratio of low-coordinated sites on the surface (Figure 4.16a).[50] This activity increase originated from facilitated H_2 evolution and CO formation over smaller NPs. However, the selectivity to hydrocarbons was drastically suppressed with decreasing size.[67] Some examples include glassy carbon-supported Cu NPs (7 nm)[65] and Cu NPs (12 nm; 40% by weight) supported on Vulcan carbon,[65] as shown in Figure 4.16b and c. To understand size-dependent trends, it is also essential to consider changes in the size and shape of NPs during the reaction. For example, the 7 nm NPs shown in Figure 4.16b grow to 23 nm during the reaction, which may explain their different selectivity from the smaller NPs shown in Figure 4.16a.

[‡]Part of this subsection is reproduced from ref. 58 with permission from Springer Nature, Copyright 2016.

Unlike the eCO_2RR occurring on Ag or Au that only yields CO, studies on single-crystals have clearly shown that both the reactivity and selectivity of Cu during the electrochemical CO_2 reduction are dependent on the crystal facets. The ratio between CH_4 and C_2H_4 depends strongly on the crystal orientation, with Cu(111) favoring the formation of CH_4, and Cu(100) supporting the formation of C_2H_4.[68] Specific steps have been shown to be selective toward individual products.[25,69] Indeed, Hori and co-workers[68] showed that steps in the (100) surface increased C_2H_4 selectivity, with an optimal selectivity of 58.9% on Cu(711). Both experimental and theoretical studies have been carried out to unravel the mechanism behind the selectivity change on (111) and (100) surfaces. It was found that Cu(100) surfaces facilitate the formation of C_2H_4 through CO dimerization (see Figure 4.17a), whereas Cu(111) surfaces favor CO protonation, which is a crucial step toward CH_4 formation, although C_2H_4 can also be formed *via* this pathway.[26–28,70,71]

Given that the selectivity toward hydrocarbons could be tuned by modifying the shapes/facets of the Cu NPs, synthesis approaches, such as electrochemical reduction/oxidation,[72,74] colloidal/wet chemistry,[75,76] and plasma treatment[63] have been implemented to control the specific nanoscale shapes to enhance the formation of hydrocarbons. Roberts *et al.*[74] recently investigated Cu nanocubes, grown by successive oxidation–reduction cycles on polycrystalline Cu in the presence of KCl, and found an improvement in C_2H_4 formation. Chen *et al.*[72] synthesized Cu nanocubes using a similar method and found enhanced C_2H_4 selectivity, as shown in Figure 4.17b, and high stability for CO_2 electroreduction. The mechanisms behind the improved activity of these structures may involve the (100) facets on the cubes, which are known to favor C_2H_4 selectivity, the nanostructured Cu cube surface or even Cl^- or Cu^+ species that may remain on the catalyst during the reaction. For the colloidal method synthesized cube-shaped Cu nanocrystals, the nanocubes with 44 nm edge length exhibited an optimized selectivity toward eCO_2RR (80%, $FE_{C_2H_4} = 41\%$) compared to other larger or smaller sized cubes (and nanospheres).[75] Instead of Cu (100) facets, the edge sites of the cubes were suggested to play the critical role in eCO_2RR and the corresponding reaction mechanism is proposed in Figure 4.17c.[73]

For eCO_2RR, especially over Cu-based catalysts, the selectivity between CH_4 and C_2H_4 is highly dependent on pH.[5,63,77] For example, the CO reduction into CH_4 process shows an evident Nernstian behavior,[78] indicating that the methane evolution requires participation of protons.[79] In contrast, C_2H_4 formation does not rely on pH, meaning that this process is not determined by the local proton concentration. As a result, it could be expected that ethylene formation is more preferred under alkaline conditions, whereas in acidic or neutral solutions CH_4 formation is boosted.[78]

Usually, the eCO_2RR is carried out in bicarbonate buffer electrolytes at a close-to-neutral pH, because the CO_2 feeding could act as a buffering agent. However, during the cathodic electrolysis, either HER or CO_2RR consumes a considerable amount of protons, alkalinizing the local solution of the double layer. Gupta *et al.* performed a computational study to model this and found

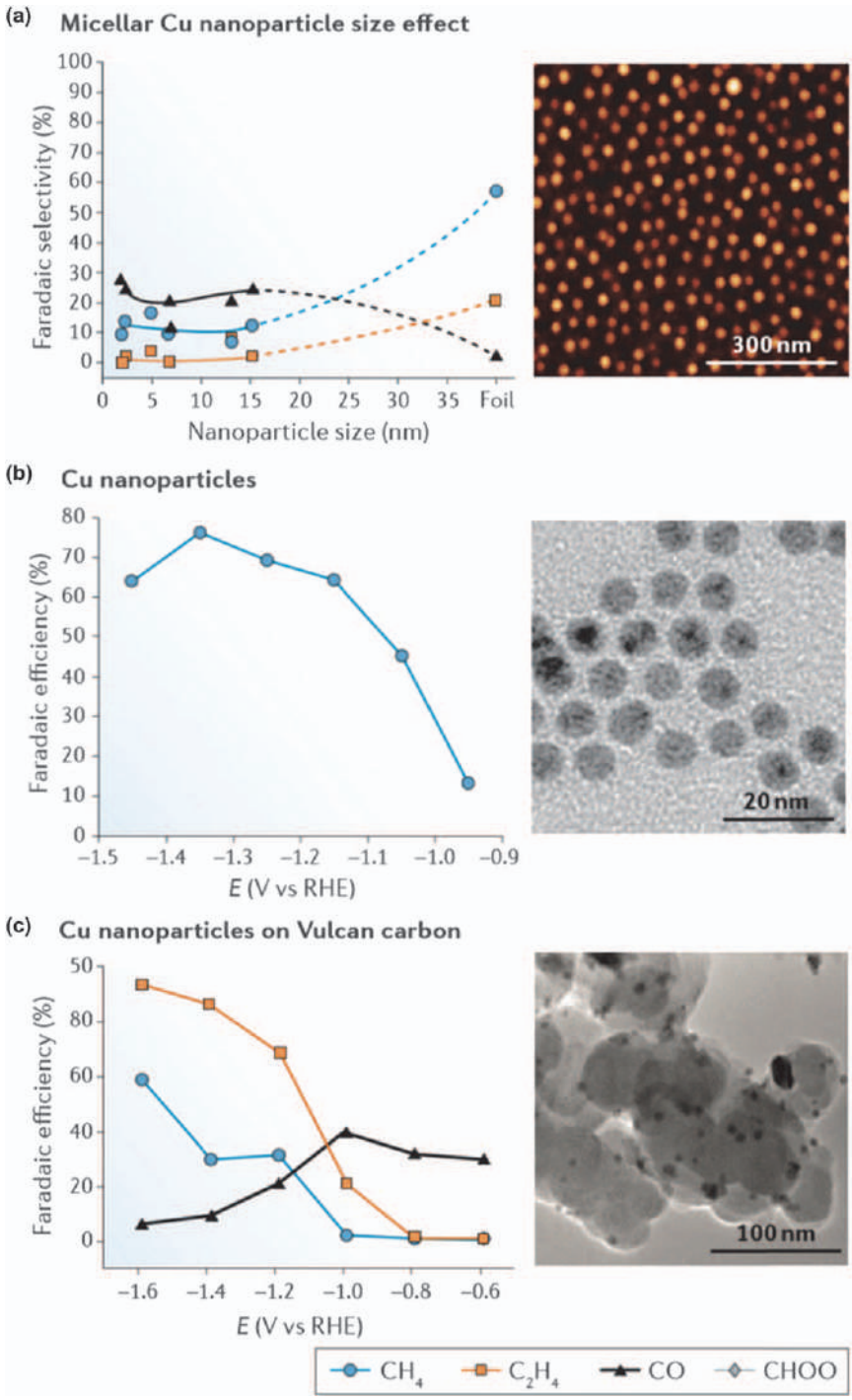
(a)
Micellar Cu nanoparticle size effect
Faradaic selectivity (%)
100
90
80
70
60
50
40
30
20
10
0
0 5 10 15 20 25 30 35 Foil
Nanoparticle size (nm)
300 nm
(b)
Cu nanoparticles
Faradaic efficiency (%)
80
70
60
50
40
30
20
10
0
−1.5 −1.4 −1.3 −1.2 −1.1 −1.0 −0.9
E (V vs RHE)
20 nm
(c)
Cu nanoparticles on Vulcan carbon
Faradaic efficiency (%)
50
80
60
40
20
0
−1.6 −1.4 −1.2 −1.0 −0.8 −0.6
E (V vs RHE)
100 nm
CH4
C2H4
CO
CHOO

that high current densities correspond to high consumption of interfacial protons and, therefore, to more dramatic changes in the local pH.[80] Accordingly, in comparison to flat electrodes, the rough/enlarged surface of nanostructured catalysts usually provides larger current densities, causing a high local pH, thus increasing the selectivity for C_2H_4 production.[81]

Another critical parameter for Cu NP catalysts is the interparticle distance. Mesoscale phenomena, such as interparticle reactant diffusion and resorption of intermediates, can have a defining role in product selectivity for a multistep reaction.[82,83] Mistry *et al.*[84] have shown that, for eCO_2RR, decreasing the interparticle spacing could increase the selectivity for CH_4 and C_2H_4. Regarding the mechanism, this was proposed to be the strengthened resorption of the CO intermediate, benefiting the further CO* protonation into hydrocarbons. This aspect could be realized on roughened Cu surfaces,[81] on highly dispersed Cu NPs with increased areal particle density,[76] and on additional CO feeding onto the catalytic Cu interface.[85]

4.4 Nanostructured Bi-metallic Catalysts[§]

One of the strategies to improve the catalytic eCO_2RR reactivity is combining one metal with another rather than the typical single-elemental metals, such as the nanostructured core-shell, deposited metal layers, and alloys. In the following sections, we discuss the recent progress on Cu-based bimetallic nanostructured catalyst systems by dividing them into three groups: i) H_2-producing metals (Pd and Pt), ii) formate-producing metals (In and Sn), and iii) CO-producing metals (Au, Ag, and Zn). We address how the combination of Cu with other metals can be used to tune both the activity and selectivity of eCO_2RR.

Figure 4.16 Faradaic selectivity of the electrochemical CO_2 reduction over various Cu NPs. (a) Particle size-dependent faradaic selectivity over micelle-synthesized Cu NPs supported on glassy carbon at −1.1 V *vs.* RHE. Atomic force microscopy image of these Cu NPs is shown on the right. (b) Faradaic efficiency for eCO_2RR to CH_4 for colloidally synthesized 7 nm Cu NPs supported on glassy carbon. The high-resolution TEM image is displayed on the right. (c) Faradaic efficiency for Cu NPs (40% by weight) supported on Vulcan carbon. The high-resolution TEM image shows the as-prepared catalyst. Reproduced from ref. 58 with permission from Springer Nature, Copyright 2016. Panel (a) adapted from ref. 50 with permission from American Chemical Society, Copyright 2014. Panel (b) adapted from ref. 65 with permission from American Chemical Society, Copyright 2014. Panel (c) adapted from ref. 66 with permission from American Chemical Society, Copyright 2014.

[§]This section is reproduced from ref. 86, with permission from John Wiley & Sons, © 2018 WILEY-VCH Verlag GmbH & Co. KGaA, Weinheim.

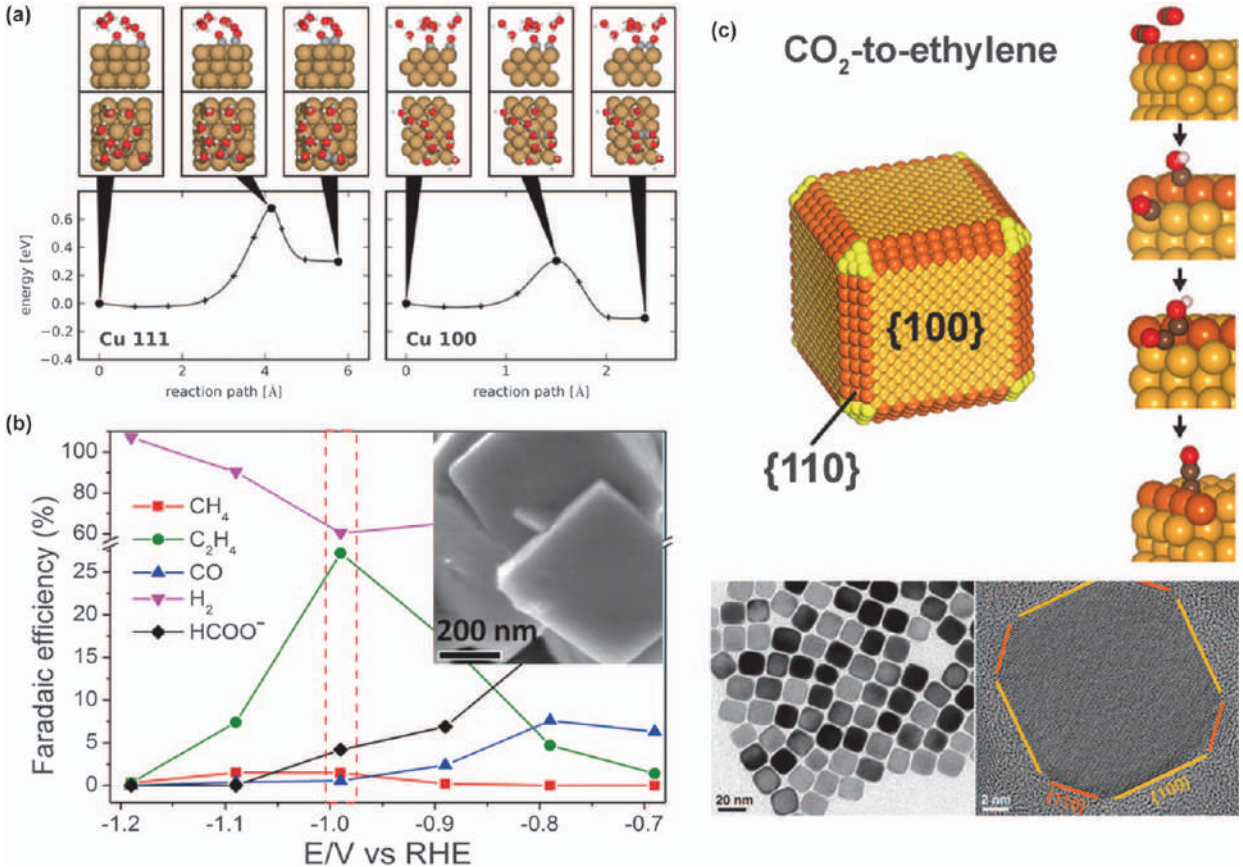
(a)
energy [eV]
0.6
0.4
0.2
0.0
−0.2
−0.4
Cu 111
Cu 100
0
2
4
6
1
reaction path [Å]
reaction path [Å]
(b)
Faradaic efficiency (%)
100
80
60
25
20
15
10
5
0
CH4
C2H4
CO
H2
HCOO−
200 nm
-1.2
-1.1
-1.0
-0.9
-0.8
-0.7
E/V vs RHE
(c)
CO2-to-ethylene
{100}
{110}
20 nm
2 nm
(110)
(100)

4.4.1 Cu–Pd/Pt Catalysts

It is well known that the formation of hydrocarbons occurs *via* the further protonation of the intermediate CO. Thus, tuning the local proton activity poses as an efficient strategy to accelerate the hydrocarbon formation, especially for methane.[63] Toward catalyst design, locally combining Cu and one traditional H* adsorber, such as Pt and Pd, would allow this reaction mechanism. Thus, Pt and Pd could adsorb atomic hydrogen (H*), while the Cu delivers and protonates the co-adsorbed CO* into CHO*.[87]

In principle, alloying Cu with Pd can tune the chemisorption strength of H* and CO* intermediates on the catalyst surface owing to geometric and electronic effects. This design enables an optimal activity and selectivity toward CO_2RR. Li *et al.* reported a well-defined mesoporous Pd–Cu, and the FE_{CO} could exceed 80% at -0.8 V_{RHE}.[88] However, the formation of hydrocarbons was not observed. It was claimed that the charge density could be altered in the Pd–Cu alloy compared with each single component. In the alloy system, the Pd atoms serve as electron donors, working as the active sites under the cathodic condition. They could therefore readily combine with the COOH* to produce CO. The Cu atoms, instead of participating in the eCO_2RR, only modify the electronic structure of the neighboring Pd atoms in the bimetal system. Consequently, the catalytic signature of Cu is to some degree hindered. Yin *et al.* prepared a series of Pd–Cu nanoalloys (supported on carbon) with various size and atomic ratios as the candidate for CO_2 reduction. They found that the particle size of 5 nm with a Pd : Cu ratio of 85 : 15 gave a significantly improved performance, which might be due to specific exposed under-coordinated steps or ad-atom sites, presumably lowering the binding toward CO*.[89]

In bimetallic systems, the strain effect is another crucial factor to consider, since it could change the electronic structure of the top-layered metal atoms, further affecting the catalytic performance. The strain effect should exist in the Cu–Pd system since the lattice constant of Cu and Pd largely deviates with each other.[90,91] To address this, Zhu *et al.* developed a facile synthesis route for Pd–Cu bimetallic NPs with various structures.[90] The concave rhombic Cu_3Pd (Cu dominant with the lattice stained by Pd) exhibits an enhanced CH_4 current density compared to Cu foil. In contrast, flower-like Pd_3Cu (Pd-rich) shows high

Figure 4.17 (a) Kinetic barriers for the formation of a CO dimer from two adsorbed CO species for Cu(111) (left) and Cu(100) (right), calculated using the NEB (nudged elastic band) method. The barriers of 0.68 eV for Cu(111) and 0.33 eV for Cu(100) suggest that Cu(100) should form CO dimers at significantly higher rates than Cu(111). Also shown are visual schematics of the initial, transition, and final states for both calculations. (b) Faradaic efficiency of CuCl derived Cu mesocrystals. The (100)-like cubic shape is shown in the TEM image. (c) Schematic ethylene formation on (100) and (110) edges proposed by Buonsanti *et al.* Figure (a) adapted from ref. 28 with permission from American Chemical Society, Copyright 2014. Figure (b) adapted from ref. 72 with permission from the Royal Society of Chemistry. Figure (c) adapted from ref. 73 with permission from American Chemical Society, Copyright 2018.

FE_{CO} in a wide overpotential range (-0.7 V_{RHE} to -1.3 V_{RHE}), while the catalytic fingerprint of Cu (hydrocarbon yields) is discarded.

In addition to single-carbon chemicals such as CO, formate, and methane, the C_2 products (basically ethylene) is also an exciting product in CO_2RR. To optimize the ethylene faradaic efficiency, Ma *et al.* prepared three Cu–Pd bimetal model catalysts with distinct patterns, *i.e.* ordered, disordered, and phase-separated configurations (see Figure 4.18a and b).[92] The ordered one (Cu : Pd = 1 : 1) shows the highest selectivity for CO (see Figure 4.18c), while the disordered Cu–Pd sample holding the same metal content favors the formation of hydrocarbons. More interestingly, the Pd–Cu sample with phase-separated patterns behaved quite differently, leading to a remarkable C_2 selectivity (>60%). The insight behind this could be attributed to the geometrically tandem effect between the Pd and Cu sites. In this system, the Cu region contributes to CO* generation and resorption, whereas the adjacent Pd-rich area could deliver the protons for a further protonation step. This observation agrees with the lately discussed "two-sites" mechanism on Cu–Ag[93] and Cu–Zn[94–96] systems.

Cu–Pd nanostructured alloys could also be coupled with organic molecules or carbon supporters, serving as dual-catalysts.[97] Liu *et al.* dispersed Cu–Pd bimetal alloys on graphene, which shows a higher eCO_2RR activity compared to the single-Cu/graphene counterpart.[98] Yang *et al.* immobilized molecular pyridine on a Cu–Pd catalyst surface,[99] and observed methanol and ethanol formation with faradaic efficiencies of 26% and 12%, respectively. The mechanistic insight provided by them is that the pyridine molecules favor methanol production, while the Cu active component facilitates the generation of ethanol.

Unlike the Pd, strong H* binding (under potential deposition) on Pt leads to active HER, restricting the applications of the Pt group alloys for eCO_2RR.[100] Therefore, there are only a few studies referring to Cu–Pt bimetallic systems. Guo *et al.* reported the utilization of a Cu–Pt catalyst with an atomic molar ratio of 3 : 1 (Cu : Pt), which improves the CH_4 formation in a 0.5 M $KHCO_3$ electrolyte.[101] The proposed mechanism is that the high atomic Cu content in the Cu–Pt alloy increases the CO* surface coverage, while the Pt sites synergistically boost the protonation process from CO* to CHO*. However, with the presence of CO formed during the eCO_2RR, the strong binding between Pt and CO* could simultaneously cause a Pt rich shell on the catalyst surface, further leading to Pt-like reactivity. Therefore, in their observation, the eCO_2RR activity largely degrades after a certain transient period, leaving the strong HER as the sole pathway.

4.4.2 Cu–In/Sn Catalysts

The next class of catalysts is based on Cu-based alloys incorporating formate-producing candidates. The interesting aspect of the latter group is that they provide weak binding strength toward the H* adsorption,[23,102] which, in principle, should diminish the competing HER during the electrochemical CO_2 reduction.

The p-block metal, In, is a formate-selective catalyst during CO_2RR with the faradaic efficiency counting up to 95%.[3] To date, several synthesis

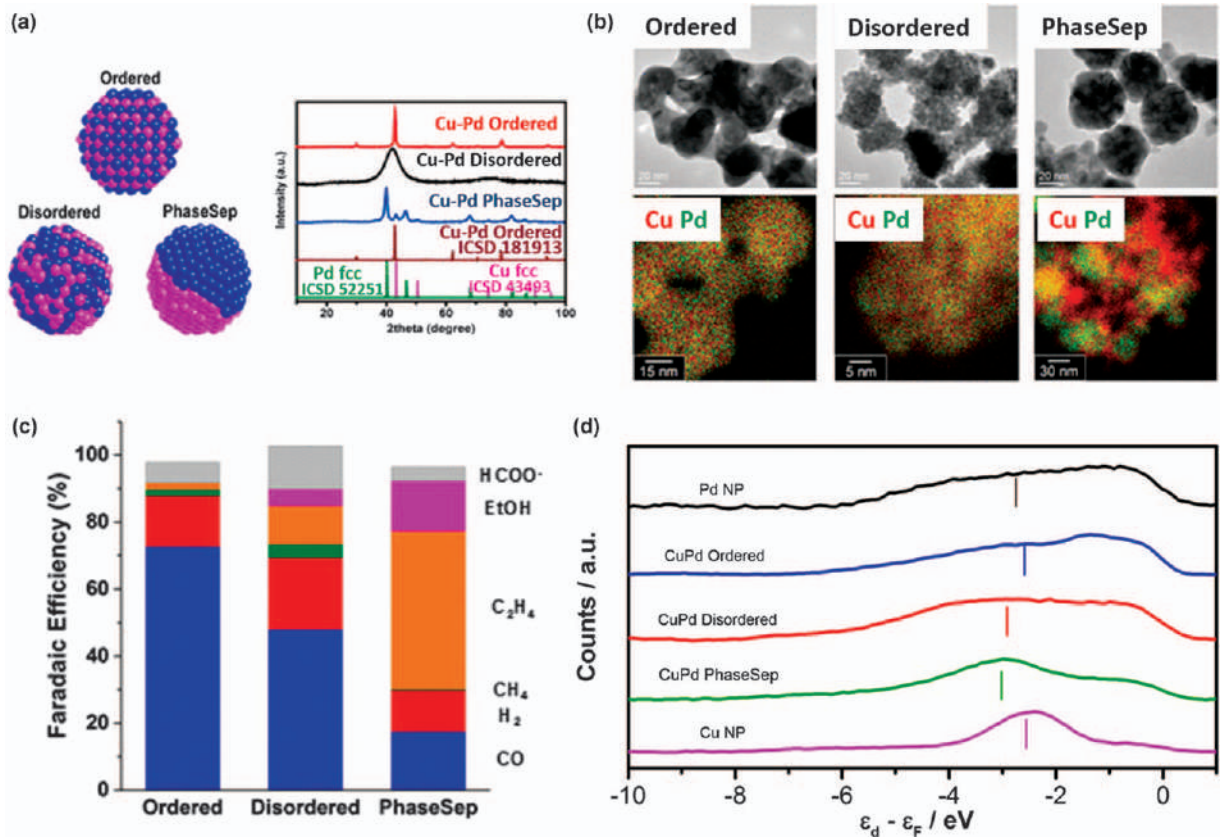

Figure 4.18 (a) Illustration of the geometric effect and X-ray diffraction (XRD) profiles, (b) TEM images and elemental mapping, (c) faradaic efficiencies toward various products, and (d) density of states of the ordered, disordered, and phase-separated (phaseSep) Cu–Pd systems.
Reproduced from ref. 92 with permission from American Chemical Society, Copyright 2017.

strategies were reported to achieve the Cu–In alloy electrodes, such as electrodeposition, electrochemical reduction, and chemical reduction. All these make the Cu–In bimetallic alloys promising catalyst systems for CO_2RR utilization. In a recent study carried out by Rasul *et al.*, a Cu–In bimetallic electrode was prepared by electrochemically depositing In in an oxide-derived Cu (OD-Cu) surface, yielding 95% FE_{CO}.[103] Such performance significantly differs from either pure Cu or In metals. To better understand the role of In atoms on the Cu surface, DFT calculations were performed, indicating that the In atoms are preferentially located on the edge sites of the Cu, inhibiting H* adsorption on the catalyst surface. This work focuses on tuning the top-layer of the catalyst, and in a subsequent work, the authors studied the Cu–In alloys with an in-bulk combination. Bimetallic $Cu_{11}In_9$ and Cu_7In_3 were synthesized by electrochemically reducing $CuInO_2$ bimetal oxides, whereas the pure Cu counterpart is produced from a Cu_2O precursor using an identical methodology.[104] These Cu–In alloys exhibited higher CO_2 conversion to HCOOH and CO compared with the monometallic Cu catalyst and remarkable stability, wherein FE_{H2} remained $<10\%$. The mechanistic insight predicted by the DFT calculation is that In could occupy the Cu step sites, hindering the adsorption of H* and CO*.

In the field of electrochemistry, core-shell type catalysts also obtained intensive scientific attention because of their specific configuration. In Larrazábal's work, Cu–In core-shell nanostructures were studied as the candidate for eCO_2RR, which were acquired by chemically depositing Cu on In_2O_3 and $In(OH)_3$ supports. Interestingly, the activity and selectivity for CO evolution over these catalysts gradually increased upon several electrocatalytic cycles, which could be associated with the segregation of Cu and In, especially the gradual formation of a shell-like $In(OH)_3$ over the Cu-rich core nanostructure (see Figure 4.19a).[105] Recently, Hoffman and co-workers used electrodeposited dendritic Cu–In alloys of various compositions as electrocatalysts.[107] At an In atomic ratio of 80%, FE_{HCOOH} could reach 62% at -1.0 V_{RHE}. At the same potential, an optimal syngas ratio ($CO:H_2 = 1:2$) could be achieved while controlling the In content at 40%.

Consistent with In, other p-block metals, Pb[102] and Sn[106,108] can strongly prohibit the hydrogen adsorption (HER activity) during the eCO_2RR on the Cu surface, namely, increasing the selectivity of carbon-based products. Sarfraz *et al.* reported a study on a Cu–Sn bimetallic catalyst generated by electrodepositing Sn atoms on an OD(oxidized-derived)-Cu substrate, showing an excellent FE_{CO} over 90% for 14 hours at -0.6 V_{RHE}.[108] In addition to the electrochemical derived bimetallic catalysts, the wet chemistry synthesized Cu–Sn core-shell nanocatalysts have also been investigated. Li *et al.* synthesized a series of SnO_2 coated Cu NPs by a seed-mediated method and suggested that the eCO_2RR activity and selectivity are contingent on the thickness of the Sn layer (Figure 4.19b).[106] The sample with the thicker Sn shell (1.8 nm) shows a Sn-like performance, and the selectivity of formate could reach ~90%. In contrast, the thinner tin shell (0.8 nm) exhibits a Sn–Cu alloy-like performance, as the CO is the major product ($FE_{CO} = 93\%$) at -0.7 V_{RHE}.

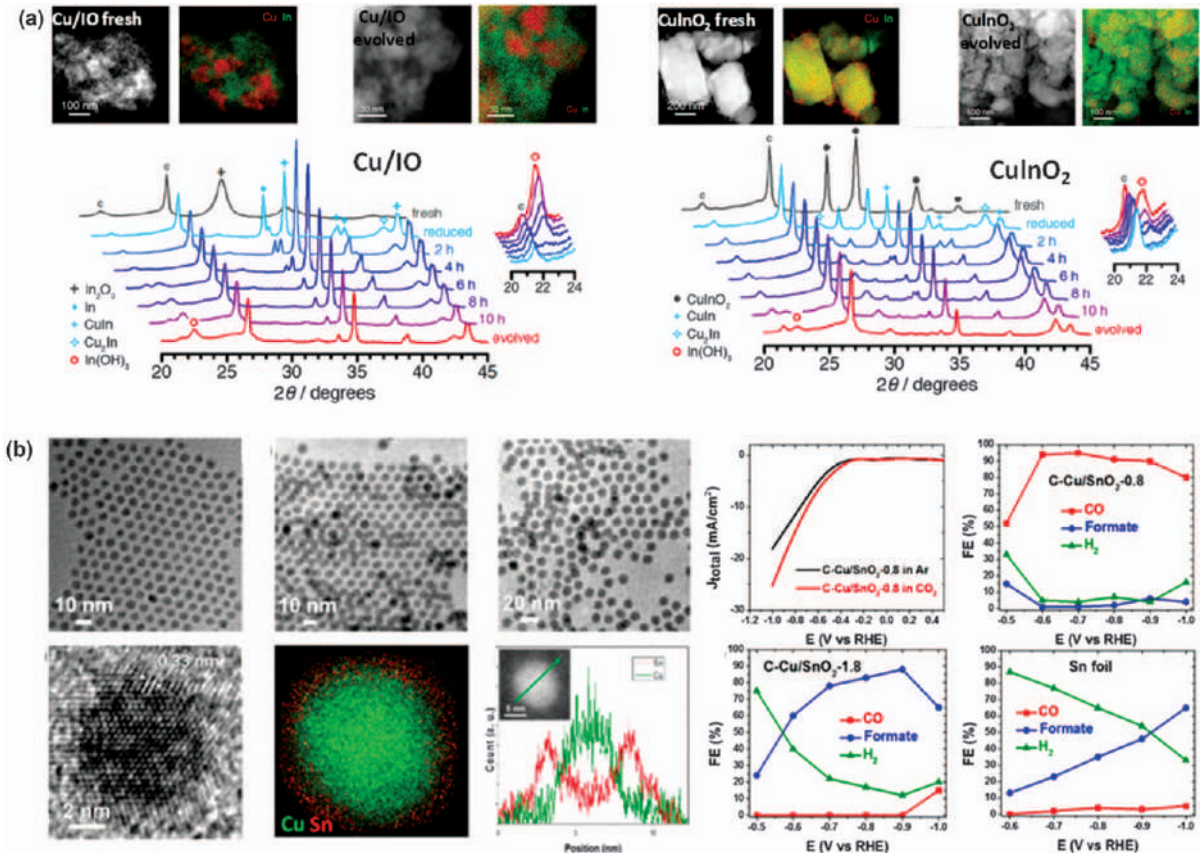

Figure 4.19 (a) HAADF-STEM (high-angle annular dark-field scanning transmission electron microscopy) images and XRD pattern of Cu-rich@In(OH)$_3$ from In_2O_3(IO) and $CuInO_2$ supported Cu NPs. Reproduced from ref. 105, http://dx.doi.org/10.1021/acscatal.6b02067, with permission from American Chemical Society, Copyright 2016. (b) TEM image of Cu@SnO2 of different thicknesses along with the electrochemical characteristics of the electrochemical CO_2 reduction.
Reproduced from ref. 106 with permission from American Chemical Society, Copyright 2017.

4.4.3 Cu–Au/Ag/Zn Catalysts

The noble metals Au and Ag are repeatedly reported as promising CO producers during the eCO_2RR. On one hand, alloying Cu into Au, Ag metals allows lowering the material cost (in comparison to pure Ag, Au metals) while maintaining even enhancement of the electrocatalytic CO yield. On the other hand, combining a CO-producing metal with Cu potentially enables a ''spill-over'' of the (intermediate) CO molecules onto the Cu sites for additional reaction steps towards products beyond CO, realizing an interesting ''tandem effect''.

To date, the most studied bimetallic system is the Au–Cu combination, because the Cu–Au could form stable and well-defined face-centered ordered and disordered alloys. Preparation methods of these bimetallic systems are commonly associated with galvanic displacement, bulk mixtures of metal melts,[109] and electrochemical deposition.[110] As expected, the increase in Au content leads to a catalytic signature of pure metallic Au, whereas some other compositions showed enhanced production of C_2H_4,[111] CO,[109] and alcohols.[110] Christophe *et al.* observed an enhanced CO production on a $Au_{50}Cu_{50}$ alloy and suggested that accelerated CO* desorption poses as the origin.[109]

It should be noticed that, for multi-metal systems, structural stability is a factor of importance as the phase evolution can readily occur, especially under an applied potential and with the presence of reactants. Friebel *et al.* have investigated the properties of Cu overlayers on a Au substrate using *in situ* X-ray absorption spectra (XAS) in an alkaline electrolyte. Although a 12.5% expansion of the Cu lattice was initially observed in the Cu overlayer, a Au-rich surface was subsequently formed under applied potentials.[112] In line with the experimental observations, the DFT prediction made by Lysgaard *et al.* addressed the stability of nanoalloys using the model of a bimetallic icosahedral composed of 309 atoms. They pinpointed that the segregation of phases into a Cu-rich core and a Au-rich shell is due to the size difference of these two metal atoms.[113]

Recent experimental studies on atomic ordering[114] and the size-reactivity relation of Au/Cu particles[115] propose segregation of Au from Au/Cu alloys to the surface. In addition, they discuss effects of compressive strain and presence of undercoordinated sites as the origin of enhanced eCO_2RR activity. The result of strain effect is further studied by Monzó *et al.*, who observed that an increasing layer thickness of Cu on a Au-core was enhancing the protonation pathway, favoring the production of H_2 and CH_4 at the cost of ethylene.[116]

Next to strain, geometric and electronic alterations are notable parameters proposed to alter catalyst reactivity. Kim *et al.* varied the Au/Cu-ratio of spherical NPs with a diameter of roughly 10 nm to investigate the influence of electronic effects on the eCO_2RR activity (Figure 4.20a). While confirming the formation of an alloy *via* XRD and Surface Plasmon Resonance, they observed an increasing FE_{CO} with increasing Au ratio, while other gaseous products were diminishing. They monitored the shift of the d-band center with varying metal ratios by XPS, which showed a decrease with higher Au-content, agreeing with the witnessed change in product distribution. Interestingly, the Au_3Cu differed from the trend and showed the highest CO mass activity. This deviation was suggested to be caused by a geometric effect,

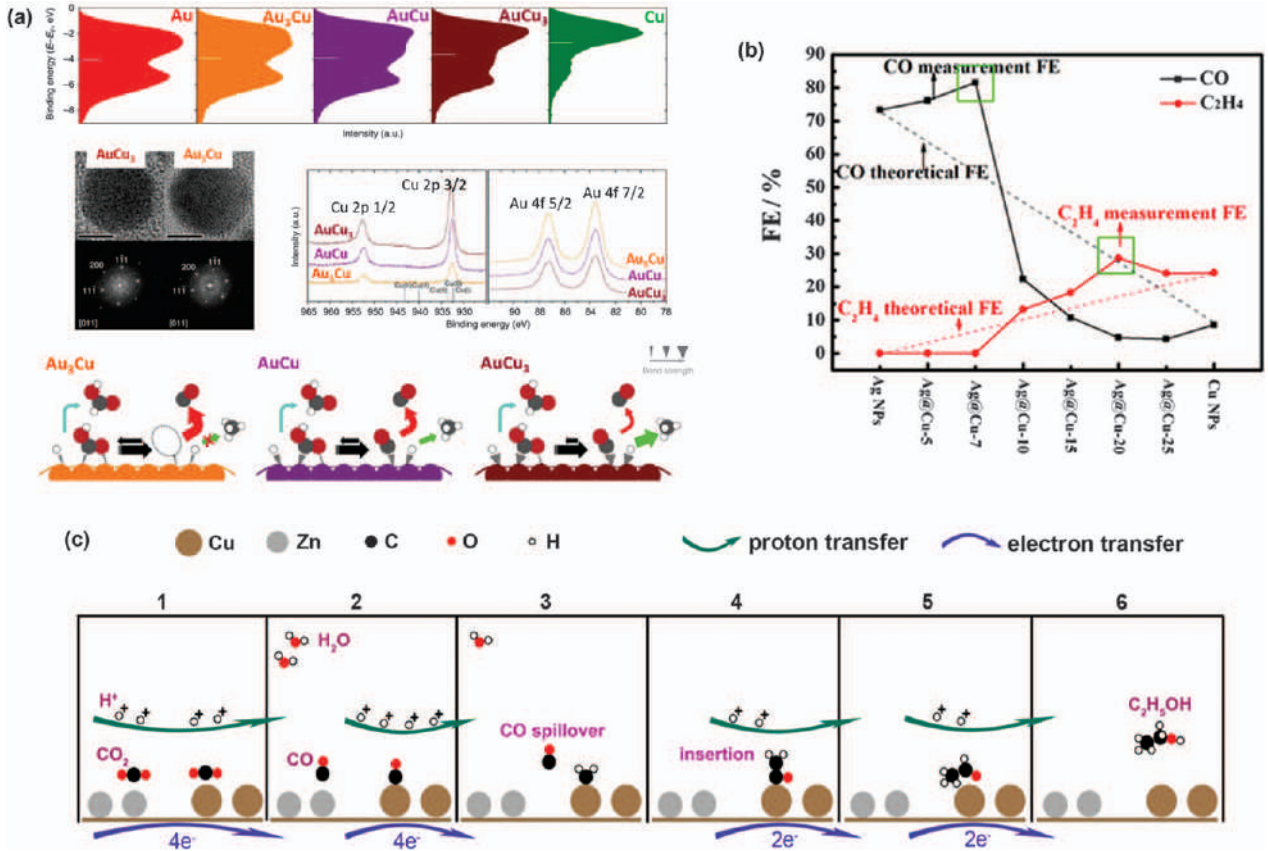

Figure 4.20 (a) Influence of variation in the Cu/Au ratio on the surface valence band. Reproduced from ref. 117 with permission from Springer Nature, Copyright 2014. (b) Change in CO2RR selectivity with increasing Cu overlayer thickness on Ag particles. Reproduced from ref. 94 with permission from American Chemical Society, Copyright 2017. (c) Proposed "CO-spillover" mechanism for a Cu/Zn system. Reproduced from ref. 118 with permission from American Chemical Society, Copyright 2016.

stabilizing the COOH* intermediate by simultaneously binding the C-end through an Au-atom and the O-end through a neighboring Cu-atom.[117] This result is similar to what Christophe *et al.* observed earlier, even though they suggested weaker CO* binding to be the cause of the improvement, highlighting the importance of geometric arrangements.

Clear analogies with the Cu–Au system are apparent in the Ag–Cu system, as well. Chang *et al.* synthesized particles composed of Cu overlayers of varying thickness on a Ag core. They could observe an increased CO production for Ag-rich NPs and an enhanced ethylene formation for Cu-rich NPs compared with the monometallic cases and claimed those ''synergistic'' effects to originate in the geometric distribution. A stronger CO binding caused by Cu-lattice expansion on the Ag substrate is suggested to enhance the ethylene formation, while the presence of oxygen-affine metals such as Cu is believed to stabilize COOH*, favoring CO formation in the Ag-rich case (Figure 4.20b).[94] In contrast, Bell and co-workers studied an Ag/Cu alloy, which showed surface-enrichment in Cu under applied electrode potential. Here, the resulting Cu-rich surface was proposed to be compressively strained, lowering the binding of H* and O*. An observed increase in the formation of oxygenated products at the expense of hydrogen and hydrocarbons was suggested to be the result of reduced amounts of adsorbed H*, limiting the cleavage of the C–O bond.[119] It is noteworthy that some studies are proposing a remarkable effect of alloying, suggesting a two-site mechanism in which one metal, as in Zn or Ag, is producing CO, which can be further reduced at neighboring Cu sites.[93,118] In the case of Ag, Hoang *et al.* deposited Cu/Ag wires on a carbon paper substrate. While X-ray absorption (extended X-ray absorption fine structure) results were suggesting an alloy formation, the relatively low content of 6% Ag showed a robust beneficial effect for ethylene selectivity, achieving almost 60%. They claimed this enhanced ethylene selectivity originates from Ag stabilizing the Cu_2O phase, as well as from Ag acting as a CO source, which can locally enhance the reactant concentration.[93]

Most studies on the Cu–Zn catalyst system report a high selectivity for $2e^-$ transfer products such as CO. After alloying with Cu, a ''two-sites'' catalyst was claimed to form, where the Zn site served as a CO producer and adjacent Cu site for further reduction.[94–96] Ren *et al.* electrodeposited Cu/Zn films and produced ethanol with a faradaic efficiency up to 29%. This exceptional selectivity for ethanol was suggested to originate from a spillover of CO from Zn sites onto Cu sites (Figure 4.20c). However, no similar observations were made in other studied Zn/Cu systems, suggesting that the geometric arrangement of the active Zn and Cu sites is of utmost importance for such effect.[118]

4.5 Activity Comparison

Throughout Sections 4.3 and 4.4, we grouped the nanostructured catalysts into two categories, monometallic-based and bimetallic-based catalysts, and mainly focused on the mechanistic aspect to improve their selectivity toward carbon-based products. Their improved activities, however, are expressed by normalizing with a geometric surface area of the applied electrodes, which is

primarily contributed by the roughness factor (increased exposed area) of the nanocatalysts. This, to some extent, makes difficulties in knowing the intrinsic activity of these nanostructured catalysts.

The CO_2RR current densities of a large number of nanostructured catalysts were plotted by Nitopi in a review paper (see Figure 4.21), to do a direct comparison of the catalytic activity of these candidates.[139] In Figure 4.21a, the geometric electrode area normalized CO_2RR current densities are presented, while the data of polycrystalline Cu by Kuhl[9] and Hori[34] are utilized as the reference. In this panel, all nanostructured materials exhibit enhanced geometric activity in the given potential window compared with the traditional polycrystal metal electrodes. However, once these current densities are normalized by the electrochemical surface area (ECSA), only a little or almost no difference appears in terms of intrinsic activity (Figure 4.21c).

The Geo- and ECSA-normalized current densities for CO evolution of various Cu-derived bimetallic catalysts are shown in Figure 4.21b and d, respectively. The same polycrystal Cu[9] and Au[129] electrodes are utilized as the control samples in this comparison. In Figure 4.21b, we can see that the OD-Au[130] outperforms all Cu-derived counterparts, while the pure Cu candidates[9,104,124,138] contribute much less faradaic activity for CO formation. This should be attributed to the further reduction of CO toward ''beyond CO'' products. We further turn to Figure 4.21d, the ECSA-normalized CO activity. The pure Au[129] still leads in this selected benchmark, showing a similar turnover frequency as the OD-Au[130] based on the active surface area.

4.6 Summary and Outlook

This chapter covers the recent progress on nanostructured metallic electrocatalysts for CO_2 reduction from the theoretical aspect to nanomaterials performance. We demonstrated how to select rational control over the material and structure of metallic nanocatalysts. This method can be used to tune the (geometric and/or gravimetric) activity and selectivity for the emerging electrochemical CO_2 conversion processes.

In light of the theoretical fundamentals, the binding energies toward key intermediates during eCO_2RR are presented, *i.e.* H*, COOH*, and CO*. However, only the later transition metals such as Au, Ag, Cu and some p-block metals, *etc.* are CO_2RR selective due to weak H* interaction. Additionally, nanoarchitecture electrocatalysts containing Au, Ag, and Cu are presented. Unsurprisingly, most of these nanostructured metallic catalysts exhibited enhanced activity and/or selectivity toward CO_2RR. To address the insight behind this selectivity, we show that both the enlarged surface area of the nanocatalysts and the lower-coordinated metal atoms on nanostructured surfaces play crucial roles in boosting the CO_2 electrolysis. In other words, specific facets, as well as the metal atoms sitting on the edge or corner, react differently from those on enclosed surfaces. This is demonstrated by computational simulations and shows that the reaction barrier of CO_2RR can be lowered on these reactive sites. With regards to the

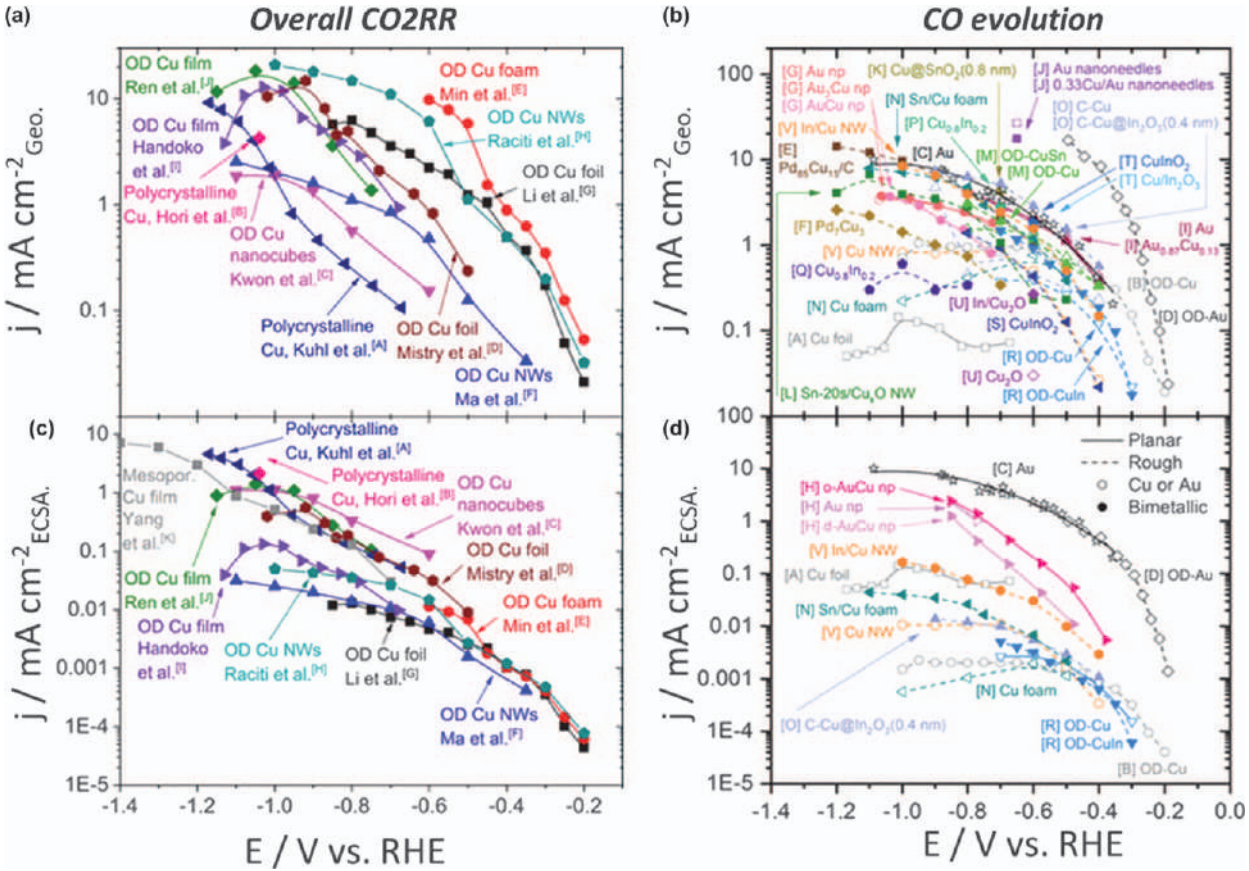
(a)
Overall CO2RR
j / mA cm-2Geo.
OD Cu film
Ren et al.[J]
OD Cu foam
Min et al.[E]
OD Cu NWs
Raciti et al.[H]
OD Cu film
Handoko
et al.[I]
OD Cu foil
Li et al.[G]
Polycrystalline
Cu, Hori et al.[B]
OD Cu
nanocubes
Kwon et al.[C]
Polycrystalline
Cu, Kuhl et al.[A]
OD Cu foil
Mistry et al.[D]
OD Cu NWs
Ma et al.[F]
(b)
CO evolution
j / mA cm-2Geo.
[G] Au np
[G] Au3Cu np
[G] AuCu np
[V] In/Cu NW
[E] Pd88Cu12/C
[K] Cu@SnO2(0.8 nm)
[J] Au nanoneedles
[J] 0.33Cu/Au nanoneedles
[N] Sn/Cu foam
[P] Cu0.8In0.2
[O] C-Cu
[O] C-Cu@In2O3(0.4 nm)
[C] Au
[M] OD-CuSn
[M] OD-Cu
[T] CuInO2
[T] Cu/In2O3
[F] Pd3Cu
[I] Au
[I] Au0.87Cu0.13
[V] Cu NW
[Q] Cu0.8In0.2
[B] OD-Cu
[N] Cu foam
[U] In/Cu2O
[S] CuInO2
[D] OD-Au
[A] Cu foil
[R] OD-Cu
[U] Cu2O
[R] OD-CuIn
[L] Sn-20s/Cu4O NW
(c)
j / mA cm-2ECSA.
Polycrystalline
Cu, Kuhl et al.[A]
Mesopor.
Cu film
Yang
et al.[K]
Polycrystalline
Cu, Hori et al.[B]
OD Cu
nanocubes
Kwon et al.[C]
OD Cu foil
Mistry et al.[D]
OD Cu film
Ren et al.[J]
OD Cu foam
Min et al.[E]
OD Cu film
Handoko
et al.[I]
OD Cu NWs
Raciti et al.[H]
OD Cu foil
Li et al.[G]
OD Cu NWs
Ma et al.[F]
(d)
j / mA cm-2ECSA.
Planar
Rough
Cu or Au
Bimetallic
[C] Au
[H] o-AuCu np
[H] Au np
[H] d-AuCu np
[V] In/Cu NW
[D] OD-Au
[A] Cu foil
[N] Sn/Cu foam
[V] Cu NW
[N] Cu foam
[O] C-Cu@In2O3(0.4 nm)
[R] OD-Cu
[R] OD-CuIn
[B] OD-Cu
E / V vs. RHE
E / V vs. RHE

commercial potential of nano electrocatalysts, nanostructuring could lower the material consumption (material-cost) and reduce the overpotential needed to achieve a larger scale (in terms of overall activity).

In comparison to the other metals, Cu based nanocatalysts are unique as they provide a broader product spectrum ''beyond CO''. Structure sensitivity of Cu facets has been studied and led to the discovery of the unique reactivity of (100) facets and the special (100)×(110) step which produces ethanol in comparison to other exposed facts.[25] However, due to the high complexity of the local condition where the CO_2RR occurs, other parameters such as the local pH (surface roughness effect)[81] and intermediate CO diffusion distance (resorption) should also be taken into account. All these could synergistically enhance the formation of multi-carbon hydrocarbons.

Cu-based alloys represent a diverse family bimetallic candidate for eCO_2RR, however, the structural stability (*e.g.* phase evolution, dealloying) of them as well as their influence on their catalytic reactivity has not been studied in detail. Although Cu is selective toward hydrocarbons and

Figure 4.21 Overview of eCO_2RR reactivity on various catalysts. (a) Geometric surface area normalized (geo-normalized) overall eCO_2RR current densities *vs.* potential. (b) Geo-normalized CO partial current densities *vs.* potential. The data were obtained from the following studies: [A] Kuhl *et al.*;[9] [B] Hori *et al.*;[34] [C] Kwon *et al.*;[120] [D] Mistry *et al.*;[63] [E] Min *et al.*;[121] [F] Ma *et al.*;[122,123] [G] Li *et al.*;[124] [H] Raciti *et al.*;[125] [I] Handoko *et al.*;[126] [J] Ren *et al.*;[127] [K] Yang *et al.*[128] Studies [A,B] are polycrystalline Cu, [C–J] are oxide-derived, nanostructured Cu and [K] is non-oxide-derived nanostructured Cu. (c) Electrochemical surface area normalized (ECSA-normalized) overall eCO_2RR current densities *vs.* potential. (d) ECSA-normalized CO partial current densities *vs.* potential. The data were obtained from the following studies: [A] Cu foil by Kuhl *et al.*;[9] [B] OD-Cu by Li *et al.*;[124] [C] Au by Hori *et al.*;[129] [D] OD-Au by Chen *et al.*;[130] [E] $Pd_{85}Cu_{15}$/C alloy NPs supported on carbon black by Yin *et al.*;[89] [F] Pd_7Cu_3 electrodeposited mesoporous films by Li *et al.*;[88] [G] AuCu, Au_3Cu, and Au NPs by Kim *et al.*;[117] [H] ordered (o-) and disordered (d-) AuCu NPs and Au NP control sample by Kim *et al.*;[114] [I] Au and $Au_{0.87}Cu_{0.13}$ prepared by pulsed laser deposition in 220 mTorr O_2 by Roy *et al.*;[131] [J] 33% Cu coverage on Au nanoneedles and Au nanoneedles by Ross *et al.*;[132] [K] Cu@SnO_2(0.8 nm) core–shell NPs by Li *et al.*;[106] [L] Sn deposited for 20 s on Cu_2O NWs by Zhao *et al.*;[133] [M] OD-CuSn and OD-Cu control sample by Sarfraz *et al.*;[108] [N] 2–3 at.% Sn on Cu10 foam (Sn/Cu foam) and Cu10 foam standard (Cu10 = 10 min electrodeposition) by Zeng *et al.*;[134] [O] Carbon-supported Cu@In_2O_3(0.4 nm) core-shell NPs and carbon-supported Cu NP control sample by Xie *et al.*;[135] [P] $Cu_{0.8}In_{0.2}$ by He *et al.*;[136] [Q] $Cu_{0.8}In_{0.2}$ by Hoffman *et al.*;[107] [R] OD-CuIn and OD-Cu control sample by Rasul *et al.*;[104] [S] $CuInO_2$-derived by Jedidi *et al.*;[104] [T] Cu/In_2O_3-derived and $CuInO_2$-derived by Larrazábal *et al.*;[105] [U] In dots microfabricated on Cu_2O substrate (In/Cu_2O) and Cu_2O control sample by Larrazábal *et al.*;[137] [V] In deposited on Cu NWs ($Cu(OH)_2$ derived) using 20 mM $InCl_3$ solution and Cu NWs control sample by Luo *et al.*[138]
Adapted from ref. 139, https://pubs.acs.org/doi/10.1021/acs.chemrev.8b00705, with permission from American Chemical Society, Copyright 2019.

oxygenates, the vast majority of Cu-based alloys in CO_2RR have been proven to favor chemical reduction products of two-electron transfer toward CO. This suggests that the chemisorption of CO intermediates on Cu sites is suppressed by the secondary metal atoms on the surface. Another challenge relates to the time stability of activity and selectivity. Faradaic efficiencies evolve over the first few hours of catalysis and, in most cases, the competing hydrogen evolution reaction outperforms the CO_2RR processed due to deposition of metal ion contaminants and/or evolution in the electrolyte which boosts hydrogen evolution.

To date, the majority of catalyst studies are performed in H-cells that suffer from massive CO_2 mass transport losses at the electrode interface. These mass transfer limitations are a barrier for projections to large-scale CO_2 electrolyzer performance. To overcome this issue, an up-scaled gas diffusion layer-based gas–liquid flow electrolyzer cell proved most suitable to test novel nanocatalysts under conditions relevant for commercial-scale electrochemical reactors.[49] The continuously circulated gas and liquid flow in electrolysis flow cell reactors diminish the mass transport limitations. Therefore, future investigations of new nanocatalysts, perhaps of all eCO_2RR catalysts, should focus on multilayer gas–liquid flow cells.

Acknowledgements

The research leading to these results has received funding from i) the European Union's Horizon 2020 research and innovation programme under grant agreement No 851441, ''SELECTCO2'', ii) the Carlsberg Foundation (Grant CF15-0165), iii) the Innovation Fund Denmark (Grand Solution Pro-ActivE 5124-00003A), and iv) the Deutsche Forschungsgemeinschaft (DFG, German Research Foundation) under Germany's Excellence Strategy – EXC 2008/1 (UniSysCat) – 390540038.

References

1. P. M. Cox, R. A. Betts, C. D. Jones, S. A. Spall and I. J. Totterdell, *Nature*, 2000, **408**, 184.
2. O. Hoegh-Guldberg, P. J. Mumby, A. J. Hooten, R. S. Steneck, P. Greenfield, E. Gomez, C. D. Harvell, P. F. Sale, A. J. Edwards, K. Caldeira, N. Knowlton, C. M. Eakin, R. Iglesias-Prieto, N. Muthiga, R. H. Bradbury, A. Dubi and M. E. Hatziolos, *Science*, 2007, **318**, 1737–1742.
3. Y. Hori, in *Modern Aspects of Electrochemistry*, ed. C. G. Vayenas, R. E. White and M. E. Gamboa-Aldeco, Springer New York, New York, NY, DOI: 10.1007/978-0-387-49489-0_3, 2008, pp. 89–189.
4. Z. P. Jovanov, H. A. Hansen, A. S. Varela, P. Malacrida, A. A. Peterson, J. K. Nørskov, I. E. L. Stephens and I. Chorkendorff, *J. Catal.*, 2016, **343**, 215–231.
5. Y. Hori, A. Murata and R. Takahashi, *J. Chem. Soc., Faraday Trans. 1*, 1989, **85**, 2309–2326.

6. E. E. Benson, C. P. Kubiak, A. J. Sathrum and J. M. Smieja, *Chem. Soc. Rev.*, 2009, **38**, 89–99.
7. J. Qiao, Y. Liu, F. Hong and J. Zhang, *Chem. Soc. Rev.*, 2014, **43**, 631–675.
8. M. Gattrell, N. Gupta and A. Co, *J. Electroanal. Chem.*, 2006, **594**, 1–19.
9. K. P. Kuhl, E. R. Cave, D. N. Abram and T. F. Jaramillo, *Energy Environ. Sci.*, 2012, **5**, 7050–7059.
10. C. W. Li, J. Ciston and M. W. Kanan, *Nature*, 2014, **508**, 504.
11. A. A. Peterson, F. Abild-Pedersen, F. Studt, J. Rossmeisl and J. K. Norskov, *Energy Environ. Sci.*, 2010, **3**, 1311–1315.
12. A. J. Medford, A. Vojvodic, J. S. Hummelshøj, J. Voss, F. Abild-Pedersen, F. Studt, T. Bligaard, A. Nilsson and J. K. Nørskov, *J. Catal.*, 2015, **328**, 36–42.
13. J. K. Nørskov, J. Rossmeisl, A. Logadottir, L. Lindqvist, J. R. Kitchin, T. Bligaard and H. Jónsson, *J. Phys. Chem. B*, 2004, **108**, 17886–17892.
14. R. Parsons, *Trans. Faraday Soc.*, 1958, **54**, 1053–1063.
15. F. Abild-Pedersen, J. Greeley, F. Studt, J. Rossmeisl, T. R. Munter, P. G. Moses, E. Skúlason, T. Bligaard and J. K. Nørskov, *Phys. Rev. Lett.*, 2007, **99**, 016105.
16. J. Rossmeisl, A. Logadottir and J. K. Nørskov, *Chem. Phys.*, 2005, **319**, 178–184.
17. M. T. M. Koper, *J. Electroanal. Chem.*, 2011, **660**, 254–260.
18. J. K. Nørskov, T. Bligaard, A. Logadottir, J. R. Kitchin, J. G. Chen, S. Pandelov and U. Stimming, *J. Electrochem. Soc.*, 2005, **152**, J23–J26.
19. I. C. Man, H.-Y. Su, F. Calle-Vallejo, H. A. Hansen, J. I. Martínez, N. G. Inoglu, J. Kitchin, T. F. Jaramillo, J. K. Nørskov and J. Rossmeisl, *ChemCatChem*, 2011, **3**, 1159–1165.
20. B. Hammer and J. K. Norskov, *Nature*, 1995, **376**, 238–240.
21. S. Dahl, A. Logadottir, R. C. Egeberg, J. H. Larsen, I. Chorkendorff, E. Törnqvist and J. K. Nørskov, *Phys. Rev. Lett.*, 1999, **83**, 1814–1817.
22. K. D. Jensen, J. Tymoczko, J. Rossmeisl, A. S. Bandarenka, I. Chorkendorff, M. Escudero-Escribano and I. E. L. Stephens, *Angew. Chem., Int. Ed.*, 2018, **57**, 2800–2805.
23. A. Bagger, W. Ju, S. Varela Ana, P. Strasser and J. Rossmeisl, *ChemPhysChem*, 2017, **18**, 3266–3273.
24. Y. Hori, I. Takahashi, O. Koga and N. Hoshi, *J. Mol. Catal. A: Chem.*, 2003, **199**, 39–47.
25. A. Bagger, L. Arnarson, M. H. Hansen, E. Spohr and J. Rossmeisl, *J. Am. Chem. Soc.*, 2019, **141**, 1506–1514.
26. F. Calle-Vallejo and M. T. M. Koper, *Angew. Chem., Int. Ed.*, 2013, **52**, 7282–7285.
27. K. J. P. Schouten, Z. Qin, E. Pérez Gallent and M. T. M. Koper, *J. Am. Chem. Soc.*, 2012, **134**, 9864–9867.
28. J. H. Montoya, C. Shi, K. Chan and J. K. Nørskov, *J. Phys. Chem. Lett.*, 2015, **6**, 2032–2037.
29. J. Hussain, H. Jónsson and E. Skúlason, *ACS Catal.*, 2018, **8**, 5240–5249.
30. S. Hedström, E. C. dos Santos, C. Liu, K. Chan, F. Abild-Pedersen and L. G. M. Pettersson, *J. Phys. Chem. C*, 2018, **122**, 12251–12258.

31. X. Nie, W. Luo, M. J. Janik and A. Asthagiri, *J. Catal.*, 2014, **312**, 108–122.
32. C. Shi, K. Chan, J. S. Yoo and J. K. Nørskov, *Org. Process Res. Dev.*, 2016, **20**, 1424–1430.
33. T. Ludwig, J. A. Gauthier, K. S. Brown, S. Ringe, J. K. Nørskov and K. Chan, *J. Phys. Chem. C*, 2019, **123**, 5999–6009.
34. Y. Hori, H. Wakebe, T. Tsukamoto and O. Koga, *Electrochim. Acta*, 1994, **39**, 1833–1839.
35. A. A. Peterson and J. K. Nørskov, *J. Phys. Chem. Lett.*, 2012, **3**, 251–258.
36. A. Bagger, W. Ju, A. S. Varela, P. Strasser and J. Rossmeisl, *ACS Catal.*, 2019, 7894–7899.
37. I. Ledezma-Yanez, E. P. Gallent, M. T. M. Koper and F. Calle-Vallejo, *Catal. Today*, 2016, **262**, 90–94.
38. E. Bertheussen, A. Verdaguer-Casadevall, D. Ravasio, J. H. Montoya, D. B. Trimarco, C. Roy, S. Meier, J. Wendland, J. K. Nørskov, I. E. L. Stephens and I. Chorkendorff, *Angew. Chem., Int. Ed.*, 2016, **55**, 1450–1454.
39. Y. Lum and J. W. Ager, *Nat. Catal.*, 2019, **2**, 86–93.
40. Q. Lu, J. Rosen and F. Jiao, *ChemCatChem*, 2015, **7**, 38–47.
41. M. E. Dry, *J. Appl. Chem. Biotechnol.*, 2002, **77**, 43–50.
42. T. Hatsukade, K. P. Kuhl, E. R. Cave, D. N. Abram and T. F. Jaramillo, *Phys. Chem. Chem. Phys.*, 2014, **16**, 13814–13819.
43. B. A. Rosen, A. Salehi-Khojin, M. R. Thorson, W. Zhu, D. T. Whipple, P. J. A. Kenis and R. I. Masel, *Science*, 2011, **334**, 643–644.
44. A. S. Varela, N. Ranjbar Sahraie, J. Steinberg, W. Ju, H.-S. Oh and P. Strasser, *Angew. Chem., Int. Ed.*, 2015, **54**, 10758–10762.
45. W. Zhu, R. Michalsky, Ö. Metin, H. Lv, S. Guo, C. J. Wright, X. Sun, A. A. Peterson and S. Sun, *J. Am. Chem. Soc.*, 2013, **135**, 16833–16836.
46. W. Zhu, Y.-J. Zhang, H. Zhang, H. Lv, Q. Li, R. Michalsky, A. A. Peterson and S. Sun, *J. Am. Chem. Soc.*, 2014, **136**, 16132–16135.
47. E. B. Nursanto, H. S. Jeon, C. Kim, M. S. Jee, J. H. Koh, Y. J. Hwang and B. K. Min, *Catal. Today*, 2016, **260**, 107–111.
48. W. Ju, A. Bagger, G.-P. Hao, A. S. Varela, I. Sinev, V. Bon, B. Roldan Cuenya, S. Kaskel, J. Rossmeisl and P. Strasser, *Nat. Commun.*, 2017, **8**, 944.
49. T. Möller, W. Ju, A. Bagger, X. Wang, F. Luo, T. Ngo Thanh, A. S. Varela, J. Rossmeisl and P. Strasser, *Energy Environ. Sci.*, 2019, DOI: 10.1039/C8EE02662A.
50. H. Mistry, R. Reske, Z. Zeng, Z.-J. Zhao, J. Greeley, P. Strasser and B. R. Cuenya, *J. Am. Chem. Soc.*, 2014, **136**, 16473–16476.
51. H. Yoshio, K. Katsuhei and S. Shin, *Chem. Lett.*, 1985, **14**, 1695–1698.
52. C.-T. Dinh, F. P. García de Arquer, D. Sinton and E. H. Sargent, *ACS Energy Lett.*, 2018, **3**, 2835–2840.
53. T. Haas, R. Krause, R. Weber, M. Demler and G. Schmid, *Nat. Catal.*, 2018, **1**, 32–39.
54. Q. Lu, J. Rosen, Y. Zhou, G. S. Hutchings, Y. C. Kimmel, J. G. Chen and F. Jiao, *Nat. Commun.*, 2014, **5**, 3242.

55. J. Rosen, G. S. Hutchings, Q. Lu, S. Rivera, Y. Zhou, D. G. Vlachos and F. Jiao, *ACS Catal.*, 2015, **5**, 4293–4299.
56. C. Kim, H. S. Jeon, T. Eom, M. S. Jee, H. Kim, C. M. Friend, B. K. Min and Y. J. Hwang, *J. Am. Chem. Soc.*, 2015, **137**, 13844–13850.
57. C. Kim, T. Eom, M. S. Jee, H. Jung, H. Kim, B. K. Min and Y. J. Hwang, *ACS Catal.*, 2017, **7**, 779–785.
58. H. Mistry, A. S. Varela, S. Kühl, P. Strasser and B. R. Cuenya, *Nat. Rev. Mater.*, 2016, **1**, 16009.
59. C.-T. Dinh, T. Burdyny, M. G. Kibria, A. Seifitokaldani, C. M. Gabardo, F. P. García de Arquer, A. Kiani, J. P. Edwards, P. De Luna, O. S. Bushuyev, C. Zou, R. Quintero-Bermudez, Y. Pang, D. Sinton and E. H. Sargent, *Science*, 2018, **360**, 783–787.
60. T.-T. Zhuang, Y. Pang, Z.-Q. Liang, Z. Wang, Y. Li, C.-S. Tan, J. Li, C. T. Dinh, P. De Luna, P.-L. Hsieh, T. Burdyny, H.-H. Li, M. Liu, Y. Wang, F. Li, A. Proppe, A. Johnston, D.-H. Nam, Z.-Y. Wu, Y.-R. Zheng, A. H. Ip, H. Tan, L.-J. Chen, S.-H. Yu, S. O. Kelley, D. Sinton and E. H. Sargent, *Nat. Catal.*, 2018, **1**, 946–951.
61. Y. Pang, J. Li, Z. Wang, C.-S. Tan, P.-L. Hsieh, T.-T. Zhuang, Z.-Q. Liang, C. Zou, X. Wang, P. De Luna, J. P. Edwards, Y. Xu, F. Li, C.-T. Dinh, M. Zhong, Y. Lou, D. Wu, L.-J. Chen, E. H. Sargent and D. Sinton, *Nat. Catal.*, 2019, **2**, 251–258.
62. A. S. Varela, M. Kroschel, T. Reier and P. Strasser, *Catal. Today*, 2016, **260**, 8–13.
63. H. Mistry, A. S. Varela, C. S. Bonifacio, I. Zegkinoglou, I. Sinev, Y.-W. Choi, K. Kisslinger, E. A. Stach, J. C. Yang, P. Strasser and B. R. Cuenya, *Nat. Commun.*, 2016, **7**, 12123.
64. S. A. Akhade, W. Luo, X. Nie, N. J. Bernstein, A. Asthagiri and M. J. Janik, *Phys. Chem. Chem. Phys.*, 2014, **16**, 20429–20435.
65. K. Manthiram, B. J. Beberwyck and A. P. Alivisatos, *J. Am. Chem. Soc.*, 2014, **136**, 13319–13325.
66. O. A. Baturina, Q. Lu, M. A. Padilla, L. Xin, W. Li, A. Serov, K. Artyushkova, P. Atanassov, F. Xu, A. Epshteyn, T. Brintlinger, M. Schuette and G. E. Collins, *ACS Catal.*, 2014, **4**, 3682–3695.
67. R. Reske, H. Mistry, F. Behafarid, B. Roldan Cuenya and P. Strasser, *J. Am. Chem. Soc.*, 2014, **136**, 6978–6986.
68. Y. Hori, I. Takahashi, O. Koga and N. Hoshi, *J. Phys. Chem. B*, 2002, **106**, 15–17.
69. W. J. Durand, A. A. Peterson, F. Studt, F. Abild-Pedersen and J. K. Nørskov, *Surf. Sci.*, 2011, **605**, 1354–1359.
70. K. J. P. Schouten, Y. Kwon, C. J. M. van der Ham, Z. Qin and M. T. M. Koper, *Chem. Sci.*, 2011, **2**, 1902–1909.
71. X. Nie, M. R. Esopi, M. J. Janik and A. Asthagiri, *Angew. Chem., Int. Ed.*, 2013, **52**, 2459–2462.
72. C. S. Chen, A. D. Handoko, J. H. Wan, L. Ma, D. Ren and B. S. Yeo, *Catal. Sci. Technol.*, 2015, **5**, 161–168.

73. G. Mangione, J. Huang, R. Buonsanti and C. Corminboeuf, *J. Phys. Chem. Lett.*, 2019, **10**, 4259–4265.
74. F. S. Roberts, K. P. Kuhl and A. Nilsson, *Angew. Chem., Int. Ed.*, 2015, **54**, 5179–5182.
75. A. Loiudice, P. Lobaccaro, E. A. Kamali, T. Thao, B. H. Huang, J. W. Ager and R. Buonsanti, *Angew. Chem., Int. Ed.*, 2016, **55**, 5789–5792.
76. X. Wang, A. S. Varela, A. Bergmann, S. Kühl and P. Strasser, *ChemSusChem*, 2017, **10**, 4642–4649.
77. M. Schreier, Y. Yoon, M. N. Jackson and Y. Surendranath, *Angew. Chem., Int. Ed.*, 2018, **57**, 10221–10225.
78. Y. Hori, R. Takahashi, Y. Yoshinami and A. Murata, *J. Phys. Chem. B*, 1997, **101**, 7075–7081.
79. M. T. M. Koper, *Chem. Sci.*, 2013, **4**, 2710–2723.
80. N. Gupta, M. Gattrell and B. MacDougall, *J. Appl. Electrochem.*, 2006, **36**, 161–172.
81. W. Tang, A. A. Peterson, A. S. Varela, Z. P. Jovanov, L. Bech, W. J. Durand, S. Dahl, J. K. Nørskov and I. Chorkendorff, *Phys. Chem. Chem. Phys.*, 2012, **14**, 76–81.
82. Y. E. Seidel, A. Schneider, Z. Jusys, B. Wickman, B. Kasemo and R. J. Behm, *Faraday Discuss.*, 2009, **140**, 167–184.
83. L. K. Ono and B. Roldán-Cuenya, *Catal. Lett.*, 2007, **113**, 86–94.
84. H. Mistry, F. Behafarid, R. Reske, A. S. Varela, P. Strasser and B. Roldan Cuenya, *ACS Catal.*, 2016, **6**, 1075–1080.
85. X. Wang, J. F. de Araújo, W. Ju, A. Bagger, H. Schmies, S. Kühl, J. Rossmeisl and P. Strasser, *Nat. Nanotechnol.*, 2019, **14**, 1063–1070.
86. C. Kim, F. Dionigi, V. Beermann, X. Wang, T. Möller and P. Strasser, *Adv. Mater.*, 2018, 1805617.
87. W. Ju, A. Bagger, X. Wang, Y. Tsai, F. Luo, T. Möller, H. Wang, J. Rossmeisl, A. S. Varela and P. Strasser, *ACS Energy Lett.*, 2019, **4**, 1663–1671.
88. M. Li, J. Wang, P. Li, K. Chang, C. Li, T. Wang, B. Jiang, H. Zhang, H. Liu, Y. Yamauchi and N. Umezawa, *J. Mater. Chem. A*, 2016, **4**, 4776–4782.
89. Z. Yin, D. Gao, S. Yao, B. Zhao, F. Cai, L. Lin, P. Tang, P. Zhai, G. Wang, D. Ma and X. Bao, *Nano Energy*, 2016, **27**, 35–43.
90. W. Zhu, L. Zhang, P. Yang, X. Chang, H. Dong, A. Li, C. Hu, Z. Huang, Z. J. Zhao and J. Gong, *Small*, 2018, **14**, 1703314.
91. D. Chen, Q. Yao, P. Cui, H. Liu, J. Xie and J. Yang, *ACS Appl. Energy Mater.*, 2018, **1**, 883–890.
92. S. Ma, M. Sadakiyo, M. Heima, R. Luo, R. T. Haasch, J. I. Gold, M. Yamauchi and P. J. Kenis, *J. Am. Chem. Soc.*, 2017, **139**, 47–50.
93. T. T. H. Hoang, S. Verma, S. Ma, T. T. Fister, J. Timoshenko, A. I. Frenkel, P. J. A. Kenis and A. A. Gewirth, *J. Am. Chem. Soc.*, 2018, **140**, 5791–5797.
94. Z. Chang, S. Huo, W. Zhang, J. Fang and H. Wang, *J. Phys. Chem. C*, 2017, **121**, 11368–11379.

95. G. Yin, H. Abe, R. Kodiyath, S. Ueda, N. Srinivasan, A. Yamaguchi and M. Miyauchi, *J. Mater. Chem. A*, 2017, **5**, 12113–12119.
96. A. Roy, D. Hursán, K. Artyushkova, P. Atanassov, C. Janáky and A. Serov, *Appl. Catal., B*, 2018, **232**, 512–520.
97. H.-P. Yang, S. Qin, H. Wang and J.-X. Lu, *Green Chem.*, 2015, **17**, 5144–5148.
98. X. Liu, L. Zhu, H. Wang, G. He and Z. Bian, *RSC Adv.*, 2016, **6**, 38380–38387.
99. H.-P. Yang, S. Qin, Y.-N. Yue, L. Liu, H. Wang and J.-X. Lu, *Catal. Sci. Technol.*, 2016, **6**, 6490–6494.
100. A. S. Varela, C. Schlaup, Z. P. Jovanov, P. Malacrida, S. Horch, I. E. L. Stephens and I. Chorkendorff, *J. Phys. Chem. C*, 2013, **117**, 20500–20508.
101. X. Guo, Y. Zhang, C. Deng, X. Li, Y. Xue, Y.-M. Yan and K. Sun, *Chem. Commun.*, 2015, **51**, 1345–1348.
102. C. Kim, T. Möller, J. Schmidt, A. Thomas and P. Strasser, *ACS Catal.*, 2019, **9**, 1482–1488.
103. S. Rasul, D. H. Anjum, A. Jedidi, Y. Minenkov, L. Cavallo and K. Takanabe, *Angew. Chem., Int. Ed.*, 2015, **54**, 2146–2150.
104. A. Jedidi, S. Rasul, D. Masih, L. Cavallo and K. Takanabe, *J. Mater. Chem. A*, 2015, **3**, 19085–19092.
105. G. O. Larrazábal, A. J. Martín, S. Mitchell, R. Hauert and J. Pérez-Ramírez, *ACS Catal.*, 2016, **6**, 6265–6274.
106. Q. Li, J. Fu, W. Zhu, Z. Chen, B. Shen, L. Wu, Z. Xi, T. Wang, G. Lu, J.-J. Zhu and S. Sun, *J. Am. Chem. Soc.*, 2017, **139**, 4290–4293.
107. Z. B. Hoffman, T. S. Gray, K. B. Moraveck, T. B. Gunnoe and G. Zangari, *ACS Catal.*, 2017, **7**, 5381–5390.
108. S. Sarfraz, A. T. Garcia-Esparza, A. Jedidi, L. Cavallo and K. Takanabe, *ACS Catal.*, 2016, **6**, 2842–2851.
109. J. Christophe, T. Doneux and C. Buess-Herman, *Electrocatalysis*, 2012, **3**, 139–146.
110. F. Jia, X. Yu and L. Zhang, *J. Power Sources*, 2014, **252**, 85–89.
111. G. Kyriacou and A. Anagnostopulos, *J. Electroanal. Chem.*, 1992, **328**, 233–243.
112. D. Friebel, F. Mbuga, S. Rajasekaran, D. J. Miller, H. Ogasawara, R. Alonso-Mori, D. Sokaras, D. Nordlund, T.-C. Weng and A. Nilsson, *J. Phys. Chem. C*, 2014, **118**, 7954–7961.
113. S. Lysgaard, J. S. Myrdal, H. A. Hansen and T. Vegge, *Phys. Chem. Chem. Phys.*, 2015, **17**, 28270–28276.
114. D. Kim, C. Xie, N. Becknell, Y. Yu, M. Karamad, K. Chan, E. J. Crumlin, J. K. Nørskov and P. Yang, *J. Am. Chem. Soc.*, 2017, **139**, 8329–8336.
115. H. Mistry, R. Reske, P. Strasser and B. Roldan Cuenya, *Catal. Today*, 2017, **288**, 30–36.
116. J. Monzó, Y. Malewski, R. Kortlever, F. J. Vidal-Iglesias, J. Solla-Gullón, M. T. M. Koper and P. Rodriguez, *J. Mater. Chem. A*, 2015, **3**, 23690–23698.
117. D. Kim, J. Resasco, Y. Yu, A. M. Asiri and P. Yang, *Nat. Commun.*, 2014, **5**, 4948.

118. D. Ren, B. S.-H. Ang and B. S. Yeo, *ACS Catal.*, 2016, **6**, 8239–8247.
119. E. L. Clark, C. Hahn, T. F. Jaramillo and A. T. Bell, *J. Am. Chem. Soc.*, 2017, **139**, 15848–15857.
120. Y. Kwon, Y. Lum, E. L. Clark, J. W. Ager and A. T. Bell, *ChemElectroChem*, 2016, **3**, 1012–1019.
121. S. Min, X. Yang, A.-Y. Lu, C.-C. Tseng, M. N. Hedhili, L.-J. Li and K.-W. Huang, *Nano Energy*, 2016, **27**, 121–129.
122. M. Ma, K. Djanashvili and W. A. Smith, *Angew. Chem., Int. Ed.*, 2016, **55**, 6680–6684.
123. M. Ma, K. Djanashvili and W. A. Smith, *Phys. Chem. Chem. Phys.*, 2015, **17**, 20861–20867.
124. C. W. Li and M. W. Kanan, *J. Am. Chem. Soc.*, 2012, **134**, 7231–7234.
125. D. Raciti, K. J. Livi and C. Wang, *Nano Lett.*, 2015, **15**, 6829–6835.
126. A. D. Handoko, C. W. Ong, Y. Huang, Z. G. Lee, L. Lin, G. B. Panetti and B. S. Yeo, *J. Phys. Chem. C*, 2016, **120**, 20058–20067.
127. D. Ren, N. T. Wong, A. D. Handoko, Y. Huang and B. S. Yeo, *J. Phys. Chem. Lett.*, 2016, **7**, 20–24.
128. K. D. Yang, W. R. Ko, J. H. Lee, S. J. Kim, H. Lee, M. H. Lee and K. T. Nam, *Angew. Chem., Int. Ed.*, 2017, **56**, 796–800.
129. Y. Hori, A. Murata, K. Kikuchi and S. Suzuki, *J. Chem. Soc., Chem. Commun.*, 1987, 728–729.
130. Y. Chen, C. W. Li and M. W. Kanan, *J. Am. Chem. Soc.*, 2012, **134**, 19969–19972.
131. C. Roy, J. Galipaud, L. Fréchette-Viens, S. Garbarino, J. Qiao and D. Guay, *Electrochim. Acta*, 2017, **246**, 115–122.
132. M. B. Ross, C. T. Dinh, Y. Li, D. Kim, P. De Luna, E. H. Sargent and P. Yang, *J. Am. Chem. Soc.*, 2017, **139**, 9359–9363.
133. Y. Zhao, C. Wang and G. G. Wallace, *J. Mater. Chem. A*, 2016, **4**, 10710–10718.
134. J. Zeng, K. Bejtka, W. Ju, M. Castellino, A. Chiodoni, A. Sacco, M. A. Farkhondehfal, S. Hernández, D. Rentsch, C. Battaglia and C. F. Pirri, *Appl. Catal., B*, 2018, **236**, 475–482.
135. H. Xie, S. Chen, F. Ma, J. Liang, Z. Miao, T. Wang, H.-L. Wang, Y. Huang and Q. Li, *ACS Appl. Mater. Interfaces*, 2018, **10**, 36996–37004.
136. J. He, K. E. Dettelbach, D. A. Salvatore, T. Li and C. P. Berlinguette, *Angew. Chem., Int. Ed.*, 2017, **56**, 6068–6072.
137. G. O. Larrazábal, T. Shinagawa, A. J. Martín and J. Pérez-Ramírez, *Nat. Commun.*, 2018, **9**, 1477.
138. W. Luo, W. Xie, R. Mutschler, E. Oveisi, G. L. De Gregorio, R. Buonsanti and A. Züttel, *ACS Catal.*, 2018, **8**, 6571–6581.
139. S. Nitopi, E. Bertheussen, S. B. Scott, X. Liu, A. K. Engstfeld, S. Horch, B. Seger, I. E. L. Stephens, K. Chan, C. Hahn, J. K. Nørskov, T. F. Jaramillo and I. Chorkendorff, *Chem. Rev.*, 2019, **119**, 7610–7672.

CHAPTER 5

Theoretical Approach to Homogeneous Catalytic Reduction of CO_2: Mechanistic Understanding to Build New Catalysts

L. ROY,[a] B. MONDAL,[b] F. NEESE[c] AND S. YE*[c,d]

[a] Institute of Chemical Technology Mumbai – IOC Odisha Campus Bhubaneswar, IIT Kharagpur Extension Centre, Bhubaneswar 751013, India; [b] School of Basic Sciences, Indian Institute of Technology Mandi, Kamand, Himachal Pradesh 175005, India; [c] Max Planck Institute for Coal Research, Kaiser Wilhelm Platz 1, Mülheim an der Ruhr 45470, Germany; [d] State Key Laboratory of Catalysis, Dalian Institute of Chemical Physics, Chinese Academy of Sciences, 457 Zhongshan Road, Dalian 116023, China
*Emails: shengfa.ye@kofo.mpg.de; shengfa.ye@dicp.ac.cn

5.1 Introduction

The extensive increase in fossil fuel depletion coupled with the rise in atmospheric CO_2 levels is alarming environmental concerns which have potentially huge impacts on climate change and the rise in ocean levels.[1,2] On one hand, CO_2, one of the key products of combustion of fossil fuel, is a major contributor to the greenhouse effect. On the other hand, CO_2 is also a source of value-added fine chemicals, in particular for fuels such as formic acid, methanol and/or for

Energy and Environment Series No. 28
Carbon Dioxide Electrochemistry: Homogeneous and Heterogeneous Catalysis
Edited by Marc Robert, Cyrille Costentin and Kim Daasbjerg

Published by the Royal Society of Chemistry, www.rsc.org

precursors such as CO or C1 source to produce industrial chemicals.[3–5] Hence, it is highly desirable to develop practical technologies, through which CO_2 can be first captured and then activated and functionalized by using artificial photosynthesis, electrochemical reduction, hydrogenation, and biochemical approaches.[1] However, the high stability and inertness of CO_2 hinder its effective reduction and instigates the design and development of appropriate catalysts. In this regard, nature has developed a range of efficient pathways to accomplish CO_2 functionalization under ambient conditions. A series of enzymes have been evolved to catalyse the breaking of the C–O bonds of CO_2 and making new C–H or C–C bonds.[1,6] Relevant examples include Ni–Fe carbon monoxide dehydrogenase (CODH) which interconverts CO_2 to CO, NADH-dependent formate dehydrogenase (FDH) which directly transfers one hydride from NADH to the C atom of CO_2, remodeled nitrogenase FeMo-cofactor which affects the eight electron reduction of CO_2 to methane, carbonic anhydrase (CA) which converts CO_2 to HCO_3^- or minerals, and decarboxylases which carries out *in vitro* biocatalytic carboxylation of epoxides, aromatics, heteroaromatics, and aliphatic compounds.[1,6] Inspired by the principles used in nature, significant scientific effort has been channelized to develop homogeneous and heterogeneous catalysts working under benign conditions for CO_2 transformations.[7] In this regard, the last few decades have witnessed fervent attempts to elucidate reaction mechanisms, in general, from both experimental and theoretical perspective to gain a better understanding of each elementary step.[6] In particular, quantum chemical calculations have been extensively used in this regard and indeed provide in-depth insights into mechanistic details, thus broadening the information on catalytic processes.[8–10] The development of large computer clusters and reliable accurate theories have united computational predictions with experimental observations in a timely manner. Along with experimental developments, computational studies have unveiled atomic-level mechanistic intricacies resulting from the change in the electronic structure of the system during chemical transformations. In fact, on the basis of detailed mechanistic understanding, several pioneering theoretical works have successfully proposed new ideas for the development of homogeneous and heterogeneous catalysts for CO_2 reduction, subjugating the traditional trial-and-error method.[11–15] Therefore, we believe that profound information and insights gained by computational studies can serve as a foundation for designing more efficient catalysts for CO_2 functionalization.[8]

5.1.1 Difficulty in CO_2 Reduction

CO_2, a linear 16 e^- molecule belonging to the $D_{\infty h}$ symmetry group, features very short C–O bond lengths (1.17 Å).[1] Furthermore, its central carbon possesses the highest oxidation state (+IV); hence, CO_2 is often the final product in many chemical and biological reactions. As a consequence, it is thermodynamically very stable and its functionalization requires high energy input. Although CO_2 is a non-polar molecule, the electronegativity

difference between C and O imparts a partial electrophilic character on the carbon centre and a weak nucleophilic character on the terminal oxygen atoms. The molecular orbitals of relevance to its reactivity are the LUMOs, the degenerate pair of antibonding $2\pi_u$ orbitals that are mainly localized on the central carbon atom with more than 60% weightage, and the doubly occupied $1\pi_g$ nonbonding HOMOs which have substantial parentage of the two oxygen atoms (Figure 5.1).[6] Hence, the basic oxygen atoms are the sites for electrophilic attack, while the acidic carbon centre is the site for nucleophilic attack. During CO_2 functionalization, one of the degenerate LUMOs is filled up by electrons, thus resulting in elongation of the C–O bonds and bending of the linear geometry. Note that $CO_2^{\bullet -}$ has an optimum O–C–O angle of 134°. Thus, CO_2 reduction involves significant geometric rearrangement as manifested by its exceedingly negative one-electron reduction potential (-1.90 V *vs.* normal hydrogen electrode (NHE)). As a result, CO_2 transformation often has to overcome a large barrier arising from this structural reorganization, leading to the significant kinetic inertness of CO_2. Taken together, CO_2 activation is a both thermodynamically and kinetically demanding process that must be achieved at a large energetic expense.[1,6]

Since a large energetic input is necessary for the one-electron reduction of CO_2, two- and multiple-electron reductions are more favorable.[7] At the same time, bi-functional activation with concerted nucleophilic and electrophilic

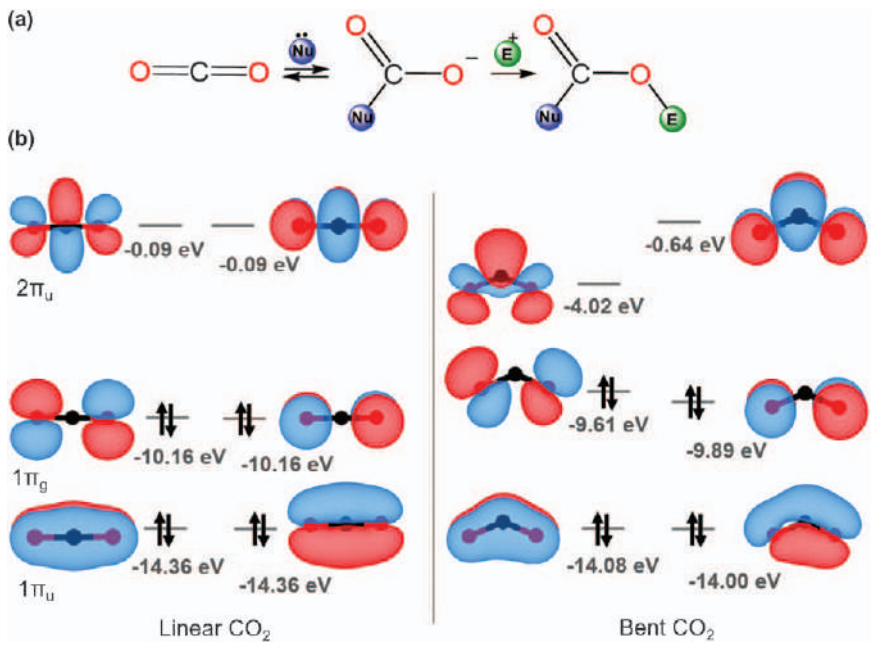

Figure 5.1 (a) Nucleophilic and electrophilic centres on CO_2. (b) Important π molecular orbitals of linear (OCO = 180°) and bent (OCO = 134°) CO_2 with corresponding orbital energies.
Reproduced from ref. 6 with permission from Elsevier, Copyright 2014.

attacks, such as proton-coupled electron transfer (PCET), is preferred. For instance, the potential for two-proton/two-electron reduction of CO_2 at neutral pH giving CO and H_2O is increased to -0.52 V *vs.* NHE. In this chapter, we present the different catalytic pathways for two-electron CO_2 reduction using homogeneous catalysts with active participation of protons (PCET) or electron-deficient metal centres (MCET, metal coupled electron transfer).

5.1.2 Present Status: Organo-catalysts and Transition Metal-based Homogeneous and Heterogeneous CO_2 Reduction

Utilization of CO_2 as a C1 building block in industrial chemical synthesis to create a renewable carbon economy is an alternative to sequestration and storage of CO_2.[16–18] Over the past few years, CO_2 has been used as a starting material for production of carbonates, polycarbonates, urea, salicylic acid, and urethanes on an industrial scale, due to its low cost, abundance, and non-toxicity.[19,20] Another approach is to convert CO_2 to formate or CO, which has promising scope for development.[21,22] In this regard, some success has recently been achieved with main-group element mediated CO_2 functionalization. One breakthrough research put forth by Stephan and co-workers demonstrated binding of CO_2 to a frustrated Lewis acid-base pair (FLP) resulting in subsequent stoichiometric conversion of CO_2 to methanol.[23] This has led to the discovery of a series of ambiphilic systems consisting of P/Al or P/B pairs for stoichiometric fixation of CO_2.[24,25] Zhang *et. al.* used N-heterocyclic carbene and silane as a hydrogen source to transform CO_2 into CH_3OH.[26] Furthermore, one study utilizes carbodiphosphoranes for the reduction of CO_2 to CO.[27] However, systematic investigations on the reactivity of CO_2 functionalization catalyzed by metal-free organo-catalysts remain scarce,[28,29] which hinders development of efficient catalytic techniques. Furthermore, in these reactions, formation of undesirable side products such as highly stable Lewis acid coordinated oxygen moieties is inevitable, which requires further work-up and largely precludes their large-scale application because of the high energy requirement.[23]

Electrochemical reduction of CO_2 by organic mediators has been less studied because organic compounds often form highly reactive species, thus promoting irrevocable reactions, inhibiting the catalytic cycle of CO_2 reduction.[7] To tackle this issue, stable organic radicals or anions are highly desired. Although Bocarsly and co-workers reported that pyridine facilitates reduction of CO_2 to methanol on Pd electrodes at -0.58 V *vs.* SCE,[30] later studies by Savéant *et al.* indicated divergent results of methanol formation on Pt electrodes which cast doubt on the reliability of the initial experiments by Bocarsly and others.[31] These contradictory results indicate that further investigations are needed to get a clear picture and rationalize all observations.[32] In general, development of metal-free systems for CO_2 reduction remains far from maturity and tremendous efforts are required to offer reliable clarifications.

Metal-based catalytic systems for CO_2 reduction are superior due to their high product selectivity and catalytic efficiency. Electrochemical reduction with both

homogeneous and heterogeneous systems has been intensively studied over the last decade. However, owing to the kinetic inertness of CO_2, large overpotentials are often required for such transformations. To date, several unconventional heterogeneous electrochemical catalysts have been discovered, which exhibit an impressive overall reaction rate and enhanced product yield, but very little knowledge about the reaction mechanism is known. Traditional catalysts in this field were primarily single-element metallic electrodes in polycrystalline forms.[33] Metals such as Pt, Ni, Fe, Al, Ga, and Ti have been tested for the CO_2 reduction reaction (CO_2RR) with CO being the major product.[33] However, the rate of the hydrogen evolution reaction (HER) on these metallic cathodes were typically higher than that of CO_2RR. This is because HER proceeds at a comparable thermodynamic potential (0 V *vs.* SHE = standard hydrogen electrode) but has a lower overpotential on most electrode surfaces.[34] Hence, efficient CO_2RR electrochemical catalysts should reduce the barrier as compared to HER, to promote selective reduction of CO_2 at a low overpotential.[35] Interestingly, Au, Ag, and Zn have been demonstrated to produce CO at a high current efficiency. Cathode surfaces were predicted to affect the rate of reaction and product selectivity by preferential binding to given intermediate species (*e.g.* CO) and changing the overall activation barrier. Sn, Pb, In, and Hg metal electrodes produce formate as the major product during CO_2RR.[33] However, Group VIB metals such as Cr, Mo, and W have been found to be poor catalysts in this regard. Cu is the most well-known bulk metal catalyst to effectuate CO_2 conversion to alcohol and hydrocarbons (methane, ethane *etc.*). It has high preferential selectivity towards CO binding which allows it to produce higher-order hydrocarbons more efficiently. Hence, it is proposed that the product selectivity on metal surfaces could be easily tuned by the differential binding energy of particular intermediates. However, Cu nanoparticle catalysts are reported to have lower faradaic efficiency for formation of CO because the low-coordinated sites on the catalyst surface promote HER over CO_2RR.[33] Besides polycrystalline metal surfaces, single-crystal surfaces of Pt, Cu, Ag, Au *etc.* are also reported for CO_2RR to CO.[33] Furthermore, copper oxides have been reported to have higher CO_2RR activity than bulk copper. Frese has investigated methanol formation on various oxidized Cu electrodes such as anodized Cu foil, thermally oxidized Cu foil in air, and air oxidized Cu electrodeposited on anodized or air-oxidized Ti foil, and found anodized Cu to give the highest rate (1×10^{-4} mol cm^{-2} h^{-1}).[36] Experiments revealed the formation of methanol to be a voltage-independent process, illustrating that the reason behind achievement of >1 faradaic efficiency is due to the contribution of several chemical (non-faradaic) and electrochemical reactions together.[33]

Apart from heterogeneous electrocatalysts, recent reports have focused on the development of homogeneous transition-metal complexes and surface-bound molecular catalysts for CO_2 reduction with higher product selectivity.[7] There has been a significant increase in the number of transition metal-based homogeneous catalytic systems that are able to selectively reduce CO_2, with metal centres encompassing the entire periodic table. The majority of homogeneous catalysts reported thus far are made up of precious noble metals such

as Ru, Rh, Pd, and Ir, while those with non-noble metals such as Mn, Fe, Co, Ni, and Cu are limited.[7] In the past, Pd complexes were always the focus of research for electrocatalytic CO_2 reduction. Dubois and co-workers reported electroreduction of CO_2 to CO and H_2O with Pd-tridentate phosphine ligands in DMF (dimethylformamide) or CH_3CN solvents, with a small amount of Brønsted acids, *e.g.* HBF_4 or H_3PO_4.[37] A plethora of catalysts based on Ru and Os coordinated to bpy ligands have been reported whose product selectivity is found to be largely influenced by pH.[38] For instance, at pH 6 the reaction catalysed by $[(bpy)_2Ru(CO)\text{-}Cl]^+$ gave a mixture of CO and H_2, while at pH 9 the reaction furnished both HCOO- and CO. Recent work focuses on the use of low-valent first-row transition metals to achieve dissociation of C–O and generate value-added intermediates. Macrocyclic complexes of soft metals such as Co(I) and Ni(I) have also been used as electrocatalysts since they are strong one-electron reductants.[1] Cyclam-based N4 complexes and their derivatives have been extensively investigated for the electroreduction of CO_2.[7,39] Success has also been achieved with surface-immobilized base metal catalysts. Berry and co-workers have utilized Co(porphyrin) appendages covalently anchored on a conductive diamond to reduce CO_2 at -1.55 V *vs.* Ag^+/Ag.[40] Cobalt mesotetraphenylporphyrin (CoTPP) immobilized on carbon nanotubes can achieve remarkable enhancement of electrocatalytic activity at a low overpotential in aqueous medium.[41] Marinescu *et al.* reported that cobalt aminopyridine macrocycles with pendant amine ligands were excellent catalysts for CO_2 reduction with high Faradaic efficiency.[42] However, most of these experimental electrokinetic studies of CO_2 reduction do not provide much insight into the rate-determining step and the origin of the product selectivity. Although several computational studies proposed the reaction mechanism of CO_2 electroreduction and underlined the role of kinetics in the elementary steps, more detailed mechanistic understanding is required to develop sustainable complex molecular systems that can work for prolonged hours under ambient conditions. Along with experimental developments, computational studies have provided valuable information that enhances the fundamental understanding of CO_2 reduction and triggers novel ideas for better catalyst design.[43] In our approach we have devoted ourselves to a comprehensive mechanistic understanding of CO_2 reduction with various homogeneous catalysts, using accurate quantum chemical computations.[6,8,11–13,40] Needless to say, such in-depth analysis may pave the way for constructing better catalysts with higher efficacy for CO_2 reduction. Hence, in this chapter, we summarize our recent theoretical works on elucidating the mechanisms of homogeneous CO_2 reduction in the hope of providing more viable solutions for sustainable CO_2 functionalization.

5.2 Theoretical Background

5.2.1 Potential Energy Surface and Reaction Energetics

Theoretical understanding of chemical reactions is absolutely necessary to decipher the underlying reaction mechanism, and rationalise different product

formation, temperature and pressure dependence, *etc.* In particular, theoretical knowledge about the thermodynamics and kinetics of a chemical reaction provides crucial insights. It will be very helpful to recapitulate some conceptual thoughts about chemical reactions, which should serve as the basis for analysing and understanding the computational results in the field of catalytic CO_2 reduction. Catalytic reactions commonly involve several elementary steps that are connected in a consecutive manner, and the overall rate of the reaction is usually governed by the slowest step, commonly known as the rate-determining step (RDS).[44] The RDS possesses the highest activation barrier in the overall catalytic cycle and the barrier of the individual steps including the RDS can be determined by, for example, the transition state theory (TST).[45] It is a common practice to connect each reaction species, *viz.* reactant, intermediates, transition states (TS), and products on a potential energy surface (PES). The basic foundation of PES is the Born–Oppenheimer (BO) approximation, which assumes that in a molecule the motions of the nuclei and electrons can be separated. As such, one can compute the electronic energy for a given nuclear arrangement and construct the PES for all possible nuclear arrangements. Therefore, within the BO approximation, molecules at their equilibrium geometries correspond to local minima on the PES and a chemical reaction can be pictured as nuclei moving from one minimum to another following a minimum-energy path (MEP). The TST assumes a quasi-equilibrium between the reactants (R) and the activated complex at the TS that decays to the product (P), $R \rightleftharpoons [TS]^{\ddagger} \rightarrow P$. In practice, such MEPs are constructed by using free energies of the individual reaction species and therefore commonly referred to as free energy profiles. The reaction barrier ($\Delta G^{\ddagger}$) for the elementary steps simply becomes the difference in free energies between the reactants and the TSs (eqn (5.1)).

$$\Delta G^{\ddagger} = G_{R} - G_{TS} \tag{5.1}$$

If one applies thermodynamic principles to the quasi-equilibrium between reactants and TS, the famous Eyring equation (k is the rate constant of the elementary step) is obtained (eqn (5.2)).

$$k = \left(\frac{k_B T}{h}\right) \exp^{(-\Delta G^{\ddagger}/RT)} \tag{5.2}$$

This simple mathematical relationship between the rate constant (k) and activation barrier ($\Delta G^{\ddagger}$) serves as the basis to compute reaction rates of each elementary step of a multi-step reaction and help identify the RDS. The key thermodynamic parameter, Gibbs free energies, of the individual species are obtained from quantum chemical calculations.

5.2.2 Relating Thermodynamics and Kinetics: Bell–Evans–Polanyi (BEP) Principle

It is often intriguing to correlate the thermodynamic and kinetic properties of a series of reactions of the same nature. Such understanding not only provides insights into the fundamental properties of the reaction but also guides the

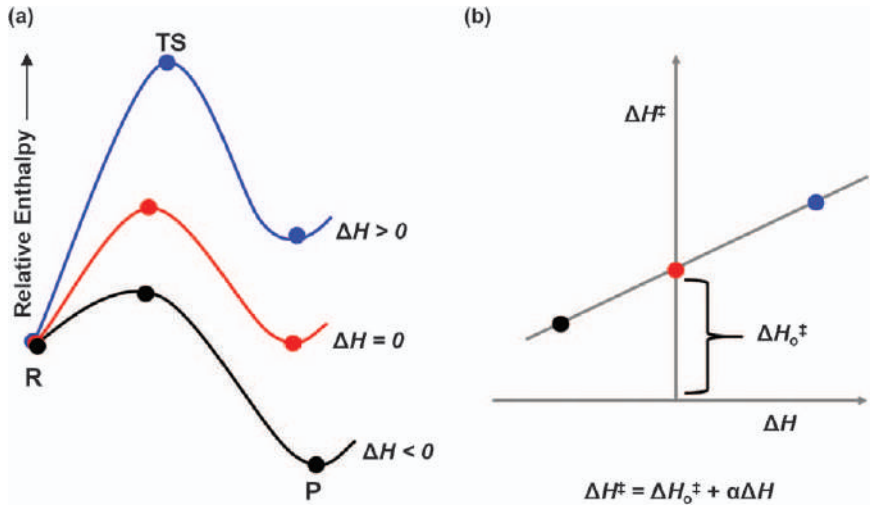

Figure 5.2 Representation of the Bell–Evans–Polanyi (BEP) principle with (a) reaction enthalpy surface and (b) linear correlation of enthalpic barrier with enthalpic change.
Reproduced from ref. 8 with permission from John Wiley and Sons, Copyright © 2019 Wiley-VCH Verlag GmbH & Co. KGaA.

design of more efficient catalysts. The Bell–Evans–Polanyi (BEP) principle represents a linear relationship between the change in the reaction enthalpy (ΔH), a thermodynamic property, and the activation enthalpy ($\Delta H^{\ddagger}$) a kinetic property, of a family of reactions as illustrated in Figure 5.2 (eqn (5.3)).[46]

$$\Delta H^{\ddagger} = \Delta H_o^{\ddagger} + \alpha \Delta H \tag{5.3}$$

This translates as, the higher the exothermicity of the reaction is, the lower the activation barrier becomes, or *vice versa* as depicted in Figure 5.2b. In Section 5.3, we will demonstrate how the key steps of homogeneous CO_2 hydrogenation follow the BEP principle. There are, of course, exceptions to the BEP principle. A prototypical example of such exception includes the oxygenation of organic substrates that encounters tremendous barriers despite having high exothermicity, which is a result of the spin-forbidden nature of the O_2 activation process.

5.2.3 Computational Methodology

Computational methods on catalytic reactions, such as homogeneous and heterogeneous CO_2 reductions, are generally aimed at calculating reaction mechanisms, activation barriers, reaction energies, and thermodynamic properties of the key intermediates. A variety of theoretical methods have been used for this purpose. For homogeneous molecular catalysts, density functional theory (DFT) is the method of choice to obtain geometries, vibrational frequencies, and energies. Recent developments of local coupled-cluster methods, such as

domain-based local pair natural orbital coupled-cluster with singles, doubles, and perturbative triple excitations, DLPNO-CCSD(T) also has made it possible to obtain highly accurate electronic energies for modelling catalytic reactions. For heterogeneous CO_2 reductions over solid surfaces, periodic DFT calculations have commonly been used. The combined quantum mechanical and molecular mechanical (QM/MM) methods are also successfully applied to model heterogeneous CO_2 reductions. In the following section, we will briefly describe the fundamental physics and working principles of the static DFT method.

5.2.3.1 Density Functional Theory (DFT)

DFT was founded upon the two Hohenberg and Kohn theorems; the first one states that there is a unique correspondence between electron density $\rho(r)$ and external potential $V(r)$ in which the electrons move. The ground-state wave function can therefore be uniquely determined by the density and *vice versa*. Thus, in principle there exists a universal functional that gives the total energy. The second theorem states that, provided that the universal density functional exists, the ground state energy can be obtained using variational principle (eqn (5.4)).

$$E_{v(r)}[\rho(r)] \geq E_{v(r)}[\rho_0(r)] = E_0 \tag{5.4}$$

Here, $\rho_0(r)$ is the exact density, and E_0 is the exact energy. However, the universal density functional is not known and DFT calculations are practiced in the framework of the Kohn–Sham (KS) approximation, which assumes a system of non-interacting electrons having the same density as the real system of interacting electrons. Analogous to the HF theory, the wavefunction of non-interacting electrons is a Slater determinant and the kinetic energy of one electron can be obtained from this one. Then the orbitals of the Slater determinant can be obtained by solving a set of eigenvalue equations as in the HF theory. The resulting equations are called KS equation and the analogue Fock operator in this case is the KS operator, which contains an effective potential consisting of three terms (eqn (5.5)).

$$V_{\text{eff}}(r) = V_{\text{ext}}(r) + \int \frac{\rho(r')}{r - r'} \mathrm{d}r + V_{\text{xc}}(r) \tag{5.5}$$

This expression contains the external potential (V_{ext}), the classic Coulomb potential, and exchange-correlation potential (V_{XC}). The energy of the KS system then can be expressed as shown in eqn (5.6).

$$E_{\text{KS}}[\rho(r)] = \sum_{i}^{N} \varepsilon_{\text{i}} - \int \frac{\rho(r)\rho(r')}{r - r'} \mathrm{d}r\mathrm{d}r' + E_{\text{XC}}[\rho(r)] - \int V_{\text{XC}}(r)\rho(r)\mathrm{d}r \tag{5.6}$$

Here, $V_{\text{XC}}(r)$ is a functional derivative of the exchange-correlation functional E_{XC}. The E_{XC} is given by eqn (5.7).

$$E_{\text{XC}}[\rho(r)] = T[\rho(r)] + T_{\text{s}}[\rho(r)] + V_{\text{ee}}[\rho(r)] - J[\rho(r)] \tag{5.7}$$

The parameter $V_{ee}[\rho(r)]$ is the exact correlation energy and $J[\rho(r)]$ is the classical Coulomb energy. If exact exchange-correlation could be used, the DFT computed energy would be exact. However, as the exact exchange-correlation is not known, various approximations to the energy functional have been developed and they are commonly referred as ''density functional''. The exchange-correlation $E_{XC}[\rho(r)]$ energy functional can be decomposed into the exchange $E_{xX}[\rho(r)]$ and correlation $E_{cC}[\rho(r)]$ functional (eqn (5.8)).

$$E_{XC}[\rho(r)] = E_{xX}[\rho(r)] + E_{cC}[\rho(r)] \tag{5.8}$$

There exist different approximations to the exchange-correlation functional, such as local density approximations (LDA), generalised gradient approximations (GGA), meta-GGA approximations, and hybrid functionals featuring a portion of the HF exchange.

5.2.3.2 *Coupled-cluster Singles, Doubles, and Perturbative Triples [CCSD(T)] and Domain-based Local Pair Natural Orbital [DLPNO-CCSD(T)]*

The coupled cluster (CC) energy expression is obtained by many-body exponential functions of cluster operators, $\check{T}1$, $\check{T}2$, $\check{T}3$, ..., $\check{T}n$ that generates excited-state determinants by exciting one, two, three, ..., n electrons from the reference ground-state Hartree–Fock (HF) wavefunction. Excitation up to the nth electron, n being the total number of electrons in a molecule, resembles the full configuration interaction (CI) method, while in practice even three electron excitations make CC calculations nearly unaffordable. Therefore, truncated versions of the CC method are used, where single and double excitations lead to the CCSD, and single, double, and triple excitations to the CCSDT methods. Fortunately, already at the CCSD level, some triple, quadrupole, and higher excitations are included owing to the fact that the higher-order excitations can be expressed as a product of linked double excitations.

$$e^{\check{T}_1+\check{T}_2} = 1 + \check{T}_1 + \check{T}_2 + \frac{\check{T}_1^2}{2} + \frac{\check{T}_2^2}{2} + \check{T}_1\check{T}_2 + \ldots \tag{5.9}$$

The approximated CC method, CCSD(T), is regarded as the best compromise between computational cost and accuracy. In this approach, the triple excitations are incorporated into the CCSD equation *via* a perturbative approach rather than a full CC approach. The CCSD(T) method proved very accurate for closed-shell systems and has been regarded as a ''gold-standard'' of computational chemistry. Unfortunately, CCSD(T) requires large one-electron basis sets to achieve the desired accuracy, which limits the routine application of this method in modelling larger systems such as metal-catalysed reactions.

In recent times, the developments of local correlation methods have come into the limelight as they have found a wide range of applications on relatively larger systems. By exploiting the local nature of electron-electron correlations in molecules, local pair natural orbital (LPNO) based CC methods (LPNO-CCSD) were rejuvenated a few years ago. Further developments gave rise to the domain-based version of the local CC, DLPNO-CCSD method. Finally, the incorporation of the perturbative triples to this method leads to the DLPNO-CCSD(T) method, which is, so far, the best (near-)linear scaling method that can compete with traditional DFT methods in terms of computational cost and can achieve the CC-level of accuracy at the same time.

5.2.3.3 General Performance of DFT and DLPNO-CCSD(T)

As demonstrated in the previous section, it is crucial to accurately compute the electronic energies for the unambiguous determination of the RDS in a catalytic process. The popular DFT often breaks down in calculating reaction barriers within the chemical accuracy ($\sim$3 kcal mol^{-1}). In fact, DFT calculations with different functionals could yield values for reaction barriers, the gap between different energy levels, *etc.* with a common error of $\sim$5 kcal mol^{-1}. The recently developed highly correlated *ab initio* method, DLPNO-CCSD(T) can, therefore, play an important role in predicting highly accurate reaction energetics and identifying the RDS.[11,12,47] Most importantly, the computational expense required for DLPNO-CCSD(T) calculations exceeds the cost of a hybrid DFT calculation (without using any approximations) by only 2–4 times.[11,12] Hence, the application of DLPNO-CCSD(T) methods on large systems like transition-metal-catalysed CO_2 reduction becomes entirely feasible on a routine basis.

5.2.4 Calculation of Hydricity

Catalytic CO_2 hydrogenation to yield formic acid often involves metal–hydride intermediates. Hydricity is an experimental measure of the nucleophilicity or hydride donating ability of a hydride donor.[48] Thus, it is important to accurately compute this parameter, for which the pioneering work has been reported by Dubois and co-workers.[49] Recently, Muckerman *et al.* proposed a simple thermodynamic scheme to estimate the hydricity, $(\Delta G^{\circ}_{H^-})(MH)$, of metal–hydride species.[50] The hydricity ($\Delta G^{\circ}_{H^-}$) of a given hydride donor (MH) is defined as the standard free energy change for the following reaction: $MH \rightarrow M^+ + H^-$ in a particular solvent, often acetonitrile. Therefore, the hydricity of a metal–hydride species is given by eqn (5.10).

$$\Delta G^{\circ}_{H^-}(MH) = G^{\circ}(M^+) + G^{\circ}(H^-) - G^{\circ}(MH) \tag{5.10}$$

However, it is difficult to calculate the absolute free energy of a solvated hydride [$G^{\circ}(H^-)$], so does $\Delta G^{\circ}_{HHR}(MH)$. Hence, the hydricity-half-reaction (HHR) $MH \rightarrow M^+$ is utilized to estimate the standard free energy change

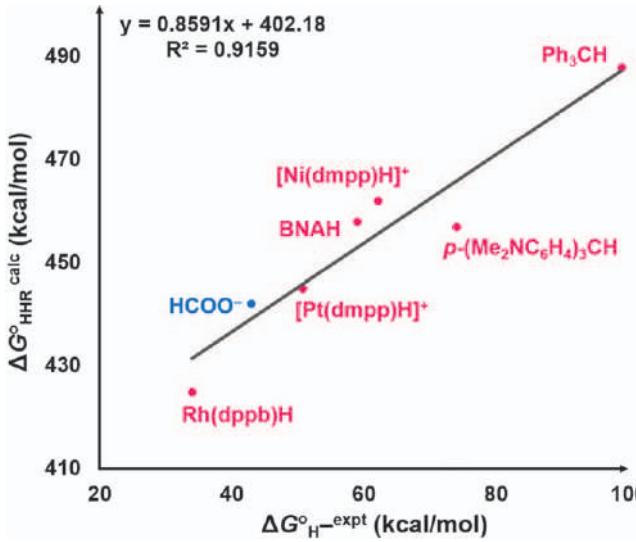

Figure 5.3 Correlation plot between experimental $\Delta G^{\circ}_{H-}{}^{expt}$ (x-axis) and calculated $\Delta G^{\circ}_{HHR}{}^{calc}$ (y-axis) of seven different species given in Table 5.1. Reproduced from ref. 11 with permission from American Chemical Society, Copyright 2015.

Table 5.1 Experimental hydricities and standard free energies of the corresponding hydricity half-reaction calculated at the M06-L/def2-TZVPP level of theory. Reproduced from ref. 11 with permission from American Chemical Society, Copyright 2015.

Species	$\Delta G^{\circ}{}_{H^-}{}^{expt}$ (kcal mol^{-1})	$\Delta G^{\circ}{}_{HHR}{}^{calc}$ (kcal mol^{-1})
$HCOO^-$	43	442
Ph_3CH	99	488
BNAH[a]	59	458
Rh(dppb)H[b]	34	425
$[Pt(dmpp)H]^{+}$[c]	50.7	445
$[Ni(dmpp)H]^{+}$[c]	62.1	462
p-$(Me_2NC_6H_4)_3CH$	74	457

[a]BNAH = 1-benzyl-1,4-dihydronicotinamide.
[b]dppb = 1,2-bis(diphenylphosphino)benzene.
[c]dmpp = bis(dimethylphosphino)propane.

$\Delta G^{\circ}_{HHR}(MH)$ to avoid calculating $G^{\circ}(H^-)$. Thereby, the HHR free energy change is given by eqn (5.11a) and (5.11b).

$$\Delta G^{\circ}_{HHR}(MH) = G^{\circ}(M^+) - G^{\circ}(MH) \quad (5.11a)$$

$$= \Delta G^{\circ}_{H-}(MH) - G^{\circ}(H^-) \quad (5.11b)$$

From eqn (5.11b) it is clear that hydricity ($\Delta G^{\circ}_{H^-}$) of a metal–hydride species should be a linear function of the standard free energy change of the hydricity half-reaction (ΔG°_{HHR}) with the slope being one and $G^{\circ}(H^-)$ being the intercept.

Table 5.2 Calculated hydricities of theoretically studied species. Reproduced from ref. 11 with permission from American Chemical Society, Copyright 2015.

Species	$\Delta G^{\circ}_{H^-}{}^{calc}$ (kcal mol^{-1})
$HCOO^-$	47.1
HCOOH	134.6
$HCOOH - NEt_3$	59.3
$Fe(H)(H)(PP_3Ph)$	66.5
$Ru(H)(H)(PP_3Ph)$	58.5
$Co(H)(H)(PP_3Ph)^{+a}$	100.0

[a] PP_3Ph = tris(2-(diphenylphosphino)phenyl)phosphine.

This approach is useful to theoretically calculate the HHR free energy change (ΔG°_{HHR}) for a series of species whose hydricities ($\Delta G^{\circ}_{H^-}{}^{expt}$) have been determined experimentally by any of the following three techniques: hydride transfer, H_2 heterolysis, and potential–pK_a methods. Hence, $\Delta G^{\circ}_{H^-}{}^{expt}$ (x-axis) is plotted against $\Delta G^{\circ}_{HHR}{}^{calc}$ (y-axis) (calculated by using eqn (5.11a)) and then a least-square linear fit is used to give a realistic value of $G^{\circ}(H^-)$ from the intercept. Using the $G^{\circ}(H^-)$ thus obtained, one can easily compute a reliable value of $\Delta G^{o}_{H^-}$ of a metal–hydride once the $\Delta G^{\circ}_{HHR}(MH^-)$ is known. Thus, the hydricity of a new species can be predicted very conveniently.

For example, from a linear regression of experimental hydricities of six hydride donor species and $HCOO^-$ against the standard free energy change of their corresponding HHR computed at the DFT M06L level of theory, the $G^{\circ}(H^-)$ value was determined to be 402.2 kcal mol^{-1} from the intercept of Figure 5.3. On the basis of that, the hydricities of a series of Fe, Ru and Co complexes of interest are calculated, as shown in Table 5.2.

5.2.5 Calculation of Standard Reduction Potential and pK_a

The standard reduction potential of a given species in solution can be conveniently calculated by using the standard Gibbs free energy change (ΔG^{EA}_{sol}) for the electron transfer process in eqn (5.12).

$$E^{\circ} = -\frac{\Delta G^{EA}_{sol}}{nF} \tag{5.12}$$

Here, F is the Faraday constant, and n is the number of electrons involved. ΔG^{EA}_{sol} is computed from the thermodynamic cycle shown in Scheme 5.1(a) using eqn (5.13).

$$\Delta G^{EA}_{sol} = \Delta G^{EA}_{g} + \Delta G_{solv}(A^-) - \Delta G_{solv}(A) - \Delta G_{solv}(e^-) \tag{5.13}$$

However, the exact solvation energy of a single electron is available neither from experiment nor from theory. Following the proposal suggested by Cramer and Truhlar, the relative standard potential rather than the exact solvation energy of a single electron was calculated by externally adding the effect in a linear fashion.[51] Hence, the standard reduction potential with respect to the NHE was obtained by a rudimentary shift of −4.48 V to the

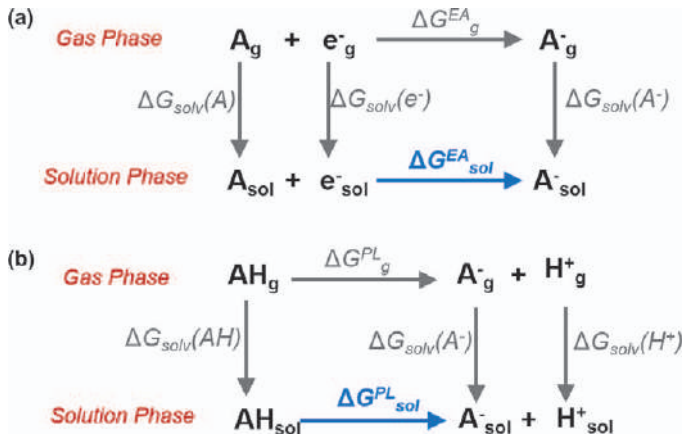

Scheme 5.1 Thermodynamic cycles used for the calculations of (a) standard reduction potential and (b) pK_a.
Reproduced from ref. 13 with permission from American Chemical Society, Copyright 2014.

relative redox potential obtained for a species in acetonitrile. Thus, the final relation of E° with free energy changes is given by eqn (5.14).

$$E^\circ = -\left[\frac{\left\{\Delta G^{EA}_g + \Delta G_{solv}(A^-) - \Delta G_{solv}(A)\right\}}{F}\right] - 4.48 \qquad (5.14)$$

Similarly, the pK_a value of a given proton dissociation reaction in solution was estimated from the thermodynamic cycle in Scheme 5.2(b).[13] Specifically, the pK_a value is computed by the Gibbs free energy change of proton affinity, ΔG^{PL}_{sol}, using eqn (5.15).

$$pK_a = \frac{\Delta G^{PL}_{sol}}{2.303\ RT} \qquad (5.15)$$

Here, R is the universal gas constant and T is the temperature in Kelvin. On the basis of the thermodynamic cycles shown in Scheme 5.1(b), eqn (5.16) ensues.

$$\Delta G^{PL}_{sol} = \Delta G^{PL}_g + \Delta G_{sol}(A^-) + \Delta G_{solv}(H^+) - \Delta G_{sol}(AH) \qquad (5.16)$$

ΔG^{PL}_g includes the gas phase standard Gibbs free energy of formation of a proton whose value was set to -6.28 kcal mol^{-1}. Furthermore, the solvation energy of a proton, $\Delta G_{solv}(H^+)$, was used from literature values (-260.2 kcal mol^{-1}).

The gas-phase Gibbs standard energy change was corrected to the standard state (1 M) using eqn (5.17) and (5.18).

$$\Delta G^{PL}_g(1\text{ M}) = \Delta G^{PL}_g(1\text{ atm}) - 1.89\text{ kcal mol}^{-1} \qquad (5.17)$$

where

$$\Delta G_g^{PL}(1\ \text{atm}) = G_g(A^-, 1\ \text{atm}) + G_g(H^+, 1\ \text{atm}) - \Delta G_g(AH, 1\ \text{atm}) \qquad (5.18)$$

In the literature, various approaches have been proposed to calculate hydricities, redox potentials, and pK_a values. Note that eqn (5.12), (5.13), and (5.16) serve as the master equations for nearly all of them. Because accurate values of solvation energies of the hydride, electron, and proton are not known, various approximations are used in different methods. Here, we only discuss those used in our own work.

5.3 Case Studies: Non-noble Metal Catalysed Homogeneous CO_2 Reduction

The large number of reactions of two-electron CO_2 reduction found in the literature can be classified into two primary categories, *i.e.* (a) CO_2 reductive dissociation and (b) CO_2 hydrogenation (Scheme 5.2). CO_2 reductive dissociation can occur *via* a C–O bond cleavage promoted by a metal ion (M^{n+}) or a proton (H^+) to yield CO (Scheme 5.2, left). Alternatively, two CO_2 molecules can couple to yield CO_3^{2-} and CO through reductive disproportionation. CO_2 hydrogenation is usually assisted by a base to form HCOOH or HCO_2^- as the primary product (Scheme 5.2, right). Here, we summarize the most fundamental aspect of two-electron reduction of CO_2 with the help of a few case studies. We focus on the mechanisms of these reactions which are extensively studied by us with theoretical tools. We begin with the discussion on electrocatalytic C–O dissociation by a Ni–Cyclam complex, followed by our understanding on Cobalt-β-diketiminate complex-mediated reductive disproportionation of CO_2. We finish with the CO_2 hydrogenation process, identifying the rate-controlling factor to design a new efficient catalyst.

5.3.1 CO_2 Reductive Dissociation

Conversion of CO_2 into CO is a promising strategy to develop fuel precursors. The reverse-water-gas-shift reaction utilizes strategies found in Nature's photosynthetic processes to dissociate CO_2 into CO according to the following reaction: $CO_2 + H_2 \rightarrow CO + H_2O$. The Fischer–Tropsch process is thereby utilized to produce higher-order hydrocarbons from CO and H_2. Several Co(II), Ni(II), Ag(II), and Pd(II) molecular electrocatalysts based on porphyrin and phthalocyanines carry out efficacious CO_2 reduction to CO and HCOOH.[1] CO_2

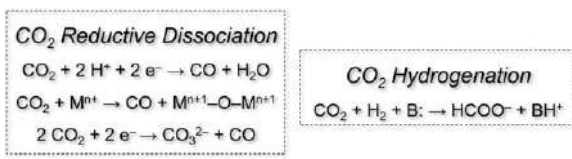

Scheme 5.2 CO_2 activation pathways *via* two-electron reduction. Here "B" denotes a base.

reduction was proposed to be initiated by the addition of CO_2 to the metal centre.

X-ray crystallographic analyses revealed that CO_2 binding to a transition metal centre adopts three different binding modes, *i.e.* η^1-C, η^2-C,O, and η^1-O (Figure 5.4a). Specifically, the η^1-C mode is proposed for electron-rich low-valent metal centres which facilitate electron transfer from metal-based *d*-orbitals to the carbon-based π^* antibonding orbitals. Experimentally, η^1-C binding to CO_2 was first observed in $[Rh(diars)_2(Cl)(CO_2)]$ (diars = o-phenylene-bis(dimethyl)arsine) as reported by Herskovitz *et al.*,[52] while η^1-O coordination has been observed with electron-poor high valent metal species. As early as 2004, Meyer and co-workers reported the first example of an η^1-O binding CO_2 ligand in a hexa-coordinated uranium(III) species.[53] The sterically very demanding adamantyl substituents on the supporting ligand produce a narrow cylindrical passage above the metal centre, instigating a linear CO_2 binding mode in η^1-OCO fashion (Figure 5.4b). The η^2-CO_2 mode featuring a bent CO_2 ligand, which was first found for $Ni(PCy_3)_2CO_2$ by Aresta and co-workers, is the most common coordination mode found for metal–CO_2 adducts.[54] This coordination mode is also found in PPMePNi(η^2-CO_2) (PPMeP = PMe[2-PiPr$_2$-C$_6$H$_4$]$_2$)[55] and (dtbpe)Ni(η^2-CO_2) (dtpbe = 1,2-bis(di-*tert*-butylphosphino)ethane).[56] Notably, computational studies predict a preference of η^2-CO_2 binding for low-valent Cr and Ni β-diketiminate complexes.[57] In particular, η^2-CO_2 adducts are often reported to undergo heterolytic C–O bond cleavage to generate CO.

Starting from η^2-CO_2 adducts, two-electron reduction of CO_2 is typically achieved by PCET or MCET. Alternatively, reductive disproportionation of two CO_2 molecules generates CO and CO_3^{2-} assisted by binuclear

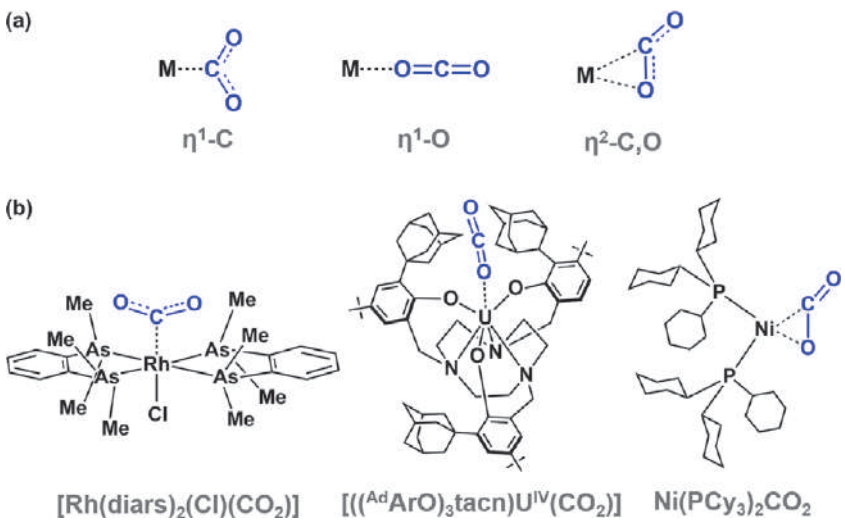

Figure 5.4 (a) Different coordination modes of CO_2 to a single metal centre. (b) Representative examples of CO_2 bound metal complexes (see text).[52–54]

macrocyclic complexes (Scheme 5.2). It is to be noted that CO_2 coordination to a reduced metal centre develops substantial negative charge on the bound CO_2 ligand. To form CO in the end, C–O bond breaking must involve transfer of an oxide-like group to protons, or to electron-deficient positively charged metal centres or even to a second molecule of CO_2. This process is expected to involve a high energetic penalty; therefore, C–O bond cleavage is often the RDS of the entire reaction.

Experimental and computational studies indicate that the proton or a second metal centre functioning as a Lewis acid can interact with the unbound oxygen atom.[13,43] As a consequence of this interaction, the electron-accepting capability of CO_2 becomes enhanced. Relevant examples include the electrochemical reduction of CO_2 to produce CO mediated by a Fe(porphyrin) system where addition of Brønsted acids, such as CF_3CH_2OH, improves the rate of catalysis.[58] Furthermore, intramolecular hydrogen bonding with ligand –NH protons has been demonstrated to provide stronger fixation of CO_2 to a Co(I) macrocyclic complex.[1,42] This favourable anchorage promotes two-electron transfer from the metal centre to CO_2, leading to the formation of a Co(III)-carboxylate adduct. In line with this reasoning, the closely placed Ni and Fe centres in the active site of [NiFe]CODH are proposed to induce cooperative C–O dissociation for reversible conversion of CO_2 to CO.[59] Similar to [NiFe]CO dehydrogenase, very high catalytic activity has been found in a bimetallic palladium complex platform in which two triphosphine units are bridged by a -CH_2 group.[60] Here, weakly coordinating solvent molecules dissociate from the metal centre to provide a vacant coordination site for binding CO_2 and assisting in C–O bond cleavage. Recent research focuses on earth-abundant complexes such as the Ni(I) –cyclam complex (cyclam = 1,4,8,11-tetraazacyclotetradecane).[61] Significant understanding on this topic has been achieved through both thermodynamic/kinetic analysis and computational studies.[13,39,58]

5.3.1.1 *Homogeneous Electrochemical CO_2 Reductive Dissociation*

Several transition metal complexes are found to selectively reduce CO_2 to formate or CO, with modest overpotential and Faradaic efficiency.[62] Among them, the reactivity of $[Ni(cyclam)]^{2+}$ is particularly interesting because it selectively furnishes CO at a low overpotential in water. On the contrary, both CO and formate (75%) are generated in low water content DMF solvent.[63] The active catalyst is believed to be the one-electron reduced $[Ni(cyclam)]^{+}$ species. Furthermore, it has been shown that the reaction predominantly takes place on a mercury electrode as $[Ni(cyclam)]^{+}$ gets adsorbed on it.[64,65] The catalytic activity plateaued with an increment in catalyst concentration due to saturation of the adsorbed complexes on the metal surface, casting doubt on the homogeneity of the reaction.[63,64] However, a recent study by Froehlich and Kubiak demonstrated homogeneous CO_2 reduction by $[Ni(cyclam)]^{2+}$ on an inert glassy carbon electrode.[61]

We hypothesized that different binding modes of CO_2 with Ni is responsible for the product selectivity.[13] An η^1-CO_2 adduct undergoes C–O bond cleavage to yield CO while $HCOO^-$ originates from a η^1-OCO intermediate. Our computational analyses revealed that the binding of CO_2 to $[Ni(cyclam)]^+$ in a η^1-CO_2 fashion is energetically more favourable (a thermoneutral process with $\Delta G = -1.6$ kcal mol^{-1}) than formation of the η^1-OCO intermediate $[Ni(\eta^1\text{-OCO})(cyclam)]^+$, ($\Delta G = 12.4$ kcal mol^{-1}) (Figure 5.5a). The thermodynamics of the CO_2 adduct controls the product selectivity. Notably, the LUMO of CO_2 is primarily C 2p centred. Hence, the overlap between the Ni dz^2 orbital with the C-centred lobe of CO_2 π^* in η^1-CO_2 mode is more effective than with the O-centred lobe of CO_2 π^* in the η^1-OCO mode which accounts for the differential binding energies. However, the frontier orbital analyses of $[Ni(\eta^1\text{-}CO_2)(cyclam)]^+$ reveal that binding of CO_2 to $[Ni(cyclam)]^+$ only causes a partial single electron transfer from Ni^+ to CO_2. Hence, the second electron transfer must proceed through an outer-sphere electron transfer mechanism assisted by a proton (Scheme 5.3). In this case, a concerted PCET pathway is found to be the feasible route rather than sequential electron-proton transfers. Our calculations therefore highlight

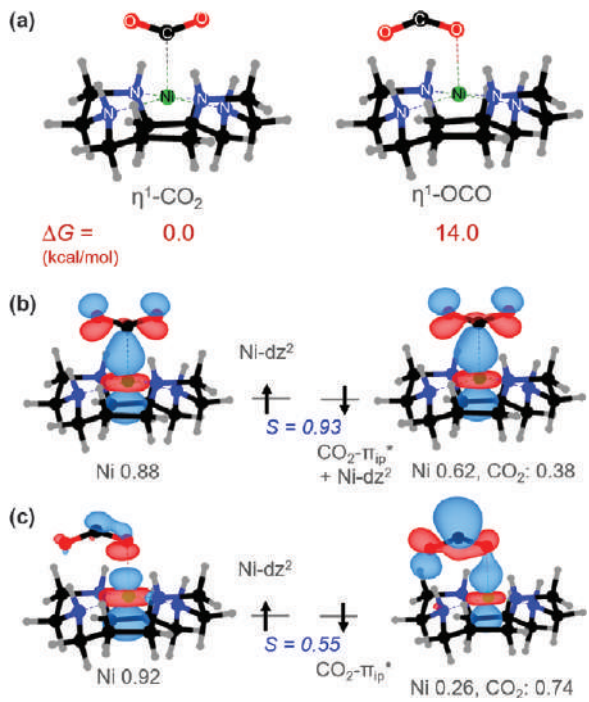

Figure 5.5 (a) η^1-CO_2 and η^1-OCO adducts of Ni-cyclam with relative free energies. Important non-orthogonal orbitals of (b) η^1-CO_2 and (c) η^1-OCO Ni complexes.
Reproduced from ref. 13 with permission from American Chemical Society, Copyright 2014.

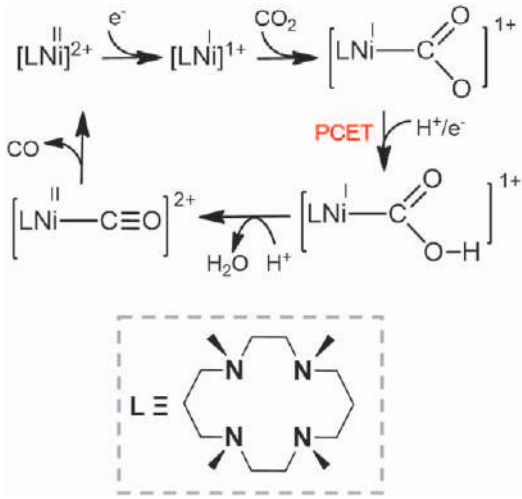

Scheme 5.3 Schematic representation of the mechanism for CO_2 reduction to CO by Ni–cyclam.
Reproduced from ref. 13 with permission from American Chemical Society, Copyright 2014.

that binding of external protons increases the electron affinity of the CO_2 in $[Ni(\eta^1\text{-}CO_2)(cyclam)]^+$ to enable acceptance of electrons from Ni^I and the electrode. Hence, a feasible C–O bond cleavage to CO is then possible, for which generation of H_2O provides the added driving force (Scheme 5.3).

5.3.1.2 *CO_2 Reductive Disproportionation by a Cobalt-β-Diketiminate Complex*

In an analogous stoichiometric reduction of CO_2 by a Co complex coordinated by β-diketiminate (L^tBu) ligands (L^tBu = 2,2,6-6-tetramethyl-3,5-bis[(2,6-diisopropylphenyl)imino]hept-4-yl), a metal carbonyl, $L^tBuCo(CO)$, and a carbonate-bridged dinuclear compound, $L^tBuCo(\mu\text{-}OCO_2)CoL^tBu$, are formed (Scheme 5.4).[43] Here, we proposed that after the rate-determining slippage of the $\kappa N,\eta^6$-arene isomer to the traditional $\kappa N,N'$ coordination mode of the ligand, CO_2 binding takes place on an uncoordinated metal site in an η^2-CO_2 fashion (Scheme 5.4). Similar to the previous case, coordination of CO_2 to the metal initiates partial electron transfer from the Co^I dz_2 orbital to the π^* of CO_2. Hence, the subsequent C–O cleavage following the CO_2 association is found to be energetically unfavourable. However, coordination of the distal oxygen atom of the CO_2 motif to a second $\kappa N,N'$ Co^I complex generates a $\kappa^1C,\kappa^2(O, O)$ CO_2 bridged dinuclear species whose formation is predicted to be highly exergonic ($\Delta G < -20$ kcal mol^{-1}). The heterolytic C–O bond cleavage assisted by bimetallic centres is found to traverse a much lower barrier which signifies the use of the second metal centre as a Lewis acid. Importantly, it is rather facile to oxidize each metal

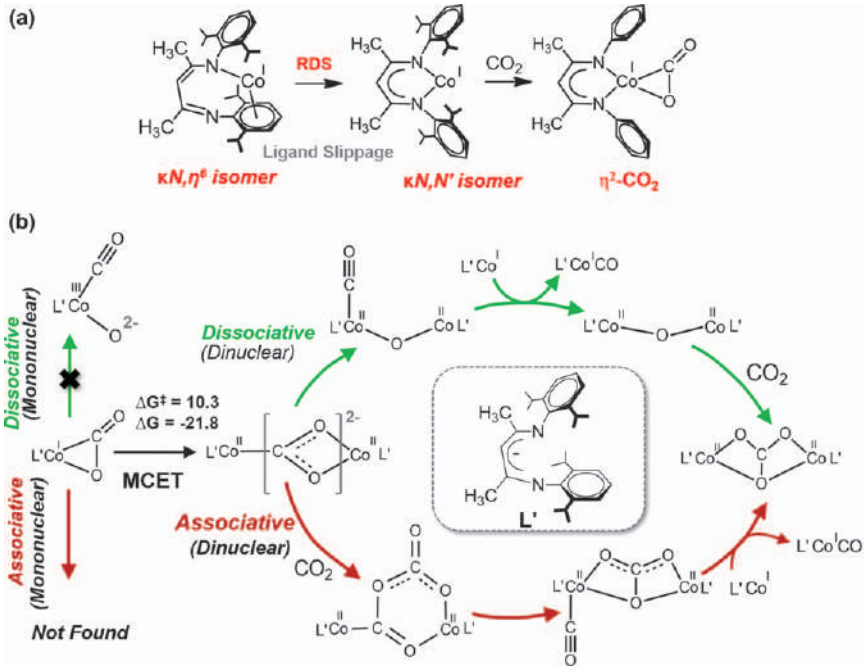

Scheme 5.4 (a) Reaction steps during the rate-determining ligand slippage for CO_2 addition to a cobalt-β-diketiminate complex. (b) Schematic representation of the mechanism for CO_2 dissociation following mononuclear and binuclear pathways. Reported Gibbs free energies are in units of kcal mol^{-1}. Reproduced from ref. 43 with permission from the Royal Society of Chemistry.

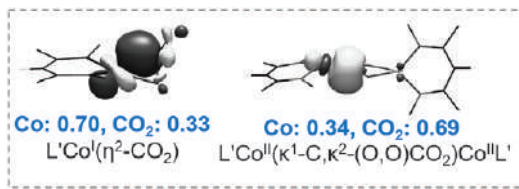

Figure 5.6 Orbital interaction between CO_2 and the Co centre in mononuclear and binuclear adducts.
Reproduced from ref. 43 with permission from the Royal Society of Chemistry.

centre by one unit rather than a single metal centre working as a two-electron reductant. Hence, binding of oxygen to a second Co centre ensures transfer of an additional electron and also facilitates complete electronic transfer from the first Co^{I} centre.

Furthermore, analyses of the frontier orbitals show that for the electron-rich $[CO_2]^{2-}$ moiety in the CO_2 bridging dinuclear species, the bonding σ orbital is predominantly carbon-based (Figure 5.6). This is essentially an

example of MCET, in principle similar to the electrochemical reduction of CO_2 by $[Ni(cyclam)]^+$ following a PCET process.[13] In both reactions, the η^1-CO_2 adduct is partially reduced and requires a proton or a second metal to recover sufficient electron affinity of CO_2 for the second electron transfer. However, unlike $[Ni(cyclam)]^+$ where an outer-sphere second electron transfer takes place, the second L^{t}BuCo species also furnishes the required additional electron to complete the reduction process. The dinuclear species then follows a heterolytic C–O bond cleavage to transform to a μ–oxo intermediate and releases CO to form the metal carbonyl. The μ–oxo intermediate subsequently reacts with a second CO_2 molecule to yield the final products. An associative pathway where a nucleophilic addition of the electron-rich $(CO_2)^{2-}$ dianion to another CO_2 to form a $(CO_2)_2{}^{2-}$ bridge is computationally identified to be another feasible channel. Further heterolytic cleavage of C–O followed by geometrical rearrangement then yields the desired products.

5.3.2 CO_2 Hydrogenation

Homogeneous hydrogenation of CO_2 using molecular H_2 is one of the most attractive ways of CO_2 functionalization with formic acid being the immediate product. The reaction is usually performed in the presence of a base, which increases the thermodynamic driving force of the reaction by forming an acid–base complex as the final product. The fundamental thermodynamic requirements of CO_2 hydrogenation are illustrated in eqn (5.19–5.21), where the use of a base clearly increases the driving force.

$$CO_2\ (g) + H_2\ (g) \rightarrow HCOOH\ (l) \tag{5.19}$$

$$\Delta G^\circ = 7.8\ \text{kcal mol}^{-1};\ \Delta H^\circ = -7.5\ \text{kcal mol}^{-1};\ \Delta S^\circ = -51.2\ \text{cal (mol K)}^{-1}$$

$$CO_2\ (g) + H_2\ (g) + NH_3\ (aq) \rightarrow HCO_2{}^-\ (aq) + NH_4{}^+\ (aq) \tag{5.20}$$

$$\Delta G^\circ = -2.3\ \text{kcal mol}^{-1};\ \Delta H^\circ = -20.1\ \text{kcal mol}^{-1};\ \Delta S^\circ = -59.5\ \text{cal (mol K)}^{-1}$$

$$CO_2\ (aq) + H_2\ (aq) + NH_3\ (aq) \rightarrow HCO_2{}^-\ (aq) + NH_4{}^+\ (aq) \tag{5.21}$$

$$\Delta G^\circ = -8.4\ \text{kcal mol}^{-1};\ \Delta H^\circ = -14.2\ \text{kcal mol}^{-1};\ \Delta S^\circ = -19.3\ \text{cal (mol K)}^{-1}$$

Since Inoue *et al.* reported the first example of homogenous CO_2 hydrogenation in 1976,[66] a plethora of noble as well as non-noble metal catalysed processes have been developed.[67,68] Some ground breaking examples based on noble metals include $[RhCl(TPPTS)_3]$ (TPPTS = tris(m-sulfonatophenyl)phosphine) developed by Leitner *et al.* (turnover number, TON = 3439), $[IrH_3(PNP^iPr)]$ (PNP^iPr = 2,6-$(CH_2P^iPr_2)_2C_5H_3N$)[69] prepared by Nozaki *et al.* (turnover frequency (TOF) = 150 000 h^{-1}; TON = 3 500 000)[70] and $[RuCl(H)(CO)(PNP^tBu)]$ (PNP^tBu = 2,6-$(CH_2P^tBu_2)_2C_5H_3N$) developed by Filonenko *et al.* (TOF = 1 100 000 h^{-1}).[71] In contrast to the noble metals, only a handful of non-noble metal-based CO_2 hydrogenation catalysts have been reported so far and

their reactivity is not comparable with their noble metal counterparts. The catalyst systems, $NiCl_2$/dcpe (dcpe = $Cy_2PCH_2CH_2PCy_2$) (TON = 4400; TOF = 20 h^{-1}) developed by Jessop and co-workers,[72] [Fe(PP_3Ph)(H_2)(H)] (PP_3Ph = tris(2-(diphenylphosphino)phenyl)phosphine) (TON = 1897; TOF = 95 h^{-1}) *in situ* generated by Beller *et al.*,[73] and [Co(dmpe)H] (dmpe = 1,2-bis-(dimethylphosphino)ethane) (TOF = 74 000 h^{-1}) developed by Appel *et al.* are some representative examples of the non-noble metal category.[74] While highly applicable ambient reaction conditions have been developed for noble metal-based reactions, non-noble metal catalysis requires harsh reaction conditions that limit their applicability. Therefore, design and developments of non-noble metal catalysed CO_2 reduction processes is now at its pinnacle. Undoubtedly, a detailed mechanistic understanding of the catalytic processes is a prerequisite for such developments and computational techniques is an irreplaceable choice in this context.

Most CO_2 hydrogenation follows a common mechanism that involves two key steps, *i.e.* (i) base-promoted heterolytic H_2 splitting to generate a metal–hydride intermediate, and (ii) hydride transfer from the metal–hydride to CO_2. More importantly, either of those two steps could function as the RDS of the overall catalytic cycle. This has been experimentally demonstrated in a single study involving $[(\eta^6\text{-}C_6Me_6)Ru(bpy)(OH_2)]^{2+}$ and $[Cp^*Ir(bpy)(OH_2)]^{2+}$ ($Cp^* = \eta^5\text{-}C_5Me_5$) catalytic systems, which showed H_2-splitting RDS for the former and hydride-transfer RDS for the latter complex.[75] Computational mechanistic investigations predicted H_2 splitting to be the RDS for CO_2 reduction with $[(PNP)Ir(H)_3]$,[76] $[(PNP)Co(H)_3]$, $[(PNP)Fe(H)_2(CO)]$ (PNP = 2,6-bis(dialkylphosphinomethyl)-pyridine), and $[Cp^*M(6,6'\text{-}O^-\text{-bpy})(H_2O)]$ (M = Co, Rh, and Ir; bpy = 2,2′-bipyridine) complexes.[8] The hydride transfer was suggested to be the RDS for a Co complex $[Co(dmpe)_2H]$ (dmpe = 1,2-bis(dimethylphosphino)ethane).[8]

The chemical nature of the RDS for CO_2 hydrogenation remains fickle. In order to pin-point the governing factor that controls the chemical identity of the RDS, we undertook computational investigations on a phosphine coordinated Fe(II) catalyst, $[Fe(H)(\eta^2\text{-}H_2)(PP_3Ph)]^+$ ($\mathbf{R_{Fe}}$) performing CO_2 hydrogenation to formate (Scheme 5.5).[11,12] The mechanistic sequence follows a base (NEt_3)-promoted heterolytic H_2-splitting for $\mathbf{R_{Fe}}$ to generate metal–hydride species $\mathbf{I_{Fe}}$ (Scheme 5.5). $\mathbf{I_{Fe}}$ undergoes hydride transfer to CO_2 to form a formate-bound complex $\mathbf{P_{Fe}}$ that eventually releases formate and regenerate $\mathbf{R_{Fe}}$. The reaction free energy profile obtained using DLPNO-CCSD(T) calculations revealed that the H_2-splitting step features the highest barrier in the catalytic cycle and is therefore the RDS (Figure 5.7). In order to investigate how a different metal with the same electronic configuration might alter the nature of the reaction, we examined the CO_2 hydrogenation reactivity with the corresponding Co(III) complex, $[Co(H)(\eta^2\text{-}H_2)(PP_3Ph)]^{2+}$ ($\mathbf{R_{Co}}$). The theoretical results revealed that the H_2-splitting by $\mathbf{R_{Co}}$ traverses a much lower barrier than that by $\mathbf{R_{Fe}}$. However, the hydride transfer starting from $\mathbf{I_{Co}}$ appeared to involve a prohibitive barrier and is hence rate-determining. Evidently, changing the metal centre from Fe(II) to Co(III)

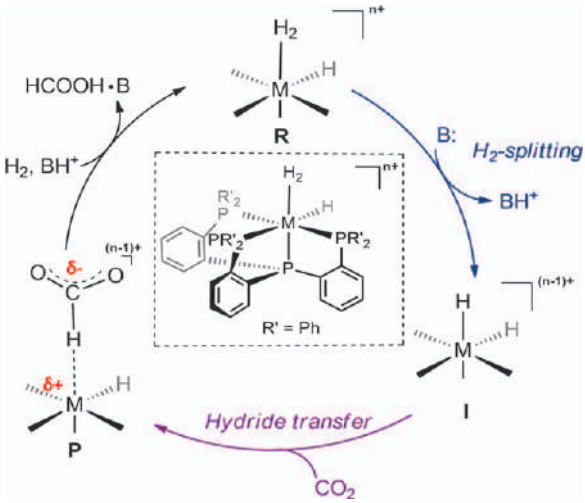

Scheme 5.5 Key steps for the CO_2 hydrogenation catalytic cycle using a metal–phosphine complex.
Reproduced from ref. 8 with permission from John Wiley and Sons, Copyright © 2019 Wiley-VCH Verlag GmbH & Co. KGaA.

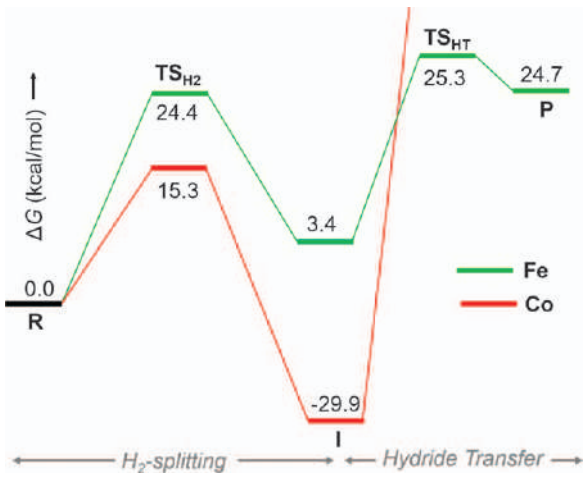

Figure 5.7 DLPNO-CCSD(T)/def2-TZVPP computed free energy profile for the crucial steps with Fe and Co catalysts.
Reproduced from ref. 8 with permission from John Wiley and Sons, Copyright © 2019 Wiley-VCH Verlag GmbH & Co. KGaA.

alters the CO_2 hydrogenation RDS from H_2-splitting to hydride transfer (Figure 5.7).

The H_2-splitting barrier for $\mathbf{R_{Fe}}$ is computed to be higher than that for $\mathbf{R_{Co}}$, and at the same time, the corresponding driving force of the former reaction

is lower than the latter. Furthermore, a correlation between barrier ($\Delta G^{\ddagger}$) and driving force (ΔG) was also observed, indicating that the reaction follows the BEP principle. The variation of the H_2-splitting driving force originates from the differential metal–hydride bonding (M–H) strength in intermediate **I**, which can be quantified by hydricity or hydride affinity, $\Delta G^{\circ}_{H-}(MH)$. In line with this analysis, the calculated hydricities of $\mathbf{I_{Fe}}$ and $\mathbf{I_{Co}}$ are 58 and 100 kcal mol^{-1}, respectively, rationalize the distinct H_2-splitting driving forces. As hydricity measures the ability of a metal–hydride complex (*e.g.* **I**) to donate its hydride, it also plays a crucial role in the hydride transfer step. As such, CO_2 hydrogenation reactions *via* the ''*in situ* generated'' metal–hydrides have to attain a delicate balance between hydride generation and hydride transfer for an overall efficient catalytic process to occur. On the basis of this analysis, we developed the following dichotomic ligand design strategies. Specifically, for low-hydricity species (*e.g.* $\mathbf{R_{Fe}}$), we used an electron-withdrawing group such as $-NO_2$ in the ligand sphere that pulls electron-density from the metal centre and increases its hydricity of the metal-hydride intermediates. For high hydricity species (*e.g.* $\mathbf{R_{Co}}$), anionic anchors C^- and Si^- were added to the phosphine ligands that push electron-density to the metal centre and thereby lower the hydricity of the metal–hydride intermediates (Figure 5.8a).[12] Following this ligand modification strategies, we designed a series of Fe and Co-based catalysts, and our calculations indeed showed that such modifications lower the RDS barriers in the respective cases.

For the parent complexes, $\mathbf{R_{Co}}$, $\mathbf{R_{Fe}}$ and their ligand modified complexes, [Co(H)(η^2-H_2)(CP_3Ph)] (CP_3Ph = tris(2-(diphenylphosphino)-phenyl)methyl) ($\mathbf{R_{Co/C}}$), [Co(H)(η^2-H_2)(SiP_3Ph)] (SiP_3Ph = tris(2-(diphenylphosphino)phenyl)silyl) ($\mathbf{R_{Co/Si}}$), [Fe(H)(η^2-H_2)(PP_3PhNO_2)]$^+$ (PP_3PhNO_2 = tris(2-(diphenylphosphino)-4-nitrophenyl)phosphine) ($\mathbf{R_{Fe/NO_2}}$), $\mathbf{R_{Fe/C}}$ and $\mathbf{R_{Fe/Si}}$ (Figure 5.8a), we observed good correlations between the hydricity of the ''*in situ* generated'' hydrides and barriers for the key steps (Figure 5.8b). In such a volcano plot, the two correlation curves cross at a point which is 59.7 kcal mol^{-1} on the hydricity scale and is the optimal hydricity that the ''*in situ* generated'' hydrides should possess to function as an efficient catalyst for CO_2 hydrogenation in the presence of NEt_3. Most importantly, the correlation suggests that beside $\mathbf{R_{Fe}}$, $\mathbf{R_{Co/Si}}$ and $\mathbf{R_{Co/C}}$ would be active catalysts for homogeneous CO_2 hydrogenation. The hydricity of CO_2 is 44 kcal mol^{-1} and any hydride donor having a hydricity value higher than that, in principle, is not a good hydride donor for CO_2 hydrogenation. One should not confuse this with the ''*in situ* generated'' metal-hydrides described above. In fact, for the ''*in situ* generated'' metal–hydrides, the optimal hydricity value should be in between the hydricity of CO_2 (44 kcal mol^{-1}) and hydricity of H_2 (76 kcal mol^{-1}) as found here.[8]

5.4 Summary and Future Outlook

To summarize, we discuss two different processes of two-electron reduction of CO_2 by non-noble metal catalysts, namely, CO_2 dissociation and CO_2

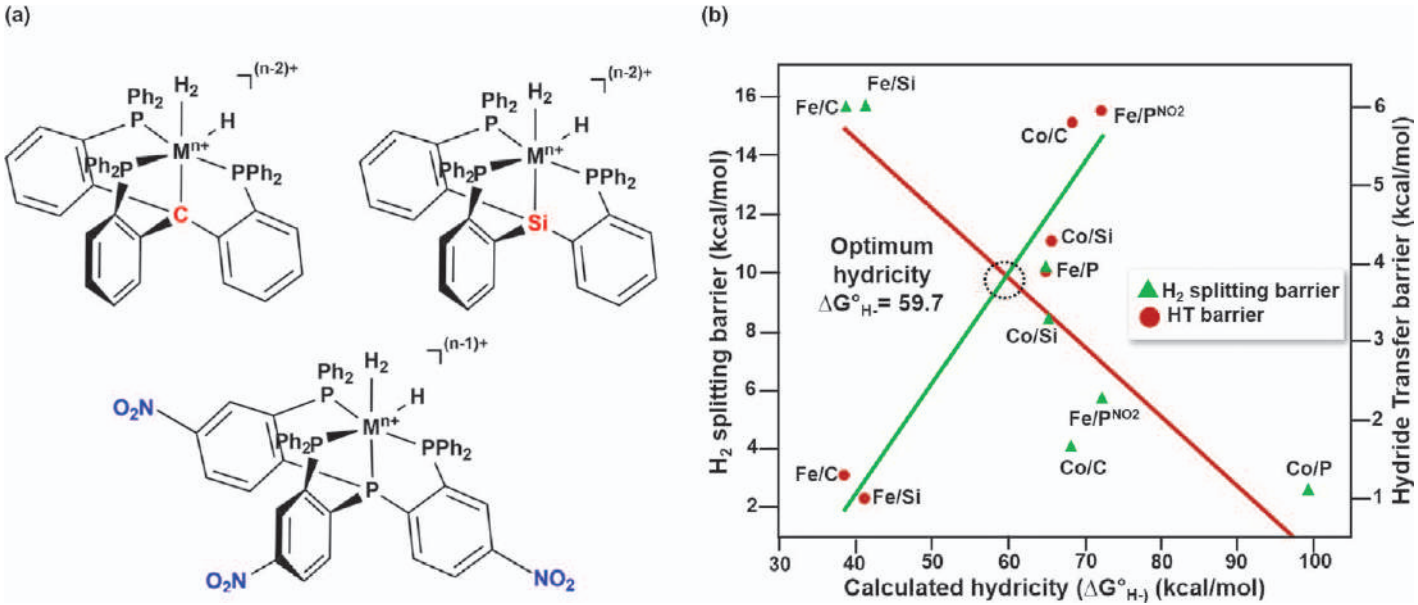

Figure 5.8 (a) Newly designed catalysts based on differential hydricity. (b) Correlation between computed hydricity and barriers of the key steps. Relative free energies are in kcal mol^{-1}.
Reproduced from ref. 8 with permission from John Wiley and Sons, Copyright © 2019 Wiley-VCH Verlag GmbH & Co. KGaA.

hydrogenation. Both are fundamental steps in formation of higher-order alkanes or fuel precursors utilizing CO_2 as a starting material. Our case studies highlight the importance of bifunctional activation for proton-coupled and metal-coupled CO_2 dissociation to CO. In this regard, formation of water or dinuclear-oxo bridged species are crucial for driving forward the C–O bond breaking. CO_2 hydrogenation to formate involves two crucial steps, namely, heterolytic H_2-splitting and hydride transfer, either of which could be the RDS. Here the hydricity or hydride affinity of the *in situ* generated metal–hydride intermediate dictate the nature of the RDS and its barrier. Based on hydricity, we show how promising catalysts could be designed with non-noble metals, to compete with noble-metal analogues. Taking CO_2 hydrogenation as an example, we further highlight how systematic computational investigations could lead to better understanding of the RDS and thereby could be translated into the design and development of more efficient systems. Such theoretical analyses are much reliant on the computational method used. Often the DFT method is preferred to understand reaction mechanisms due to their lower computational cost. However, relative energetics computed by DFT methods are found to have an error of up to 10 kcal mol^{-1}, depending on the choice of the exchange–correlation functional. Hence, it is important to use wavefunction based highly-correlated *ab initio* approaches to compute the relative energetics and more reliably determine the RDS. Calculations with DLPNO-CCSD(T) can furnish chemical accuracy in the order of $\sim$2 kcal mol^{-1} and are particularly helpful in predicting reliable potential energy surfaces. Thus, this theory could be utilized for better understanding of the catalytic steps which open up the possibility of discovery of *in silico* designed *3d* transition metal catalysts.

References

1. A. M. Appel, J. E. Bercaw, A. B. Bocarsly, H. Dobbek, D. L. DuBois, M. Dupuis, J. G. Ferry, E. Fujita, R. Hille, P. J. A. Kenis, C. A. Kerfeld, R. H. Morris, C. H. F. Peden, A. R. Portis, S. W. Ragsdale, T. B. Rauchfuss, J. N. H. Reek, L. C. Seefeldt, R. K. Thauer and G. L. Waldrop, *Chem. Rev.*, 2013, **113**, 6621.
2. S. Solomon, G.-K. Plattner, R. Knutti and P. Friedlingstein, *Proc. Natl. Acad. Sci. U. S. A.*, 2009, **106**, 1704.
3. L. Wu, L. Q. Liu, I. Fleischer, R. Jackstell and M. Beller, *Nat. Commun.*, 2014, **5**, 3091.
4. Y. Li, X. Cui, K. Dong, K. Jung and M. Beller, *ACS Catal.*, 2017, **7**, 1077.
5. H. Schönherr and T. Cernak, *Angew. Chem., Int. Ed.*, 2013, **52**, 12256.
6. B. Mondal, J. Song, F. Neese and S. Ye, *Curr. Opin. Chem. Biol.*, 2015, **25**, 103.
7. R. Francke, B. Schille and M. Roemelt, *Chem. Rev.*, 2018, **118**, 4631.
8. B. Mondal, F. Neese and S. Ye, Computational Insights into Chemical Reactivity and Road to Catalyst Design: The Paradigm of CO_2

Hydrogenation, *Non-Noble Metal Catalysis: Molecular Approaches and Reactions*, Wiley-VcH, 2019, pp. 33–48.
9. M. Drees, M. Cokoja and F. E. Kühn, *ChemCatChem*, 2012, **4**, 1703.
10. D. J. Darensbourg and A. D. Yeung, *Polym. Chem.*, 2014, **5**, 3949.
11. B. Mondal, F. Neese and S. Ye, *Inorg. Chem.*, 2015, **54**, 7192.
12. B. Mondal, F. Neese and S. Ye, *Inorg. Chem.*, 2016, **55**, 5438.
13. J. Song, E. L. Klein, F. Neese and S. Ye, *Inorg. Chem.*, 2014, **53**, 7500.
14. J. A. Keith and E. A. Carter, *Chem. Sci.*, 2013, **4**, 1490.
15. C.-H. Lim, A. M. Holder and C. B. Musgrave, *J. Am. Chem. Soc.*, 2013, **135**, 142.
16. R. Banerjee, A. Phan, B. Wang, C. Knobler, H. Furukawa, M. O'Keeffe and O. M. Yaghi, *Science*, 2008, **319**, 939.
17. T. Sakakura, J.-C. Choi and H. Yasuda, *Chem. Rev.*, 2007, **107**, 2365.
18. H. Arakawa, M. Aresta, J. N. Armor, M. A. Barteau, E. J. Beckman, A. T. Bell, J. E. Bercaw, C. Creutz, E. Dinjus and D. A. Dixon, *et al.*, *Chem. Rev.*, 2001, **101**, 953.
19. G. W. Coates and D. R. Moore, *Angew. Chem., Int. Ed.*, 2004, **43**, 6618.
20. T. Sakakura and K. Kohno, *Chem. Commun.*, 2009, **11**, 1312.
21. C. Federsel, R. Jackstell and M. Beller, *Angew. Chem., Int. Ed.*, 2010, **49**, 6254.
22. C. Steinlechner and H. Junge, *Angew. Chem., Int. Ed.*, 2018, **57**, 44.
23. G. Menard and D. W. Stephan, *J. Am. Chem. Soc.*, 2010, **132**, 1796.
24. M.-A. Courtemanche, M.-A. Legaré, L. Maron and F.-G. Fontaine, *J. Am. Chem. Soc.*, 2014, **136**, 10708.
25. B. M. Barry, D. A. Dickie, L. J. Murphy, J. A. C. Clyburne and R. A. Kemp, *Inorg. Chem.*, 2013, **52**, 8312.
26. S. N. Riduan, Y. G. Zhang and J. Y. Ying, *Angew. Chem., Int. Ed.*, 2009, **48**, 3322.
27. R. Dobrovetsky and D. W. Stephan, *Angew. Chem., Int. Ed.*, 2013, **52**, 2516.
28. L. Roy, P. M. Zimmerman and A. Paul, *Chem. – Eur. J*, 2011, **17**, 435.
29. L. Roy, B. Ghosh and A. Paul, *J. Phys. Chem. A*, 2017, **121**, 5204.
30. G. Seshadri, C. Lin and A. B. Bocarsly, *J. Electroanal. Chem.*, 1994, **372**, 145.
31. H. Dridi, C. Comminges, C. Morais, J.-C. Meledje, K. B. Kokoh, C. Costentin and J.-M. Savéant, *J. Am. Chem. Soc.*, 2017, **139**, 13922.
32. C. Costentin, J.-M. Savéant and C. Tard, *ACS Energy Lett.*, 2018, **3**, 695.
33. B. Kumar, J. P. Brian, V. Atla, S. Kumari, K. A. Bertram, R. T. White and J. M. Spurgeon, *Catal. Today*, 2016, **270**, 19.
34. R. Kortlever, J. Shen, K. J. P. Schouten, F. Calle-Vallejo and M. T. M. Koper, *J. Phys. Chem. Lett.*, 2015, **6**, 4073.
35. E. E. Benson, C. P. Kubiak, A. J. Sathrum and J. M. Smieja, *Chem. Soc. Rev.*, 2009, **38**, 89.
36. K. W. Frese Jr., *J. Electrochem. Soc.*, 1991, **138**, 3338.
37. D. L. DuBois, *J. Am. Chem. Soc.*, 1987, **109**, 113.
38. H. Ishida, K. Tanaka and T. Tanaka, *Organometallics*, 1987, **6**, 181.

39. J. P. Collin and J. P. Sauvage, *Coord. Chem. Rev.*, 1989, **93**, 245.
40. S. A. Yao, R. E. Ruther, L. H. Zhang, R. A. Franking, R. J. Hamers and J. F. Berry, *J. Am. Chem. Soc.*, 2012, **134**, 15632.
41. X. M. Hu, M. H. Ronne, S. U. Pedersen, T. Skrydstrup and K. Daasbjerg, *Angew. Chem., Int. Ed.*, 2017, **56**, 6468.
42. A. Chapovetsky, T. H. Do, R. Haiges, M. K. Takase and S. C. Marinescu, *J. Am. Chem. Soc.*, 2016, **138**, 5765.
43. L. Roy, M. H. Al-Afyouni, D. E. DeRosha, B. Mondal, I. M. DiMucci, K. M. Lancaster, J. Shearer, E. Bill, W. W. Brennessel, F. Neese, S. Ye and P. L. Holland, *Chem. Sci.*, 2019, **10**, 918.
44. D. A. McQuarrie and J. D. Simon, *Physical Chemistry: A Molecular Approach*, University Science Books, Sausalito, CA, 1997, p. 1190.
45. K. J. Laidler and M. C. King, *J. Phys. Chem.*, 1983, **87**, 2657.
46. M. G. Evans and M. Polanyi, *Trans. Faraday Soc.*, 1938, **34**, 11.
47. M. Sparta and F. Neese, *Chem. Soc. Rev.*, 2014, **43**, 5032.
48. E. S. Wiedner, M. B. Chambers, C. L. Pitman, R. M. Bullock, A. J. M. Miller and A. M. Appel, *Chem. Rev.*, 2016, **116**, 8655.
49. C. J. Curtis, A. Miedaner, W. W. Ellis and D. L. Dubois, *J. Am. Chem. Soc.*, 2002, **124**, 1918.
50. J. T. Muckerman, P. Achord, C. Creutz, D. E. Polyansky and E. Fujita, *Proc. Natl. Acad. Sci. U. S. A.*, 2012, **109**, 15965.
51. C. P. Kelly, C. J. Cramer and D. G. Truhlar, *J. Phys. Chem. B*, 2006, **111**, 408.
52. J. C. Calabrese, T. Herskovitz and J. B. Kinney, *J. Am. Chem. Soc.*, 1983, **105**, 5914.
53. I. Castro-Rodriguez, H. Nakai, L. N. Zakharov, A. L. Rheingold and K. Meyer, *Science*, 2004, **305**, 1757.
54. M. Aresta, C. F. Nobile, V. G. Albano, E. Forni and M. Manassero, *J. Chem. Soc., Chem. Commun.*, 1975, **15**, 636.
55. Y. E. Kim, J. Kim and Y. Lee, *Chem. Commun.*, 2014, **50**, 11458.
56. J. S. Anderson, V. M. Iluc and G. L. Hillhouse, *Inorg. Chem.*, 2010, **49**, 10203.
57. C. Liu, L. Munjanja, T. R. Cundari and A. K. Wilson, *J. Phys. Chem. A*, 2010, **114**, 6207.
58. C. Costentin, S. Drouet, G. Passard, M. Robert and J.-M. Savéant, *J. Am. Chem. Soc.*, 2013, **135**, 9023.
59. J.-H. Jeoung and H. Dobbek, *Science*, 2007, **318**, 1461.
60. B. D. Steffey, C. J. Curtis and D. L. Dubois, *Organometallics*, 1995, **14**, 4937.
61. J. D. Froehlich and C. P. Kubiak, *Inorg. Chem.*, 2012, **51**, 3932.
62. J.-M. Savéant, *Chem. Rev.*, 2008, **108**, 2348.
63. J. P. Collin, A. Jouaiti and J. P. Sauvage, *Inorg. Chem.*, 1988, **27**, 1986.
64. M. Beley, J. P. Collin, R. Ruppert and J. P. Sauvage, *J. Am. Chem. Soc.*, 1986, **108**, 7461.
65. G. B. Balazs and F. C. Anson, *J. Electroanal. Chem.*, 1992, **322**, 325.

66. Y. Inoue, H. Izumida, Y. Sasaki and H. Hashimoto, *Chem. Lett.*, 1976, **5**, 863.
67. S. Klaus, M. W. Lehenmeier, C. E. Anderson and B. Rieger, *Coord. Chem. Rev.*, 2011, **255**, 1460.
68. X.-B. Lu, W.-M. Ren and G.-P. Wu, *Acc. Chem. Res.*, 2012, **45**, 1721.
69. F. Gassner and W. Leitner, *J. Chem. Soc., Chem. Commun.*, 1993, 1465.
70. R. Tanaka, M. Yamashita and K. Nozaki, *J. Am. Chem. Soc.*, 2009, **131**, 14168.
71. G. A. Filonenko, M. P. Conley and C. Copéret, *ACS Catal.*, 2013, **3**, 2522.
72. C.-C. Tai, T. Chang, B. Roller and P. G. Jessop, *Inorg. Chem.*, 2003, **42**, 7340.
73. C. Ziebart, C. Federsel, P. Anbarasan, R. Jackstell, W. Baumann, A. Spannenberg and M. Beller, *J. Am. Chem. Soc.*, 2012, **134**, 20701.
74. M. S. Jeletic, M. T. Mock, A. M. Appel and J. C. Linehan, *J. Am. Chem. Soc.*, 2013, **135**, 11533.
75. S. Ogo, R. Kabe, H. Hayashi, R. Harada and S. Fukuzumi, *Dalton Trans.*, 2006, 4657.
76. M. R. S. G. Ahlquist, *J. Mol. Catal. A: Chem.*, 2010, **324**, 3.

CHAPTER 6

Bridging Homogeneous and Heterogeneous Systems: Atomically Dispersed Metal Atoms in Carbon Matrices for Electrocatalytic CO_2 Reduction

HUI-YUN JEONG,[a,†] MANI BALAMURUGAN,[a,†] CHANG HYUCK CHOI*[b] AND KI TAE NAM*[a]

[a] Department of Materials Science and Engineering, Seoul National University, 1 Gwanak-ro, Gwanak-gu, Seoul 08826, Korea; [b] School of Materials Science and Engineering, Gwangju Institute of Science and Technology (GIST), Gwangju 61005, Republic of Korea
*Email: nkitae@snu.ac.kr; chchoi@gist.ac.kr

6.1 Introduction

The continuous usage of fossil fuel materials as energy and fine chemical sources have raised greenhouse gas emissions leading to global climate change.[1] Current statistics suggest that the level of carbon dioxide will reach up to 800 ppm by the end of this century, and may increase up to 2000 ppm by 2300, which will cause intense temperature increase and ocean acidification.[2,3] To maintain, or even reduce, the CO_2 level in the atmosphere,

[†]These authors contributed equally.

Energy and Environment Series No. 28
Carbon Dioxide Electrochemistry: Homogeneous and Heterogeneous Catalysis
Edited by Marc Robert, Cyrille Costentin and Kim Daasbjerg

Published by the Royal Society of Chemistry, www.rsc.org

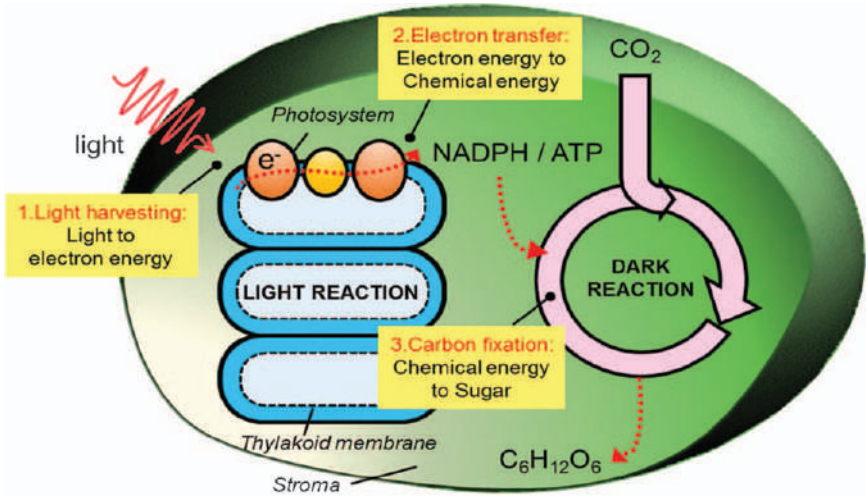

Figure 6.1 Carbon fixation in oxygenic photosynthesis processes. Reproduced from ref. 4, https://dx.doi.org/10.1186%2Fs40580-016-0079-5, under the terms of the CC BY 4.0 license, http://creativecommons.org/licenses/by/4.0/.

shifting towards more sustainable pathways are essential; such as utilization of CO_2 as a feedstock material for chemicals. Interestingly, plants and certain bacteria use photosynthesis (see Figure 6.1) as a key process for the conversion of carbon dioxide and water into sugar and oxygen using sunlight as an energy source ($6CO_2 + 6H_2O + \text{light} \rightarrow C_6H_{12}O_6 + 6O_2$).[4] Inspired from this natural process, various approaches have been suggested, and one among them is the electrochemical conversion of CO_2 to fuels and chemicals.

6.1.1 Bridging Homogeneous and Heterogeneous Catalysts

The electrocatalyst is the most important component in an electrochemical system because it is involved in the chemical transformation of the reactants. Both homogeneous and heterogeneous electrocatalysts have been extensively studied and utilised for the electrochemical CO_2 reduction reaction (eCO_2RR).[5–12] Homogeneous catalysts can exhibit high activity and selectivity towards specific reactions because of their well-defined active sites and tunability by adopting different ligand environments.[5–9] However, they usually exhibit low current density due to their low solubility in aqueous electrolytes, and limited current density caused by the diffusional kinetics (substrates and catalysts) and catalytic kinetics.[13–15] In comparison, only the catalytic kinetics is the dominant factor as the active sites and electrodes are electronically coupled in the heterogeneous catalysts and high current density can be attained easily.[10–13] However, as the

reactions occur at the heterogeneous interface between a solid (catalyst) and liquid (electrolytes), only the atoms at the catalyst surface can be directly involved in the reaction. As a consequence, heterogeneous catalysts have disadvantages with respect to atom utilization. Furthermore, as the surface of the heterogeneous catalysts consists of various kinds of crystallographic surfaces, selective production of desired products is challenging due to the heterogeneity of the active sites.

To increase the atom efficiency and selectivity of catalysts, enormous efforts have been devoted to developing nanostructured electrocatalysts.[16–18] By adopting nanostructures, a high surface area to volume ratio can be obtained and higher catalytic current can be achieved (see Figure 6.2a). By controlling the morphology of nanoparticles, selectivity towards specific CO_2RR products can be enhanced.[19–22] However, even the nanostructured electrode surfaces consist of various kinds of crystallographic phases which can exhibit different activities. Furthermore, it is difficult to identify which surface sites are active for a reaction, especially, in the case of CO_2RR where

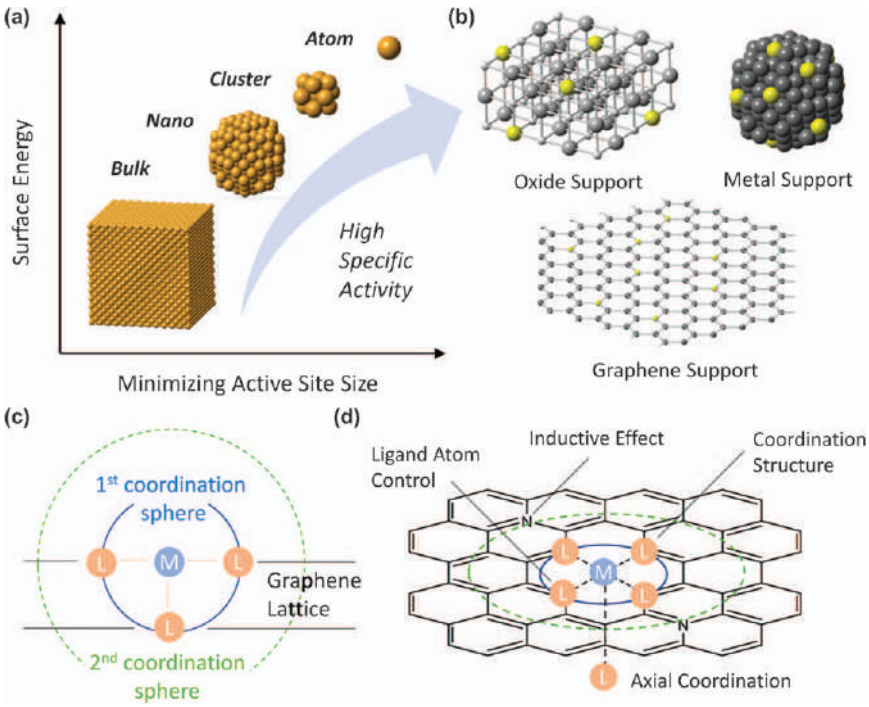

Figure 6.2 (a) Relationship between metal sizes *vs.* surface free energy and specific activity. (b) Schematic representation of atomically-dispersed metal atoms anchored on a metal oxide, metal surface, and graphene. (c) Schematic representation of coordination spheres of metal atoms on a graphene lattice. (d) Most important factors affecting the catalytic ability of the metal center.

various reaction pathways are possible. To achieve both high product selectivity and high current density, it is important to design catalysts which bridge the merits of both homogeneous and heterogeneous catalysts.

The simple way to bridge homogeneous and heterogeneous catalysts is through immobilization of homogeneous catalysts to heterogeneous supports.[23–27] By immobilizing the homogeneous catalysts on the electroconductive supports, such as carbon nanotubes, graphene sheets, or carbon black, the current density can be increased due to the high surface area of nanostructured carbon supports and by decreasing the effect of diffusion limiting current of the catalytic active sites. The other approach is to directly create atomically-defined active sites similar to those of homogeneous catalysts on the surface of heterogeneous catalysts. To make atomically-defined active sites, it is necessary to reduce the size of the active sites from the nano to sub-nano level. In such a context, the ADMAs will be the ultimate size-limit of active sites.

Recently, atomically dispersed metal atom catalysts (ADMCs) emerged as an alternative catalyst to bridge the gap between homogenous and heterogeneous catalysts.[28–32] Various supports such as oxides, metal nanoparticles, and carbon materials can be used to stabilize the ADMAs (see Figure 6.2b). ADMCs can have the merits of two different catalytic systems. With atomically-defined and uniform local structure, ADMAs can exhibit high activity and selectivity similar to that of homogeneous catalysts. Furthermore, ADMAs can maximize the efficiency of metal atom use, which is particularly important for supported noble-metal catalysts. Furthermore, as the active sites can be directly embedded in the electroconductive supports, facile electron transfer from electrodes to active sites and the effect of diffusion limiting current is significantly lowered.[33–35]

6.1.2 Carbon-based Electrocatalysts

The utilization of ADMAs on the catalytic reaction was first introduced in oxide-supported heterogeneous catalysts.[36] In heterogeneous catalysis, it is important to increase the exposed active surface area to increase the partially-coordinated metal atoms which act as the catalytically active sites. By reducing the size of the metal particles, the active surface area can be increased to enhance both the performance and atom efficiencies of such catalysts. In fact, by reducing the size of active sites to the atomic level, catalysts can achieve 100% active-metal atom utilization and high specific activity. Such efficiency of atom utilization is necessary, in particular for rare earth metal porphyrins or noble metal-based catalysts, such as Platinum (Pt), Palladium (Pd), Ruthenium (Ru), Iridium (Ir), *etc.*

However, as the surface free energy of metals increases significantly with decreasing particle size, the use of an appropriate support material becomes indispensable to compensate for the high surface energy and stabilize the small-sized active sites or ADMAs. As the surfaces of oxides are full of oxygen ligands that can strongly coordinate with the metal atoms, oxide materials

have been extensively studied as supports for nano-sized catalysts.[37] In 2011, Qiao *et al.* successfully demonstrated the stabilization of atomically dispersed Pt atoms by iron oxide (FeOx).[36] By atomically dispersing Pt active sites, extremely high atom-efficiency can be achieved and the catalyst shows excellent stability and high activity for CO oxidation. The Pt atoms embedded in the FeOx are suggested to have a high oxidation state because of oxygen coordination, significantly different from that of Pt atoms in clusters or metal surfaces. Density functional theory (DFT) calculations suggested that the partially vacant 5d orbitals of Pt atoms, induced by the electron transfer to FeOx, is responsible for its high catalytic activity.[36] Since this seminal work, numerous ADMAs supported on various supports have been developed across a wide array of catalytic systems.[28,38–42]

The oxide materials are excellent supports for ADMAs, which are suitable for thermal reactions but not suitable as the electrocatalysts for the reduction reactions. In eCO_2RRs, the reactions typically occur at a high reductive potential due to the sluggish kinetics which requires a high overpotential. At this potential, most of the oxide supports can be reduced to zero-valent metal species, resulting in severe structural deformation of supports and weakening of the interaction with the ADMAs. Therefore, desirable support materials, which are not only inert under the reductive potentials but also allow strong interaction with metallic atoms, are needed. Among the suitable candidate materials to support metal atoms, carbon-based materials stand out because they exhibit high stability, good electron conductivity, and large surface areas. In addition, their structures and surface environments can be rationally designed for the stabilization of the atomically dispersed metal catalysts.[43–46]

To achieve strong stabilization of the ADMAs on the surface of carbon-based materials, it is important to understand the interactions between the carbon support and the ADMAs, and how this can affect catalytic activities of metal atoms (see Figure 6.2c). Incorporation of heteroatoms such as oxygen (O), nitrogen (N), phosphorus (P), and sulphur (S) is typically indispensable, not only to activate chemically inert π-conjugated carbon surfaces but also to develop active sites which have similar environments to those of homogeneous catalysts. In particular, nitrogen atoms in carbon lattices can coordinate with metal atoms (M) to form M–Nx active sites. The electrocatalytic activities of various kinds of metal and nitrogen-doped carbon materials have been studied for renewable energy applications, including the hydrogen evolution reaction (HER), the oxygen reduction reaction (ORR), and CO_2RR.[47]

In this chapter, recent advancement in carbon-based ADMCs for CO_2RR will be reviewed, with emphasis on the unique structure of those catalysts in comparison with homogeneous catalysts and biological enzymes. For example, in nature, enzymes catalyse many different reactions with slightly modified local structures and by adopting different local environments to match the required energetics of the reactions. Inspired by the active sites of the enzymes, we endeavoured to understand how the local coordination

structure can affect the activity of metal centres (see Figure 6.2c and d). In Section 2 and 3, the synthetic methodology adopted for preparing ADMCs, and the characterisation methodology utilised for the identification of the local structure, will be discussed. In Section 4, the structure–activity relationship of the ADMCs is discussed by adopting the structure–function strategy used by Nature in various aspects such as M–N4–C and M–Nx–Cy structures, axial ligand coordination, inductive effect as well as the effect of the secondary coordination sphere. In Section 5, the perspectives to expand the catalytic selectivity towards C1 hydrocarbons and C2–Cn products are discussed.

6.2 Preparation of Carbon-based Atomically Dispersed Metal Catalysts

Developing new synthetic methodologies for ADMCs is one of the main research focuses in this field because of the challenging issues related to the fabrication of atomic level dispersion on the carbon support. However, many different methods have been successfully adopted for the synthesis of ADMAs on the carbon support using various precursor molecules. The important methods include atomic layered deposition (ALD), wet chemistry, and high-temperature pyrolysis. Each method has its own merits and demerits in terms of cost and yield of the final product. ALD has a unique ability to deposit the atoms in a well-controlled manner. Wet chemistry is considered to be the most cost-effective method for the synthesis of ADMCs. Pyrolysis is especially beneficial for making carbon materials as the ADMAs-doped carbon materials can be directly prepared by carbonizing various kinds of precursor.

6.2.1 Atomic Layer Deposition

ALD is a vapour phase technique typically used for preparing high-quality conformal thin films on three-dimensional substrates. This technique is a special variant of chemical vapour deposition (CVD), in which gaseous reactants are introduced into the reactor to form the desired products through chemical surface reactions. The sequential and self-limiting nature of the ALD technique offers many advantages such as thickness control with near-atomic precision. Due to these features, ALD has been used to stabilize ADMAs (Pt and Pd, in particular) on 2D carbon materials. For example, ALD with (methylcyclopentadienyl)trimethylplatinum ($MeCpPtMe_3$) and O_2 as the precursors and N_2 as the purging/carrier gas has been used to deposit Pt species from nanoparticle-to-sub-nanometer clusters and atomically-dispersed Pt atoms over (N-doped) graphene.[48,49] The Pt size and site-density can be controlled by adjusting the number of ALD cycles. Atomically-dispersed Pt species with a loading of 2.1 wt% have been obtained after 50 ALD cycles. Despite the controlled ALD process,

diffusion and agglomeration of metal atoms are a risk and likely to occur if the interactions between the atoms and the support are weak, resulting in the failure of their stabilization. This suggests that the selection of optimum supporting materials is crucial for the preparation of atomically-dispersed metal catalysts using the ALD process. As mentioned earlier, the introduction of heteroatoms, such as nitrogen, enhances the interaction between the metal atoms and the graphene support. The grain boundary and edge site of the graphene supports can also provide stabilization sites for metal atoms during the ALD process.[50,51] The synthesis of catalysts with atomically-dispersed Pd active sites by the alternate exposure of palladium hexafluoroacetylacetate ($Pd(hfac)_2$) and formalin precursors on anchor sites generated by the oxidation of graphene in acid, and its subsequent thermal deoxygenation prior to the ALD process, has been reported.[52] Although ALD is an efficient method to achieve atomic-dispersion of active metal sites, its application is limited by sluggish kinetics and the use of expensive metal precursors.

6.2.2 Wet Chemistry Process

6.2.2.1 Conventional Wet Impregnation Method

In heterogeneous catalysis, wet impregnation is one of the most widely used and simplest method to prepare supported metal catalysts. In this process, a solid support is brought into contact with a liquid solvent containing the active metal precursors to be deposited on the solid surface. After a certain time, the liquid solvent is removed by drying/evaporation and the solid compound is separated. The active metal precursors deposited on the support are then transferred to active metal species by H_2 reduction at a relatively high temperature ($<500\ ^\circ C$, typically 200–300 $^\circ C$). Since active metal precursors are dissolved as ion species in the solvent, the purpose of the process is to bind those ions strongly on the support and to maintain a good dispersion during the post-treatments and reactions. However, since the carbon surface is chemically inert, the stable isolation of metal atoms/ions is highly limited to very low metal loadings of <0.5 wt%. For example, Pd/carbon nanofibers, which are prepared by impregnation with an aqueous palladium dichloride ($PdCl_2$) solution, and the subsequent H_2 reduction at 250 $^\circ C$, have a maximum Pd atom loading of 0.2 wt%.[53] To increase the metal loading as stable atomic species, carbon supports with a large surface area and strong anchoring sites are required. Among the various kinds of carbonaceous material, zeolite-templated carbon (ZTC) is a promising candidate for ADMAs stabilization. ZTC consists of highly curved three-dimensional networks of graphene nanoribbons with abundant edge sites and has a microporous structure and extremely high surface area of $>2500\ m^2\,g^{-1}$. Owing to its unique carbon structure, ZTC can be doped with a large amount of S (17 wt%) to effectively stabilize Pt atoms (5 wt%).[54]

6.2.2.2 In Situ *Generation of Atomically Dispersed Metal Sites*

The wet impregnation method typically involves a H_2 reduction process at high temperatures. Another suggested way to stabilize ADMAs on carbon supports is to attach the metal atoms on N-doped carbon materials during CO_2RRs. Under the reductive conditions, metal ions are preferentially adsorbed on the electron-rich N sites, thus inducing metal-N interactions. The feasibility of the *in situ* generation of metal active sites on carbon was demonstrated in a CO_2RR system.[55] In electrolytes containing iron ions, the applied potential for the CO_2RR leads to the selective adsorption of iron ions from the electrolyte on the electron-rich N sites, resulting in the formation of highly dispersed metal-N sites. It has been confirmed that the *in situ* generation of atomically-dispersed metal species can also occur in the presence of other metal impurities such as nickel (Ni), zinc (Zn) and copper (Cu). The CO_2RR activity of these catalysts depends on the type of metal impurity, and the *in situ* generated metal–N sites improve the durability of the resulting catalysts. Nevertheless, further research is required to improve and validate this method.

6.2.3 Pyrolysis at High Temperature

Pyrolysis methods have been extensively used for the preparation of carbon materials with ADMAs by thermal decomposition of a mixture of precursors at elevated temperatures in a controlled atmosphere (Ar, N_2, NH_3, or H_2). In general, the stabilization of transition-metal atoms/ions on carbonaceous supports is achieved by the ligation of precursor metal ions with heteroatom moieties (typically nitrogen) in the presence of carbon materials or their precursors. This is followed by the subsequent pyrolysis of the precursor mixture at temperatures $>800\ ^{\circ}C$ in the presence of an inert gas. Since this method involves the impregnation of metal and nitrogen precursors on carbon or carbon precursors, this method can be considered as a part of the wet impregnation process. However, this method involves a pyrolysis step, which requires a temperature higher than that required for H_2-treatment or calcination during the wet impregnation process. Furthermore, the wet chemical mixing process is not a prerequisite, *i.e.* physical mixing of precursors under dry conditions is also possible before pyrolysis.[56] The objective of the pyrolysis step is the simultaneous introduction of nitrogen moieties and the anchoring of atomically dispersed metal species within the graphitic network, resulting in the formation of $M–N_x$ moieties on the support. To improve the physicochemical properties of atomically dispersed metal sites, additional pyrolysis steps such as pyrolysis under an NH_3 atmosphere have been used. Pyrolysis at high temperatures can induce agglomeration of transition metal atoms, resulting in the formation of bulk metal species. These bulk metal species can be easily removed by post-acid treatment owing to their instability in acidic environments.[57] Unfortunately, all the bulk metal species exposed to the acid solution cannot be completely eliminated by the post-treatment, and the acid treatment introduces

unintended oxygen functionalities on the carbon surface. Hence, many different methods have been put forward to develop an efficient pyrolysis process for producing atomically-dispersed metal catalysts with effective anchoring sites and minimum agglomerations.

6.2.3.1 Carbonization of Metal-doped Polymer Complexes

This method involves the formation of polymers with abundant functional groups and metal ions coordinated with them. Then, carbonaceous materials with metal active sites were produced *via* high-temperature pyrolysis. Synthesis of the catalysts from polymer precursors is highly advantageous because it offers mass production using inexpensive precursors. Polymers with low vapour pressure like polyacrylonitrile, polyaniline, and polypyrrole are well-known precursors for preparing carbon materials.[58–61] Also, as these polymers have a large number of anchoring N-sites for the metal atoms, they can serve as both the carbon and nitrogen sources for the ADMAs.[62–66] Atomically-dispersed metal nitrogen carbon can be synthesized by formamide condensation followed by a pyrolysis method.[67] Carbon nitride also allows the atomic dispersion of dense metal sites stabilized by multiple nitrogen ligands.[68,69] Since polymers exhibit good adhesivity with other materials, activated carbon, carbon nanotubes, or graphene oxides can be introduced during the polymerization process to increase the surface area and electric conductivity of the resulting catalysts.[70–72]

6.2.3.2 Carbonization of Ionic Liquids

Most organic molecules with low molecular weight are usually evaporated or decomposed to gaseous products during high-temperature carbonization. However, ionic liquids with low-vapour-pressure can endure and yield carbonaceous materials under harsh carbonization conditions.[73] Lee *et al.* successfully demonstrated that the nitrogen-rich porous carbons can be produced from ionic liquids with cross-linkable nitrile-functionalized cations (1-cyanomethyl-3-methylimidazolium ($[MCNIm]^+$) and 1,3-bis(cyanomethyl)imidazolium ($[BCNIm]^+$)).[74] Similarly, Paraknowitsch *et al.* prepared nitrogen-rich carbon by direct carbonization of dicyanamide-anion-based ionic liquids.[75] These ionic liquids possess high nitrogen contents, so carbon materials with high nitrogen contents can be obtained.[76] As these precursors are liquids at room temperature, they are ideal candidates for making nanomaterials with various geometries.[75] Furthermore, metal salts can be easily dissolved in ionic liquids to produce nitrogen-coordinated metal active sites after the carbonization process.[77]

6.2.3.3 Carbonization of Metal–Organic Frameworks

Metal–organic frameworks (MOFs), in particular zeolitic imidazolate frameworks (ZIFs), are considered as promising platforms for stabilizing

atomically-dispersed metal sites on N-doped carbon substrates. ZIFs consisting of tetrahedral-coordinated transition metal ions [*e.g.*, Fe, Co (cobalt), Cu, Zn] connected by imidazolate linkers is an all-in-one platform providing atomically-dispersed metal sites and carbon/nitrogen sources. Their pyrolysis leads to the formation of carbon-based materials with $M–N_x$ active species. Synthesis of atomically-dispersed metal catalysts using MOF substrates offers some potential advantages. First, the size, surface area, and porosity of the pyrolyzed carbon can be tailored by controlling the synthesis conditions of MOFs. Second, the target metals can be easily and uniformly introduced in the metal nodes, ligands, or MOF pores. Besides, the tuneable carbon structure, metal type, abundant node sites and nitrogen content from imidazolate linkers can effectively anchor the metal at an atomic level even after the pyrolysis. Furthermore, when zinc is used to construct the ZIF structure, the pyrolysis at temperatures >900 °C leads to the evaporation of zinc because of its lower boiling temperature of 907 °C. This introduces microporous structures in the carbon support which is advantageous for increasing the surface area of the resulting catalysts and for stabilizing the atomic metal species. This approach has been further developed to synthesize bimetallic catalysts and to prepare structurally more complex carbon materials.[78–80] The target metal ions are introduced during the initial MOF synthesis step, or by mixing the metal precursors with the MOF prior to the pyrolysis. For the latter case, other nitrogen sources (*e.g.*, phenanthroline) are typically introduced into the metal precursor/MOF mixture to increase the number of anchoring sites for metal atoms.

6.2.3.4 Other Methods

The silica-protective-layer-assisted approach also offers preferential generation of atomically-dispersed metal catalysts while suppressing the formation of bulk metal particles.[81] This method involves the adsorption of metal porphyrin precursors on carbon substrates, silica layer over-coating, pyrolysis, and subsequent silica layer etching. During the pyrolysis, the silica layer prevents the sintering of metal species to their bulk form.

Unlike conventional pyrolysis methods, thermal emitting and the subsequent trapping of metal atoms uses bulk metallic foams or nets as the metal precursors for the preparation of atomically-dispersed metal catalysts. In this method, the metal, nitrogen, and carbon precursors are not homogenized before the pyrolysis. However, they are separately introduced into the reactor. For example, the carbon precursor (*e.g.*, graphite oxide and ZIF-8) is loaded on one side of a quartz boat and a piece of a bulk metal is located at the other side.[82] The quartz boat is placed at the middle of a furnace chamber and heated for pyrolysis under a continuous flow of ammonia gas. During the pyrolysis, ammonia coordinates with the bulk metal and forms volatile $M(NH_3)_x$ species owing to the strong Lewis acid–base interactions. After the transportation of the $M(NH_3)_x$ species under the ammonia atmosphere, they are trapped at the defect sites on the carbon

support, producing isolated metal sites. As alternatives to the toxic ammonia gas, solid-phase nitrogen sources such as dicyandiamide can be used.[83] Except for its *in situ* generation of gaseous reactants, this technique is similar to CVD.

6.2.4 Graphite-conjugated Catalysts

To achieve the atomic level decoration of the molecular systems on the graphitic substrate, a molecular conjugation strategy has been successfully used, which enhances the catalytic activity of the molecular systems.[33] It has been established that the level of electronic coupling of the molecular system with the electrode surface plays an important role in maximizing the activity of the covalently linked molecular systems. The edge sites of the graphitic carbon substrate can have acidic and *o*-quinone functionalities, which can be utilised to conjugate the molecular systems with amine functionalities. The covalent linking of the molecular systems with the graphitic substrate can enhance the electronic coupling of the substrate with the catalytic sites to boost the activity of the system. Such a strong electronic coupling of the redox sites with the substrate is limited in the molecular systems dissolved in the solvents due to the distance between the substrate and redox sites, which is separated by the solvents.[34,35,84]

6.3 Characterization of Atomically-dispersed Metal Catalysts

The local structures of ADMAs are strongly related to their electrocatalytic properties. In order to design high-performing catalysts with atomically-dispersed active metal moieties, a better understanding of their morphological/electronic structures and coordination is imperative. Unfortunately, this information cannot be successfully provided by conventional characterization tools such as X-ray diffraction (XRD), X-ray photoelectron spectroscopy (XPS), scanning electron microscopy (SEM), and Raman spectroscopy. Hence, various *ex/in situ* techniques have been developed to examine the local structures of atomically-dispersed metal sites. Complementary analyses with other tools should be adopted for comprehensive identification of the active sites.

6.3.1 Identification of Atomically-dispersed Metal Atoms

The presence of isolated metal sites on carbon has been investigated using a combination of aberration-corrected high-angle-annular-dark-field scanning transmission electron microscopy (HAADF-STEM) and X-ray absorption fine structure (XAFS) spectroscopy. Furthermore, conventional spectroscopy techniques, such as infrared (IR) and nuclear magnetic resonance (NMR) spectroscopies are very useful to investigate how the substrate interacts with

active sites. In the case of iron active sites, Mössbauer spectroscopy is also useful to understand the spin state of metal sites.

6.3.1.1 Electron Microscopy Techniques

Among the various kinds of characterization methods, direct imaging of ADMAs on supports is the most convincing and intuitive approach to prove their presence. The direct observation of ADMAs was achieved using electron microscopy techniques due to an improvement of their resolution to the angstrom scale. HAADF-STEM is a powerful tool to examine ADMAs on carbon supports. As the HAADF detector collects electrons that undergo Rutherford scattering, images can be acquired at an intensity that is approximately proportional to the atomic number of the scattering atoms (Z-contrast).[85–87] In particular, ADMAs on carbon supports can be easily distinguished by the HAADF-STEM analysis because of the significant difference in atomic numbers between metal and carbon atoms. As shown in Figure 6.3a, bright spots in aberration-corrected HAADF-STEM images correspond to isolated metal atoms.[88] In addition, it was observed that the metal atoms are stabilized by the vacancy site in the graphene lattices (see Figure 6.3b and c).

Another benefit of STEM is that it can be simultaneously combined with techniques such as electron energy-loss spectroscopy (EELS) and energy-dispersive X-ray spectroscopy (EDS). Using simultaneous spectroscopy measurements, not only the metal atoms are distinguished by Z contrast, but also the local electronic states of the metal atoms and bonding configurations can be characterized.[89–92]

From HAADF-STEM images, it is difficult to distinguish whether the iron atoms in graphene lattices are coordinated with carbon atoms (Fe@DV) or nitrogen atoms (Fe + 4N) (see Figure 6.3d and e).[91] From measuring with EELS, one can clearly see the characteristic peak around 410 eV which indicates the presence of nitrogen atoms around iron atoms (see Figure 6.3f). Furthermore, the change in the fine structure of the L_{23} edge of the transition metal in the spectrum can also be noticed. By comparing L_3/L_2 intensity ratios, it can be shown that the Fe@DV retains the high-spin state ($L_3/L_2 \approx 3.38$), while Fe + 4N shows a significantly smaller value ($L_3/L_2 \approx 1.91$) signifying the lower oxidation state than the Fe@DV site. In other words, the lone pair of pyridinic-like nitrogen can interact with iron atoms at Fe + 4N and electrons can be transferred from the nitrogen to the iron atoms.[91]

6.3.1.2 Spectroscopy Techniques

Considering that the activity and stability of ADMAs on carbon supports are greatly affected by how the metal atoms are coordinated with the carbon supports, it is important to study the metal–carbon support interaction. X-ray absorption spectroscopy (XAS) is one of the few techniques that can investigate the metal–support interaction in detail. XAS is highly

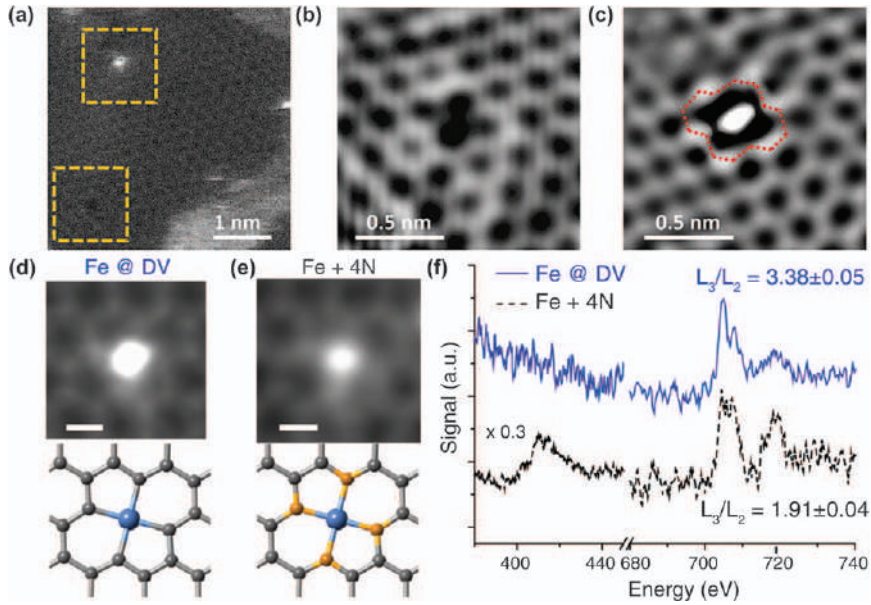

Figure 6.3 Electron microscopic characterisation: (a) HADDF–STEM image of atomically-dispersed nickel atoms on defected graphene. (b) Zoomed-in view of a di-vacancy site on graphene. (c) Zoomed-in view of nickel trapped in a di-vacancy site. (d) HADDF–STEM images of iron at di-valent sites with a simulated atomic model. (e) HADDF–STEM images of iron at 4N sites with a simulated atomic model. (f) Comparison of the electron energy loss spectra of iron at di-valent and 4N sites.
Reproduced from ref. 88 with permission from Elsevier, Copyright 2017, and from ref. 91, http://dx.doi.org/10.1103/PhysRevLett.115.206803, with permission from the American Physical Society, Copyright 2015.

sensitive to the oxidation state, bond length, coordination number, and coordination structure. Hence, this technique provides a practical and relatively simple approach to examine the chemical state and local geometric structure of active sites. In general, XAS is implemented at a synchrotron radiation facility with a tuneable and intense X-ray source. As the energy of X-ray radiation is scanning through the binding energy regime of a core-level electron, a sudden increase of absorption appears when X-rays have sufficient energy to eject a core electron from an atom. This sharp increase in absorption is called the absorption edge. As the core electron binding energy is strongly dependent on the atomic number, each atom has a different absorption edge position.

However, the absorption edge is not just a simple discontinuous increase in absorption. There are typically two different regimes on an XAS spectrum. The structure in the vicinity of the absorption edge is referred to as X-ray absorption near-edge structure (XANES). The potential from 50 to 1000 eV above the edge is referred to as the extended X-ray absorption fine structure (EXAFS).[93] XANES and EXAFS complement each other and XANES spectra are

inevitably measured when measuring EXAFS spectra. XANES spectra can provide information about the oxidation state of the absorbing atom and the coordination structure. EXAFS can provide information on the radial distribution of atoms around the absorbing metal atom.[93]

Usually, XANES spectra are much easier to measure than EXAFS spectra due to their higher intensities. However, the complexity of XANES spectra makes it difficult to carry out anything but a qualitative analysis. The absorption edge energy of XANES is sensitive to the oxidation state of the metal atoms and very useful for comparing the oxidation state with metal active sites. As higher X-ray energy is required to eject a core electron from a metal centre with a higher oxidation state, linear relationships between the absorption edge energy and the oxidation state have been observed.[94] In addition, several features in the XANES spectra can explain specific features in the electronic structure of X-ray absorbing metal centres. For example, several specific features can be seen in the XANES spectra of iron and nitrogen-doped carbon materials (see Figure 6.4a).[95] The pre-edge peak A was assigned to a dipole forbidden 1s → 3d transition.[96] The second peak B

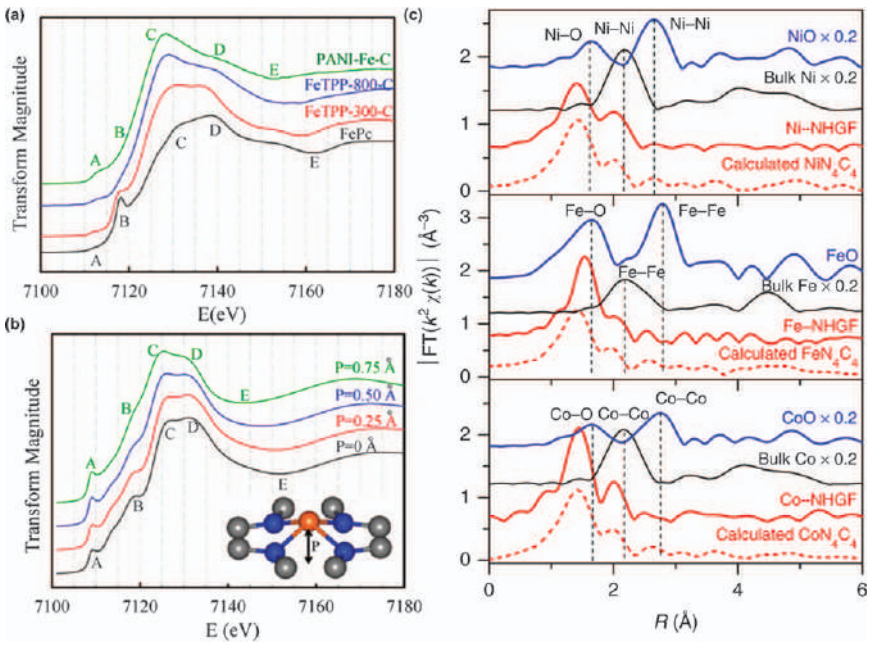

Figure 6.4 X-ray absorption spectroscopy: (a) XANES spectra of various iron materials. (b) Calculated XANES spectra of the Fe–N4–C8 model (inset) with different iron atom displacements. (c) Fourier transformed K-edge EXAFS of atomically-dispersed metal centres (Ni, Fe, Co) with their reference samples with calculated EXAFS spectra.
Reproduced from ref. 95 with permission from American Chemical Society, Copyright 2015, and from ref. 99 with permission from Springer Nature, Copyright 2018.

can be assigned to the $1s \rightarrow 4p_z$ transition which is a fingerprint of the compounds with D_{4h} symmetry.[96–98] Peak C can be attributed to the $1s \rightarrow 4p_{xy}$ transition, and peak D can be attributed to the multiple scattering processes of the metal centres.[95] Finally, the structural change of metal centres can be estimated with the computational approaches to XANES analysis (see Figure 6.4b).

XAFS can provide information about how metal atoms are dispersed on the carbon supports. By comparing EXAFS spectra with those of other related materials such as metal or metal oxide, the co-existence/absence of bulk metal particles can be revealed (see Figure 6.4c).[99] Furthermore, EXAFS fitting analysis can provide quantitative information on the average coordination number of metal atoms with surrounding atoms and the average interatomic distance between them.[99] However, it is difficult to attribute an EXAFS oscillation to a specific structural feature of the metal centre since EXAFS spectra are spectroscopically detected scattering patterns. The structure of the metal centre should be analysed using both XANES and EXAFS.

Mössbauer spectroscopy is a powerful tool to investigate the electronic structure of iron (or other selected elements) containing coordination complexes and materials.[100] The basic principles rely on the 'Mössbauer effect' which describes a nucleus that can emit or absorb gamma rays without loss of energy to a nuclear recoil. Using this method, the transitions between the nuclear ground state ($I_g = 1/2$) to the excited state ($I_e = 3/2$) can be measured. Importantly, the oxidation and spin state of a particular metal centre and coordination environment can be identified using Mössbauer spectroscopy because of the interaction of electron spin with magnetic nuclei, called hyperfine splitting.[95,100–102]

From the Mössbauer spectra, which usually consists of doublet signals, two important kinds of information can be obtained, *i.e.* quadrupole splitting (ΔE_Q) and isomer shift (δ_{iso}). The information on valence state and ligand contribution can be obtained from the ΔE_Q. The δ_{iso} parameter measures the s-electron density around the nucleus and provides information on the oxidation state and spin states of the metal centre due to the shielding effect of the d-electrons population. The nature of the atomically-dispersed iron centre can be identified by numerous doublet signals obtained from the Mössbauer spectra corresponding to different iron local structures with different spin states (see Figure 6.5). The quantification of each iron site can be carried out by peak analysis and the results are correlated with the electrocatalytic performance of atomically-dispersed iron catalysts to identify the active site structure (see Figure 6.5a – c).

6.3.2 *In Situ/Operando* Measurement Techniques

In situ/operando characterizations provide the fundamental information about the molecular structure–activity/selectivity/stability relationships of

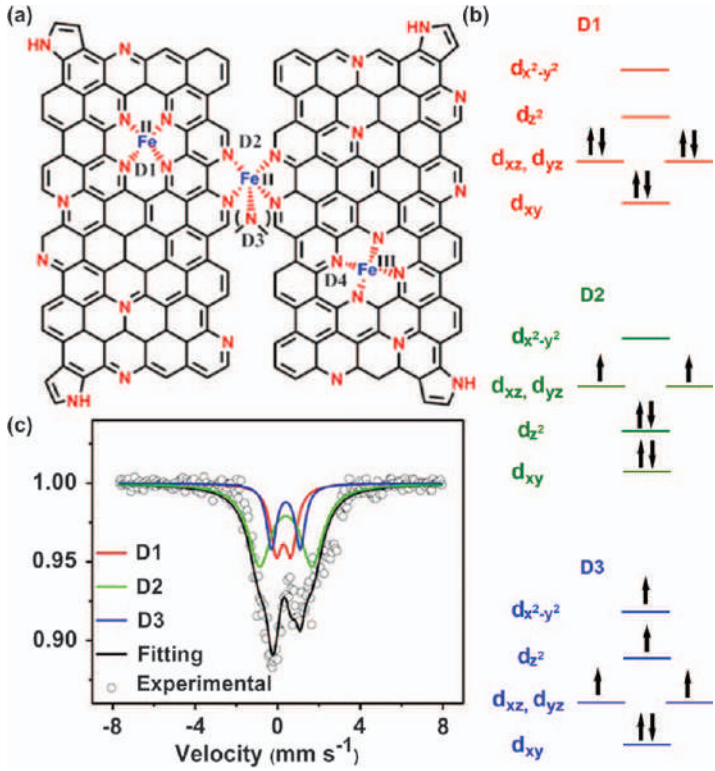

Figure 6.5 Mössbauer spectral characterisation. (a) Schematic representation of various kinds of iron sites at graphene. (b) Various spin-states of the Fe(II) center. (c) Mössbauer spectral signals for the different spin-states of the iron center.
Reproduced from ref. 101 with permission from Royal Society of Chemistry, and from ref. 102 with permission from the National Academy of Sciences, Copyright 2018.

atomically-dispersed metal catalysts under realistic operating conditions. These methods can identify the nature of catalytic sites and can even monitor the dynamic behaviour of the active sites at the atomic scale during the reactions. *In situ/operando* TEM,[103,104] Fourier-transform IR spectroscopy,[105,106] and ambient-pressure XPS (APXPS)[107,108] have been developed for the direct observation of the dynamic process of stabilization of metal atoms, to confirm the existence of isolated metal atoms, and to examine the surface chemistry of atomically-dispersed metal catalysts, respectively. In this section, we highlight *in situ/operando* characterization methods based on XAS and online mass spectroscopy, which provide key information about the nature of active species and structural dependence of the activity/selectivity/stability of atomically-dispersed metal catalysts.

6.3.2.1 In Situ *X-ray Absorption Spectroscopy*

In situ/operando XAS has been extensively used to study electrocatalysis on ADMCs. For example, nickel atoms on N-doped carbon catalysts were suggested to have a Ni(I) valence state during CO_2RR through an *in situ* XANES study.[109] The change in Ni–N bond length with CO_2 adsorption on active nickel moieties can be examined by means of *in situ* EXAFS. The combination of *in situ* XANES and EXAFS spectra enables the analysis of the role of atomically-dispersed Fe(II) sites or polyatomic iron sites in improving the faradaic efficiency (FE) of the catalysts and their selectivity towards acetic acid.[110] Furthermore, *in situ* XAFS studies with cobalt phthalocyanine (CoPc) catalysts revealed insignificant modifications in the spectra at CO_2RR conditions, showing a stable presence of Co(II) moieties at the highly reduced potentials.[111] These observations highlight the advantages of the *in situ/operando* XAFS techniques for monitoring changes in the geometric structure and electronic environment at the atomic scale during the reactions. However, the complexity of the reaction mechanisms and the heterogeneity of active species can induce large variations in the data interpretation. Since the variations in the XAFS spectra of ADMAs may originate from very complex changes in their valance states, coordination environments, and electronic states, other *ex/in situ* methods are typically required to obtain a deeper insight into the complex electrocatalysis mechanism of atomically dispersed metal catalysts.

6.3.2.2 *Online Electrochemical Mass Spectrometry*

Identifying reaction intermediates and products is highly important to understand the electrocatalytic reaction mechanism of atomically-dispersed metal catalysts. Since the intermediates and products stabilized at a certain potential are not identical, their identification on the basis of potential changes can elucidate the underlying reaction mechanism. Online differential electrochemical mass spectroscopy (DEMS) is a powerful tool to analyse gas and volatile intermediates and products obtained during electrochemical reactions. Several designs of the DEMS measurements have been suggested.[112–115] However, the electrochemical cell connected with the mass spectrometer typically consists of highly porous hydrophobic membranes, at which the gas and volatile species are separated from the liquid electrolyte and transported to the mass spectrometer. In principle, both qualitative and quantitative measurements are possible. On the other hand, metal dissolution during the electrochemical measurements can be observed when the scanning flow cell is connected to an inductively coupled plasma mass spectrometer (ICP–MS).[116,117] This technique provides information about the catalytic stability, *i.e.* the dissolution of active species. An identical tool with an atomic/optical emission spectrometry (AES/OES) detector can also be used for this purpose. However, online ICP–MS provides much more sensitive resolution.

6.4 Structure and Activity of Atomically-dispersed Metal Catalysts

In this section, we attempt to highlight how the coordination structure of the ADMAs decorated on carbon materials play crucial roles in determining their CO_2RR activities using the available experimental and DFT studies and by correlating with the strategy used by natural enzymes. To correlate the structure–activity relationship of the ADMAs, we have also used the structure–function versatility of the enzymes in this section. In our opinion, this approach may enhance the understanding further, and may help in finding the missing structural aspects to improve the activity and selectivity of the ADMAs. In nature, many different enzymes carry out various kinds of extraordinary chemical reactions. The functions of enzymes are primarily dependent on the local electronic structures of the active sites. Inspired by natural enzymes, various kinds of molecular catalysts have been developed to understand and mimic the function of enzymes. The type and number of ligand donors coordinated with the metal center play crucial roles in determining the efficiency and activity of catalysts. Therefore, understanding the key factors such as coordination number and asymmetry in local structure is crucial to improve the catalytic performances.

Similar to the homogeneous system, the local coordination structure plays an important role in the heterogeneous counterpart. For example, in metal nanoparticles, generalised coordination number (GCN) can be used as a descriptor for the catalytic activity. The GCN which can be varied based on the crystal facet and size of the nanoparticle directly affects the catalytic activity. Previously, it has been studied thoroughly for platinum nanoparticles catalyzing CO oxidation.[118] In addition, DFT calculations have been performed to study the effect of GCN in CO_2 reduction catalyzed on a copper surface. It was suggested that an average coordination number of 7.5 is appropriate for high CO_2 reduction activity.[119]

In particular, supported active sites are beneficial for controlling the coordination number. As the active metal atoms are stabilized by the surface ligands on the supports, they can be designed to possess different coordination numbers by introducing metal atomic clusters on the support surface. In the previous study, copper ad-particles were formed on the metallic copper surface to acquire a high density of low coordinated copper active sites (see Figure 6.6a).[120] The low-coordinated surface sites increased both the adsorption of CO and stabilized two-carbon intermediates to promote the generation of propanol as a product. Furthermore, the surface adatoms can affect the lattice structure of the inactive supports to give unexpected catalytic activity. For example, photoexcitation of atomically-doped copper on titanium dioxide (TiO_2) undergo structural reorganisation on the TiO_2 surface leading to the reversible photocatalytic ability of the system towards HER (see Figure 6.6b).[121]

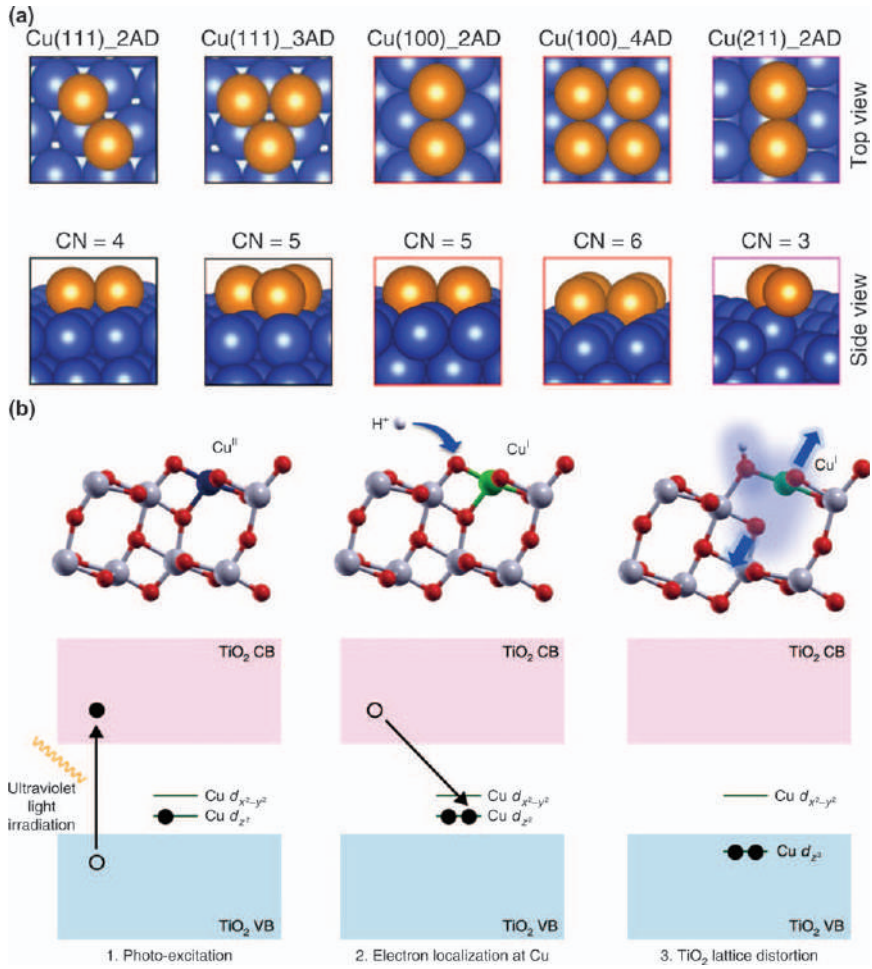

Figure 6.6 Importance of coordination number: (a) Various coordination structures of copper adparticles on a copper crystal. (b) Schematics of the generation of local structural distortion during the photo excitation process of atomically-dispersed copper atoms on TiO_2.
Reproduced from ref. 120, https://doi.org/10.1038/s41467-018-07032-0, under the terms of the CC BY 4.0 license, http://creativecommons.org/licenses/by/4.0/, and from ref. 121 with permission from Springer Nature, Copyright 2019.

The understanding of the structure–activity relationship of ADMAs is particularly interesting as they can bridge the structural tunability of homogeneous catalysts and the stability of heterogeneous catalysts. Various ADMCs having different metals with various local coordination structure have been developed as catalysts for CO_2RR.[122–124] Below, we review the CO_2RR activities of individual catalysts and discuss how differences in the local structure and secondary coordination sphere of ADMAs can affect the activities.

6.4.1 Structure of Dispersed Metal Atoms on Carbon Supports

To understand the activity of ADMAs, it is important to know how the metal atoms can be stabilized by carbon supports as they determine the coordination structure of ADMAs. Since atomically-dispersed active metal moieties are highly unstable and prone to agglomerate, the stabilization of ADMAs with specific sites on the supporting materials is important. The basal plane surfaces of defect-free pristine graphene consist of sp^2 carbon. Three possible metal adsorption sites are suggested: on top of a carbon atom (T), on the bridge of a C–C bond (B), and at the centre of hollow hexagons sites (H) (see Figure 6.7a).[125] Among them, H sites are considered as the most stable sites for the ADMAs.[125–127]

To investigate if the pristine graphene layers can effectively stabilize the ADMAs, the binding energies of selected metal atoms on the H sites were calculated.[128] The adsorption energies of metal atoms on defect-free H sites are calculated to be $0.2 - 1.5$ eV. The adsorption energies are lower than the corresponding cohesive energies of the transition metal (TM) atoms.[129] As a result, the metal atoms on the pristine graphene surfaces are prone to

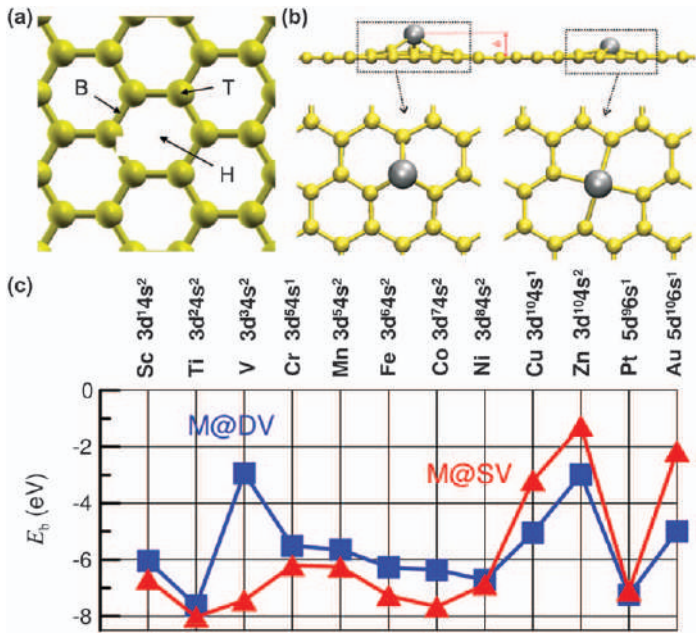

Figure 6.7 (a) Hollow (H), bridge (B), and top (T) metal adsorption sites on graphene. (b) Typical atomic configurations of TM atoms adsorbed on SV and DV in a graphene sheet. (c) Binding energies of selected metal atoms at SV and DV sites.
Reproduced from ref. 125 and ref. 130 with permission from the American Physical Society, Copyright 2008 and 2009.

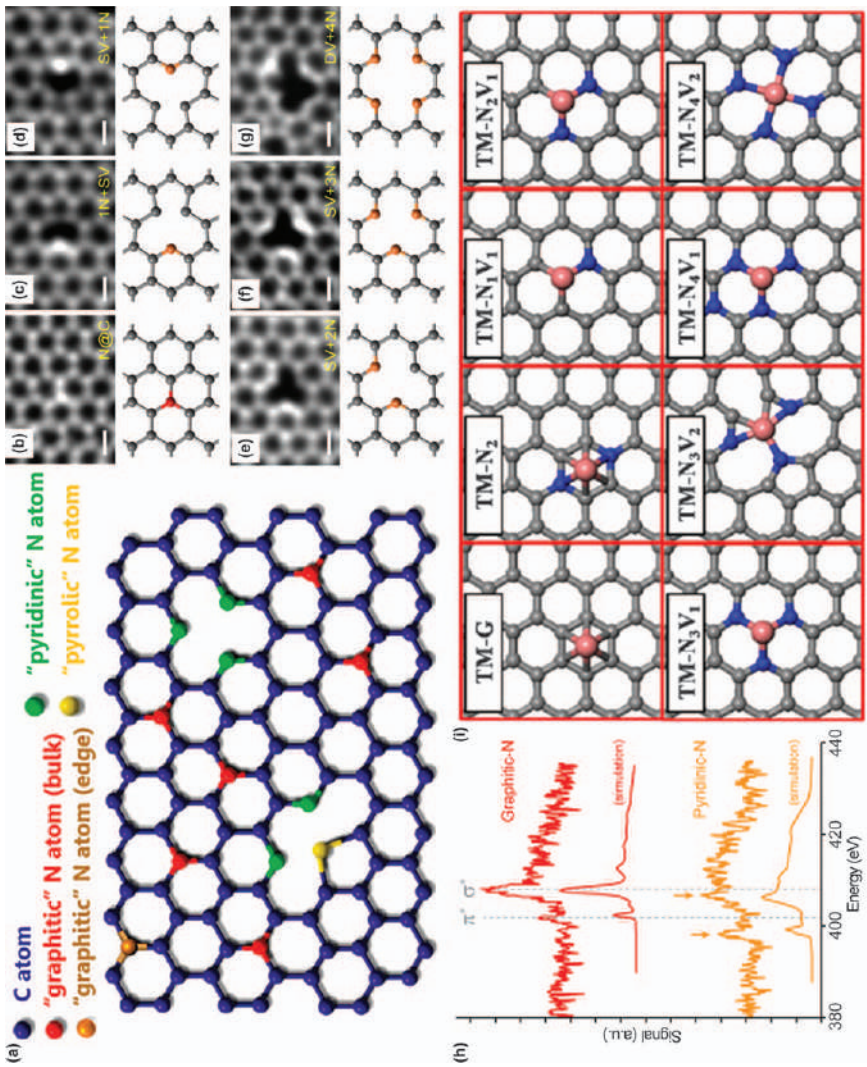
(a)
C atom
"graphitic" N atom (bulk)
"graphitic" N atom (edge)
"pyridinic" N atom
"pyrrolic" N atom
(b)
N@c
(c)
1N-SV
(d)
SV+1N
(e)
SV+2N
(f)
SV+3N
(g)
DV+4N
(h)
Graphitic-N
(simulation)
Pyridinic-N
(simulation)
π*
σ*
Signal (a.u.)
380
400
420
440
Energy (eV)
(i)
TM-G
TM-N2
TM-N1V1
TM-N2V1
TM-N3V1
TM-N3V2
TM-N4V1
TM-N4V2

agglomerate forming metal nanoparticles. Also, migration barriers for metal atoms on the H sites are low and calculated to be in the range of $0.2 - 0.8$ eV.[126,130] Therefore, pristine graphene surfaces are not appropriate to stabilize the ADMAs and specific binding sites on the graphene lattice acting as trap sites for the metal atoms are necessary.

Edge sites in the graphene lattice are one of the possible defects that can stabilize the metal atoms.[131] However, due to the high surface area of the basal plane compared to the edge site, only a small fraction of the graphene layer can be utilized. Vacancies in the graphene are excellent sites for trapping and stabilisation of the ADMAs. Mostly, two kinds of vacant sites are considered, *i.e.* single vacancy (SV) where one of the carbon atoms in the graphene lattice is removed, and double vacancy (DV) where two of the adjacent carbon atoms are removed from the graphene lattice. Typical atomic configurations of ADMAs stabilized by the SV and DV in a graphene lattice are shown in Figure 6.7b. Binding energies of selected metal atoms on SV and DV are shown in Figure 6.7c.[130] Most of the metal atoms in the SV shows strong binding energies of ~7 eV which is significantly higher than the adsorption energies on a pristine graphene layer (<1.5 eV). Some atoms with almost fully occupied d-shells, such as copper and zinc, show slightly lower binding energies, but still over 1 eV. The metal atoms in the DV show similar trends in the binding energies, the exception being the vanadium atoms suggested to have a different configuration.[130] As metal atoms in SV/DV defect sites show higher adsorption energy than cohesive energies of metal atoms, their atomically-dispersed states are stable without agglomeration on the surface.

The other interesting defect sites on graphene lattices are heteroatom substituted sites. In particular, nitrogen-doped carbon materials have attracted much attention due to their unique electrochemical activities toward HER, ORR, and CO_2RR. The nitrogen atoms can be doped in graphene lattices *via* three different ways: pyridinic, graphitic, or pyrrolic (see Figure 6.8a).[132] Nitrogen atoms in the graphene lattice play several important roles in the formation of ADMAs on carbon materials. First, nitrogen doping during the synthesis promotes the formation of defects on the carbon surfaces that can facilitate metal doping.[18] Nitrogen atoms have a lower thermal stability than carbon atoms. During the high-temperature annealing

Figure 6.8 (a) Schematic representation of various kinds of nitrogen atom on the graphene surface. (b–g) HAADF images and corresponding atomic models of various nitrogen decorated vacant sites on graphene. (h) Difference in electron energy loss spectra of the graphitic-N and pyridinic-N along with the DFT calculated spectra. (i) Various configurations of TM atoms embedded in nitrogen-doped graphene.
Reproduced from ref. 132 with permission from American Chemical Society, Copyright 2009, from ref. 92 with permission from American Chemical Society, Copyright 2015, and from ref. 133, https://doi.org/10.1063/1.4922841, under the terms of the CC BY 3.0 license, https://creativecommons.org/licenses/by/3.0/.

or carbonization process, nitrogen atoms can thus evaporate from the carbon lattice leaving vacancies where metal atoms can be trapped. Second, nitrogen atoms enhance the structural stability of ADMAs on the carbon supports as nitrogen atoms have lone pairs of electrons and bind with ADMAs more strongly than carbon atoms.[133] Third, the N-doping contributes to the tuning of the local density of state around the Fermi level of the material. This plays a pivotal role in tuning the electronic and catalytic properties of ADMAs.[134]

The ADMAs in nitrogen-doped carbon materials can have various kinds of local coordination structures based on the defect structure of carbon lattices. Figure 6.8b – g show HAADF-STEM images of nitrogen-substituted vacancy sites on graphene lattices.[92] The presence of pyridinic nitrogen that can be coordinated with metal atoms is revealed by the EELS measurement (see Figure 6.8h).[92] The structural stability of 3d TM adatoms embedded in N-doped graphene was investigated using DFT calculations.[133] Since the pyrrolic nitrogen in the graphene lattice is thermodynamically less stable compared to the graphitic or pyridinic nitrogen, graphitic or pyridinic nitrogen was considered in the DFT calculations.[58] Among the various defect structures, it is suggested that the ADMAs on the 4N-centered structure (N_4V_2) with the highest binding energies of >7 eV are the most stable configurations (see Figure 6.8i). It is worth mentioning that the ADMAs stabilized by the N_4V_2 sites of the graphene lattice have a coordination structure similar to that of heme enzymes or porphyrin-based metal complexes. In particular, iron or cobalt porphyrins and phthalocyanines have been widely investigated for their oxygen activation or CO2RR activity.[135,136]

6.4.2 CO_2 Reduction Activities of Atomically-dispersed Metal Catalysts

The activity and selectivity of catalysts are determined by the way the active sites stabilize the reaction intermediates. Among the various kinds of possible CO_2RR products, CO and formic acid are the simple reduction products of CO_2 requiring two electrons and two protons. Spectroscopic measurements on metal electrodes during CO_2RR have shown that the reaction intermediates, such as *COOH, *OCOH, and *CO, are key reaction intermediates.[137–140] Moreover, the CO_2RR products are determined by what kinds of intermediates are involved and stabilized on the active sites. For example, CO will be produced when *COOH intermediates are stabilized, and formic acid will be produced with *OCOH intermediates (see Figure 6.9a). The reduction path of CO_2 to CO is suggested in eqn (6.1) – (6.3).[111,138]

$$CO_2(g) + * + H^+(aq) + e^- \leftrightarrow *COOH \quad (6.1)$$

$$*COOH + H^+(aq) + e^- \leftrightarrow *CO + H_2O \quad (6.2)$$

$$*CO \leftrightarrow * + CO(g) \quad (6.3)$$

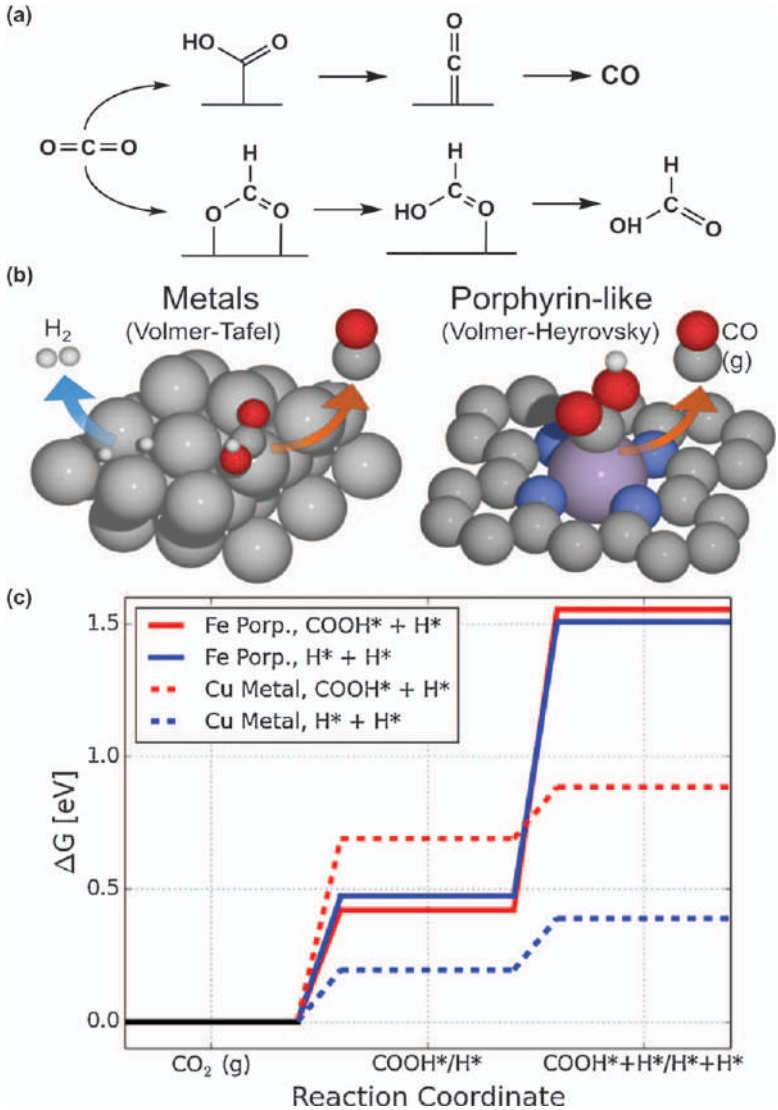

Figure 6.9 (a) Possible reaction intermediates involved in CO_2RR. (b) Illustration of a metal surface (left) and porphyrin-like structure (right) for the Volmer–Tafel *vs.* Volmer–Heyrovsky mechanism. (c) Comparison of the free energy diagram of binding of either COOH* + H* or H* + H* on the Fe porphyrin-like structure and the Cu metal.
Adapted from ref. 144 with permission from American Chemical Society, Copyright 2017, and from ref. 154 with permission from Elsevier, Copyright 2017.

To facilitate the CO production, the metal surfaces should favorably absorb the CO_2 to form the *COOH intermediate. At the same time, *CO should not bind too strongly to allow its desorption from the metal surface to

produce the gaseous CO. The adsorption energy of *COOH can serve as an indicator of the CO production activity since a linear relationship between the COOH and CO adsorption energies is expected.[141,142] A so-called volcano-type relationship has been established between the *COOH adsorption energy and the catalytic activity.[143,144]

Therefore, developing a highly efficient CO generating electrocatalyst requires precise tuning of the *COOH adsorption energies on the active sites. In the case of homogenous catalysts such as iron or cobalt-modified porphyrin complexes with *COOH and *CO intermediates, the binding affinity can be tuned by substitution in the porphyrin ring for the selective CO_2-to-CO reduction activity.[145–148] Several nickel macrocyclic complexes have shown selective CO-producing activity suggesting that the nitrogen coordinated metal active sites can be active for the CO_2-to-CO reduction.[149–153] Furthermore, DFT calculations on the M–N_4 sites on the carbon supports suggested that they can have favourable COOH adsorption to promote the CO_2RR.[154–157]

Importantly, to have an efficient and dominant CO_2RR the competing HER in the aqueous electrolyte should be suppressed. Bagger *et al.* suggested on the basis of DFT calculations that the atomically-dispersed Fe–N_4 active sites in the graphitic lattice have an advantage in this respect by limiting the competing HER.[154] The activity of Fe–N_4 active sites was evaluated by calculating the formation energies of *COOH and *H, used as activity descriptors for CO_2RR and HER, respectively. The binding of COOH* or *H intermediates on the Fe–N_4 ADMAs is compared with what is occurring on a Cu metal surface. In the latter case, the first and second H* intermediates interact with two similar metal sites, so the energy required for the second H* binding is similar to that of the first H* binding.[154] This means that the Tafel reaction is possible (see Figure 6.9b and c). In contrast for the Fe–N_4 sites, the second H* binding requires considerably more energy as it should be bound at the metal–nitrogen bond.[154] Thus, it is suggested that the HER now occurs by the Heyrovsky reaction mechanism which is not as energetically favoured as the Tafel mechanism in the ADMA case (see Figure 6.9b and c). In this manner, the HER on the Fe–N_4 sites becomes successfully suppressed. On top of this, the selective CO_2RR on ADMA is benefitted by the Fe–N_4 active sites having an overpotential for the reduction of CO_2 to *COOH that is lower than the corresponding one for adsorbing H^+ followed by reduction. In comparison, Cu shows lower H* formation overpotentials than what is required for the first CO_2 reduction step, resulting in this case in a dominant HER instead of CO_2RR.[154]

In nature, the M–N4 structure can be found in heme-containing iron proteins and enzymes which carry out a wide range of biologically important redox reactions.[158] The M–N4 planar structure shows both stability and versatility towards many different functions such as oxidation, reduction and hydrolysis reactions. Inspired by the natural enzymes, and to understand the reaction mechanism of the enzymes, synthetic metalloporphyrin catalysts have been developed[159–161] and later it was extended to ADMCs.[136]

To corroborate the activity of $M–N_4$ sites experimentally, metal and nitrogen co-doped carbon catalysts (M–N–C) were prepared and investigated. Varela *et al.* synthesized M–N–C by pyrolyzing a mixture of polyaniline and metal salts.[162] Mn (Manganese), Fe, and MnFe on N-doped carbon catalysts showed higher activity compared to polycrystalline gold with 100 mV reduced onset potential. Furthermore, the CO selectivity was high [80% at −0.5 V *vs.* Reversible Hydrogen Electrode (RHE)] compared to carbon-supported gold catalysts. Although the nitrogen-doped carbon catalyst prepared with no metal centres also shows selectivity toward CO production, but the current density was much lower. Likewise, the current density for CO production was increased eight times by the presence of the metal active centre, underlining the central role of the metal active sites for CO production.

Later efforts have been made to understand the trends in the activity of a series of M–N–C catalysts (M = Mn, Fe, Co, Ni, Cu). Ju *et al.* used a two-step protocol to prepare M–N–C catalysts, involving the synthesis of N-doped porous carbon and metallation by a solution impregnation method followed by high-temperature pyrolysis (see Figure 6.10a).[163] The electrochemical measurements revealed that Fe–N–C shows the lowest overpotential for CO production and Ni–N–C shows the highest selectivity for CO production (see Figure 6.10c). In terms of the CO production per unit weight of catalysts, Ni-N-C shows the highest CO_2-to-CO conversion activity with the trend following Ni > Fe > Co (see Figure 6.10c). To understand this, binding energies of *H, *COOH, and *CO on the $M–N_4$ active sites were investigated using DFT calculations and correlated with the experimental results. Based on the computational hydrogen electrode model, the proton-coupled electron transfer reduction of CO_2 to adsorbed *COOH is suggested to be the potential-determining step. Accordingly, the Co, Fe, and Mn with low *COOH formation energy exhibit a small overpotential for CO production, while Ni and Cu require a higher overpotential (see Figure 6.10e).

Besides the COOH* formation energy, the $M–N_4$ active sites should have a high overpotential for H* formation to show selectivity for CO_2RR. In fact, if the *H formation is more favoured than the *COOH formation, the active sites will produce H_2 rather than reduce CO_2 to CO. As shown in Figure 6.10d, downhill HER energy pathways of the Fe-, Co- and Mn-based catalysts suggest that they can strongly catalyse the HER (see Figure 6.10c). As a result, they show low CO_2RR selectivity in a highly reductive potential range, even though they have a low CO_2RR overpotential. In contrast, the Ni- and Cu-based catalysts exhibit very weak binding of *H which makes the HER thermodynamically unfavourable, giving rise to high FE_{CO} for the CO_2-to-CO conversion. In this respect, $Ni–N_4$ becomes the most preferable for selective CO_2RR, while Fe-, Co- and Mn–N4 are more suitable for HER than CO_2RR.

Another key factor for efficient CO_2-to-CO conversion is the binding energy of CO*. In the case of $Ni–N_4$ and $Cu–N_4$, their weak binding of CO* promotes the facile desorption of CO from the active sites and CO (*g*) can be easily produced. However, $Fe–N_4$ and $Co–N_4$ with strong CO affinity make the

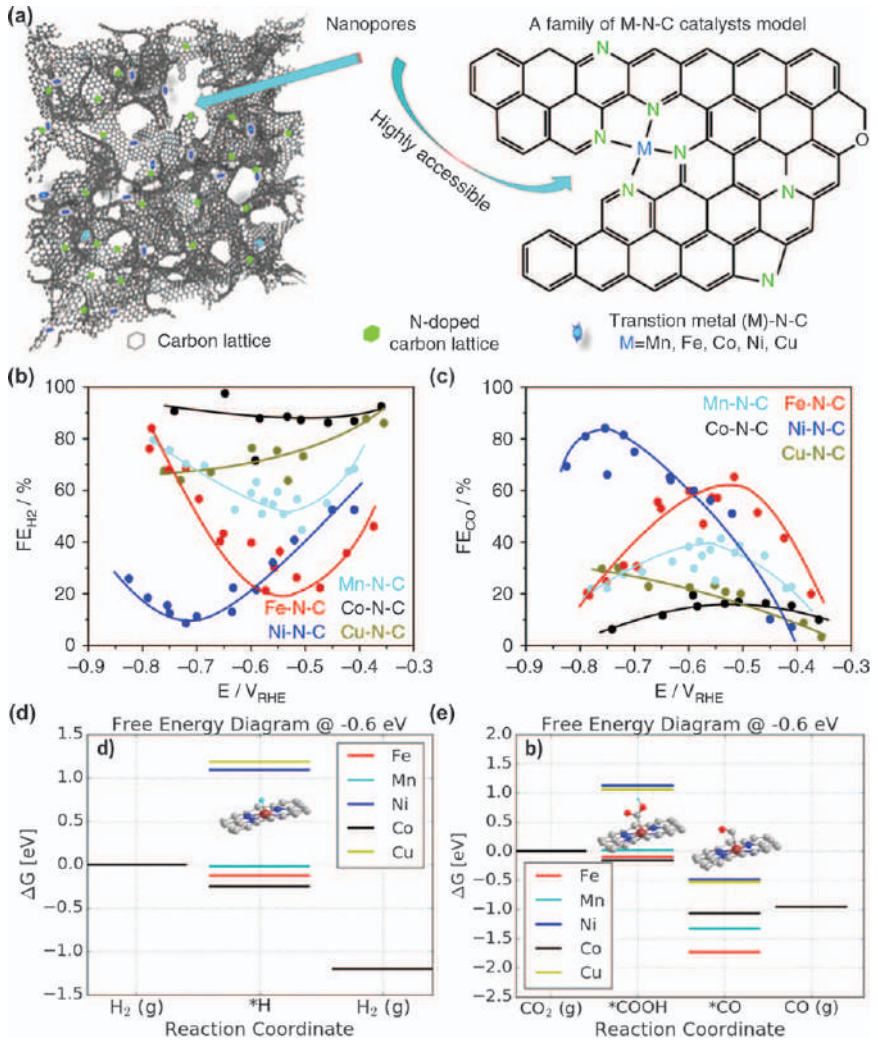

Figure 6.10 (a) Schematics of the local structure of atomically-dispersed metal atom catalysts (*i.e.* M–N–C). (b and c) FE_{H2} and FE_{CO} as a function of applied potential using M–N–C catalysts respectively. (d and e) Free energy diagram for H_2 and CO production at −0.6 V *vs.* RHE, respectively. Reproduced from ref. 163, https://doi.org/10.1038/s41467-017-01035-z, under the terms of the CC BY 4.0 license, http://creativecommons.org/licenses/by/4.0/.

potential-independent chemical CO desorption process become the rate-determining step (RDS), *i.e.* the active sites can be poisoned by strong *CO binding.

Similar activity trends among the first-row transition metal-based active sites can be found in other studies.[164–166] Hu *et al.* compared the CO_2RR activity of M–N–C (M = Fe, Co, and Ni) prepared by carbonization of

phenylenediamine and metal salts precursors with silica templates.[57] A selectivity trend for CO_2-to-CO conversion was observed as Ni > Fe ≫ Co. Jeong *et al.* also found a similar selectivity trend with metal and nitrogen-doped reduced graphene oxides (N–RGO). M–Nx sites were fabricated on the RGO surfaces using metal complexes of tris(2-benzimidazolylmethyl)amine ligands.[165]

To prepare atomically-dispersed Ni active sites (Ni ADMAs), it is important to avoid agglomeration. Various synthetic methodologies using different precursors have been adopted to synthesize Ni ADMAs on the electroconductive carbon supports. These include the metal complex precursor method, immobilization of transition metals on N-doped graphene, and ZIF-8 based topochemical transformation.[167–170]

Su *et al.* developed nickel and nitrogen-doped graphene by stabilizing the nickel ions with pentaethylenehexamine (PEHA) on graphene oxide (GO).[167] PEHA can adsorb on the surface of GO, and subsequently coordinate with nickel ions, due to electrostatic interaction. By annealing this precursor mixture at 900 °C, nickel and nitrogen-doped reduced GOs were prepared. The isolated nickel atoms were revealed by XAS. The nickel ADMAs exhibit high electrocatalytic activity for CO_2RR with FE_{CO} exceeding 90%, significantly outperforming that of N-doped graphene and the Ni metal electrode. Although the nickel ADMAs were proven to be active sites for CO_2-to-CO conversion, the local coordination structure was not well characterized.

To achieve well defined Ni–N_4 sites, Li *et al.* developed a topochemical transformation strategy where nickel and nitrogen-doped carbon was derived from a nickel doped carbon nitride precursor (see Figure 6.11a).[168] In this method, carbon nitride was used as supports for nickel atoms to prevent their agglomeration. The Ni-doped graphitic carbon nitride (g-C_3N_4) were synthesized by a polycondensation reaction of the mixture of dicyandiamide, ammonium chloride (NH_4Cl), and nickel dichloride ($NiCl_2$) at 550 °C followed by carbonizing the prepared Ni doped g-C_3N_4 with glucose as a carbon source. Well-dispersed nickel atoms can be observed by TEM analysis (see Figure 6.11b). The catalysts exhibit a high CO_2-to-CO reduction activity with a current density of 28.6 mA cm^{-2} and a maximum FE of 99% at −0.81 V *vs.* RHE. The active sites are determined to be Ni–N_4 sites since an introduction of thiocyanate anion (SCN^-) to the electrolyte causes a dramatic depression of the catalytic activity due to the blockage of metal centres by SCN^-.

Zhao *et al.* produced nitrogen-doped carbon with atomically-dispersed nickel sites (NiSACs/N–C) by carbonizing Ni-doped ZIF (see Figure 6.11c).[170] Ni-doped ZIF was prepared by an ionic exchange reaction involving nickel ions and Zn-nodes MOF. During the carbonization step of Ni-doped ZIF, the imidazole molecules are decomposed and carbonized. While the Zn-nodes evaporates, it leaves the N-rich defect sites which can anchor Ni^{2+} ions. Nickel ADMAs were confirmed by TEM analysis (see Figure 6.11d). On the basis of the EXAFS fitting analysis, it was suggested that the nickel atoms are coordinated by three nitrogen atoms. The NiSACs/N–C showed a high

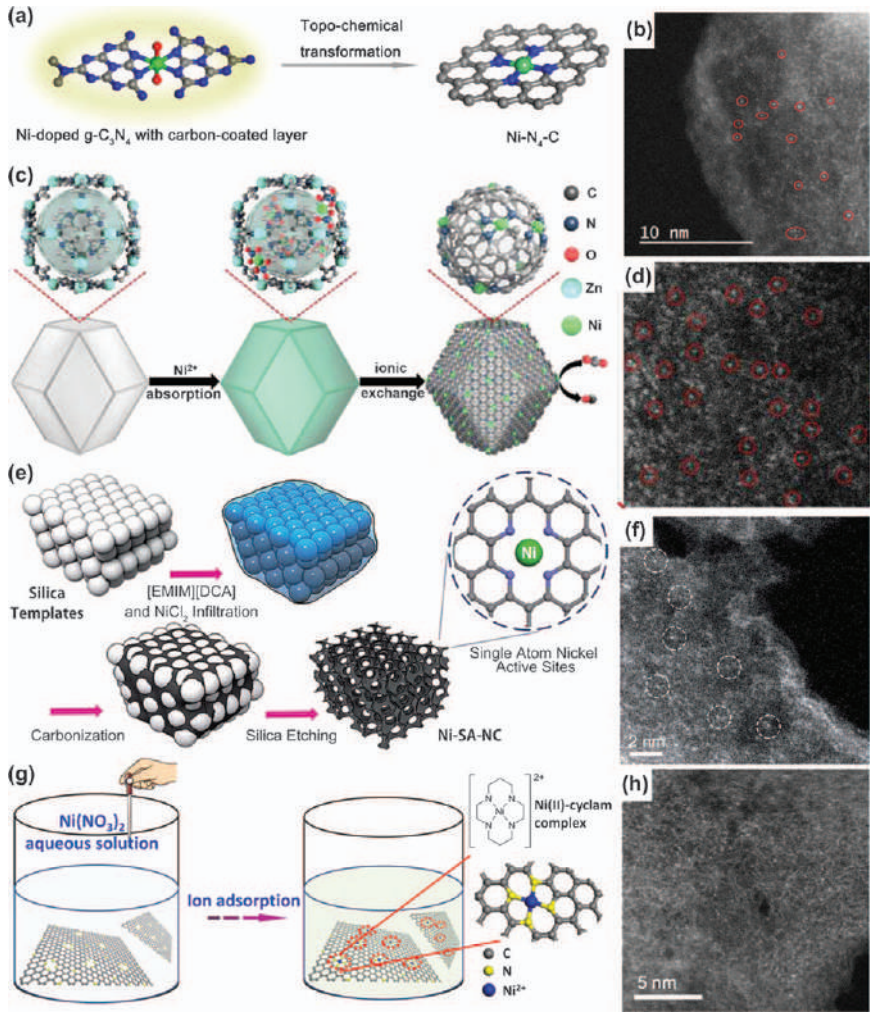

Figure 6.11 Synthetic protocols for preparing ADMAs: (a) Topo-chemical transformation strategy for the formation of atomically-dispersed Ni along with (b) HAADF–STEM image. (c) Scheme of the formation of ZIF derived atomically-dispersed Ni along with (d) magnified HAADF–STEM images. (e) Template assisted synthetic strategy of atomically-dispersed nickel on N-doped 3D porous carbon along with (f) HAADF–STEM images. (g) Ion adsorption methodology for Ni-doping on N-doped nanographene along with (h) HAADF–STEM images.
Reproduced from ref. 168 and 170 with permission from American Chemical Society, Copyright 2017, from ref. 171 with permission from the Royal Society of Chemistry, and from ref. 169 with permission from John Wiley and Sons, Copyright © 2018 WILEY-VCH Verlag GmbH & Co. KGaA, Weinheim.

current density of 10.48 mA cm^{-2} for CO production at an overpotential of 0.89 V *vs.* RHE.

Jeong *et al.* produced porous carbon catalysts with nickel ADMAs using nickel ion-dissolved ionic liquids as precursors (see Figure 6.11d).[171] Silica spheres were used as templates and etched away after carbonization to generate a three-dimensional porous structure. After etching, the interconnected porous structure and nickel ADMAs can be characterized by TEM (see Figure 6.11f). The porous catalyst structure was beneficial for CO_2 transport, allowing a high current density exceeding 300 mA cm^{-2} for CO production to be obtained.[171]

Bi *et al.* used an ion adsorption method (wet impregnation method) to decorate nickel atoms on the surface of N-doped graphene to avoid conventional harsh pyrolysis and acid-leaching procedures (see Figure 6.11g).[169] The N-doped graphene was produced from pyrolyzing the mixture of carbon nitride and glucose. Then, nickel ions were immobilised on N-doped graphene *via* an ion adsorption process in aqueous solution, followed by mild annealing at 300 °C in Ar atmosphere to improve the stability. Absence of metal agglomeration after the annealing process can be confirmed with TEM (see Figure 6.11h). The synthesised catalysts show high CO selectivity (92%) compared to the Fe- or Co-doped counterpart and N-doped graphene samples.[169]

Other nickel-based ADMCs also exhibited high selectivity for CO production.[172–176] However, the low CO_2RR activity of Fe–N_4 or Co–N_4 sites in previous studies are particularly interesting, in that, the porphyrin-complex of iron and cobalt with similar M–N_4 coordination structure exhibited high activity.[57,154,165] This suggests that the trends observed on homogeneous catalysts cannot be directly translated to M–N–C materials. This could be attributed to a different chemical environment surrounding the metal centre. The defects on the carbon lattices can also affect the surrounding environment of ADMAs and can alter their activity trends. The possible coordination structure of those active sites will be discussed.

Several other ADMCs containing metal centres such as Mn,[162,177] Fe,[163,178–187] Co,[188–191] Ni,[167,192–207] Cu,[208] Zn,[209–211] Sn,[212,213] and Bi[214] have been reported which usually exhibit high selectivity and stability towards eCO_2RR. Moreover, most of the Mn, Fe, Co, Ni, Sn, and Zn ADMCs are able to produce CO dominantly. Copper-based ADMC is able to produce methanol and tin-based ADMCs can produce formic acid. Recently, it has been reported that atomically-dispersed bismuth can produce CO selectively.

6.4.3 Metal Active Sites with Low Coordination Number

In molecular catalysts, the coordination number of the active metal centre plays a crucial role in determining the activity and stability of the system. Similarly, the control of the coordination number of ADMAs on carbon catalysts is particularly interesting to manifest their CO_2RR activity. Several attempts have been made to study the role of coordination number on the

catalytic activity of the catalysts. In particular, the M–N–C catalysts prepared by carbonizing the ZIF supports are suggested to have low coordination numbers.[215,216]

Wang *et al.* prepared and compared the CO_2RR activities of series of atomically-dispersed cobalt catalysts with different nitrogen coordination numbers.[215] Cobalt and nitrogen co-doped carbon catalysts were prepared by carbonization of cobalt doped ZIF-8 (see Figure 6.12a). The EXAFS analysis shows the change in the coordination number on the carbonization temperature (see Figure 6.12b). By controlling the carbonization temperature, catalysts with different coordination number, *i.e.* Co–N_4, Co–N_3, and Co–N_2 were prepared at 800, 900, and 1000 °C, respectively. While the catalyst with Co–N_4 active sites prepared at 800 °C exhibits negligible CO_2RR activity and mainly produces hydrogen, the catalyst with Co–N_2 active sites

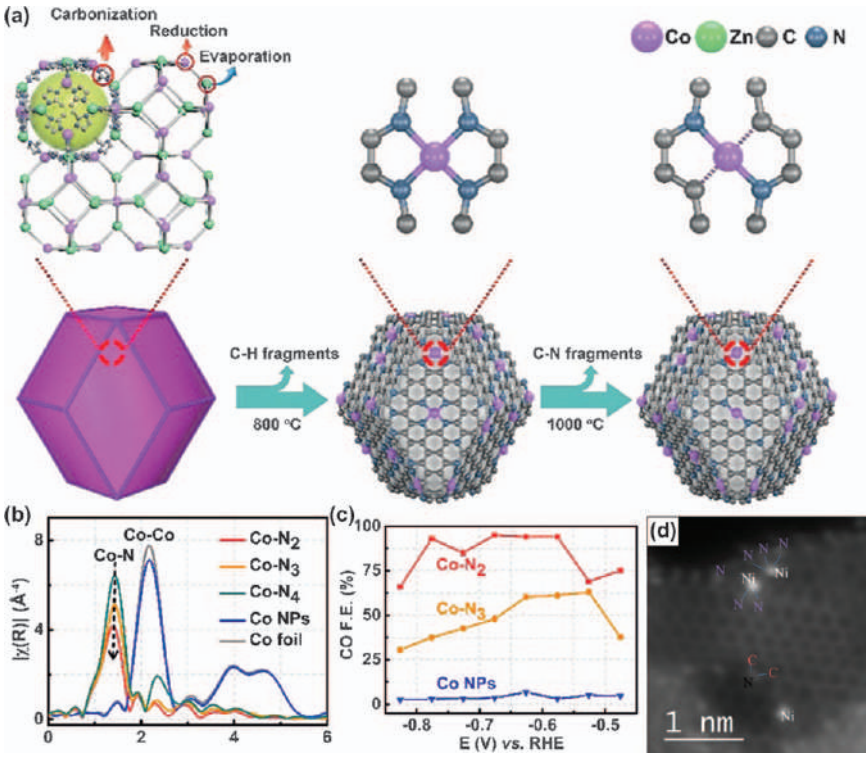

Figure 6.12 Low coordinated ADMAs for CO_2RR: (a) Synthetic protocol for Co–N4 and Co–N2 sites. (b) EXAFS spectra of the atomic-dispersion of Co with low coordination number Co–N2, Co–N3, and Co–N4. (c) FE_{CO} of Co–N2, Co–N3, and cobalt nanoparticles as a function of applied potential. (d) Local defects of N dopants and Ni–Nx single-atom sites identified by the atomic column intensity.
Reproduced from ref. 188 with permission from John Wiley and Sons, Copyright © 2018 WILEY-VCH Verlag GmbH & Co. KGaA, Weinheim, and from ref. 205 with permission from Elsevier, Copyright 2018.

prepared at 1000 °C exhibits selective CO_2RR activity (see Figure 6.12c). The high HER activity of Co–N_4 active sites matches with other reported experimental observations and DFT calculations. The easier formation of *H intermediates relative to the formation of $*CO_2^-$ promotes the HER on Co–N_4 moiety. Based on the DFT calculation, usually the Co–N4 moiety can exhibit smaller hydrogen adsorption energy than that of the binding with the CO_2. Also, the potential RDS in the CO_2 reduction is the formation of a *COOH intermediate from CO_2, which is unfavourable at the Co–N4 sites.[163] On the other hand, catalysts with a low coordinated Co–N_2 structural motif exhibit high CO_2-to-CO activity with a current density of 18.1 mA cm^{-2} at −0.63 V *vs.* RHE and a maximum FE_{CO} of 95% at −0.68 V *vs.* RHE in 0.5 M potassium bicarbonate ($KHCO_3$). From the DFT calculations, the formation energy of the $*CO_2^-$ intermediate on Co–N_2 is revealed to be low compared to Co–N_4 active sites which should facilitate CO_2RR, in accordance with experimental observations. Co–N_3 exhibit a moderate selectivity that is between that of Co–N_2 and Co–N_4 with $FE_{CO} = 63\%$ at −0.53 V *vs.* RHE.

With a similar approach, Yan *et al.* prepared a porous Ni ADMAs-doped nitrogenated carbon through pyrolysis of Ni-doped ZIF.[216] From EXAFS fitting analysis, it is suggested that the Ni ADMAs were coordinated with two nitrogen atoms, forming unsaturated Ni–N active sites. The catalysts exhibited a current density of 71.5 mA cm^{-2} and a high FE_{CO} of 98.0% at −1.03 V *vs.* RHE. The DFT calculation indicated that *COOH can be more easily adsorbed on these unsaturated nickel active sites than on fully coordinated Ni–N_4 active sites, implying the superior CO_2RR activity of the Ni ADMAs with low coordination number.[216]

Cheng *et al.* developed a Ni ADMAs on three-dimensional microwave exfoliated GO (Ni-N-MEGO).[217] Ni-N-MEGO was prepared by annealing the mixture of MEGO, nickel nitrate, and urea under an ammonia atmosphere. Interestingly, the atomically-dispersed nickel atoms were found to be predominantly anchored along the edges of nanopores (<6 nm) by HAADF–STEM (see Figure 6.12d). The Ni-N-MEGO exhibits a CO2RR current density of 53.6 mA mg^{-1} and $FE_{CO} = 92.1\%$ at an overpotential of 0.59 V *vs.* RHE.[217] The high CO_2RR activity was suggested to originate from the high loading of unsaturated nickel single-atoms on edge sites. The DFT calculation suggested that the edge-anchored unsaturated nickel sites with three nitrogen coordination would exhibit better CO_2RR activity compared with in-plane Ni–N_4 active sites.

6.4.4 Metal Active Sites with Carbon Coordination

ADMAs dispersed on the nitrogen-doped carbon are usually suggested to be coordinated with nitrogen atoms as the metal-nitrogen bonds are stronger than metal-carbon bonds. However, it is also possible that the metal atoms are co-coordinated by both carbon and nitrogen. Metal on graphene layers can have different numbers of nitrogen coordination as shown experimentally by Lin *et al.*[91] Various defect sites were introduced by treating

graphene layers with the ozone (O_3) and N_2 mixed plasma. Chromium (Cr) atoms were deposited on the plasma-treated graphene by thermal evaporation and heated at 500 °C to fill up the Cr atoms on defect sites. The spin state of chromium atoms on the graphene layers with different coordination numbers of nitrogen atoms was investigated by means of HAADF-STEM and EELS. In particular, the $L_3 : L_2$ branching ratio of chromium with surrounding nitrogen atoms was thoroughly investigated. With an increasing number of nitrogen coordination, the $L_3 : L_2$ ratio shows a gradual decrease as the electrons from N atoms can be transferred to chromium atoms.[91] This observation showed that chromium with a different number of coordinated nitrogen atoms can be present on the surface of graphene with different amounts of charge transfer occurring between the nitrogen and chromium atoms.

Furthermore, Jiang *et al.* demonstrated that the carbon coordinated nickel atoms can be active for CO_2RR.[218] Nickel-doped carbon nanowire was prepared by carbonizing a nickel-containing electrospun polymeric nanofiber. As the nickel nanoparticles produced during the carbonization are covered by a graphene shell, it seems that the nickel active sites in the catalysts are passivated (see Figure 6.13a). Nevertheless, the catalyst shows a CO current density of 60 mA mg^{-1} with $FE_{CO} > 90\%$ in $KHCO_3$. On this basis it is suggested that the graphene shell possesses atomically-dispersed nickel atoms as active sites. The local chemical structure of nickel sites in the graphene shell was proven by three-dimensional atom probe tomography (APT).

The APT analysis revealed that most of the nickel atoms are ADMAs with no neighbouring nickel atoms closer than 2.2 Å (see Figure 6.13b). It was proposed that nickel atoms are stabilized by the vacancy sites in the graphene lattice, while nitrogen atoms promote the generation of vacancy. Interestingly, only 0.2% of the nickel atoms were suggested to be directly anchored with nitrogen atoms, while 98% were anchored within carbon defects in the graphene vacancies. To understand the activity of the catalysts, free energies of reaction intermediates on possible nickel sites were obtained by DFT calculations (see Figure 6.13c). Nickel atoms trapped in single or double vacancies of the graphene sheet, with a variety of N coordination to nickel sites, were considered as possible active sites. Among the various kinds of nickel coordination structure considered, Ni@SV and Ni@DV showed a more favourable reaction pathway because of facile *COOH formation and weak CO binding. Recalling the finding of carbon coordinated nickel atoms in APT, the DFT calculations suggested that the nickel atoms coordinated in the graphene vacancies without nitrogen coordination, such as Ni@SV and Ni@DV, can also be active for CO_2 reduction to CO. The benefit of having mixed nitrogen and carbon coordination for improving the activity of nickel atoms was also suggested by Möller *et al.*[173] Although no experimental evidence for the carbon coordination was presented, the DFT results clearly showed that the carbon coordination enhances the activity of the Ni-based ADMAs on carbon supports. Compared to the Ni–N_4 coordination motif, the Ni–N_3C and Ni–N_2C_2 motifs are active towards *COOH

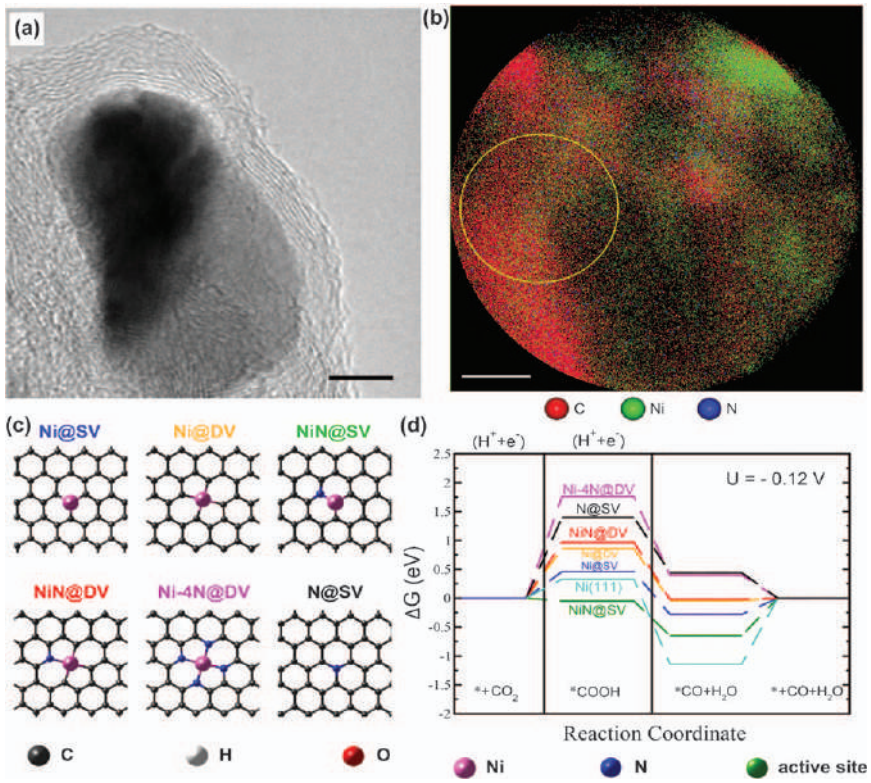

Figure 6.13 Importance of carbon coordination: (a) TEM image of NiN–graphene sheet (NiN–GS) after catalysis. (b) 2D atom map of NiN–GS. (c) DFT structures of different atomic configurations in graphene. (d) Free energy diagram of CO_2RR pathways on different atomic structures at −0.12 V *vs.* RHE.
Reproduced from ref. 192 with permission from Elsevier, Copyright 2017.

intermediates formation and *CO desorption (see Figure 6.13d), while the Ni–C_4 and Ni–NC_3 motifs are highly active for *COOH formation but tend to bind CO too strongly.

6.4.5 Metal Active Sites with Axial Coordination

To understand the importance of axial coordination in CO_2RR catalyzed by the M–N5 motif, we have adopted the approach used by nature in biological enzymes. Even though both cytochromes P450 (cyt P450) and Horseradish peroxidase (HRP) utilize high-valent iron–oxo species as active intermediates during their reactions, HRP catalyzes monooxygenation of thioethers and acts as a poor oxidant for C=C epoxidation and C–H hydroxylation which, in contrast, can be catalyzed by cyt P450.[219] The intrinsic reactivity differences between the intermediate species of these two enzymes depend on the axial

ligands. Cyt P450s have a thiolate ligand in the axial position, while most of the peroxidases have histidine as an axial ligand.[220] The electrostatic effects of the neutral histidine ligand and anionic cysteine ligand on the catalytic centres are very different for HRP and cyt P450. Cysteinate can push electrons to the iron centre, while histidine can pull electrons from the iron centre.[220]

The activity enhancement induced by the axial coordination has also been verified in CO_2RR using metalloporphyrin and phthalocyanine catalysts.[221–223] The coordination of an axial ligand on the Co–N_4 moiety increases the energy level of the cobalt dz^2 orbital compared to the Co–N_4 moiety, leading to the Co(I) centre becoming a stronger nucleophile that binds with the Lewis acidic carbon of CO_2 during CO_2RR.[224] Furthermore, it is anticipated that the electrostatic and covalent contributions of an axial ligand enhance the push effect, which makes the CO desorption easier. Also, DFT calculations suggest that the axial ligand is not only enhancing the CO_2-to-CO conversion but also the formic acid production over hydrogen in the metal–porphyrin-like active sites on graphene (G–Por–M).[225] When the axial ligand is coordinated to G–Por–M, the stronger binding of *OCHO intermediates than that of *H was observed to favour the formic acid production and suppress HER.

The nitrogen atoms in N-doped carbon materials can also act as axial ligands to the molecular complex system. The CO_2RR activity enhancement by means of axial coordination has been demonstrated with CoPc anchored on polymer-derived hollow N-doped porous carbon spheres (NHPCS) (see Figure 6.14a).[226] The CoPc anchored on NHPCS leads to the formation of Co–N_5 sites *via* axial ligation of the nitrogen atoms in NHPCS. Compared to the CoPc without axial coordination, CoPc on NHPCS exhibited both higher current density and selectivity (see Figure 6.14b).[226] A high CO selectivity with $FE_{CO} = 99.4\%$ can be reached at -0.79 V *vs.* RHE, which is significantly higher than for CoPc itself at the same potential. DFT calculations suggested that the Co–N_5 site is efficient in CO_2 activation by favouring the rapid formation of the COOH* intermediate and CO desorption to a much higher extent than if CoPc is without axial ligands.

Axial ligand coordination can also affect the activity and spin-state of the metal atoms in nitrogenated carbon. For example, it has been suggested that the iron atoms on Fe–N–C can have different spin-states based on their geometry such as axial coordination.[95,100] Mainly three different doublets corresponding to low (D1), intermediate (D2), and high (D3) spin-states are assigned to Fe–N_4 sites with a +2 oxidation state determined by Mössbauer spectroscopy.[100] Interestingly, iron active sites exhibited spin-state dependent reactivity towards ORR. The low-spin (D1) and, in particular, high-spin (D3) states are suggested to be responsible for the high ORR activity of Fe–N–C.[95]

Interestingly, high oxidase-like activity was observed with the Fe–N_5 motif on a carbon nanoframe (Fe–N_5–CNF).[227] Iron phthalocyanine (FePc) has been used as an iron precursor and ZIF has been used as a N-confined

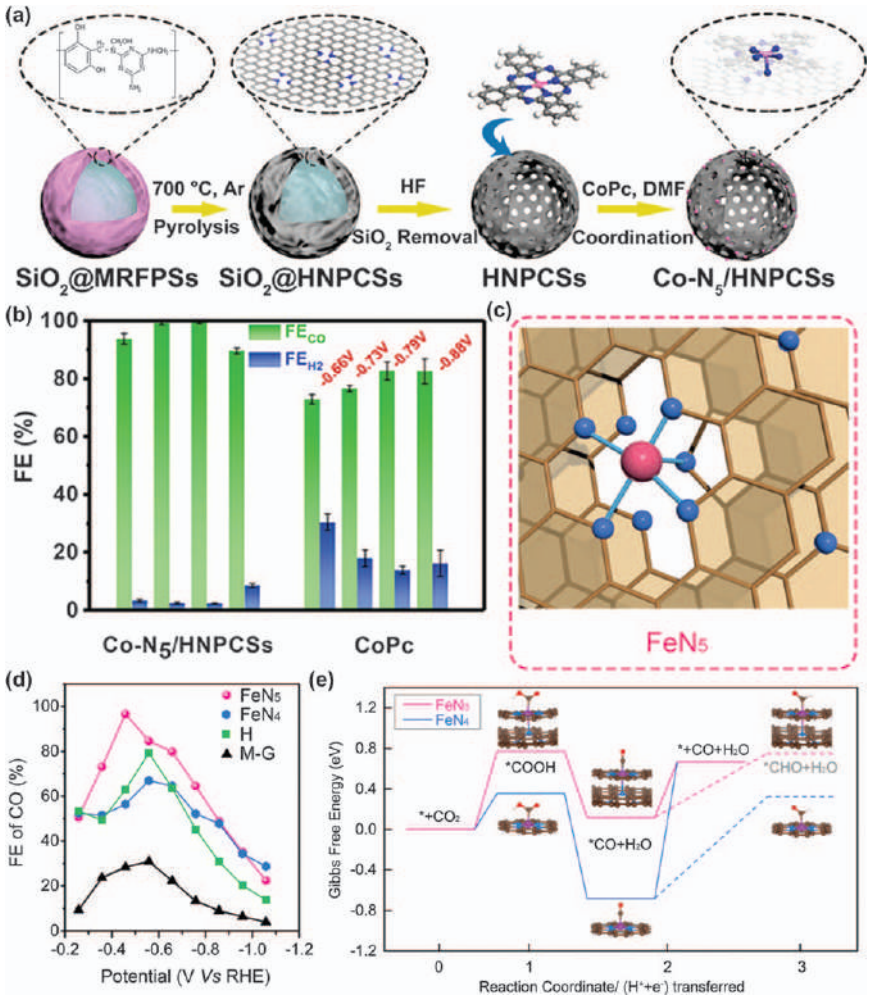

Figure 6.14 Effect of axial ligation on catalytic activity: (a) Schematic illustration of the synthesis of Co–N5 sites. (b) FE of CO and H_2 production of Co–N5 and CoPc. (c) Graphene-supported atomically-dispersed Fe–N5 sites. (d) Comparison of CO production efficiencies of Fe–N4 and Fe–N5 sites. (e) Comparative free energy diagram of the intermediates in the electro-reduction of CO_2 to CO for the Fe–N4 and Fe–N5 sites.
Reproduced from ref. 190 with permission from American Chemical Society, Copyright 2018, and from ref. 228 with permission from John Wiley and Sons, Copyright © 2019 Wiley-VCHVerlag GmbH & Co. KGaA, Weinheim.

carbon precursor acting as an axial ligand provider during the carbonization process. Fe–N_5–CNF was suggested to have a similar structure to the natural heme enzyme with an axial ligand and oxidase-like activity was tested. Fe–N_5–CNF exhibited enhanced oxidase-like activity, which is 17 and

70 times higher than that of the square planar Fe–N_4 catalyst and commercial Pt/C catalysts, respectively. Theoretical calculations identified that the electron donation mechanism of axial N coordination in Fe–N_5–CNF plays a vital role in the high oxidase activity.[227]

For the application of Fe–N–C to CO_2RR, the strong binding affinity of CO on the iron sites can be a problem causing poisoning and a decreased CO_2RR activity. Recently, the positive effect of axial coordination on the CO_2RR activity of Fe–N–C was demonstrated.[228] The pyrolysis method was utilised to decorate atomically dispersed Fe–N_5 sites on the graphene layer using hemin and melamine as precursors and graphene as the carbon support (see Figure 6.14c). Interestingly, the atomically-dispersed Fe–N5 catalyst displayed high FE_{CO} (~97%) at low overpotential (0.35 V *vs.* RHE) for CO production from CO_2 (see Figure 6.14d). The DFT calculations suggested that the axial coordination plays a crucial role in reducing the binding strength of *CO (Fe–N_5 site = 0.54 eV; Fe–N_4 site = 1.35 eV), thus facilitating the CO desorption step (see Figure 6.14e).

Moreover, the formation of heterostructures with other inorganic materials can enhance the activity of metal centres. Cheng *et al.* prepared an iron and nitrogen co-doped carbon nanofiber (Fe–N–CNF) featuring a core–shell structure consisting of iron nitride nanoparticles encapsulated within iron and N co-doped carbon layers.[229] The experimental results and DFT calculations illustrate that the introduction of an iron nitride core can facilitate the CO intermediate desorption from the Fe active sites by means of the axial coordination, thus enhancing the catalytic performance of CO_2 reduction. Only few attempts have been made to study the axial N-ligand coordination to enhance the CO_2 reduction ability of the ADMACs. The axial ligand effect of other dopants such as S and P may be considered as well.

6.4.6 Effect of Second Coordination Sphere (SCS): Inductive Effect

The central metal ions and the ligands attached directly to the active sites are called the first coordination sphere, while the atoms around the first coordination sphere constitute a SCS. The active site structure and function are affected by not only changing the ligand donor functionalities coordinated with the metal center but also by the SCS (not directly bonded with the metal center). Similarly, substituent nearby ligating atoms can influence the active site electronically. In particular, the substituent nearby ligating atoms can change the electronic nature of the metal centre through the inductive effect, triggered by their electron-withdrawing/donating properties.

Nature has utilised various heme proteins to carry out a variety of both oxidation and reduction reactions. The nature of the central metal atom is tuned by many different factors such as the type of porphyrin (categorized by substituents on the heme moiety), axial ligand, spin-state of the metal centre, distortion in the macrocyclic ring, surrounding protein side chains *etc.* These structural factors are responsible for the tuning of the reduction

potentials of naturally occurring heme proteins in the range from −550 to +450 mV *vs.* SHE.[230] Among various factors, the inductive effect of the substituents is important in varying the nature of the active site. In particular, the redox properties can be altered due to the electronic influence exerted by the substituents on the heme moiety.

For synthetic porphyrins and phthalocyanines the inductive effect has been systematically investigated by introducing various substituents and studying their role in tuning the active sites and catalytic ability in ORR and CO_2RR. Zhu *et al.* sequentially varied the substituents on the immobilised cobalt porphyrins and demonstrated the key role of the inductive effect in tuning the redox properties of the metal centre and, consequently, the catalytic activity.[231] Furthermore, it has been established that the electron-donating substituents enhanced the activity by increasing the electron density on the cobalt centre and facilitated the electrosorption of CO_2, while the cationic substituents tend to increase the CO_2 reduction activity by the electrostatic stabilization of the transition state associated with the rate-determining electron transfer to carbon dioxide. Furthermore, the relationship between the turnover frequency (TOF) of cobalt porphyrin derivatives for CO production *vs.* calculated Hammett σ values demonstrated the inductive effect of substituents on the tuning of the redox potentials and, thus, the CO_2 reduction activity.[231]

As is the case for homogenous catalysts, the inductive effect can influence the activity of the metal centre in graphene lattices. Here, the heteroatoms at the SCS of ADMAs can act as an electron-acceptor or donor, tuning the activity of ADMAs. In particular, the enhancement of catalytic activity caused by using more than two types of dopants such as nitrogen, sulphur, and phosphorous was extensively investigated for the development of ORR catalysts. The electronic influence of the doping atom has been successfully observed in ORR catalyzed by the atomically-dispersed Fe atoms supported on the nitrogen, phosphorus and sulphur co-doped hollow carbon.[226] The sulphur and phosphorus-doping resulted in an increase of the catalyst performance with enhanced kinetics and activity for oxygen reduction in both alkaline and acidic media. It was suggested that the electronic effect from surrounding S and P atoms contributes favourably to the ORR activity of iron centres. The DFT calculation supported that sulphur and phosphorus in the SCS can donate electrons to the iron centres making the charge of iron less positive to weaken the binding of adsorbed hydroxyl (–OH) species.[226]

Zhang *et al.* suggested a synergic effect of the nitrogen dopant around the metal active centres for CO_2RR.[184] To study the inductive effect of doped nitrogen, the amount of nitrogen on the graphene layer was controlled by annealing under a NH_3 atmosphere and using various pyrolysis temperatures. The synthesized materials exhibit variations in the reactivity, dependent on the pyrolysis temperature, suggesting that the level of nitrogen-doping plays a crucial role in the CO_2 reduction activity (see Figure 6.15a). Fe–N4 moieties with different amounts of nitrogen dopant in the secondary coordination sphere was modelled for DFT calculations

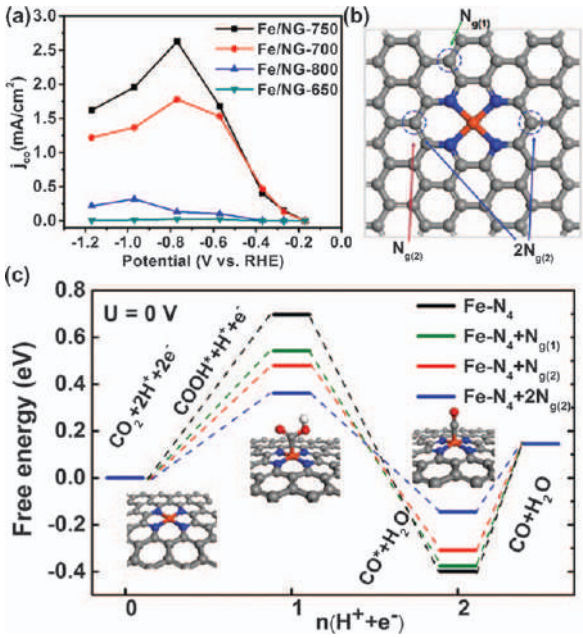

Figure 6.15 Importance of the inductive effect: (a) Partial current densities of CO on Fe–nanographene catalysts with different nitrogen content. (b) Optimised structure of Fe–N4 sites on a graphene layer along with potential nitrogen-doping sites. (c) Free energy diagram for CO_2 to CO conversion on Fe–N4 moieties with various nitrogen-doping.
Reproduced from ref. 122 with permission from John Wiley and Sons, Copyright © 2018 Wiley-VCHVerlag GmbH & Co. KGaA, Weinheim.

(see Figure 6.15b). Different graphitic nitrogen-doping configurations illustrated that the additional nitrogen substitution on graphene improves the catalytic activity by lowering the energy barrier of *COOH formation, as well as by facilitating the *CO desorption step through the change of occupied density of states (DOS) (see Figure 6.15c). The inductive effect of nitrogen-doping near the single-atomic sites on the electrochemical CO_2 reduction has been documented using DFT calculations.

6.4.7 Effect of SCS: Local Proton Environment

In natural enzymes, the active site is surrounded by protein side-chains, which make unique SCSs around the active sites, enhancing the activity of the enzymes during their catalytic reactions.[232] Various factors in the SCS can affect the activity of the metal centre, *i.e.* a pendant proton source, charged moieties, steric functional groups, and bimetallic active species. Among them, a pendant proton source near the active site can enhance the CO_2RR catalytic activity by stabilizing the CO_2 bound metal centre and facilitating the proton transfer/shuttling (see Figure 6.16a).[233]

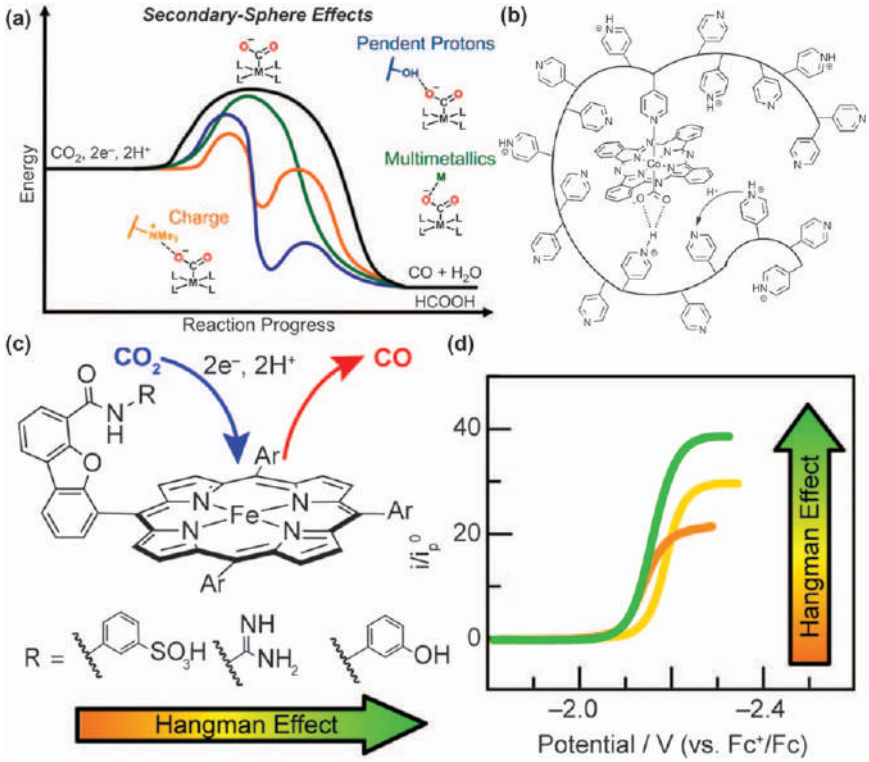

Figure 6.16 Importance of the SCS: (a) Possible effects of the SCS on the catalytic selectivity. (b) Structure of CoPc encapsulated within a hydrophobic poly-4-vinylpyridine (P4VP) membrane highlighting SCS effects. (c and d) Hangman effect on CO_2RR.
Reproduced from ref. 233, https://doi.org/10.3389/fchem.2019.00397, under the terms of the CC BY 4.0 license, https://creativecommons.org/licenses/by/4.0/, from ref. 234, https://doi.org/10.1038/s41467-019-09626-8, under the terms of the CC BY 4.0 license, https://creativecommons.org/licenses/by/4.0/, and from ref. 236 with permission from American Chemical Society, Copyright 2018.

In the [NiFe] CO dehydrogenase enzyme the histidine (H93) and lysine (K563) residues in the SCS play crucial roles in the activation and conversion of CO to CO_2. While binding the CO at the nickel center, the hydroxide bound to the iron becomes deprotonated by the lysine residue (K563) and then the Fe–oxo species interacts with the carbon of CO to form a new C–O bond and generate the μ^2–η^2–CO_2 adduct. This CO_2 bound NiFe centre with the μ^2–η^2–CO_2 binding mode is stabilized by two hydrogen bonds, one from the histidine residue (H93) and the other from the lysine residue (K563), showing the importance of the SCS.[232]

The McCrory group attempted to elucidate the mechanism of the proton transport through the polymer chain. The encapsulated CoPc on the polymers such as polystyrene, poly-2-vinylpyridine and poly-4-vinylpyridine and

exhibited involvement of protons in the RDS during CO_2 reduction reaction.[224,234] It was demonstrated that the axial-coordination of the pyridyl moieties in poly-4-vinylpyridine with the metal centre enhanced the catalytic activity. Moreover, the involvement of proton transfer in the RDS was experimentally observed by measuring the kinetic isotopic effect (KIE) value (see Figure 6.16b and c). It is known that if the KIE > 1, the proton is involved in the RDS. Interestingly, the observed high KIE of 3.1 for the py-CoPc was diminished to ~2 for the CoPc encapsulated in the poly-2-vinylpyridine and poly-4-vinylpyridine. From these results, it was suggested that the proton relay mechanism was involved in the RDS in the coordination polymers. Also, it was suggested that controlling the proton supply to the active site during CO_2RR is important to achieve high selectivity and to limit the competitive HER.[234]

Likewise, the 5,10,15,20-tetrakis-(2,6-dihydroxyphenyl)-porphyrin with 8 local –OH protons as substituents showed high activity for the CO_2-to-CO production compared to the catalyst without –OH groups. The pendant OH moieties caused appreciable catalytic current enhancement at a decreased overpotential. It was proposed that the $CO_2^{\bullet -}$ radical anion coordinated with the iron centre is stabilized *via* hydrogen-bonding interactions with the pendant proton donor.[147,235]

It is noteworthy to mention the effect of SCS in CO_2 reduction, catalyzed by a few molecular complexes, where the substituents on the ligand backbone stabilized the CO_2 intermediate bound with the metal center. Nocera and co-workers utilised different kinds of ''Hangman-type'' porphyrin architecture to understand the role of pendant groups on the catalytic activity towards CO_2-to-CO conversion (see Figure 6.16d).[236] Based on functional groups such as phenol, guanidinium, and sulfonate, the hangman effect on the catalytic activity has been observed (phenol > guanidinium > sulphonate). DFT calculations predicted that the intramolecular hydrogen bonding ability of the phenol and guanidinium groups (2.1–6.6 kcal mol^{-1}) stabilized the CO_2 within the hangman active site pocket, while hanging sulfonate group destabilized the CO_2 adduct because of the unfavourable electrostatic interactions. Consequently, the rate of CO_2 reduction activity was altered.

Accordingly, along with the change of ligand–donor functionalities, the introduction of other useful functionalities such as hydrogen-bonding groups on the carbon matrices is expected to enhance the proton shuttling pathway or stabilize the intermediates during the catalytic CO_2 reduction reactions of the ADMAs on the carbon support. So far, no attempt has been made to study the effect of the secondary coordination sphere during the ADMAs catalyzed CO_2 reduction reactions. Thus, the introduction of a functional group on the carbon needs to be considered to improve the CO_2 reduction activity of ADMCs.

6.4.8 Effect of the Oxidation State of the Metal Centre

During eCO_2RR most of the metal centers are reduced to a low-valent state to bind and activate the CO_2. As such, not only the local structure of the ADMAs

but also the electronic structure of the metal center can play crucial roles in activating the substrate and reducing the overpotential of the eCO_2RR. Recently, it has been demonstrated that by introducing a sulphur-containing molecule such as L-cysteine in the pyrolysing mixture or by increasing the population of pyrrolic nitrogen atoms in the carbon lattice, the atomically-dispersed Ni(I) sites can be stabilized. The synthesized catalysts exhibited a low overpotential for the eCO_2RR compared to the Ni(II) sites (see Figure 6.17).[200] Similarly, it has been demonstrated that the overpotential of eCO_2RR catalyzed by an atomically-dispersed iron(III) centre is reduced compared to the other ADMCs based on iron. The iron(III) center has been stabilized by increasing the population of pyrrolic nitrogen contents in the carbon matrix. It has been achieved by pyrolyzing the Fe-doped ZIF-8 at 900 °C. The reported catalysts displayed the production of CO at a very low

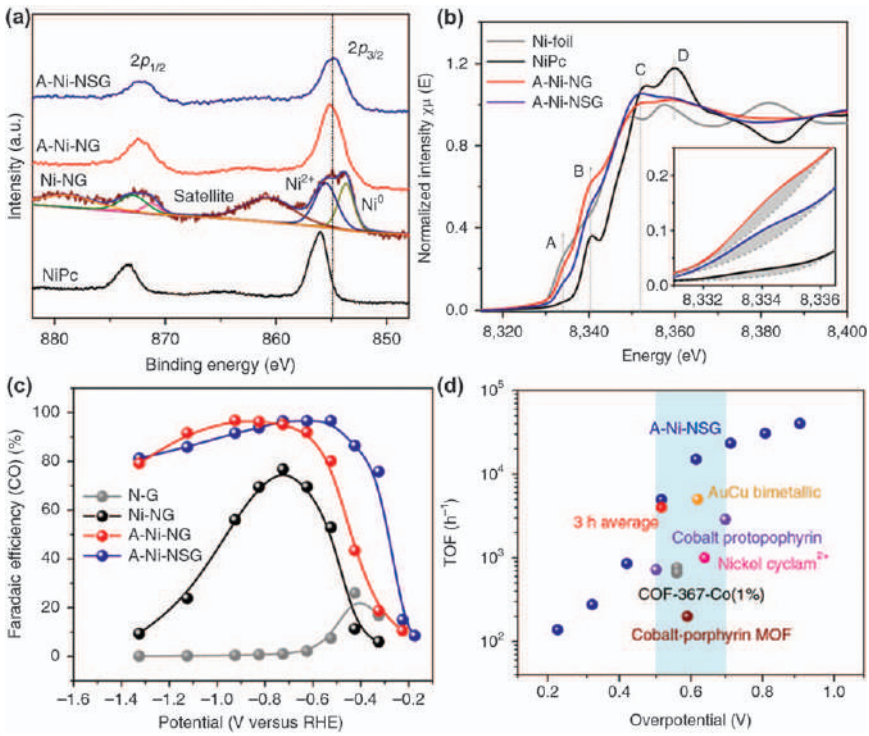

Figure 6.17 Effect of oxidation state of the metal center: (a) High-resolution XPS Ni 2p spectra for the Ni(I) species; (b) Ni K-edge XANES spectra of various Ni materials (peak A: 1s→3d transition; peak B: 1s→4pz transition; peak C and D: 1s→4px,y transitions and multiple scattering processes respectively; (c) CO Faradaic efficiency of Ni materials at various applied potentials; (d) TOF of low-valent Ni material compared with other CO-producing catalysts.
Reproduced from ref. 109 with permission from Springer Nature, Copyright 2018.

overpotential (80 mV). Furthermore, it was suggested that the Fe(III) center enables faster CO_2 adsorption and decreased the CO absorption compared to the Fe(II) sites, displaying better activity.[237] Moreover, the atomically-dispersed $Sn^{\delta+}$ sites ($0 < \delta < 4$) displayed a very low overpotential (60 mV) for the eCO_2RR to formate production.[213] Interestingly, the atomically-dispersed Sn(II) sites exhibited only CO production, so the oxidation state of the ADMAs plays crucial roles in both reducing the overpotential, as well as in product selectivity.[212]

6.5 Production of Highly-reduced C1 and Multi-carbon Products

Most of the ADMAs-based catalysts exhibit good selectivity and stability towards CO production from CO_2. To expand the applicability of the ADMAs towards the production of other valuable hydrocarbons such as C1 to Cn products, a different approach is needed. Their production is considered promising because of the applicability and high energy density of those molecules. C1 products such as methane and methanol have high energy densities and can be directly used as fuels, storing renewable energies harvested from photovoltaics or wind turbines. Furthermore, C2 products, such as ethylene, are versatile chemical feedstocks in the chemical industry.

6.5.1 Production of C_1 Hydrocarbons

To produce highly reduced C1 products such as methane and methanol from CO_2, controlling the CO binding energy is crucial because CO is suggested to be a key intermediate in the formation of hydrocarbons from CO_2. Unfortunately, the ADMCs favour the CO desorption due to the weak binding affinity of the CO molecule, but by tuning the local structure of the ADMCs it can be achieved nevertheless.

Varela *et al.* showed that Fe- or Mn-doped nitrogenated carbon derived from polyaniline can produce traces of CH_4 from CO_2.[162] Later, Ju *et al.* noted that the relatively strong binding of *CO on Fe–N_x and Mn–N_x active sites is responsible for the ability of these two catalysts to produce CH_4.[154] In simple terms, the CO molecule must be bound strongly and long enough with active sites to undergo subsequent dissociation and hydrogenation steps to arrive at CH_4. For comparison, further transformation of CO to hydrocarbons is prevented by Ni ADMAs because of the energetically-favoured *CO desorption.

To understand the mechanism of CH_4 production in detail, the Strasser group studied the effect of the pH of the electrolyte on the product selectivity catalyzed by Fe-N-C (see Figure 6.18). It was found that the selectivity of CO was unaltered by pH during CO_2RR. The proton-decoupled electron-transfer pathway was therefore suggested to explain the pH independency of the CO production. However, at low pH, methane was detected due to the higher

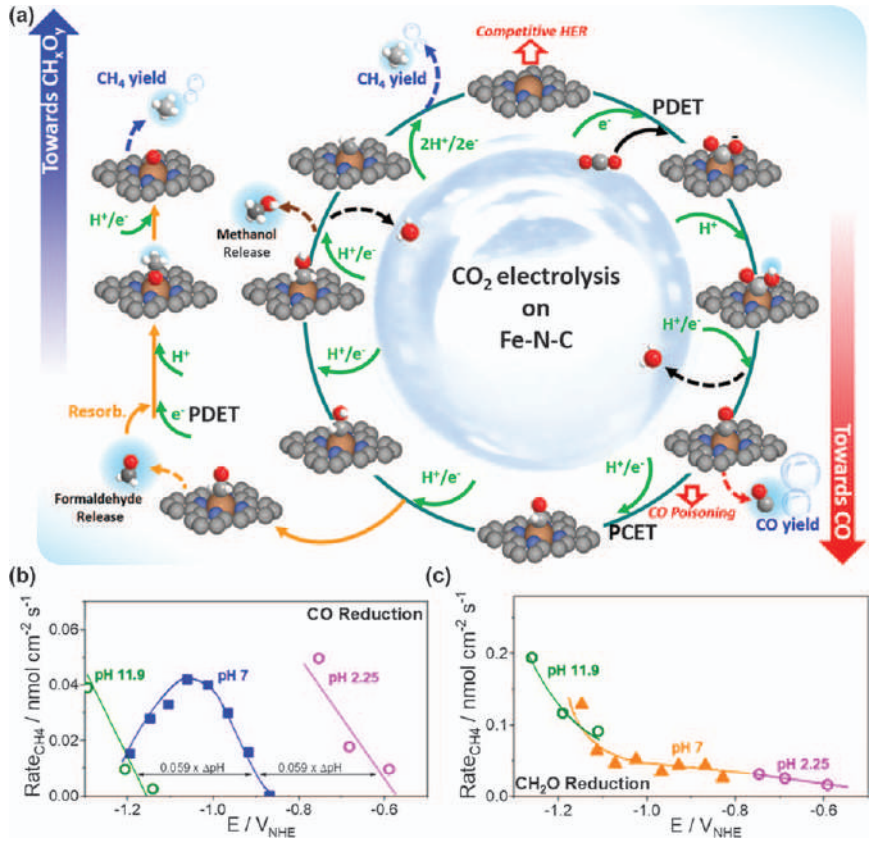

Figure 6.18 (a) Comparative mechanistic pathways of CH_4 formation from CO and CH_2O catalyzed by Fe–N–C. (b) Rate of methane formation from CO at various pH and applied potential. (c) Rate of methane formation from formaldehyde at various pH and applied potential.
Reproduced from ref. 239 with permission from American Chemical Society, Copyright 2019.

proton concentration which favours the hydrogenation of CO. Still, the FE of CH_4 was very low due to the dominant HER.[238] To understand what kind of intermediate is involved in the CO_2-to-CH_4 conversion, CO and formaldehyde were considered as seed reactants and the reduction products were analysed at different pH and applied potential (see Figure 6.18b and c). Based on the CH_4 formation from formaldehyde, but not CO, it was suggested that the most favourable pathway of CO_2-to-CH_4 conversion is the formaldehyde formation pathway, while the CO reduction pathway produces methanol. Indeed, DFT calculations suggest that the CH_2O-to-CH_4 conversion follows a low energy pathway compared to the CO-to-CH_4 pathway. In particular, the Fe–N–C catalysts followed the second hydrogenation step of the *CHO intermediate into CH_2O rather than *CHOH, which leads to the formation of methane rather than methanol.[239] Moreover, the effect of

controlling the local pH by means of electrode morphology needs to be considered, in that a shift in product selectivity from ethylene to ethane has been demonstrated in the heterogeneous system.[240]

Interestingly, atomically-dispersed copper-decorated carbon nanofibers have exhibited high methanol production with FE of 44% at −0.9 V *vs.* RHE.[241] According to DFT calculations, Cu–N_4 active sites possess a relatively higher binding energy for the *CO intermediate than the Ni–N_4 sites. Therefore, *CO could be further reduced to products such as methanol, instead of being released from the catalyst surface as CO.[241] However, it should be noted that the Cu–N_x sites under the reductive potential can become unstable as the d-orbital of Cu^0 and Cu^{1+} is fully occupied.[242] Also, during the CO_2RR experiments with copper phthalocyanine, the formation of Cu nanoparticles was found after prolonged bulk electrolysis under a reductive potential. Hence, the actual active sites of the catalysts were derived from metallic copper particles.[243] *In situ* XAS analysis of the Cu–N–C revealed the formation of Cu agglomeration under CO_2RR conditions. Cu–N–C with atomically-dispersed copper atoms was prepared *via* a typical ZIF pyrolytic route. During electrolysis, the isolated sites transiently convert into metallic copper which are likely to be the catalytically-active species.[243] Interestingly, it is found that the initial Cu ADMAs can be recovered after electrolysis suggesting that further agglomeration of Cu atoms was efficiently inhibited and only sub-nanometer sized copper agglomerations (∼0.5 nm) were formed. This uncommon behaviour of Cu–N–C emphasizes the unique interaction between metal atoms and the carbon support, and can provide a new approach to develop CO_2RR electrocatalysts.

Previously, to study the effect of metal dimers towards CO_2 reduction, the metal dopant pairs M2@2SV on graphene supports were considered. It was found that MnCu@2SV sites selectively produced methane and NiCu@2SV sites produced CH_3OH. The crucial role played by the oxophilicity of the incorporated metal dimer on the product selectivity was explored.[244] The strategy used in binary metal alloy catalysts to enhance the catalytic activity for CO_2RR through the binding mode of CO_2 could be extended to ADMCs to alter the product selectivity.[245] In other words, decoration of ADMAs on carbon matrices might be considered to achieve highly selective production of methane/methanol from CO_2. Also, the lessons learned from other catalytic systems, such as controlling the pH and oxophilicity of the metal center, can be adopted to control the CO binding energy to achieve methanol or methane from CO_2 by ADMCs before desorption from the active site.

6.5.2 Production of Multi-carbon Products

Producing C2 to long-chain hydrocarbons are considered more advantageous than the production of C_1 products, in terms of volumetric energy density. The higher volumetric energy density of long-chain products [*e.g.* butanol (26.9 MJ L^{-1}) > ethanol (21.4 MJ L^{-1}) > methanol (15.9 MJ L^{-1})] produced from CO_2 makes them suitable candidates for replacing at least

some of the petroleum-based fuels.[246] However, the production of C_2 or long-chain hydrocarbons from CO_2 is challenging because it requires C–C bond formation steps.[247]

Nature has addressed the issues in making long-chain hydrocarbons using efficient CO_2 fixation. This has inspired the scientific community to develop synthetic catalysts for producing the desired value-added fuels with high selectivity.[248] For instance, acetyl-coenzyme A (acetyl-CoA) participate in more than 100 different reactions and among these the most important one is C–C coupling of short-chain carbon building blocks.[249] *Clostridium acetobutylicum* can biochemically produce butanol by the direct condensation of two acetyl monomers followed by subsequent reduction reactions.[250] Initially, the C–C coupling pathway of acetyl groups are triggered through the Claisen condensation reaction and then the produced butyryl-CoA is reduced to butanol with the help from other electron-transfer proteins (see Figure 6.19).

Among the various CO_2 reduction electrocatalysts, copper-based catalysts have displayed exceptional abilities in C–C coupling, and produced C_2–C_3 products such as ethylene, ethanol, and propanol. A moderate binding affinity of the *CO intermediate at copper-based catalysts is suggested to be responsible for the formation of hydrocarbons.[251–253] The possible reaction pathways for the reduced C_1 and C_2 products are described in Figure 6.20. DFT calculations predicted that the direct reduction of CO follows different pathways, depending on the pH at the copper (111) electrode. At acidic pH,

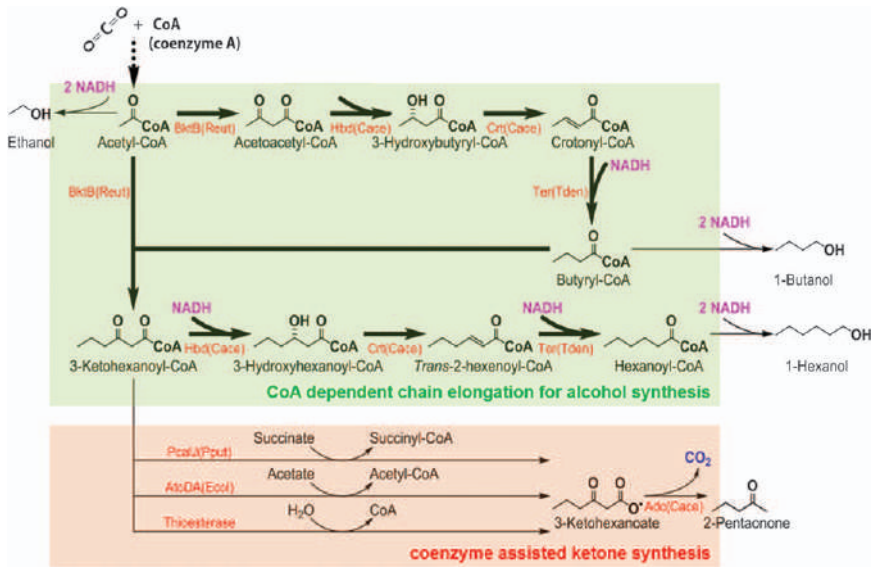

Figure 6.19 Schematic illustration of the biological synthesis of long-chain liquid fuels.
Reproduced from ref. 248 with permission from American Chemical Society, Copyright 2017.

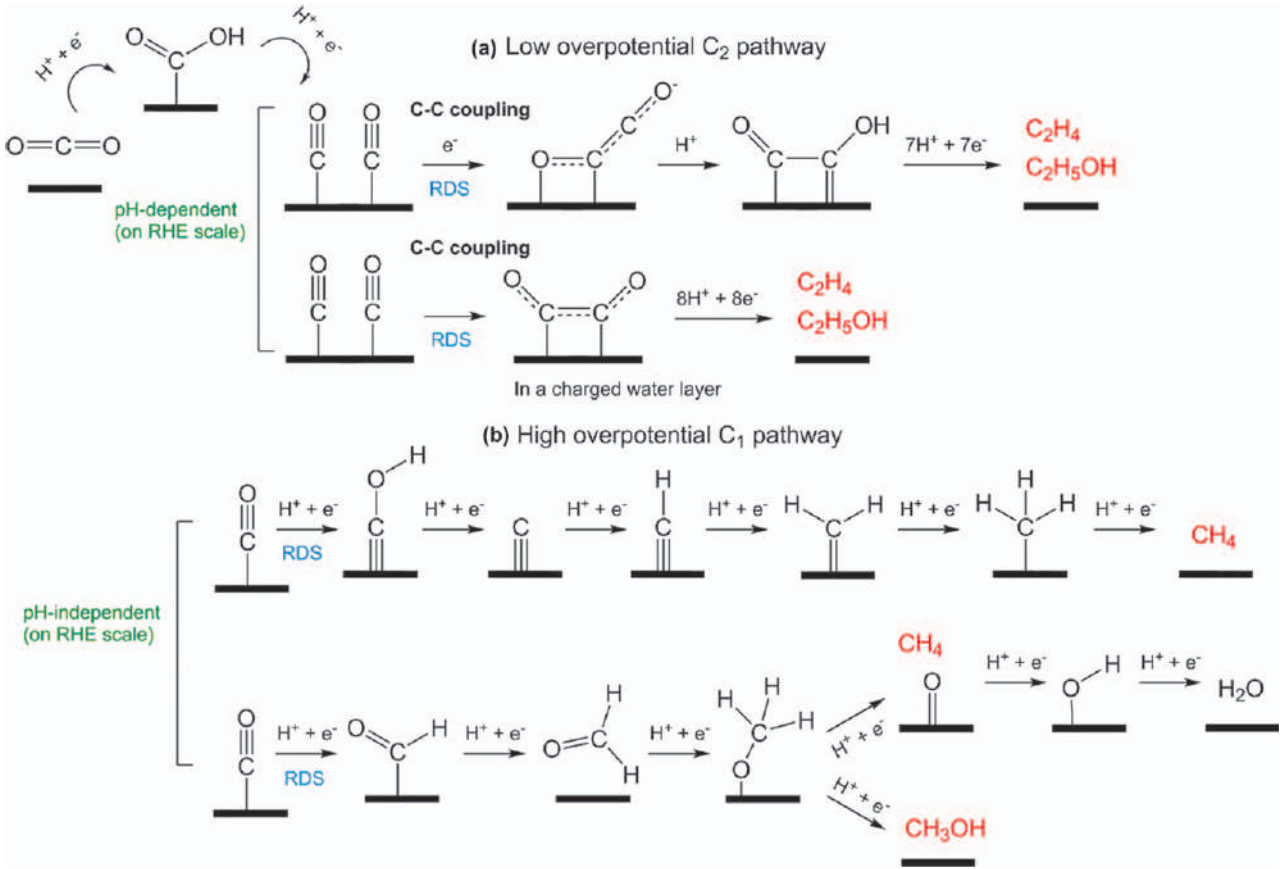

Figure 6.20 Proposed CO dimerization or reduction pathways for the electrochemical reduction of CO_2 to C1–C2 products on the Cu surface.
Adapted from ref. 248 with permission from American Chemical Society, Copyright 2017.

the C_1 pathway is favoured while the C_2 pathway is kinetically blocked. In contrast, at neutral pH the C–C coupling is dominant through adsorbed CO dimerization, while the C_1 pathways are suppressed to give high selectivity for C2 products.[254] As depicted in Figure 6.20, the *CO dimerization proceeds through various intermediates such as *OCCHO, *OCHCHO, *OCHCHOH, *OCHCH, and *$OCHCH_2$ on the copper surface.

As the CO dimerization step is crucial for producing multi-carbon products, metal–dimer or bi-atom active sites, where two CO molecules can be bound simultaneously, may be beneficial to achieve C–C coupling. In homogeneous catalysis, it has been previously reported that dimeric copper complexes with nitrogen and/or sulphur coordination have produced oxalic acid by coupling two CO_2 molecules, either chemically or electrochemically.[255,256] Decoration of copper dimers on carbon matrices may be considered as a good option for achieving selective production of C_2 products in high yield. DFT calculations also predicted that copper dimers supported on a nitrogenated holey graphene (C_2N) layer boost the CO_2RR.[257] $Cu_2@C_2N$ exhibits a high catalytic ability to produce CH_4 rather than CH_3OH, while at the same time favouring the effective CO coupling to make ethylene.

However, the decoration of targeted dimeric or multimeric metal atoms on carbon matrices is challenging. He *et al.* studied the structure of an iron dimer in the lattice of monolayer graphene.[246] Fe dopant atoms were loaded on the clean surface of graphene by drop-casting iron(III) chloride ($FeCl_3$) solutions. HAADF–STEM was used to investigate the atomic structure of iron pairs and real-time dynamics of iron atoms in graphene vacancies. Several iron dimer structures were observed embedded in the tri-vacancy, quad-vacancy, or two adjacent mono-vacancies of the graphene lattice. The dimer structures were found to evolve from an initial single iron atom which acts as trapping centre for the second Fe atom. The energy driving this process comes primarily from the focused electron beam.[246] Lu *et al.* fabricated Pt dimers on reduced-GO with a bottom-up approach using the ALD technique.[38] During this process, the preliminarily deposited monomeric Pt atoms act as nucleation sites to selectively attach secondary Pt atoms, forming Pt dimers. The Pt dimers exhibited superior activity in hydrolytic dehydrogenation of ammonia borane compared with monomeric Pt atoms or nanoparticles on graphene.[38] Instead of using the high vacuum method such as ALD, Zeng *et al.* tried a wet-chemical route to fabricate dimeric active sites on carbon materials.[258] First, Fe–N–C was prepared by conventional pyrolysis methods using ZIF-8, 1,10-phenanthroline, and iron acetate as precursors. The then-prepared Fe–N–Cs was treated with a solution of chloroplatinic acid (H_2PtCl_6) and exposed to a mild heat treatment at 450 °C under an Ar atmosphere. Pt atoms were suggested to be preferentially grafted onto the iron centre through a bridging oxygen atom creating a new active moiety of $Pt_1–O_2–Fe_1–N_4$. The active sites showed high catalytic activities toward OER and HER by outperforming the benchmark ruthenium oxide (RuO_2) and were comparable with Pt/C, with overpotentials of 310 mV

for OER in alkaline solution and 60 mV for HER in acidic media. Thus, in future work, attempts need to be made to explore and understand the importance of metal nuclearity in the C–C bond formation during CO_2RR.

6.6 Conclusions

This chapter highlighted the CO_2RR activities of ADMAs on carbon supports and focused on the structure–activity relationship of their active centres. The methods to synthesize various ADMCs and the approaches to tune the activity using structural modifications were discussed. Various ADMCs have shown promising CO_2 reduction activity, mainly for CO production and in a few cases minor C1 hydrocarbon production. Despite the recent advances in the synthetic and characterization methods, preparation of ADMCs with well-defined coordination structures comparable to the corresponding homogenous catalysts is still challenging. Based on the above discussions, we believe that the approaches for the future development of ADMAs on electrocatalytic CO_2RR may focus on: (1) finding suitable synthetic methods to decorate appropriate active sites for a particular CO_2 reduction product, and (2) detailed characterization of ADMAs to understand the structure–function relationship at the atomic level. Furthermore, the cooperative effects used by the natural enzymes should be adopted to advance the performance of the electrocatalysts. By controlling the second coordination sphere around the active centres, the activities of ADMAs can be tuned by exploiting the inductive effects from nearby dopants or from changes in the local proton environments. Furthermore, production of multi-carbon products requires further exploration to expand the applicability of the ADMCs. Compared to processes in Nature, producing multi-carbon products by efficiently catalyzing C–C coupling reactions using CO_2 as a feedstock, electrochemical C_2 product formation with ADMCs is still challenging. To this end, the formation of atomically-controlled bi- or multi-metallic active sites on the supports is a great challenge.

References

1. M. Meinshausen, N. Meinshausen, W. Hare, S. C. B. Raper, K. Frieler, R. Knutti, D. J. Frame and M. R. Allen, *Nature*, 2009, **458**, 1158–U1196.
2. K. Caldeira and M. E. Wickett, *Nature*, 2003, **425**, 365.
3. H. Baumann, S. C. Talmage and C. J. Gobler, *Nat. Clim. Change*, 2012, **2**, 38–41.
4. Y. Kim, J. H. Lee, H. Ha, S. W. Im and K. T. Nam, *Nano Converg.*, 2016, **3**, 19.
5. C. D. Windle and R. N. Perutz, *Coord. Chem. Rev.*, 2012, **256**, 2562–2570.
6. D. L. DuBois, *Inorg. Chem.*, 2014, **53**, 3935–3960.
7. M. Rakowski Dubois and D. L. Dubois, *Acc. Chem. Res.*, 2009, **42**, 1974–1982.

8. C. Costentin, M. Robert and J.-M. Savéant, *Chem. Soc. Rev.*, 2013, **42**, 2423–2436.
9. N. Elgrishi, M. B. Chambers, X. Wang and M. Fontecave, *Chem. Soc. Rev.*, 2017, **46**, 761–796.
10. D. D. Zhu, J. L. Liu and S. Z. Qiao, *Adv. Mater.*, 2016, **28**, 3423–3452.
11. A. J. Martín, G. O. Larrazábal and J. Pérez-Ramírez, *Green Chem.*, 2015, **17**, 5114–5130.
12. S. Nitopi, E. Bertheussen, S. B. Scott, X. Liu, A. K. Engstfeld, S. Horch, B. Seger, I. E. L. Stephens, K. Chan, C. Hahn, J. K. Nørskov, T. F. Jaramillo and I. Chorkendorff, *Chem. Rev.*, 2019, **119**, 7610–7672.
13. A. J. Sathrum and C. P. Kubiak, *J. Phys. Chem. Lett.*, 2011, **2**, 2372–2379.
14. R. Francke and R. D. Little, *Chem. Soc. Rev.*, 2014, **43**, 2492–2521.
15. E. S. Rountree, B. D. McCarthy, T. T. Eisenhart and J. L. Dempsey, *Inorg. Chem.*, 2014, **53**, 9983–10002.
16. Q. Lu, J. Rosen and F. Jiao, *ChemCatChem*, 2015, **7**, 38–47.
17. H. Mistry, A. S. Varela, S. Kühl, P. Strasser and B. R. Cuenya, *Nat. Rev. Mater.*, 2016, **1**, 16009.
18. X.-F. Li, K.-Y. Lian, L. Liu, Y. Wu, Q. Qiu, J. Jiang, M. Deng and Y. Luo, *Sci. Rep.*, 2016, **6**, 23495.
19. W. Zhu, R. Michalsky, Ö. Metin, H. Lv, S. Guo, C. J. Wright, X. Sun, A. A. Peterson and S. Sun, *J. Am. Chem. Soc.*, 2013, **135**, 16833–16836.
20. W. Zhu, Y.-J. Zhang, H. Zhang, H. Lv, Q. Li, R. Michalsky, A. A. Peterson and S. Sun, *J. Am. Chem. Soc.*, 2014, **136**, 16132–16135.
21. C. Kim, H. S. Jeon, T. Eom, M. S. Jee, H. Kim, C. M. Friend, B. K. Min and Y. J. Hwang, *J. Am. Chem. Soc.*, 2015, **137**, 13844–13850.
22. M. Ma, B. J. Trześniewski, J. Xie and W. A. Smith, *Angew. Chem., Int. Ed.*, 2016, **55**, 9748–9752.
23. S. A. Yao, R. E. Ruther, L. Zhang, R. A. Franking, R. J. Hamers and J. F. Berry, *J. Am. Chem. Soc.*, 2012, **134**, 15632–15635.
24. J. Shen, R. Kortlever, R. Kas, Y. Y. Birdja, O. Diaz-Morales, Y. Kwon, I. Ledezma-Yanez, K. J. P. Schouten, G. Mul and M. T. M. Koper, *Nat. Commun.*, 2015, **6**, 8177.
25. A. Maurin and M. Robert, *J. Am. Chem. Soc.*, 2016, **138**, 2492–2495.
26. X. Zhang, Z. Wu, X. Zhang, L. Li, Y. Li, H. Xu, X. Li, X. Yu, Z. Zhang, Y. Liang and H. Wang, *Nat. Commun.*, 2017, **8**, 14675.
27. X.-M. Hu, M. H. Rønne, S. U. Pedersen, T. Skrydstrup and K. Daasbjerg, *Angew. Chem., Int. Ed.*, 2017, **56**, 6468–6472.
28. X. F. Yang, A. Q. Wang, B. T. Qiao, J. Li, J. Y. Liu and T. Zhang, *Acc. Chem. Res.*, 2013, **46**, 1740–1748.
29. H. B. Zhang, G. G. Liu, L. Shi and J. H. Ye, *Adv. Energy Mater.*, 2018, **8**, 1701343.
30. J. Liu, *ACS Catal.*, 2017, **7**, 34–59.
31. L. Zhang, Y. Ren, W. Liu, A. Wang and T. Zhang, *Natl. Sci. Rev.*, 2018, **5**, 653–672.
32. X. Cui, W. Li, P. Ryabchuk, K. Junge and M. Beller, *Nat. Catal.*, 2018, **1**, 385–397.

33. M. N. Jackson, S. Oh, C. J. Kaminsky, S. B. Chu, G. H. Zhang, J. T. Miller and Y. Surendranath, *J. Am. Chem. Soc.*, 2018, **140**, 1004–1010.
34. C. J. Kaminsky, J. Wright and Y. Surendranath, *ACS Catal.*, 2019, **9**, 3667–3671.
35. M. N. Jackson and Y. Surendranath, *Acc. Chem. Res.*, 2019, **52**, 3432–3441.
36. B. Qiao, A. Wang, X. Yang, L. F. Allard, Z. Jiang, Y. Cui, J. Liu, J. Li and T. Zhang, *Nat. Chem.*, 2011, **3**, 634–641.
37. P. Munnik, P. E. de Jongh and K. P. de Jong, *Chem. Rev.*, 2015, **115**, 6687–6718.
38. H. Yan, Y. Lin, H. Wu, W. Zhang, Z. Sun, H. Cheng, W. Liu, C. Wang, J. Li, X. Huang, T. Yao, J. Yang, S. Wei and J. Lu, *Nat. Commun.*, 2017, **8**, 1070.
39. J. Lin, A. Q. Wang, B. T. Qiao, X. Y. Liu, X. F. Yang, X. D. Wang, J. X. Liang, J. X. Li, J. Y. Liu and T. Zhang, *J. Am. Chem. Soc.*, 2013, **135**, 15314–15317.
40. Q. Liu and Z. L. Zhang, *Catal. Sci. Technol.*, 2019, **9**, 4821–4834.
41. A. Q. Wang, J. Li and T. Zhang, *Nat. Rev. Chem.*, 2018, **2**, 65–81.
42. L. C. Liu and A. Corma, *Chem. Rev.*, 2018, **118**, 4981–5079.
43. P. Trogadas, T. F. Fuller and P. Strasser, *Carbon*, 2014, **75**, 5–42.
44. Y. Peng, B. Lu and S. Chen, *Adv. Mater.*, 2018, **30**, 1801995.
45. C. Rivera-Cárcamo and P. Serp, *ChemCatChem*, 2018, **10**, 5058–5091.
46. N. Yang, S. R. Waldvogel and X. Jiang, *ACS Appl. Mater. Interfaces*, 2016, **8**, 28357–28371.
47. J. Masa, W. Xia, M. Muhler and W. Schuhmann, *Angew. Chem., Int. Ed.*, 2015, **54**, 10102–10120.
48. S. Sun, G. Zhang, N. Gauquelin, N. Chen, J. Zhou, S. Yang, W. Chen, X. Meng, D. Geng, M. N. Banis, R. Li, S. Ye, S. Knights, G. A. Botton, T.-K. Sham and X. Sun, *Sci. Rep.*, 2013, **3**, 1775.
49. N. Cheng, S. Stambula, D. Wang, M. N. Banis, J. Liu, A. Riese, B. Xiao, R. Li, T.-K. Sham, L.-M. Liu, G. A. Botton and X. Sun, *Nat. Commun.*, 2016, **7**, 13638.
50. S. Stambula, N. Gauquelin, M. Bugnet, S. Gorantla, S. Turner, S. Sun, J. Liu, G. Zhang, X. Sun and G. A. Botton, *J. Phys. Chem. C*, 2014, **118**, 3890–3900.
51. M. Kim, K.-J. Kim, S.-J. Lee, H.-M. Kim, S.-Y. Cho, M.-S. Kim, S.-H. Kim and K.-B. Kim, *ACS Appl. Mater. Interfaces*, 2017, **9**, 701–709.
52. H. Yan, H. Cheng, H. Yi, Y. Lin, T. Yao, C. Wang, J. Li, S. Wei and J. Lu, *J. Am. Chem. Soc.*, 2015, **137**, 10484–10487.
53. D. I. Kochubey, V. V. Chesnokov and S. E. Malykhin, *Carbon*, 2012, **50**, 2782–2787.
54. C. H. Choi, M. Kim, H. C. Kwon, S. J. Cho, S. Yun, H.-T. Kim, K. J. J. Mayrhofer, H. Kim and M. Choi, *Nat. Commun.*, 2016, **7**, 10922.
55. D. H. Won, H. Shin, M. W. Chung, H. Jung, K. H. Chae, H.-S. Oh, Y. J. Hwang and B. K. Min, *Appl. Catal., B*, 2019, **258**, 117961.
56. A. Zitolo, V. Goellner, V. Armel, M.-T. Sougrati, T. Mineva, L. Stievano, E. Fonda and F. Jaouen, *Nat. Mater.*, 2015, **14**, 937.

57. J.-C. Li, Z.-Q. Yang, D.-M. Tang, L. Zhang, P.-X. Hou, S.-Y. Zhao, C. Liu, M. Cheng, G.-X. Li, F. Zhang and H.-M. Cheng, *NPG Asia Mater.*, 2018, **10**, e461.
58. J. R. Pels, F. Kapteijn, J. A. Moulijn, Q. Zhu and K. M. Thomas, *Carbon*, 1995, **33**, 1641–1653.
59. E. Zussman, X. Chen, W. Ding, L. Calabri, D. A. Dikin, J. P. Quintana and R. S. Ruoff, *Carbon*, 2005, **43**, 2175–2185.
60. R. Silva, D. Voiry, M. Chhowalla and T. Asefa, *J. Am. Chem. Soc.*, 2013, **135**, 7823–7826.
61. F. Su, C. K. Poh, J. S. Chen, G. Xu, D. Wang, Q. Li, J. Lin and X. W. Lou, *Energy Environ. Sci.*, 2011, **4**, 717–724.
62. G. Wu, K. L. More, C. M. Johnston and P. Zelenay, *Science*, 2011, **332**, 443.
63. G. Wu, C. M. Johnston, N. H. Mack, K. Artyushkova, M. Ferrandon, M. Nelson, J. S. Lezama-Pacheco, S. D. Conradson, K. L. More, D. J. Myers and P. Zelenay, *J. Mater. Chem.*, 2011, **21**, 11392–11405.
64. F. Jaouen, E. Proietti, M. Lefèvre, R. Chenitz, J.-P. Dodelet, G. Wu, H. T. Chung, C. M. Johnston and P. Zelenay, *Energy Environ. Sci.*, 2011, **4**, 114–130.
65. H.-W. Liang, W. Wei, Z.-S. Wu, X. Feng and K. Müllen, *J. Am. Chem. Soc.*, 2013, **135**, 16002–16005.
66. H. Peng, Z. Mo, S. Liao, H. Liang, L. Yang, F. Luo, H. Song, Y. Zhong and B. Zhang, *Sci. Rep.*, 2013, **3**, 1765.
67. G. Zhang, Y. Jia, C. Zhang, X. Xiong, K. Sun, R. Chen, W. Chen, Y. Kuang, L. Zheng, H. Tang, W. Liu, J. Liu, X. Sun, W.-F. Lin and H. Dai, *Energy Environ. Sci.*, 2019, **12**, 1317–1325.
68. X. Wang, X. Chen, A. Thomas, X. Fu and M. Antonietti, *Adv. Mater.*, 2009, **21**, 1609–1612.
69. Z. Chen, S. Mitchell, E. Vorobyeva, R. K. Leary, R. Hauert, T. Furnival, Q. M. Ramasse, J. M. Thomas, P. A. Midgley, D. Dontsova, M. Antonietti, S. Pogodin, N. López and J. Pérez-Ramírez, *Adv. Funct. Mater.*, 2017, **27**, 1605785.
70. L. Lai, J. R. Potts, D. Zhan, L. Wang, C. K. Poh, C. Tang, H. Gong, Z. Shen, J. Lin and R. S. Ruoff, *Energy Environ. Sci.*, 2012, **5**, 7936–7942.
71. K. Zhang, L. L. Zhang, X. S. Zhao and J. Wu, *Chem. Mater.*, 2010, **22**, 1392–1401.
72. T.-M. Wu, Y.-W. Lin and C.-S. Liao, *Carbon*, 2005, **43**, 734–740.
73. S. Zhang, K. Dokko and M. Watanabe, *Mater. Horizons*, 2015, **2**, 168–197.
74. J. S. Lee, X. Wang, H. Luo, G. A. Baker and S. Dai, *J. Am. Chem. Soc.*, 2009, **131**, 4596–4597.
75. J. P. Paraknowitsch, J. Zhang, D. Su, A. Thomas and M. Antonietti, *Adv. Mater.*, 2010, **22**, 87–92.
76. W. Yang, T.-P. Fellinger and M. Antonietti, *J. Am. Chem. Soc.*, 2011, **133**, 206–209.
77. N. Ranjbar Sahraie, J. P. Paraknowitsch, C. Göbel, A. Thomas and P. Strasser, *J. Am. Chem. Soc.*, 2014, **136**, 14486–14497.

78. J. Wang, Z. Huang, W. Liu, C. Chang, H. Tang, Z. Li, W. Chen, C. Jia, T. Yao, S. Wei, Y. Wu and Y. Li, *J. Am. Chem. Soc.*, 2017, **139**, 17281–17284.
79. D. Zhang, W. Chen, Z. Li, Y. Chen, L. Zheng, Y. Gong, Q. Li, R. Shen, Y. Han, W.-C. Cheong, L. Gu and Y. Li, *Chem. Commun.*, 2018, **54**, 4274–4277.
80. Y. Pan, K. Sun, S. Liu, X. Cao, K. Wu, W.-C. Cheong, Z. Chen, Y. Wang, Y. Li, Y. Liu, D. Wang, Q. Peng, C. Chen and Y. Li, *J. Am. Chem. Soc.*, 2018, **140**, 2610–2618.
81. Y. J. Sa, D.-J. Seo, J. Woo, J. T. Lim, J. Y. Cheon, S. Y. Yang, J. M. Lee, D. Kang, T. J. Shin, H. S. Shin, H. Y. Jeong, C. S. Kim, M. G. Kim, T.-Y. Kim and S. H. Joo, *J. Am. Chem. Soc.*, 2016, **138**, 15046–15056.
82. Y. Qu, Z. Li, W. Chen, Y. Lin, T. Yuan, Z. Yang, C. Zhao, J. Wang, C. Zhao, X. Wang, F. Zhou, Z. Zhuang, Y. Wu and Y. Li, *Nat. Catal.*, 2018, **1**, 781–786.
83. Y. Qu, B. Chen, Z. Li, X. Duan, L. Wang, Y. Lin, T. Yuan, F. Zhou, Y. Hu, Z. Yang, C. Zhao, J. Wang, C. Zhao, Y. Hu, G. Wu, Q. Zhang, Q. Xu, B. Liu, P. Gao, R. You, W. Huang, L. Zheng, L. Gu, Y. Wu and Y. Li, *J. Am. Chem. Soc.*, 2019, **141**, 4505–4509.
84. M. N. Jackson, C. J. Kaminsky, S. Oh, J. F. Melville and Y. Surendranath, *J. Am. Chem. Soc.*, 2019, **141**, 14160–14167.
85. S. J. Pennycook and D. E. Jesson, *Ultramicroscopy*, 1991, **37**, 14–38.
86. O. L. Krivanek, M. F. Chisholm, V. Nicolosi, T. J. Pennycook, G. J. Corbin, N. Dellby, M. F. Murfitt, C. S. Own, Z. S. Szilagyi, M. P. Oxley, S. T. Pantelides and S. J. Pennycook, *Nature*, 2010, **464**, 571–574.
87. P. A. Midgley, M. Weyland, J. M. Thomas and B. F. G. Johnson, *Chem. Commun.*, 2001, 907–908.
88. L. Zhang, Y. Jia, G. Gao, X. Yan, N. Chen, J. Chen, M. T. Soo, B. Wood, D. Yang, A. Du and X. Yao, *Chem*, 2018, **4**, 285–297.
89. K. Suenaga and M. Koshino, *Nature*, 2010, **468**, 1088–1090.
90. J. H. Warner, Y.-C. Lin, K. He, M. Koshino and K. Suenaga, *Nano Lett.*, 2014, **14**, 6155–6159.
91. Y.-C. Lin, P.-Y. Teng, P.-W. Chiu and K. Suenaga, *Phys. Rev. Lett.*, 2015, **115**, 206803.
92. Y.-C. Lin, P.-Y. Teng, C.-H. Yeh, M. Koshino, P.-W. Chiu and K. Suenaga, *Nano Lett.*, 2015, **15**, 7408–7413.
93. J. E. Penner-Hahn, in *Comprehensive Coordination Chemistry II*, ed. J. A. McCleverty and T. J. Meyer, Pergamon, Oxford, 2003, pp. 159–186, , DOI: 10.1016/B0-08-043748-6/01063-X.
94. J. A. Kirby, D. B. Goodin, T. Wydrzynski, A. S. Robertson and M. P. Klein, *J. Am. Chem. Soc.*, 1981, **103**, 5537–5542.
95. Q. Jia, N. Ramaswamy, H. Hafiz, U. Tylus, K. Strickland, G. Wu, B. Barbiellini, A. Bansil, E. F. Holby, P. Zelenay and S. Mukerjee, *ACS Nano*, 2015, **9**, 12496–12505.
96. M. C. M. Alves, J. P. Dodelet, D. Guay, M. Ladouceur and G. Tourillon, *J. Phys. Chem.*, 1992, **96**, 10898–10905.

97. T. A. Smith, J. E. Penner-Hahn, M. A. Berding, S. Doniach and K. O. Hodgson, *J. Am. Chem. Soc.*, 1985, **107**, 5945–5955.
98. S. Kim, I. T. Bae, M. Sandifer, P. N. Ross, R. Carr, J. Woicik, M. R. Antonio and D. A. Scherson, *J. Am. Chem. Soc.*, 1991, **113**, 9063–9066.
99. H. Fei, J. Dong, Y. Feng, C. S. Allen, C. Wan, B. Volosskiy, M. Li, Z. Zhao, Y. Wang, H. Sun, P. An, W. Chen, Z. Guo, C. Lee, D. Chen, I. Shakir, M. Liu, T. Hu, Y. Li, A. I. Kirkland, X. Duan and Y. Huang, *Nat. Catal.*, 2018, **1**, 63–72.
100. U. I. Kramm, J. Herranz, N. Larouche, T. M. Arruda, M. Lefèvre, F. Jaouen, P. Bogdanoff, S. Fiechter, I. Abs-Wurmbach, S. Mukerjee and J.-P. Dodelet, *Phys. Chem. Chem. Phys.*, 2012, **14**, 11673–11688.
101. Q. X. Lai, Q. W. Gao, Q. Su, Y. Y. Liang, Y. X. Wang and Z. Yang, *Nanoscale*, 2015, **7**, 14707–14714.
102. L. Yang, D. J. Cheng, X. F. Zeng, X. Wan, J. L. Shui, Z. H. Xiang and D. P. Cao, *Proc. Natl. Acad. Sci. U. S. A.*, 2018, **115**, 6626–6631.
103. J. Zhao, Q. Deng, S. M. Avdoshenko, L. Fu, J. Eckert and M. H. Rümmeli, *Proc. Natl. Acad. Sci.*, 2014, **111**, 15641.
104. S. Wei, A. Li, J.-C. Liu, Z. Li, W. Chen, Y. Gong, Q. Zhang, W.-C. Cheong, Y. Wang, L. Zheng, H. Xiao, C. Chen, D. Wang, Q. Peng, L. Gu, X. Han, J. Li and Y. Li, *Nat. Nanotechnol.*, 2018, **13**, 856–861.
105. S. Yang, Y. J. Tak, J. Kim, A. Soon and H. Lee, *ACS Catal.*, 2017, **7**, 1301–1307.
106. G. X. Pei, X. Y. Liu, A. Wang, A. F. Lee, M. A. Isaacs, L. Li, X. Pan, X. Yang, X. Wang, Z. Tai, K. Wilson and T. Zhang, *ACS Catal.*, 2015, **5**, 3717–3725.
107. L. Nguyen, S. Zhang, L. Wang, Y. Li, H. Yoshida, A. Patlolla, S. Takeda, A. I. Frenkel and F. Tao, *ACS Catal.*, 2016, **6**, 840–850.
108. J. P. Simonovis, A. Hunt, R. M. Palomino, S. D. Senanayake and I. Waluyo, *J. Phys. Chem. C*, 2018, **122**, 4488–4495.
109. H. B. Yang, S.-F. Hung, S. Liu, K. Yuan, S. Miao, L. Zhang, X. Huang, H.-Y. Wang, W. Cai, R. Chen, J. Gao, X. Yang, W. Chen, Y. Huang, H. M. Chen, C. M. Li, T. Zhang and B. Liu, *Nat. Energy*, 2018, **3**, 140–147.
110. C. Genovese, M. E. Schuster, E. K. Gibson, D. Gianolio, V. Posligua, R. Grau-Crespo, G. Cibin, P. P. Wells, D. Garai, V. Solokha, S. Krick Calderon, J. J. Velasco-Velez, C. Ampelli, S. Perathoner, G. Held, G. Centi and R. Arrigo, *Nat. Commun.*, 2018, **9**, 935.
111. Z. Zhang, J. Xiao, X.-J. Chen, S. Yu, L. Yu, R. Si, Y. Wang, S. Wang, X. Meng, Y. Wang, Z.-Q. Tian and D. Deng, *Angew. Chem., Int. Ed.*, 2018, **57**, 16339–16342.
112. A. H. Wonders, T. H. M. Housmans, V. Rosca and M. T. M. Koper, *J. Appl. Electrochem.*, 2006, **36**, 1215–1221.
113. S. J. Ashton and M. Arenz, *J. Power Sources*, 2012, **217**, 392–399.
114. J.-P. Grote, A. R. Zeradjanin, S. Cherevko and K. J. J. Mayrhofer, *Rev. Sci. Instrum.*, 2014, **85**, 104101.

115. E. L. Clark and A. T. Bell, *J. Am. Chem. Soc.*, 2018, **140**, 7012–7020.
116. S. O. Klemm, A. A. Topalov, C. A. Laska and K. J. J. Mayrhofer, *Electrochem. Commun.*, 2011, **13**, 1533–1535.
117. A. A. Topalov, I. Katsounaros, M. Auinger, S. Cherevko, J. C. Meier, S. O. Klemm and K. J. J. Mayrhofer, *Angew. Chem., Int. Ed.*, 2012, **51**, 12613–12615.
118. F. Calle-Vallejo, J. Tymoczko, V. Colic, Q. H. Vu, M. D. Pohl, K. Morgenstern, D. Loffreda, P. Sautet, W. Schuhmann and A. S. Bandarenka, *Science*, 2015, **350**, 185.
119. Z. Zhao, Z. Chen, X. Zhang and G. Lu, *J. Phys. Chem. C*, 2016, **120**, 28125–28130.
120. J. Li, F. Che, Y. Pang, C. Zou, J. Y. Howe, T. Burdyny, J. P. Edwards, Y. Wang, F. Li, Z. Wang, P. De Luna, C.-T. Dinh, T.-T. Zhuang, M. I. Saidaminov, S. Cheng, T. Wu, Y. Z. Finfrock, L. Ma, S.-H. Hsieh, Y.-S. Liu, G. A. Botton, W.-F. Pong, X. Du, J. Guo, T.-K. Sham, E. H. Sargent and D. Sinton, *Nat. Commun.*, 2018, **9**, 4614.
121. B.-H. Lee, S. Park, M. Kim, A. K. Sinha, S. C. Lee, E. Jung, W. J. Chang, K.-S. Lee, J. H. Kim, S.-P. Cho, H. Kim, K. T. Nam and T. Hyeon, *Nat. Mater.*, 2019, **18**, 620–626.
122. A. S. Varela, W. Ju and P. Strasser, *Adv. Energy Mater.*, 2018, **8**, 1703614.
123. Y. Cheng, S. Yang, S. P. Jiang and S. Wang, *Small Methods*, 2019, **3**, 1800440.
124. X. Su, X.-F. Yang, Y. Huang, B. Liu and T. Zhang, *Acc. Chem. Res.*, 2019, **52**, 656–664.
125. K. T. Chan, J. B. Neaton and M. L. Cohen, *Phys. Rev. B*, 2008, **77**, 235430.
126. H. Sevinçli, M. Topsakal, E. Durgun and S. Ciraci, *Phys. Rev. B*, 2008, **77**, 195434.
127. H. Valencia, A. Gil and G. Frapper, *J. Phys. Chem. C*, 2010, **114**, 14141–14153.
128. A. Bhattacharya, S. Bhattacharya, C. Majumder and G. P. Das, *J. Phys. Chem. C*, 2010, **114**, 10297–10301.
129. P. H. T. Philipsen and E. J. Baerends, *Phys. Rev. B*, 1996, **54**, 5326–5333.
130. A. V. Krasheninnikov, P. O. Lehtinen, A. S. Foster, P. Pyykkö and R. M. Nieminen, *Phys. Rev. Lett.*, 2009, **102**, 126807.
131. H. Wang, K. Li, Y. Cheng, Q. Wang, Y. Yao, U. Schwingenschlögl, X. Zhang and W. Yang, *Nanoscale*, 2012, **4**, 2920–2925.
132. D. Wei, Y. Liu, Y. Wang, H. Zhang, L. Huang and G. Yu, *Nano Lett.*, 2009, **9**, 1752–1758.
133. M. Yang, L. Wang, M. Li, T. Hou and Y. Li, *AIP Adv.*, 2015, **5**, 067136.
134. X. Liu and L. Dai, *Nat. Rev. Mater.*, 2016, **1**, 16064.
135. R. A. Baglia, J. P. T. Zaragoza and D. P. Goldberg, *Chem. Rev.*, 2017, **117**, 13320–13352.
136. G. F. Manbeck and E. Fujita, *J. Porphyrins Phthalocyanines*, 2015, **19**, 45–64.
137. S. Zhu, T. Li, W.-B. Cai and M. Shao, *ACS Energy Lett.*, 2019, **4**, 682–689.
138. N. J. Firet and W. A. Smith, *ACS Catal.*, 2017, **7**, 606–612.

139. M. F. Baruch, J. E. Pander, J. L. White and A. B. Bocarsly, *ACS Catal.*, 2015, **5**, 3148–3156.
140. M. Dunwell, Q. Lu, J. M. Heyes, J. Rosen, J. G. Chen, Y. Yan, F. Jiao and B. Xu, *J. Am. Chem. Soc.*, 2017, **139**, 3774–3783.
141. K. P. Kuhl, T. Hatsukade, E. R. Cave, D. N. Abram, J. Kibsgaard and T. F. Jaramillo, *J. Am. Chem. Soc.*, 2014, **136**, 14107–14113.
142. A. A. Peterson and J. K. Nørskov, *J. Phys. Chem. Lett.*, 2012, **3**, 251–258.
143. H. A. Hansen, J. B. Varley, A. A. Peterson and J. K. Nørskov, *J. Phys. Chem. Lett.*, 2013, **4**, 388–392.
144. J. T. Feaster, C. Shi, E. R. Cave, T. Hatsukade, D. N. Abram, K. P. Kuhl, C. Hahn, J. K. Nørskov and T. F. Jaramillo, *ACS Catal.*, 2017, **7**, 4822–4827.
145. I. Bhugun, D. Lexa and J.-M. Saveant, *J. Am. Chem. Soc.*, 1994, **116**, 5015–5016.
146. I. Bhugun, D. Lexa and J.-M. Savéant, *J. Am. Chem. Soc.*, 1996, **118**, 1769–1776.
147. C. Costentin, S. Drouet, M. Robert and J.-M. Savéant, *Science*, 2012, **338**, 90.
148. C. Costentin, M. Robert, J.-M. Savéant and A. Tatin, *Proc. Natl. Acad. Sci.*, 2015, **112**, 6882.
149. K.-M. Lam, K.-Y. Wong, S.-M. Yang and C.-M. Che, *J. Chem. Soc., Dalton Trans.*, 1995, 1103–1107.
150. B. J. Fisher and R. Eisenberg, *J. Am. Chem. Soc.*, 1980, **102**, 7361–7363.
151. J. Schneider, H. Jia, K. Kobiro, D. E. Cabelli, J. T. Muckerman and E. Fujita, *Energy Environ. Sci.*, 2012, **5**, 9502–9510.
152. J. D. Froehlich and C. P. Kubiak, *Inorg. Chem.*, 2012, **51**, 3932–3934.
153. M. Fujihira, Y. Hirata and K. Suga, *J. Electroanal. Chem. Interfacial Electrochem.*, 1990, **292**, 199–215.
154. A. Bagger, W. Ju, A. S. Varela, P. Strasser and J. Rossmeisl, *Catal. Today*, 2017, **288**, 74–78.
155. V. Tripkovic, M. Vanin, M. Karamad, M. E. Björketun, K. W. Jacobsen, K. S. Thygesen and J. Rossmeisl, *J. Phys. Chem. C*, 2013, **117**, 9187–9195.
156. H. He and Y. Jagvaral, *Phys. Chem. Chem. Phys.*, 2017, **19**, 11436–11446.
157. S. Back, J. Lim, N.-Y. Kim, Y.-H. Kim and Y. Jung, *Chem. Sci.*, 2017, **8**, 1090–1096.
158. T. L. Poulos, *Chem. Rev.*, 2014, **114**, 3919–3962.
159. C. Costentin, S. Drouet, M. Robert and J. M. Saveant, *Science*, 2012, **338**, 90–94.
160. C. Costentin, M. Robert, J. M. Saveant and A. Tatin, *Proc. Natl. Acad. Sci. U. S. A.*, 2015, **112**, 6882–6886.
161. S. Fukuzumi, Y. M. Lee, H. S. Ahn and W. Nam, *Chem. Sci.*, 2018, **9**, 6017–6034.
162. A. S. Varela, N. Ranjbar Sahraie, J. Steinberg, W. Ju, H.-S. Oh and P. Strasser, *Angew. Chem., Int. Ed.*, 2015, **54**, 10758–10762.
163. W. Ju, A. Bagger, G.-P. Hao, A. S. Varela, I. Sinev, V. Bon, B. Roldan Cuenya, S. Kaskel, J. Rossmeisl and P. Strasser, *Nat. Commun.*, 2017, **8**, 944.

164. X.-M. Hu, H. H. Hval, E. T. Bjerglund, K. J. Dalgaard, M. R. Madsen, M.-M. Pohl, E. Welter, P. Lamagni, K. B. Buhl, M. Bremholm, M. Beller, S. U. Pedersen, T. Skrydstrup and K. Daasbjerg, *ACS Catal.*, 2018, **8**, 6255–6264.
165. H.-Y. Jeong, M. Balamurugan, V. S. K. Choutipalli, J. Jo, H. Baik, V. Subramanian, M. Kim, U. Sim and K. T. Nam, *Chem. – Eur. J.*, 2018, **24**, 18444–18454.
166. F. Pan, W. Deng, C. Justiniano and Y. Li, *Appl. Catal., B*, 2018, **226**, 463–472.
167. P. Su, K. Iwase, S. Nakanishi, K. Hashimoto and K. Kamiya, *Small*, 2016, **12**, 6083–6089.
168. X. Li, W. Bi, M. Chen, Y. Sun, H. Ju, W. Yan, J. Zhu, X. Wu, W. Chu, C. Wu and Y. Xie, *J. Am. Chem. Soc.*, 2017, **139**, 14889–14892.
169. W. Bi, X. Li, R. You, M. Chen, R. Yuan, W. Huang, X. Wu, W. Chu, C. Wu and Y. Xie, *Adv. Mater.*, 2018, **30**, 1706617.
170. C. Zhao, X. Dai, T. Yao, W. Chen, X. Wang, J. Wang, J. Yang, S. Wei, Y. Wu and Y. Li, *J. Am. Chem. Soc.*, 2017, **139**, 8078–8081.
171. H.-Y. Jeong, M. Balamurugan, V. S. K. Choutipalli, E.-S. Jeong, V. Subramanian, U. Sim and K. T. Nam, *J. Mater. Chem. A*, 2019, **7**, 10651–10661.
172. P. Lu, Y. Yang, J. Yao, M. Wang, S. Dipazir, M. Yuan, J. Zhang, X. Wang, Z. Xie and G. Zhang, *Appl. Catal., B*, 2019, **241**, 113–119.
173. T. Möller, W. Ju, A. Bagger, X. Wang, F. Luo, T. Ngo Thanh, A. S. Varela, J. Rossmeisl and P. Strasser, *Energy Environ. Sci.*, 2019, **12**, 640–647.
174. L. Zhao, Y. Zhang, L.-B. Huang, X.-Z. Liu, Q.-H. Zhang, C. He, Z.-Y. Wu, L.-J. Zhang, J. Wu, W. Yang, L. Gu, J.-S. Hu and L.-J. Wan, *Nat. Commun.*, 2019, **10**, 1278.
175. T. Zheng, K. Jiang, N. Ta, Y. Hu, J. Zeng, J. Liu and H. Wang, *Joule*, 2019, **3**, 265–278.
176. Y. Cheng, S. Zhao, B. Johannessen, J.-P. Veder, M. Saunders, M. R. Rowles, M. Cheng, C. Liu, M. F. Chisholm, R. De Marco, H.-M. Cheng, S.-Z. Yang and S. P. Jiang, *Adv. Mater.*, 2018, **30**, 1706287.
177. B. X. Zhang, J. L. Zhang, J. B. Shi, D. X. Tan, L. F. Liu, F. Y. Zhang, C. Lu, Z. Z. Su, X. N. Tan, X. Y. Cheng, B. X. Han, L. R. Zheng and J. Zhang, *Nat. Commun.*, 2019, **10**, 2980.
178. Y. F. Ye, F. Cai, H. B. Li, H. H. Wu, G. X. Wang, Y. S. Li, S. Miao, S. H. Xie, R. Si, J. Wang and X. H. Bao, *Nano Energy*, 2017, **38**, 281–289.
179. T. N. Huan, N. Ranjbar, G. Rousse, M. Sougrati, A. Zitolo, V. Mougel, F. Jaouen and M. Fontecave, *ACS Catal.*, 2017, **7**, 1520–1525.
180. F. P. Pan, H. G. Zhang, K. X. Liu, D. Cullen, K. More, M. Y. Wang, Z. X. Feng, G. F. Wang, G. Wu and Y. Li, *ACS Catal.*, 2018, **8**, 3116–3122.
181. H. N. Zhang, J. Wang, Z. Zhao, H. F. Zhao, M. Cheng, A. N. Li, C. W. Wang, J. Y. Wang and J. Z. Wang, *Green Chem.*, 2018, **20**, 3521–3529.
182. A. S. Varela, M. Kroschel, N. D. Leonard, W. Ju, J. Steinberg, A. Bagger, J. Rossmeisl and P. Strasser, *ACS Energy Lett.*, 2018, **3**, 812–817.

183. Q. Q. Cheng, K. Mao, L. S. Ma, L. J. Yang, L. L. Zou, Z. Q. Zou, Z. Hu and H. Yang, *ACS Energy Lett.*, 2018, **3**, 1205–1211.
184. C. H. Zhang, S. Z. Yang, J. J. Wu, M. J. Liu, S. Yazdi, M. Q. Ren, J. W. Sha, J. Zhong, K. Q. Nie, A. S. Jalilov, Z. Y. Li, H. M. Li, B. I. Yakobson, Q. Wu, E. L. Ringe, H. Xu, P. M. Ajayan and J. M. Tour, *Adv. Energy Mater.*, 2018, **8**, 1703487.
185. E. L. Li, F. Yang, Z. M. Wu, Y. Wang, M. B. Ruan, P. Song, W. Xing and W. L. Xu, *Small*, 2018, **14**, 1702827.
186. N. Leonard, W. Ju, I. Sinev, J. Steinberg, F. Luo, A. S. Varela, B. Roldan Cuenya and P. Strasser, *Chem. Sci.*, 2018, **9**, 5064–5073.
187. Z. Zhang, C. Ma, Y. C. Tu, R. Si, J. Wei, S. H. Zhang, Z. Wang, J. F. Li, Y. Wang and D. H. Deng, *Nano Res.*, 2019, **12**, 2313–2317.
188. X. Q. Wang, Z. Chen, X. Y. Zhao, T. Yao, W. X. Chen, R. You, C. M. Zhao, G. Wu, J. Wang, W. X. Huang, J. L. Yang, X. Hong, S. Q. Wei, Y. Wu and Y. D. Li, *Angew. Chem., Int. Ed.*, 2018, **57**, 1944–1948.
189. X. K. Song, H. Zhang, Y. Q. Yang, B. Zhang, M. Zuo, X. Cao, J. H. Sun, C. Lin, X. P. Li and Z. Jiang, *Adv. Sci.*, 2018, **5**, 1800177.
190. Y. Pan, R. Lin, Y. J. Chen, S. J. Liu, W. Zhu, X. Cao, W. X. Chen, K. L. Wu, W. C. Cheong, Y. Wang, L. R. Zheng, J. Luo, Y. Lin, Y. Q. Liu, C. G. Liu, J. Li, Q. Lu, X. Chen, D. S. Wang, Q. Peng, C. Chen and Y. D. Li, *J. Am. Chem. Soc.*, 2018, **140**, 4218–4221.
191. Z. G. Geng, Y. J. Cao, W. X. Chen, X. D. Kong, Y. Liu, T. Yao and Y. Lin, *Appl. Catal. B – Environ.*, 2019, **240**, 234–240.
192. K. Jiang, S. Siahrostami, A. J. Akey, Y. B. Li, Z. Y. Lu, J. Lattimer, Y. F. Hu, C. Stokes, M. Gangishetty, G. X. Chen, Y. W. Zhou, W. Hill, W. B. Cai, D. Bell, K. R. Chan, J. K. Norskov, Y. Cui and H. T. Wang, *Chem*, 2017, **3**, 950–960.
193. X. G. Li, W. T. Bi, M. L. Chen, Y. X. Sun, H. X. Ju, W. S. Yan, J. F. Zhu, X. J. Wu, W. S. Chu, C. Z. Wu and Y. Xie, *J. Am. Chem. Soc.*, 2017, **139**, 14889–14892.
194. W. T. Bi, X. G. Li, R. You, M. L. Chen, R. L. Yuan, W. X. Huang, X. J. Wu, W. S. Chu, C. Z. Wu and Y. Xie, *Adv. Mater.*, 2018, **30**, 1706617.
195. X. M. Hu, H. H. Hval, E. T. Bjerglund, K. J. Dalgaard, M. R. Madsen, M. M. Pohl, E. Welter, P. Lamagni, K. B. Buhl, M. Bremholm, M. Beller, S. U. Pedersen, T. Skrydstrup and K. Daasbjerg, *ACS Catal.*, 2018, **8**, 6255–6264.
196. S. Y. Zhao, Y. Cheng, J. P. Veder, B. Johannessen, M. Saunders, L. J. Zhang, C. Liu, M. F. Chisholm, R. De Marco, J. Liu, S. Z. Yang and S. P. Jiang, *ACS Appl. Energy Mater.*, 2018, **1**, 5286–5297.
197. K. Jiang, S. Siahrostami, T. T. Zheng, Y. F. Hu, S. Hwang, E. Stavitski, Y. D. Peng, J. Dynes, M. Gangisetty, D. Su, K. Attenkofer and H. T. Wang, *Energy Environ. Sci.*, 2018, **11**, 893–903.
198. F. P. Pan, W. Deng, C. Justiniano and Y. Li, *Appl. Catal. B – Environ.*, 2018, **226**, 463–472.

199. Y. Cheng, S. Y. Zhao, B. Johannessen, J. P. Veder, M. Saunders, M. R. Rowles, M. Cheng, C. Liu, M. F. Chisholm, R. De Marco, H. M. Cheng, S. Z. Yang and S. P. Jiang, *Adv. Mater.*, 2018, **30**, 1706287.
200. H. B. Yang, S. F. Hung, S. Liu, K. D. Yuan, S. Miao, L. P. Zhang, X. Huang, H. Y. Wang, W. Z. Cai, R. Chen, J. J. Gao, X. F. Yang, W. Chen, Y. Q. Huang, H. M. Chen, C. M. Li, T. Zhang and B. Liu, *Nat. Energy*, 2018, **3**, 140–147.
201. T. T. Zheng, K. Jiang, N. Ta, Y. F. Hu, J. Zeng, J. Y. Liu and H. T. Wang, *Joule*, 2019, **3**, 265–278.
202. C. C. Yan, H. B. Li, Y. F. Ye, H. H. Wu, F. Cai, R. Si, J. P. Xiao, S. Miao, S. H. Xie, F. Yang, Y. S. Li, G. X. Wang and X. H. Bao, *Energy Environ. Sci.*, 2018, **11**, 1204–1210.
203. T. Moller, W. Ju, A. Bagger, X. L. Wang, F. Luo, T. N. Thanh, A. S. Varela, J. Rossmeisl and P. Strasser, *Energy Environ. Sci.*, 2019, **12**, 640–647.
204. H. Y. Jeong, M. Balamurugan, V. S. K. Choutipalli, E. S. Jeong, V. Subramanian, U. Sim and K. T. Nam, *J. Mater. Chem. A*, 2019, **7**, 10651–10661.
205. Y. Cheng, S. Y. Zhao, H. B. Li, S. He, J. P. Veder, B. Johannessen, J. P. Xiao, S. F. Lu, J. Pan, M. F. Chisholm, S. Z. Yang, C. Liu, J. G. Chen and S. P. Jiang, *Appl. Catal. B – Environ.*, 2019, **243**, 294–303.
206. P. L. Lu, Y. J. Yang, J. N. Yao, M. Wang, S. Dipazir, M. L. Yuan, J. X. Zhang, X. Wang, Z. J. Xie and G. J. Zhang, *Appl. Catal. B – Environ.*, 2019, **241**, 113–119.
207. S. S. Ma, P. P. Su, W. J. Huang, S. Jiang, S. Y. Bai and J. Liu, *ChemCatChem*, 2019, **11**, 6092.
208. H. P. Yang, Y. Wu, G. D. Li, Q. Lin, Q. Hu, Q. L. Zhang, J. H. Liu and C. He, *J. Am. Chem. Soc.*, 2019, **141**, 12717–12723.
209. F. Yang, P. Song, X. Z. Liu, B. B. Mei, W. Xing, Z. Jiang, L. Gu and W. L. Xu, *Angew. Chem., Int. Ed.*, 2018, **57**, 12303–12307.
210. Z. P. Chen, K. W. Mou, S. Y. Yao and L. C. Liu, *ChemSusChem*, 2018, **11**, 2944–2952.
211. Q. H. Yang, C. C. Yang, C. H. Lin and H. L. Jiang, *Angew. Chem., Int. Ed.*, 2019, **58**, 3511–3515.
212. Y. Zhao, J. J. Liang, C. Y. Wang, J. M. Ma and G. G. Wallace, *Adv. Energy Mater.*, 2018, **8**, 1702524.
213. X. L. Zu, X. D. Li, W. Liu, Y. F. Sun, J. Q. Xu, T. Yao, W. S. Yan, S. Gao, C. M. Wang, S. Q. Wei and Y. Xie, *Adv. Mater.*, 2019, **31**, 1808135.
214. E. H. Zhang, T. Wang, K. Yu, J. Liu, W. X. Chen, A. Li, H. P. Rong, R. Lin, S. F. Ji, X. S. Zhene, Y. Wang, L. R. Zheng, C. Chen, D. S. Wang, J. T. Zhang and Y. D. Li, *J. Am. Chem. Soc.*, 2019, **141**, 16569–16573.
215. X. Wang, Z. Chen, X. Zhao, T. Yao, W. Chen, R. You, C. Zhao, G. Wu, J. Wang, W. Huang, J. Yang, X. Hong, S. Wei, Y. Wu and Y. Li, *Angew. Chem., Int. Ed.*, 2018, **57**, 1944–1948.
216. C. Yan, H. Li, Y. Ye, H. Wu, F. Cai, R. Si, J. Xiao, S. Miao, S. Xie, F. Yang, Y. Li, G. Wang and X. Bao, *Energy Environ. Sci.*, 2018, **11**, 1204–1210.

217. Y. Cheng, S. Zhao, H. Li, S. He, J.-P. Veder, B. Johannessen, J. Xiao, S. Lu, J. Pan, M. F. Chisholm, S.-Z. Yang, C. Liu, J. G. Chen and S. P. Jiang, *Appl. Catal., B*, 2019, **243**, 294–303.
218. K. Jiang, S. Siahrostami, A. J. Akey, Y. Li, Z. Lu, J. Lattimer, Y. Hu, C. Stokes, M. Gangishetty, G. Chen, Y. Zhou, W. Hill, W.-B. Cai, D. Bell, K. Chan, J. K. Nørskov, Y. Cui and H. Wang, *Chem*, 2017, **3**, 950–960.
219. P. R. Ortiz de Montellano, *Annu. Rev. Pharmacol. Toxicol.*, 1992, **32**, 89–107.
220. M. Sono, M. P. Roach, E. D. Coulter and J. H. Dawson, *Chem. Rev.*, 1996, **96**, 2841–2888.
221. T. Atoguchi, A. Aramata, A. Kazusaka and M. Enyo, *J. Electroanal. Chem. Interfacial Electrochem.*, 1991, **318**, 309–320.
222. T. Abe, T. Yoshida, S. Tokita, F. Taguchi, H. Imaya and M. Kaneko, *J. Electroanal. Chem.*, 1996, **412**, 125–132.
223. H. Aga, A. Aramata and Y. Hisaeda, *J. Electroanal. Chem.*, 1997, **437**, 111–118.
224. W. W. Kramer and C. C. L. McCrory, *Chem. Sci.*, 2016, **7**, 2506–2515.
225. M.-J. Cheng, Y. Kwon, M. Head-Gordon and A. T. Bell, *J. Phys. Chem. C*, 2015, **119**, 21345–21352.
226. Y. Pan, R. Lin, Y. Chen, S. Liu, W. Zhu, X. Cao, W. Chen, K. Wu, W.-C. Cheong, Y. Wang, L. Zheng, J. Luo, Y. Lin, Y. Liu, C. Liu, J. Li, Q. Lu, X. Chen, D. Wang, Q. Peng, C. Chen and Y. Li, *J. Am. Chem. Soc.*, 2018, **140**, 4218–4221.
227. L. Huang, J. Chen, L. Gan, J. Wang and S. Dong, *Sci. Adv.*, 2019, **5**, eaav5490.
228. H. Zhang, J. Li, S. Xi, Y. Du, X. Hai, J. Wang, H. Xu, G. Wu, J. Zhang, J. Lu and J. Wang, *Angew. Chem., Int. Ed.*, 2019, **58**, 14871–14876.
229. Q. Cheng, K. Mao, L. Ma, L. Yang, L. Zou, Z. Zou, Z. Hu and H. Yang, *ACS Energy Lett.*, 2018, **3**, 1205–1211.
230. C. J. Reedy, M. M. Elvekrog and B. R. Gibney, *Nucleic Acids Res.*, 2007, **36**, D307–D313.
231. M. Zhu, D.-T. Yang, R. Ye, J. Zeng, N. Corbin and K. Manthiram, *Catal. Sci. Technol.*, 2019, **9**, 974–980.
232. J.-H. Jeoung and H. Dobbek, *Science*, 2007, **318**, 1461.
233. A. W. Nichols and C. W. Machan, *Front Chem.*, 2019, **7**, 397.
234. Y. Liu and C. C. L. McCrory, *Nat. Commun.*, 2019, **10**, 1683.
235. C. Costentin, G. Passard, M. Robert and J.-M. Savéant, *J. Am. Chem. Soc.*, 2014, **136**, 11821–11829.
236. C. G. Margarit, C. Schnedermann, N. G. Asimow and D. G. Nocera, *Organometallics*, 2019, **38**, 1219–1223.
237. J. Gu, C. S. Hsu, L. C. Bai, H. M. Chen and X. L. Hu, *Science*, 2019, **364**, 1091–1094.
238. A. S. Varela, M. Kroschel, N. D. Leonard, W. Ju, J. Steinberg, A. Bagger, J. Rossmeisl and P. Strasser, *ACS Energy Lett.*, 2018, **3**, 812–817.
239. W. Ju, A. Bagger, X. Wang, Y. Tsai, F. Luo, T. Möller, H. Wang, J. Rossmeisl, A. S. Varela and P. Strasser, *ACS Energy Lett.*, 2019, **4**, 1663–1671.

240. K. D. Yang, W. R. Ko, J. H. Lee, S. J. Kim, H. Lee, M. H. Lee and K. T. Nam, *Angew. Chem., Int. Ed.*, 2017, **56**, 796–800.
241. H. Yang, Y. Wu, G. Li, Q. Lin, Q. Hu, Q. Zhang, J. Liu and C. He, *J. Am. Chem. Soc.*, 2019, **141**, 12717–12723.
242. A. S. Varela, W. Ju, A. Bagger, P. Franco, J. Rossmeisl and P. Strasser, *ACS Catal.*, 2019, **9**, 7270–7284.
243. Z. Weng, Y. Wu, M. Wang, J. Jiang, K. Yang, S. Huo, X.-F. Wang, Q. Ma, G. W. Brudvig, V. S. Batista, Y. Liang, Z. Feng and H. Wang, *Nat. Commun.*, 2018, **9**, 415.
244. Y. W. Li, H. B. Su, S. H. Chan and Q. Sun, *ACS Catal.*, 2015, **5**, 6658–6664.
245. C. W. Lee, K. D. Yang, D. H. Nam, J. H. Jang, N. H. Cho, S. W. Im and K. T. Nam, *Adv. Mater.*, 2018, **30**, 1704717.
246. L. Tao, E. C. D. Tan, R. McCormick, M. Zhang, A. Aden, X. He and B. T. Zigler, *Biofuels, Bioprod. Biorefin.*, 2014, **8**, 30–48.
247. C. W. Lee, N. H. Cho, S. W. Im, M. S. Jee, Y. J. Hwang, B. K. Min and K. T. Nam, *J. Mater. Chem. A*, 2018, **6**, 14043–14057.
248. K. D. Yang, C. W. Lee, K. Jin, S. W. Im and K. T. Nam, *J. Phys. Chem. Lett.*, 2017, **8**, 538–545.
249. C. R. Shen, E. I. Lan, Y. Dekishima, A. Baez, K. M. Cho and J. C. Liao, *Appl. Environ. Microbiol.*, 2011, **77**, 2905.
250. B. B. Bond-Watts, R. J. Bellerose and M. C. Y. Chang, *Nat. Chem. Biol.*, 2011, **7**, 222.
251. J. H. Montoya, C. Shi, K. Chan and J. K. Nørskov, *J. Phys. Chem. Lett.*, 2015, **6**, 2032–2037.
252. R. Kortlever, J. Shen, K. J. P. Schouten, F. Calle-Vallejo and M. T. M. Koper, *J. Phys. Chem. Lett.*, 2015, **6**, 4073–4082.
253. J. H. Montoya, A. A. Peterson and J. K. Nørskov, *ChemCatChem*, 2013, **5**, 737–742.
254. H. Xiao, T. Cheng, W. A. Goddard and R. Sundararaman, *J. Am. Chem. Soc.*, 2016, **138**, 483–486.
255. R. Angamuthu, P. Byers, M. Lutz, A. L. Spek and E. Bouwman, *Science*, 2010, **327**, 313.
256. U. R. Pokharel, F. R. Fronczek and A. W. Maverick, *Nat. Commun.*, 2014, **5**, 5883.
257. J. Zhao, J. Zhao, F. Li and Z. Chen, *J. Phys. Chem. C*, 2018, **122**, 19712–19721.
258. X. Zeng, J. Shui, X. Liu, Q. Liu, Y. Li, J. Shang, L. Zheng and R. Yu, *Adv. Energy Mater.*, 2018, **8**, 1701345.

CHAPTER 7

Bridging Homogeneous and Heterogeneous Systems—Photoelectrodes for CO_2 Electrochemical Conversion

ZHILIANG WANG AND LIANZHOU WANG*

Nanomaterials Centre, School of Chemical Engineering and Australian Institute for Bioengineering and Nanotechnology, The University of Queensland, St Lucia, QLD 4072, Australia
*Email: l.wang@uq.edu.au

7.1 Introduction

The fast development of our society requires a vigorous increase in energy demand, which is currently provided by fossil fuels.[1] However, the limited supply of fossil fuels cannot sustain usage over a long period and the resultant carbon footprint (*e.g.* CO_2) will threaten the living environment through the greenhouse effect and ocean acidification. To address both the potential energy crisis and CO_2 issue, achieving the so-called artificial photosynthesis *via* a photoelectrocatalytic (PEC) process is highly desirable.[2] During this process, sunlight will drive the CO_2 reduction reaction (CO_2RR) on a semiconductor photoelectrode with CO_2 and H_2O as the feedstock. Different from the electrocatalytic (EC) process, where a high overpotential is needed for CO_2RR,[3] the PEC process can reduce the energy requirement since the solar energy will compensate a large ratio of the overpotenial.[4,5]

Energy and Environment Series No. 28
Carbon Dioxide Electrochemistry: Homogeneous and Heterogeneous Catalysis
Edited by Marc Robert, Cyrille Costentin and Kim Daasbjerg

Published by the Royal Society of Chemistry, www.rsc.org

Ideally, an unbiased PEC process is desired where the CO_2RR on the cathode and water oxidation on the anode will occur spontaneously once the photoelectrode is stimulated, mimicking photosynthesis in plants.[2]

CO_2 can be converted into potential platform chemicals for industrial production. For example, CO_2 has been reported to be converted into olefin, CO, or methanol *via* the PEC process.[4,6] CO is an important source of syngas for the Fischer–Tropsch reaction, while methanol is used either directly as a fuel or in the methanol-to-olefin (MTO) process. In order to make CO_2RR viable, three key parameters require attention during the CO_2RR process on photoelectrodes:[4,7]

(i) CO_2 reduction activity. This indicates how much CO_2 can be reduced during the CO_2RR as indicated by the CO_2RR photocurrent (j_{CO_2}). This is not only limited by the surface reaction kinetics but is also significantly affected by the dissolved CO_2 concentration during the reaction. Moreover, since some competitive reactions occur during CO_2RR (*e.g.* H_2 evolution reaction), not all photocurrent will be applied for CO_2 reduction. Besides the j_{CO_2}, the onset potential (E_{onset}) also indicates the effectiveness of the photoelectrodes: the higher the E_{onset} is, the easier the CO_2RR will be processed in the PEC process.

(ii) Product selectivity. CO_2RR normally has wide product distribution, including CO, HCOOH, CH_3OH, CH_4, and various C_{2+} products. To achieve a highly selective CO_2RR process not only means less cost in product separation, but also provides insights into the CO_2RR pathway. The selectivity is normally described with the product faradaic efficiency (FE) following eqn (7.1):

$$FE = n{\cdot}N{\cdot}F/Q = n{\cdot}N{\cdot}F/(j{\cdot}t) \tag{7.1}$$

where n is the number of electrons transferred during the CO_2RR (*e.g.*, $n = 2$ for CO production; $n = 6$ for CH_3OH production), N is the mole amount of the production, F is the Faradaic constant (96 485 C mol^{-1}), Q is the total charge amount passing the electrode, which can be calculated from the total current (j) and the reaction time (t).

(iii) Stability of the photoelectrode. A long-term stable photocathode is critical for the practical application of CO_2RR. Two major corrosion processes may happen on a photocathode: chemical corrosion and photo-chemical corrosion. The chemical corrosion is caused by the reaction between the electrolyte solution and the semiconductor, *e.g.* Si in an alkaline solution or Cu_2O in an acidic solution. The photochemical corrosion is due to the presence of photogenerated charges (electrons or holes) which can trigger the corrosion reaction in solution. For example, CuO can remain stable in the electrolyte, but will be reduced further with light. Coating the electrode with robust layers (*e.g.* TiO_2, Al_2O_3) and adjusting the pH of the electrolyte can effectively suppress the corrosion. Herein, our focus is not as much on corrosion issues as on the design of effective photocathodes for CO_2RR.

Considering that many good reviews have been published to comprehensively discuss the materials applied in PEC CO_2RR,[7–10] we are not going to add another one but rather address some fundamental understanding of this process. In this chapter, we will discuss the photoconversion process in a photoelectrode and the thermodynamics and kinetics of the surface reactions of PEC CO_2RR. In the following part, three major topics will be focused on to highlight the research statues in PEC CO_2RR, *i.e.* (1) the physicochemical process in semiconductor photoelectrodes; (2) the co-catalyst selection for CO_2 conversion; and (3) the influence of the electrolyte solution. We mainly focus on the aqueous electrolyte unless otherwise mentioned.

7.2 The Physicochemical Process at the Semiconductor Photoelectrode

To convert solar energy, semiconductor materials are used for photoelectrode fabrication. A semiconductor with a suitable bandgap (E_g) can absorb light, and an electron from the valence band (VB) can be excited to the conductive band (CB), leading to the generation of electron–hole pairs provided the semiconductor is stimulated with light that has a higher energy than the absorption threshold. The energy carried by photons is stored in electron–hole pairs for further chemical reactions.[11–13] Further driven by the photovoltaic (PV) effect of the semiconductors, the photogenerated electrons can be used in CO_2RR and holes in water oxidation. Generally speaking, due to the PV effect, the applied bias for CO_2RR on photoelectrodes can be largely compensated, leading to less applied bias compared to the traditional EC.[14,15] Depending on the structure of the photoelectrode design, the PV effect can be generated from either a semiconductor/electrolyte (S|E) junction or a buried junction, as shown in Figure 7.1. In the following section, we will briefly introduce them.

7.2.1 The Semiconductor/Electrolyte Junction

Figure 7.1(a and c) shows that the S|E junction is formed at the interface between the semiconductor and the electrolyte solution.[16,17] There exists a Schottky contact between the semiconductor and the electrolyte. At the S|E interface, the energy level of VB and CB is pinned. Since the photogenerated electron needs to be transferred from the CB to CO_2 (see Figure 7.1c), the CB position is strictly required to be high enough for the CO_2RR to occur at the S|E interface. Taking this into consideration, it is helpful to compare the standard redox potential (E°) of various CO_2 reduction reaction potentials with the band structure of the semiconductors (Figure 7.2). As shown, some available semiconductors for CO_2RR are Si, GaP, InP *etc.* Moreover, the CO_2 reduction potential is within a narrow range of -0.2 to $\sim$0.17 V *vs.* Standard Hydrogen Electrode (V_{SHE}) for different products, including HCOOH, CO,

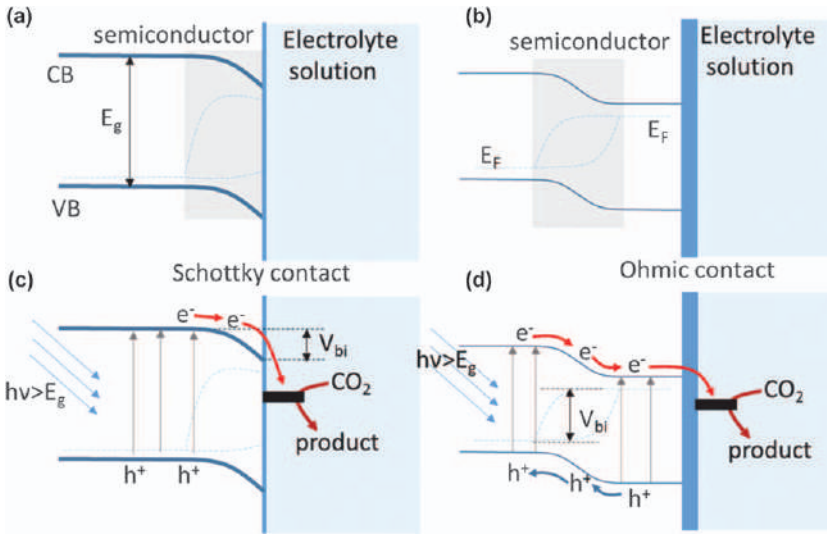

Figure 7.1 (a and b) Schematic band bending at the S|E junction and the buried junction. The grey zone shows the junction. (c and d) Schematic charge transfer during CO_2RR at the S|E junction and buried junction. The built-in electric field is indicated by V_{bi}.

HCHO, CH_3OH, and CH_4. The small thermodynamics difference among these CO_2RR processes indicates the challenges in controlling the product selectivity.

In the semiconductor, band bending will happen at the S|E interface due to the Fermi Level (E_F) flatting between semiconductors and the electrolyte (see Figure 7.1c).[18] For the CO_2RR, the adopted p-type semiconductor (photocathode) normally has a lower E_F than the electrolyte, which will result in downwards band bending (Figure 7.3a). In this case, a built-in electric field (V_{bi}) directed towards the electrolyte will be established with a field strength expressed as eqn (7.2) and (7.3).[14,18]

$$V(z) = \frac{eN_a}{\varepsilon_{sc}}(z - W_0) \tag{7.2}$$

$$W(E) = \left[\frac{2\varepsilon_{sc}(E - V_{fb})}{eN_a}\right]^{1/2} \tag{7.3}$$

Here, $W(E)$ is the width of the electric field (also called space charge layer) under the applied potential of E, *as* shown in Figure 7.3a, in particular W_0 is the width without applied bias, e is the elemental charge, ε_{sc} is the dielectric constant of the semiconductor, N_a is the carrier concentration in the semiconductor, and V_{fb} is the flat band potential.

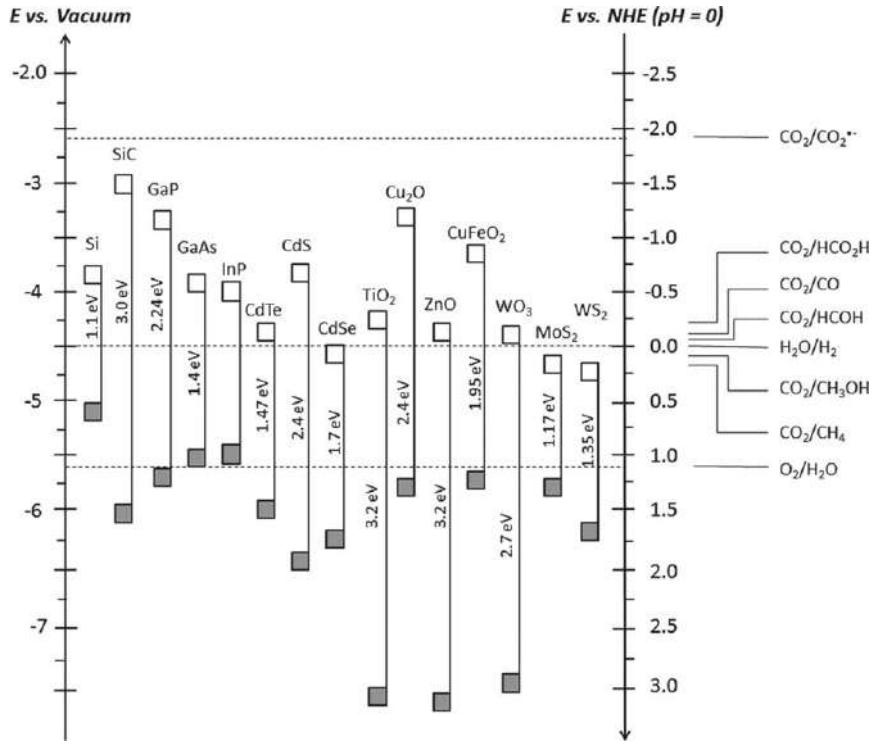

Figure 7.2 Band structure of different semiconductors and standard reduction potential for CO_2RR.
Reproduced from ref. 6 with permission from American Chemical Society, Copyright 2015.

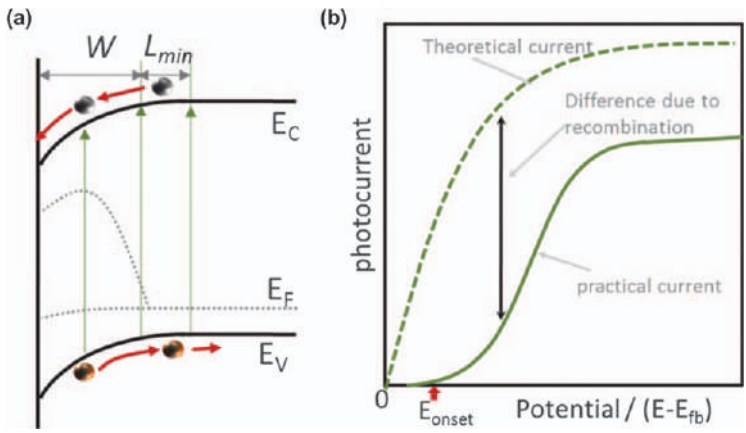

Figure 7.3 (a) Detailed band bending of a photocathode at the semiconductor–electrolyte interface. (b) Ideal *j–V* curve (dashed line) derived from the Gartner equation and the schematic practical curve (solid line).
Reproduced from ref. 19 with permission from Elsevier, Copyright 2018.

Once the photoexcited electrons exist on the CB in the space charge layer, they will be swept to the surface for reaction. By assuming the ideal surface catalytic process without resistance, the photocurrent of the PEC process (*j–E* curve) can be predicted *via* the Gartner equation (eqn (7.4)).[14,19]

$$j/I_0 = 1 - \exp(-\alpha W)/(1 + \alpha L_{\min}) \tag{7.4}$$

The parameter α is the light absorption coefficient, I_0 is the incident light intensity and $L_{\min}$ is the diffusion length of minority carrier (electrons for p-type semiconductor, see Figure 7.3a). According to the equation, the E_{onset} of an ideal PEC process is predicted to be close to the V_{fb} of a semiconductor (see Figure 7.3b) and the theoretical photocurrent is determined by its light absorption (I_0 and α), *i.e.* the light intensity and bandgap.

The S|E junction model is frequently used to illustrate the PEC process at the junction. In this simple structure, it does not need very strict interface modification since the semiconductors are directly in touch with the solution. Therefore, nanostructure engineering can be applied in fabricating a complex structure for facilitating charge transfer and surface reaction.[20–23] For example, the nanobranched Cu_2O/CuO has been reported to exhibit much better CO_2RR performance than the corresponding nanorod arrays.[22] Jang *et al.* loaded the ZnTe on ZnO arrays for highly selective CO production during the PEC process.[23] However, the S|E junction is not the best choice for solar conversion since the produced photovoltage is normally low, limited by the band bending. This normally results in serious charge recombination at the S|E interface or in the bulk of the semiconductors. It will lead to a large fraction of photocurrent loss as indicated by Figure 7.3b. To realize more efficient PEC CO_2RR, a buried junction structure can be a better choice for the photoelectrode design.

7.2.2 The Buried Junction

A buried junction is created with a p–n junction beneath the electrode/electrolyte interface as shown in Figure 7.1(b and d). At the top layer, an Ohmic contact is built between the surface catalyst layer and the buried junction (Figure 7.1b).[24] Due to the absence of direct contact with the electrolyte, the VB and CB of the buried structure are no longer pinned. In this case, the CB can be easily shifted with the applied bias to make it suitable for CO_2RR. The buried junction, normally a p–n junction, can produce a much larger space charge layer for photocharge separation and transfer.[25,26] The photovoltage will be determined by the Fermi level difference of the two semiconductors. For the photoelectrode with a buried junction, it works like an all-in-one PV driven EC system, with the buried junction functionalized as the PV part and the electrocatalyst layer coated outside. Actually, most of the buried junction photoelectrode can be correlated with similar heterojunction cells as shown in Table 7.1.

The resemblance between the buried junction photoelectrode and the heterojunction solar cells allows us to apply well-developed strategies in

Table 7.1 Comparison between buried junction photoelectrode and heterojunction solar cells.[a]

Photoelectrode			
Buried junction	Catalyst	Correlated solar cell	Ref.
p–i–n Si/TiO_2	Au	p–i–n amorphous Si solar cell	34,81
p–n^+ Si/Ti	Au	Si solar cell	82,83
$Cu_2O|Al:ZnO|TiO_2$	Re molecular catalyst	Cu_2O–TCO solar cell	27,84
CZTS/CdS $CZTS/In_2S_3$	N.A.	CZTS solar cell	85,86
$PTAA|MAPbI_3|C_{60}|BCP|Cu$	In–Bi alloy	Perovskite solar cell	87,88

[a]CZTS: Cu_2ZnSnS_4; PTAA: poly(triaryl)amine; TCO: transparent conductive oxide; BCP: Bathocuproine.

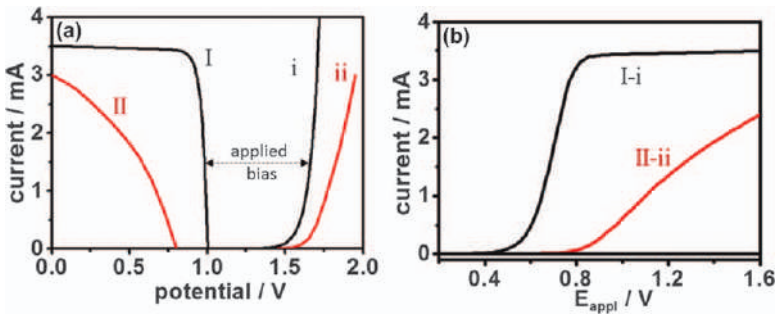

Figure 7.4 Simulating the PEC process based on the PV and EC responses. (a) Current–potential curves for PV (I, II) and EC processes (i, ii), respectively. For the PV processes, they are featured with different short circuit current, open voltage, and fill factor. The EC processes, featured with different Tafel slopes and overpotentials. (b) The calculated PEC response curves (I-i and II-ii) based on the numeric simulation in (a). The applied potential is produced by calculating the potential gap at the same current for the PV and EC processes in (a).
Reproduced from ref. 28 with permission from the Royal Society of Chemistry.

heterojunction solar cell for improving the CO_2RR in PEC processes. For example, to facilitate the selected electron transfer, an electron transfer layer (ETL) will be applied in the solar cell. In the photoelectrode, it is normally the TiO_2 layer taking similar roles in $CuZnSnS_4$ (CZTS), Cu_2O or Si-based photocathodes.[25–27] According to the PV performance of the buried junction and the EC performance of the surface catalyst, we can predict the performance of CO_2RR on the buried junction photoelectrodes.[28] Figure 7.4 shows that the PV + EC (PVEC) processes can be well reproduced from the response of the individual parts. The applied bias (E_{appl}) in the PVEC process can be calculated as shown in Figure 7.4a and the maximum photocurrent is determined by the buried junctions.

7.3 Co-catalyst Selection for CO_2 Reduction

CO_2 molecules have a very stable structure with a C=O bond energy of 732 kJ mol^{-1}. The highly symmetric linear structure (O=C=O) leads to a very low ground state. Meanwhile, the additional π bond further strengthens the linkage of C and O (Figure 7.5).[29] As a result, it needs a huge activation energy to initiate the CO_2RR, leading to weak reactivity on bare semiconductors. In order to accelerate the surface reaction process, a suitable co-catalyst is needed. As an important component of effective photoelectrodes, the co-catalyst plays multiple roles in CO_2RR: on the one hand it can accelerate the surface reaction by reducing the reaction barrier; on the other hand, it can change the surface property of the photocathode and modulate the product selectivity.

It is commonly realized that the CO_2RR starts from the formation of $CO_2^{\bullet-}$ (an intermediate of CO_2 with one electron). According to the molecular orbital of CO_2 in Figure 7.5b, the additional electron will be accommodated on the anti-bond (π*) orbital, which will weaken the C=O bond for further reaction. A further *ab initio* study indicates that the $CO_2^{\bullet-}$ is no longer a linear molecular but with an angle of 135.3° between the two C–O bonds.[30] A possible reaction pathway for the CO_2RR is shown in Figure 7.6.[31] The CO_2 is absorbed on the surface of the catalyst first, followed by an electron transfer (ET) to form the $CO_2^{\bullet-}$. In Figure 7.2, it is shown that the $CO_2/CO_2^{\bullet-}$ has a standard potential of −1.9 V_{SHE}, which makes the $CO_2^{\bullet-}$ formation the rate-determining step. Then, a series of proton coupled electron transfer (PCET) processes will happen, leading to the formation of different products, such as HCOOH, CO, CH_3OH, and CH_4.[3] If the catalyst can realize a dimerization process, it can also produce C_{2+} compounds, *e.g.*, C_2H_4, C_2H_5OH, C_2H_6 *etc.* The product selectivity is determined by the adsorption–desorption

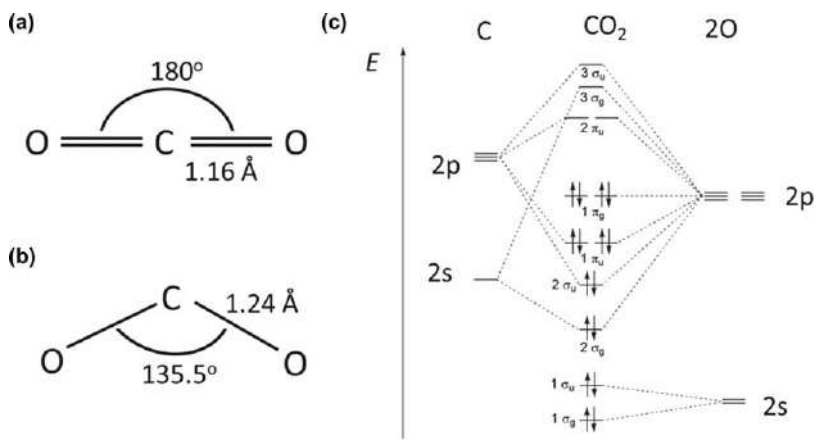

Figure 7.5 (a and b) Geometric structures of CO_2 and $CO_2^{\bullet-}$. Redrawn from ref. 30. (c) CO_2 molecular orbital. Reproduced from ref. 29 with permission from American Chemical Society, Copyright 2018.

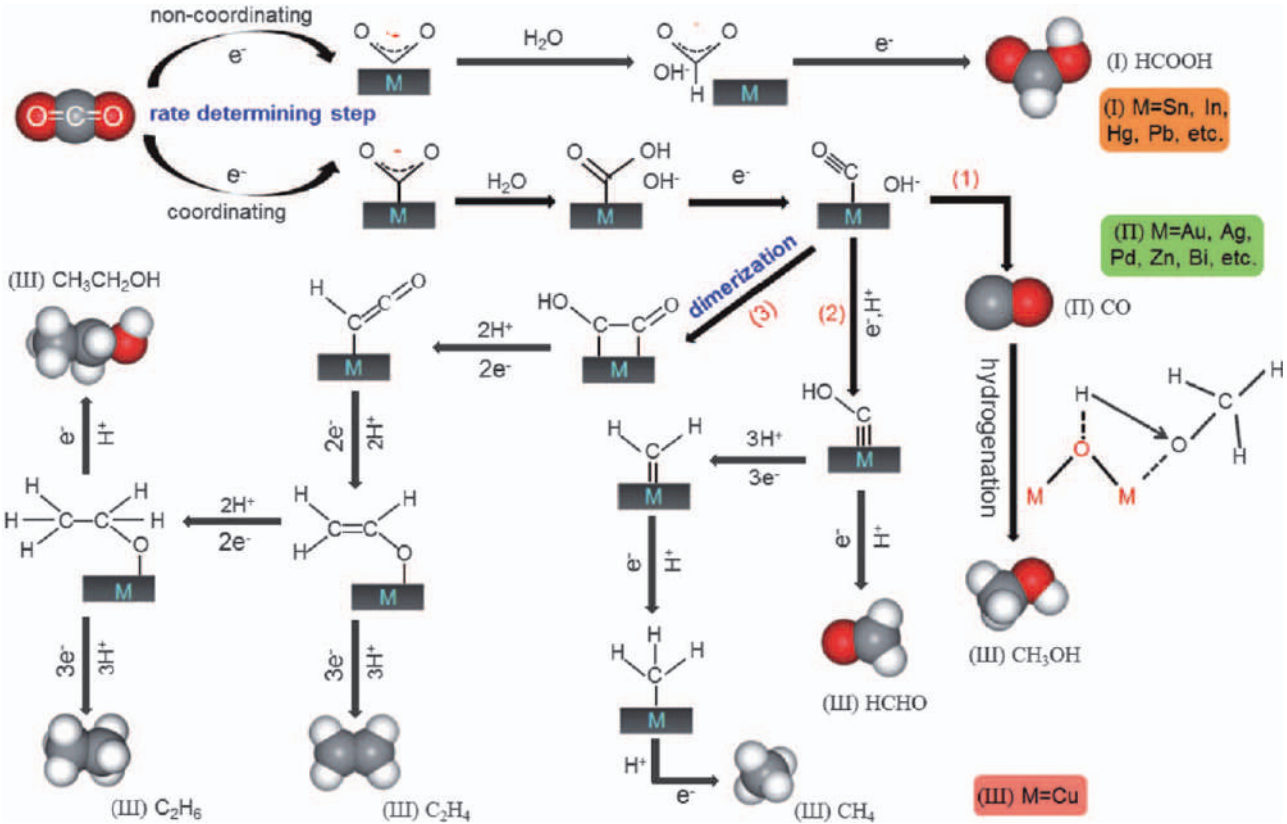

Figure 7.6 Possible CO_2 reduction pathways for the production of HCOOH, CO, CH_3OH, HCHO, CH_4, C_2H_4, C_2H_6, and C_2H_5OH. Reproduced from ref. 31, https://doi.org/10.1002/advs.201700275, under the terms of the CC BY 4.0 licence, https://creativecommons.org/licenses/by/4.0/.

capability of the intermediates. Therefore, it is helpful to further understand the intrinsic properties of different co-catalysts for CO_2RR.

Three categories of co-catalyst exist for PEC CO_2RR: (1) heterogeneous catalysts, which include transition metals and the derived metal oxides; (2) homogeneous catalysts, which are mainly composed of transition metal molecular complexes; (3) enzyme catalysts. Due to the significant differences among these three different co-catalysts, the interaction between co-catalyst and photoelectrode is also drastically different. Below, we will discuss how these co-catalysts cooperate with the photoelectrode to achieve efficient CO_2RR.

7.3.1 Heterogeneous Catalysts

The heterogeneous catalysts include transition metal clusters and the corresponding metal oxides. They are widely used to accelerate the CO_2RR on photoelectrodes since they are robust and can create intimate contact with the photoelectrodes. These co-catalysts normally show electrocatalytic CO_2RR capabilities even without light stimulation, therefore, referring to their EC capability can shed light on the design of co-catalysts on photoelectrodes. Hori has summarized the electrochemical CO_2RR on metal electrodes (Figure 7.7),[6,30] indicating that the H_2 evolution reaction (HER) is favoured on many metal electrodes, *e.g.* Ti, Pt, Ir, Ni, Fe, and Co. As for CO production, it can be observed on Zn, Ag, Au, Pd *etc.* Other metals, such as Bi, Sn, In, and Pb show high selectivity in HCOOH formation. Especially on Hg, it shows almost a single product of HCOOH.

Moreover, Lee *et al.* have compared the binding energy of four different intermediates (COOH*, CO*, OCHO* and OH*) on different metals (Figure 7.8), including Pt, Cu, Au, Ag, Zn, Ni *etc.*[3] The volcano shape curves are observed when plotting the binding energy *versus* CO_2RR activity. Since the adsorption capability of these intermediates is strongly related to the product selectivity, this result provides insights into the co-catalyst choice in pursuit of high selectivity. Among all the reported metals, Cu is the most unique catalyst since it can lead to a wide range of products, including CO, hydrocarbons, formate, olefine *etc.*[30,32]

In PEC CO_2RR, the catalyst choice is within the candidates for EC, and the final products are in accordance with the EC as well. Kaneco *et al.* investigated a series of metals, including Pb, Ag, Au, Pd, Cu, and Ni on a p-InP photocathode for CO_2RR.[33] It is observed that CO is mainly produced on Pd, Ag, and Au, while H_2 is produced on Ni. Moreover, they also observed that the loading amount can affect the final products. An increase of Cu can lead to a gradual decrease of CO and increase of HCOOH.

Au is the most frequently used metal catalyst in PEC CO_2RR (Table 7.2). With p-Si as the photocathode, the CO selectivity is profoundly improved after Au loading.[34] A FE of ~50% was achieved on a Au coated Si photocathode. Similar promotion effects of Au is observed in p-GaN, copper–oxide photocathodes.[25,35] Alloying Au with another metal such as Cu is also

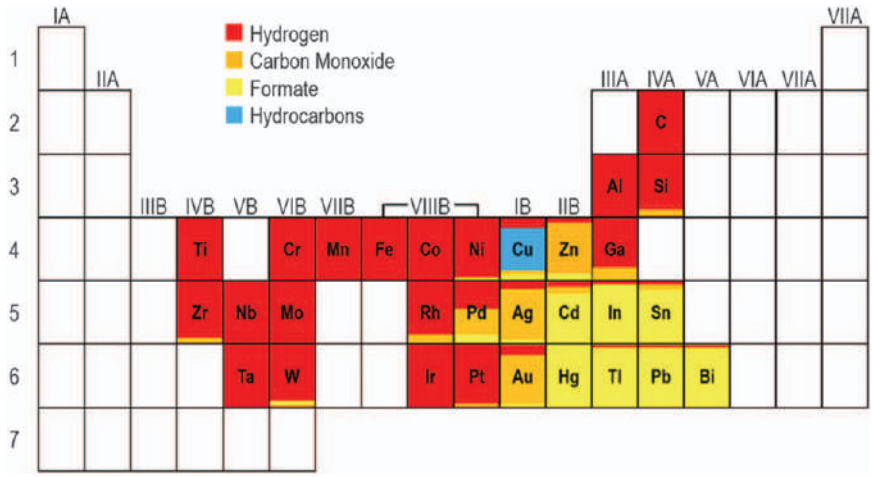

Figure 7.7 The periodic table showing metal catalysts for CO_2RR in EC processes. Reproduced from ref. 6 with permission from American Chemical Society, Copyright 2015. Data from Hori.[30]

reported to have promoted CO_2RR efficiency.[36] Kong *et al.* reported that assembling an Au_3Cu alloy on Si nanowire arrays not only improves the CO_2RR photocurrent but also leads to higher CO selectivity.[36] Other kinds of alloys, *e.g.* Cu–In, Cu–Sn, Cu–Pd, Sn–In–Bi *etc.*, have been explored for electrocatalytic CO_2RR.[31] The alloy metal catalyst deserves our attention in photoelectrode design since the alloying effect can greatly change the electron structure of the metal and adjust the surface absorption/desorption capability. Finely tuning the alloy composition is promising to realize highly active CO_2RR catalysts.[31] Other metals such as Cu,[25] Sn,[37] Ag[38] *etc.* have been applied in different photocathodes, with the majority of products being CO or HCOOH during the PEC CO_2RR.

Besides metal catalysts, the metal-oxides have also been reported to promote the CO_2RR on photoelectrodes. TiO_2 has been reported to work as a co-catalyst on p-GaP and Cu_2O photocathodes to realize a CO_2-to-methanol conversion.[39–41] Kang *et al.*, deposited TiO_2 on the top of a Cu_2O photocathode and achieved over 90% FE of methanol production.[41] RuO_x was also reported to promote the conversion of CO_2 into CO on a Cu_2O photocathode.[42] Moreover, reduced tin oxide (SnO_x) can efficiently convert CO_2. With SnO_x coated on a CuO electrode, Schreier *et al.* successfully demonstrated stable CO production from CO_2 with FE over 70%.[43] It is also interesting to note that a metal-oxide can be used to modify metal catalysts. Taking the Cr_2O_3 coated Rh as an example, after forming this core–shell Rh/Cr_2O_3 on a p-GaN photocathode, the CO_2RR is promoted with improved CO selectivity.[44] Actually, in EC CO_2RR, it has been reported that there exists a promotion effect at the interface between the metal and metal-oxide substrates.[45,46] This indicates that a more efficient CO_2RR process can be achieved by taking advantage of metal–substrate interactions.

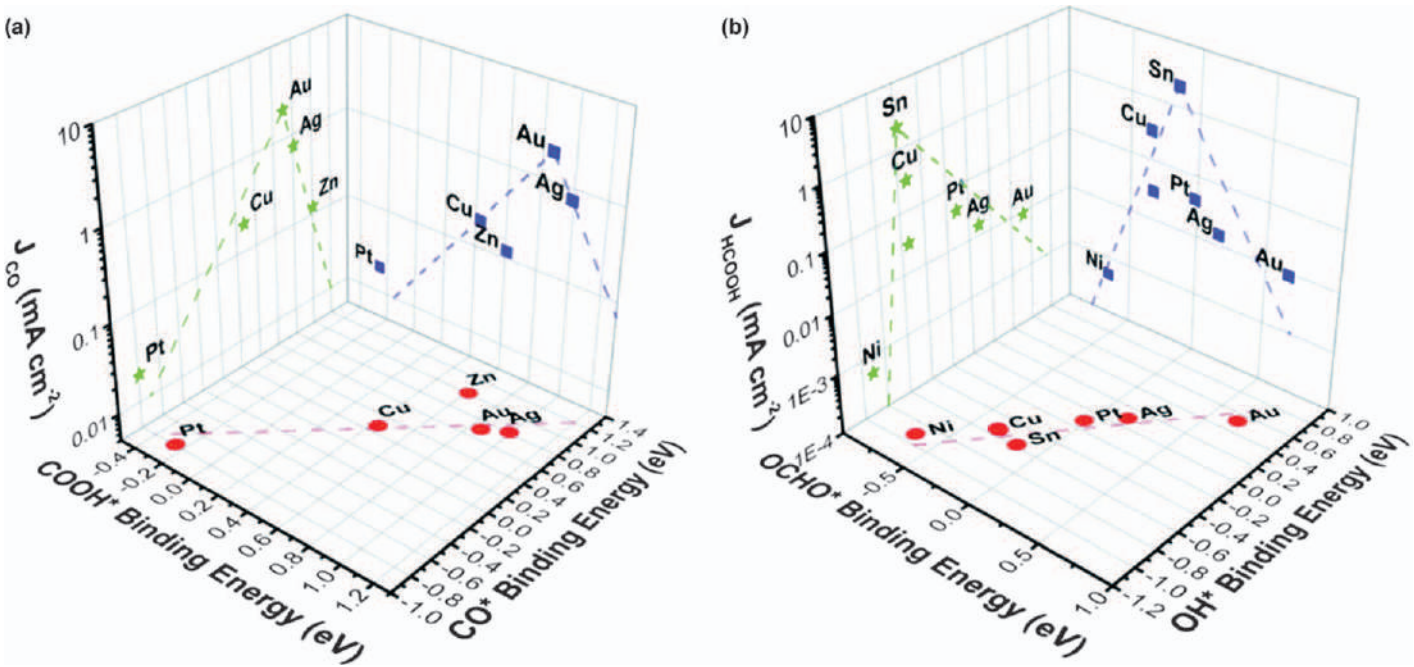

Figure 7.8 Calculated binding energy for different absorbed intermediates, including (a) COOH* and CO*; (b) OCHO* and OH*. Reproduced from ref. 3 with permission from the Royal Society of Chemistry.

Table 7.2 Metals and metal-oxide catalysts applied in PEC CO_2RR.[a]

Catalyst	Photocathode	Photocurrent	Major product	Ref.
Au	ZnTe/ZnO	$-16\ mA\,cm^{-2}$@ $-0.7\ V_{SHE}$ (0.5 M $KHCO_3$ aqueous solution, 100 $mW\,cm^{-2}$ simulated sunlight)	CO, FE = 63%	23
Au	p–i–n Si	$-6\ mA\,cm^{-2}$@ $-0.1\ V_{SHE}$ (0.1 M $KHCO_3$ aqueous solution, 100 $mW\,cm^{-2}$ simulated sunlight)	CO, FE = 70%	34
Au	p–n Si	$-12.5\ mA\,cm^{-2}$@ $-2.0\ V_{SHE}$ (0.2 M $KHCO_3$ aqueous solution, 100 $mW\,cm^{-2}$ simulated sunlight)	CO, FE = 91%	82
Au	p-GaN	$-1.8\ \mu A\,cm^{-2}$@ $-0.8\ V_{SHE}$ (0.05 M K_2CO_3, 500 $mW\,cm^{-2}$, $\lambda > 495$ nm)	$CO:H_2 = 5:1$	35
Au_3Cu	p-Si	$-6.8\ mA\,cm^{-2}$@ $-0.6\ V_{SHE}$ (0.1 M $KHCO_3$, 20 $mW\,cm^{-2}$ $\lambda = 740$ nm)	CO, FE = 67.2%	36
In0.4Bi0.6	PTAA|$MAPbI_3$|C_{60}|BCP	$-5.5\ mA\,cm^{-2}$@ $-0.6\ V_{SHE}$ (0.1 M $KHCO_3$, 100 $mW\,cm^{-2}$ simulated sunlight)	HCOOH, FE = 92%	87
Cu–In	$CuInS_2$	$-2.5\ mA\,cm^{-2}$@ $-0.8\ V_{SHE}$ (0.1 M $KHCO_3$, 100 $mW\,cm^{-2}$ Xenon lamp)	C_2H_5OH, FE = 80%	89
Sn	p-Si	$-4\ mA\,cm^{-2}$@ $-1.6\ V_{SHE}$ (0.1 M $KHCO_3$, 100 $mW\,cm^{-2}$ simulated sunlight)	HCOOH, FE = 39%	37
Ag	p-Si	$-10\ mA\,cm^{-2}$@ $-0.6\ V_{SHE}$ (0.5 M $KHCO_3$, 50 $mW\,cm^{-2}$ simulated sunlight)	CO, FE = 90%	38
Cu	GaN/p–n+ Si	$-10\ mA\,cm^{-2}$@ $-0.33\ V_{SHE}$ (0.5 M $KHCO_3$, 800 $mW\,cm^{-2}$ Xenon lamp)	CO, FE = 20%	25
TiO_2	Cu_2O	$-1\ mA\,cm^{-2}$@ $0.4\ V_{SHE}$ (0.5 M $KHCO_3$, 100 $mW\,cm^{-2}$ simulated sunlight)	CH_3OH, FE = 70%	41

[a]SHE: standard hydrogen electrode.

7.3.2 Molecular Catalysts

Molecular catalysts are an important category of CO_2RR catalysts.[29] Due to the flexible structure of molecules and their abundant coordination sites, it is much easier to bond with and activate the CO_2 molecule, which is the most energy-consuming step in CO_2RR. In Table 7.3, many different

Table 7.3 Molecular catalysts applied in PEC CO_2RR.[a]

Catalyst structure	Photocathode	Photocurrent	Major product	Ref.
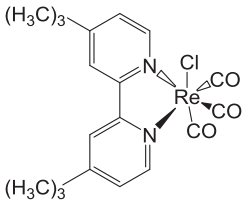	p-Si	−30 mA@ −1.6 $V_{Ag/AgCl}$ (0.1 M Bu_4NPF_6/MeCN solution, 95 mW cm^{-2}, $\lambda = 661$ nm)	CO, FE = 97%	47
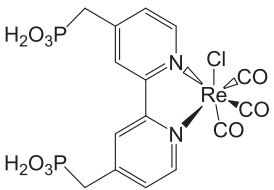	Cu_2O/AZO/TiO_2	−25 mA cm^{-2}@ −2 V *vs.* $Fc^{+/0}$ (0.1 M Bu_4NPF_6/MeCN solution, 100 mW cm^{-2}, simulated sunlight)	CO, FE = 90%	27
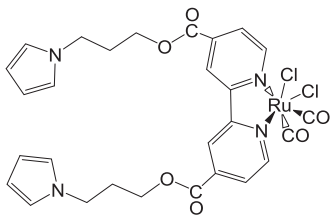	p-InP	−0.12 mA cm^{-2}@ −0.8 $V_{Ag/AgCl}$ (0.1 M Bu_4NClO_4/MeCN solution, visible light)	HCOOH, FE = 62.3%	48

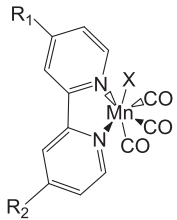	p-Si	−1.8 mA cm^{-2}@ −1.5 V_{SCE} (0.1 M Bu_4NClO_4/MeCN solution, visible light)	CO, FE = 35%	49
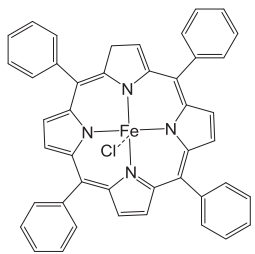	p-Si	−3 mA cm^{-2}@ −1.2 V_{SCE} (0.1 M Bu_4NPF_6/MeCN solution, 90 mW cm^{-2}, $\lambda = 650$ nm)	CO, FE = 80%	50
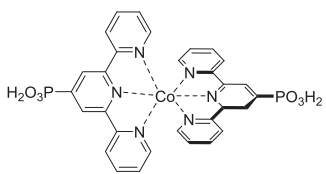	p-Si/TiO_2	−0.2 mA cm^{-2}@ −0.9 V *vs.* $Fc^{+/0}$ (0.1 M Bu_4NPF_6/MeCN solution, 100 mW cm^{-2}, $\lambda > 400$ nm)	CO, FE = 47.6%	54

[a]Bu: butyl; MeCN: acetonitrile; SCE: saturated calomel electrode; Fc: $Fe(C_5H_5)_2$.

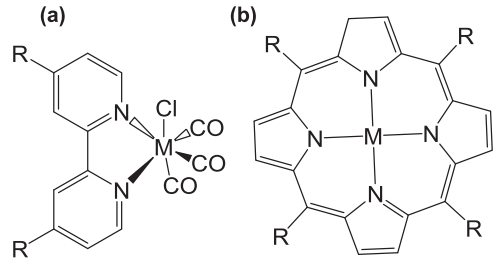

Figure 7.9 Structure of the (a) metal bipyridine tricarbonyl catalyst and (b) porphyrin-based catalyst. R represents different functional groups, M represents different metal atoms.

complexes are listed, including the bipyridine, porphyrin, and bis(terpyridine) structures *etc*.

Although many different molecular catalysts exist for EC CO_2RR, most of the catalysts applied in PEC processes share a similar scaffold of bipyridine tricarbonyl (Figure 7.9a) with different metal centres (M(bpy)$(CO)_3$), including Ru, Re, Mn *etc.*[26,27,47–49] The additional ligands R can be used to adjust the hydrophilic/hydrophobic property of the catalysts. They can also work as anchors to form bonds with the photosensitiser considering that the catalysts do not have a photoresponse. Meanwhile, inspired by the enzyme structure for photosynthesis, the porphyrin-based metallomacrocycles (Figure 7.9b) have also been applied for CO_2RR on photoelectrodes with high current efficiency.[50,51] Alenezi *et al.* applied Fe porphyrin as a surface catalyst on a p-Si photocathode. In non-aqueous solution, they achieved a CO_2RR photocurrent of over 3 mA cm^{-2} with around 80% FE for CO production.[50]

Three different matrices are used to host the molecular catalysts, including the planar photoelectrode, mesoporous photoelectrode, and molecular photosensitiser. For planar photoelectrodes, such as Si wafer, p-Fe_2O_3 and $CuZnSnS_4$ photoelectrodes,[26,47,49,52] the immobilization between matrix and the molecular catalyst is significant for achieving high catalyst loading. By adjusting the R ligand in the molecular catalyst, it is possible to create an intimate interaction. For example, the H_2 treated p-Si photocathode shows a hydrophobic surface, which can interact with the alkyl group in a Re(bpy)$(CO)_3$-based molecular catalyst for CO_2RR with a long lifetime.[47] For mesoporous structures, such as a NiO photocathode, they can be directly used as a light-harvesting semiconductor to capture solar energy and pass the photogenerated electrons onto the molecular catalyst for CO_2RR.[53] Alternatively, the porous structure of TiO_2 or NiO can be coated on the top of a planar photocathode, such as Cu_2O[27] or Si,[54] to increase the catalyst loading area and improve the CO_2RR of the photocathode. In Figure 7.10a, it is shown that with a mesoporous TiO_2 layer on Cu_2O, the Re(bpy)$(CO)_3$ catalyst can be effectively immobilized on the electrode and promote the CO_2RR.[27] In this research, it is found that the $-PO_3H_2$ terminal group of the Re molecular catalyst is significant for creating the strong

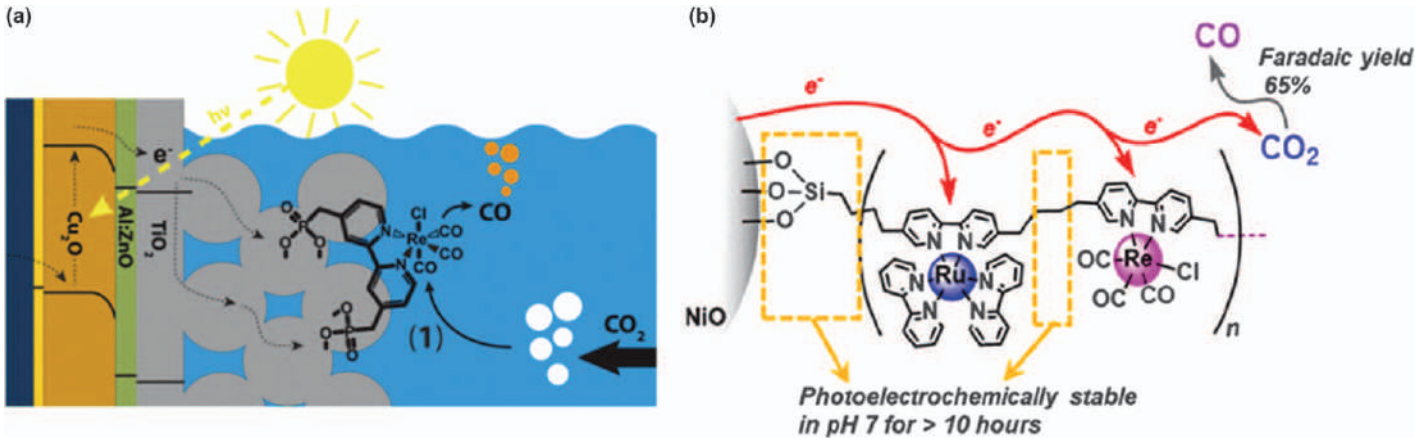

Figure 7.10 (a) Schematic structures of the Cu_2O photocathode with the $(bipy)_2Re(CO)_3Cl$ molecular catalyst immobilized on mesoporous TiO_2. Reproduced from ref. 27 with permission from American Chemical Society, Copyright 2016. (b) Schematic structure of N3 dye loaded NiO with the $(bipy)_2Re(CO)_3Cl$ molecular catalyst for CO_2 reduction. Reproduced from ref. 55 with permission from American Chemical Society, Copyright 2019.

linkage between the catalyst and substrate. The NiO mesoporous layer can also be used for loading the photosensitizer as shown in Figure 7.10b.[53] In the dye sensitized photoelectrodes, the strong light absorption coefficient of the dye molecular [normally the N3 dye (*i.e.*, cis-bis(isothiocyanato)bis(2,2′-bipyridyl-4,4′-dicarboxylato)ruthenium(II)) and metallophthalocyanine][6,55] can ensure enough light harvest, which makes it significantly different from the classical PEC system where the light is captured by the semiconductors. The terminal groups of $-SiO_3H_2$ can have strong interactions with the hydrophilic surface of NiO, creating a strong linkage for charge transfer between the molecular catalyst and the substrate. When the dye is stimulated by photons, the electrons will be promoted to the lowest unoccupied molecular orbitals (LUMO) for CO_2RR *via* the molecular catalysts, further bridging with the Re(bpy)$(CO)_3$-based molecular catalyst (Figure 7.10b).[53] The as-prepared molecular-based photoelectrode shows high CO selectivity (FE > 65%) in CO_2RR.

For the molecular catalyst-based PEC CO_2RR, there are two features: 1) current is relatively low compared to the heterogeneous catalyst system; 2) the product in most cases is CO. The low photocurrent for the homogenous system may be a result of low catalyst loading. For example, a photocurrent of -1 mA cm^{-2} means the turn over frequency (TOF) of CO_2-to-CO conversion is in the order of 10^{15} s^{-1} cm^{-2}. Suppose that there are 10^{11} cm^{-2} catalyst molecules, the catalytic capability of the molecular catalysts of over 10^4 s^{-1} would be required, which is a harsh requirement. Moreover, due to the coordination of the central metal in the molecular catalyst, it may be difficult for further hydrogenation of CO_2 after formation of the intermediate of the CO product. Therefore, CO is the dominate product in many cases. Notwithstanding these features, the insight into molecular catalysts can help to obtain a better understanding of heterogeneous reactions for further achieving more efficient and higher selectivity of CO_2RR.

7.3.3 Enzyme Catalysts

CO_2 conversion is one of the most important processes that occur in plants. Under the synergetic effect of serials of enzymes, CO_2 can be converted into various carbohydrates. Inspired by Nature, researchers attempt to couple an enzyme with a photocathode for CO_2RR. Due to the protection of the protein around the active centre in the enzyme, it is impossible to directly pass electrons between the photoelectrode and the enzyme. Therefore, it needs some mediator for the electron communication. One good example is the application of the formate dehydrogenase (FDH) enzyme as the catalyst on p-InP and methyl viologen (MV) as the electron mediator to achieve highly selective HCOOH production through the PEC process.[56] The MV works as an electron shuttle to ensure the charge-transfer between the p-InP photocathode and the active centre of the FDH enzyme. Bachmeier also reported the application of a long chain dye molecule to couple with the

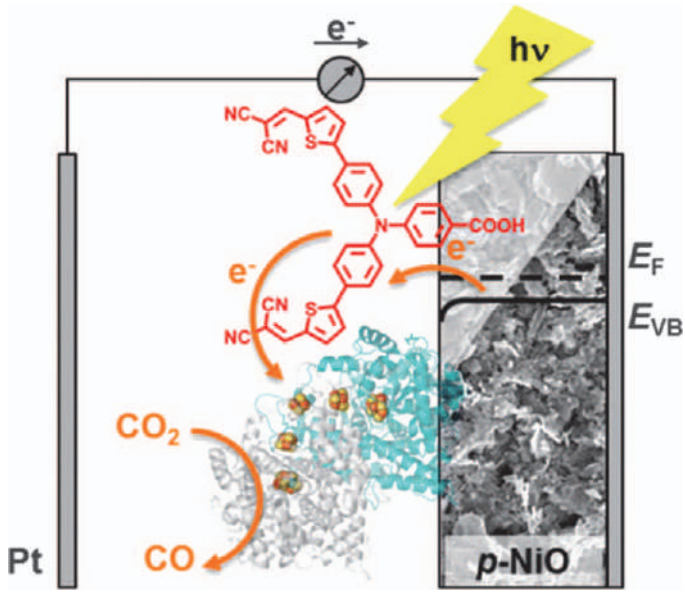

Figure 7.11 Schematic illustration of an enzyme-loaded photocathode for CO_2RR. Reproduced from ref. 57 with permission from American Chemical Society, Copyright 2014.

carboxydothermus hydrogenoformans (CODH) enzyme.[57] As shown in Figure 7.11, on the one hand the dye molecule can work as a light absorber, on the other hand it is capable of close contact with the CODH enzyme to ensure the charge-transfer. This system was able to convert CO_2 into CO under visible light irradiation. Besides the single enzyme catalyst, Kuk *et al.* reported that they were able to combine three different functional enzymes together on a $BiFeO_3$ photocathode and realized the CO_2-to-CH_3OH conversion in a PEC process.[58] Eventually, Peidong Yang's group has reported coupling a Si nanowire with bacteria to convert CO_2 into valuable chemicals.[59,60] All these results indicate the potential of applying bio-hybrid photoelectrodes to achieve an effective CO_2RR process.

7.4 Electrolyte Solution Selection

Besides the photoelectrode and surface catalyst, the electrolyte solution exerts significant influence on the CO_2RR. Normally, the electrolyte solution is composed of two essential components, *i.e.* solvent and electrolyte. Additionally, some additives have also been reported to affect the CO_2RR. The electrolyte is used to provide ion conductivity, while the solvent has two major roles of providing protons and hosting the CO_2. Below, we will discuss how the solution, electrolyte, and additives affect the CO_2RR on photoelectrodes.

7.4.1 Solvent

Both aqueous and non-aqueous electrolyte solutions are used for CO_2RR. In aqueous solution, it is well known that there is an equilibrium for CO_2 dissolving (eqn (7.5)).[30]

$$CO_2 + H_2O \leftrightarrow H_2CO_3 \leftrightarrow H^+ + HCO_3^- \leftrightarrow 2H^+ + CO_3^{2-} \quad (7.5)$$

The equilibrium under different pH values will determine the form of carbonate ions (HCO_3^-, CO_3^{2-}, or molecular CO_2), which will finally affect CO_2 activation. Actually, there is still debate on whether the adsorbed species are CO_2 or carbonate ions on the surface of electrode.[31] If liquid products (*e.g.*, HCOOH, CH_3OH) are produced in the CO_2RR, a more complicated equilibrium will be established in the system. The Pourbaix diagram offers a good reference to show the species balance in the solution.[61–63] Taking the CO_2-HCOOH system as an example, the Pourbaix diagram (Figure 7.12) shows the equilibrium between different species, including H_2CO_3, HCO_3^-, CO_3^{2-} and $HCOO^-$.[62,63] The thermodynamic requirement for these species conversion can also be identified from the diagram. For example, according to Figure 7.12, the HER is thermodynamically more favoured than the CO_2RR (with the product of formic acid) in all pH ranges. Moreover, when taking both the reduction (CO_2RR) and oxidation (water oxidation) into consideration, they need the lowest theoretical bias over the pH range of 7–10, since the potential gap between E($HCOO^-/HCO_3^-$) and E (H_2/H^+) is the lowest.

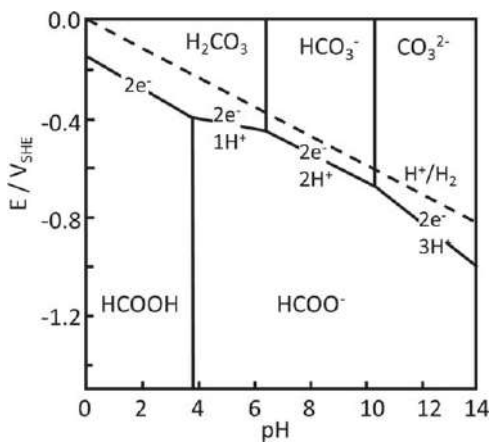

Figure 7.12 Pourbaix diagram showing the pH-potential thermodynamic relationship for HCOOH and dissolved CO_2. The proton reduction curve in the Pourbaix diagram is indicated by the dashed line.
Reproduced from ref. 62 with permission from the Royal Society of Chemistry. The proton-coupled electron transfer processes as indicated by $2e^-/H^+$, $2e^-/2H^+$ and $2e^-/3H^+$ are referred to in ref. 63.

For CO_2RR, the performance is closely related to the dissolved CO_2 concentration. Improving the CO_2 solubility normally leads to increased CO_2RR current. Water, the most widely used solvent, is a good proton source, but the CO_2 solubility is very low. At room temperature, 0.1 MPa (1 atm) CO_2 only gives 0.06 mol % in water. Increasing the temperature can suppress the CO_2 dissolution, while increasing the CO_2 pressure can efficiently improve its solubility.[64,65] Taniguchi *et al.* investigated the CO_2RR on p-CdTe under different CO_2 pressures, and found that the photocurrent increased linearly with the increase of CO_2 pressure.[69] Alternatively, some small molecular organic solvents are reported to have high CO_2 dissolution.[65] For example, methanol has been used as a commercial solvent to realize CO_2 capture. It is reported to have 7 times higher CO_2 solubility than water. Acetone is reported to have a much better CO_2 absorbtion capability, but is hard to handle due to its volatility and toxicity.[66] In any case, we also need to consider the solubility of the electrolyte in the solvent to provide sufficient ion conductivity.

In the literature, *N*,*N*-dimethylformamide (DMF) and acetonitrile (MeCN) are usually used for non-aqueous CO_2RR in the PEC process. A comparison of the standard reduction potential for CO_2 reduction in H_2O, DMF, and MeCN has been provided by Mayer's group (Table 7.4).[67] It is noticed that the CO_2RR in MeCN also holds a higher potential that in DMF, indicating the CO_2RR is easier in MeCN solution. Moreover, the CO_2RR in non-aqueous solution usually leads to CO production. Shreier *et al.* reported that in MeCN a hybrid Re molecular catalyst modified Cu_2O photocathode can also realize highly CO_2-to-CO conversion.[68] More interesting, they also find that after adding another organic solvent, MeOH, the CO_2RR activity is profoundly improved (Figure 7.13). Taniguchi *et al.* systematically investigated the reduction of CO_2 in non-aqueous media on a p-CdTe photocathode, including DMF, MeCN, DMSO, and polycarbonate.[69] They all show over 60% FE for CO production. It should be mentioned that it is essential to have a little amount of water in the organic solvent. In pure solvent, the surface of the photocathode will be totally covered by organic solvent molecules without a proton source, which will hinder the CO_2RR from happening.[70]

Table 7.4 Standard reduction potential for CO_2RR in various solvents. Reproduced from ref. 67, https://protect-eu.mimecast.com/s/CnNZC91EgFJPq4UoqL6s?domain=pubs.acs.org, with permission from American Chemical Society, Copyright 2015.

Reaction	E° in H_2O (*vs.* SHE)	E° in MeCN (*vs.* $Fc^{+/0}$)	E° in DMF (*vs.* $Fc^{+/0}$)
$2H^+_{(solv)} + 2e^- \leftrightarrow 2H_{2(g)}$	0	−0.028	−0.662
$O_{2(g)} + 4e^- + 4H^+_{(solv)} \leftrightarrow 2H_2O_{(solv)}$	+1.229	+1.21	+0.60
$CO_{2(g)} + 2e^- + 2H^+_{(solv)} \leftrightarrow CO_{(g)} + H_2O_{(solv)}$	−0.104	−0.12	−0.73
$CO_{2(g)} + 8e^- + 8H^+_{(solv)} \leftrightarrow CH_{4(g)} + 2H_2O_{(solv)}$	+0.169	+0.15	−0.48

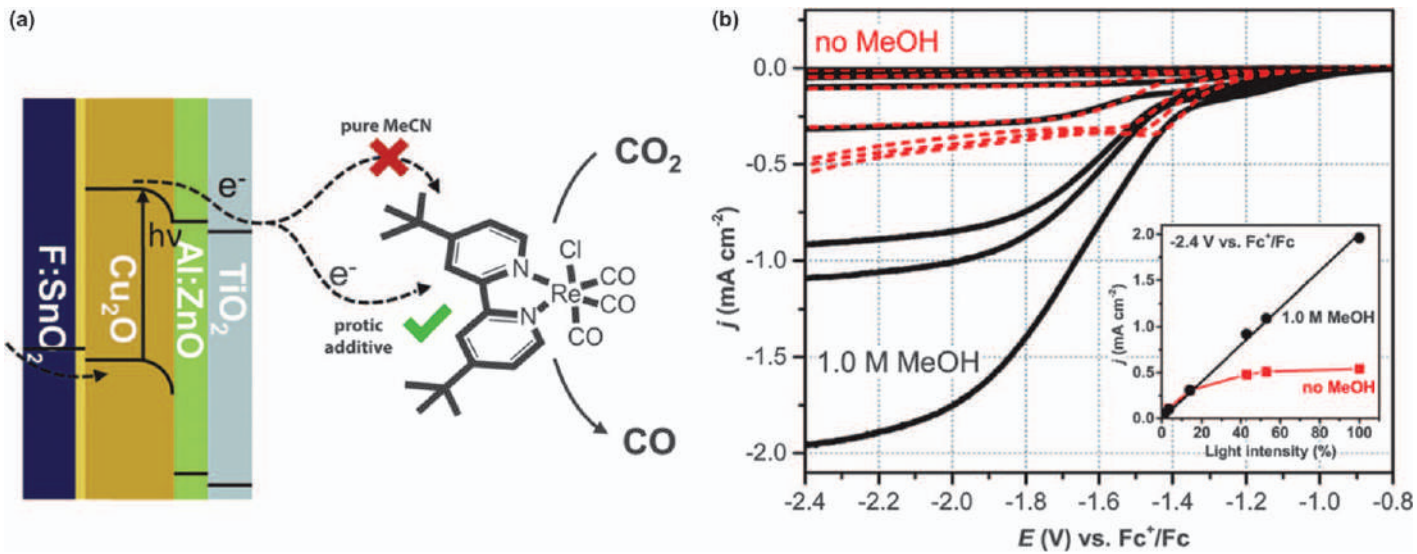

Figure 7.13 (a) Schematic structure of the Cu_2O-based photocathode with an Re molecular catalyst for CO_2RR. (b) Photocurrent of the photocathode recorded without (red dashed line) and with (black solid line) MeOH in the electrolyte solution. Reproduced from ref. 68 with permission from the Royal Society of Chemistry.

7.4.2 Electrolyte

Depending on the solvent, different kinds of electrolyte are used to provide ionic conductivity. In aqueous solution, the electrolyte is usually bicarbonate, such as $NaHCO_3$ and $KHCO_3$. It has also been reported that some alkaline, phosphate, or sulphate solution are used in CO_2RR, but considering the CO_2 dissolving equilibrium, there also exist large amounts of bicarbonate salts. According to the research of Yoneyama *et al.* on the p-CdTe photocathode, both the cation and the anion have significant influence on the product of CO_2RR.[71] Figure 7.14 shows that when using the same anion, *e.g.* CO_3^{2-}, the CO selectivity gradually increases in the order of Li, Na, K; but the HCOOH selectivity does not change much. When using the same cation, *e.g.*, Na^+, the HCOOH selectivity is gradually decreased in the order of CO_3^{2-}. SO_4^{2-}, PO_4^{3-}; the CO selectivity remains close to each other.

Besides inorganic salts, other electrolytes have been widely used in CO_2RR. Hu *et al.* summarized organic molecule-based electrolytes in electrocatalytic CO_2RR and showed how these organic mediators can activate CO_2 during the reduction reaction.[72] In PEC, the use of hybrid salts and ion liquids has been reported as well. Hybrid salts based on tetraalkyammonium (NR_4^+) ions are applied in both aqueous and non-aqueous solutions.[69,71,73] By changing the chain length of the alkyl group, a large group of hybrid electrolytes has been investigated based on the p-CdTe photocathode (Table 7.5).[69] The catalytic effect of NR_4^+ declined upon increasing the chain length, which is attributed to the difficulty in NR_4^+ absorption on the surface of the photoelectrodes. Comparing to the inorganic electrolyte, the hybrid one shows better CO selectivity and higher CO_2 conversion efficiency.

Another kind of electrolyte, ionic liquid, has been used in non-aqueous solution for CO_2RR in the PEC process.[74] Many different ionic liquids have been designed (Figure 7.15a).[72] Zeng *et al.* applied 1-ethyl-3-methylimidazolium tetrafluoroborate ([EMIM]BF_4) in MeCN as the

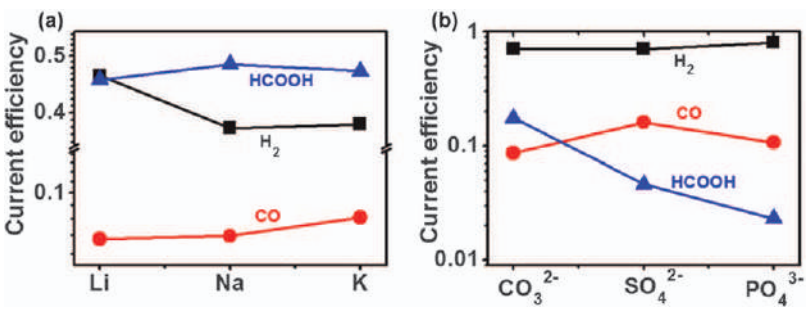

Figure 7.14 Effect of cation and anion on the selectivity of CO_2RR on the p-CdTe photocathode.
Data from Yoneyama *et al.*[71]

Table 7.5 Effect of alky-group length on CO_2RR. Reproduced from ref. 69 with permission from Elsevier, Copyright 1984.[a]

Supporting electrolyte	Cathode potential (V *vs.* SCE)	Electricity passed (C)	CO formed	
			μmoles	Current efficiency (%)
Me_4NCl	−1.6	8.2	34.0	80.0
Me_4NPF_6	−1.6	7.3	31.1	82.2
Et_4NClO_4	−1.6	6.8	26.8	76.1
Pr_4NClO_4	−1.6	5.1	19.5	73.8
Bu_4NClO_4	−1.6	7.8	30.9	76.5
Hex_4NClO_4	−1.6	5.1	20.1	77.2
Oct_4NClO_4	−1.6	3.2	11.7	70.6

[a]Me: methyl; Et: ethyl; Pr: propyl; Bu: butyl; Hex: hexyl; Oct: octyl.

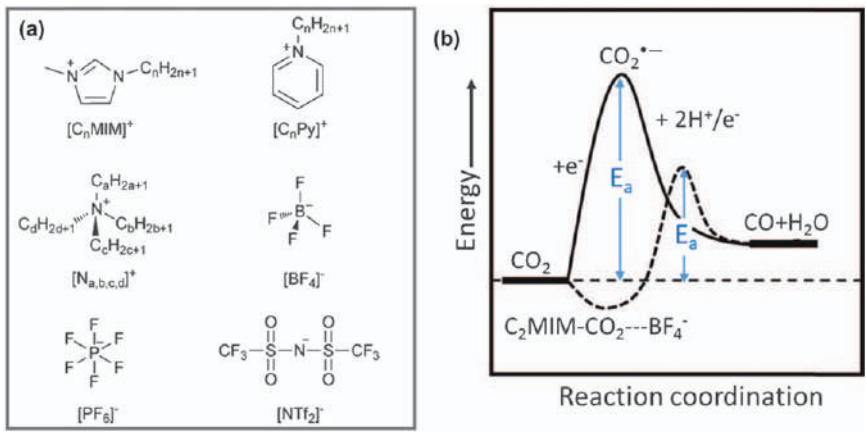

Figure 7.15 (a) Structures of cations and anions for typical ionic liquids used as the electrolyte for CO_2RR. Reproduced from ref. 72 with permission from the Royal Society of Chemistry. (b) Schematic illustration of the activation energy (E_a) decrease by ionic liquid, $[C_2MIM]BF_4$.[74]

electrolyte solution, using p-InP as the photocathode, to achieve CO_2RR with FE > 99%.[75] It is claimed that the ionic liquid can bond with CO_2 and largely decrease the $CO_2^{\bullet-}$ formation energy as shown in Figure 7.15b.[72,74,75]

7.4.3 Additives

Additives normally contribute little to the ionic conductivity due to their low concentration and dissociation constant. Nevertheless, they can significantly change the CO_2RR pathway, leading to high selectivity/CO_2 conversion efficiency. Two kinds of interesting additive have been reported, *i.e.* crown ethers and pyridine.

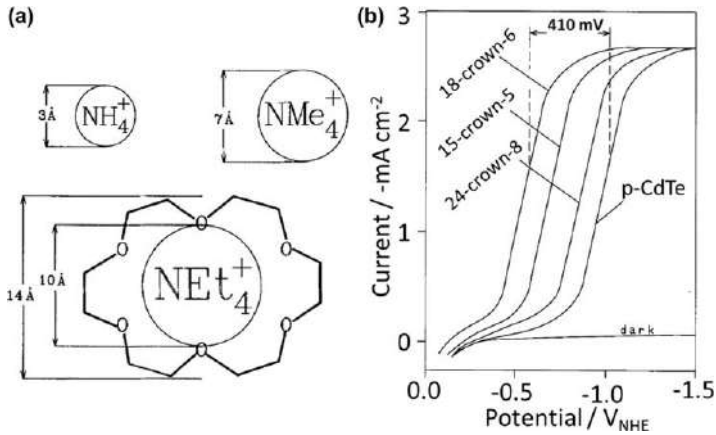

Figure 7.16 (a) Comparison of ion size to the void in 18-crown-6 ether. (b) Effect of crown ethers on the CO_2RR on a p-CdTe photocathode. Reproduced from ref. 70 with permission from Elsevier, Copyright 1989.

Crown ethers are cyclic chemical compounds consisting of several ether groups. The ether oxygen atoms are reported to be CO_2-philic, which will effectively increase the CO_2 concentration near the photocathode surface.[65] And the large void of the crown ether can accommodate ammonia ions (as indicated in Figure 7.16a), which has been reported to promote the CO_2 catalytic process. Bockris and Wass have investigated the promotion effect of different crown ethers on a p-CdTe photocathode (Figure 7.16).[70] The best one is 18-crown-6, showing over 400 mV voltage shift compared to the pristine CdTe photocathode. This indicates the significant role of the crown ether in decreasing the activation energy of the CO_2RR. Taniguchi *et al.* found that on a p-GaP photocathode, 15-crown-5 can drastically increase the FE of methanol from 6.5% to 44%.[76]

Pyridine is another interesting additive for CO_2RR. On the p-GaP photocathode, Barton *et al.* reported that the FE of CH_3OH generation increases to >90% with the presence of pyridine, as shown in Figure 7.17.[77] The investigation of the mechanism claimed that the pyridine works as a one electron shuttle to realize the multiple electron–proton transfer from CO_2 to methanol.[78] The protonation of the pyridine molecular leads to a significant decrease of the energy barrier for CO_2 activation.[79,80] However, it should be noted that the high CH_3OH FE is achieved only at low photocurrent density (<0.5 mA cm^{-2}), which may bring great uncertainty or even error to the product analysis due to this very little amount.[90] Applying a simple molecular to complete this multiple electron–proton transfer process is also debatable.[91] Moreover, it has been reported that the FE could pass from close to 100% to nearly 0 when the ultrapure electrolyte solution (99.999% salt, 17 M Ω cm water) was applied, suggesting a possible catalytic effect from the impurities.[92] Extreme attention should therefore be paid to the situation where high FE is achieved at low CO_2RR activity.

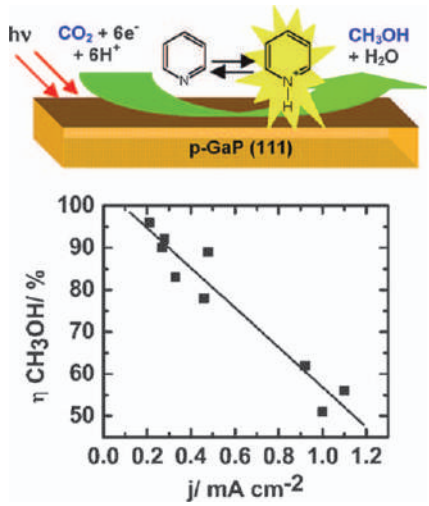

Figure 7.17 Schematic illustration of pyridine promoted CH_3OH production and the CH_3OH selectivity on the p-GaP photocathode at different current densities during CO_2RR.
Reproduced from ref. 77 with permission from American Chemical Society, Copyright 2008.

7.5 Summary

Herein, we have summarized the development of photoelectrochemical CO_2 reduction reaction in terms of three aspects of photoelectrode candidates, surface catalyst loading, and electrolyte choice. Two categories of photoelectrodes have been reviewed, one is based on the semiconductor/electrolyte junction, the other is based on the buried junction. Moreover, various catalysts have been developed to facilitate the surface CO_2RR, including metal/metal oxides, molecular catalysts, and enzyme catalysts. They provide a wide choice for optimizing the activity and selectivity of CO_2RR. In addition, the electrolyte solution is also thought to be critical for the CO_2 reduction due to the influence of the solvent, electrolyte and additives.

Although photoelectrochemical CO_2RR has been developed a lot, we should be aware that we are still at the very early stage when taking the efficiency, selectivity, and stability into consideration. In the CO_2RR, we face not only the challenge of photocharge separation and transfer in the photoelectrode, but also the mass diffusion issue for this gas–solid phase reaction. In the future, we need to address the following three challenges:

1. reactor design to promote the interaction time between CO_2 and the photoelectrode.
2. photocathode optimization to realize high photocurrent.
3. catalyst and electrolyte solution optimization to realize high selectivity.

The photoelectrochemical CO_2 reduction reaction is an ambitious reaction since it can realize the utilization of waste CO_2 for platform chemicals production driven by clean sunlight. The realization of this process is significant for the sustainable development of our society. Therefore, the PEC CO_2RR deserves our greatest attention and efforts.

References

1. R. Perez and M. Perez, *The IEA SHC Solar Update*, 2009, p. 50.
2. T. J. Meyer, *Acc. Chem. Res.*, 1989, **22**, 163.
3. C. W. Lee, N. H. Cho, S. W. Im, M. S. Jee, Y. J. Hwang, B. K. Min and K. T. Nam, *J. Mater. Chem. A*, 2018, **6**, 14043.
4. B. Kumar, M. Llorente, J. Froehlich, T. Dang, A. Sathrum and C. P. Kubiak, *Annual Rev. Phy. Chem.*, 2012, **63**, 541.
5. P. Wang, S. Wang, H. Wang, Z. Wu and L. Wang, *Part. Part. Syst. Character.*, 2018, **35**, 1700371.
6. J. L. White, M. F. Baruch, J. E. Pander III, Y. Hu, I. C. Fortmeyer, J. E. Park, T. Zhang, K. Liao, J. Gu and Y. Yan, *Chem. Rev.*, 2015, **115**, 12888.
7. N. Zhang, R. Long, C. Gao and Y. Xiong, *Sci. China Mater.*, 2018, **61**, 771.
8. X. Li, J. Yu, M. Jaroniec and X. Chen, *Chem. Rev.*, 2019, **119**, 3962.
9. M. B. Ross, P. De Luna, Y. Li, C.-T. Dinh, D. Kim, P. Yang and E. H. Sargent, *Nature Catal*, 2019, 1.
10. H. Pang, T. Masuda and J. Ye, *Chem. – Asian J.*, 2018, **13**, 127.
11. Z. Wang and L. Wang, *Sci. China Mater.*, 2018, 1.
12. Z. Chen, T. F. Jaramillo, T. G. Deutsch, A. Kleiman-Shwarsctein, A. J. Forman, N. Gaillard, R. Garland, K. Takanabe, C. Heske and M. Sunkara, *J. Mater. Res.*, 2010, **25**, 3.
13. M. Xiao, Z. Wang, M. Lyu, B. Luo, S. Wang, G. Liu, H. M. Cheng and L. Wang, *Adv. Mater.*, 2018, 1801369.
14. H. Gerischer, in *Photovoltaic and Photoelectrochemical Solar Energy Conversion*, Springer, 1981, pp. 199.
15. R. Wilson, *Crit. Rev. Sol. St. Mate. Sci.*, 1980, **10**, 1.
16. J. Reichman, *Appl. Phy. Lett.*, 1980, **36**, 574.
17. D. Boudreaux, F. Williams and A. Nozik, *J. Appl. Phy.*, 1980, **51**, 2158.
18. Z. Zhang and J. T. Yates Jr., *Chem. Rev.*, 2012, **112**, 5520.
19. Z. Wang and L. Wang, *Chinese. J. Catal.*, 2018, **39**, 369.
20. J. Gu, A. Wuttig, J. W. Krizan, Y. Hu, Z. M. Detweiler, R. J. Cava and A. B. Bocarsly, *J. Phys. Chem. C*, 2013, **117**, 12415.
21. U. Kang, S. K. Choi, D. J. Ham, S. M. Ji, W. Choi, D. S. Han, A. Abdel-Wahab and H. Park, *Energy Environ. Sci.*, 2015, **8**, 2638.
22. G. Ghadimkhani, N. R. de Tacconi, W. Chanmanee, C. Janaky and K. Rajeshwar, *Chem. Commun.*, 2013, **49**, 1297.
23. Y. J. Jang, J.-W. Jang, J. Lee, J. H. Kim, H. Kumagai, J. Lee, T. Minegishi, J. Kubota, K. Domen and J. S. Lee, *Energy Environ. Sci.*, 2015, **8**, 3597.

24. S. Wenham, C. Honsberg and M. Green, *Sol. Energy Mat. Sol. Cells*, 1994, **34**, 101.
25. S. Chu, S. Fan, Y. Wang, D. Rossouw, Y. Wang, G. A. Botton and Z. Mi, *Angew. Chem., Int. Ed.*, 2016, **55**, 14262.
26. T. Arai, S. Tajima, S. Sato, K. Uemura, T. Morikawa and T. Kajino, *Chem. Commun.*, 2011, **47**, 12664.
27. M. Schreier, J. Luo, P. Gao, T. Moehl, M. T. Mayer and M. Grätzel, *J. Am. Chem. Soc.*, 2016, **138**, 1938.
28. Z. Wang, M. Lyu, P. Chen, S. Wang and L. Wang, *Phy. Chem. Chem. Phy.*, 2018, **20**, 22629.
29. R. Francke, B. Schille and M. Roemelt, *Chem. Rev.*, 2018, **118**, 4631.
30. Y. Hori, in *Modern Aspects of Electrochemistry*, ed. C. G. Vayenas, R. E. White and M. E. Gamboa-Aldeco, 2008, p. 89.
31. W. Zhang, Y. Hu, L. Ma, G. Zhu, Y. Wang, X. Xue, R. Chen, S. Yang and Z. Jin, *Adv. Sci.*, 2018, **5**, 1700275.
32. T. J. LaTempa, S. Rani, N. Bao and C. A. Grimes, *Nanoscale*, 2012, **4**, 2245.
33. S. Kaneco, H. Katsumata, T. Suzuki and K. Ohta, *Appl. Cataly. B: Environ.*, 2006, **64**, 139.
34. C. Li, T. Wang, B. Liu, M. Chen, A. Li, G. Zhang, M. Du, H. Wang, S. F. Liu and J. Gong, *Energy Environ. Sci.*, 2019, **12**, 923.
35. J. S. DuChene, G. Tagliabue, A. J. Welch, W.-H. Cheng and H. A. Atwater, *Nano Lett.*, 2018, **18**, 2545.
36. Q. Kong, D. Kim, C. Liu, Y. Yu, Y. Su, Y. Li and P. Yang, *Nano Lett.*, 2016, **16**, 5675.
37. S. K. Choi, U. Kang, S. Lee, D. J. Ham, S. M. Ji and H. Park, *Adv. Energy Mater.*, 2014, **4**, 1301614.
38. Y. Hu, F. Chen, P. Ding, H. Yang, J. Chen, C. Zha and Y. Li, *J. Mater. Chem. A*, 2018, **6**, 21906.
39. G. Zeng, J. Qiu, Z. Li, P. Pavaskar and S. B. Cronin, *ACS Catal.*, 2014, **4**, 3512–3516.
40. E. Szaniawska, K. Bienkowski, I. A. Rutkowska, P. J. Kulesza and R. Solarska, *Catal. Today*, 2018, **300**, 145.
41. H.-Y. Kang, D.-H. Nam, K. D. Yang, W. Joo, H. Kwak, H.-H. Kim, S.-H. Hong, K. T. Nam and Y.-C. Joo, *ACS Nano*, 2018, **12**, 8187.
42. E. Pastor, F. M. Pesci, A. Reynal, A. D. Handoko, M. Guo, X. An, A. J. Cowan, D. R. Klug, J. R. Durrant and J. Tang, *Phys. Chem. Chem. Phy.*, 2014, **16**, 5922.
43. M. Schreier, F. Héroguel, L. Steier, S. Ahmad, J. S. Luterbacher, M. T. Mayer, J. Luo and M. Grätzel, *Nat. Energy*, 2017, **2**, 17087.
44. B. AlOtaibi, S. Fan, D. Wang, J. Ye and Z. Mi, *ACS Catal.*, 2015, **5**, 5342.
45. D. Gao, Y. Zhang, Z. Zhou, F. Cai, X. Zhao, W. Huang, Y. Li, J. Zhu, P. Liu and F. Yang, *J. Am. Chem. Soc.*, 2017, **139**, 5652.
46. S. Chu, P. Ou, P. Ghamari, S. Vanka, B. Zhou, I. Shih, J. Song and Z. Mi, *J. Am. Chem. Soc.*, 2018, **140**, 7869.
47. B. Kumar, J. M. Smieja and C. P. Kubiak, *J. Phys. Chem. C*, 2010, **114**, 14220.

48. T. Arai, S. Sato, K. Uemura, T. Morikawa, T. Kajino and T. Motohiro, *Chem. Commun.*, 2010, **46**, 6944.
49. E. N. Torralba-Peñalver, Y. Luo, J.-D. Compain, S. Chardon-Noblat and B. Fabre, *ACS Catal.*, 2015, **5**, 6138.
50. K. Alenezi, S. K. Ibrahim, P. Li and C. J. Pickett, *Chem. – Eur. J.*, 2013, **19**, 13522.
51. J. Bonin, A. Maurin and M. Robert, *Coord. Chem. Rev.*, 2017, **334**, 184.
52. K. Sekizawa, S. Sato, T. Arai and T. Morikawa, *ACS Catal.*, 2018, **8**, 1405.
53. G. Sahara, H. Kumagai, K. Maeda, N. Kaeffer, V. Artero, M. Higashi, R. Abe and O. Ishitani, *J. Am. Chem. Soc.*, 2016, **138**, 14152.
54. J. J. Leung, J. Warnan, K. H. Ly, N. Heidary, D. H. Nam, M. F. Kuehnel and E. Reisner, *Nat. Catal.*, 2019, **2**, 354.
55. T.-T. Li, B. Shan and T. J. Meyer, *ACS Energy Lett.*, 2019, **4**, 629.
56. B. A. Parkinson and P. F. Weaver, *Nature*, 1984, **309**, 148.
57. A. Bachmeier, S. Hall, S. W. Ragsdale and F. A. Armstrong, *J. Am. Chem. Soc.*, 2014, **136**, 13518.
58. S. K. Kuk, R. K. Singh, D. H. Nam, R. Singh, J. K. Lee and C. B. Park, *Angew. Chem., Int. Ed.*, 2017, **56**, 3827.
59. C. Liu, J. J. Gallagher, K. K. Sakimoto, E. M. Nichols, C. J. Chang, M. C. Chang and P. Yang, *Nano Lett.*, 2015, **15**, 3634.
60. K. K. Sakimoto, A. B. Wong and P. Yang, *Science*, 2016, **351**, 74.
61. C. Costentin, S. Drouet, G. Passard, M. Robert and J.-M. Savéant, *J. Am. Chem. Soc.*, 2013, **135**, 9023.
62. K. Saravanan, Y. Basdogan, J. Dean and J. A. Keith, *J. Mater. Chem. A*, 2017, **5**, 11756.
63. T. Reda, C. M. Plugge, N. J. Abram and J. Hirst, *Proc. Natl. Acad. Sci. U. S. A.*, 2008, **105**, 10654.
64. J. J. Carroll, J. D. Slupsky and A. E. Mather, *J. Phys. Chem. Ref. Data*, 1991, **20**, 1201.
65. M. B. Miller, D.-L. Chen, D. R. Luebke, J. K. Johnson and R. M. Enick, *J. Chem. Eng. Data*, 2011, **56**, 1565.
66. M. Jödecke, J. Xia, Á. Pérez-Salado Kamps and G. Maurer, *Chem. Eng. Tech.*, 2004, **27**, 31.
67. M. L. Pegis, J. A. Roberts, D. J. Wasylenko, E. A. Mader, A. M. Appel and J. M. Mayer, *Inorg. Chem.*, 2015, **54**, 11883.
68. M. Schreier, P. Gao, M. T. Mayer, J. Luo, T. Moehl, M. K. Nazeeruddin, S. D. Tilley and M. Grätzel, *Energy Environ. Sci.*, 2015, **8**, 855.
69. I. Taniguchi, B. Aurian-Blajeni and B. Jo'm, *Electrochim. Acta*, 1984, **29**, 923.
70. B. Jo'm and J. Wass, *Mater. Chem. Phys.*, 1989, **22**, 249.
71. H. Yoneyama, K. Sugimura and S. Kuwabata, *J. Electroanaly. Chem. Interf. Electrochem.*, 1988, **249**, 143.
72. Y. Oh and X. Hu, *Chem. Soc. Rev.*, 2013, **42**, 2253.
73. M. G. Bradley, T. Tysak, D. J. Graves and N. A. Viachiopoulos, *J. Chem. Soc., Chem. Commun.*, 1983, 349.

74. B. A. Rosen, A. Salehi-Khojin, M. R. Thorson, W. Zhu, D. T. Whipple, P. J. Kenis and R. I. Masel, *Science*, 2011, **334**, 643.
75. G. Zeng, J. Qiu, B. Hou, H. Shi, Y. Lin, M. Hettick, A. Javey and S. B. Cronin, *Chem. Euro. J.*, 2015, **21**, 13502.
76. Y. Taniguchi, H. Yoneyama and H. Tamura, *Bull. Chem. Soc. Jap.*, 1982, **55**, 2034.
77. E. E. Barton, D. M. Rampulla and A. B. Bocarsly, *J. Am. Chem. Soc.*, 2008, **130**, 6342.
78. E. Barton Cole, P. S. Lakkaraju, D. M. Rampulla, A. J. Morris, E. Abelev and A. B. Bocarsly, *J. Am. Chem. Soc.*, 2010, **132**, 11539.
79. C.-H. Lim, A. M. Holder and C. B. Musgrave, *J. Am. Chem. Soc.*, 2012, **135**, 142.
80. J. A. Keith and E. A. Carter, *J. Am. Chem. Soc.*, 2012, **134**, 7580.
81. Y. Arai, M. Ishii, H. Shinohara and S. Yamazaki, *IEEE Electron Device Lett.*, 1991, **12**, 460.
82. J. T. Song, H. Ryoo, M. Cho, J. Kim, J. G. Kim, S. Y. Chung and J. Oh, *Adv. Energy Mater.*, 2017, **7**, 1601103.
83. C. Battaglia, A. Cuevas and S. De Wolf, *Energy Environ. Sci.*, 2016, **9**, 1552.
84. H. Tanaka, T. Shimakawa, T. Miyata, H. Sato and T. Minami, *Thin Solid Films*, 2004, **469**, 80.
85. S. Kamimura, Y. Sasaki, M. Kanaya, T. Tsubota and T. Ohno, *RSC Adv.*, 2016, **6**, 112594.
86. C. Yan, F. Liu, K. Sun, N. Song, J. A. Stride, F. Zhou, X. Hao and M. Green, *Sol. Energy Mater. Sol. Cells*, 2016, **144**, 700.
87. J. Chen, J. Yin, X. Zheng, H. Ait Ahsaine, Y. Zhou, C. Dong, O. F. Mohammed, K. Takanabe and O. M. Bakr, *ACS Energy Lett.*, 2019, **4**, 1279.
88. N.-G. Park, *Mater. Today*, 2015, **18**, 65.
89. C. An, J. Yuan and J. Zhu, *J. Electrochem. Soc.*, 2018, **165**, H1066.
90. C. Costentin, J. M. Savéant and C. Tard, *ACS Energy Lett.*, 2018, **3**, 695.
91. H. Dridi, C. Comminges, C. Morais, J. C. Meledje, K. B. Kokoh, C. Costentin and J. M. Savéant, *J. Am. Chem. Soc.*, 2017, **139**, 13922.
92. K. W. Frese and D. Canfield, *J. Electrochem. Soc.*, 1984, **131**, 2518.

CHAPTER 8

Hybrid Biological–Inorganic Systems for CO_2 Conversion to Fuels

REBECCA S. SHERBO,[a,b] DANIEL M. LOH[a] AND DANIEL G. NOCERA*[a]

[a] Department of Chemistry and Chemical Biology, Harvard University, Cambridge, MA 02138, USA; [b] Department of Systems Biology, Harvard Medical School, Boston, MA 02115, USA
*Email: dnocera@fas.harvard.edu

8.1 Introduction

The biological reduction of CO_2 into organic carbon is integral to the formation and maintenance of all life on earth. An urgent need to mitigate the effects of CO_2 on our atmosphere[1,2] has provided an imperative to exploit biological CO_2 fixation for the conversion of CO_2 into valuable and energy-rich fuels. Photosynthesis uses only sunlight, water, and CO_2 as starting materials to form all biomass according to the reaction given in eqn (8.1).

$$\text{sunlight} + n\text{H}_2\text{O} + n\text{CO}_2 \rightarrow (\text{CH}_2\text{O})_n + n\text{O}_2 \tag{8.1}$$

Key lessons learned from photosynthesis are that sunlight is used only to split water into H_2 ($NADPH/H^+$) and O_2, and that this process is separated from CO_2 reduction processes (Figure 8.1).[3] Solar absorption occurs in Photosystems II and I where water is oxidized to O_2 and protons, which are then translated to produce NADPH, and ATP is formed as an energy source

Energy and Environment Series No. 28
Carbon Dioxide Electrochemistry: Homogeneous and Heterogeneous Catalysis
Edited by Marc Robert, Cyrille Costentin and Kim Daasbjerg

Published by the Royal Society of Chemistry, www.rsc.org

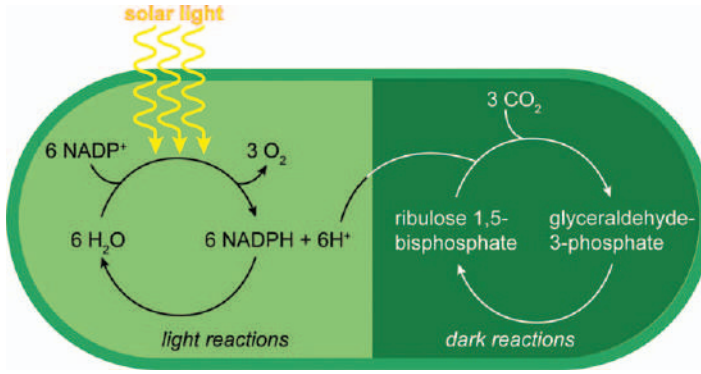

Figure 8.1 Light and dark reactions separate hydrogen formation and CO_2 reduction in photosynthesis.

from the resulting proton gradient.[4] NADPH and ATP are then appropriated as a hydrogen (hydride/proton) source and energy supply, respectively, in the separate dark reactions that fix CO_2 by carboxylation in the so-called Calvin–Benson (CB) cycle (Figure 8.1).[5]

By separating the formation of hydrogen equivalents in the form of $NADPH/H^+$ from CO_2 reduction, nature is able to overcome a significant challenge confronting CO_2 fixation: namely, hydrogen evolution is almost always more kinetically facile than the reduction of CO_2. This issue only becomes more prevalent when complex carbon products are desired that involve large inventories of protons and electrons (*e.g.* ethanol requires $8H^+/8e^-$; glucose requires $24H^+/24e^-$).[3,6] As evidenced from chemical strategies to achieve CO_2 reduction, suppressing the more kinetically favourable hydrogen evolution reaction (HER) relative to CO_2 reduction to complex carbon fuels selectively and in high yields is a major challenge.[7–9]

Despite nature's proclivity to successfully execute CO_2 reduction by (i) managing large proton-electron inventories, (ii) the extensive formation of C–C bonds and (iii) furnishing selective carbon products, there are limitations to solely relying on photosynthetic processes to address climate and energy challenges.[10] Light absorption and the energetics associated with the water splitting reaction in Photosystems I and II present a roadblock to high energy efficiencies. A simple model predicts that carbon fixation pathways, limited by enzyme concentrations and rates, can use between 3–18% of the absorbed light.[11,12] Solar-to-biomass efficiencies in plants are naturally only ~1–2%,[13] while efficiencies in microalgae reach ~3%.[14,15] Meanwhile, the efficiencies of photovoltaics have increased significantly in recent years, with devices commonly achieving efficiencies of ~20%.[16] A potentially superior approach to utilizing photosynthesis directly is to use efficient solar cells to produce an electron donor either directly or indirectly *via* a redox mediator/intermediate such as hydrogen from water splitting. That electron donor can then be used in tandem with CO_2 as a carbon source to feed lithoautotrophic microorganisms and produce fuels. With this hybrid approach, the energy

efficiency associated with producing the electron donor and protons with solar photovoltaic materials/catalysts overcomes the low energy efficiency of Photosystems I and II while simultaneously exploiting the ability of biology to fix carbon to form complex molecules with high selectivity.

All microorganisms require both an electron/proton source and a carbon source to sustain life. Autotrophic organisms fix CO_2 as the carbon source into biomass; lithoautotrophs use an electron donor directly for reducing power.[15] We term the combination of a synthetically-produced electron-donor with a lithoautotrophic microorganism a ''Hybrid Biological–Inorganic'' (HBI) system.[17] HBIs are able to fix CO_2 at atmospheric (400 ppm) concentrations at reasonable solar efficiencies,[18] and thus they do not require the large land areas and volumes of water required by plants, nor do they affect potential food sources.[19] Furthermore, HBI systems are advantageous over photosynthetic microorganisms because they do not require large surface area reactors in order to pass sufficient light for photosynthesis.[20] The surface area required for HBIs is defined by the photovoltaic array, whereas the microorganism can be grown in a dark reactor.

In this chapter, we will discuss three different HBI systems as classified by reducing sources: (1) direct H_2; (2) indirect H_2 ($2H^+/2e^-$) *via* small molecule organic mediators; and (3) electron transfer, either direct or indirect *via* redox mediators. Differences in carbon fixation pathways between aerobic and anaerobic microorganisms will be delineated, in addition to engineered metabolic pathways to selectively deliver targeted products. A comprehensive energy efficiency metric for HBI systems will be presented, thus allowing for the direct comparison of the various HBI systems.

8.2 Carbon Fixation Cycles

Carbon fixation pathways are key processes that transform CO_2 into carbon products and fuels. There are six known natural CO_2 fixation pathways: the Calvin–Benson (CB) cycle, the Wood–Ljungdahl (WL) pathway, the reductive citric acid cycle, the hydroxypropionate bi-cycle, the 3-hydroxypropionate/4-hydroxybutyrate cycle, and the dicarboxylate/4-hydroxybutyrate cycle.[15,21] The two most common pathways in HBI systems are the aerobic CB cycle and the anaerobic WL pathway (also known as the reductive acetyl-CoA pathway).[15,17,19,20,22,23] As shown in Table 8.1, these pathways have very different energetic demands as well as potential products.

8.2.1 Aerobic Carbon Fixation

The CB cycle is the most common carbon fixation cycle found in nature, and is utilized by plants as well as a number of microorganisms (Figure 8.2).[24] Figure 8.2 shows the steps in this pathway, as well as the carbon and electron sources. The key enzyme in this pathway is ribulose-1,5-bisphophate carboxylase/oxygenase (RuBisCO), which activates CO_2 for carboxylation of the pathway intermediate, 3-phosphoglycerate.[15] Despite being the most

Table 8.1 Comparison between the Calvin–Benson cycle and the Wood–Ljungdahl pathway.

	Calvin–Benson cycle	Wood–Ljungdahl pathway
ATP/pyruvate	7	<1
Oxygen tolerance	Yes	No
CO_2 incorporation	Carboxylation	Direct reduction
Products	Variable	Acetate/methane
Energy efficiency	~20–35%	~70–90%
Cell growth	High	Low

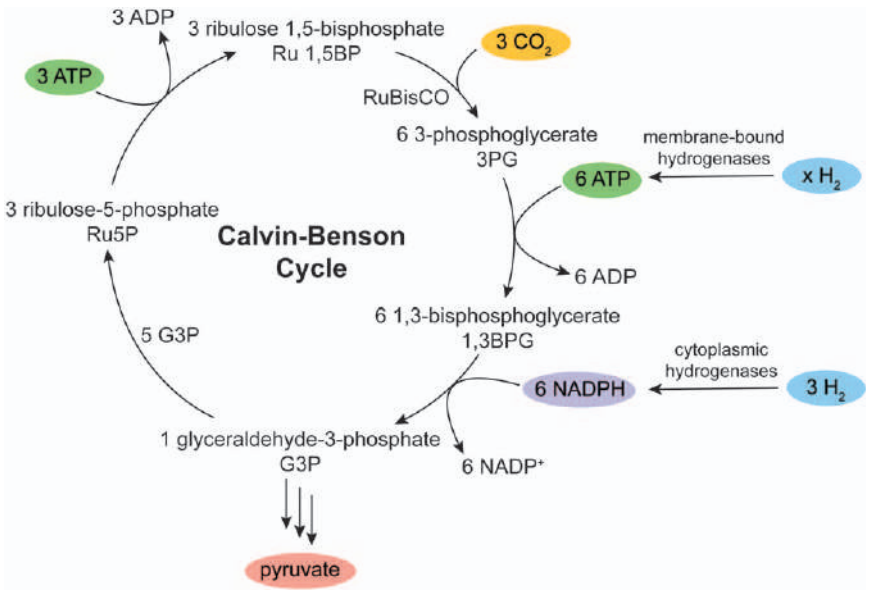

Figure 8.2 The CB cycle incorporates CO_2 by carboxylation and produces glyceraldehyde-3-phosphate, which can then produce pyruvate and acetyl-CoA. Yellow indicates carbon source, blue indicates electron source, green indicates energy equivalents, purple indicates reducing equivalents, and red indicates carbon product.

highly utilized and best understood carbon fixation mechanism,[25] CB cycle inefficiencies stemming from the main enzyme RuBisCO significantly affect product output for the production of biofuels. RuBisCO can utilize O_2 as an alternate substrate to CO_2, leading to photorespiration which decreases carbon fixation by ~30% in microorganisms.[17] Improving enzyme selectivity for CO_2 reduces photorespiration, but also leads to a decrease in reaction kinetics.[24]

The CB cycle consumes more ATP than most other carbon fixation pathways (7 ATP per pyruvate or acetyl-CoA),[15] and therefore the energy efficiency for fuel production is suppressed (~20–35% for any given product).[19] Another disadvantage of this cycle is that acetyl-CoA, which is a common

precursor for many carbon fuels, is produced from pyruvate (a C3 intermediate) by decarboxylation; thus, a third of all fixed carbon is lost and the maximum carbon yield that can be achieved is limited to 66.6%.[20] Despite these disadvantages, the acetyl-CoA produced in the CB cycle acts as an intermediate for the production of a large number of potential carbon fuels. Additionally, cell growth is more vigorous than for the WL pathway (see Section 8.2.2), allowing for higher cell densities and therefore higher product titres.[19]

8.2.1.1 Engineering the CB Cycle

RuBisCO is the main constraint in the CB cycle for both efficiency and carboxylation kinetics. Increasing RuBisCO selectivity improves cycle efficiency, but also decreases reaction rates, while the opposite occurs when reaction rates are improved.[24] The enzyme has therefore evolved to favour either selectivity or kinetics based on the oxygen content of the natural growth environment: a more highly oxygenated environment favours better selectivity over faster turnover.[24] Efforts to improve the enzyme for biofuel production typically use selective evolution based on the desired CO_2/O_2 growth ratio or the addition of a RuBisCO system from a different autotroph that is naturally adapted to the desired gas-mixture environment.[26,27] In some organisms, synthetic[28] or alternative[29,30] photorespiration routes that bypass RuBisCO but supplement the CB cycle have been introduced. This approach has been successful in increasing plant growth[29] but, to date, has not led to improved growth in cyanobacterial systems,[15,30] illustrating the challenges confronted in bypassing natural carbon fixation pathways to improve reaction rates. Such a metabolic engineering strategy has not yet been used in HBI CO_2-fixing systems.

8.2.1.2 Carbon-concentrating Mechanisms

Two important components of carbon fixation in aerobic microorganisms are the cellular storage of carbon and its conversion to an active form. These mechanisms (known as carbon-concentrating mechanisms, or CCMs) alleviate mass-transport limitations and increase CO_2 concentrations in the cell.[24] CCMs also enable microorganisms to fix low concentrations of CO_2 directly from the atmosphere, which is a significant advantage in biological systems. CO_2-fixing carboxysomes are icosahedral intracellular microcompartments comprised of a protein complex that concentrates CO_2 and encapsulates RuBisCO and the enzyme carbonic anhydrase (CA), which converts HCO_3^- to CO_2 (Figure 8.3).[31] Carbonic anhydrase is a necessary component within these compartments because HCO_3^-, present both intra- and extracellularly, cannot be used as a substrate for RuBisCO. It has been proposed that intracellular carboxysomes are a key factor in achieving higher RuBisCO selectivity because the CO_2 concentrations therein are much higher than in the environment or in the cytoplasm, and at the same time they may exclude O_2.[15,32]

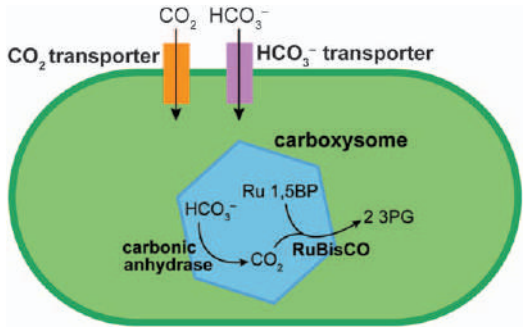

Figure 8.3 Carbon-concentrating mechanisms present in aerobic cells increase carbon fixation reaction rates and selectivity.

Carbonic anhydrase enzymes and HCO_3^- transport proteins (Figure 8.3) are important components for maintaining high CO_2 concentrations. CA enzymes and transport proteins in HBI systems are particularly valuable for operating in aqueous conditions where CO_2 solubility is low and HCO_3^- concentrations are high. The growth rate of the cyanobacterium *Synechocystis* sp. PCC6803 can be nearly doubled when HCO_3^- transporters are overexpressed, an effect most notable when microorganisms are grown with only air or low concentrations of CO_2.[33] Studies of the lithoautotroph *Cupriavidus necator* have shown that CA enzymes are crucial for autotrophic growth, especially when grown only in air. Mutants that do not produce CA are capable of only growing under the presence of high CO_2 concentrations; growth plateaus in the absence of excess CO_2.[34,35] Figure 8.3 shows how the combination of HCO_3^- transporters and carboxysomes containing RuBisCO, CA, and concentrated CO_2 work together as CCMs for aerobic carbon fixation, particularly when using atmospheric CO_2 as a carbon source.

8.2.2 Anaerobic Carbon Fixation

The primary alternative for carbon fixation in HBI systems is the Wood–Ljungdahl, or reductive acetyl-CoA, pathway (Figure 8.4).[19,36] The key enzymes of the WL pathway, such as carbon monoxide dehydrogenase (CODH), are sensitive to oxygen, and therefore CO_2 conversion must be performed in an anaerobic environment.[37] Unlike the CB cycle, where CO_2 incorporation occurs *via* carboxylation, CO_2 is directly reduced to formate or CO in the WL pathway.[36] This pathway is unique among all other fixation strategies in that ATP is conserved (<1 ATP used per cycle, Figure 8.4) and because of this, most of the cell's energy is devoted to product formation;[19] these products are acetate/acetic acid in acetogenic microorganisms and methane in methanogenic microbes.[38]

Accordingly, the energetic efficiency of the WL pathway for the production of acetate from acetogenic microbes can be up to 70–90% (as opposed to 20–35% in aerobic microbes), with the remainder directed to cell growth and

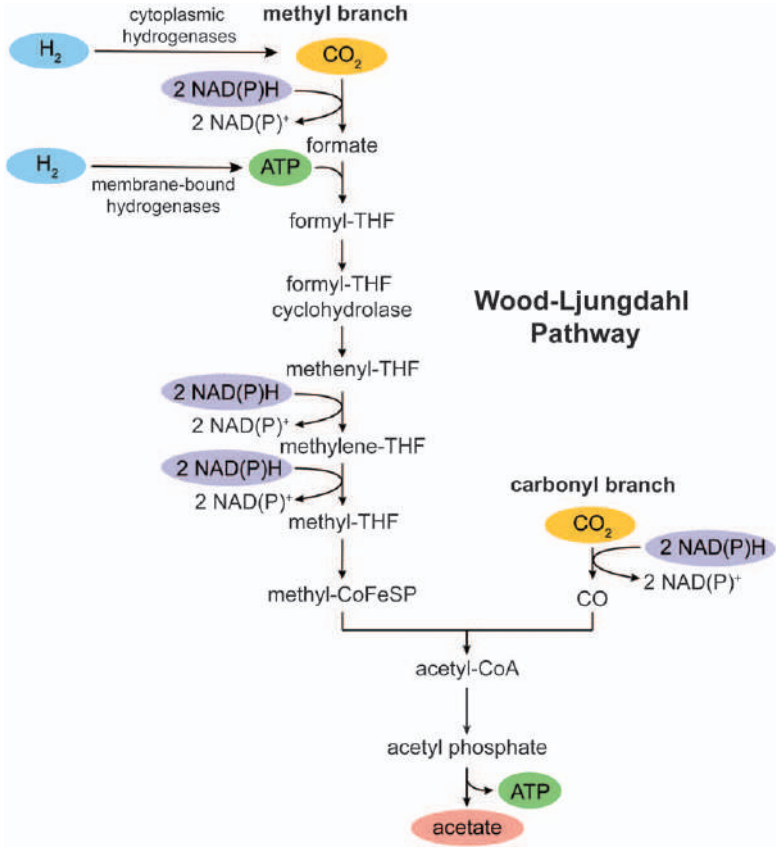

Figure 8.4 The Wood–Ljungdahl pathway directly reduces CO_2 using both a methyl and carbonyl branch that converge to form acetyl-CoA and produce acetate (or methane). Yellow indicates carbon source, blue indicates electron source, green indicates energy equivalents, purple indicates reducing equivalents, and red indicates carbon product.

maintenance. Acetogens can consume electrons at a rate of 100 $\mu mol\,s^{-1}\,g$ dry cell weight $(DCW)^{-1}$, and methanogens, under thermophilic conditions, can consume electrons up to a rate of 500 $\mu mol\,s^{-1}\,g\,DCW^{-1}$. These consumption rates are very fast as compared to those in aerobic microorganisms, which support electron consumption rates typically in the range of $\sim 25-45\ \mu mol\,s^{-1}\,g\,DCW^{-1}$.[19] The disadvantage of the WL pathway, however, is that it is very challenging to make products other than acetate/acetic acid and methane. More complex products demand more energy consumption, and these microorganisms operate at the boundary of what is thermodynamically possible. Additionally, with minimal excess ATP, growth rates of $<0.05\ h^{-1}$ and cell concentrations $<5\ g\,L^{-1}$ are lower than their aerobic counterparts by as much as an order of magnitude,[19,39,40] limiting the titre of the desired carbon product.

Due to the high energy efficiency of the WL pathway, schemes have been developed to use microorganisms with this pathway in HBI systems. To overcome limitations in carbon products, organisms with the WL pathway have been engineered or used in combination with heterotrophs. These systems will be discussed in more detail in Sections 8.4.1.2 and 8.4.3.

8.3 Efficiency Metrics

Evaluating the efficiency of HBI systems for CO_2 reduction requires thermodynamic and kinetic analysis. The thermodynamic efficiency of the system (η_{elec}) is defined as the ratio of the free energies of the products and that of the solar/electrical input (eqn (8.2)):

$$\eta_{elec} = \frac{\Delta_r G^\circ \times N}{Q \times E_{appl}} \tag{8.2}$$

where $\Delta_r G^\circ$ is the Gibb's free energy change of the system under standard conditions for N moles of product, and Q is the total charge passed at the applied voltage E_{appl}. In the case where HBI systems are not designed for fuel synthesis, the $\Delta_r G^\circ$ for biomass as a fuel equivalent can be approximated as -46 kJ $(\text{mol carbon})^{-1}$. The solar-to-fuels (/biomass) efficiency, η_{SFE}, is then obtained by multiplying η_{elec} with η_{PV}, the solar-to-electricity efficiency (*e.g.*, photovoltaic efficiency):

$$\eta_{SFE} = \eta_{PV}\eta_{elec} \tag{8.3}$$

The η_{elec} can be improved by maximizing electron conversion or faradaic efficiency (FE), decreasing the overpotential, and increasing the chemical energy of the products. Loss of FE commonly manifests from cathodic side reactions, such as the production of excess H_2 or reactive oxygen species (ROS).[18,41] Cell overpotentials can be minimized by optimization of the water-splitting catalyst and microbe-electrode interfacing.[15,22] Lastly, the thermal energy of products in $\text{J g}^{-1}\text{ L}^{-1}$ can generally be enhanced by increasing the carbon chain length.[20,42]

We note that in most HBI systems, a FE is reported as a metric of efficiency for electrode-driven reactions, and quantum yield is similarly reported for photo-driven processes.[43] As eqn (8.2) shows for electrode processes, however, a high FE is a necessary but not sufficient condition for high overall η_{SFE}. A high applied voltage can lead to a greatly reduced overall efficiency. Indeed, many HBI systems are run at constant current; to maintain that current, the applied voltage of typical potentiostats can be driven up to $10-20$ V. Unfortunately, the voltage is often not reported with a FE. Hence the overall energy efficiency and, ultimately, η_{SFE} for these constant current-driven HBIs may be abysmally small. The same goes for photo-driven processes, where the energy content of the absorbed photons must be determined together with the quantum yield.

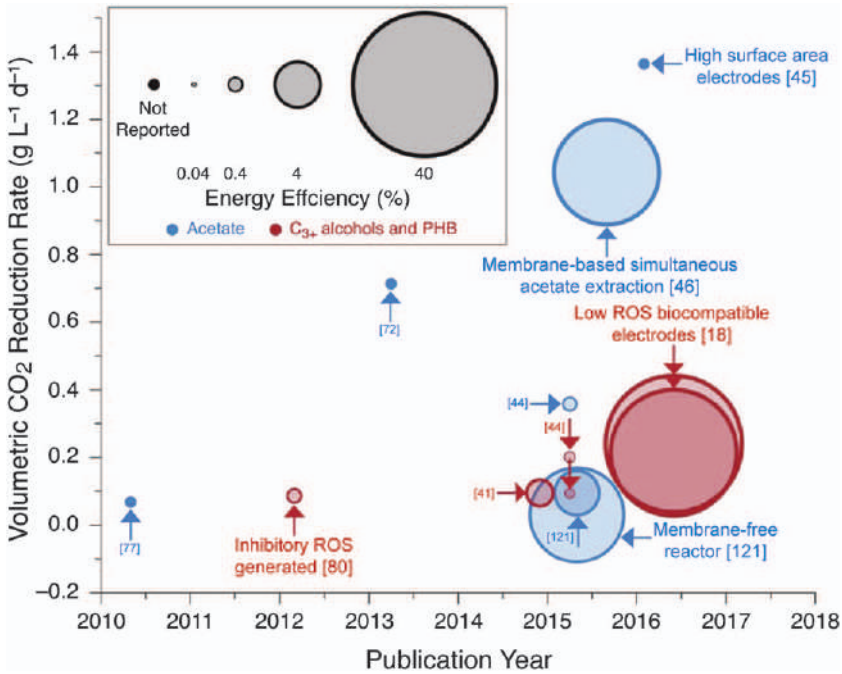

Figure 8.5 Comparison of recent HBI systems.
Adapted from ref. 17 with permission from Elsevier, Copyright 2017.

Though largely ignored as the basic science of HBIs has advanced, the kinetic performance of HBI systems, expressed in volumetric CO_2 reduction or product formation ($g\,L^{-1}$ per day), is an important measure of throughput, or product made per unit of time. The kinetics can be enhanced largely by engineering metabolic pathways within the organism and by engineering reactor design for improved gaseous mass transport. In systems where direct microbe–electrode contact is necessary, increasing the electrode surface area and porosity has been implemented to increase the kinetics of fuel production.[44,45] Additionally, ion-exchange membranes have been used to improve these HBI systems through continuous product extraction.[46] Alternatively, it is possible to improve the solubility and transfer kinetics of electron mediators such as H_2 or to introduce a solubilized small molecule H_2 ($2H^+/2e^-$) source such as formate or methanol.[47] Figure 8.5 plots key developments in the energy efficiencies and kinetic performances of HBI systems over the last decade.

8.4 Classes of Hybrid Biological–Inorganic (HBI) Systems

In order to fix CO_2 and produce carbon fuels, microorganisms require an electron donor that acts as a reducing equivalent. In this section, we define three main classes of HBI systems based on their electron donor as shown in

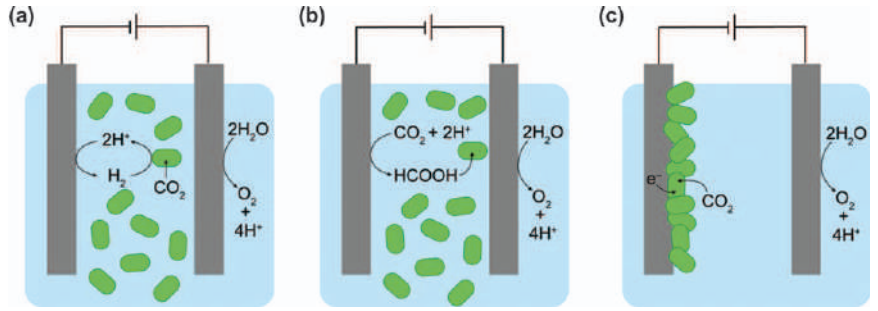

Figure 8.6 The three major categories of hybrid biological–inorganic (HBI) systems as classified by electron source are: (a) direct H_2; (b) indirect H_2 ($2H^+/2e^-$) source *via* a small molecule organic mediator; and (c) electron transfer, either direct or indirect *via* a redox mediator.

Figure 8.6: (1) direct H_2; (2) indirect H_2 ($2H^+/2e^-$) source *via* a small molecule organic mediator; and (3) electron transfer, either direct or indirect *via* a redox mediator.[17,48,49] For these three classifications of HBI systems, the organisms, carbon products, and methodologies and challenges of interfacing biological systems with abiotic materials will now be presented.

8.4.1 Direct H_2 HBI Systems

H_2 is a commonly utilized donor because it is a natural $2H^+/2e^-$ source for carbon fixation cycles. H_2 as an electron-donor or reducing equivalent is used irreversibly and therefore must be consistently produced for growth, which may be solar driven by electrochemical or photochemical methods with low kinetic barriers. The low solubility of H_2 in growth media (the Henry's constant is 7.8×10^{-4} atm^{-1}, as compared to 3.4×10^{-2} atm^{-1} for CO_2)[19,22] is a general challenge for growing H_2-fed autotrophs in HBI systems. Local H_2 concentrations are therefore often a limiting factor in growth and carbon-product formation.

8.4.1.1 Aerobic Microorganisms

Aerobic microbes that use the CB cycle commonly use H_2 as an electron source for reducing equivalents. A crucial component of these systems is the introduction of H_2 into the CO_2 fixation of the organism. H_2 may be relayed to the organism by membrane-bound hydrogenases and/or cytoplasmic hydrogenases. Membrane-bound hydrogenases oxidize H_2 to protons and use the resulting proton gradient for the formation of ATP, which acts as an energy source for the CB cycle and other cellular processes. Cytoplasmic hydrogenases use H_2 to reduce $NAD(P)^+$ to NAD(P)H with the attendant formation of protons.[15,24] NAD(P)H then acts as a hydride ($H^+/2e^-$) source. The availability of H_2 is crucial to cellular growth in aerobic microorganisms

due to the requirement of 7 ATP and 7 NAD(P)H molecules for the fixation of a single CO_2 molecule.

A large proportion of the research on aerobic, H_2-fed autotrophs focuses on engineering the organisms for the selective formation of valuable carbon products and fuels. A commonly-studied organism in this category is *Cupriavidus necator* (also called *Ralstonia eutropha*), a model aerobic lithoautotroph that can be grown to high densities autotrophically,[17,24,50,51] and for which a number of engineering tools have been developed.[52] This organism also directs much of its fixed carbon, using acetyl-CoA as an intermediate, toward the polymer polyhydroxybutyrate (PHB), which can be produced in yields of up to 85% dry-cell weight under nitrogen or phosphorus starvation conditions.[24,53] Disrupting this polymerization pathway to make other products, such as alcohols, from acetyl-CoA has been a key strategy to control carbon fuel production in *C. necator*.[54]

When a PHB-impaired *C. necator* mutant is grown under nitrogen-starvation conditions, the bacteria excretes large amounts of pyruvate into the growth medium,[55] from which carbon fuels may be produced.[54] Along with an increase in pyruvate, there is build-up of NAD(P)H in the cells, indicating that PHB acts as both a carbon and energy storage polymer. Adding an operon with enzymes for branched alcohol synthesis results in the formation of small amounts of isobutanol when fructose is used as a carbon source. With additional genetic modifications and conversion to a semi-continuous culturing setup (to prevent toxicity of *C. necator*), total branched alcohol yields between 200–500 $mg\,L^{-1}$ may be achieved in 1 day, with the majority of the product being isobutanol and the additional formation of some 3-methyl-1-butanol.[56] Though these experiments were performed heterotrophically using fructose as a carbon source, they demonstrate that an autotrophic bacterium can be modified to create valuable carbon fuels.

Subsequent work has shown that isopropanol in the same *C. necator* host may be selectively produced once again with a PHB pathway deletion and the addition of only three enzymatic steps (Figure 8.7a). A number of additional alterations were made to the engineered bacteria to ensure high selectivity of isopropanol over acetone and pyruvic acid, as well as to ensure high growth and production rates. Ultimately, a titre of 3.44 $g\,L^{-1}$ was achieved in 96 h with minimal production of acetone or other side products, as shown in Figure 8.7b. Although higher titres have been achieved in *E. coli* (4.9 $g\,L^{-1}$) and other organisms, the main advantage of the *C. necator* system is that only 0.82 $g\,L^{-1}$ biomass is produced, indicating that a large portion of the metabolism is directed toward product formation rather than growth and maintenance processes [OD_{600} (optical density at 600 nm) = 20 for *E. coli*; $OD_{600} = 2.25$ for *C. necator*]. Although the bacterium was also grown on fructose as a carbon source in this study, this modified strain of *C. necator* has since been used for autotrophic growth (*vide infra*).[57]

C. necator may also be engineered to furnish other valuable carbon products such as long-chain fatty acids, methyl ketones, and terpenes.[54,58,59] The readily-available tools for metabolic engineering of these model

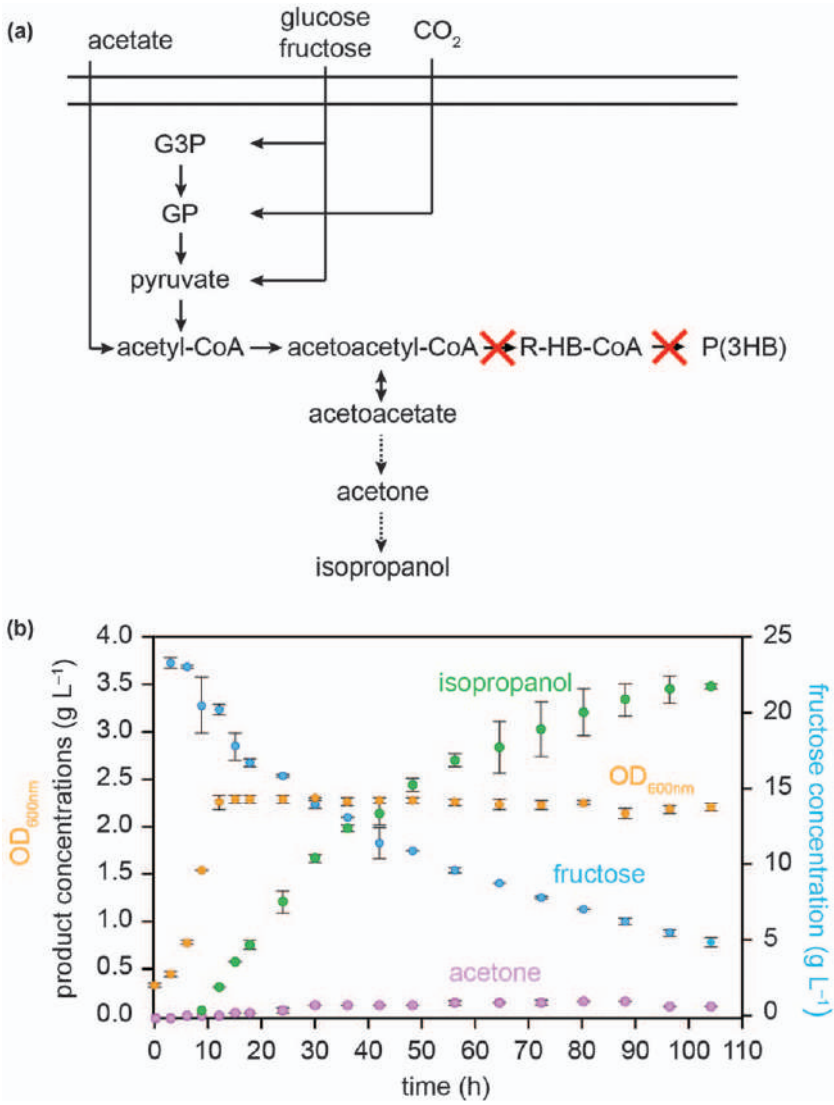

Figure 8.7 (a) Native and engineered pathways in *C. necator*. Red crosses indicate that the PHB synthesis pathway has been disrupted, and dashed arrows indicate enzymes that have been introduced for the production of isopropanol. (b) Isopropanol and acetone formation, fructose consumption, and OD_{600} over time in engineered *C. necator*, demonstrating constant and selective isopropanol formation during growth on fructose.
Adapted from ref. 57 with permission from Springer Nature, Copyright 2014.

autotrophs as well as the ability to redirect the energy and carbon storage pathway on nutrient starvation[60] have enabled the subsequent use of these organisms for CO_2 conversion in HBI systems.

Solar-driven HBI systems may be constructed by integrating H_2-fed aerobic autotrophs with H_2 produced by renewable water electrolysis directly *via* buried junctions[61] or indirectly by photovoltaics.[62] Initial work on *Pseudomonas hydrogenomonas* established that autotrophs could survive in combination with water electrolysis.[63]

C. necator has been adapted for the solar production of isopropanol selectively by interfacing the organism with a cobalt-phosphate (CoP_i) water splitting anode and a NiMoZn cathode, which produced the H_2 to fix CO_2 in the form of biomass (Figure 8.8).[41] The integration of bacteria with electrodes was enabled by the design of catalysts able to operate in pH neutral phosphate buffer,[64] owing to the special ''self-healing'' properties of the catalysts.[65–67] At low potentials between $1.8 - 2.3$ V, very little cell growth was observed (Figure 8.9a), which was shown to be due to the formation of H_2O_2 and other reactive oxygen species (ROS) from O_2 reduction at the cathode. ROS production was evidenced by facile cell growth when a superoxide dismutase was introduced into solution (see Figure 8.9b and c). When the cell potentials were raised to 2.7 or 3 V, cell vitality was maintained; OD_{600} values of 2 and 3 were recorded after 4 days of growth (Figure 8.9a). At these large overpotentials, hydrogen evolution outcompeted the formation of ROS to enable cell growth (Figure 8.9b and c). However, at these high overpotentials, the overall energy efficiency was low ($\eta_{elec} = 1.5\%$ for isopropanol), owing to a high E_{appl} as calculated using eqn (8.2).

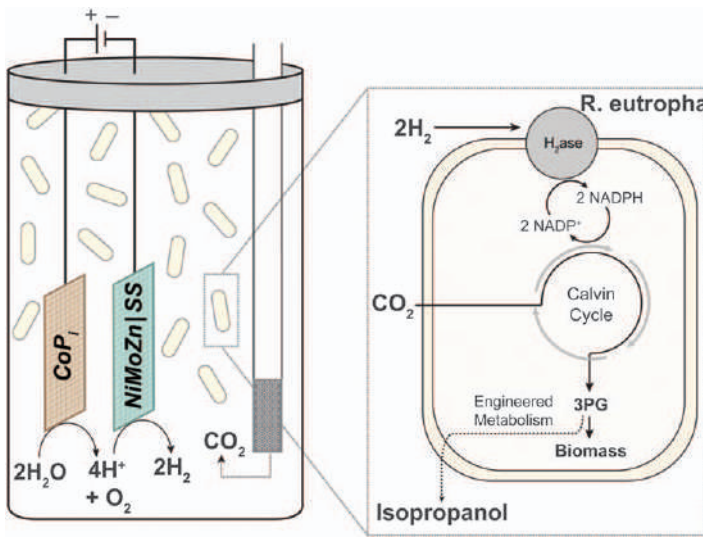

Figure 8.8 Incorporation of *C. necator* (previously *R. eutropha*) modified for isopropanol production into an electrochemical system with CO_2 as a carbon source and H_2 produced from water splitting as an electron source. Adapted from ref. 41 with permission from the National Academy of Sciences, Copyright 2015.

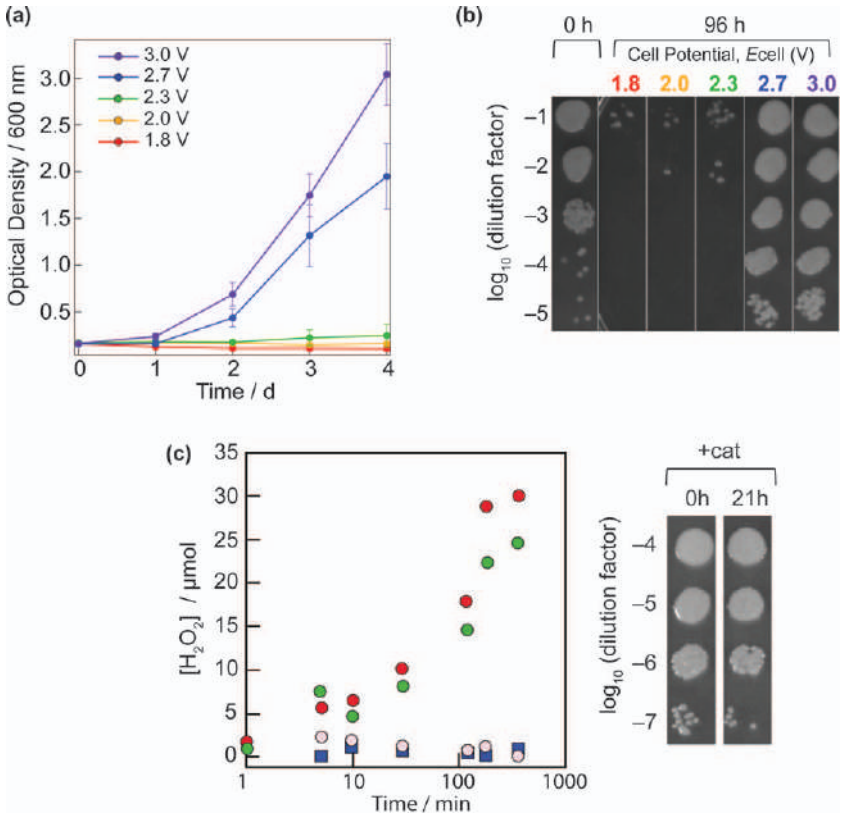

Figure 8.9 (a) OD_{600} of *C. necator* with a H_2O splitting system shown in Figure 8.8 over time at varying potentials, demonstrating the lack of growth in intermediate (ROS-producing) potentials and significant growth at higher (HER) potentials. (b) Cell viability spot assay for *C. necator* at 0 and 96 h of electrolysis at varying cell potentials. (c) H_2O_2 measurements at the anode (blue squares) and cathode (red circles) at 1 mA current ($E_{cell} = 1.8$–2.1 V) over time. Bovine liver catalase (gray circles), an enzyme that can consume H_2O_2, and heat-inactivated bovine liver catalase (green circles) were added to confirm H_2O_2 effect. Accompanying spot assay of *C. necator* in the presence of catalase corresponding to grey circles in (c). Adapted from ref. 41 with permission from the National Academy of Sciences, Copyright 2015.

Accordingly, subsequent work was directed to lowering E_{appl}. A cobalt–phosphorus alloy cathode (Co–P) was developed that did not produce ROS.[18] This cathode was found to be highly active for H_2 production at neutral pH, and enabled considerable H_2 evolution at $E_{appl} = 2.0$ V. As shown in Figure 8.10, high η_{elec} was obtained for biomass growth. As per eqn (8.3), a biomass yield of $\eta_{SFE} = 10.8\%$ was achieved with a typical Si photovoltaic η_{PV} of 20%, a η_{SFE} greatly exceeding those of the best growing crops or grasses (1%) by natural photosynthesis. Furthermore, metabolically-engineered *C. necator* produced longer-chain alcohols at

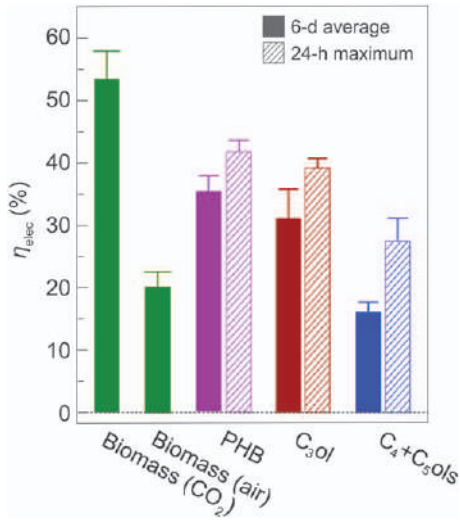

Figure 8.10 Electricity-to-fuel (biomass) efficiencies (η_{elec}) at 2.0 V over 6 days (solid) or at a 24 h maximum (hatched). The biomass efficiency is shown under 1 atm of CO_2 or under air. Error bars denote SEM; $n \geq 3$.
Adapted from ref. 18. with permission from AAAS, Copyright 2016.

$\eta_{SFE} = 5–8\%$, also at efficiencies significantly outperforming the efficiency of natural photosynthesis.[18] We note that as eqn (8.2) is an authentic efficiency due to the limitations arising from H_2, energy associated with maintaining the HBI system, *etc.*, are included in the reported η_{SFE}. Another important outcome of this work was the successful production of *C. necator* biomass from CO_2 derived from air. The $\eta_{elec} = 20\%$ was only 2.7 times lower than η_{elec} for the HBI operating under pure CO_2 (Figure 8.10), despite a CO_2 concentration difference between air and pure CO_2 of 2500, indicating that CO_2 was not limiting.[18] The high product yield obtained for organisms under air demonstrates that the CCMs outlined in Section 8.2.1.2 are active in this system.

The ability of this HBI system, called the Bionic Leaf, to significantly outperform photosynthesis reflects the significant promise of HBIs for CO_2 to fuels conversion. Such high efficiencies are intrinsic to HBIs as they combine the high efficiencies of light harvesting and H_2 formation offered by the inorganic part of the HBI with the advantages of carbon management by the biological part of the system. Furthermore, the HBI approach described in this section has implications beyond fuel, as it offers a general strategy for renewable chemical synthesis.[68]

8.4.1.2 Acetogens and Methanogens

Acetogens and methanogens can also be grown with H_2 as the sole electron donor[15,19,51] to reduce CO_2 to CO and/or formate, followed by further reduction to acetate/acetic acid (acetogens) or methane (methanogens) (see

Figure 8.4). Whereas electron donors containing carbon (*e.g.* formate, methanol) actually result in a higher energy efficiency for growth of these bacteria, due to ease of formation through electrolysis or photolysis, H_2 is often a preferred choice for these HBI systems.[19] Acetogens and methanogens form products of less value than those that can be produced in aerobic systems. Accordingly, effort has been devoted to engineering new pathways into acetogens,[38] but tools for genetically engineering these microorganisms have been less well developed compared to those for aerobic autotrophs. Acetogens often contain restriction systems that hamper the transformations targeted by genetic engineering.[24] An early engineered, non-native pathway (butanol synthesis from CO_2 and H_2) in the acetogen *Clostridium ljungdahlii* involved the introduction of a plasmid with butanol synthesis genes from *Clostridium acetobutylicum*, a similar species with a native butanol synthesis pathway. In this initial attempt, only ~2 mM butanol was detected during growth. The absence of butanol in the stationary phase suggests that the alcohol was subsequently used by the organism as an additional carbon source.[69] Despite low product concentrations, this initial work has been valuable for the development of tools for acetogens. Other tools for engineering acetogens have since been developed[24,60,70] that have led to higher yields of products, such as acetone and butyrate.[70,71]

An alternative approach to engineering the metabolism of acetogens is to maintain high efficiencies of acetate production and to use that acetate to feed heterotrophs and produce more complex products.[48,72,73] A successful example of a mixed bacterial system entailed the growth of *Moorella thermoacetica* on a CO_2/H_2 or CO/CO_2 gas mixture to furnish acetic acid, which was then fed to the yeast *Yarrowia lipolytica* for triacylglyceride production. Yields of acetic acid and lipids in *M. thermoacetica* and *Y. lipolytica*, respectively, were optimized individually, and then the systems were combined. The bioreactors of the two organisms must be separate due to the anaerobic nature of the acetogen. Acetic acid concentrations of ~25 $g\,L^{-1}$ were achieved over 250 h in the anaerobic reactor, and subsequently ~18 $g\,L^{-1}$ of lipid was formed in the second reactor, accounting for ~36% of the produced biomass (Figure 8.11).[74]

A similar dual bacterial approach has recently been pursued to produce food protein by using *C. ljungdahlii* to create acetic acid for *Saccharomyces cerevisiae* growth and protein production. Protein formation rates of 1.56 $g\,L^{-1}$ per day are achieved in the first 12 days of fermentation.[75] These approaches are significantly simpler than engineering new pathways into acetogenic bacteria and result in more complex and valuable products with higher yields.

H_2-fed anaerobic autotrophs have been successfully incorporated into HBI systems as demonstrated by the use of the methanogen *Methanosarcina bakeri* in electrochemical, photoelectrochemical, and photochemical HBI systems.[76] To avoid oxygen contamination of the anaerobic growth medium, cathodic H_2 evolution must be separated from anodic O_2 evolution by an ion-permeable membrane with the cathodic chamber sealed from the

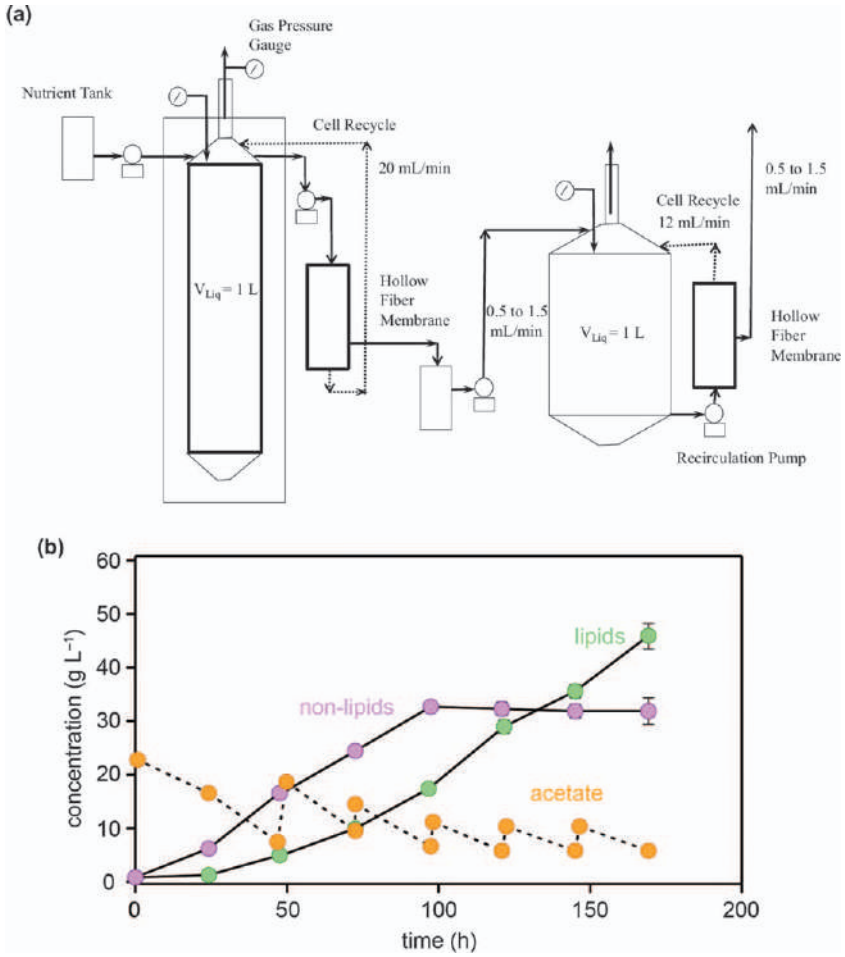

Figure 8.11 Acetic acid consumption (produced from M. thermoacetica) and lipid and non-lipid production by Y. lypolytica in a semi-continuous mode over time. Data indicates standard deviation for triplicate runs. Adapted from ref. 74 with permission from the National Academy of Sciences, Copyright 2016.

atmosphere (Figure 8.12a). In the electrochemical setup, a 2.5 mA current maintained at a Pt cathode for H_2 production furnished 16.8 mL of methane over a 3-day period (Figure 8.12b).[76] An improved result of 17.6 mL methane over 3 days was observed in the photoelectrochemical system, where a 2.5 mA current was applied to a n^+/p-Si/NiMo photocathode, with concurrent 740 nm light illumination (Figure 8.12c and d).[76] Finally, an unassisted, light-driven system was developed using a *p*-InP/Pt cathode for H_2 production and a TiO_2 anode for O_2 evolution. Lower yields of 1.75 mL methane were detected over 3 days, but no electricity input was needed for the system (Figure 8.12e and f).[76]

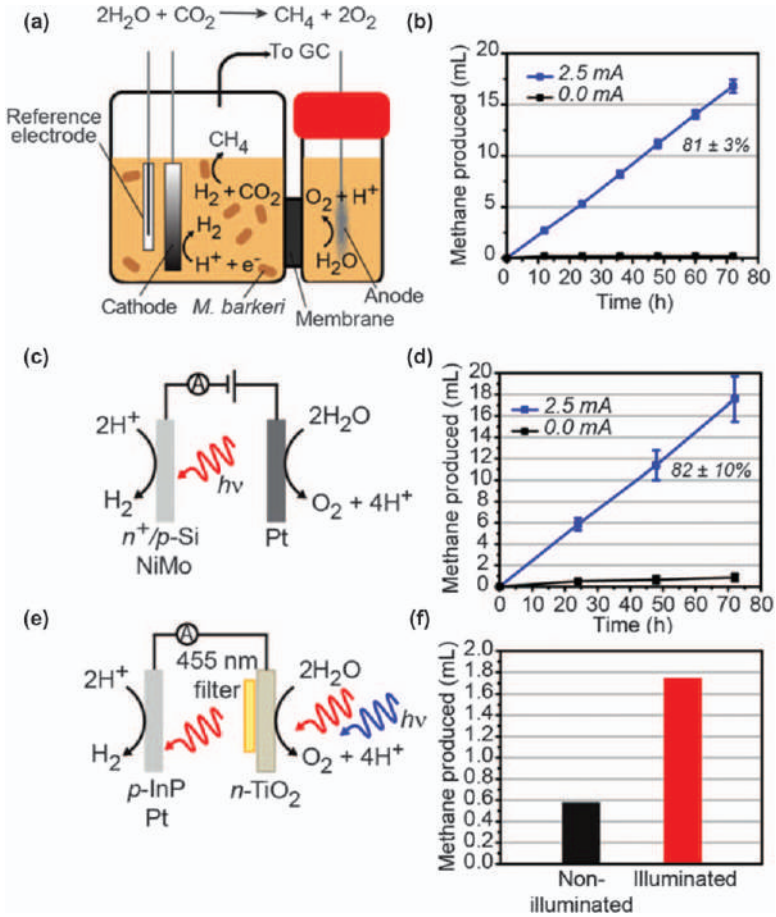

Figure 8.12 (a) Cell setup and (b) methane produced in *M. bakeri* using electrochemically-produced H_2 as an electron source. (c) Cell setup and (d) methane produced with photoelectrochemical H_2 formation. (e) Cell setup and (f) methane produced for a purely photochemical system. Reproduced from ref. 76 with permission from the National Academy of Sciences, Copyright 2015.

Acetogens can also be grown with electrochemically-generated H_2; however, research generally focuses on HBI systems that transfer electrons directly to acetogens in an electrochemical cell rather than utilizing H_2 as an intermediate.[22,77,78] There is debate as to whether direct electron transfer is the dominating mechanism or whether electrochemically-produced H_2 may still be feeding the bacteria in these cases.[79] For example, nanowire arrays are driven at such high voltages to maintain a constant current that, rather than direct electron transfer, the overvoltage for H_2 production may be met and the organism may be using H_2 as its electron source.

8.4.2 Indirect H_2 HBI Systems *via* Organic Mediators

Organic compounds can act as electron donors in two ways: as an energy carrier that is used irreversibly within the cell, as is the case with H_2; or as a reversible mediator carrying electrons and protons from the electrode to the cell. Both options have been explored in HBI systems.

8.4.2.1 Organic Mediators as Carbon and Electron/Proton Sources

One of the first uses of an organic electron donor involved the model aerobic autotroph *C. necator*, with the recognition that introducing a reduced carbon source such as formate[80] held two advantages. First, formate is highly soluble in water and therefore confronts less mass transport limitations than a combination of H_2 and CO_2. Second, formate is a more reduced carbon form than CO_2 and can therefore act as both a carbon and electron source.[80] In this HBI system, CO_2 was reduced to formate at an indium cathode, and the generated formate was converted into CO_2 and NADH intracellularly. The bacteria were engineered to produce both isobutanol and 3-methyl-1-butanol fuels by again disrupting the PHB production pathway to funnel energy and carbon to product formation. Growth of these bacteria with formic acid as a chemical feedstock, as opposed to its electrochemical production, yielded ~846 mg L^{-1} isobutanol and ~570 mg L^{-1} 3-methyl-1-butanol.[80]

Integrating these bacteria in an HBI setup posed challenges. Initially, no bacterial growth could be detected under electrolytic conditions. It was thought that NO and O_2^- were being produced at the anode to result in inhibited growth.[80] We note, however, that subsequent work on *C. necator*, as described above,[18] shows that it is ROS at the cathode that results in inhibited growth of *C. necator*, an insight that was not known at the time of these initial studies. With the supposition of ROS production at the anode, a simple physical barrier was created around the anode as shown in Figure 8.13a to maintain ionic conductivity between the electrodes but increase the diffusion length of the harmful anodic species, with the goal of quenching the ROS before they reached regions of cell growth. With this setup, an OD_{600} ~2.5 was achieved and ~140 mg L^{-1} total branched alcohols (peak η_{elec} ~ 0.4% and ~0.2% for isobutanol and 3-methyl-1-butanol, respectively) were made after 100 h using only formate created *in situ* from CO_2 and electricity (Figure 8.13b).[80]

8.4.2.2 Organic Mediators as an Electron/Proton Source

A reversible organic mediator provides electrons and protons without being consumed, shuttling them between an electrode and the microorganism.[22,81] The neutral red dye is one proposed example of such a system.[82,84] Studies on *E. coli* have indicated that neutral red donates both electrons and protons in a reversible fashion to a mediator in the inner bacterial

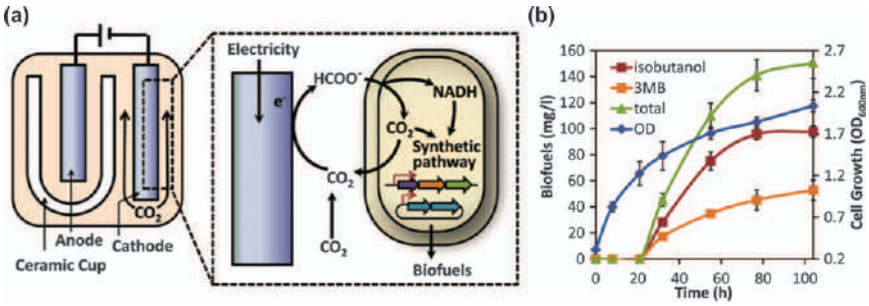

Figure 8.13 (a) Cell setup for CO_2 reduction to formate and subsequent use of that formate as a carbon and electron source for *C. necator* fuel production. A ceramic cup separates reactive species formed at the anode from cell growth. (b) Isobutanol, 3-methyl-1-butanol, and OD_{600} of *C. necator* over time.
Reproduced from ref. 80 with permission from AAAS, Copyright 2012.

membrane and then the dye is re-protonated in solution and re-reduced at an electrode to continue the cycle.[84] There has been mechanistic debate as to whether neutral red acts as a proton and electron donor or simply as an electron donor. Initial studies using neutral red with *Actinobacillus succinogenes* for the conversion of (i) CO_2 into methane and (ii) fumarate into succinate postulated that the dye solely acts as an electron channel in the bacterial membrane that directly reduces NAD^+ to NADH within the cell, as well as establishes a proton gradient for ATP formation.[82,83] An advantage of using neutral red as a soluble mediator is that bacteria grown with the dye yielded product more quickly than those grown using H_2 as the electron donor, possibly due to the higher solubility and concentration of the dye.[82,83]

8.4.3 Electron Transfer HBI Systems

In addition to oxidizing H_2 and $2H^+/2e^-$ equivalents, autotrophs may also obtain reducing equivalents through proton-decoupled extracellular electron transfer (EET). Autotrophic growth by EET can occur indirectly through electron-redox mediators such as iron or directly through conductive electrode contact. These two routes, outlined in Figure 8.14, allow for novel interfacing in HBI systems, but are currently limited by mediator solubility and electrode surface area.

8.4.3.1 Indirect EET with Iron Mediators

Many lithoautotrophic bacteria populating geological transition zones, where the earth's deoxygenated crust contacts oxygenated water, evolved the ability to oxidize Fe^{2+} to Fe^{3+}.[85,86] Ferrous iron and other inorganic reducing equivalents, including H_2 and sulfides, are created abiotically at geological boundaries such as the rhizosphere and hydrothermal vents. Under acidic conditions, Fe^{2+} becomes much more soluble and less prone to abiotic

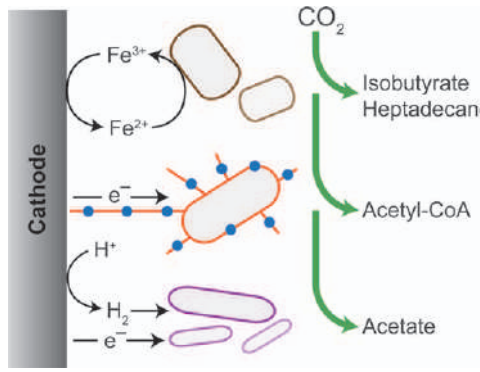

Figure 8.14 Autotrophic growth by extracellular electron transfer by either direct or indirect electron transfer. In HBI systems, possible mechanisms include EET by Fe^{2+} oxidation, direct conduction by bacterial pili, and a potential combination of H_2 evolution and direct electron uptake.

oxidation than under neutral conditions.[87,88] As such, many iron-oxidizing bacteria (FeOB) including model organism *Acidithiobacillus ferrooxidans* are acidophilic.[89–91] In addition to obtaining energy through the oxidation of Fe^{2+}, *A. ferrooxidans* utilizes the electrons to reduce $NAD(P)^+$ and O_2 to form NAD(P)H and H_2O, respectively. NAD(P)H is then used in the CB cycle to fix CO_2, while consumption of protons creates a proton gradient with the acidic environment that drives ATP synthesis.

A. ferrooxidans has been cultured under acidic, aerobic conditions by electrically regenerating Fe^{2+} from Fe^{3+}.[90,92] Engineering this bacteria allowed the organism to synthesize isobutyric acid and heptadecane from electricity and CO_2 with an η_{elec} of 0.93% and 1.6%, respectively.[93] Microbial growth by electrochemical Fe^{3+}/Fe^{2+} regeneration requires a high reduction potential at low pH ($E^\circ = 700$ mV),[87] however, which limits the efficiency at which fuels can be generated. Additionally, these systems operated at a low current density ~10 mA cm^{-2}.[90,92] It was also demonstrated, however, that *A. ferrooxidans* grows directly on cathodes in the absence of an $Fe^{3+/2+}$ mediator,[94] suggesting that its outer membrane cytochromes may be able to obtain reducing equivalents directly from electrodes, or by an as-of-yet unknown mediator.

Though not traditionally considered FeOB, several aerobic and anaerobic bacteria exhibit the ability to obtain reducing equivalents solely by oxidizing solid Fe^0 substrates.[95] The application of these bacteria in HBI systems is discussed in the following section.

8.4.3.2 Direct EET

Several microbial CO_2 reduction schemes have been demonstrated and proposed to operate by direct EET from an electrode to bacteria.[96,97] Termed 'exoelectrogens', these bacteria use protein scaffolds to form a conducting contact between electrodes and cellular electron transport chains. The

genera *Shewanella* and *Geobacter* are two such exoelectrogens, initially coming into prominence as organisms for microbial fuel cell applications. In contrast to the various CO_2 reductive schemes outlined above, microbial fuel cells utilize microbes oxidatively to convert chemical energy in organic waste to electrical current. As such, investigations initially focused on understanding how *Shewanella* and *Geobacter* species were able to donate electrons directly to anodes.[98,99] These exoelectrogens were later shown to grow in the reverse scheme, receiving electrons only from an electrode.[100,101] In combination with techniques of synthetic biology, these bacteria have been genetically engineered to produce organic fuels using reducing equivalents obtained directly from cathode surfaces.[102]

One of the most thoroughly characterized and well understood EET pathways is the Mtr pathway in *Shewanella oneidensis* MR-1.[103–105] The Mtr pathway uses several multi-heme *c*-type cytochromes (*c*-Cyts), structural proteins, and flavin cofactors to link the intracellular quinone-based electron transport chain to the bacterial surface, which can then be linked to other surfaces such as other bacteria or electrodes.[106–108] Studies of the Mtr pathway have demonstrated that EET by *S. oneidensis* is kinetically controlled by outer membrane *c*-Cyts,[109] while secreted flavins can supplement total EET to these proteins.[110]

The Pcc pathway, an equivalent to the Mtr pathway, is responsible for EET in *Geobacter sulfurreducens* and is also composed of several multi-heme *c*-Cyts.[111–113] EET by the Pcc pathway is heavily reliant on OmcZ, an extracellular octaheme *c*-Cyts that can transfer electrons to and from Cr, Mn, Fe, Au, and U.[114] When *G. sulfurreducens* is grown electrochemically, OmcZ localizes heavily at the electrode surface in a biofilm matrix and is able to store charge for as long as 12 hours.[111,114]

Both *Geobacter* and *Shewanella* bacteria have been observed to extrude pili, which can form contacts with electrodes and other cells. A single pilus of *S. oneidensis* can conduct on the order of 1 nA at 100 mV and exhibit resistivity of $\sim 1\ \Omega\,\mathrm{cm}$.[115] Genetic and microscopic studies revealed that these pili are formed from joined outer membrane vesicles containing *c*-Cyts MtrA and MtrC, which are suspected to conduct electrons through a combination of flavin mediators and direct hopping.[116] Pili conductivity in *G. sulfurreducens* is seemingly dependent on the organism's capacitive biofilm, possibly extending from cells to access the charge stored in distal matrix-bound OmcZ.[117,118]

Exoelectrogenic bacteria were first demonstrated to uptake electrons from cathodes to enable the two-electron reduction of fumarate to succinate by both wildtype *G. sulfurreducens* and by a mutant lacking the gene encoding its essential uptake hydrogenase.[101] Later, it was shown that *S. oneidensis* could similarly reduce fumarate to succinate, with the study also proving that such electroreduction is highly dependent on the previously described Mtr pathway.[100] With an increase in genetic tractability, these organisms have now also been used for biofuel synthesis from CO_2. *G. sulfurreducens* expressing ATP-dependent citrate lyase for CO_2 fixation *via* the reverse

tricarboxylic acid cycle grew autotrophically on a graphite cathode with fumarate as the terminal electron acceptor.[102] Though autotrophic growth by modified *G. sulfurreducens* was not quantified, reduction of fumarate to succinate occurred with 100% FE at −500 mV, resulting in a η_{elec} of 4.3%. Additional modifications to *G. sulfurreducens* that deleted the hydrogenase and formate dehydrogenase genes still maintained the ability to grow on solid Fe^0 as the sole electron source.[119] These cases definitively demonstrate the unique ability of these organisms to catalyze carbon reduction through direct bacteria–cathode contact, but applications of these systems have been limited by low current density, achieving a maximum of 80 $\mu A\,cm^{-2}$ for pure autotrophic growth.[102] Additionally, the lack of natural carbon fixation pathways means that the production of biofuels requires significant metabolic engineering.

8.4.3.3 Combined Direct and Indirect EET

Acetogenic bacteria possess two advantages over the *Shewanella* and *Geobacter*: carbon fixation is endogenous to acetogens; and acetate is a feedstock for heterotrophic biofuel producers.[120] *Sporomusa ovata*, a model organism for acetogen studies, has been shown to grow and produce acetate anaerobically using electrons from a cathode as the sole reducing source and CO_2 as the sole carbon source.[44,77] In both of these studies, the biocatalyzed reduction of CO_2 to acetate was coupled to anodic water splitting, mimicking natural photosynthesis. Nanostructured electrodes were implemented both to increase surface area and to facilitate anaerobic metabolism in aerobic media by excluding oxygen diffusion between the nanostructures. An ~85% FE for acetate production was achieved with a peak current of 0.35 $mA\,cm^{-2}$ at 1.08 V. The resulting production of 600 mg acetate L^{-1} d^{-1} equated to an $\eta_{SFE} = 0.38\%$, which is within an order of magnitude of plant growth. Downstream of *S. ovata*, engineered *E. coli* converted the produced acetate to acetyl-coA for the biosynthesis of butanol, PHB, and isoprenoids. Notwithstanding, nanostructured-HBI constructs will confront significant limitations to throughput due to surface area constraints and device fabrication.

Reactors have also been designed to generate H_2 as an electron mediator for *S. ovata*,[121] with cathodic H_2 evolution producing >18 g acetate L^{-1} per day at $\eta_{elec} = 12\%$ ($\eta_{SFE} = 2.4\%$ assuming $\eta_{PV} = 20\%$).[122] The lack of observed H_2, low driving potentials, and varying Tafel slopes,[44,77,121] however, suggest that acetate electrosynthesis may proceed through direct electron transfer.[44,77] Growth of acetogens on Fe^0 without applied current has been similarly cited as evidence for direct EET pathways.[95,123,124] These claims were later questioned once it was demonstrated that surface-adsorbed hydrogenases catalyzed H_2 evolution to serve as electron mediators during the biocorrosion of Fe^0.[124,125] Though *S. ovata* is incapable of Fe^0 oxidation, similar processes may be important to its electrochemical growth, as its cell-free spent media also catalyzes H_2 generation at cathodes, possibly through surface adsorption of

Ni-containing hydrogenases.[126] These studies show that H_2 is important for electrochemical growth of acetogens, but that direct EET cannot be ruled out as a supplementary mechanism. *S. ovata* may indeed obtain reducing equivalents through a combination of indirect mediators and direct electron transfer as with *Shewanella* and *Geobacter*. Nevertheless, mediation by H_2 will be an important consideration in the scale-up and optimization of acetogenic bioreactors.[127]

8.5 Conclusions

Hybrid biological–inorganic systems provide an avenue for capitalizing on the high efficiency of inorganic systems to provide solar-derived reducing equivalents as well as the advantages of biological systems for CO_2 conversion to complex carbon products with high selectivity. Three different HBI systems may be categorized by the electron/reducing source: direct H_2; indirect H_2 ($2H^+/2e^-$) *via* molecular mediators; and electron-transfer (direct and indirect). Aerobic microorganisms can be used to produce a wide range of carbon fuels with comparatively lower energy efficiencies, whereas anaerobic microorganisms operate at higher energy efficiencies with a more limited product scope. All of these HBI systems, whether they be aerobic or anaerobic, have been developed by genetically modifying the microorganisms to selectively produce desired carbon fuels, identifying methods of incorporating the microorganisms with synthetic inorganic systems, and overcoming limitations of combining the two. Importantly, the energy efficiency of these systems may be placed on equal footing with proper analysis that accounts for the energy of reducing equivalents in conjunction with electron-to-product yields. Research in the development of HBIs for CO_2 to fuels production at energy efficiencies that exceed photosynthesis encourage further studies to be undertaken to diversify the organismic scope of the approach as well as to increase fuel yields/titres and diversity.

Abbreviations

CB	Calvin–Benson
WL	Wood–Ljungdahl
HER	Hydrogen evolution reaction
HBI	Hybrid biological–inorganic
RuBisCO	Ribulose-1,5-bisphosphate carboxylase/oxygenase
CCM	Carbon-concentrating mechanism
CA	Carbonic anhydrase
DCW	Dry cell weight
η_{elec}	Electrical efficiency
η_{PV}	Photovoltaic efficiency
η_{SFE}	Solar-to-fuels (/biomass) efficiency
$\Delta_r G^\circ$	Gibb's free energy change standard conditions
PHB	Polyhydroxybutyrate

CODH	Carbon monoxide dehydrogenase
OD_{600}	Optical density at 600 nm
CoP_i	Cobalt phosphate
Co–P	Cobalt–phosphorus alloy
ROS	Reactive oxygen species
E_{appl}	Applied electrical potential
FeOB	Iron oxidizing bacteria

Acknowledgements

This material is based upon work supported by the Air Force Office of Scientific Research, Award number: FA9550-19-1-0246.

References

1. N. S. Lewis and D. G. Nocera, *Proc. Natl. Acad. Sci. U. S. A.*, 2006, **103**, 15729–15735.
2. T. R. Cook, D. K. Dogutan, S. Y. Reece, Y. Surendranath, T. S. Teets and D. G. Nocera, *Chem. Rev.*, 2010, **110**, 6474–6502.
3. D. K. Dogutan and D. G. Nocera, *Acc. Chem. Res.*, 2019, **52**, 3143–3148.
4. N. Nelson and C. F. Yocum, *Annu. Rev. Plant Biol.*, 2006, **57**, 521–565.
5. M. D. Hatch and C. R. Slack, *Annu. Rev. Plant Physiol.*, 1970, **21**, 141–162.
6. J. Qiao, Y. Liu, F. Hong and J. Zhang, *Chem. Soc. Rev.*, 2014, **43**, 631–675.
7. C. H. Lee and M. W. Kanan, *ACS Catal.*, 2015, **5**, 465–469.
8. A. Wuttig, C. Liu, Q. Peng, M. Yaguchi, C. H. Hendon, K. Motobayashi, S. Ye, M. Osawa and Y. Surendranath, *ACS Cent. Sci.*, 2016, **2**, 522–528.
9. B. A. Zhang, C. Costentin and D. G. Nocera, *Joule*, 2019, **3**, 1565–1568.
10. R. E. Blankenship, D. M. Tiede, J. Barber, G. W. Brudvig, G. Fleming, M. Ghirardi, M. R. Gunner, W. Junge, D. M. Kramer, A. Melis, T. A. Moore, C. C. Moser, D. G. Nocera, A. J. Nozik, D. R. Ort, W. W. Parson, R. C. Prince and R. T. Sayre, *Science*, 2011, **332**, 805–809.
11. O. Adesina, I. A. Anzai, J. L. Avalos and B. Barstow, *Chem*, 2017, **2**, 20–51.
12. F. Salimijazi, E. Parra and B. Barstow, *J. Biol. Eng.*, 2019, **13**, 38.
13. X.-G. Zhu, S. P. Long and D. R. Ort, *Annu. Rev. Plant Biol.*, 2010, **61**, 235–261.
14. R. H. Wijffels and M. J. Barbosa, *Science*, 2010, **329**, 796–799.
15. N. J. Claassens, D. Z. Sousa, V. A. P. M. dos Santos, W. M. de Vos and J. van der Oost, *Nat. Rev. Microbiol.*, 2016, **14**, 692–706.
16. P. K. Nayak, S. Mahesh, H. J. Snaith and D. Cahen, *Nat. Rev. Mater.*, 2019, **4**, 269–285.
17. S. N. Nangle, K. K. Sakimoto, P. A. Silver and D. G. Nocera, *Curr. Opin. Biotech.*, 2017, **41**, 107–113.
18. C. Liu, B. C. Colón, M. Ziesack, P. A. Silver and D. G. Nocera, *Science*, 2016, **352**, 1210–1213.

19. N. J. Claassens, C. A. R. Cotton, D. Kopljar and A. Bar-Even, *Nat. Catal.*, 2019, **2**, 437–447.
20. J. C. Liao, L. Mi, S. Pontrelli and S. Luo, *Nat. Rev. Microbiol.*, 2016, **14**, 288–304.
21. I. A. Berg, *Appl. Environ. Microbiol.*, 2011, **77**, 1925–1936.
22. K. Rabaey and R. A. Rozendal, *Nat. Rev. Microbiol.*, 2010, **8**, 706–716.
23. R. Takors, M. Kopf, J. Mampel, W. Bluemke, B. Blombach, B. Eikmanns, F. R. Bengelsdorf, D. Weuster-Botz and P. Dürre, *Microb. Biotechnol.*, 2018, **11**, 606–625.
24. S. E. Nybo, N. E. Khan, B. M. Woolston and W. R. Curtis, *Metab. Eng.*, 2015, **30**, 105–120.
25. H. Yu, X. Li, F. Duchoud, D. S. Chuang and J. C. Liao, *Nat. Commun.*, 2018, **9**, 2008.
26. S. Satagopan and F. R. Tabita, *FEBS J.*, 2016, **283**, 2869–2880.
27. Y.-C. C. Tsai, M. C. Lapina, S. Bhushan and O. Mueller-Cajar, *Nat. Commun.*, 2015, **6**, 8883.
28. A. Bar-Even, E. Noor, N. E. Lewis and R. Milo, *Proc. Natl. Acad. Sci. U. S. A.*, 2010, **107**, 8889–8894.
29. R. Kebeish, M. Niessen, K. Thiruveedhi, R. Bari, H.-J. Hirsch, R. Rosenkranz, N. Stäbler, B. Schönfeld, F. Kreuzaler and C. Peterhänsel, *Nat. Biotechnol.*, 2007, **25**, 593–599.
30. P. M. Shih, J. Zarzycki, K. K. Niyogi and C. A. Kerfeld, *J. Biol. Chem.*, 2014, **289**, 9493–9500.
31. B. D. Rae, B. M. Long, M. R. Badger and G. D. Price, *Microbiol. Mol. Biol. Rev.*, 2013, **77**, 357–379.
32. W. Bonacci, P. K. Teng, B. Afonso, H. Niederholtmeyer, P. Grob, P. A. Silver and D. F. Savage, *Proc. Natl. Acad. Sci. U. S. A.*, 2012, **109**, 478–483.
33. N. A. Kamennaya, S. Ahn, H. Park, R. Bartal, K. A. Sasaki, H.-Y. Holman and C. Jansson, *Metab. Eng.*, 2015, **29**, 76–85.
34. C. S. Gai, J. Lu, C. J. Brigham, A. C. Bernardi and A. J. Sinskey, *AMB Express*, 2014, **4**, 2.
35. B. Kusian, D. Sultemeyer and B. Bowien, *J. Bacteriol.*, 2002, **184**, 5018–5026.
36. K. Schuchmann and V. Müller, *Nat. Rev. Microbiol.*, 2014, **12**, 809–821.
37. S. W. Ragsdale and E. Pierce, *Biochim. Biophys. Acta*, 2008, **1784**, 1873–1898.
38. B. Schiel-Bengelsdorf and P. Dürre, *FEBS Lett.*, 2012, **586**, 2191–2198.
39. H. N. Abubackar, M. C. Veiga and C. Kennes, *Biofuel. Bioprod. Bioref.*, 2011, **5**, 93–114.
40. L. Garcia-Gonzalez, M. S. I. Mozumder, M. Dubreuil, E. I. P. Volcke and H. De Wever, *Catal. Today*, 2015, **257**, 237–245.
41. J. P. Torella, C. J. Gagliardi, J. S. Chen, D. K. Bediako, B. Colón, J. C. Way, P. A. Silver and D. G. Nocera, *Proc. Natl. Acad. Sci. U. S. A.*, 2015, **112**, 2337–2342.
42. H. R. Beller, T. S. Lee and L. Katz, *Nat. Prod. Rep.*, 2015, **32**, 1508–1526.

43. S. Cestellos-Blanco, H. Zhang, J. M. Kim, Y.-X. Shen and P. Yang, *Nat. Catal.*, 2020, **3**, 245–255.
44. C. Liu, J. J. Gallagher, K. K. Sakimoto, E. M. Nichols, C. J. Chang, M. C. Y. Chang and P. Yang, *Nano Lett.*, 2015, **15**, 3634–3639.
45. L. Jourdin, S. Freguia, V. Flexer and J. Keller, *Environ. Sci. Technol.*, 2016, **50**, 1982–1989.
46. S. Gildemyn, K. Verbeeck, R. Slabbinck, S. J. Andersen, A. Prévoteau and K. Rabaey, *Environ. Sci. Tech. Lett.*, 2015, **2**, 325–328.
47. R. M. Rodrigues, X. Guan, J. A. Iñiguez, D. A. Estabrook, J. O. Chapman, S. Huang, E. M. Sletten and C. Liu, *Nat. Catal.*, 2019, **2**, 407–414.
48. K. K. Sakimoto, N. Kornienko and P. Yang, *Acc. Chem. Res.*, 2017, **50**, 476–481.
49. R. J. Conrado, C. A. Haynes, B. E. Haendler and E. J. Toone, in *Advanced Biofuels and Bioproducts*, ed. J. W. Lee, Springer New York, New York, NY, 2013, pp. 1037–1064.
50. A. S. Hawkins, P. M. McTernan, H. Lian, R. M. Kelly and M. W. W. Adams, *Curr. Opin. Biotech.*, 2013, **24**, 376–384.
51. P. Dürre and B. J. Eikmanns, *Curr. Opin. Biotech.*, 2015, **35**, 63–72.
52. C. Bi, P. Su, J. Müller, Y.-C. Yeh, S. R. Chhabra, H. R. Beller, S. W. Singer and N. J. Hillson, *Microb. Cell Fact.*, 2013, **12**, 107.
53. M. Beeby, M. Cho, J. Stubbe and G. J. Jensen, *J. Bacteriol.*, 2012, **194**, 1092–1099.
54. J. Muller, D. MacEachran, H. Burd, N. Sathitsuksanoh, C. Bi, Y. C. Yeh, T. S. Lee, N. J. Hillson, S. R. Chhabra, S. W. Singer and H. R. Beller, *Appl. Environ. Microbiol.*, 2013, **79**, 4433–4439.
55. A. Steinbchel and H. G. Schlegel, *Appl. Environ. Microbiol.*, 1989, **31**, 168–175.
56. J. Lu, C. J. Brigham, C. S. Gai and A. J. Sinskey, *Appl. Microbiol. Biotechnol.*, 2012, **96**, 283–297.
57. E. Grousseau, J. Lu, N. Gorret, S. E. Guillouet and A. J. Sinskey, *Appl. Microbiol. Biotechnol.*, 2014, **98**, 4277–4290.
58. J. S. Chen, B. Colón, B. Dusel, M. Ziesack, J. C. Way and J. P. Torella, *PeerJ*, 2015, **3**, e1468.
59. T. Krieg, A. Sydow, S. Faust, I. Huth and D. Holtmann, *Angew. Chem., Int. Ed.*, 2018, **57**, 1879–1882.
60. C. Leang, T. Ueki, K. P. Nevin and D. R. Lovley, *Appl. Environ. Microbiol.*, 2013, **79**, 1102–1109.
61. S. Y. Reece, J. A. Hamel, K. Sung, T. D. Jarvi, A. J. Esswein, J. J. H. Pijpers and D. G. Nocera, *Science*, 2011, **334**, 645–648.
62. C. Liu, B. E. Colón, P. A. Silver and D. G. Nocera, *J. Photochem. Photobiol., A*, 2018, **358**, 411–415.
63. H. G. Schlegel and R. Lafferty, *Nature*, 1965, **205**, 308–309.
64. M. W. Kanan and D. G. Nocera, *Science*, 2008, **321**, 1072–1075.
65. D. A. Lutterman, Y. Surendranath and D. G. Nocera, *J. Am. Chem. Soc.*, 2009, **131**, 3838–3839.

66. D. K. Bediako, A. M. Ullman and D. G. Nocera, *Top. Curr. Chem.*, 2016, **371**, 173–213.
67. C. Costentin and D. G. Nocera, *Proc. Natl. Acad. Sci. U. S. A.*, 2017, **114**, 13380–13384.
68. D. G. Nocera, *Acc. Chem. Res.*, 2017, **50**, 616–619.
69. M. Kopke, C. Held, S. Hujer, H. Liesegang, A. Wiezer, A. Wollherr, A. Ehrenreich, W. Liebl, G. Gottschalk and P. Durre, *Proc. Natl. Acad. Sci. U. S. A.*, 2010, **107**, 13087–13092.
70. A. Banerjee, C. Leang, T. Ueki, K. P. Nevin and D. R. Lovley, *Appl. Environ. Microbiol.*, 2014, **80**, 2410–2416.
71. T. Ueki, K. P. Nevin, T. L. Woodard and D. R. Lovley, *mBio*, 2014, **5**, e01636–01614.
72. C. W. Marshall, D. E. Ross, E. B. Fichot, R. S. Norman and H. D. May, *Environ. Sci. Technol.*, 2013, **47**, 6023–6029.
73. E. V. LaBelle, C. W. Marshall and H. D. May, *Acc. Chem. Res.*, 2020, **53**, 62–71.
74. P. Hu, S. Chakraborty, A. Kumar, B. Woolston, H. Liu, D. Emerson and G. Stephanopoulos, *Proc. Natl. Acad. Sci. U. S. A.*, 2016, **113**, 3773–3778.
75. B. Molitor, A. Mishra and L. T. Angenent, *Energ. Environ. Sci.*, 2019, **12**, 3515–3521.
76. E. M. Nichols, J. J. Gallagher, C. Liu, Y. Su, J. Resasco, Y. Yu, Y. Sun, P. Yang, M. C. Y. Chang and C. J. Chang, *Proc. Natl. Acad. Sci. U. S. A.*, 2015, **112**, 11461–11466.
77. K. P. Nevin, T. L. Woodard, A. E. Franks, Z. M. Summers and D. R. Lovley, *mBio*, 2010, **1**, e00103–00110.
78. D. R. Lovley and K. P. Nevin, *Curr. Opin. Biotech.*, 2013, **24**, 385–390.
79. J. Philips, *Front. Microbiol.*, 2020, **10**, 2997.
80. H. Li, P. H. Opgenorth, D. G. Wernick, S. Rogers, T. Y. Wu, W. Higashide, P. Malati, Y. X. Huo, K. M. Cho and J. C. Liao, *Science*, 2012, **335**, 1596.
81. H. Chen, F. Dong and S. D. Minteer, *Nat. Catal.*, 2020, **3**, 225–244.
82. D. H. Park, M. Laivenieks, M. V. Guettler, M. K. Jain and J. G. Zeikus, *Appl. Environ. Microbiol.*, 1999, **65**, 2912–2917.
83. D. H. Park and J. G. Zeikus, *J. Bacteriol.*, 1999, **181**, 2403–2410.
84. T. D. Harrington, V. N. Tran, A. Mohamed, R. Renslow, S. Biria, L. Orfe, D. R. Call and H. Beyenal, *Bioresour. Technol.*, 2015, **192**, 689–695.
85. F. Widdel, S. Schnell, S. Heising, A. Ehrenreich, B. Assmus and B. Schink, *Nature*, 1993, **362**, 834–836.
86. D. Emerson, E. J. Fleming and J. M. McBeth, *Annu. Rev. Microbiol.*, 2010, **64**, 561–583.
87. D. B. Johnson, T. Kanao and S. Hedrich, *Front. Microbiol.*, 2012, **3**, 96.
88. M. Ilbert and V. Bonnefoy, *Biochim. Biophys. Acta*, 2013, **1827**, 161–175.
89. W. J. Ingledew, *Biochim. Biophys. Acta*, 1982, **683**, 89–117.

90. N. Matsumoto, H. Yoshinaga, N. Ohmura, A. Ando and H. Saiki, in *Process Metallurgy*, ed. R. Amils and A. Ballester, Elsevier, **vol. 9**, 1999, pp. 757–766.
91. Y. Zhang, S. Zhang, D. Zhao, Y. Ni, W. Wang and L. Yan, *Microorganisms*, 2019, **8**, 2.
92. S. Nakasono, N. Matsumoto and H. Saiki, *Bioelectrochem. Bioenerg.*, 1997, **43**, 61–66.
93. T. Kernan, S. Majumdar, X. Li, J. Guan, A. C. West and S. Banta, *Biotechnol. Bioeng.*, 2016, **113**, 189–197.
94. T. Ishii, S. Kawaichi, H. Nakagawa, K. Hashimoto and R. Nakamura, *Front. Microbiol.*, 2015, **6**, 994.
95. S. Kato, *Microb. Biotechnol.*, 2016, **9**, 141–148.
96. F. Kracke, I. Vassilev and J. O. Krömer, *Front. Microbiol.*, 2015, **6**, 575.
97. O. Choi and B.-I. Sang, *Biotechnol. Biofuels*, 2016, **9**, 11.
98. H. J. Kim, H. S. Park, M. S. Hyun, I. S. Chang, M. Kim and B. H. Kim, *Enzyme Microb. Technol.*, 2002, **30**, 145–152.
99. D. R. Bond and D. R. Lovley, *Appl. Environ. Microbiol.*, 2003, **69**, 1548–1555.
100. D. E. Ross, J. M. Flynn, D. B. Baron, J. A. Gralnick and D. R. Bond, *PLoS One*, 2011, **6**, e16649.
101. K. B. Gregory, D. R. Bond and D. R. Lovley, *Environ. Microbiol.*, 2004, **6**, 596–604.
102. T. Ueki, K. P. Nevin, T. L. Woodard, M. A. Aklujkar, D. E. Holmes and D. R. Lovley, *Front. Microbiol.*, 2018, **9**, 1512.
103. O. Bretschger, A. Obraztsova, C. A. Sturm, I. S. Chang, Y. A. Gorby, S. B. Reed, D. E. Culley, C. L. Reardon, S. Barua, M. F. Romine, J. Zhou, A. S. Beliaev, R. Bouhenni, D. Saffarini, F. Mansfeld, B.-H. Kim, J. K. Fredrickson and K. H. Nealson, *Appl. Environ. Microbiol.*, 2007, **73**, 7003–7012.
104. L. A. Meitl, C. M. Eggleston, P. J. S. Colberg, N. Khare, C. L. Reardon and L. Shi, *Geochim. Cosmochim. Acta*, 2009, **73**, 5292–5307.
105. D. Coursolle, D. B. Baron, D. R. Bond and J. A. Gralnick, *J. Bacteriol.*, 2010, **192**, 467–474.
106. E. Marsili, D. B. Baron, I. D. Shikhare, D. Coursolle, J. A. Gralnick and D. R. Bond, *Proc. Natl. Acad. Sci. U. S. A.*, 2008, **105**, 3968–3973.
107. A. R. Rowe, P. Rajeev, A. Jain, S. Pirbadian, A. Okamoto, J. A. Gralnick, M. Y. El-Naggar and K. H. Nealson, *mBio*, 2018, **9**, e02203–02217.
108. S. Xu, A. Barrozo, L. M. Tender, A. I. Krylov and M. Y. El-Naggar, *J. Am. Chem. Soc.*, 2018, **140**, 10085–10089.
109. A. Okamoto, K. Hashimoto, K. H. Nealson and R. Nakamura, *Proc. Natl. Acad. Sci. U. S. A.*, 2013, **110**, 7856–7861.
110. N. J. Kotloski and J. A. Gralnick, *mBio*, 2013, **4**, e00553–00512.
111. K. Inoue, C. Leang, A. E. Franks, T. L. Woodard, K. P. Nevin and D. R. Lovley, *Environ. Microbiol. Rep.*, 2011, **3**, 211–217.
112. C. H. Chan, C. E. Levar, F. Jiménez-Otero and D. R. Bond, *J. Bacteriol.*, 2017, **199**, e00340–00317.

113. J. Golden, M. D. Yates, M. Halsted and L. Tender, *Phys. Chem. Chem. Phys.*, 2018, **20**, 25648–25656.
114. K. Inoue, X. Qian, L. Morgado, B.-C. Kim, T. Mester, M. Izallalen, C. A. Salgueiro and D. R. Lovley, *Appl. Environ. Microbiol.*, 2010, **76**, 3999–4007.
115. M. Y. El-Naggar, G. Wanger, K. M. Leung, T. D. Yuzvinsky, G. Southam, J. Yang, W. M. Lau, K. H. Nealson and Y. A. Gorby, *Proc. Natl. Acad. Sci. U. S. A.*, 2010, **107**, 18127–18131.
116. P. Subramanian, S. Pirbadian, M. Y. El-Naggar and G. J. Jensen, *Proc. Natl. Acad. Sci. U. S. A.*, 2018, **115**, E3246–E3255.
117. G. Reguera, K. D. McCarthy, T. Mehta, J. S. Nicoll, M. T. Tuominen and D. R. Lovley, *Nature*, 2005, **435**, 1098–1101.
118. R. J. Steidl, S. Lampa-Pastirk and G. Reguera, *Nat. Commun.*, 2016, **7**, 12217.
119. H.-Y. Tang, D. E. Holmes, T. Ueki, P. A. Palacios and D. R. Lovley, *mBio*, 2019, **10**, e00303–00319.
120. K. Novak and S. Pflügl, *FEMS Microbiol. Lett.*, 2018, **365**, 20.
121. C. G. S. Giddings, K. P. Nevin, T. Woodward, D. R. Lovley and C. S. Butler, *Front. Microbiol.*, 2015, **6**, 468.
122. E. V. LaBelle and H. D. May, *Front. Microbiol.*, 2017, **8**, 756.
123. S. Kato, I. Yumoto and Y. Kamagata, *Appl. Environ. Microbiol.*, 2015, **81**, 67–73.
124. J. Philips, E. Monballyu, S. Georg, K. De Paepe, A. Prévoteau, K. Rabaey and J. B. A. Arends, *FEMS Microbiol. Ecol.*, 2018, **95**, 2.
125. J. S. Deutzmann, M. Sahin and A. M. Spormann, *mBio*, 2015, **6**, e00496–00415.
126. P.-L. Tremblay, N. Faraghiparapari and T. Zhang, *Catalysts*, 2019, **9**, 166.
127. E. Blanchet, F. Duquenne, Y. Rafrafi, L. Etcheverry, B. Erable and A. Bergel, *Energ. Environ. Sci.*, 2015, **8**, 3731–3744.

CHAPTER 9

In Situ *Spectroscopic Methods to Study Electrochemical CO_2 Reduction*

S. BUNEA AND A. URAKAWA*

Catalysis Engineering, Department of Chemical Engineering,
Delft University of Technology, Van der Maasweg 9, Delft, 2629 HZ,
The Netherlands
*Email: a.urakawa@tudelft.nl

9.1 Introduction

Modern approaches towards investigation of electrochemical reactions seldom rely solely on voltammetric techniques. The reasons for this are, on one hand, the increasing level of complexity of the electrochemical experiments and methodologies, involving nanostructured electrocatalysts, molecular complexes, or solid electrolytes and, on the other hand, the necessity to deepen our understanding of the reactions taking place at or near the electrodes. In these reactions solid–liquid or gas–solid–liquid interfaces often play key roles in the rational discovery of new reactions and electrochemically active materials. While the use of voltammetric techniques is widely accepted to study electrochemical surfaces, the information gained is indirect, and is not able to give a precise picture of what is happening at the electrodes and/or in solutions. The nature of intermediate species, possible reaction mechanisms, the oxidation state of the electrocatalysts under operating conditions, and changes in the structure of molecular electrocatalysts under applied potential are just a few questions which cannot be

Energy and Environment Series No. 28
Carbon Dioxide Electrochemistry: Homogeneous and Heterogeneous Catalysis
Edited by Marc Robert, Cyrille Costentin and Kim Daasbjerg

Published by the Royal Society of Chemistry, www.rsc.org

answered using the traditional approach. Answering these questions generally requires spectroscopic studies performed under relevant electrochemical conditions.

Nowadays, there are numerous analytical techniques used for the study of catalysts under *in situ* and *operando* conditions.[1–5] However, only a few are pertinent for the investigation of electrochemical reactions, mainly due to the experimental restrictions or the presence of liquid phase. Most *in situ* and *operando* studies use (i) infrared (IR) spectroscopy or (ii) Raman spectroscopy to identify the state or structures of chemical species in solution and on the electrode surface, (iii) UV–Vis spectroscopy to learn about the electronic structures of molecular complexes and (iv) X-ray absorption spectroscopy to understand the local geometric environment and the electronic state of molecular complexes or the electrode itself. All these techniques have been successfully used for the study of the electrochemical CO_2 reduction reaction (CO_2RR), greatly increasing our knowledge of the reaction mechanisms, selectivity trends, and oxidation state of the electrodes during electrolysis, among others. These analytical techniques are described in this chapter with their working principles, practical aspects, and some selected examples.

9.2 Vibrational Spectroscopy for the Investigation of Electrochemical CO_2 Reduction

9.2.1 Infrared Spectroscopy

In general, the CO_2 molecule, as well as its possible reduction products, possess highly polarised chemical bonds with vibrational modes that can be detected by IR spectroscopy. IR spectroscopy can often detect intermediate species, which makes it particularly interesting for the elucidation of reaction mechanisms and thus for the investigation of CO_2RR. IR spectroscopic investigations can be implemented for the study of both heterogeneous systems (with bulk metallic electrodes) and homogeneous systems (with molecular catalysts). There are two measurement configurations that are widely used for the study of electrochemical reactions, namely transmission and reflection configurations. Each configuration will be discussed in the following, highlighting their advantages and drawbacks, along with some implementation examples.

Most of the studies of CO_2RR involve the use of a liquid electrolyte. Usually, this is an aqueous bicarbonate solution for heterogeneous systems and various protic or aprotic solvents for homogeneous systems. This poses a significant challenge for IR spectroscopic experiments, mainly due to the strong IR absorption by the electrolyte, particularly by aqueous ones. A way to overcome this challenge is to use D_2O instead of H_2O as the electrolyte/solvent. Another practical solution is the use of the internal reflection (or more-commonly called attenuated total reflection, ATR) configuration,

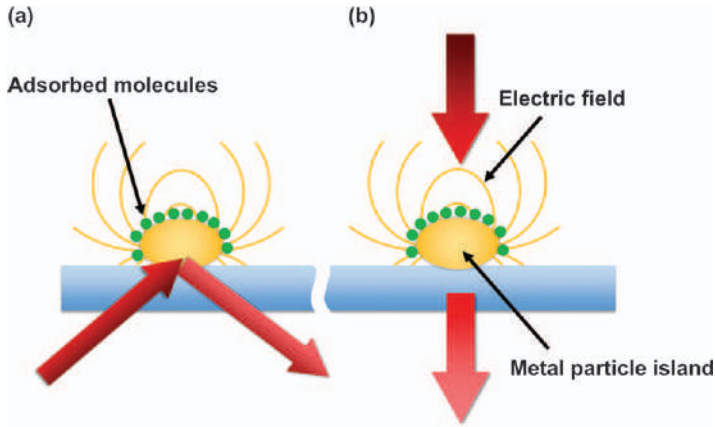

Figure 9.1 The SEIRA effect: (a) internal reflection configuration and (b) transmission configuration.

which maximizes the signal from the sample and minimizes that of the solution.

Modern Fourier transform infrared (FTIR) spectrometers allow fast acquisition of spectra, making it possible to study CO_2RR *in situ* in real time. An important feature of IR spectroscopy for the study of electrochemical reactions is the effect of signal enhancement near the surface, of up to three orders of magnitude, which can be observed for some metals.[6–9] This enhancement effect is known as the surface enhanced infrared absorption (SEIRA) effect and is due to the presence of a strong electric field created around small metal particles (see Figure 9.1a and b). The highest signal enhancement can be observed for noble metals, *i.e.* silver, gold, copper, or platinum, but it was also reported for non-noble metals.[10–15] It is worth mentioning that even though the SEIRA effect provides a significant IR signal enhancement for metallic electrodes, the preparation of SEIRA active metallic surfaces can be intricate, as only thin-enough metallic films are known to exhibit the effect. This poses challenges for making use of the SEIRA effect for other types of electrocatalysts. Consequently, the advantages of the SEIRA effect are prominent in the internal reflection configuration, when the thin metal films are deposited over the ATR crystal directly (Section 9.2.1.2).

9.2.1.1 External Reflection Configuration

The external reflection configuration is historical and one of the most commonly used measurement configurations in IR spectroelectrochemical experiments.[16–18] The IR beam is directed at the electrode surface under an incidence angle of 60–70° and then reflected towards the detector (see Figure 9.2a). By design, the IR beam strikes the electrode surface from outside the electrochemical cell, through a window made of IR transparent

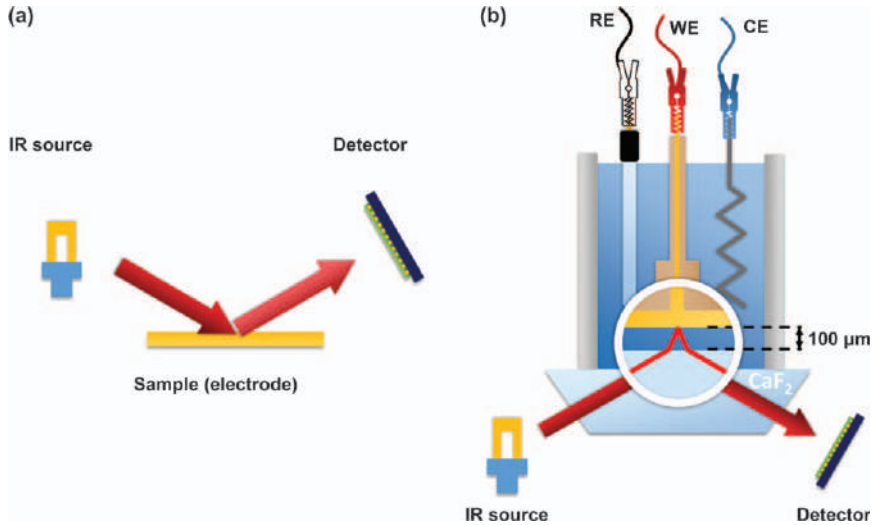

Figure 9.2 (a) Schematic representation of the external reflection configuration and (b) its implementation in a thin layer cell design.

material and exits the electrochemical cell through another window on its way to the detector. Despite the conceptual simplicity, the external reflection configuration has a drawback that restricts its potential for the investigation of CO_2RR. This drawback is the presence of the electrolyte layer in the path of the IR beam, which absorbs IR light, and leads to a decrease in signal intensity and to a poor signal-to-noise ratio. To mitigate this problem, the working electrode is placed at a very small distance from the IR transparent window. Such a design approach is known as the thin layer cell design (see Figure 9.2b). In this way, the IR beam travels only $\leq$100 µm through the electrolyte layer. The IR signal that reaches the detector contains information about both bulk species and species at the electrode surface. In order to differentiate between the two, polarization modulation infrared reflection absorption spectroscopy (PM-IRRAS) can be used. The technique is based on the different interaction of molecules in the vicinity of the electrode surface and of those in the bulk with polarized IR radiation.[19] In this way, the contribution of molecules in the bulk to IR spectra can be cancelled out or at least minimized.

A challenge associated with thin layer spectroelectrochemical cells is the mass transport limitations in the thin layer of the electrolyte between the electrode and the IR window. The accumulation of electrolysis products can lead to erroneous interpretation of spectra. To avoid this, it is recommended to continuously replenish the thin electrolyte layer, either by stirring the solution or by using a flow cell.

The choice of IR windows is also important to consider when setting up spectroelectrochemical experiments in the external reflection configuration. First, the IR window material should not be corroded or dissolved by the

electrolyte. Second, the window material should be chosen in accordance with its transmission properties in the IR range of interest. Last, but not least, the refractive index of the IR transparent material should not be too high for external reflection spectroscopy. The most used material, which satisfies most of the aforementioned conditions, is CaF_2 offering good chemical stability towards corrosion and a transmission range from 50000–1000 cm^{-1}. BaF_2 has similar properties to CaF_2 and its transmission range is slightly wider with 50 000–750 cm^{-1}, but it possesses slightly less chemical resistance. Thus, it could be used if one is interested in slightly extending the spectral range towards the far-infrared region. Alternatively, ZnSe can be considered as window material. Its transmission range is 20 000–454 cm^{-1}, and it has a good stability in aqueous solutions (only corroded by strong acids).

The use of external reflection IR spectroscopy for the investigation of electrochemical reactions was pioneered by Bewick, Kunimatsu, and Pons at the beginning of the 1980s.[20–22] For the investigation of CO_2RR it was used for the first time by Beden for a Pt electrode in 1982.[23] At that time, the technique used was electrochemically modulated infrared spectroscopy (EMIRS) where the electric potential was modulated. The aim was to improve the signal-to-noise ratio, in accordance with the phase-sensitive detection (PSD) method. At that time, this was the most suitable PSD method to be used with dispersive spectrometers. Later, as FTIR spectrometers emerged, the need for potential modulation was no longer needed to increase the quality of the signal, as this was achieved by means of averaging a high number of interferograms which the FTIR spectrometer can acquire. The FTIR technique was then often used as subtractively normalized interfacial Fourier transform infrared spectroscopy (SNIFTIRS). In SNIFTIRS, IR spectra are presented as a difference between reflectivity at the potential of interest and at the reference potential, divided by the reflectivity at the reference potential. In this way, positive band formation is associated with formation of spectroscopically active species and negative band formation is associated with the depletion of species.

A few years later, in 1984, PM-IRRAS was used by Golden and Kunimatsu to investigate the CO oxidation on a Pt electrode.[24] In this method, the polarization of IR light is modulated between the surface parallel and perpendicular components. PM-IRRAS allows one to discern between bulk and surface species, and can be applied to the investigation of CO_2RR.[25,26]

9.2.1.1.1 Application in Heterogeneous Systems. The external reflection configuration is a very good choice for the investigation of the heterogeneous CO_2RR. However, it is important to consider the applicability of the external reflection exclusively to flat, mirror finish electrode surfaces. This is needed for the IR light to be efficiently reflected by the electrode surface to reach the detector as well as to maximize the signals from the surface species at a glazing incident angle.[27]

Many reports have appeared over the years since the first by Beden in 1982, making use of the external reflection spectroscopy for the investigation of CO_2RR. The technique was extensively used in fundamental studies of the mechanisms of CO_2RR over various metal electrodes, such as Pt, Pd, Au, Cu, and Pb.[28–33] A thorough review of IR spectroscopic studies using the external configuration measurement with different metal electrodes was reported by Pastor, to which the interested reader is referred.[34]

At a Pt electrode in acetonitrile during CO_2RR, bands at 1682, 1303, and 1274 cm^{-1} emerged at potentials more negative than −2.0 V *vs.* Saturated Calomel Electrode (SCE). They were assigned to carbonate species by Christensen *et al.* (see Figure 9.3A).[28] As no other products were observed, the authors concluded that carbonate formation follows eqn (9.1), as also suggested by Amatore and Savéant.[35]

$$2CO_2 + 2e^- \rightarrow {CO_3}^{2-} + CO \tag{9.1}$$

No bands that could be associated with CO were observed, probably because CO has low solubility in acetonitrile and a low dipole moment. In the same study, when using a gold electrode, the emergence of a band at 1606 cm^{-1} was attributed to formate species, while a band at 2140 cm^{-1} was assigned to dissolved CO (see Figure 9.3B).[28]

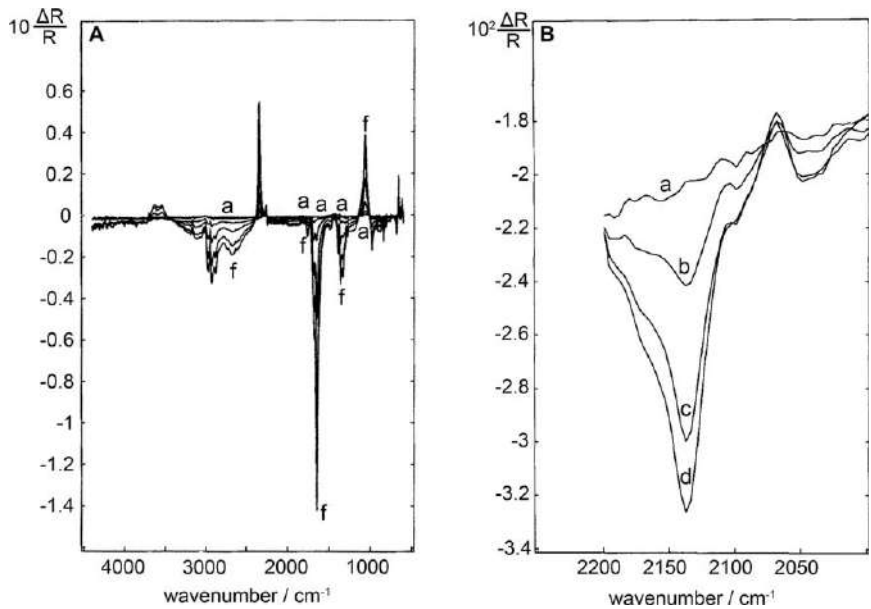

Figure 9.3 (a) IR spectra recorded in external reflection configuration at a Pt electrode in CO_2 saturated 0.1 M tetra-n-butylammonium fluoride (TBAF)/acetonitrile (with a background recorded at −0.8 V *vs.* SCE) at (a) −1.0 and (f) −1.9 V *vs.* SCE. (B) Reflectance IR spectra for an Au electrode in CO_2 saturated 0.1 M TBAF/acetonitrile at (a) −1.6, (b) −1.8, (c) −1.9, and (d) −2.0 V *vs.* SCE.
Adapted from ref. 28 with permission from Elsevier, Copyright 1990.

Pd is a more active metal for CO_2RR than Pt. In a neutral phosphate buffer solution, Taguchi *et al.* identified adsorbed CO in a bridged configuration (two-fold coordination to surface Pt atoms) at 1898 cm^{-1} and that on a hollow site (three-fold coordination) at 1838 cm^{-1} (see Figure 9.4).[29] The band at 1898 cm^{-1} shifted towards higher wavenumbers when the applied potential was shifted to more positive values. This was attributed to the decreasing electron back donation to the CO π^* orbital or the Stark effect, demonstrating the high sensitivity of IR spectroscopy on the electronic structure of adsorbates.

Cu is one of the few metals that show high selectivity towards hydrocarbons as CO_2RR products, making its spectroscopic investigation particularly interesting for understanding the underlying reaction mechanisms.[36] Hori identified CO as reaction intermediate at 2083 cm^{-1} in a $KHCO_3$ electrolyte solution using a Cu electrode at -0.9 V *vs.* NHE (see Figure 9.5).[30] Note that *s*-polarized light is not sensitive to surface species while *p*-polarised light is sensitive to both surface and liquid-phase species. To confirm their band assignment, the authors recorded IR spectra of a CO-saturated electrolyte solution to detect the CO-characteristic band at the same position as the band observed during CO_2RR.

Besides methane, Cu is also known to give C_2 hydrocarbons such as ethylene from CO_2RR. A hydrogenated dimer intermediate was experimentally observed by Pérez-Gallent *et al.* at a Cu(100) electrode. A CO-saturated LiOH solution was used as the electrolyte. The characteristic band for CO stretching on Cu(100) hollow sites at 1677 cm^{-1} was observed upon varying the potential from 0.1 to -0.2 V *vs.* RHE (see Figure 9.6). In addition, a new band emerged at 1191 cm^{-1} along with another band at 1584 cm^{-1} in D_2O solution. Based on

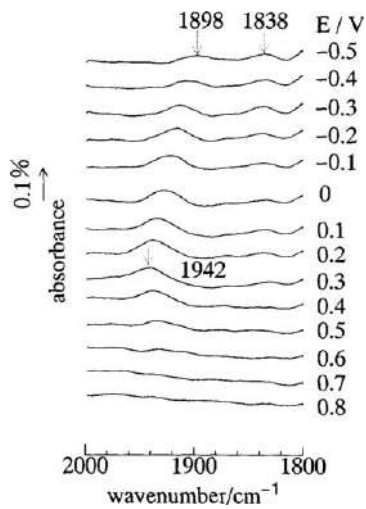

Figure 9.4 *In situ* IR spectra recorded of a CO_2 saturated phosphate buffer solution at a Pd electrode at various applied potentials (*vs.* Reversible Hydrogen Electrode (RHE)).
Reproduced from ref. 29 with permission from Elsevier, Copyright 1994.

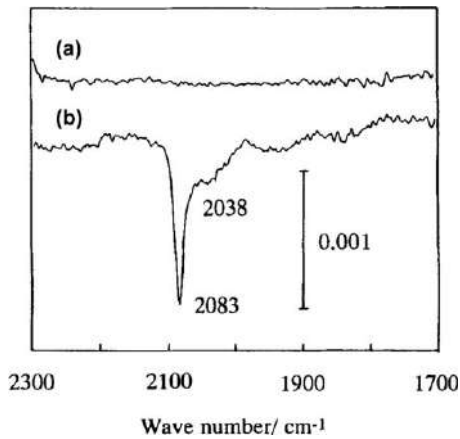

Figure 9.5 (a) s-Polarized light IR spectrum of CO_2RR on a Cu electrode in 0.2 M $KHCO_3$ (potential values reported *vs.* Normal Hydrogen Electrode (NHE)). (b) p-polarized light IR spectrum at the surface of a Cu electrode, showing the adsorbed CO bands at 2083 cm^{-1} and 2038 cm^{-1}.
Reproduced from ref. 30 with permission from Elsevier, Copyright 1995.

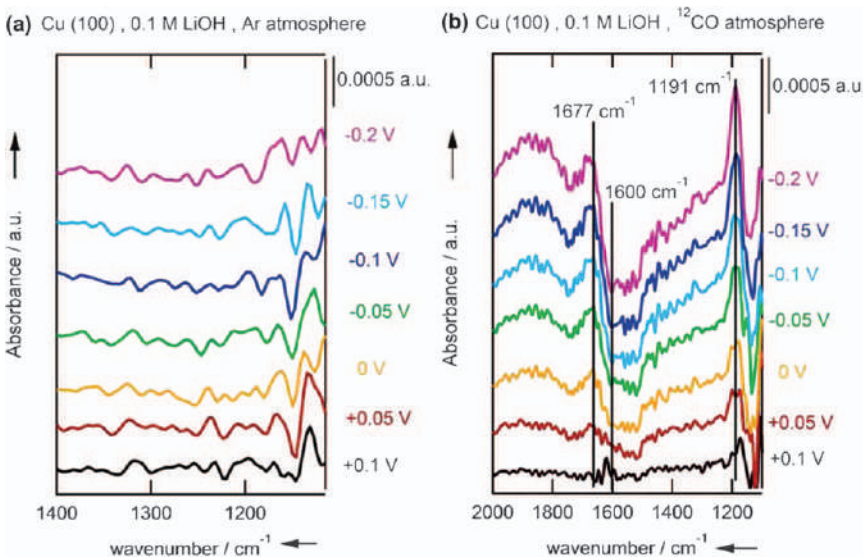

Figure 9.6 IR spectra at a Cu(100) electrode (potential values reported *vs.* RHE) in (a) Ar and (b) CO_2 atmosphere.
Reproduced from ref. 31 with permission from John Wiley and Sons, Copyright © 2017 Wiley-VCH Verlag GmbH & Co. KGaA, Weinheim.

calculated IR spectra of potential C_2 intermediates, the authors ascribed the latter two bands to a hydrogenated CO dimer (OCCOH), suggesting its formation for the first time.[31]

Figueiredo *et al.* studied CO_2RR at a Cu electrolyte in acetonitrile. Spectroscopic studies indicated that even residual amounts of water in the electrolyte lead to CO and carbonate formation from CO_2. Carbonate formation was confirmed by the appearance of specific IR bands at 1681, 1646, 1364, 1328, and 1305 cm^{-1}. These became increasingly prominent when the potential of the working electrode was shifted from −1.4 V to −2.4 V *vs.* $Ag/AgClO_4$, along with the appearance of bands which were assigned to bicarbonate species at 1607 and 1388 cm^{-1} (see Figure 9.7).[37] The formation of CO was observed by Raman spectroscopy (see also the section on Raman spectroscopy).

Detailed studies have been performed for non-Cu elements. Innocent *et al.* investigated CO_2RR in a NaOH electrolyte at a Pb electrode. A band at 1394 cm^{-1}, characteristic for carbonate species, emerged as soon as bubbling of CO_2 started. After 100 s of bubbling, a band characteristic for bicarbonate species was observed at 1397 cm^{-1} along with the band associated with CO_2 in solution at 2346 cm^{-1} (see Figure 9.8a–c). The potential was gradually increased from −1.8 (reference spectrum taken at this value) to −1.0 V *vs.* SCE while recording the IR spectra (see Figure 9.8d and e). The consumption of bicarbonate (at 1397 cm^{-1}) was observed, in that a new band emerging at 1104 cm^{-1} at −1.45 V *vs.* SCE was assigned to the ν_{C-H} bending vibration of the formate anion. Between −1.5 and −1.7 V *vs.* SCE, a band at 1633 cm^{-1} was observed and assigned to the $\nu_{s(OCO)}$ symmetric stretch vibration of formate. On this basis the authors concluded that bicarbonate undergoes reduction to formate in alkaline solution at a Pb electrode.[32]

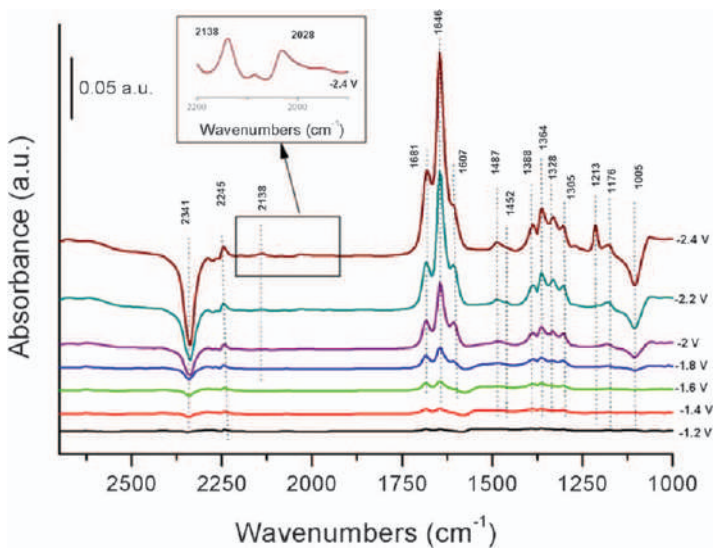

Figure 9.7 *In situ* IR spectra recorded during CO_2RR at a Cu electrode in acetonitrile (reference spectrum recorded at −1 V *vs.* $Ag/AgClO_4$).
Reproduced from ref. 37 with permission from American Chemical Society, Copyright 2016.

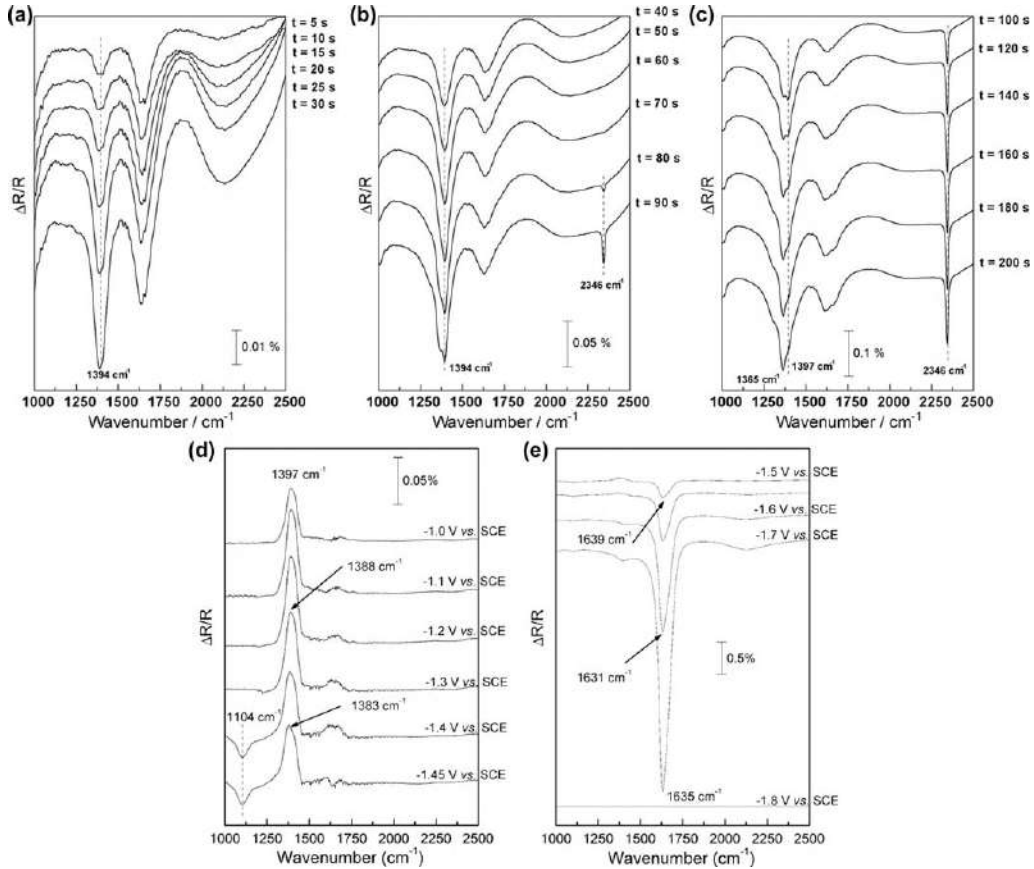

Figure 9.8 IR spectra recorded under CO_2 bubbling conditions in 0.5 M NaOH (reference spectrum recorded at 0 s) with bubbling between (a) 5–30 s, (b) 40–90 s, and (c) 100–200 s. IR spectra at a Pb electrode during CO_2RR (reference spectrum recorded at −1.8 V *vs.* SCE) between (d) −1.0 and −1.45 V *vs.* SCE and (e) −1.5 and −1.8 V *vs.* SCE.
Adapted from ref. 32 with permission from Elsevier, Copyright 2010.

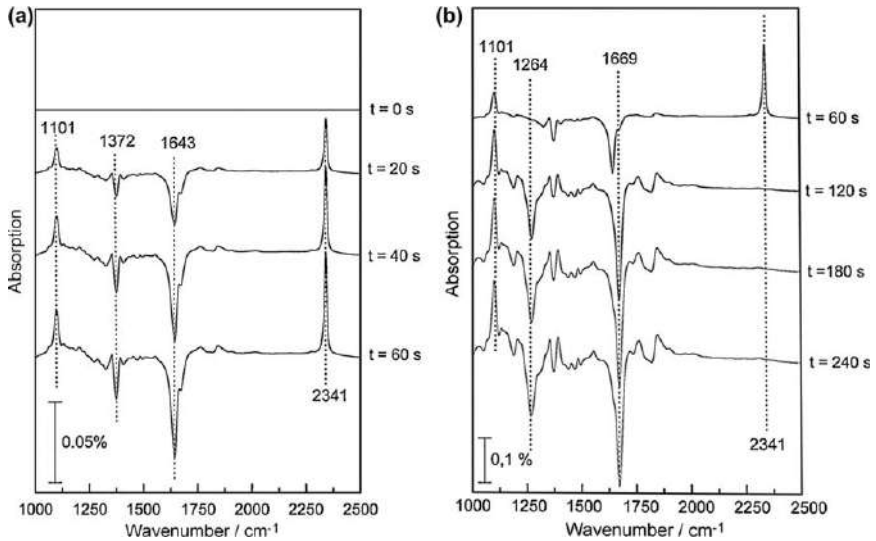

Figure 9.9 IR spectra of CO_2RR at a Pb electrode in 0.2 M tetraethylammonium perchlorate (TEAP)/propylene carbonate recorded at −2.5 V *vs.* Ag/AgCl from (a) 0–60 s and (b) 60–240 s.
Adapted from ref. 33 with permission from Elsevier, Copyright 2010.

The authors also reported CO_2RR at a Pb electrode in a propylene carbonate electrolyte.[33] At −2.5 V *vs.* Ag/AgCl, the appearance of a band at 1642 cm^{-1} was assigned to oxalate species (see Figure 9.9a and b) which are often speculated as the reaction intermediate in CO_2RR. Another band at 1371 cm^{-1} was tentatively assigned to Pb-CO_2^- species. The decrease in intensity of the band at 2341 cm^{-1} suggests that dissolved CO_2 is undergoing reduction in propylene carbonate electrolyte.

IR spectroscopy in external reflection configuration was applied to study most metal electrodes that are active towards CO_2RR. The information acquired from the spectroelectrochemical experiments in the 1980s and 1990s has offered a great level of insight into the selectivity trends for most transition and noble metals towards different CO_2RR products. Careful studies in this configuration allow separation of chemical processes taking place at the electrode surface and bulk liquid (electrolyte).

9.2.1.1.2 Application in Homogeneous Systems. The external reflection IR spectroscopy found great popularity for the study of homogeneous CO_2RR systems. By sweeping the potential of the working electrode while simultaneously recording spectra, it is possible to identify intermediates and understand the catalytic mechanisms involving molecular complexes present in the liquid phase. Band formation or disappearance indicates species formation or consumption, respectively. The assignment of the bands is not always straightforward, because the *in situ* emerging bands are often compared to the bands corresponding to the intermediate

structures measured *ex situ* which are not always representative. Nowadays, thanks to the methodological and technological developments in atomistic simulation, it is possible to simulate IR spectra with high accuracy, facilitating band assignment. Experimentally, isotopes such as ^{13}C-labelled CO_2 can be conveniently used to elucidate whether the appearing bands are related to CO_2RR or other changes in the structure of the catalysts.

In homogeneous CO_2RR, glassy carbon (GC) is most often the material of choice for the working electrode, as Pt or Au electrodes can catalyse CO_2RR and therefore interfere with the investigation of molecular catalysts.[38–40] Furthermore, due to its high activity towards the hydrogen evolution reaction (HER) at low overpotentials, particularly in protic media, the use of Pt as a working electrode material is not recommended.[41] Spectroelectrochemical studies on molecular catalysts can also indicate reversibility of the reaction in question, by the presence of well-defined isosbestic points.

The first cell design for IR spectroelectrochemistry in external reflection configuration, for the investigation of molecular electrocatalysts for CO_2RR, was proposed by Christensen *et al.*[42] Their cell was similar to the cells reported in the previous section, with a GC electrode placed at a small distance from a CaF_2 window (see Figure 9.10a). A cell design using an optical fibre probe was proposed by Shaw in 1996 (see Figure 9.10b).[43] The cell design approach was perhaps ''ahead of its time'' and was not widely implemented. A second-generation external reflection spectroelectrochemical cell was developed by the group of Kubiak (see Figure 9.10c).[44] The design of this cell was inspired by Christensen's, but the authors were able to assemble the components in a more compact fashion. It made possible the use of commercial, PEEK-jacketed concentric ring disk electrodes such as Pt, Au, or GC disk electrodes encircled by a Ag pseudo reference and a Pt counter ring electrode. The cell also allows temperature control during electrochemical experiments.

In the paper by Christensen *et al.*, the authors also investigated Re tricarbonyl bipyridyl (bipy) complexes for CO_2RR.[42] In a CO_2-saturated acetonitrile solution, the appearance of a weak characteristic band for CO was observed at 2150 cm^{-1}, as the potential was decreased from -1.1 to -2 V *vs.* SCE, along with a decreasing band at 2342 cm^{-1}, associated with CO_2 consumption (see Figure 9.11a). As the potential was further decreased, the bands emerging at 2010, 1902, and 1878 cm^{-1} were assigned to a *fac*-[Re(dmbipy)$(CO)_3(CO_2H)$] intermediate (dmbipy = 4,4′-dimethyl-2,2′-bipyridine), and the bands at 1997 and 1860 cm^{-1} were assigned to a *fac*-[Re(dmbipy$^{\bullet-}$)$(CO)_3(CO_2H)$] intermediate (see Figure 9.11b and c). At the most negative potential of -2 V *vs.* SCE, the bands at 1930 and 1823 cm^{-1} were assigned to the *fac*-[Re(dmbipy$^{\bullet-}$)$(CO)_3(CO_2H)]^-$ species (see Figure 9.11d). The band assignment was based on the empirical method of calculating energy-factored k_{CO} force constants reported by Timney, from which ν_{CO} stretching vibration frequencies were predicted with high accuracy.[45]

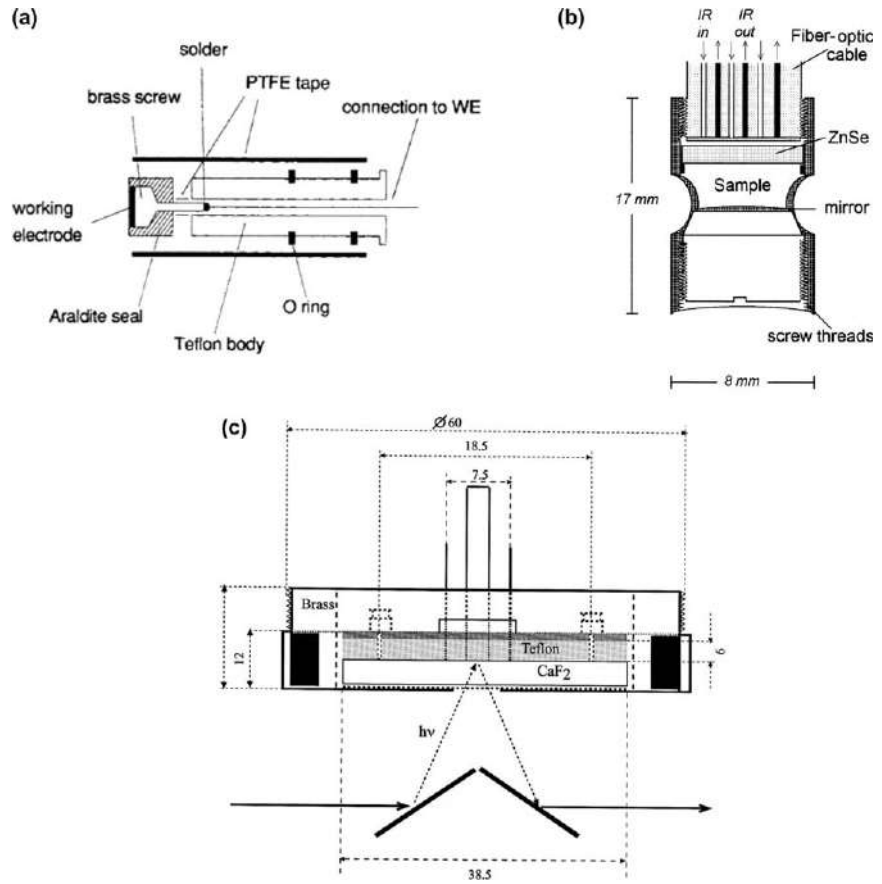

Figure 9.10 Schematic representation of various IR spectroelectrochemical cell designs proposed by (a) Christensen *et al.*,[42] (b) Shaw and Geiger,[43] and (c) Zavarine and Kubiak.[44] Adapted from ref. 42 with permission from the Royal Society of Chemistry. Adapted from ref. 43 with permission from American Chemical Society, Copyright 1996. Adapted from ref. 44, with permission from Elsevier, Copyright 2001.

This was the first paper to elucidate the reaction mechanism of CO_2RR using a Re-based molecular catalyst. The reaction mechanism was suggested to follow eqn (9.2)–(9.6).

$$[Re(dmbipy)(CO)_3Cl] + e^- \rightarrow [Re(dmbipy^{\bullet -})(CO)_3Cl] \quad (9.2)$$

$$[Re(dmbipy^{\bullet -})(CO)_3Cl] + CO_2 \rightarrow [Re(dmbipy)(CO)_3(CO_2)] + Cl^- \quad (9.3)$$

$$[Re(dmbipy)(CO)_3(CO_2)] + e^- + H_2O \rightarrow [Re(dmbipy)(CO)_3(CO_2H)] + OH^- \quad (9.4)$$

$$OH^- + CO_2 \rightarrow {CO_3}^{2-} + H^+ \quad (9.5a)$$

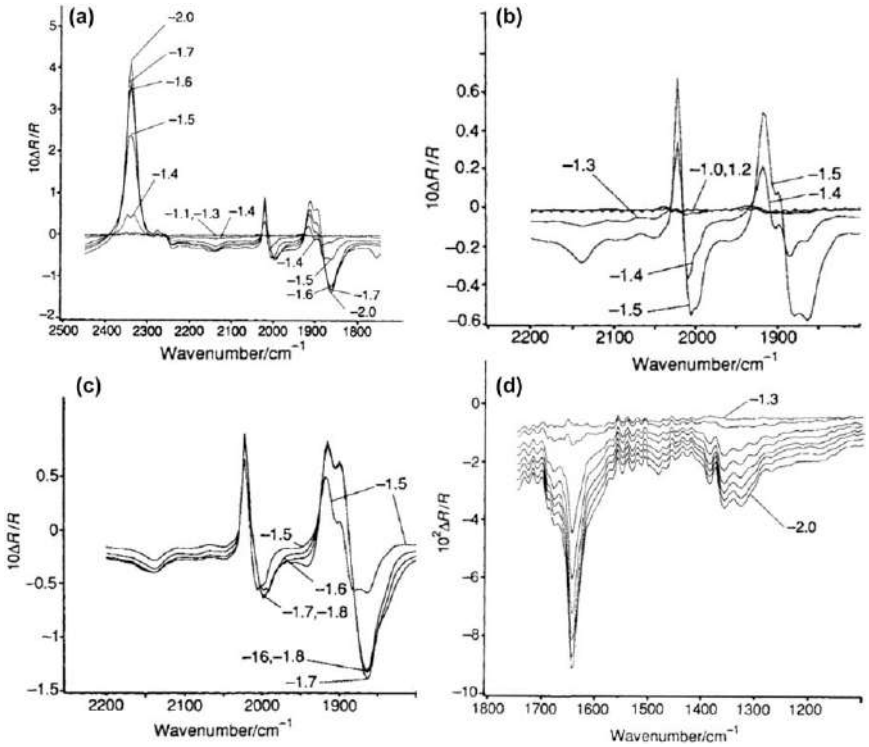

Figure 9.11 (a) IR spectra recorded during CO_2RR by [Re(dmbipy)$(CO)_3$Cl] in 0.2 M tetraethylammonium tetrafluoroborate ($TEABF_4$)/acetonitrile (reference spectrum taken at −1.0 V *vs.* SCE) showing the (b) 2200–1800 cm^{-1} region at potentials between −1.1 and −1.5 V *vs.* SCE, (c) 2200–1800 cm^{-1} region at potentials between −1.5 to −1.8 V *vs.* SCE and (d) 1750–1100 cm^{-1} region at potentials between −1.3 and −2.0 V *vs.* SCE. Adapted from ref. 42 with permission from the Royal Society of Chemistry.

or

$$2[\text{Re(dmbipy)(CO)}_3(\text{CO}_2)] + 2\text{Cl}^- \rightarrow [\text{Re(dmbipy}^{\bullet -})(\text{CO})_3\text{Cl}] + \text{CO} + \text{CO}_3{}^{2-} \quad (9.5b)$$

$$[\text{Re(dmbipy)(CO)}_3(\text{CO}_2\text{H})] + \text{e}^- \rightarrow [\text{Re(dmbipy}^{\bullet -})(\text{CO})_3(\text{CO}_2\text{H})] \quad (9.6a)$$

or

$$[\text{Re(dmbipy)(CO)}_3(\text{CO}_2\text{H})] + \text{e}^- \rightarrow [\text{Re(dmbipy)(CO)}_3(\text{CO}_2{}^-)] + \tfrac{1}{2}\,\text{H}_2 \quad (9.6b)$$

A more efficient Re complex, Re(bipy-*tert*-butyl)$(CO)_3$Cl, was developed by the group of Kubiak by changing the methyl substituents at the 4,4′ positions of the bipyridine ligand with *tert*-butyl substituents.[46,47] The enhanced catalytic activity of this complex was elucidated by spectroelectrochemical

studies. The most important feature is the absence of bands characteristic for the $[Re(bipy\text{-}tBu)(CO)_3]_2$ dimer, reported by Johnson *et al.*, at 1986, 1950, 1888, and 1850 cm^{-1}.[48] The lower degree of dimerization of this complex leads to its superior catalytic performance.

The indirect detection of reaction products is also possible using IR spectroscopy. Often, CO is one of the reduction products of CO_2RR using molecular catalysts. However, detection of CO formation using IR spectroscopy is not straightforward, because of its low solubility in the solvents commonly used with molecular catalysts (*e.g.* acetonitrile) and its low dipole moment. For the detection of generated CO from the electrochemical reduction of CO_2 with $Re^{I}(dmb)(CO)_3Cl$ (dmb = 4,4′-dimethyl-2,2′-bipyridyl), the Kubiak group used nickelocene ($Ni^{II}Cp_2$) to capture the formed CO (see Figure 9.12a). The emergence of bands associated with $[Ni^{I}(\mu_1\text{-}CO)Cp]_2$ at ~1840 cm^{-1} and with $Ni^0(CO)_4$ at 2045 cm^{-1} (see Figure 9.12b,c,d), to which nickelocene is transformed. Along with the decrease of the CO_2 band at 2340 cm^{-1}, this confirms the formation of CO as a reaction product of CO_2RR.[47,49]

Pun *et al.* elucidated the mechanism of CO_2RR with iron(I) 2,9-bis(2-hydroxyphenyl)-1,10-phenanthroline (H_2dophen) complexes using IR spectroelectrochemistry.[50] In a CO_2-saturated dimethyl sulfoxide (DMSO) solution at −2.16 V *vs.* ferrocenium/ferrocene ($Cp_2Fe^{+/0}$), they correlated the band at 2140 cm^{-1} with the formation of CO and the band at 2340 cm^{-1} with the consumption of CO_2 (see Figure 9.13a). The bands at 1934 and 1881 cm^{-1} were attributed to an iron carbonyl species and the band at

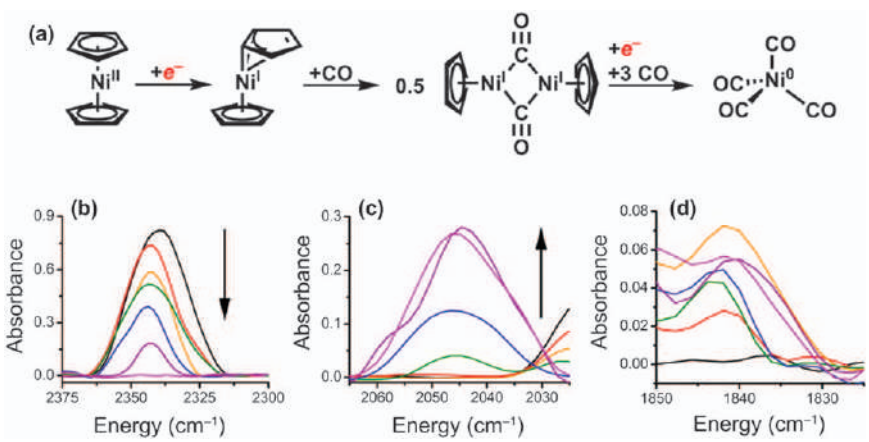

Figure 9.12 (a) Proposed reaction scheme of reduced nickelocene with CO. IR spectra of $Re^{I}(dmb)(CO)_3Cl$ under a CO_2 atmosphere at −2.0 V *vs.* Ag quasi-reference electrode showing the (b) decrease of the 2340 cm^{-1} band associated with CO_2, (c) emergence of the band at 2045 cm^{-1} associated with $Ni^0(CO)_4$, and (d) the band at ~1845 cm^{-1} associated with $Ni^{I}(\mu_1\text{-}CO)Cp]_2$.
Adapted from ref. 47 with permission from American Chemical Society, Copyright 2014.

1328 cm^{-1} to a formato iron species (Fe–OC(O)H). The authors supported their band assignment by conducting experiments with $^{13}CO_2$ and monitoring the band associated with it at 2278 cm^{-1} (see Figure 9.13b). At the same time, they were able to observe the emergence of bands associated with ^{13}CO at 2110 cm^{-1}, Fe–^{13}CO at 1867 and 1814 cm^{-1} and Fe–O^{13}C(O)H at 1288 cm^{-1}. They used DMSO as a solvent instead of *N*,*N*-dimethylformamide to avoid the high absorbance of the latter in the 1600–1400 cm^{-1} region. By a similar approach, the mechanisms of CO_2RR were elucidated for multiple molecular catalysts, including Mn, Re, Ru and Ni-based complexes.[51–55]

9.2.1.2 Internal Reflection Configuration

In the internal reflection configuration, the IR beam does not travel through the electrolyte to reach the electrode surface. Instead, an ATR crystal is used as a propagation medium for the IR radiation. The ATR crystal has a high refractive index and the IR beam is directed through the crystal in such a fashion that it undergoes total internal reflection (see Figure 9.14a). Above the surface of the crystal, an electric field arises, called the evanescent wave. When the crystal is put in contact with the sample under study, the evanescent wave can penetrate a few hundreds of nanometres to a few micrometres inside the sample. The molecules or species that can absorb IR radiation interact with the evanescent wave, which is attenuated when absorption takes place. Then, as the IR beam exits the crystal, it reaches the detector, where the spectrum is recorded.

Related to the study of CO_2RR, the internal reflection configuration can be used for both homogeneous and heterogeneous systems. Compared to the external reflection configuration, the ATR configuration does not suffer from the solution absorption issue because of its inherent near-surface sensitivity. For these reasons, it is particularly interesting for the investigation of reaction mechanisms at the surface of metallic electrodes. Furthermore, the SEIRA effect which can be achieved in the ATR configuration, increases the intensity of the signal and therefore the sensitivity of the method, making possible the detection of species that are present in low amounts. The sensitivity of the measurements can also be tuned by varying the effective path length of the IR beam through the crystal or by choosing a suited crystal material. The effective path length is a function of the penetration depth of the evanescent wave, which is defined by the refractive index of the crystal material and the medium above, by the angle of incidence, and by the number of reflections that the IR beam undergoes as it travels through the crystal. The ATR crystal should be chosen so that it is chemically stable in the electrolyte solution. The thermal stability and optical properties of the crystal should be carefully considered, as the material state or optical properties of the crystal can change at elevated temperatures as well as due to applied electric potential. The commonly used ATR crystals are ZnSe, Ge, Si, or diamond.

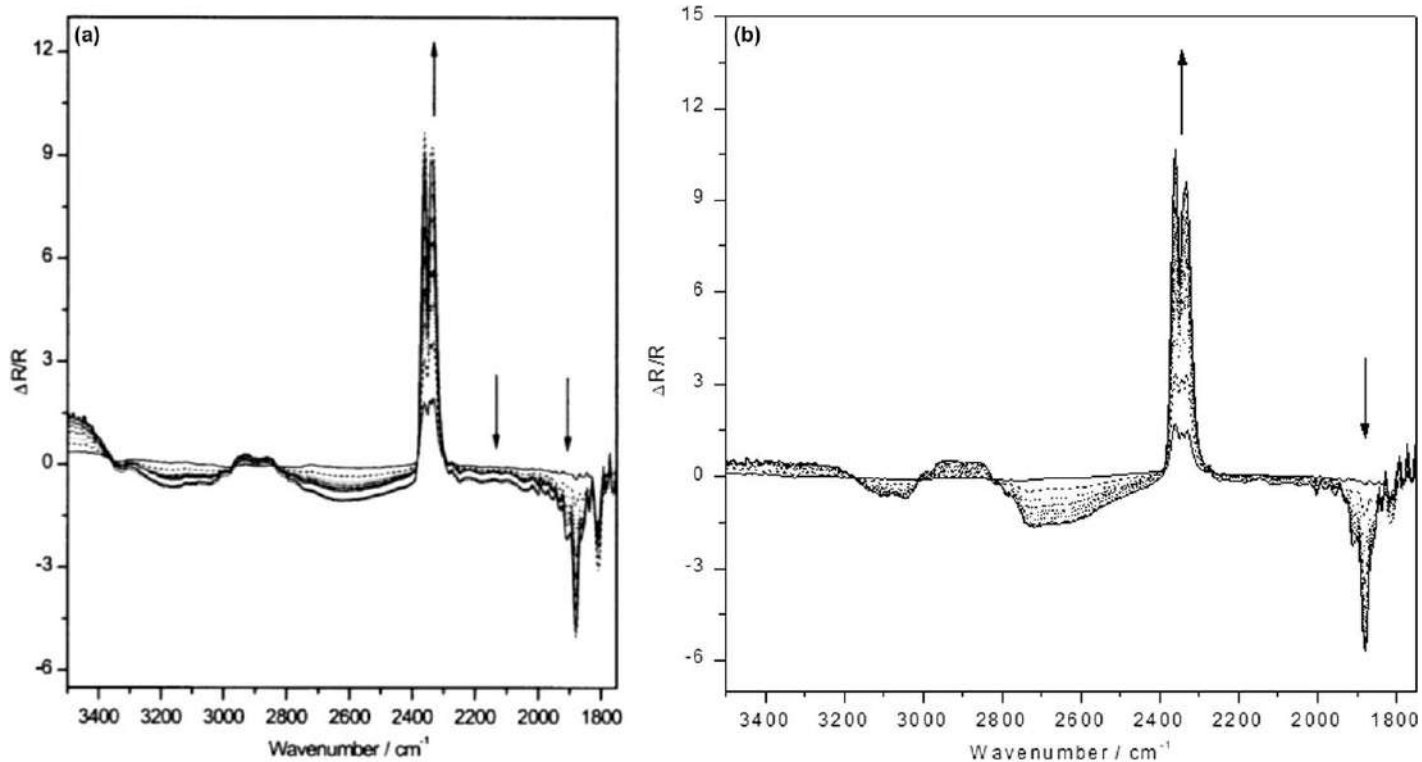

Figure 9.13 (a) *In situ* IR spectra recorded during CO_2RR with $[Fe^{III}(dophen)(1\text{-methylimidazole})_2]ClO_4$ at a GC electrode in DMSO at -2.16 V *vs.* $Cp_2Fe^{+/0}$ (reference spectrum recorded at -0.46 V *vs.* $Cp_2Fe^{+/0}$). (b) *In situ* IR spectra recorded under the same conditions with a $^{13}CO_2$-saturated electrolyte.
Adapted from ref. 50 with permission from the Royal Society of Chemistry.

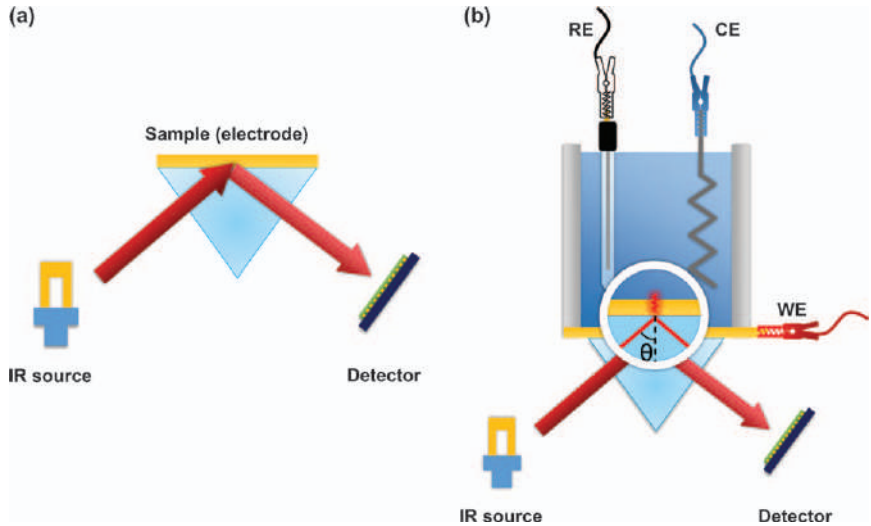

Figure 9.14 (a) Internal (or attenuated total) reflection IR measurement configuration and (b) its implementation in a spectroelectrochemical cell for the study of thin metal film electrodes.

The first application of the ATR configuration for the investigation of an electrochemical reaction dates back to 1964, when a Ge plate was used both as an ATR crystal and the working electrode.[56] Ge is not the common material of choice for a working electrode, but the experiment proved the feasibility of such an approach. The method was later improved by the deposition of thin metallic films over the ATR crystal, acting as the working electrode. This configuration is known as the Kretschmann configuration (see Figure 9.14b). Thin metal films can be deposited over the ATR crystal using various methods such as electroless chemical deposition, sputtering, or electroless deposition followed by electrochemical deposition for the deposition of an additional film.[57–61]

9.2.1.2.1 Application in Heterogeneous Systems. Many reports on the reaction mechanisms of CO_2RR at the surface of various metallic films, including Pt, Au, Sn, Cu, Ag, In, Pb, and Bi, are available in the literature.[57–66] The metal film-coated ATR crystal is usually placed at the bottom of the cell. Electrical contact with the metallic film working electrode is ensured by using electrically conductive tape. The counter electrode can be placed either in the same compartment with the working electrode, or in another compartment separated by a membrane. Commercial reference electrodes can be used and simply immersed in the solution above the electrode surface. To avoid the accumulation of electrolysis products near the surface of the electrode, which can lead to erroneous interpretations of the spectra, it is recommended that the

electrolyte solution above the ATR crystal is stirred during experiments. Alternatively, flow cells can be used.

A thorough review of the most central papers reported over the last few years on this topic was published by Zhu *et al.* and by Cowan.[67,68] The use of ATR-IR spectroscopy allowed identification of surface-bound CO, formate and methoxy species, among others, at the surface of thin film working electrodes during CO_2RR.

Baruch *et al.* used ATR-IR spectroscopy to elucidate the mechanism of CO_2RR at a Sn electrode in aqueous electrolyte.[58] The electrical potential of the working electrode was varied while acquiring IR spectra. Under CO_2 purge, at −1.4 V *vs.* Ag/AgCl, bands at 1500, 1385, and 1100 cm^{-1} emerged, which were assigned to monodentate tin carbonate species (see Figure 9.15). Based on the spectroscopic data, a reaction mechanism was proposed, with the surface-bound tin carbonate as the key intermediate, and a CE mechanism where the CO_2-carbonate equilibrium precedes the rate-limiting electron transfer step, thus ruling out the CO_2-to-$CO_2^{\bullet-}$ reduction as an intermediate step for the reduction.

The behaviour of an adsorbed CO intermediate formed at the surface of Cu during CO_2RR in 0.1 M $NaHCO_3$ was studied by ATR-IR spectroscopy by Wuttig *et al.*[59] The potential was swept between 0.03 to −0.89 V *vs.* RHE, with the reference spectrum recorded at 0.25 V *vs.* RHE. Already at 0.03 V *vs.* RHE, a negative band at 1524 cm^{-1} was observed in the IR spectrum, indicating the desorption of (bi)carbonate from the surface of the electrode (see Figure 9.16a). The appearance of the positive band at 1620 cm^{-1} was attributed to the δ_{HOH} bending mode, suggesting water adsorption at the electrode surface. At −0.66 V *vs.* RHE, the adsorption of CO at the electrode

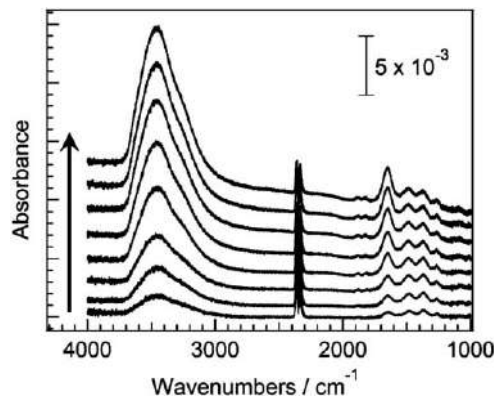

Figure 9.15 *In situ* IR spectra showing the time evolution of CO_2RR at −1.4 V *vs.* Ag/AgCl at a SnO_2 thin film electrode in 0.1 M K_2SO_4. Spectra recorded 1, 3, 5, 10, 15, 20, 25, and 30 min after the introduction of CO_2 in the electrolyte solution (indicated by the direction of the arrow).
Reproduced from ref. 58 with permission from American Chemical Society, Copyright 2015.

surface was indicated by the appearance of the positive band in the IR spectrum between 2104 and 1970 cm^{-1}. The broad shape of the band suggests different binding modes of CO with the surface. Experiments with ^{13}CO show that adsorbed CO is exchanged at −0.8 V *vs.* RHE with the labelled CO in the solution, accompanied by the shift of the adsorbed CO band from 2077 to 2032 cm^{-1} (by 45 cm^{-1}), consistent with the shift expected from the harmonic oscillator model (see Figure 9.16b and c).

ATR-IR spectroscopy is not restricted to the study of metallic thin film electrodes. There are reports of using a Au-coated ATR crystal, which provides a good surface enhancement effect, over which a catalyst was deposited. A Li–Zn and a Pd–Au catalyst were investigated in this way.[69,70] Nanostructured electrocatalysts have different, and often superior, catalytic properties from those of metallic films. In our view, this is a potential future direction for the evolution of IR spectroscopy in internal reflection configuration applied to electrochemical reactions.

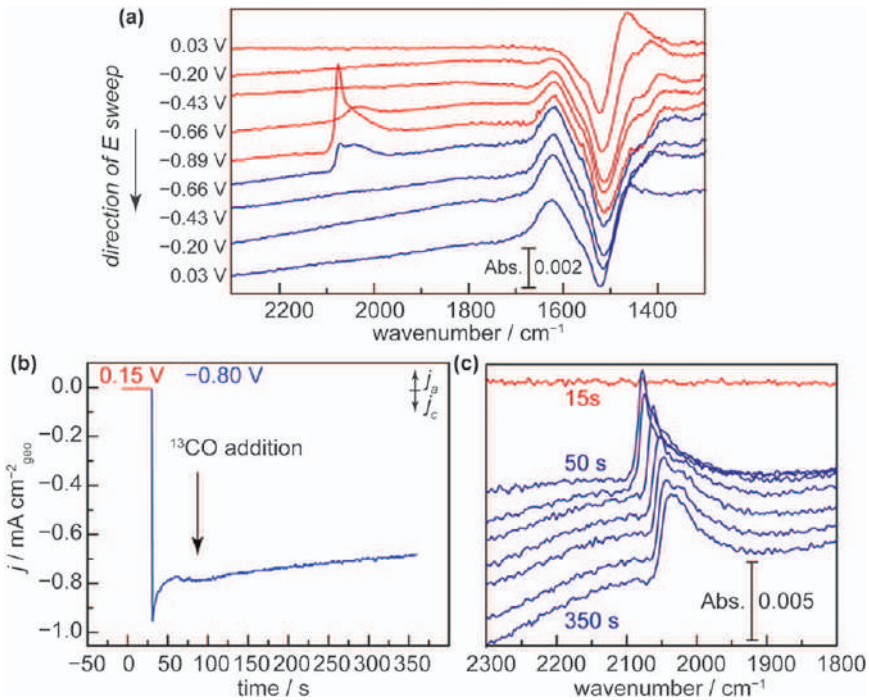

Figure 9.16 (a) *In situ* IR spectra during CO_2RR at a Cu electrode in 0.1 M $NaHCO_3$. (b) Chronoamperometric experiment indicating the addition of ^{13}CO in the electrolyte solution. (c) IR spectra recorded after the addition of ^{13}CO showing the evolution of the characteristic CO band at 2032 cm^{-1} as adsorbed CO is exchanged with ^{13}CO.
Reproduced from ref. 59, http://dx.doi.org/10.1021/acscentsci.6b00155, with permission from American Chemical Society, Copyright 2016.

9.2.1.2.2 Application in Homogeneous Systems. Although ATR-IR spectroscopy is used more and more for the investigation of heterogeneous CO_2RR, to our knowledge, there is only one report describing its use for the study of a molecular complex during CO_2RR. The authors cast a graphene suspension over a ZnSe crystal, which formed a thin graphene film acting as the working electrode (see Figure 9.17a).[71]

The measurement configuration reassembles the ATR configuration for studying electrochemical reactions at metal films, described in the previous section. When translating this approach to the investigation of molecular complexes, it is important to have a thin enough graphene layer deposited on the ATR crystal to allow the evanescent wave to penetrate deep enough into the electrolyte bulk to detect signals related to the molecular complex. The recorded spectra indicate the adsorption of the Cu(II)(1,10-phenanthroline)$_2$ complex (phen–Cu) at the surface of graphene at −0.9 V *vs.* RHE, suggested by the increasing intensity of the peaks specific to the phen ligands of the molecular complex (see Figure 9.17b). Emerging bands at 800/823 and 1110/1135 cm^{-1} are related to C–H bond out-of-plane and in-plane deformations, respectively. The stretching of the C=C and C=N bonds in the aromatic ring of the phen ligands was associated with bands between 1380 and 1510 cm^{-1}. Based on the intensity of the band increase, the authors suggest that adsorption of the phen–Cu catalyst takes place rapidly in the first 10 min upon applying an electric potential, reaching a plateau after about one hour. The phen–Cu complex is desorbed from the surface of the working electrode once the potential is no longer applied (see Figure 9.17c). This shows the reversibility of the phen–Cu adsorption at the graphene surface. The slight red shift of the bands observed in the desorption spectrum is suggested to happen due to the increased electron density on the phen ligands during electrolysis. A blue shift of the R branch of the CO_2 asymmetric stretching band from 2336.5 to 2342.2 cm^{-1} was observed when the potential was applied (see Figure 9.17d). In the absence of the phen–Cu complex, the blue shift was smaller, from 2336.5 to 2343.2 cm^{-1}. Based on this observation, the authors claim the ability of the phen–Cu catalyst to tune the electronic density of CO_2 near the electrode surface.

We envision the use of immersion ATR probes for the investigation of homogeneous systems. The immersion ATR probe can be placed either in the bulk electrolyte solution or in the vicinity of the working electrode. In this way, issues associated with the thin layer external configuration, such as mass transport limitations, can be mitigated. A recent example of the use of ATR-IR spectroscopy with the use of an immersion probe for the elucidation of the reaction mechanism of the conversion of CO_2 into a cyclic carbonate, was reported by Huang *et al.*[72] The same approach can be used for mechanistic investigations of CO_2RR by molecular catalysts (see Figure 9.18). It is important to note, however, that observation of intermediate species, which are confined in a thin diffusion-reaction layer (few μm, for moderate catalytic rates), would still require the placement of the immersion probe at a distance close to the working electrode surface (<1 μm for common ATR crystals).

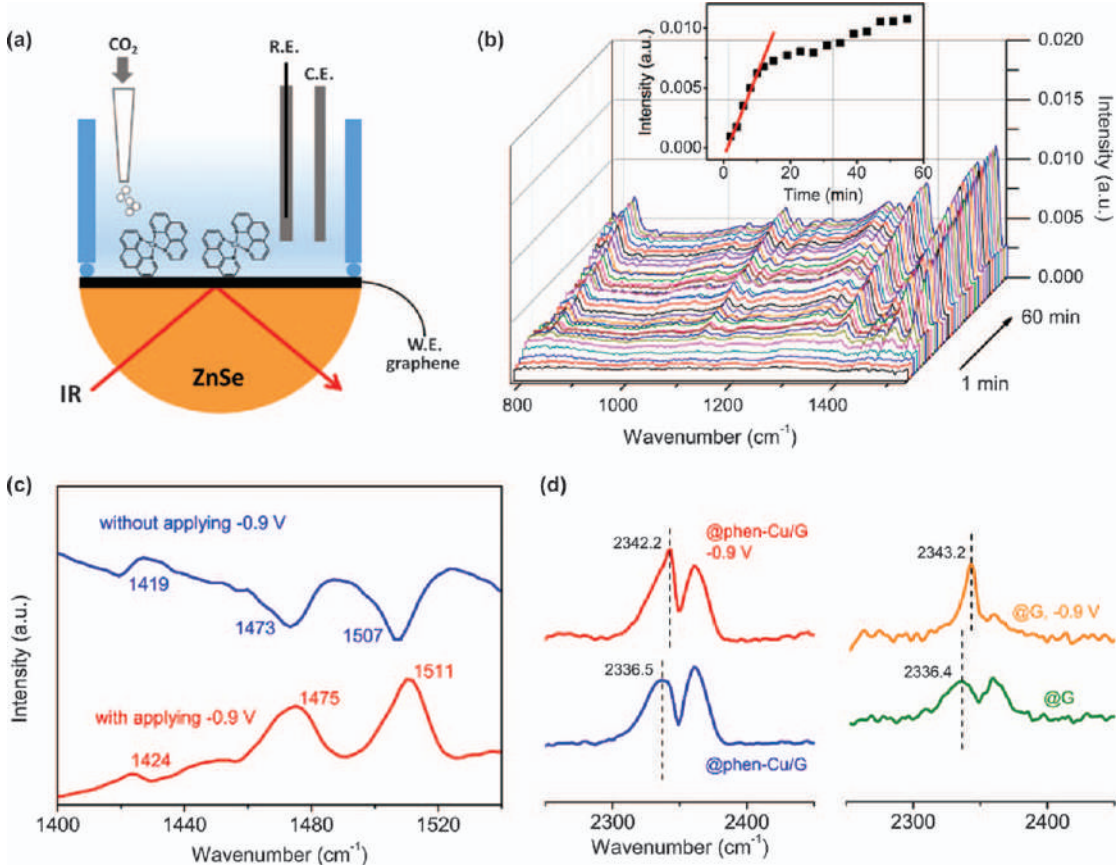

Figure 9.17 (a) Schematic representation of the measurement configuration, (b) IR absorption spectra as a function of time in a CO_2 saturated 0.1 M $KHCO_3$ solution with 0.6 mM phen-Cu catalyst at −0.9 V *vs.* RHE at the graphene working electrode surface (adsorption kinetics shown in inset), (c) IR spectra recorded while applying potential and at the open circuit potential, and (d) variations of the asymmetric stretching band of CO_2 under different potential conditions.
Reproduced from ref. 71 with permission from John Wiley and Sons, Copyright © 2018 WILEY-VCH Verlag GmbH & Co. KGaA, Weinheim.

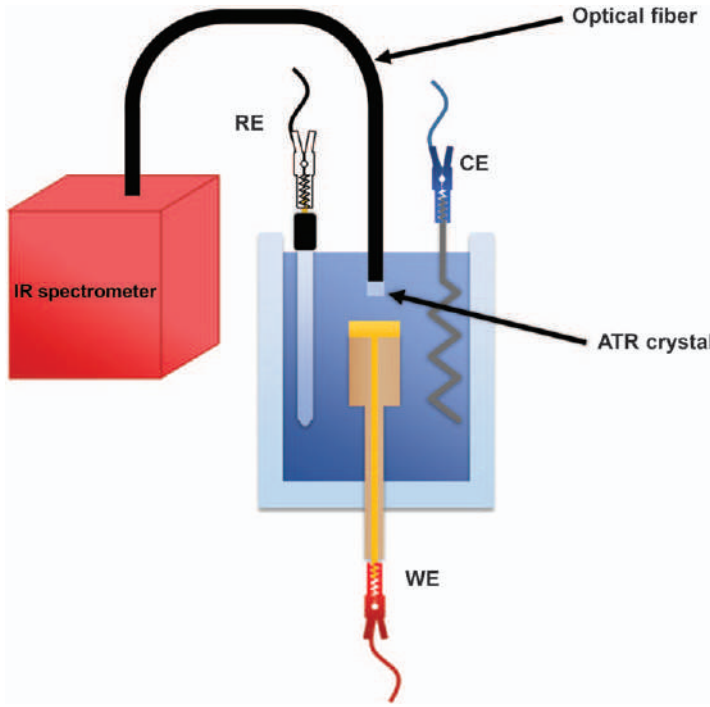

Figure 9.18 Schematic representation of ATR-IR spectroscopy using an immersion probe.

9.2.1.3 Transmission Configuration

The transmission geometry is the oldest sampling configuration used in IR spectroscopy, where the theory based on Beer–Lambert law is firmly established. The sample of interest, which can be either in solid, liquid or gaseous form, is placed between the IR source and the detector (see Figure 9.19a).

For the investigation of electrochemical reactions using transmission configuration, as an obvious requisite, the IR beam needs to pass through the electrolyte solution. For this reason, electrochemical cells with IR transparent windows are used. As the IR beam cannot penetrate through metallic electrodes, the transmission configuration is limited to the study of species in the electrolyte solution or species in the close vicinity of the working electrode.

Most of the cell designs reported for the transmission IR spectroscopy are based on optically transparent electrodes (OTEs), which date back to the 1960s.[73] OTEs consist of Pt or Au grids, which allow the IR beam to pass through micrometric holes in its pathway from the source to the detector. This working electrode is placed in an electrochemical cell with IR transparent windows. To minimise IR absorption by the electrolyte solution, the pathway of the IR beam through the cell must be as small as possible.

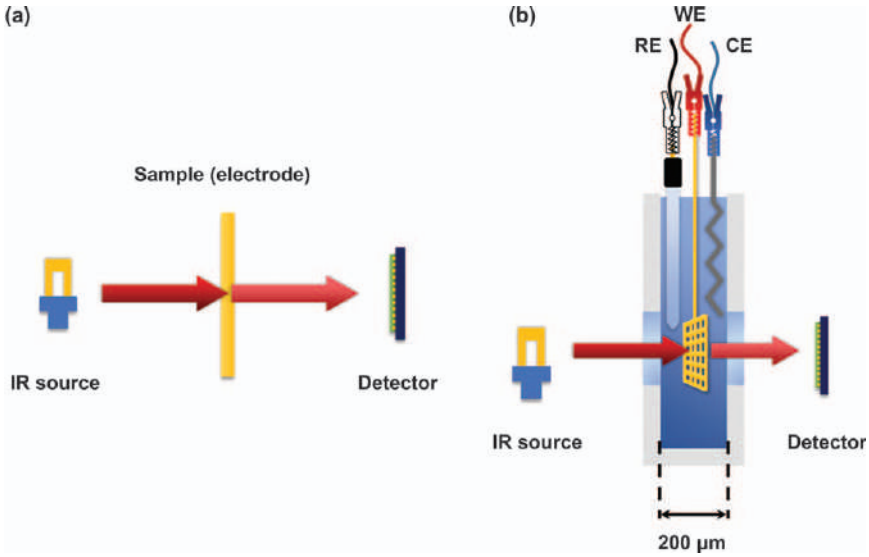

Figure 9.19 (a) Schematic representation of the transmission IR measurement configuration and (b) its implementation with a minigrid working electrode.

To achieve this, thin layer cells are used (see Figure 9.19b). A typical value for the IR beam path length through an optically transparent thin layer electrolyte (OTTLE) cell is 200 μm.[74] Multiple cell designs were reported later, with improvements in cell tightness and counter and reference electrode positioning, but the working principle of OTTLE cells remained unchanged (see Figure 9.20a–c).[75–78]

9.2.1.3.1 Application in Homogeneous Systems. A clear advantage of OTTLE cells for the study of CO_2RR with molecular catalysts is the possibility of using the same cell for IR and UV–vis spectroscopy. By this complementary approach, it becomes possible to acquire knowledge that cannot be gained by a single spectroscopic technique. The transmission configuration was extensively developed and used by the group of Hartl.[78] The catalytic mechanisms of multiple molecular catalysts, including Mo, Cr, W, Re, and Os-based complexes, for CO_2RR were formulated based on spectroelectrochemical experiments in the thin layer configuration, in a similar fashion to the studies using the external reflection configuration mentioned in an earlier section.[38,48,79] The main advantage of the OTTLE cells is the ease of assembly and the possibility of coupling IR spectroscopy and UV–vis spectroscopy, as the latter is less susceptible to radiation absorption by the electrolyte. For further reading on the application of IR spectroelectrochemistry for the investigation of molecular electrocatalysts, the reader is referred to the review by Lee *et al.*[80]

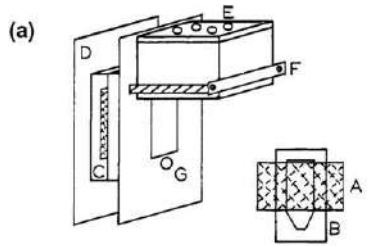

Infrared transparent thin-layer electrode

A. Gold minigrid electrode
B. Teflon spacer
C. NaCl plates
D. Steel frame
E. Holes for reference and auxilary electrodes, nitrogen inlet and outlet
F. Teflon cup and support bar
G. Outlet to draw solution from cell

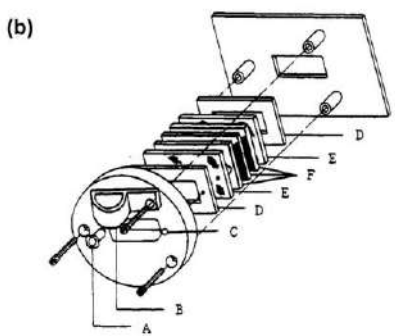

Construction of the OTTLE cell. The key is as follows: (A) inlet; (B) reservoir; (C) connection to reservoir; (D) Teflon gasket; (E) CaF_2 window; (F) gold minigrids (82% transmission) with spacers.

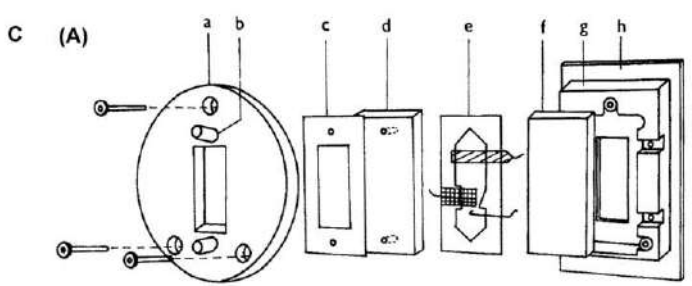

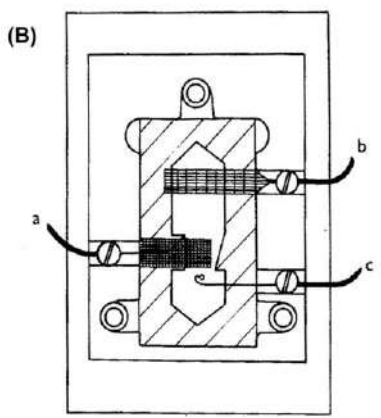

(A) Schematic diagram of the IR OTTLE cell with the three-electrode system placed inside the thin layer. (a) Steel pressure plate; (b) inlet; (c) Teflon gasket; (d, f) front and back KBr windows; (e) polyethylene spacer with melt-sealed electrodes; (g) Teflon holder; (h) back plate. (B) Front view of the cell composed of the parts (e)–(h) of (A) showing the position of the electrodes and their soldered contacts with Cu conductors fixed by screws. (a) Au minigrid working electrode with twinned contact Ag wire; (b) Pt mesh auxiliary electrode; (c) Ag wire pseudoreference electrode.

Figure 9.20 Cell design for IR spectroelectrochemistry reported by (a) Heineman *et al.*,[75] (b) Brisdon *et al.*,[76] and (c) Krejčic *et al.*[78] Adapted from ref. 75 with permission from American Chemical Society, Copyright 1968. Adapted from ref. 76 with permission from American Chemical Society, Copyright 1987. Adapted from ref. 78 with permission from Elsevier, Copyright 1991.

9.2.2 Raman Spectroscopy

Raman spectroscopy possesses a few key features that make it particularly relevant for the investigation of CO_2RR. Compared to IR spectroscopy, Raman spectroscopy does not suffer from the strong absorption by aqueous electrolytes. Furthermore, although Raman scattering in general struggles with low signal intensities, this drawback is mitigated by the surface enhancement Raman scattering (SERS) effect, similar to the SEIRAS effect for IR spectroscopy. The surface enhancement effect is much stronger in Raman spectroscopy, showing signal enhancements of up to a factor of 10^{14}.[9,81] Because of these features and the essential analytical information about surface species and the oxidation state of metallic electrodes, Raman spectroscopy is widely and successfully used for the investigation of electrochemical reactions.

Fleischmann *et al.* were the first to report the SERS effect in 1973.[82] Nowadays, it is generally accepted that the SERS effect arises from the contributions of two mechanisms, *i.e.* an electromagnetic enhancement mechanism due to the excitation of the localized surface plasmon resonance, and a chemical enhancement mechanism due to charge transfer between the electrode and molecules under investigation.[83–85] The SERS effect was initially observed mainly with coinage metals such as Au, Ag, and Cu, as these exhibit localized surface plasmon resonance covering the visible and near-infrared (NIR) radiation range due to their electronic structure. This property makes possible the use of NIR or visible lasers as excitation sources. Later, a few methods to prepare SERS active surfaces were developed.[86]

Depending on the electrode surface, there are a few possibilities to obtain the surface enhancement effect, as thoroughly described in the review by Tian.[85] The first approach is the enhancement of the Raman scattering signal by surface roughening, which can be conducted electrochemically by cycling the potential of the working electrode (see Figure 9.21a and b). Another approach is to deposit SERS-active NPs over a SERS inactive,

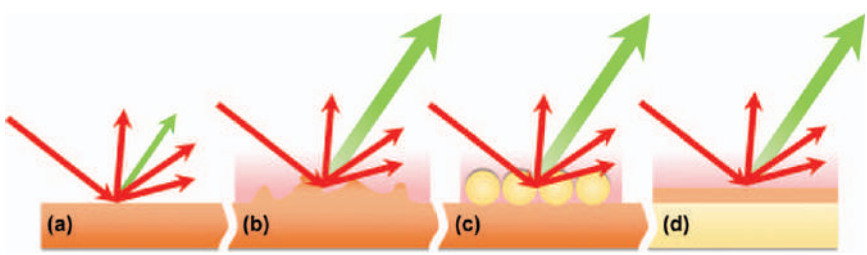

Figure 9.21 The surface enhancement Raman effect: (a) no enhancement, (b) enhancement due to surface roughness, (c) enhancement due to enhancing nanoparticles (NPs) on the surface, and (d) enhancement due to enhancing substrate, over which the material of interest is deposed. Red arrows: Rayleigh scattering; green arrows: Raman scattering.

electrically conductive substrate (see Figure 9.21c). Alternatively, a thin film made of the electrode material of interest can be deposited on a SERS active substrate (*e.g.* Au) (see Figure 9.21d). A drawback of SERS is the fact that it can be only applied to bulk metallic electrodes, pre-treated in such a way that they exhibit the surface enhancement effect, limiting the applicability of the surface enhancement effect to powdered electrocatalysts. However, SERS studies are very useful due to the high sensitivity of the technique, for detecting reaction species present in low concentrations close to the electrode surface. This leads to a better understanding of the mechanisms governing CO_2RR with various metals.

The experimental setup for Raman spectroscopy involves the use of a monochromatic radiation source (a laser) to excite the substrate, a filter which blocks the elastically scattered light and lets only the inelastically scattered light pass through an edge filter, a notch filter or a laser-line filter and finally a detector, *e.g.* a charge-coupled device (CCD) detector (see Figure 9.22a). The most widely used lasers for SERS studies are the 632.8 nm He–Ne laser and the 514 nm Ar^+ laser. With increasing wavelength, the intensity of the Raman signal decreases, but the negative effect of fluorescence on the Raman signal is also mitigated. A Nd:YAG 1064 nm laser was reported for a Fourier transform Raman (FT-Raman) study of CO_2RR on Cu in the 1-*n*-butyl-3-methyl imidazolium tetrafluoroborate ionic liquid.[87] However, FT-Raman is not so commonly used, as it has several disadvantages in terms of the presence of moving components in the devices and long acquisition time of the spectra.

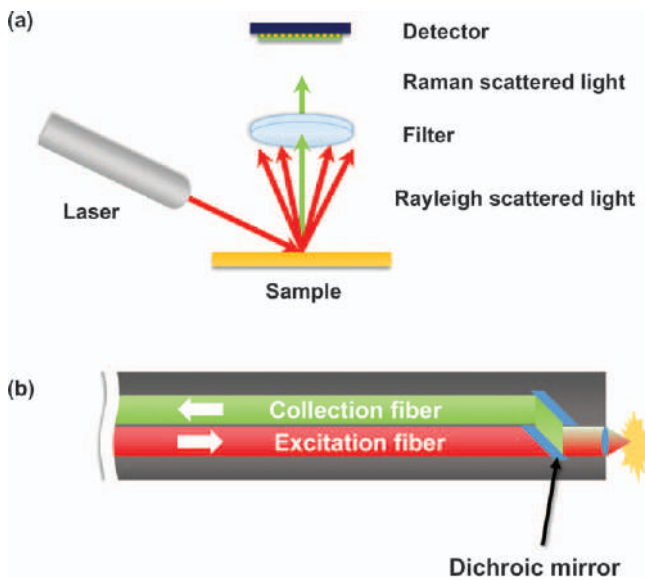

Figure 9.22 (a) Schematic representation of a Raman scattering experiment and the (b) immersion probe for Raman spectroscopy.

Modern Raman apparatus often use optical fibre immersion probes or confocal microscopes. With immersion probes, it is possible to investigate the electrode of interest *in situ*, as long as the electrolyte solution is not corrosive, or its temperature does not fall outside the operational temperature of the probe (see Figure 9.22b). The immersion probe combines an excitation fibre, a collection fibre, and a filter in a robust and compact assembly, which makes the application of Raman spectroscopy in electrochemical systems straightforward. Despite these advantages, Raman spectroscopy using immersion probes is seldom used in the spectroelectrochemical community, most likely due to the relatively poor sensitivity compared to IR spectroscopy.

The first cell design for Raman spectroelectrochemistry was reported by Fleischmann *et al.* (see Figure 9.23a).[88] They used a mirror finish silver working electrode, which was subjected to potential cycling to increase the roughness of the surface to achieve the SERS effect. Although the measured signal of adsorbed pyridine was higher than expected at that time due to the SERS effect, nowadays, this cell design can be regarded as outdated due to technological advances of Raman apparatus. Modern cell design of Raman spectroelectrochemical cells makes use of confocal Raman microscopes.

Ren *et al.* proposed a Teflon spectroelectrochemical cell with the working electrode facing upwards, without cell windows (see Figure 9.23b, left).[89] The motivation for this approach is the fact that Raman scattering is not influenced by air, glass, or (aqueous) electrolyte in its path. A confocal Raman microscope was used, with the lens pointing towards the working electrode from outside the solution, focusing the laser beam on a 3 μm spot on the working electrode surface.

This cell was later improved by the same group by adding a quartz window on top of the cell and using a thin electrolyte layer configuration, as gaseous species forming above the electrolyte solution can damage the objective and interfere with the Raman signal from the electrode surface (see Figure 9.23b, right).[90] Furthermore, if the solution is sensitive to air, the quartz window helps to avoid contamination. However, the mismatch of the refractive indices of the electrolyte, quartz, and air leads to distortion of the light as it travels from the source to the sample and back to the detector. Later, the authors proposed a water immersion objective approach, by placing a droplet of water between a long working distance (2.8 mm) objective and the quartz window of the spectroelectrochemical cell (see Figure 9.23c).[91] The electrolyte layer between the working electrode and the 0.17 mm quartz glass window in their study was 2 mm. The authors highlight that the Raman signal intensity is decreased by 50% using this approach, but, compared to the thin layer approach where the electrolyte layer thickness is ~0.2 mm, mass transport limitation issues are mitigated. By using the water immersion objective, the refractive index mismatch issue is diminished, and at the same time, the objective is protected from potential chemical degradation caused by the electrolyte solution. Another cell design approach using a water immersion objective was proposed by the group of Bell. This consists

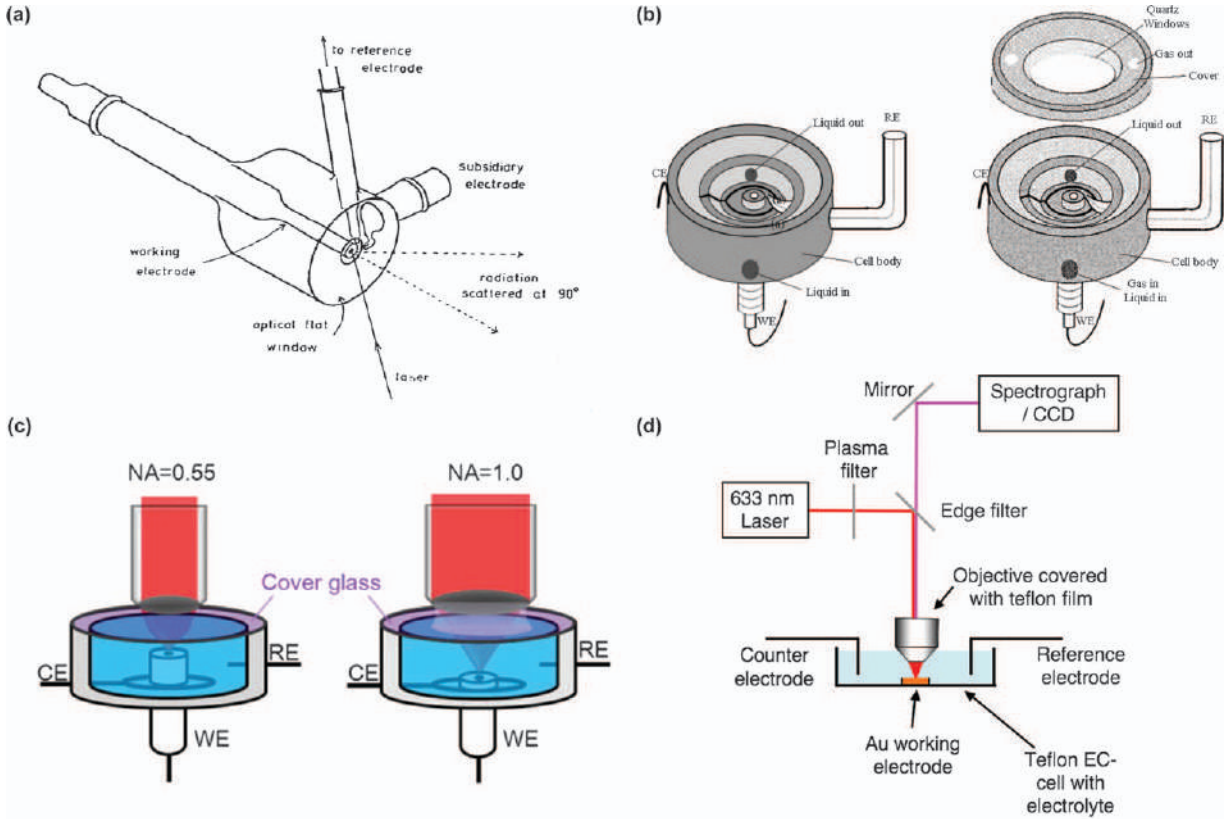

Figure 9.23 Raman spectroelectrochemical cell reported by (a) Fleischmann *et al.*, and further developed by (b) Ren *et al.* with a Teflon cell without windows (left) and a Teflon cell with a quartz window and a thin electrolyte layer (right). (c) Raman spectroelectrochemical cells with air-exposed objective (left) and water immersion objective (right) developed by the group of Ren. (d) Spectroelectrochemical cell design for Raman studies with PTFE-coated immersion objective developed by the group of Bell.
Adapted from ref. 88 with permission from Elsevier, Copyright 1974. Adapted from ref. 89 with permission from Elsevier, Copyright 2000. Adapted from ref. 90 with permission from SAGE Publications, Copyright 2003. Adapted from ref. 91 with permission from American Chemical Society, Copyright 2016. Adapted from ref. 92 with permission from John Wiley and Sons, Copyright © 2010 WILEY-VCH Verlag GmbH & Co. KGaA, Weinheim.

of covering the objective with a PTFE film to protect it from any destructive influence from the electrolyte and, as the refractive index of PTFE is almost similar to that of water, the issue related to the distortion of light is avoided (see Figure 9.23d).[92]

For a detailed review of the application of Raman spectroscopy to electrochemical reactions and a more thorough discussion on cell design, the reader is referred to the perspective paper by Deng and Yeo.[93]

9.2.2.1 Application in Heterogeneous Systems

Raman spectroscopy was successfully applied to the investigation of CO_2RR with various metallic electrodes, including Au, Ag, Cu, Cu–Zn, and Sn.[87,94–104] Most of the literature reports of Raman spectroelectrochemical studies of heterogeneous CO_2RR involve the preparation of SERS active substrates by electrochemical roughening. In this way, SERS active substrates are easily achieved for metals such as Ag, Au, Pt, and Cu.

Oberst *et al.* investigated CO_2RR at a SERS-active Au electrode in a KOH electrolyte solution.[95] In a previous study with organometallic Ag catalysts, it was found that nitrogen-containing ligands, such as pyrazole, phtalocyanine, 3,5-diamino-1,2,4-triazole, and tris(2-pyridylmethyl)amine increase the efficiency of CO_2RR.[105] Based on these findings, the influence of a few nitrogen-containing additives on the efficiency of CO_2RR was studied. Taking advantage of the SERS effect, the authors observed a band characteristic to adsorbed CO on atop Au sites at 2120 cm^{-1}, if either pyrazole, ethanolamine, or benzotriazole were present in the electrolyte solution purged with CO_2 (see Figure 9.24b and c). A Stark shift of 30–40 $cm^{-1}\,V^{-1}$ for this band was observed, consistent with previous literature reports (see Figure 9.24d).[106] The CO characteristic band was not observed without the presence of additives in the electrolyte (see Figure 9.24a). Correlating the spectroscopic observations with results of voltammetric experiments, indicating no increased activity towards CO_2RR due to additives, the authors concluded that the role of the additives is to increase the CO_2 concentration near the electrode surface, due to the CO_2 scavenging abilities of *e.g.* ethanolamine.

In their spectroscopic study of CO_2RR by Cu in acetonitrile (see also the section on IR spectroscopy), Figueiredo *et al.* made use of SERS spectroscopy to observe CO formation. Since this would be challenging to observe solely by FTIR, this study elegantly shows the complementarity of the two vibrational techniques (see Figure 9.25).[37] Emerging bands at 283 and 382 cm^{-1} at potentials more negative than −1.4 V *vs.* Ag/Ag^+ were assigned to the restricted rotation of bound CO and the Cu-CO stretching mode, respectively.[97,99,107] A band at 423 cm^{-1} was tentatively attributed to either (bi)carbonate species or a poisoning species formed during the course of reaction. Bands between 2028 and 1999 cm^{-1}, 2066 and 2030 cm^{-1}, and 2102 and 2087 cm^{-1} were assigned to adsorbed CO stretching on Cu. The redshift of the bands with increasingly negative potential can be attributed

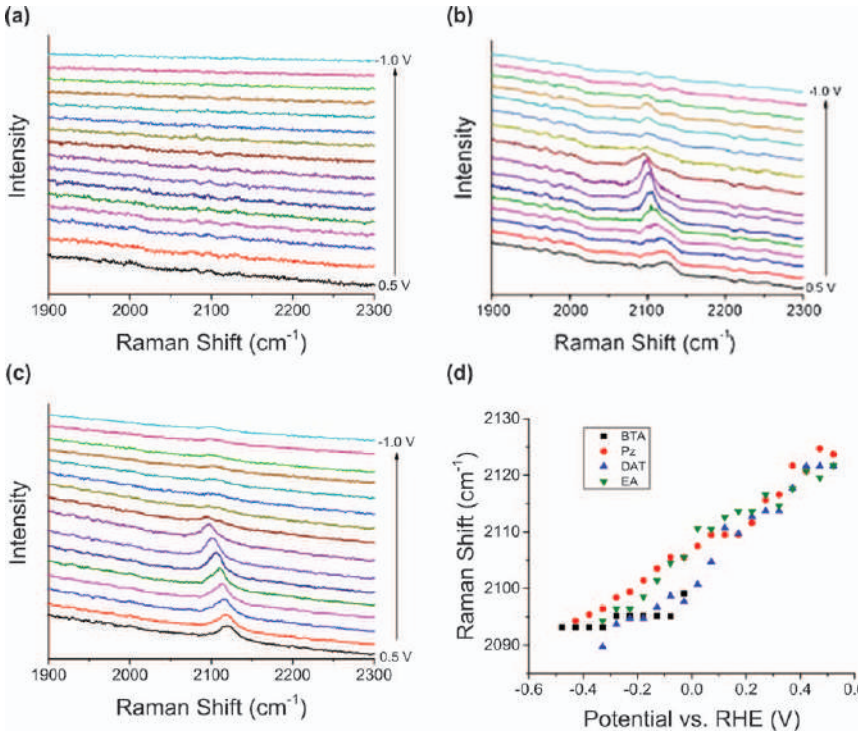

Figure 9.24 *In situ* Raman spectra at a Au electrode recorded between 0.5 and −1.0 V *vs.* Ag/AgCl in a 1 M KOH + saturated $Ca(OH)_2$ electrolyte with (a) CO_2 sparging and in presence of 10 mM (b) pyrazole and (c) ethanolamine. (d) Stark shift of the CO stretching peak as a function of applied potential for electrolytes containing different additives.
Reproduced from ref. 95 with permission from Springer Nature, Copyright 2015.

to the Stark effect. The degree of redshift indicates the adsorption strength of CO on Cu, *i.e.* the bands at 2030 and 2070 cm^{-1} correspond to strongly bound CO, as they are shifted by 29 $cm^{-1}V^{-1}$ and 36 $cm^{-1}V^{-1}$, respectively. The band at 2102 cm^{-1} corresponds to weakly physisorbed CO, as it only shifts by 13 $cm^{-1}V^{-1}$. The appearance of CO-characteristic bands in the Raman spectra at a potential as low as −1.2 V *vs.* Ag/Ag^+ indicates that CO is formed before bicarbonates, which form at −1.8 V *vs.* Ag/Ag^+. The authors concluded that the two reaction products are formed *via* two different reaction pathways when wet solvent is used, *i.e.* CO is formed from CO_2 reduction by residual water, and carbonates by the reaction of CO_2 with OH^- species.

For a Cu electrode in $NaHCO_3$ electrolyte, Smith *et al.* also observed bands emerging at 280, 358, and 2090 cm^{-1} at −1.06 V *vs.* NHE, which were assigned to adsorbed CO (see Figure 9.26).[99] The authors associated the decrease of the bands over time with poisoning of the reaction at the

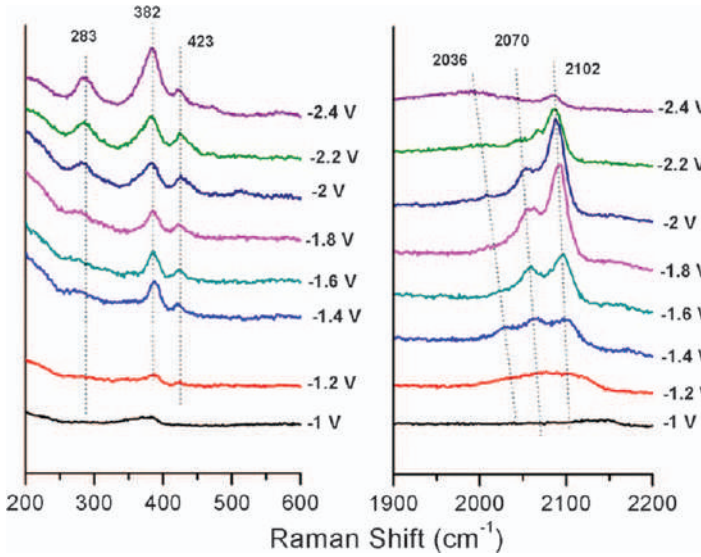

Figure 9.25 *In situ* Raman spectra recorded during CO_2RR at a Cu electrode in 0.1 M $TEABF_4$ in acetonitrile as a function of applied potential. Reproduced from ref. 37 with permission from American Chemical Society, Copyright 2016.

electrode surface. A band at 1050 cm^{-1} was attributed to carbonate species, and the broad band at 2900 cm^{-1} and the weak band at 1450 cm^{-1} were assigned to the C–H stretching vibrations of an intermediate species. The authors correlated the band appearing at 523 cm^{-1}, and increasing with time, to a poisoning species, presumed to be a copper patina consisting of either surface copper oxide, copper hydroxide, or copper carbonate.

Dutta *et al.* investigated the change in the oxidation state of SnO_2 NPs during CO_2RR in NaOH electrolyte solution at pH values of 8.5, 9.7, and 12.[104] SnO_2 exhibits a strong Raman band at 623 cm^{-1} corresponding to the A_{1g} mode of SnO_2 (see Figure 9.27a). The evolution of this band with potential variation was monitored, and it was observed that the reduction of SnO_2 to metallic Sn takes place at potential values much lower than those predicted by Pourbaix diagrams, at all pH values investigated (see Figure 9.27b). The highest efficiency towards CO_2RR does not correspond to fully reduced Sn NPs, but rather to partially reduced tin oxide at around −1 V *vs.* Ag/AgCl (see Figure 9.27c). It is notable in this report that the SnO_2 NPs were drop-cast over a GC electrode, which exhibits no SERS effect. This explains why no species related to CO_2RR were observed during the experiments and only strong bands of SnO_2 were detected. We envision that the approach of NP deposition over a SERS active metallic electrode (*e.g.* Au) could lead to a more detailed level of spectral information and would contribute to the development of the field of Raman spectroscopy applied to the investigation of powdered electrocatalysts.

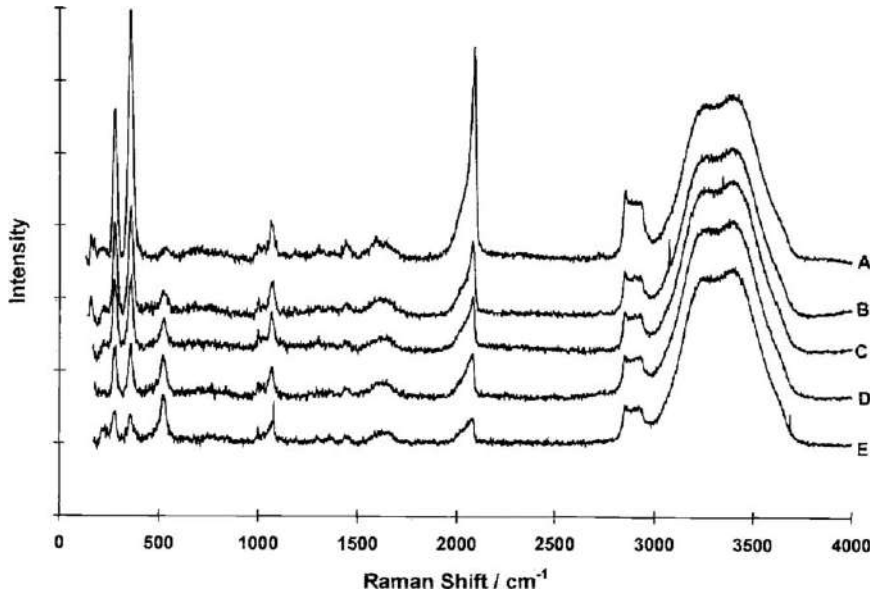

Figure 9.26 *In situ* Raman spectra of CO_2RR at a Cu electrode in $NaHCO_3$ electrolyte at −1.06 V *vs.* NHE as a function of time, *i.e.* (A) 13, (B) 61, (C) 105, (D) 144, and (E) 215 min.
Reproduced from ref. 99 with permission from IOP Publishing, Copyright 1997.

9.2.2.2 Application in Homogeneous Systems

For the study of homogeneous systems for CO_2RR, resonance Raman is a particularly attractive technique. The particularity of the technique is the use of lasers with a wavelength frequency close to the frequency of an electronic transition in the molecular complex under investigation. Resonance Raman allows one to obtain significant signal enhancements of up to 10^6. The electronic transitions in the molecule enhance certain Raman active modes, offering information about the structure of molecular electrocatalysts. By tuning the laser wavelength, excitation of different electronic transitions can be targeted, *e.g.* metal-to-ligand charge-transfer (MLCT) or intraligand charge-transfer (ILCT) transitions, which exhibit different Raman spectra. For example, if resonance Raman spectra in resonance with an MLCT transition in a molecular catalyst are recorded while the electrode potential is varied, changes in the ligand structure of the catalyst induced by a change in the oxidation state of the metal centre can be observed. If the excitation of ILCT transitions is targeted, recorded resonance spectra can indicate changes of the ligands' structure induced by electronic charge redistribution in the ligands. Unfortunately, the number of reports of *in situ* resonance Raman studies on molecular electrocatalysts is scarce due to the rather limited versatility of this technique.[108,109] However, it can be very powerful

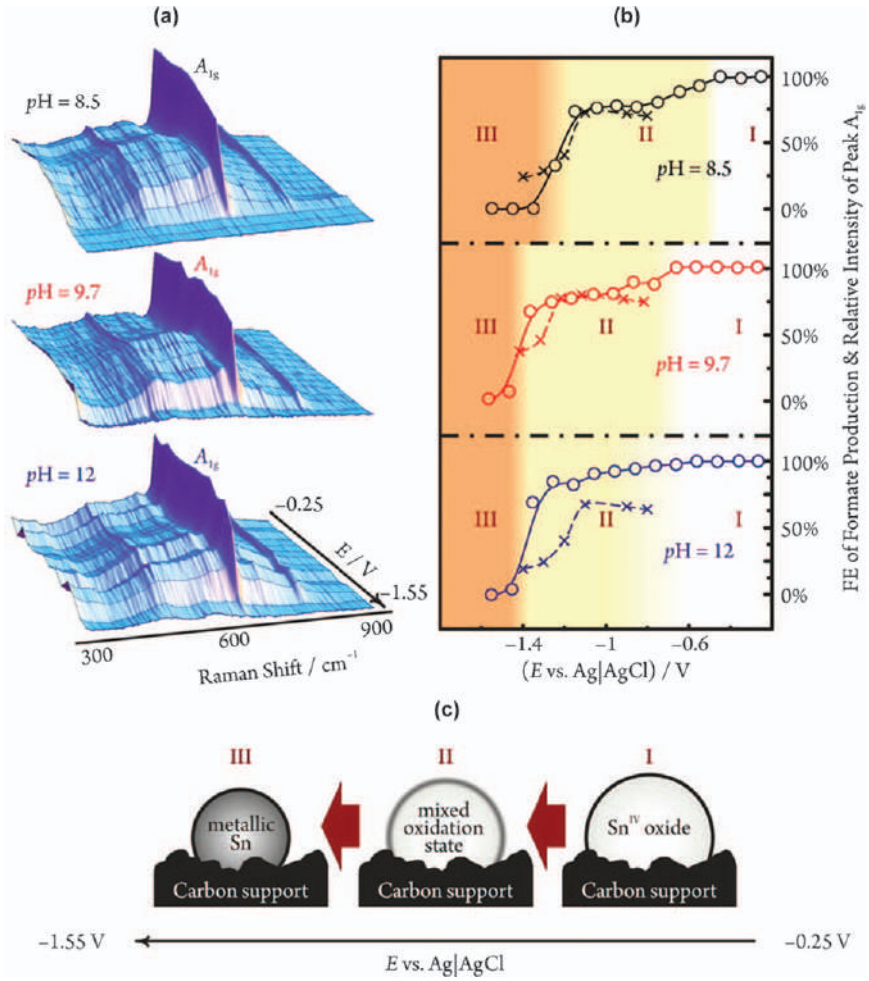

Figure 9.27 (a) Raman spectra of a SnO_2 electrocatalyst for CO_2RR in NaOH electrolyte. (b) Evolution of the A_{1g} band of SnO_2 (circles, solid line) as a function of applied potential and pH of the electrolyte solution and faradaic efficiency towards formate (crosses, dashed line). (c) Schematic representation of the reduction of SnO_2 NPs as a function of applied potential. Reproduced from ref. 104 with permission from American Chemical Society, Copyright 2015.

for elucidating catalyst structure changes induced by the electric potential. Spectroelectrochemical cells using the OTTLE approach can be coupled to Raman spectrometers or confocal microscopes that allow for laser frequency tuning for experimental implementation.

The use of Raman spectroscopy for the investigation of the [Re(Cl)(bpy-R)(CO)$_3$] molecular complex, which is active for CO_2RR was reported by van Gastel.[110] The authors investigated *ex situ* the structure of the oxidized, the

monoreduced and the doubly reduced complexes in acetonitrile solution using a Raman microscope. Based on spectroscopic data, the authors proved that the bipyridine ligand is involved in the activation of CO_2 along with the rhenium metal centre.

9.3 X-ray Absorption Spectroscopy for the Investigation of Electrochemical CO_2 Reduction

X-ray absorption spectroscopy (XAS) is one of the newest of the spectroscopic techniques, applied for the study of CO_2RR, gaining interest and popularity with the development of synchrotron X-ray sources in the 20th century. *In situ* XAS is used to determine changes in the local environment of atoms and in the oxidation state of either the electrodes in heterogeneous systems, or of the molecular catalysts in homogeneous systems under reaction conditions. The use of ''hard'' X-rays for XAS reduces the absorption of radiation by light elements such as H, C, N, and O, which makes cell design for *in situ* XAS studies a much easier task compared to cell design for vibrational spectroscopic studies. XAS is, traditionally, a bulk technique compared to the vibrational spectroscopic techniques, which can have some degree of surface sensitivity, depending on the sampling configurations as described in earlier sections.

The mechanism of X-ray absorption follows the Beer–Lambert law. A typical X-ray absorption spectrum is a plot of the absorption coefficient *vs.* the energy of X-ray photons. Every element exhibits specific X-ray absorption edges corresponding to promotion of electrons from core levels to either empty valence levels or into the continuum. The energy of the absorption edge depends on the oxidation state of the element. In this way, the latter can be identified from the position of the absorption edge, by comparing it to that of a reference material. When the energy of X-ray photons is increased further after the absorption edge, generated photoelectrons are ejected into the continuum, accompanied by the formation of a wave. When the probed atoms are in a lattice, the photoelectrons which form due to the absorption of X-ray radiation are scattered by the neighbouring atoms. The wave formed due to the scattering of the photoelectrons can interfere (constructively or destructively) with the wave formed due to the photoelectron ejection to the continuum. This interference phenomenon gives rise to a fine structure after the absorption edge, and information regarding the neighbouring atoms, interatomic distances, and coordination can be extracted.

Two measurement configurations are common for XAS studies, *i.e.* transmission and fluorescence (see Figure 9.28a and b). The choice of configuration is determined by the sample type under investigation. Typically, the transmission mode is used for thinner samples (<1 μm) and samples of higher concentration. Here, the uniform thickness of the sample is critical for obtaining accurate results. The fluorescence mode is used for the

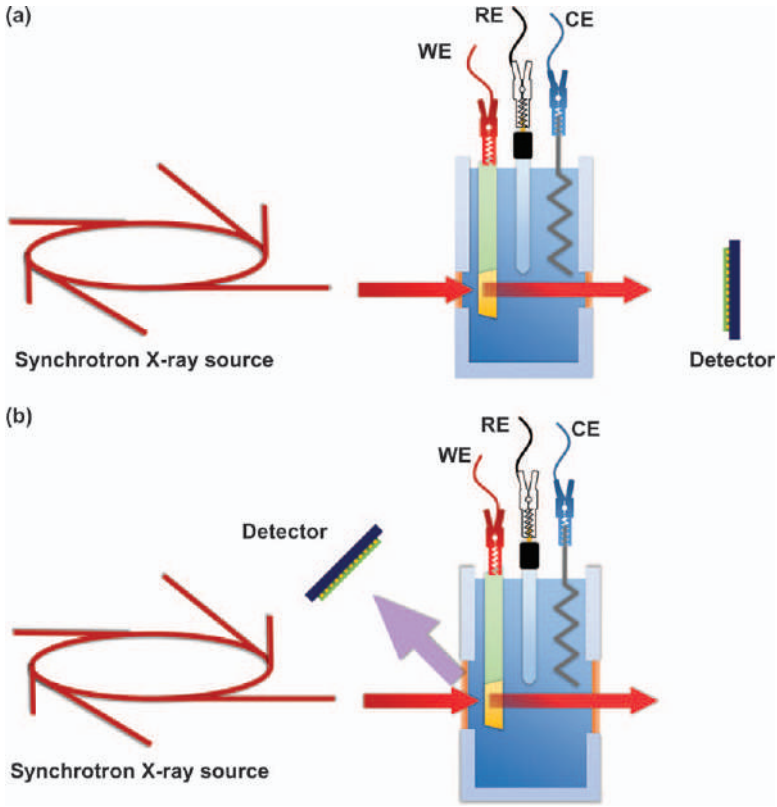

Figure 9.28 XAS measurement configurations for the investigation of electrochemical reactions, *i.e.* (a) transmission and (b) fluorescence configuration.

analysis of thick samples and for highly diluted samples. The use of fluorescence mode for samples of high concentration is not advised, as self-absorption can occur, which attenuates the fluorescence signal. The study of nanostructured electrocatalysts is possible and more easily implemented for XAS compared to vibrational techniques. This is done by directly depositing the catalyst materials on conductive support materials, *e.g.* carbon paper which acts as working electrode.

Nevertheless, there are a few considerations to keep in mind when designing cells for *in situ* XAS. Although water is less of a problem in XAS, the electrolyte solution, which for CO_2RR often contains potassium or sodium (bi)carbonate can give some attenuation of the X-ray beam travelling through the cell. Therefore, the thickness of the electrolyte layer is an important factor that can influence the quality of the acquired data, although this is not as critical as with IR spectroelectrochemistry where the thin electrolyte layer approach is used. The cell windows should be manufactured from a chemically inert, resistant, and X-ray transparent polymer material, such as Kapton.

For more information on the historical development and applications of XAS, as well as for a detailed explanation of the X-ray absorption mechanism and some implementation examples, the review paper by Sharpe *et al.* and the more recent one by Wang *et al.*, as well as the chapter by Minguzzi and Ghigna, offer very useful insights.[111–113]

9.3.1 Application in Heterogeneous Systems

One may argue on the necessity of applying *in situ* XAS, taking into account its main inherent challenge, *i.e.* the need of synchrotron radiation for the investigation of electrode materials. In principle, information regarding the oxidation state of the metals can be derived from less technically demanding and time-consuming means. The oxidation state of metals at different applied potentials as a function of pH, for example, is available from Pourbaix diagrams. However, Pourbaix diagrams only indicate the most thermodynamically stable phases and, as already mentioned in the earlier sections, the suggested oxidation states do not always coincide with data acquired by spectroscopic techniques, which are more accurate for the specific electrodes and electrolyte solutions used.

The use of XAS for investigating CO_2RR is gaining more and more interest in recent years, with several reports emerging for various metal electrodes and nanoparticulate electrocatalysts, including Zn, Cu, Fe, Sn, Fe_3S_4 and Ni.[114–123] A robust flow electrochemical cell design for *in situ* XAS for the investigation of heterogeneous electrocatalysts was proposed by Binninger *et al.*[124] The cell is designed for both transmission and fluorescence configurations and consists of three parts (see Figure 9.29a). The window material is Kapton. The electrolyte layer thickness in the path of the X-ray beam is 2 mm. The working electrode consists of an electrically conductive Kapton film, over which the powdered catalyst is deposited by spray coating (see Figure 9.29b). The counter electrode also consists of an electrically conductive Kapton film, spray-coated with high surface area active carbon. A commercial Ag/AgCl reference electrode can be connected and used for the cell (see Figure 9.29c).

Although the authors did not use their cell for the study of CO_2RR, it would be feasible, by spray-depositing the catalysts over the conductive Kapton tape and choosing the appropriate electrolyte. The main advantage of the cell is that the electrolyte flows through the cell during measurements, carrying away bubbles that might form at the electrode surface. At the same time, mass transport limitations are diminished by the continuous replenishment of the electrolyte. A similar cell for small angle X-ray scattering studies on a laboratory-scale diffractometer was reported by the same group.[125]

A notable case of this technique is the so-called soft XAS (sXAS). Although the experimental implementation and data treatment of sXAS is more difficult, it offers the possibility to investigate light elements, such as oxygen, carbon, or nitrogen that are often present in the composition of

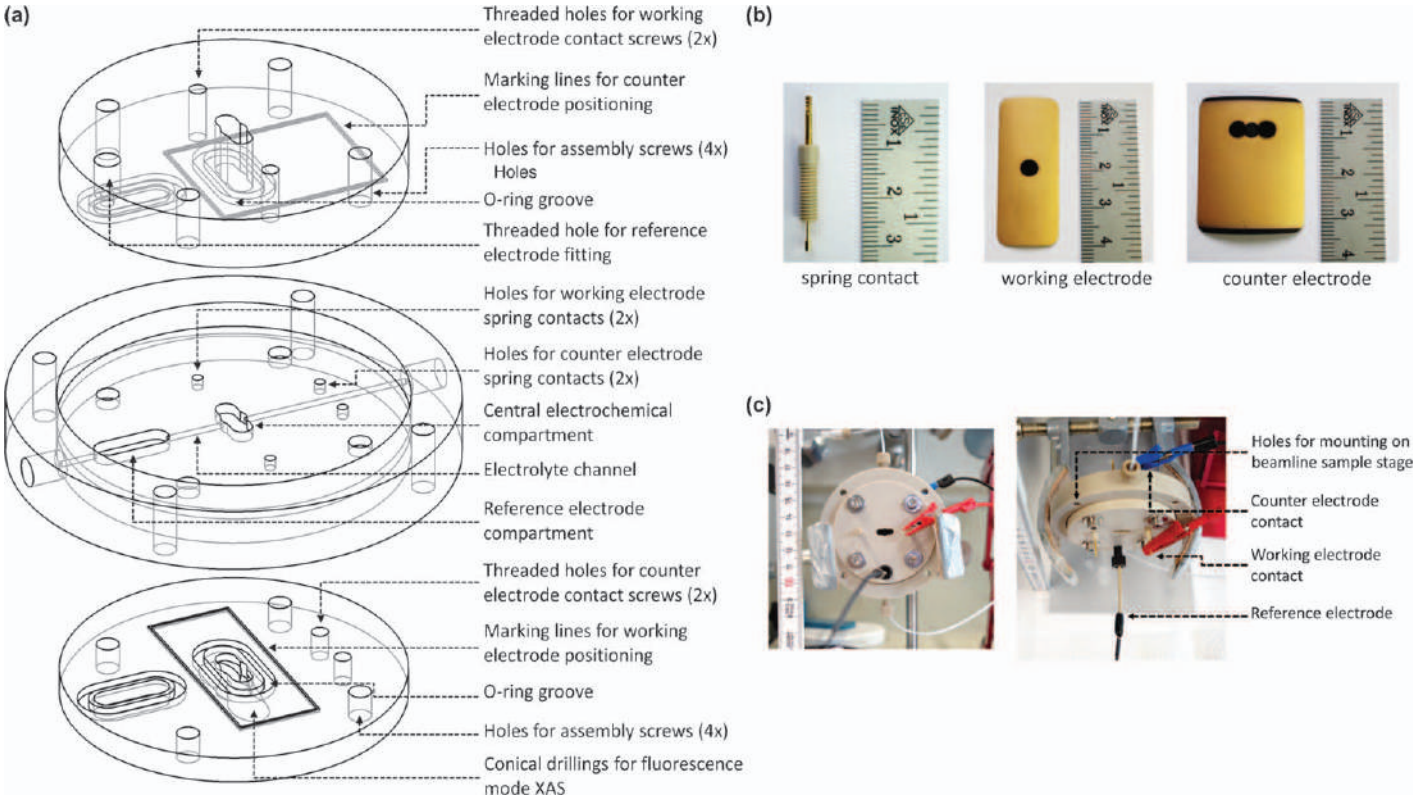

Figure 9.29 (a) Exploded view of a XAS flow cell, (b) spring contact and Kapton tape spray-coated working and reference electrodes, and (c) assembled view of the cell.
Adapted from ref. 124, http://dx.doi.org/10.1149/2.0201610jes, under the terms of the CC BY 4.0 license, http://creativecommons.org/licenses/by/4.0/.

electrocatalysts. In this way, the formation and reduction of oxides can be monitored *in situ*. The main challenge is the low penetration depth of soft X-ray in liquids and the need of placing the cell and the detector in vacuum chambers because of the high absorption of soft X-rays by gas. Ishihara *et al.* proposed a noteworthy cell design for sXAS.[126]

Rosen *et al.* investigated CO_2RR to CO in 0.5 M $NaHCO_3$ using a nanostructured Zn dendrites catalyst.[114] The stability of the electrode at different applied potentials was tested using *in situ* XAS. At −0.5 V *vs.* RHE, the oxidation of metallic Zn to Zn^{2+} was observed, associated with the shifting of the Zn K-edge towards higher energy values (see Figure 9.30a). Starting from −0.7 V *vs.* RHE and lower potentials, the Zn dendrites electrode is stabilized, as the absorption edge during electrolysis matches the K-edge of metallic Zn. In the Fourier transform extended X-ray absorption fine structure (EXAFS) spectra, the distance of ∼2.3 Å agrees with a Zn–Zn bond (see Figure 9.30b). The EXAFS spectrum of the material after reaction does not fully match either the reference spectrum of metallic Zn foil, or that of ZnO (see Figure 9.30c). The authors suggest the formation of an amorphous ZnO. The change in oxidation state of Zn during 1 h of electrolysis at −0.5 V *vs.* RHE was monitored. The shift of the absorption edge towards higher energy is a clear indication of the oxidation of Zn to ZnO (see Figure 9.30d).

Mistry *et al.* studied CO_2RR to ethylene over plasma-activated Cu foils.[115] Cu_2O and CuO form at the surface of the foils after O_2 plasma treatment. During electrolysis at −1.2 V *vs.* RHE in 0.1 M $KHCO_3$, X-ray absorption near edge structure (XANES) spectra indicated the reduction of copper oxides to metallic Cu after one hour (see Figure 9.31a). However, the selectivity towards ethylene did not change during the course of the reaction and the authors concluded that Cu^+ species are still present at the surface of the foils after the 1 h electrolysis. This was confirmed by scanning transmission electron microscopy (STEM) studies but not observed in the XANES spectra, which reflect to a higher degree the bulk composition of the samples, rather than the surface. EXAFS spectra of the plasma-activated Cu foils before electrolysis confirm the presence of metallic Cu and copper oxides (see Figure 9.31b). *In situ* EXAFS spectra clearly indicate the reduction of CuO and Cu_2O to metallic Cu within one hour of electrolysis (see Figure 9.31c).

In situ sXAS was used by De Luna *et al.* to investigate CO_2RR to ethylene with a electroredeposited (ERD) Cu catalyst in 0.5 M $KHCO_3$.[116] Unlike hard X-rays which are able to probe high-energy transitions, soft X-rays are able to measure lower energy 2p electron excitations to the 3d shell. Such transitions are more sensitive to electronic structure changes and the acquired spectra can offer more information than the high-energy transitions. The reduction of copper from Cu^{2+} to Cu^0 with increasingly negative potential was observed by following changes in the L-edge of Cu (see Figure 9.32a). At an applied potential of 0.28 V *vs.* RHE, Cu^{2+} was quickly reduced to Cu^+. It is notable that the reduction of Cu^{2+} to Cu^+ takes place within 5 min after the application of the potential, but the reduction of Cu^+ to Cu^0 is much slower. After one hour of electrolysis, ∼23% of the copper in

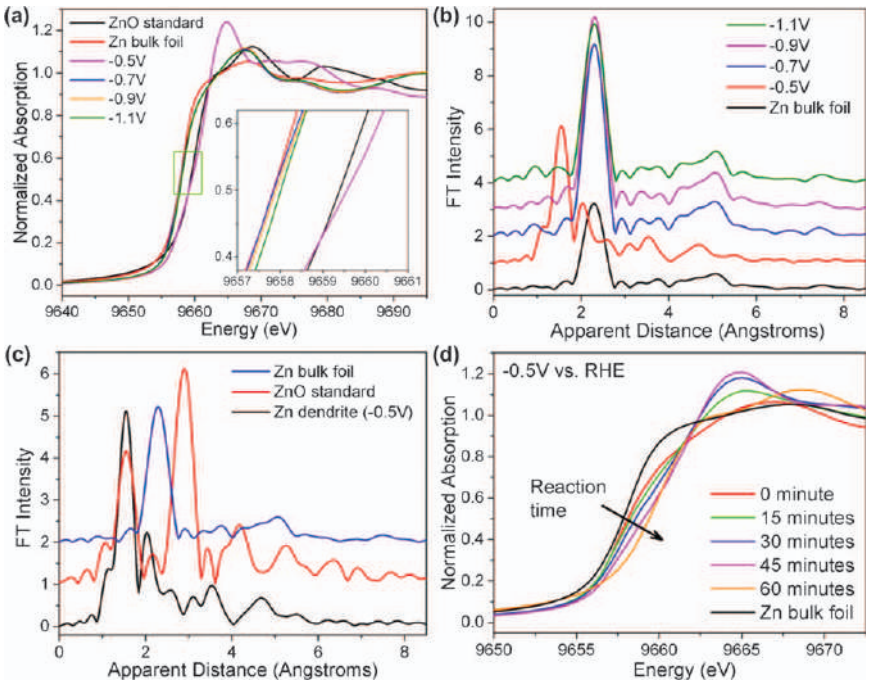

Figure 9.30 *In situ* (a) XANES and (b) EXAFS spectra of the Zn dendrites electrode at different applied potentials, (c) EXAFS spectra of a Zn dendrite electrode after 1 h of electrolysis at −0.5 V *vs.* RHE, and (d) *in situ* XANES spectra of the catalyst as a function of electrolysis time.
Reproduced from ref. 114 with permission from American Chemical Society, Copyright 2015.

the electrocatalyst is present as Cu^+ species (see Figure 9.32b–e). From DFT studies, the authors concluded that Cu^+ species are responsible for shifting the product selectivity from C_1 to C_2 compounds. The stability of Cu^+ species is a key factor of the efficiency of these catalysts.

XAS was used for *in situ* studies on highly active CO_2RR catalysts consisting of O- and N-doped carbon-supported Fe oxyhydroxide clusters. The oxidation state of iron in the catalysts was first determined from XANES spectra recorded *ex situ*.[118] By comparing the spectra of the catalysts to the spectra of Fe_3O_4 and Fe_2O_3, the authors concluded that Fe is present as Fe(III) species. Furthermore, *in situ* measurements under CO_2 electrolysis conditions were conducted. For the N-doped carbon support, the decrease in intensity of the pre-edge feature at 7114.5 eV, and the shift of the absorption edge towards lower energy by 2 eV as the potential is varied from the open circuit potential (OCP) to −0.5 V *vs.* Ag/AgCl, were observed. At −2 V *vs.* Ag/AgCl the iron species are reduced to Fe^0 (see Figure 9.33a). The changes in the XANES spectra at OCP and at −0.5 V *vs.* Ag/AgCl do not clearly indicate the formation of Fe(II) species, so the authors fitted a spectrum arising from both Fe(III)

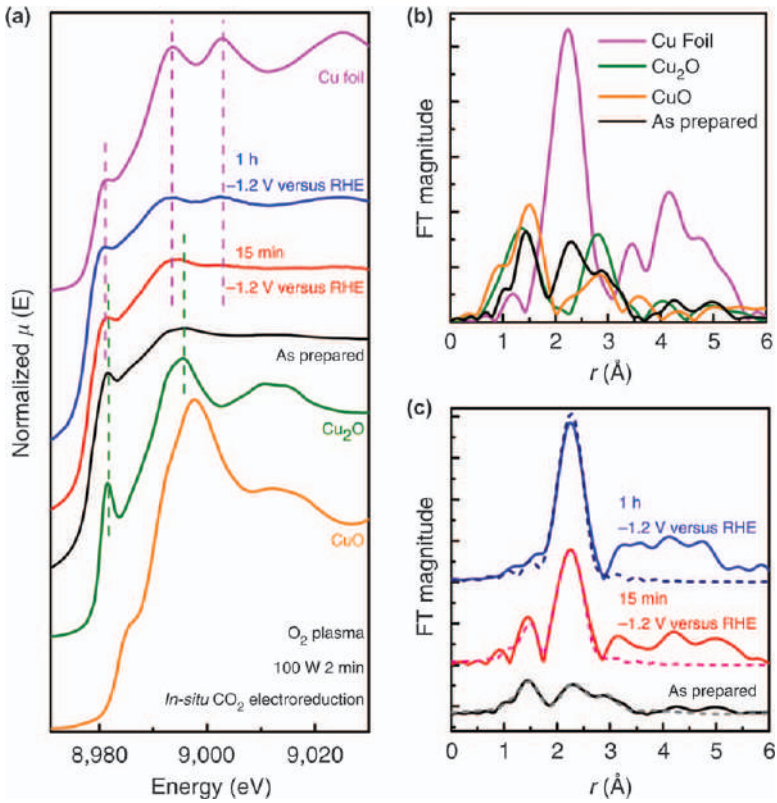

Figure 9.31 (a) *In situ* XANES spectra of plasma–activated Cu foil during electrolysis, (b) Fourier transform EXAFS spectra of the Cu foil along with the reference spectra, and (c) *in situ* Fourier transfer EXAFS spectra of the plasma–activated Cu foil.
Reproduced from ref. 115, https://doi.org/10.1038/ncomms12123, under the terms of the CC BY 4.0 license, http://creativecommons.org/licenses/by/4.0/.

species and Fe^0. After calculating the difference between the experimentally acquired spectrum and the fitted spectrum, a new spectrum resembling the structure of FeO (wüstite) was obtained (see Figure 9.33b). For determining the coordination of the iron atoms under reaction conditions, the EXAFS spectrum of the Fe/N–C catalyst was compared to the simulated spectra of ferrihydrite and wüstite. The authors concluded that the EXAFS spectrum represents a mixed valence Fe(III)/Fe(II) compound (see Figure 9.33c).

Changes in the oxidation state with applied potential for a tin oxide-containing catalyst for CO_2RR to formate in a bicarbonate solution (pH 8.5) were monitored by Dutta *et al.*[120] The XANES spectrum of the as-synthesized catalysts resembles the spectrum of a SnO_2 reference, with the Sn K-edge position at 29 205 eV (see Figure 9.34a). The −1.15 V *vs.* Ag/AgCl negative potential is not enough to start the reduction of the SnO_2 NPs, but at −1.55

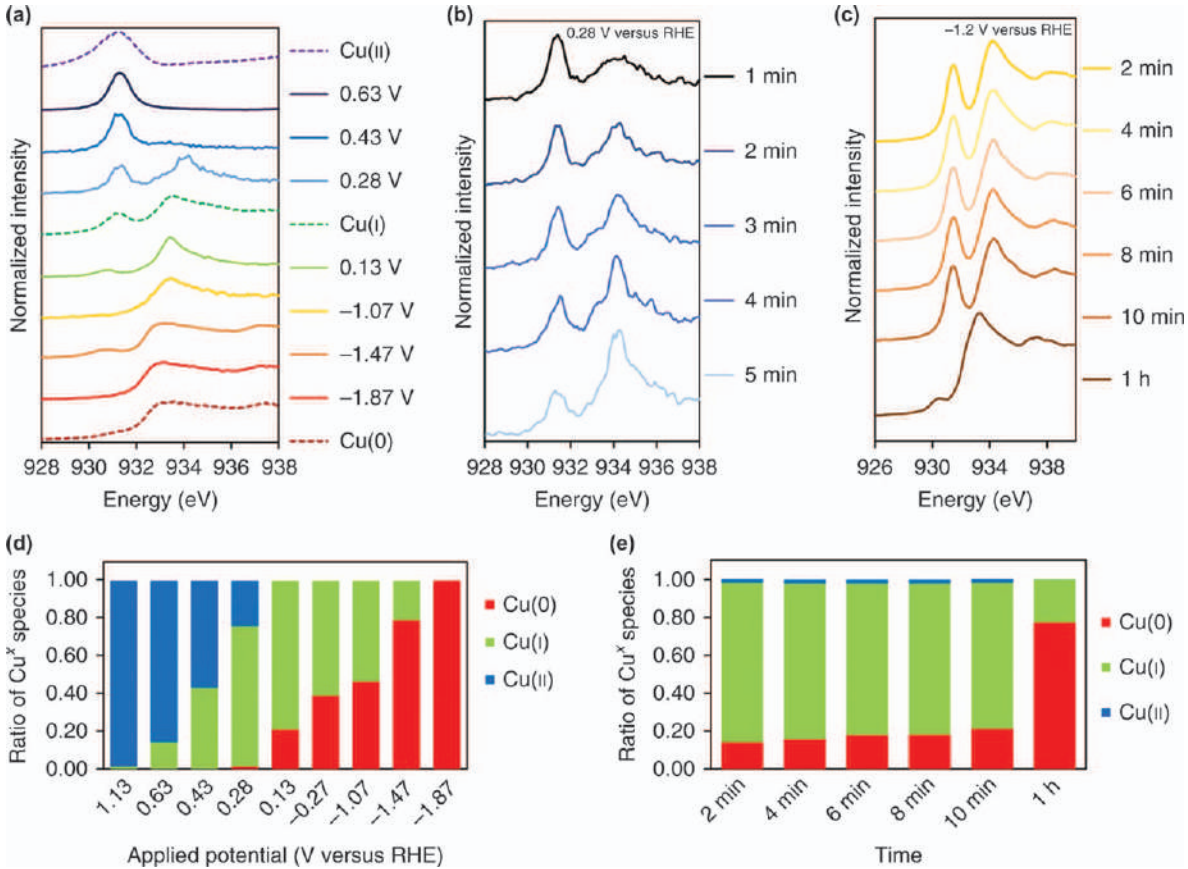

Figure 9.32 (a) Cu L-edge sXAS spectra of ERD Cu catalysts at different potentials, (b) sXAS spectra of Cu ERD catalysts at 0.28 V *vs.* RHE as a function of time, (c) sXAS spectra of Cu ERD catalysts at −1.2 V *vs.* RHE as a function of time, and (d) ratio of Cu species as a function of electrolysis time, determined by fitting sXAS spectra.
Adapted from ref. 116 with permission from Springer Nature, Copyright 2018.

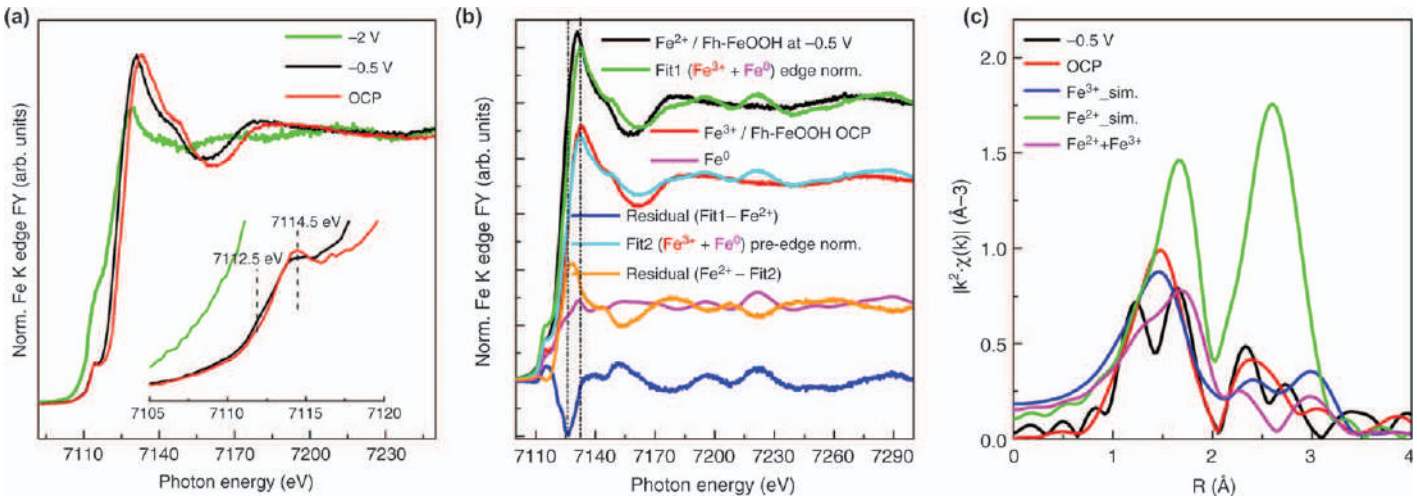

Figure 9.33 (a) XANES spectra of Fe/N–C catalysts in 0.05 M $KHCO_3$, (b) normalized Fe K edge spectra of Fe/N–C at −0.5 V *vs.* Ag/AgCl in 0.05 M $KHCO_3$ (black line); Fe/N–C at OCP in 0.05 M $KHCO_3$ component of the fit (red line); Fe foil component of the fit (magenta line); envelope of Fe/N–C at −0.5 V *vs.* Ag/AgCl with the Fe(III) component (Fe/N–C at OCP) and Fe^0 component (Fe foil) in "Fit 1" (green line); difference spectrum: "Fit 1" – Fe/N–C at −0.5 V *vs.* Ag/AgCl (blue line); "Fit 1" normalized to the pre-edge in Fe/N–C at −0.5 V *vs.* Ag/AgCl in 0.05 M $KHCO_3$ (cyan line); difference spectrum: Fe/N–C at −0.5 V *vs.* Ag/AgCl – "Fit 2" (orange line), (c) Fourier transform EXAFS spectra of: Fe/N–C at −0.5 V *vs.* Ag/AgCl in 0.05 M $KHCO_3$ (black line); Fe/N–C at OCP in 0.05 M $KHCO_3$ (red line); simulations of EXAFS signal for ferrihydrite (Fh)–FeOOH (blue line), wüstite (green line), and a mixture of Fh–FeOOH and wüstite 1 : 1 (magenta line).

and −1.70 V *vs.* Ag/AgCl, the shift of the Sn K-edge towards lower energy values indicates the reduction of SnO_2. By fitting the experimental XANES spectra, the authors were able to determine the ratio of SnO_2 to Sn in the catalysts as a function of applied potential (see Figure 9.34b). In the EXAFS spectra, the intensity of the peak characteristic for Sn–O bonds in SnO_2 gradually decreased in size, and at the same time, the peak characteristic for Sn–Sn bonds increased with more negative potential (see Figure 9.34c). Interestingly, SnO, which should be an intermediate in the reduction of SnO_2 to metallic Sn, was not clearly observed, although a low-intensity peak in the EXAFS spectra was tentatively attributed to it.

The activation and reduction of CO_2 were experimentally observed for a single-Ni-atom catalyst using *in situ* XAS by Yang *et al.*[122] When the $KHCO_3$ electrolyte solution purging was changed from Ar to CO_2, a shift of the absorption edge by 0.4 eV to higher energy indicated the increase of Ni oxidation state. The authors correlated this to the delocalization of the unpaired electron in the $3d_{x2-y2}$ orbital and the charge transfer from Ni(I) to the 2p orbital of carbon in CO_2, leading to the formation of $CO_2^{\delta-}$ species (see Figure 9.35a). At −0.7 V *vs.* RHE, the absorption edge shifted by −0.2 eV to a lower energy, which indicates the reduction of Ni after one cycle of CO_2RR. The EXAFS spectrum showed an increase in intensity of the peak at 1.45 Å, associated with the Ni–N bond, due to a contribution from the Ni–C bond overlapping with the Ni–N bond (see Figure 9.35b). Applying −0.7 V *vs.* RHE leads to a shift of the peak by 0.04 Å, indicating a Ni–N bond length increase during the reduction of CO_2.

9.3.2 Application in Homogeneous Systems

Despite the popularity of XAS for the study of heterogeneous CO_2RR, reports of using this technique for the investigation of molecular catalysts are limited. Wei *et al.* reported an *in situ* XAS cell for the investigation of molecular catalysts, including heterogenised molecular catalysts (see Figure 9.36).[127–129]

The XAS investigation of a heterogenised, carbon nanotube-anchored Zn–porphyrin complex active for CO_2RR indicated no changes in the XANES spectra under *in situ* conditions in a potential range from −1.7 V to +0.2 V *vs.* SHE (see Figure 9.37a).[128] Based on this observation, the authors concluded that the Zn metal centre does not change its oxidation state during electrolysis and keeps its +2 oxidation state. *In situ* EXAFS spectra also exhibited minor changes in the investigated potential range which could indicate reduction of the porphyrin ligand or binding of molecules to the Zn site, but not oxidation state changes (see Figure 9.37b). Experiments with the metal-free porphyrin precursor showed no activity towards CO_2RR, indicating the critical role of Zn metal centre for CO_2RR, although its oxidation state did not change during electrolysis.

Weng *et al.* investigated three Cu complexes for CO_2RR by *in situ* XAS: copper(II) phthalocyanine (CuPc), copper(II) benzene-1,3,5-tricarboxylate (btc) MOF (HKUST-1) and copper(II) 1,4,8,11-tetraazacyclotetradecane

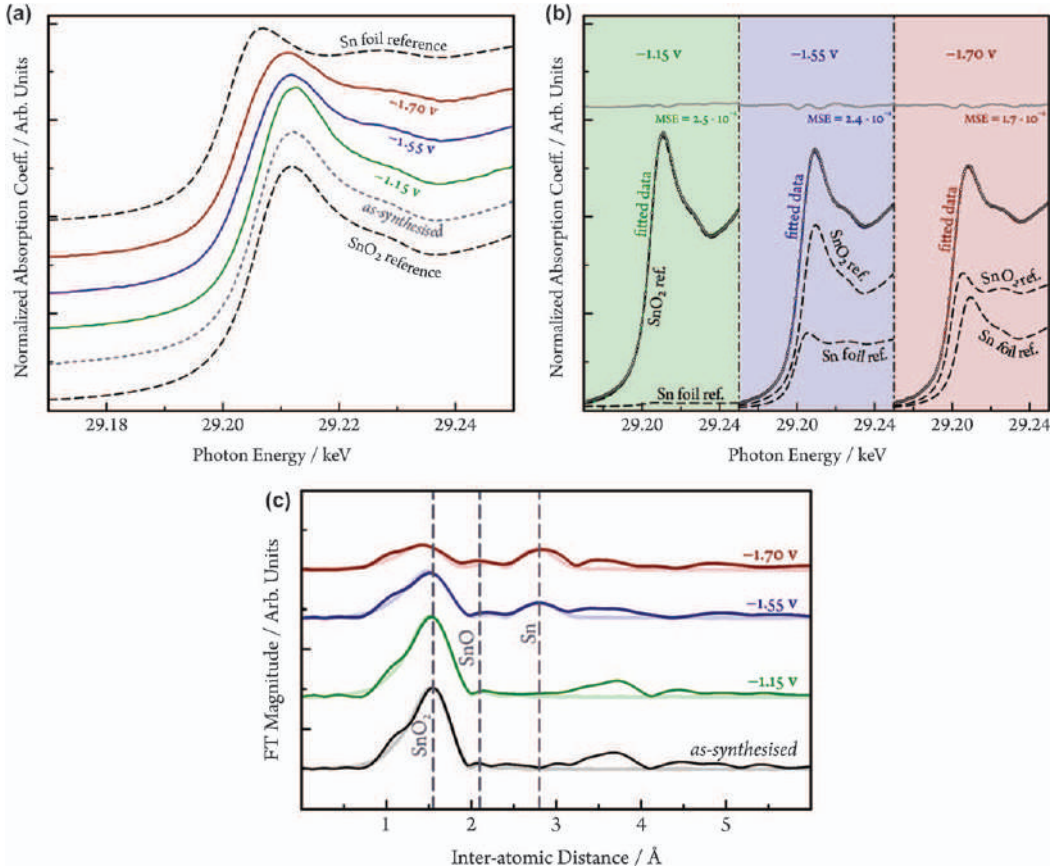

Figure 9.34 (a) *In situ* Sn–K edge XANES spectra of SnO_2 NPs@reduced graphene oxide (rGO) at different applied potentials, (b) fitted XANES spectra of SnO_2 NPs@rGO, showing the SnO_2 and Sn components, and (c) Fourier transform EXAFS spectra of SnO_2 NPs@rGO catalysts as a function of applied potential.
Adapted from ref. 120 with permission from Elsevier, Copyright 2018.

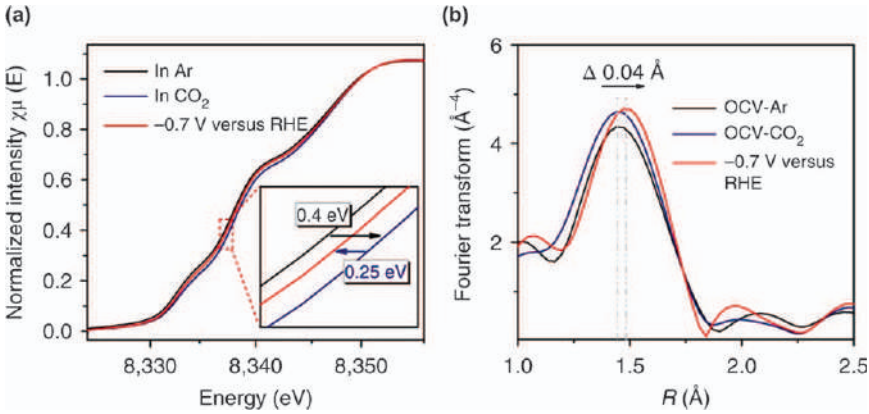

Figure 9.35 (a) *In situ* XANES spectra of the single-Ni-atom catalyst under Ar, CO_2 and at −0.7 V *vs.* RHE applied potential, and (b) *in situ* EXAFS spectra of the single-Ni-atom catalyst.
Adapted from ref. 122 with permission from Springer Nature, Copyright 2018.

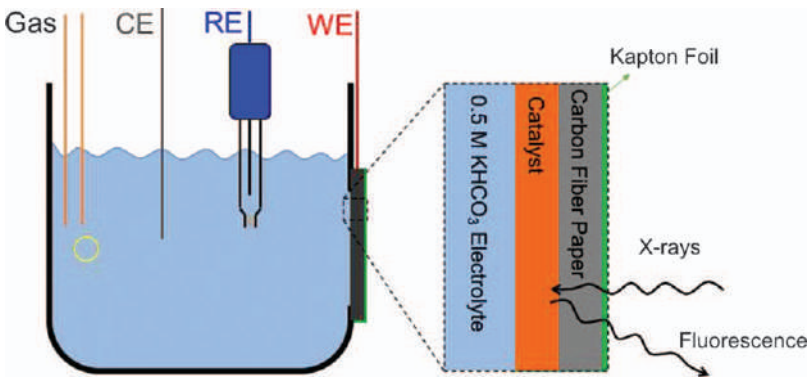

Figure 9.36 Schematic representation of cell design for *in situ* XAS reported by Wei *et al.* and used by Weng *et al.* for the study of Zn and Cu-based complexes for CO_2RR.[127–129]
Reproduced from ref. 129, https://doi.org/10.1038/s41467-018-02819-7, under the terms of the CC BY 4.0 license, http://creativecommons.org/licenses/by/4.0/.

chloride ([Cu(cyclam)]Cl_2).[129] XANES spectra recorded during electrolysis revealed distinct behaviour of the three materials. The potential was decreased stepwise from the open circuit voltage (OCV) value (~0.8 V *vs.* RHE) to −1.06 V *vs.* RHE and increased to 0.64 V *vs.* RHE. At OCV, copper is present as Cu(II) species in all three complexes, indicated by the characteristic peak at ~8985 eV of the 1s → 3d transition (see Figure 9.38a and 9.39a and d). At −0.66 V *vs.* RHE, the appearance of a peak at ~8981 eV in the

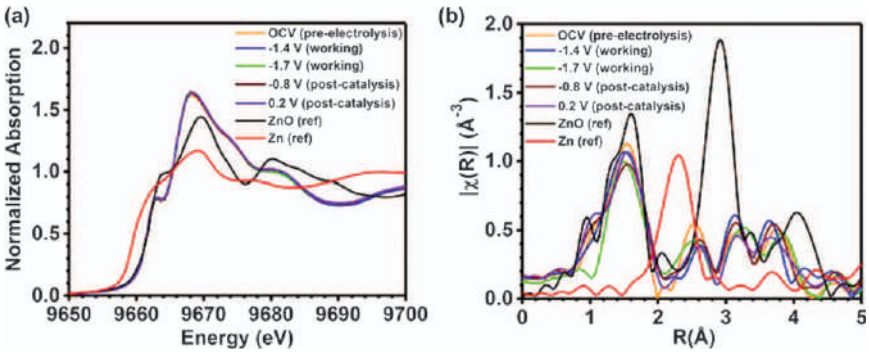

Figure 9.37 (a) *In situ* XANES spectra and (b) *in situ* Fourier transform EXAFS spectra of the Zn–porphyrin catalyst during CO_2RR (potential values reported *vs.* Ag/AgCl).
Adapted from ref. 128 with permission from American Chemical Society, Copyright 2017.

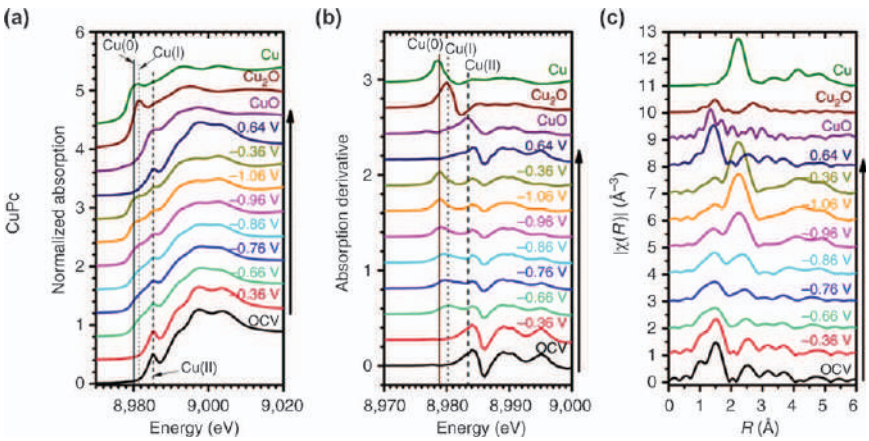

Figure 9.38 (a) *In situ* XANES spectra of CuPc at different applied potentials, (b) first-order derivatives of XANES spectra, and (c) *in situ* Fourier transform Cu K-edge EXAFS spectra of CuPc during CO_2RR.
Adapted from ref. 129, https://doi.org/10.1038/s41467-018-02819-7, under the terms of the CC BY 4.0 license, http://creativecommons.org/licenses/by/4.0/.

XANES spectrum of CuPc, indicates the reduction of Cu(II) species to Cu(I) (see Figure 9.38a). At a potential of −1.06 V, Cu(I) species were further reduced to metallic Cu(0), indicated by the increase of the feature at ∼8980 eV, characteristic for Cu(0). The Cu(II) peak was still present at −1.06 V *vs.* RHE in the XANES spectra. Increasing the potential to 0.64 V *vs.* RHE led to the oxidation of Cu(0) species to Cu(II). The reversibility of the oxidation state change of Cu in CuPc with applied potential was more clearly observed in the derivative curves of the XANES spectra (see Figure 9.38b).

HKUST-1 and [Cu(cyclam)]Cl_2 complexes did not exhibit the reversible oxidation change of Cu with applied potential. At −1.06 V *vs.* RHE, XANES spectra indicated the presence of Cu(0) species (see Figure 9.39a,b,d,e) for both complexes. However, when the potential was increased to 0.64 V *vs.* RHE, the XANES spectrum of HKUST-1 predominantly indicated that Cu(I) species and metallic Cu were observed for [Cu(cyclam)]Cl_2.

EXAFS investigations strengthened the conclusions from XANES measurements regarding oxidation state changes of Cu in the three complexes. At −1.06 V *vs.* RHE, all three complexes exhibited a peak at $R = 2.2$ Å in the Fourier transform EXAFS spectra, characteristic for the metallic Cu–Cu bond (see Figure 9.38c, and 9.39c and f).

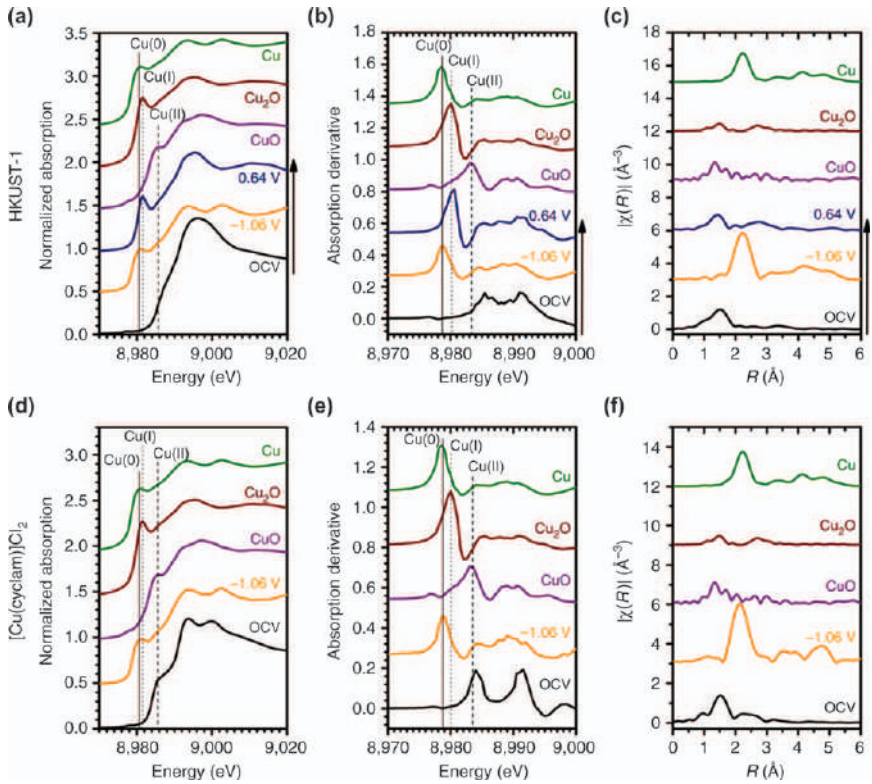

Figure 9.39 (a) *In situ* XANES spectra of HKUST-1 at different applied potentials, (b) first-order derivatives of XANES spectra for HKUST-1, (c) *in situ* Fourier transform Cu K-edge EXAFS spectra of HKUST-1 during CO_2RR, (d) *in situ* XANES spectra of [Cu(cyclam)]Cl_2 at different applied potentials, (e) first-order derivatives of XANES spectra for [Cu(cyclam)]Cl_2, and (f) *in situ* Fourier transform Cu K-edge EXAFS spectra of [Cu(cyclam)]Cl_2 during CO_2RR.
Adapted from ref. 129, https://doi.org/10.1038/s41467-018-02819-7, under the terms of the CC BY 4.0 license, http://creativecommons.org/licenses/by/4.0/.

For the CuPc complex, the potential-induced structural reversibility was revealed (see Figure 9.38c). At −1.06 V *vs.* RHE, besides the characteristic Cu–Cu peak, a feature in the $R = 1$ to ~2 Å range was assigned to the CuPc structure. At 0.64 V *vs.* RHE, the EXAFS spectrum exhibits a strong resemblance to the EXAFS spectrum recorded at OCV.

Based on the pronounced similarity between the metal Cu standard spectrum and the spectra of HKUST-1 and [Cu(cyclam)]Cl_2 at −1.06 V *vs.* RHE, the authors suggested that for these complexes, formation of bulk metallic Cu takes place (see Figure 9.39c and f). Formation of Cu_2O from HKUST-1 at 0.64 V *vs.* RHE was suggested, based on the resemblance of the EXAFS spectrum to the reference spectrum of Cu_2O standard. In the experiments with [Cu(cyclam)]Cl_2, the formation of a reddish sheen on the electrode caused noise in the EXAFS spectra, indicating the formation of metallic Cu, irreversible upon potential cycling.

9.4 UV–Vis Spectroscopy for the Investigation of Electrochemical CO_2 Reduction

UV–Vis spectroscopy is, along with IR spectroscopy, a pioneering spectroscopic technique that is applied to the study of electrochemical reactions. Both techniques were developed in the same period, but compared to IR spectroelectrochemistry, UV–Vis spectroelectrochemistry has the advantage of easier experimental implementation. Absorption of UV–Vis light by the electrolyte solution and the subsequent attenuation of the signal encountered in IR spectroelectrochemistry is a less critical concern in UV–Vis spectroelectrochemistry. In addition, the material of choice for cell design is quartz, which is more stable at the conditions used in the electrochemical experiments than the materials used as radiation transparent windows in IR spectroelectrochemistry.

The technique is used to study electronic transitions accompanying electrochemical transformations in molecular catalysts, as will be shown in a few examples. UV–Vis spectroscopy can be applied to investigate electrochemical reactions in external reflection, internal reflection, or transmission configuration (see Figure 9.40a and b).

The internal reflection configuration was developed and applied in the late 1960s, but later became less popular in favour of the external reflection configuration and the transmission configuration.[130,131] An interesting cell design using the external reflection configuration was proposed by Neudeck *et al.*[132] The group of Kubiak used one cell for both IR and UV–Vis spectroelectrochemical studies using the external reflection configuration.[44] The transmission configuration makes use of optically transparent thin layer electrodes, consisting of Au or Pt minigrids, similar to those mentioned in the section on IR spectroelectrochemistry. The application of UV–Vis spectroscopy for the investigation of species formed at the surface of metallic

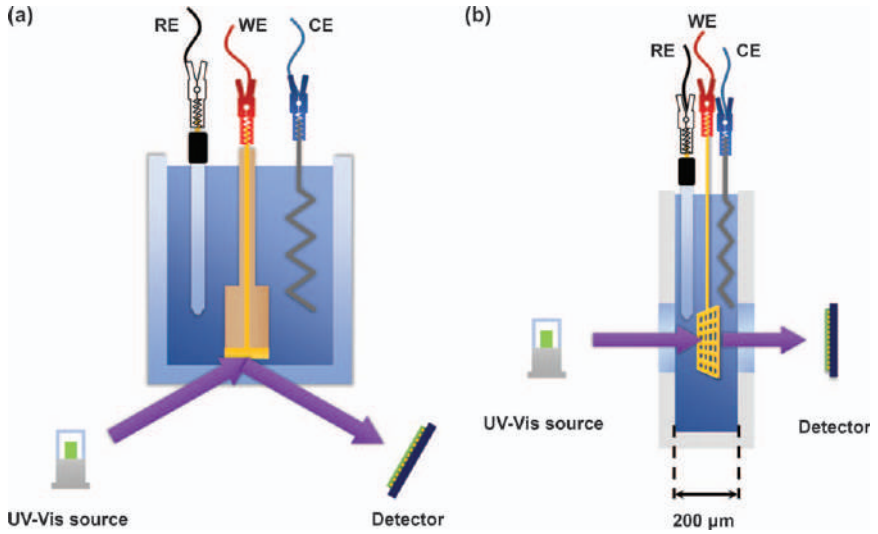

Figure 9.40 (a) External reflection configuration for UV–Vis spectroelectrochemistry and (b) transmission configuration.

electrodes is challenging, as very often such intermediates are not susceptible to UV–Vis radiation.

9.4.1 Application in Homogeneous Systems

In homogeneous CO_2RR, UV–Vis spectroscopy is used to elucidate the nature of redox species arising with changes in applied potential. In this way, it is possible to determine if the electron transfer involves the metal centre or the ligands, and how the latter participates in electrolysis. Together with the equivalent information extracted from IR spectroelectrochemistry, this allows one to derive reaction mechanisms.

The group of Hartl extensively investigated CO_2RR using UV–Vis and IR spectroelectrochemistry for various molecular complexes, including $[M(CO)_4(2,2\text{-bipyridine})]$ complexes with M = Cr, Mo, W, $[Os(CO)(2,2'\text{-bipyridine})(L)Cl_2]$ with $L = Cl^-$, PrCN, $[Mn(CO)_3(\text{isopropyl-1,4-diazabuta-1,3-diene})]^-$ and $[Mo(CO)_2(\eta^3\text{-allyl})(\alpha\text{-diimine})(NCS)]$.[38,79,133,134]

For $[Mo(CO)_4(bpy)]$, at −2.07 V *vs.* $Cp_2Fe^{+/0}$, the peaks at $\lambda_{max} = 258$, 297, 393, and 462 nm, characteristic to $[Mo(CO)_4(bpy)]$ (see the red line in Figure 9.41), are replaced by new peaks at $\lambda_{max} = 260$, 306, 366, and 463, and the bifurcated band at 491 and 532 nm, indicating a reduced 2,2-bipyridine ligand. The authors associated this spectrum to the $[Mo(CO)_4(bpy)]^{\bullet -}$ complex (see the green line in Figure 9.41). At −2.16 V *vs.* $Cp_2Fe^{+/0}$, the complex was further reduced to $[Mo(CO)_3(bpy)]^{2-}$, indicated by the appearance of characteristic absorption bands at $\lambda_{max} = 258$, 369, 580, and 644 nm in the UV–Vis spectrum (see the blue line in Figure 9.41).

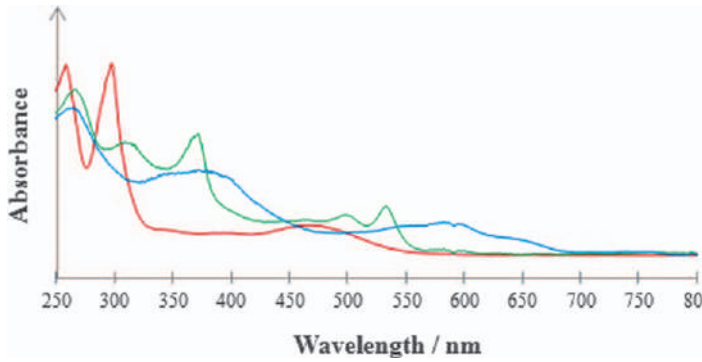

Figure 9.41 UV–Vis spectra of $[Mo(CO)_4(bpy)]$ (red), $[Mo(CO)_4(bpy)]^{\bullet -}$ (green), and $[Mo(CO)_3(bpy)]^{2-}$ (blue) recorded in 0.3 M Bu_4NPF_6/tetrahydrofuran using an OTTLE cell.
Adapted from ref. 38 with permission from John Wiley and Sons, Copyright © 2015 The Authors. Published by Wiley-VCH Verlag GmbH & Co. KGaA.

Bourrez *et al.* used UV–Vis spectroscopy to confirm the intermediates of the reduction of the $[Mn(bpy)(CO)_3Br]$ complex in acetonitrile.[135] Two irreversible reduction peaks were observed in the cyclic voltammograms. The first one, at −1.65 V *vs.* Ag/Ag^+ was associated with the formation of the $[Mn(bpy)(CO)_3]_2$ dimer, accompanied by the appearance of three bands in the UV–Vis spectra at 394, 461, 633, and 806 nm (see Figure 9.42a). For the second reduction peak, at −1.85 V *vs.* Ag/Ag^+, the appearance of bands at 370 and 560 nm was associated with the formation of $[Mn(bpy)(CO)_3]^-$ (see Figure 9.42b).

Machan *et al.* replaced the Br^- ligand with CN^-, to form $[Mn(bpy)(CO)_3CN]$, for which the formation of the $[Mn(bpy)(CO)_3]_2$ dimer is supressed.[52] UV–Vis spectroscopy confirmed the substitution of Br^- with CN^- by a blue shift of the band at 416 nm in the parent compound to 377 nm in $[Mn(bpy)(CO)_3CN]$ (see Figure 9.43a). The formation of $[Mn(bpy)(CO)_3]^-$ was observed, indicated by bands at 352 and 559 nm, when decamethylcobaltocene ($CoCp^*_2$) was added as a reductant (see Figure 9.43b).

Isaacs *et al.* applied UV–Vis spectroscopy to a series of poly-*M*-aminophtalocyanine complexes (M = Co, Ni, Fe) for CO_2RR.[136] Phthalocyanines exhibit two features in UV–Vis spectra associated with π–π transitions of the ligands: the Q band at low energies (HOMO–LUMO) and the Soret band at high energies ($HOMO^{-1}$–LUMO). The spectroelectrochemical experiments were conducted using a fluorine-doped tin oxide glass working electrode, on which the complexes were electropolymerized in a quartz cuvette, in 1 mM $NaClO_4$. Poly-Co-tetrakis aminophthalocyanine (poly-Co-TaPc) and poly-Ni-tetrakis aminophthalocyanine (poly-Ni-TaPc) exhibit different selectivity trends in CO_2RR. *In situ* UV–vis spectra of the two complexes also showed significant differences when the electric potential was applied. In the case of poly-Co-TaPc, under a N_2 atmosphere, the Q band appeared at 725 nm and a

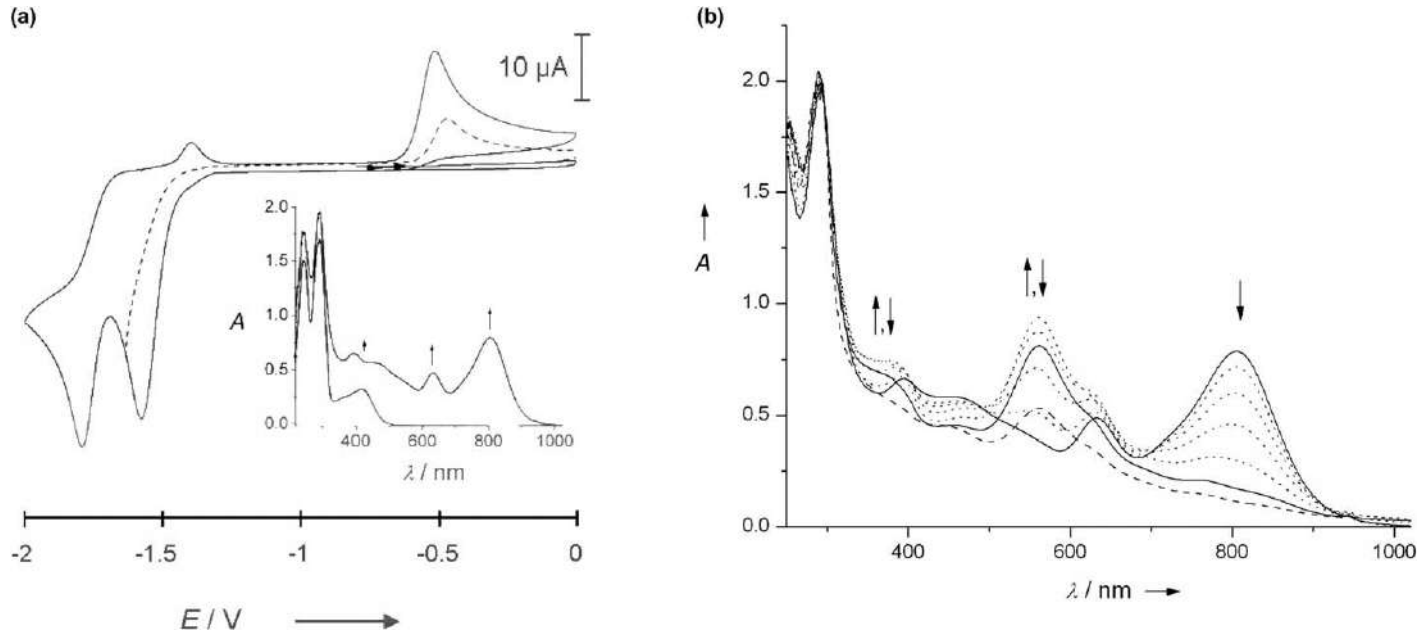

Figure 9.42 (a) Cyclic voltammogram and UV–Vis spectrum (inset) at −1.65 V *vs.* Ag/Ag^+ for $[Mn(bpy)(CO)_3Br]_2$ and (b) UV–Vis spectrum of $[Mn(bpy)(CO)_3Br]^-$ at −1.85 V *vs.* Ag/Ag^+ in 0.1 M Bu_4NClO_4/acetonitrile.
Adapted from ref. 135 with permission from John Wiley and Sons, Copyright © 2011 WILEY-VCH Verlag GmbH & Co. KGaA, Weinheim.

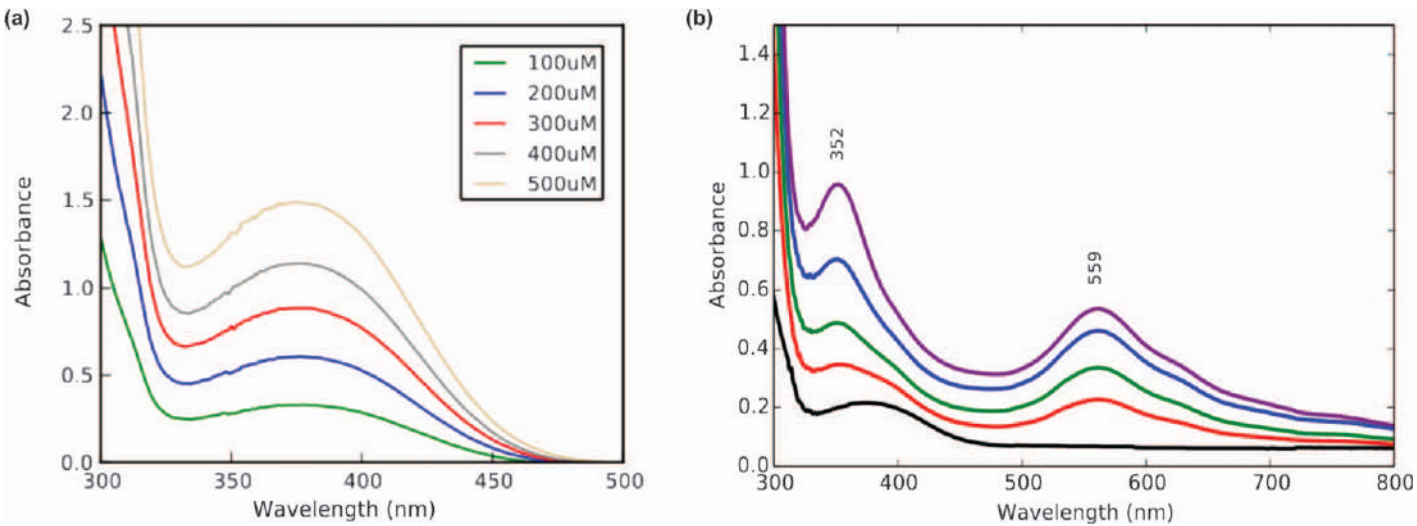

Figure 9.43 (a) UV–Vis spectrum of $[Mn(CN)(bpy)(CO)_3]$, (b) UV–Vis spectrum of the titration of $[Mn(CN)(bpy)(CO)_3]$ with $CoCp^*_2$ (black → purple: 0 → 2.1 equiv).
Adapted from ref. 52 with permission from American Chemical Society, Copyright 2015.

part of the Soret band was observed between 300 and 400 nm at OCP (see Figure 9.44a). At −0.4 V *vs.* Ag/AgCl, a new band at 480 nm emerged, ascribed by the authors to a MLCT (see Figure 9.44b) transition. Under CO_2 bubbling of the electrolyte solution, the Q band and the Soret band decreased in intensity. In contrast, for poly-Ni-TaPc, the Q band showed almost no change in intensity when the potential was changed from OCP to −0.8 V *vs.* Ag/AgCl (see Figure 9.44c). Under CO_2 bubbling, the Q band significantly decreased in intensity (see Figure 9.44d). Based on the appearance of UV–Vis spectra of the two complexes under CO_2 bubbling, the authors concluded that CO_2 interacts differently with the two complexes, which results in the different selectivity trends.

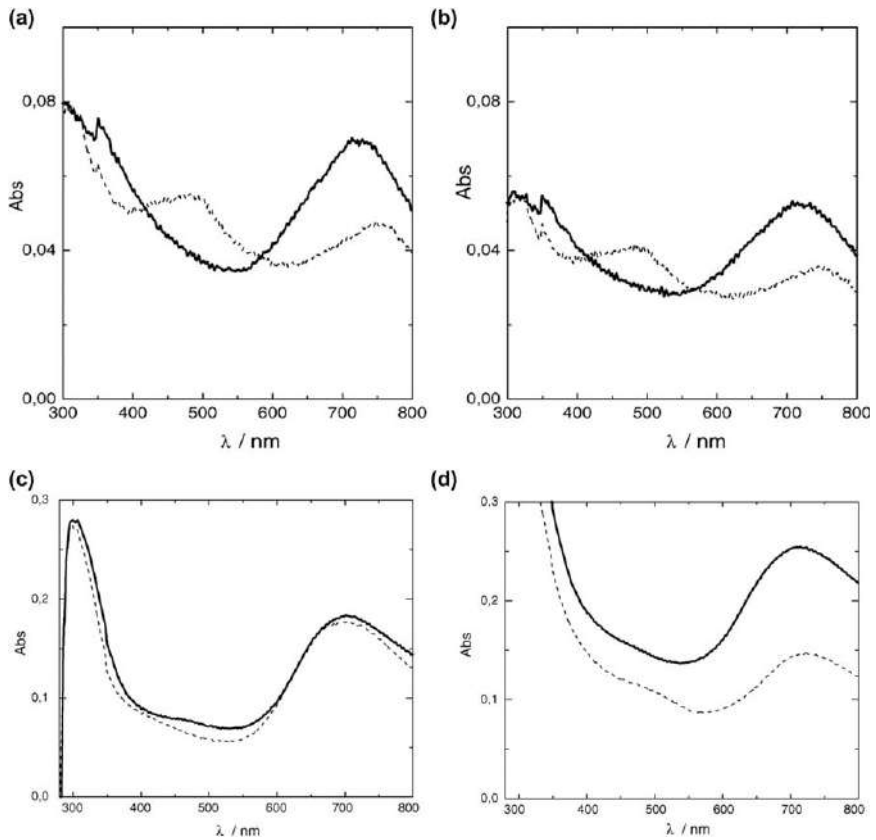

Figure 9.44 (a) UV–Vis spectra of poly-Co-TaPc under a N_2 atmosphere at OCP (solid line) and −0.4 V *vs.* Ag/AgCl (dashed line), (b) UV–Vis spectra of poly-Co-TaPc under CO_2 bubbling at OCP (solid line) and −0.4 V *vs.* Ag/AgCl, (c) UV–Vis spectra of poly-Ni-TaPc under a N_2 atmosphere at OCP (solid line) and −0.8 V *vs.* Ag/AgCl (dashed line), and (d) UV–Vis spectra of poly-Ni-TaPc under CO_2 bubbling at OCP (solid line) and −0.8 V *vs.* Ag/AgCl (dashed line).
Adapted from ref. 136 with permission from Elsevier, Copyright 2005.

9.5 Summary and Outlook

The contribution of spectroscopy to the understanding of electrochemical reactions cannot be underestimated. The information on selectivity trends and reaction mechanisms determined by IR spectroscopy for bulk metallic electrodes over the years is of great practical importance towards the rational design of more efficient electrocatalysts. We hope that more effort will be done in the future to extend the use of spectroscopic methods to the study of nanostructured electrocatalysts, as these behave differently to bulk electrodes. As highlighted above, different analytical techniques have different characteristics in the information gained and methodological limitations. Knowing these is of utmost importance to increase the feasibility of such experiments and extract as much information as possible.

Raman spectroscopy and X-ray absorption spectroscopy have shown that the oxidation state of the metals during electrolysis do not always match those predicted by Pourbaix diagrams. This information is very useful for determining the optimum electrolysis conditions, in terms of applied potential, and for understanding the deactivation and long-term stability of electrode materials. For molecular electrocatalysts, UV-Vis spectroscopy and IR spectroscopy both brought a significant contribution to the identification of intermediate structures formed during electrolysis and to the formulation of reaction mechanisms.

What is clearly needed for the further development of the field of spectroelectrochemistry, is the improvement of the design of current cells. As discussed, there are still challenges in the state-of-the-art cell design, particularly for IR spectroscopic studies, such as mass transport limitations in thin layer cells or stability issues of metallic films in ATR-IR. New approaches and measurement configuration should target the diminishment of such constraints.

Most of the time, only one, or rarely two, spectroscopic techniques are combined to investigate electrochemical reactions. However, for a full understanding of all the underlying processes happening during the reaction, it would be of great interest to combine as many complementary spectroscopic techniques as possible (in a multiprobe or multimodal approach), which we expect to happen in the future.

References

1. B. M. Weckhuysen, *PCCP*, 2003, **5**, 4351.
2. B. M. Weckhuysen, *In-situ Spectroscopy of Catalysts*, American Scientific Publishers, San Diego, 2004.
3. M. A. Bañares, *Catal. Today*, 2005, **100**, 71.
4. J. A. Rodriguez, J. C. Hanson and P. J. Chupas, *Inupasuezdaracterization of Heterogeneous Catalysts*, Wiley, Hoboken, 2013.

5. A. Chakrabarti, M. E. Ford, D. Gregory, R. Hu, C. J. Keturakis, S. Lwin, Y. Tang, Z. Yang, M. Zhu, M. A. Bañares and I. E. Wachs, *Catal. Today*, 2017, **283**, 27.
6. M. Osawa, in *Handbook of Vibrational Spectroscopy*, ed. J. Chalmers and P. Griffiths, Wiley, 2002, p. 1.
7. M. Osawa, in *Near-Field Optics and Surface Plasmon Polaritons*, ed. S. Kawata, Springer, Berlin, Heidelberg, **vol. 81**, 2001, pp. 163–187.
8. M. Osawa, in *In-situ Spectroscopic Studies of Adsorption at the Electrode and Electrocatalysis*, ed. S.-G. Sun, P. A. Christensen and A. Wieckowski, Elsevier, Amsterdam, Boston, **vol. 7**, 2007, pp. 209–246.
9. A. J. Wain and M. A. O'Connell, *Adv. Phys.: X*, 2017, **2**, 188.
10. A. Hartstein, J. R. Kirtley and J. C. Tsang, *Phys. Rev. Lett.*, 1980, **45**, 201.
11. A. Hatta, Y. Suzuki and W. Suëtaka, *Appl. Phys. A: Mater. Sci. Process.*, 1984, **35**, 135.
12. A. Hatta, Y. Chiba and W. Suëtaka, *Surf. Sci.*, 1985, **158**, 616.
13. G. T. Merklin and P. R. Griffiths, *Langmuir*, 1997, **13**, 6159.
14. R. Aroca and B. Price, *J. Phys. Chem. B*, 1997, **101**, 6537.
15. T. Yoshidome, T. Inoue and S. Kamata, *Chem. Lett.*, 1997, **26**, 533.
16. C. Korzeniewski, *Crit. Rev. Anal. Chem.*, 1997, **27**, 81.
17. C. Korzeniewski, in *In-situ Spectroscopic Studies of Adsorption at the Electrode and Electrocatalysis*, ed. S.-G. Sun, P. A. Christensen and A. Wieckowski, Elsevier, Amsterdam, Boston, **vol. 6**, 2007, pp. 179–208.
18. P. A. Christensen and A. Hamnett, in *New Techniques for the Study of Electrodes and Their Reactions*, ed. R. G. Compton, Elsevier, **vol. 29**, 1, 1989, pp. 1–77.
19. E. A. Monyoncho, V. Zamlynny, T. K. Woo and E. A. Baranova, *Analyst*, 2018, **143**, 2563.
20. A. Bewick and K. Kunimatsu, *Surf. Sci.*, 1980, **101**, 131.
21. A. Bewick, K. Kunimatsu and B. Stanley Pons, *Electrochim. Acta*, 1980, **25**, 465.
22. S. Pons, T. Davidson and A. Bewick, *J. Electroanal. Chem. Interfacial Electrochem.*, 1984, **160**, 63.
23. B. Beden, A. Bewick, M. Razaq and J. Weber, *J. Electroanal. Chem. Interfacial Electrochem.*, 1982, **139**, 203.
24. W. G. Golden, K. Kunimatsu and H. Seki, *J. Phys. Chem.*, 1984, **88**, 1275.
25. A. Urakawa, T. Bürgi, H.-P. Schläpfer and A. Baiker, *J. Chem. Phys.*, 2006, **124**, 054717.
26. D. M. Meier, A. Urakawa and A. Baiker, *Analyst*, 2009, **134**, 1779.
27. R. G. Greenler, *J. Chem. Phys.*, 1966, **44**, 310.
28. P. A. Christensen, A. Hamnett, A. V. G. Muir and N. A. Freeman, *J. Electroanal. Chem. Interfacial Electrochem.*, 1990, **288**, 197.
29. S. Taguchi, A. Aramata and M. Enyo, *J. Electroanal. Chem.*, 1994, **372**, 161.
30. Y. Hori, O. Koga, H. Yamazaki and T. Matsuo, *Electrochim. Acta*, 1995, **40**, 2617.
31. E. Perez-Gallent, M. C. Figueiredo, F. Calle-Vallejo and M. T. M. Koper, *Angew. Chem., Int. Ed.*, 2017, **56**, 3621.

32. B. Innocent, D. Pasquier, F. Ropital, F. Hahn, J. M. Léger and K. B. Kokoh, *Appl. Catal., B*, 2010, **94**, 219.
33. B. Eneau-Innocent, D. Pasquier, F. Ropital, J. M. Léger and K. B. Kokoh, *Appl. Catal., B*, 2010, **98**, 65.
34. S. Pérez-Rodríguez, G. García, M. J. Lázaro and E. Pastor, in *Electrochemical Reduction of Carbon Dioxide: Overcoming the Limitations of Photosynthesis*, ed. F. Marken and D. Fermin, The Royal Society of Chemistry, **vol. 9**, 2018, pp. 212–243.
35. C. Amatore and J. M. Saveant, *J. Am. Chem. Soc.*, 1981, **103**, 5021.
36. M. Gattrell, N. Gupta and A. Co, *J. Electroanal. Chem.*, 2006, **594**, 1.
37. M. C. Figueiredo, I. Ledezma-Yanez and M. T. M. Koper, *ACS Catal.*, 2016, **6**, 2382.
38. J. Tory, B. Setterfield-Price, R. A. W. Dryfe and F. Hartl, *ChemElectroChem*, 2015, **2**, 213.
39. J. D. Froehlich and C. P. Kubiak, *Inorg. Chem.*, 2012, **51**, 3932.
40. C. Costentin, G. Passard, M. Robert and J.-M. Savéant, *Proc. Natl. Acad. Sci. U. S. A.*, 2014, **111**, 14990.
41. R. Francke, B. Schille and M. Roemelt, *Chem. Rev.*, 2018, **118**, 4631.
42. P. Christensen, A. Hamnett, A. V. G. Muir and J. A. Timney, *J. Chem. Soc., Dalton Trans.*, 1992, 1455.
43. M. J. Shaw and W. E. Geiger, *Organometallics*, 1996, **15**, 13.
44. I. S. Zavarine and C. P. Kubiak, *J. Electroanal. Chem.*, 2001, **495**, 106.
45. J. A. Timney, *Inorg. Chem.*, 1979, **18**, 2502.
46. J. M. Smieja and C. P. Kubiak, *Inorg. Chem.*, 2010, **49**, 9283.
47. C. W. Machan, M. D. Sampson, S. A. Chabolla, T. Dang and C. P. Kubiak, *Organometallics*, 2014, **33**, 4550.
48. F. P. A. Johnson, M. W. George, F. Hartl and J. J. Turner, *Organometallics*, 1996, **15**, 3374.
49. J. D. Froehlich and C. P. Kubiak, *J. Am. Chem. Soc.*, 2015, **137**, 3565.
50. S.-N. Pun, W.-H. Chung, K.-M. Lam, P. Guo, P.-H. Chan, K.-Y. Wong, C.-M. Che, T.-Y. Chen and S.-M. Peng, *J. Chem. Soc., Dalton Trans.*, 2002, 575.
51. K. A. Grice and C. P. Kubiak, in *Adv. Inorg. Chem.*, ed. M. Aresta and R. van Eldik, Academic Press, **vol. 66**, 5, 2014, pp. 163–188.
52. C. W. Machan, C. J. Stanton, 3rd, J. E. Vandezande, G. F. Majetich, H. F. Schaefer, C. P. Kubiak and J. Agarwal, *Inorg. Chem.*, 2015, **54**, 8849.
53. M. V. Vollmer, C. W. Machan, M. L. Clark, W. E. Antholine, J. Agarwal, H. F. Schaefer, 3rd, C. P. Kubiak and J. R. Walensky, *Organometallics*, 2014, **34**, 3.
54. D. J. Boston, Y. M. Pachon, R. O. Lezna, N. R. de Tacconi and F. M. MacDonnell, *Inorg. Chem.*, 2014, **53**, 6544.
55. E. Simón-Manso and C. P. Kubiak, *Organometallics*, 2005, **24**, 96.
56. H. B. Mark and B. S. Pons, *Anal. Chem.*, 1966, **38**, 119.
57. M. Dunwell, Q. Lu, J. M. Heyes, J. Rosen, J. G. Chen, Y. Yan, F. Jiao and B. Xu, *J. Am. Chem. Soc.*, 2017, **139**, 3774.

58. M. F. Baruch, J. E. Pander, J. L. White and A. B. Bocarsly, *ACS Catal.*, 2015, **5**, 3148.
59. A. Wuttig, C. Liu, Q. Peng, M. Yaguchi, C. H. Hendon, K. Motobayashi, S. Ye, M. Osawa and Y. Surendranath, *ACS Cent. Sci.*, 2016, **2**, 522.
60. N. J. Firet and W. A. Smith, *ACS Catal.*, 2016, **7**, 606.
61. J. Heyes, M. Dunwell and B. Xu, *J. Phys. Chem. C*, 2016, **120**, 17334.
62. M. Dunwell, Y. Yan and B. Xu, *ACS Catal.*, 2017, **7**, 5410.
63. C. M. Gunathunge, X. Li, J. Li, R. P. Hicks, V. J. Ovalle and M. M. Waegele, *J. Phys. Chem. C*, 2017, **121**, 12337.
64. J. E. Pander, M. F. Baruch and A. B. Bocarsly, *ACS Catal.*, 2016, **6**, 7824.
65. S. Zhu, B. Jiang, W. B. Cai and M. Shao, *J. Am. Chem. Soc.*, 2017, **139**, 15664.
66. Y. Katayama, F. Nattino, L. Giordano, J. Hwang, R. R. Rao, O. Andreussi, N. Marzari and Y. Shao-Horn, *J. Phys. Chem. C*, 2019, **123**, 5951.
67. S. Zhu, T. Li, W.-B. Cai and M. Shao, *ACS Energy Lett.*, 2019, **4**, 682.
68. A. J. Cowan, in *Electrochemical Reduction of Carbon Dioxide: Overcoming the Limitations of Photosynthesis*, The Royal Society of Chemistry, 2018, pp. 244–263.
69. S. Zhu, Q. Wang, X. Qin, M. Gu, R. Tao, B. P. Lee, L. Zhang, Y. Yao, T. Li and M. Shao, *Adv. Energy Mater.*, 2018, **8**, 1802238.
70. K. Jiang, H. Wang, W. B. Cai and H. Wang, *ACS Nano*, 2017, **11**, 6451.
71. J. Wang, L. Gan, Q. Zhang, V. Reddu, Y. Peng, Z. Liu, X. Xia, C. Wang and X. Wang, *Adv. Energy Mater.*, 2019, **9**, 1803151.
72. R. Huang, J. Rintjema, J. González-Fabra, E. Martín, E. C. Escudero-Adán, C. Bo, A. Urakawa and A. W. Kleij, *Nat. Catal.*, 2019, **2**, 62.
73. R. W. Murray, W. R. Heineman and G. W. O'Dom, *Anal. Chem.*, 1967, **39**, 1666.
74. C. L. Yao, F. J. Capdevielle, K. M. Kadish and J. L. Bear, *Anal. Chem.*, 1989, **61**, 2805.
75. W. R. Heineman, J. N. Burnett and R. W. Murray, *Anal. Chem.*, 1968, **40**, 1974.
76. B. J. Brisdon, S. K. Enger, M. J. Weaver and R. A. Walton, *Inorg. Chem.*, 1987, **26**, 3340.
77. R. S. K. A. Gamage, S. Umapathy and A. J. McQuillan, *J. Electroanal. Chem. Interfacial Electrochem.*, 1990, **284**, 229.
78. M. Krejčik, M. Daněk and F. Hartl, *J. Electroanal. Chem. Interfacial Electrochem.*, 1991, **317**, 179.
79. J. Tory, L. King, A. Maroulis, M. Haukka, M. J. Calhorda and F. Hartl, *Inorg. Chem.*, 2014, **53**, 1382.
80. K. J. Lee, N. Elgrishi, B. Kandemir and J. L. Dempsey, *Nat. Rev. Chem.*, 2017, **1**, 0039.
81. E. C. Le Ru, E. Blackie, M. Meyer and P. G. Etchegoin, *J. Phys. Chem. C*, 2007, **111**, 13794.

82. M. Fleischmann, P. J. Hendra and A. J. McQuillan, *J. Chem. Soc., Chem. Commun.*, 1973, 80.
83. B. Sharma, R. R. Frontiera, A.-I. Henry, E. Ringe and R. P. Van Duyne, *Mater. Today*, 2012, **15**, 16.
84. Z. Q. Tian and B. Ren, in *Encyclopedia of Electrochemistry*, ed. A. J. Bard, Wileylopedia of Electrochemistry, **vol. 3**, 6, 2007, pp. 572–659.
85. D.-Y. Wu, J.-F. Li, B. Ren and Z.-Q. Tian, *Chem. Soc. Rev.*, 2008, **37**, 1025.
86. S. Lal, N. K. Grady, J. Kundu, C. S. Levin, J. B. Lassiter and N. J. Halas, *Chem. Soc. Rev.*, 2008, **37**, 898.
87. V. O. Santos, I. R. Leite, A. G. Brolo and J. C. Rubim, *J. Raman Spectrosc.*, 2016, **47**, 674.
88. M. Fleischmann, P. J. Hendra and A. J. McQuillan, *Chem. Phys. Lett.*, 1974, **26**, 163.
89. B. Ren, X. Q. Li, C. X. She, D. Y. Wu and Z. Q. Tian, *Electrochim. Acta*, 2000, **46**, 193.
90. B. Ren, X.-F. Lin, Y.-X. Jiang, P.-G. Cao, Y. Xie, Q.-J. Huang and Z.-Q. Tian, *Appl. Spectrosc.*, 2003, **57**, 419.
91. Z. C. Zeng, S. Hu, S. C. Huang, Y. J. Zhang, W. X. Zhao, J. F. Li, C. Jiang and B. Ren, *Anal. Chem.*, 2016, **88**, 9381.
92. B. S. Yeo, S. L. Klaus, P. N. Ross, R. A. Mathies and A. T. Bell, *ChemPhysChem*, 2010, **11**, 1854.
93. Y. Deng and B. S. Yeo, *ACS Catal.*, 2017, **7**, 7873.
94. B. M. Setterfield-Price and R. A. W. Dryfe, *J. Electroanal. Chem.*, 2014, **730**, 48.
95. J. L. Oberst, H.-R. M. Jhong, P. J. A. Kenis and A. A. Gewirth, *J. Solid State Electrochem.*, 2016, **20**, 1149.
96. A. J. McQuillan, P. J. Hendra and M. Fleischmann, *J. Electroanal. Chem. Interfacial Electrochem.*, 1975, **65**, 933.
97. I. Oda, H. Ogasawara and M. Ito, *Langmuir*, 1996, **12**, 1094.
98. K. G. Schmitt and A. A. Gewirth, *J. Phys. Chem. C*, 2014, **118**, 17567.
99. B. D. Smith, D. E. Irish, P. Kedzierzawski and J. Augustynski, *J. Electrochem. Soc.*, 1997, **144**, 4288.
100. E. A. Batista and M. L. A. Temperini, *J. Electroanal. Chem.*, 2009, **629**, 158.
101. D. Ren, Y. Deng, A. D. Handoko, C. S. Chen, S. Malkhandi and B. S. Yeo, *ACS Catal.*, 2015, **5**, 2814.
102. D. Ren, B. S.-H. Ang and B. S. Yeo, *ACS Catal.*, 2016, **6**, 8239.
103. S. Jiang, K. Klingan, C. Pasquini and H. Dau, *J. Chem. Phys.*, 2019, **150**, 041718.
104. A. Dutta, A. Kuzume, M. Rahaman, S. Vesztergom and P. Broekmann, *ACS Catal.*, 2015, **5**, 7498.
105. C. E. Tornow, M. R. Thorson, S. Ma, A. A. Gewirth and P. J. Kenis, *J. Am. Chem. Soc.*, 2012, **134**, 19520.
106. Y. Zhang and M. J. Weaver, *J. Electroanal. Chem.*, 1993, **354**, 173.
107. W. Akemann and A. Otto, *Surf. Sci.*, 1993, **287–288**, 104.

108. L. Zedler, J. Guthmuller, I. Rabelo de Moraes, S. Kupfer, S. Krieck, M. Schmitt, J. Popp, S. Rau and B. Dietzek, *Chem. Commun.*, 2014, **50**, 5227.
109. K. Sengupta, S. Chatterjee and A. Dey, *ACS Catal.*, 2016, **6**, 6838.
110. S. I. Kalläne and M. van Gastel, *J. Phys. Chem. A*, 2016, **120**, 7465.
111. L. R. Sharpe, W. R. Heineman and R. C. Elder, *Chem. Rev.*, 1990, **90**, 705.
112. M. Wang, L. Árnadóttir, Z. J. Xu and Z. Feng, *Nano-Micro Lett.*, 2019, **11**, 47.
113. A. Minguzzi and P. Ghigna, in *Electroanalytical Chemistry*, ed. A. J. Bard and C. G. Zoski, CRC Press, Boca Raton, Florida, **vol. 27**, 3, 2017, pp. 119–181.
114. J. Rosen, G. S. Hutchings, Q. Lu, R. V. Forest, A. Moore and F. Jiao, *ACS Catal.*, 2015, **5**, 4586.
115. H. Mistry, A. S. Varela, C. S. Bonifacio, I. Zegkinoglou, I. Sinev, Y. W. Choi, K. Kisslinger, E. A. Stach, J. C. Yang, P. Strasser and B. R. Cuenya, *Nat. Commun.*, 2016, **7**, 12123.
116. P. De Luna, R. Quintero-Bermudez, C.-T. Dinh, M. B. Ross, O. S. Bushuyev, P. Todorović, T. Regier, S. O. Kelley, P. Yang and E. H. Sargent, *Nat. Catal.*, 2018, **1**, 103.
117. A. Eilert, F. S. Roberts, D. Friebel and A. Nilsson, *J. Phys. Chem. Lett.*, 2016, **7**, 1466.
118. C. Genovese, M. E. Schuster, E. K. Gibson, D. Gianolio, V. Posligua, R. Grau-Crespo, G. Cibin, P. P. Wells, D. Garai, V. Solokha, S. Krick Calderon, J. J. Velasco-Velez, C. Ampelli, S. Perathoner, G. Held, G. Centi and R. Arrigo, *Nat. Commun.*, 2018, **9**, 935.
119. S. N. A. Zakaria, N. Hollingsworth, H. U. Islam, A. Roffey, D. Santos-Carballal, A. Roldan, W. Bras, G. Sankar, G. Hogarth, K. B. Holt and N. H. de Leeuw, *ACS Appl. Mater. Interfaces*, 2018, **10**, 32078.
120. A. Dutta, A. Kuzume, V. Kaliginedi, M. Rahaman, I. Sinev, M. Ahmadi, B. Roldán Cuenya, S. Vesztergom and P. Broekmann, *Nano Energy*, 2018, **53**, 828.
121. X. Zheng, P. De Luna, F. P. García de Arquer, B. Zhang, N. Becknell, M. B. Ross, Y. Li, M. N. Banis, Y. Li, M. Liu, O. Voznyy, C. T. Dinh, T. Zhuang, P. Stadler, Y. Cui, X. Du, P. Yang and E. H. Sargent, *Joule*, 2017, **1**, 794.
122. H. B. Yang, S.-F. Hung, S. Liu, K. Yuan, S. Miao, L. Zhang, X. Huang, H.-Y. Wang, W. Cai, R. Chen, J. Gao, X. Yang, W. Chen, Y. Huang, H. M. Chen, C. M. Li, T. Zhang and B. Liu, *Nat. Energy*, 2018, **3**, 140.
123. X. Li, W. Bi, M. Chen, Y. Sun, H. Ju, W. Yan, J. Zhu, X. Wu, W. Chu, C. Wu and Y. Xie, *J. Am. Chem. Soc.*, 2017, **139**, 14889.
124. T. Binninger, E. Fabbri, A. Patru, M. Garganourakis, J. Han, D. F. Abbott, O. Sereda, R. Kötz, A. Menzel, M. Nachtegaal and T. J. Schmidt, *J. Electrochem. Soc.*, 2016, **163**, H906.
125. J. Tillier, T. Binninger, M. Garganourakis, A. Patru, E. Fabbri, T. J. Schmidt and O. Sereda, *J. Electrochem. Soc.*, 2016, **163**, H913.

126. T. Ishihara, T. Tokushima, Y. Horikawa, M. Kato and I. Yagi, *Rev. Sci. Instrum.*, 2017, **88**, 104101.
127. C. Wei, Z. Feng, M. Baisariyev, L. Yu, L. Zeng, T. Wu, H. Zhao, Y. Huang, M. J. Bedzyk, T. Sritharan and Z. J. Xu, *Chem. Mater.*, 2016, **28**, 4129.
128. Y. Wu, J. Jiang, Z. Weng, M. Wang, D. L. J. Broere, Y. Zhong, G. W. Brudvig, Z. Feng and H. Wang, *ACS Cent. Sci.*, 2017, **3**, 847.
129. Z. Weng, Y. Wu, M. Wang, J. Jiang, K. Yang, S. Huo, X.-F. Wang, Q. Ma, G. W. Brudvig, V. S. Batista, Y. Liang, Z. Feng and H. Wang, *Nat. Commun.*, 2018, **9**, 415.
130. T. Kuwana and J. W. Strojek, *Discuss. Faraday Soc.*, 1968, **45**, 134.
131. N. Winograd and T. Kuwana, *J. Electroanal. Chem. Interfacial Electrochem.*, 1969, **23**, 333.
132. A. Neudeck, F. Marken and R. G. Compton, in *Electroanalytical Methods*, ed. F. Scholz, A. M. Bond, R. G. Compton, D. A. Fiedler, G. Inzelt, H. Kahlert, Š. Komorsky-Lovrić, H. Lohse, M. Lovrić, F. Marken, A. Neudeck, U. Retter, F. Scholz and Z. Stojek, Springer, Heidelberg, Dordrecht, London, New York, **vol. II.6**, 2010, pp. 179–200.
133. Q. Zeng, J. Tory and F. Hartl, *Organometallics*, 2014, **33**, 5002.
134. J. Tory, G. Gobaille-Shaw, A. M. Chippindale and F. Hartl, *J. Organomet. Chem.*, 2014, **760**, 30.
135. M. Bourrez, F. Molton, S. Chardon-Noblat and A. Deronzier, *Angew. Chem., Int. Ed.*, 2011, **50**, 9903.
136. M. Isaacs, F. Armijo, G. Ramírez, E. Trollund, S. R. Biaggio, J. Costamagna and M. J. Aguirre, *J. Mol. Catal. A: Chem.*, 2005, **229**, 249.

CHAPTER 10

Electrochemical Reactors

MAXWELL GOLDMAN,[a,†] ERIC W. LEES,[b,†] PALOMA L. PRIETO,[a] BENJAMIN A. W. MOWBRAY,[a] DAVID M. WEEKES,[c] ANGELICA REYES,[b] TENGFEI LI,[a] DANIELLE A. SALVATORE,[b] WILSON A. SMITH*[d,e] AND CURTIS P. BERLINGUETTE*[a,b,c,f]

[a] Department of Chemistry, The University of British Columbia, 2036 Main Mall, Vancouver, British Columbia V6T 1Z1, Canada; [b] Department of Chemical and Biological Engineering, The University of British Columbia, 2360 East Mall, Vancouver, British Columbia V6T 1Z3, Canada; [c] Stewart Blusson Quantum Matter Institute, The University of British Columbia, 2355 East Mall, Vancouver, British Columbia V6T 1Z4, Canada; [d] Department of Chemical and Biological Engineering, University of Colorado Boulder, Boulder, CO 80309, USA; [e] National Renewable Energy Laboratory, Golden, CO 80401, USA; [f] Canadian Institute for Advanced Research (CIFAR), 661 University Avenue, Toronto M5G 1M1 Ontario, Canada
*Emails: W.Smith@tudelft.nl; cberling@chem.ubc.ca

10.1 Introduction

Scalable energy storage technologies are needed to enable a renewable energy economy.[1] Converting electrical energy into chemical energy in the form of liquid fuels is an appealing storage strategy for addressing seasonal energy storage, as well as for the heavy transportation and aeronautical

[†]These authors contributed equally.

Energy and Environment Series No. 28
Carbon Dioxide Electrochemistry: Homogeneous and Heterogeneous Catalysis
Edited by Marc Robert, Cyrille Costentin and Kim Daasbjerg

Published by the Royal Society of Chemistry, www.rsc.org

industries. The electrochemical production of H_2 fuel from H_2O is one pathway that has seen considerable advancements in efficiencies and rates of product formation in the past few decades, yet it remains relatively expensive to relative to producing H_2 from steam methane reforming.[2,3] Consequently, less than 5% of global hydrogen production is produced by non-thermal methods.[3] An alternative strategy for converting renewable electricity into chemical energy is to electrolytically produce carbon-based chemicals and fuels from CO_2. These processes offer the advantage of being easier to integrate into our existing infrastructure than hydrogen and have motivated academia and industry to design "low-temperature" (*i.e.*, those that operate at $\sim 20-150\ ^{\circ}C$) CO_2 reduction reaction (CO_2RR) electrolyzers capable of producing value-added chemicals such as CO, methanol, ethylene, and propanol (Figure 10.1)[4] without fossil fuel feedstocks.[5]

The commercial viability of CO_2 electrolyzers is contingent on achieving high current densities ($J > 200\ mA\,cm^{-2}$) with reasonable single-pass conversions (>50%) at high CO_2RR faradaic efficiencies (FE > 90%) for extended time periods (>1 year) while maintaining low operating cell potentials ($E_{cell} < 3.0$ V).[6–8] An emerging body of data indicates that pilot CO_2 electrolyzers are capable of competitive performance across a limited set of these metrics [*e.g.*, a combination of high J and FE,[9,10] or the simultaneous achievement of moderate J ($100\ mA\,cm^{-2}$) and extended lifetimes ($\sim$100 h)[11,12]] but realizing all key figures-of-merit (including J, single-pass CO_2 conversion, FE, lifetime, and E_{cell}) in a single technology has not yet been demonstrated.[4] This situation demands major advances in electrocatalyst and membrane material design as well as electrolyzer stack engineering.[13–17]

How CO_2 electrolyzers are integrated with both upstream and downstream processes needs to be considered along with the market size and price of

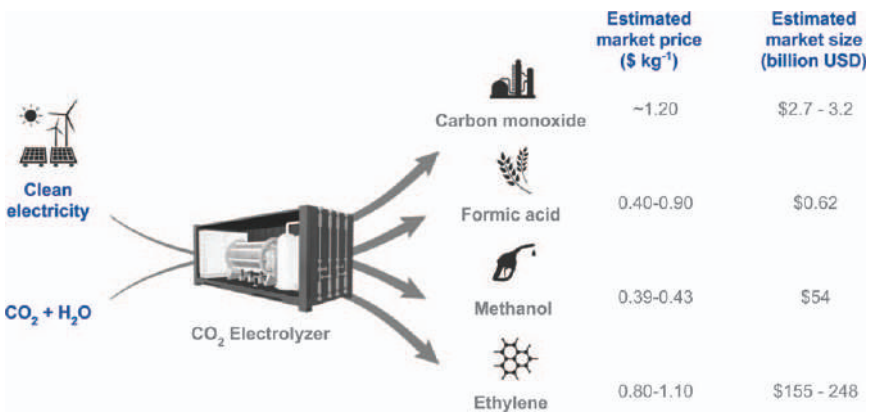

Figure 10.1 An overview of the approximate market sizes (in USD) and prices (in $ per kg) for chemicals directly accessible *via* CO_2 electrochemical reduction. Reproduced from ref. 4 with permission from American Chemical Society, Copyright 2018.

target CO_2RR products.[6] C1 and C2 hydrocarbons are particularly appealing CO_2 electroreduction targets due to their sizeable markets (*e.g.*, CO and C_2H_4 estimated at $\$2.7-3.2$ and $\$155-248$ billion USD, respectively).[4] The challenge is to electrolytically produce these chemicals at a cost that is competitive with conventional industrial production (<$1USD per kg). Indeed, currently known electrocatalysts are unable to electrosynthesize alcohols (methanol, ethanol) or any C2 product with high selectivity, potentially disqualifying them as viable CO_2RR products.[18–20] In contrast, formate and CO are attractive target products for CO_2 electrolysis because they can be produced with FE exceeding 90% and have higher ''product value per electron'' than other CO_2RR products ($0.016 USD per electron and $0.008 USD per electron for formate and CO, respectively, *cf.* remaining accessible CO_2RR products including propanol, ethylene, and methane have product values of <$0.005 USD per electron).[21–23] CO is appealing because there exists a significant global demand for downstream products of syngas (CO, H_2), including synthetic diesel and methanol.[4,8] Furthermore, CO_2-to-CO electrolysis has been demonstrated at high FE (>90%) and high J (>200 mA cm^{-2}).[4] Notwithstanding, a commercially viable CO_2RR reactor remains outstanding and the supply chains and capital expenditure costs are poorly defined, thus it is too early to make strong judgements on the exact CO_2RR product that should be targeted.

The electrocatalyst is one of the most important components of a CO_2 electrolyzer because it dictates both the product selectivity and energy efficiency of the CO_2RR. The search for new catalysts that can simultaneously increase energy efficiency and selectivity is complicated by various factors which can impact catalyst activity, including intermediate binding energy,[24–26] coordination[27,28] and active site availability,[29–31] catalyst particle geometry,[32,33] kinetic supply of reactants,[34] desorption of products,[35] and adsorbate-adsorbate interactions.[36] The local environment of the catalyst also plays a significant role in modulating the selectivity of the CO_2RR and the reduction potential of the competing hydrogen evolution reaction (HER), including local pH,[37–41] electrolytes,[42,43] and cations.[44–47] Moreover, these factors are highly sensitive to current density and applied potential. Most academic investigations of CO_2RR electrocatalysts are typically performed in three-compartment aqueous ''H-cells'' that restrict J to <100 mA cm^{-2} due to mass transfer limitations and low CO_2 solubility.[15,19,48] Given that the applied current density affects the chemical environment of a catalyst and the catalytic activity, catalyst testing in an H-cell is generally not representative of commercial operating conditions that require $J>200$ mA cm^{-2}. One must also consider that the performance of an electrocatalyst will be a mixture of both the material and the local environment, as opposed to solely the catalyst surface characteristics (*e.g.*, morphology, crystallographic face, *etc.*).[49]

These constraints make it imperative to study catalytic performance at $J>100$ mA cm^{-2}. Such studies must be performed in continuous flow reactors that exhibit decreased mass transfer resistances relative to

batch-type H-cell reactors by driving fluid flow across the catalyst surface. Furthermore, the implementation of catalysts in flow reactors can open up entirely new fields of CO_2RR research. A clear example of this phenomenon is our demonstration that molecular catalysts achieve stable, selective CO production in a flow reactor, but not in an H-cell environment.[50] Another advantage of the flow reactor architecture is that benchtop flow reactor design can inform the scale up of CO_2 electrolyzers to multi-cell stacks that are compatible with commercial operation. Such an approach has previously been effective in developing other industrial electrolysis technologies such as fuel cells and H_2O electrolyzers.[51] Notwithstanding, strikingly few studies exist of the CO_2RR in a flow reactor relative to H-cell.

This chapter highlights the challenges and opportunities of testing CO_2RR flow cells to better account for the local environment at the catalyst surface (*e.g.*, pH, electrolyte), transport phenomena, and ion and charge transfer properties. We examine the various flow reactor architectures that are currently being studied in this field, and outline strategies for catalyst testing at high current densities.

10.2 Differentiated CO_2RR Chemistry in an H-Cell and Flow Reactor

A key difference between a continuous flow reactor and an H-cell is the roughly 3 orders of magnitude difference in the CO_2 diffusion boundary layer thickness (*i.e.*, ~50 μm in an H-cell *c.f.* ~50 nm in a gas-diffusion layer).[52,53] This difference allows for higher maximum current densities in a flow reactor. Our reaction-diffusion model predicts that the maximum current density (J_{max}) in an aqueous-fed system is <35 mA cm^{-2} for two-electron CO_2RR processes. For gas-fed reactors, J_{max} values can reach >200 mA cm^{-2} with gas-diffusion layers (GDLs) because of the smaller CO_2 diffusion boundary layer thickness relative to H-cell setups.[53] These predictions are corroborated by experimental literature, including the first report of gas-diffusion layers for CO_2RR by Cook *et al.* in 1990.[54,55]

A simple 1D reaction-diffusion model teaches that the local environment directly influences CO_2RR pathways and kinetics, and that the CO_2RR itself has a profound impact on the local environment.[9,56–59] This reaction-driven sensitivity arises from the fact that H_3O^+, HCO_3^-, and H_2O are reactants in the CO_2RR chemistry, as well as the competing HER. In most cases, the HER is thermodynamically favorable relative to the relevant CO_2RR. This situation creates a competition for protons and electrons between CO_2RR and HER that must be carefully managed.

At $J<1$ mA cm^{-2}, H_3O^+ present in the local electrolyte can directly mediate both the CO_2RR and HER.[60] As J is increased and H_3O^+ is depleted, H_2O is reduced to provide the requisite H^+ (Figure 10.2a), and concomitant formation of OH^- increases the local electrolyte pH (Figure 10.2c).[61,62] At slightly higher CO_2RR current densities (*e.g.*, $\sim 35-100$ mA cm^{-2} [38,42]) in

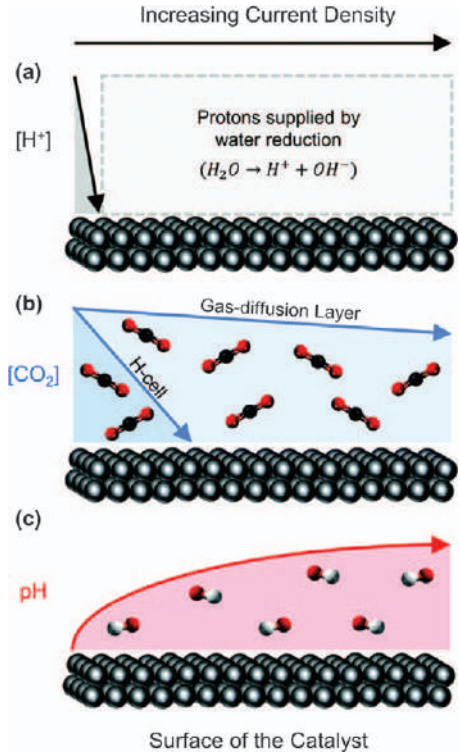

Figure 10.2 The relative effect of current density on the CO_2 reduction reaction reaction (a) proton source, (b) concentration of CO_2 and (c) pH at the surface of a CO_2 reduction catalyst.
Reproduced from ref. 53 with permission from the Royal Society of Chemistry.

aqueous-fed systems, the catalyst is starved of CO_2 due to diffusion limitations and the equilibrium is shifted towards HCO_3^- because of the higher local pH (Figure 10.2b and c).[56,57] The conversion of CO_2 into HCO_3^- results in the deleterious consumption of the feedstock and enhancement of the HER.[63] As the reaction current density is increased from zero to the point where CO_2 is depleted at the catalyst layer, the surface coverage and binding energies of key intermediates at the catalyst surface are affected by changes in the local environment.[62,64,65] These changes are reminiscent of surface effects incurred by varying material composition, structure or morphology. The activity of a CO_2RR electrocatalyst is clearly defined as much by the environment around it as by the composition and geometry.

Modeling CO_2 reduction reactivity as a function of current density shows that the CO_2 concentration and pH in the electrolyte at low current densities are relatively similar for both the H-cell and the gas-fed flow reactor (Figure 10.3). These similarities are expected because the smaller CO_2 diffusion boundary layer thickness does not impact the availability of CO_2 in

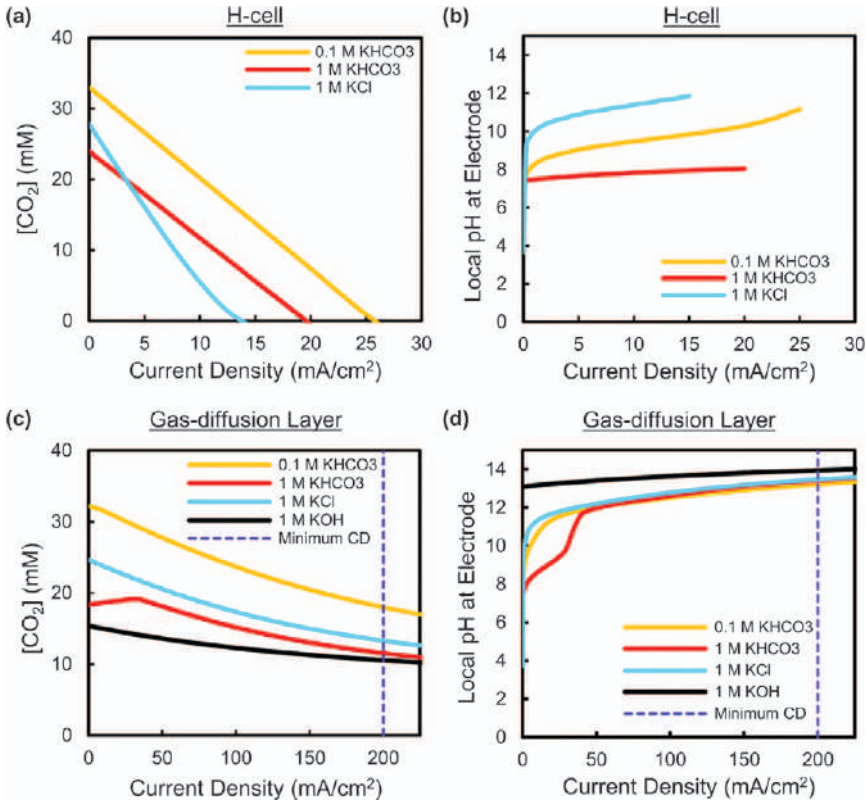

Figure 10.3 Simplified predictions of the electrode concentration of CO_2 and pH for commonly-used electrolytes as a function of current density in an (a and b) H-cell with a 50 μm CO_2 diffusion thickness and (c and d) a gas-diffusion layer with a 50 nm CO_2 diffusion thickness and liquid diffusion layer of 200 μm. A Faradaic efficiency of CO_2-to-CO of 90% is assumed.
Reproduced from ref. 53 with permission from the Royal Society of Chemistry.

the electrolyte to a significant extent, and OH^- diffusion is moderated by the catholyte. In both cases, the local pH increases quickly for weakly-buffered electrolytes (1 M KCl, 0.1 M $KHCO_3$) because the OH^- by-product cannot diffuse from the catalyst at a sufficient rate, nor can it be immediately buffered (Figure 10.3b and d). Indeed, the pH at the catalyst can shift by as much as 6 units within the first $1-2$ mA cm^{-2}.[60] These large pH swings not only impact CO_2 reduction reactivity, but they also impact the reference and working electrodes to complicate the measurement of equilibrium potentials, and, in turn, onset potentials and Tafel slopes. Our results also highlight how, at low current densities, the solvent can act as the sole proton source when using slightly acidic CO_2-saturated electrolytes (Figure 10.3a). This situation creates the possibility for a CO_2RR electrocatalyst to be

effective within the Tafel region, but exhibit slower kinetics at higher potentials/current densities if H_2O reduction becomes rate-determining. These results illuminate the challenges of studying electrocatalysts at low current densities.

An extrapolation of this model to commercially relevant current densities (>200 mA cm^{-2}) indicates that the environment near the CO_2RR electrocatalyst will be very basic (pH >12) regardless of the electrocatalyst or electrolyte (Figure 10.3d). Indeed, the formation of OH^- will drive the pH at the catalyst layer to >12, even when using a 1 M $KHCO_3$ buffered electrolyte. While a 0.1 M $KHCO_3$ electrolyte can be used in an H-cell to approach the local pH values reached at high current densities (Figure 10.3), these conditions are reached only when CO_2 is largely depleted and over a small current density/potential range. The local alkaline conditions could, in principle, be avoided with an acidic electrolyte, but the reaction kinetics would have to favor the CO_2RR over HER in a concentrated protic environment. Moreover, changes in local pH will drive up the overall cell potential (even if the locally corrected cathode potential is not affected). These results all point to the importance of the local environment on the CO_2RR chemistry, and that this environment will be affected by the cell configuration.

10.3 Catalyst Testing at High Current Densities

It is widely known that the composition and structure of an electrocatalyst can impact the binding energies of substrates to the surface, which effectively gate reaction pathways to converge on a specific product. The previous section highlighted how the local chemical environment of the catalyst provides a similar function. Several studies have noted that higher local pH conditions are needed to favour CO and multi-carbon products over H_2 and CH_4 formation at Ag and Cu catalysts.[38,42] At high current densities, this effect is pushed to an extremely alkaline environment with or without a buffer. This section discusses how pH affects the relative rates of CO_2RR and HER.

The HER is the key competing reaction to CO_2RR at the cathode. In a basic environment, the HER proceeds through direct H_2O reduction and the Volmer–Tafel or Volmer–Heyrovsky steps (Figure 10.4). The Volmer step is particularly slow for widely used Cu, Au, and Ag electrocatalysts in basic media due to poor H_2O dissociation and the weak adsorbed H (*H) binding energies that are to the right of the peak of the HER volcano plot (Figure 10.5).[66–69] Simultaneous CO_2RR at a catalyst surface also suppresses HER activity by weakening hydrogen binding to the surface, blocking surface sites, and consuming protons.[70,71] For catalysts on the left side of the HER activity volcano plot (*e.g.*, W, Mo, Co, Ni), HER activity in a basic environment may increase for the same fundamental reasons.

For most metals, operating at current densities >200 mA cm^{-2} provides a secondary means of suppressing HER by acting to weaken hydrogen binding energies at a higher local pH. Secondary approaches for suppressing HER

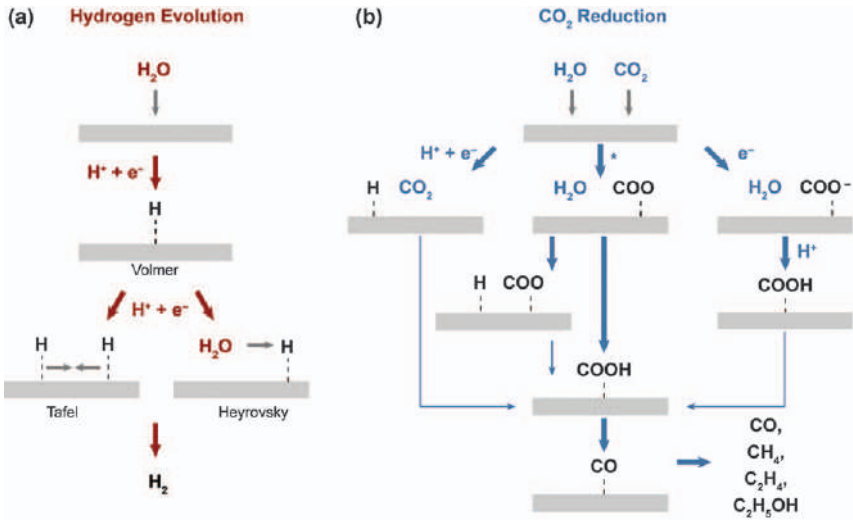

Figure 10.4 (a) The general reaction pathway for the hydrogen evolution reaction (HER) in neutral and basic media; HER is the primary competing reaction to CO_2 reduction. (b) Possible reaction pathways for electrochemical CO_2 reduction to adsorbed CO (*CO) showing variations of the initial proton-electron transfer step that may be thermodynamically or kinetically affected by changes in the local reaction environment. Adapted from ref. 53 with permission from the Royal Society of Chemistry.

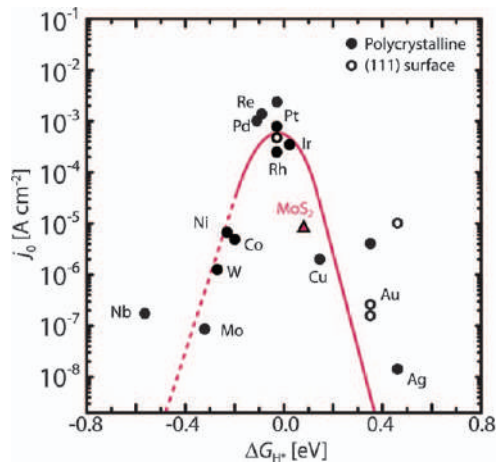

Figure 10.5 Schematic representation of the relationship between the exchange current density and hydrogen binding Gibbs energy of intermediates (*H) in the HER of multiple transition metals and MoS_2. Reproduced from ref. 68 with permission from American Chemical Society, Copyright 2010, and from ref. 69 with permission from The American Association for the Advancement of Science, Copyright 2017.

are especially important for multi-carbon product formation. For example, 100-fold differences in C2 formation over C1 formation can be achieved in an H-cell, but H_2 still represents $20-30\%$ of the electrolytic product.[54,72–74] When the same catalyst system operates at elevated current densities in a flow reactor, the selectivity for carbon-based products can be increased simply because of HER suppression (Figure 10.3).

The local pH environment influences the energetics of different CO_2RR products. For catalysts capable of producing only CO and H_2, HER suppression leads to higher CO selectivity. The observation that CO is formed at a Ag catalyst (under alkaline conditions) at close to the equilibrium potential of -0.11 V *vs.* RHE[9,10] indicates that the actual CO_2RR reaction is improved (and it is not just HER suppression). How CO is formed at a Cu surface in a flow reactor also differs from that of a more neutral H-cell environment. In H-cell tests, CO selectivity of >20% is observed only at very low current densities (<5 mA cm^{-2}), with methane, ethylene, and ethanol favoured at higher current densities. Under alkaline conditions performed in a flow reactor, high CO selectivities can be maintained over a much broader range ($0-200$ mA cm^{-2}).[11,75] These results suggest that the binding energy of CO at a Cu surface may be weakened in the flow reactor environment promoting faster desorption of the formed *CO intermediate under neutral conditions.[11] The selectivity towards CO does eventually decrease in favour of higher-order products similar to what is observed in an H-cell, but at much higher current densities (>200 mA cm^{-2}).

While some studies at elevated current densities have used neutral-pH catholytes (*e.g.*, KCl, HCO_3^-)[4,13,16,75–77] the majority of experiments performed in reactors have used KOH as the bulk catholyte.[9–11,74,78–81] An alkaline catholyte enables the catalyst performance to be probed across both low and high current densities with a similar local reaction environment.[10,74,78,79,81] In a 1 M KOH environment, CO_2 reduction products have been observed with Cu, Au, and Ag catalysts at earlier overall onset potentials than in neutral conditions.[11,78,82,83] These experiments do not pay the same overpotential price associated with the large local pH swing from neutral to alkaline conditions. Additionally, the interaction between unreacted CO_2 and OH^- is problematic for overall stability (*vide infra*). Using an alkaline electrolyte for testing and characterizing catalyst performance is, however, a promising means of mimicking the local environment of high current densities (>200 mA cm^{-2}) while being able to measure catalytic activity even at lower current densities (<100 mA cm^{-2}).

An additional reaction constraint at >200 mA cm^{-2} is the choice of electrolyte. The ohmic losses of many electrolytes, regardless of the catalyst or substrate used, are prohibitive. Figure 10.6 shows an example of how a combined catholyte and anolyte thickness of 3 mm yields prohibitively high ohmic losses. The 0.1 M $KHCO_3$ electrolyte used in the majority of the highest selectivity C_2H_4 studies, for instance, results in heating losses of 6 V at 200 mA cm^{-2}. This voltage is *ca.* 5-fold higher than the thermodynamic cell potential of a H_2O electrolyzer. Consequently, a low-conductivity

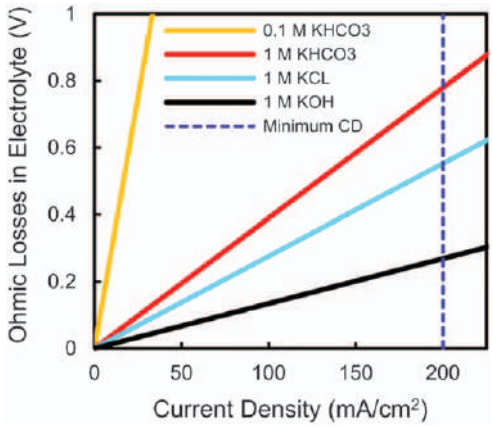

Figure 10.6 Expected ohmic losses as a function of current density for commonly-used electrolytes in an electrochemical cell with a combined 3 mm catholyte and anolyte thickness at 25 °C.
Reproduced from ref. 53 with permission from the Royal Society of Chemistry.

electrolyte can never be used in a functioning system unless the electrolyte pathway between the anode and cathode is eliminated or greatly reduced (*vide infra*).[13,16] This issue is exacerbated for multi-carbon products such as C_2H_4. These ohmic drops also cast light on how components of a flow reactor other than the electrocatalyst need to be fully addressed.

Finally, high current densities (>200 mA cm^{-2}) and high local pH (pH > 10) will also affect catalyst stability and GDL stability. These conditions may result in the dissolution of metals into solution and/or the unfavourable modification of the GDL surface properties such as hydrophobicity.[82] While this effect does not currently appear to dominate many Cu and Ag catalysts in flow reactors, this will prove to be the ultimate test in building commercially relevant reactor assemblies.

10.4 Flow Reactor Architectures

Electrochemical CO_2 reduction has been investigated in four different types of flow reactors: H-cells; zero-gap membrane reactors; alkaline flow-reactors (microfluidic flow reactors); and hybrid reactors (Figure 10.7). H-cells (Figure 10.7a) are batch type reactors that separate the anodic and cathodic compartments using a polymer electrolyte membrane (PEM). In these types of reactors, CO_2 is sourced from a CO_2-saturated electrolyte and the diffusion of CO_2 through the hydrodynamic boundary layer controls reagent delivery to the cathode surface. Zero-gap membrane reactors (Figure 10.7b) are continuous flow reactors that contain a PEM in direct contact with both the anode and cathode to form a membrane electrode assembly (MEA). This design, which is similar to PEM fuel cells and H_2O electrolyzers, serves to minimize ohmic losses by largely eliminating ionic transport through the

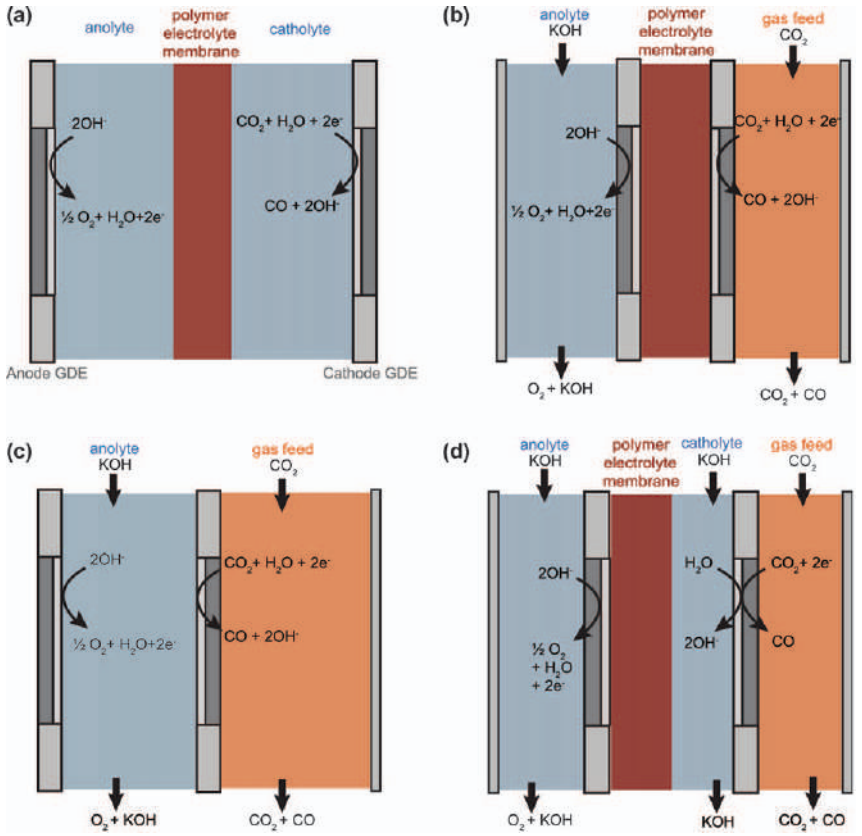

Figure 10.7 Schematics of the four different types of CO_2 reactors: (a) H-cell, (b) zero-gap membrane reactor, (c) microfluidic reactor, and (d) hybrid reactor.

liquid electrolyte layer. An alkaline flow reactor (or microfluidic reactor) design separates the anode and cathode with a conductive OH^- solution (*e.g.*, KOH, NaOH) instead of a PEM. Finally, a hybrid reactor (Figure 10.7d) borrows design principles from a zero-gap membrane reactor and a microfluidic reactor by using a PEM to separate the anode and cathode (similar to zero-gap membrane reactors) as well as a microfluidic catholyte conduit (similar to an alkaline flow reactor) that flows between the cathode and the PEM. The vast majority of CO_2RR catalyst research has been performed in batch-type H-cell architectures (Figure 10.7a),[84] but the inherent mass transfer limitations of this setup constrain current densities to $\sim$35 mA cm^{-2}.[85] It is largely for this reason that testing in other architectures is required.

Zero-gap membrane reactors, alkaline flow reactors, and hybrid reactors are continuous systems that enable higher CO_2RR current densities than

H-cells by enhancing mass transport of CO_2 to the catalyst.[9–11,73–75,78–80,86] Water electrolyzers do not encounter the same mass transport issues as aqueous CO_2 electrolyzers because of the high concentration of water (55 M) relative to CO_2 in aqueous media at ambient conditions (33 mM) (Figure 10.8b). Utilizing gaseous CO_2 gas feedstocks in these configurations provides a means of increasing the local concentration of CO_2 at the catalyst layer by circumventing the aqueous solubility limit of CO_2 and decreasing the diffusion boundary layer thickness relative to H-cell configurations (Figure 10.8c).[87] The geometry and operational parameters of each of these continuous gas-fed reactors varies significantly;[9–11,73–75,78–80,86] however, each architecture uses a porous gas diffusion electrode (GDE) as the cathode to increase catalyst dispersion and contact time between reactants and active sites relative to H-cells fitted with planar electrodes.

Experiments with zero-gap flow reactors have revealed the need for a solid-support aqueous layer between the GDE and membrane, or highly humidified CO_2, to achieve high CO_2RR selectivity compared to HER selectivity.[13,16,88] These studies provide evidence that the CO_2RR in the cathode compartments of microfluidic/hybrid reactors (Figure 10.7c and d) and zero-gap reactors (Figure 10.7b) likely both proceed at a liquid–solid interface as opposed to a triple-phase boundary. These two cathode variations then similarly require the diffusion of CO_2 across a gas–liquid interface and through a thin electrolyte to a porous catalyst layer. For this reason, appropriate H_2O management within the GDE is essential for all gas-fed CO_2 reactor architectures to ensure the stability of the gas–liquid interface and to prevent flooding or catholyte evaporation for gas-fed CO_2 reactors.[11,16,89] The anode chemistry is also germane to the design of CO_2 flow reactors because the oxygen evolution reaction (OER) suffers from sluggish kinetics and yields low-value oxygen gas. The remainder of this section will expand upon the

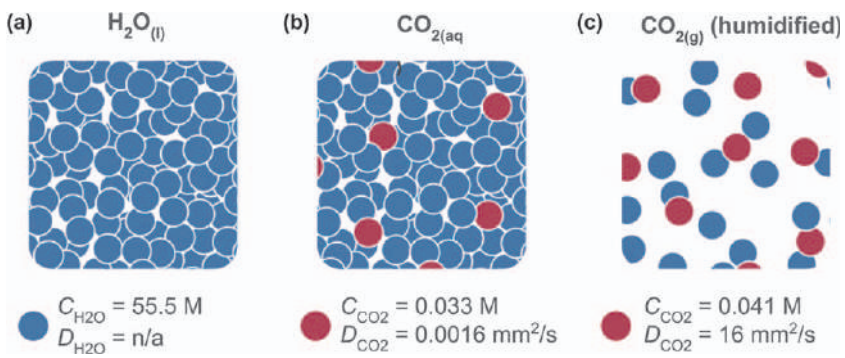

Figure 10.8 Cartoon illustrating the relative saturated concentrations, C, and diffusion coefficients, D, for (a) water, (b) CO_2 in aqueous solution, and (c) humidified gaseous CO_2. Values at room temperature and pressure are indicated.
Adapted from ref. 4 with permission from American Chemical Society, Copyright 2018.

operational details of zero-gap membrane reactors and microfluidic/hybrid flow reactors to provide an overview of the benefits and shortcomings of both configurations.

In a typical zero-gap membrane reactor, the membrane electrode assembly consists of a cathode GDE, membrane, and anode (which is either a porous free-standing electrode or a GDE) sandwiched between two flow plates. This configuration leaves no gap between the membrane and electrodes. The membrane serves to transport ionic species (*i.e.*, H^+ and OH^-) and prevent crossover of CO_2 and electrochemical products. Three classes of membranes are used in CO_2 flow reactors: anion exchange membranes (AEMs); cation exchange membranes (CEMs); and bipolar membranes (BPMs). The choice of membrane allows for the transport of ions to produce either acidic or basic conditions at the anode and cathode. AEMs mediate transport of anions from a basic cathode to the anode, CEMs transport cations from an acidic anode to the cathode, and BPMs enable the dissociation of H_2O under an applied potential and transport H^+ to the cathode and OH^- to the anode.

Microfluidic or alkaline reactors utilize a liquid-filled conduit to separate the anode and cathode compartments.[90,91] Microfluidic reactors operate without membranes by relying on differences in the diffusivity of gas species to separate reduced and oxidized products. A membrane can also be incorporated into microfluidic reactors, to form ''hybrid reactors'', to prevent reduction of oxidized products at the anode (Figure 10.7d).[83] The cathodic chemistry in hybrid reactors occurs at a liquid catholyte-solid interface, as opposed to the polymeric-solid interface encountered in zero-gap membrane reactors. The ability to modulate the pH and other catholyte properties in these systems has been effective in suppressing HER and enabling high CO_2RR current densities.[90,91]

The preferred choice of catalyst materials, catholyte, anolyte, and membrane will differ depending on the constraints of the selected CO_2 electrolyzer architecture. Each continuous reactor design (zero-gap membrane reactor, microfluidic reactor, and hybrid reactor) has different operational challenges that it must overcome by means of material and system design to achieve CO_2RR at industrially relevant current densities for prolonged times. Regardless of the reactor being utilized, each component must work in concert to transport ions, electrons, and gases to and from the active sites while sustaining a high conductivity to prevent ohmic losses. Research efforts focused on all three reactors are therefore synergistic in informing the fundamental science and engineering of CO_2RR technologies.

10.5 Membranes

There are three distinct classes of ion exchange membranes (AEM, CEM, and BPM) that are utilized in membrane-containing CO_2RR reactors. These membranes are classified by the type of ion they conduct (cations, anions, or both). The choice of membrane is pivotal in reactor design because the membrane defines the pH at both the anode and cathode. This section

describes the function and limitations of the three classes of ion exchange membranes in regards to their application in a CO_2 electrolyzer, and highlights specific examples where the membrane is leveraged to increase the selectivity and activity of the CO_2RR.

10.5.1 Anion Exchange Membranes

In an AEM, positively-charged functional groups facilitate anion (*e.g.*, OH^-, HCO_3^- and CO_3^{2-}) transport from the cathode to the anode during CO_2 reduction (Figure 10.9a). AEMs enable CO_2 reduction to occur in a basic environment by transporting OH^- produced from the CO_2RR to facilitate the flow of ionic current. The basic catalyst interface increases the selectivity for the CO_2RR by means of reducing the local H^+ concentration at the catalyst surface, and, in turn, suppressing the HER. Indeed, the highest CO_2-to-CO conversion rates reported to date are achieved in an AEM-based electrolyzer.[12] For example, Zhuang and co-workers tested a Au cathode interfaced with a quaternary ammonia poly(*N*-methyl-piperidine-*co*-*p*-terphenyl) AEM at 3.0 V and reached current densities of 500 mA cm^{-2} and a $FE_{CO} > 85\%$ while operating at 50 °C.[12]

There are operational challenges encountered when utilizing AEMs in both zero-gap and hybrid reactors. Acid–base reactions between the CO_2 feed and OH^- at the basic catalyst interface generate HCO_3^- and CO_3^{2-} and suffocate the catalyst of catalytically active CO_2.[81] In hybrid reactors, the HCO_3^- and CO_3^{2-} produced can readily contaminate the KOH catholyte solution by decreasing the pH and precipitating $KHCO_3$ and K_2CO_3 crystals on the electrode/membrane surfaces.[52] Crystal formation can also occur without a KOH catholyte solution: in zero-gap membrane reactors K^+ can be transported from the anode to the cathode and react with HCO_3^- and CO_3^{2-} to form $KHCO_3$ and K_2CO_3 crystals. The use of pure H_2O as opposed to KOH at the anode has been demonstrated as a means of reducing CO_3^{2-} and HCO_3^- crystal formation, however, this reduces the ionic conductivity of AEMs and drives up the cell potential. The polarity of AEMs permits HCO_3^- and CO_3^{2-} to cross the membrane from the cathode to the anode in both zero-gap membrane and hybrid reactors, which results in parasitic loss of the CO_2 feedstock and re-release of the CO_2 gas by reaction between H^+ and HCO_3^-/CO_3^{2-} at the anode.[92,93]

Masel and co-workers developed a highly conductive anion exchange membrane, Sustainion®, that exhibits a stability of >1000 h under specific operating conditions.[70,94] Improved ion conductivity through the membrane is needed to decrease the full cell potential (due to reduced ohmic resistance) and to inhibit co-ion transport through the membrane.[95] Anions have inherently lower mobilities than cations, which is why the reported ion conductivities through AEMs are typically lower than for CEMs.[96,97] Improving OH^-, HCO_3^-, and CO_3^{2-} conduction through AEMs has the potential to boost CO_2 electrolyzer performance by decreasing the ohmic resistance within the polymer electrolyte. A suitable AEM that inhibits product

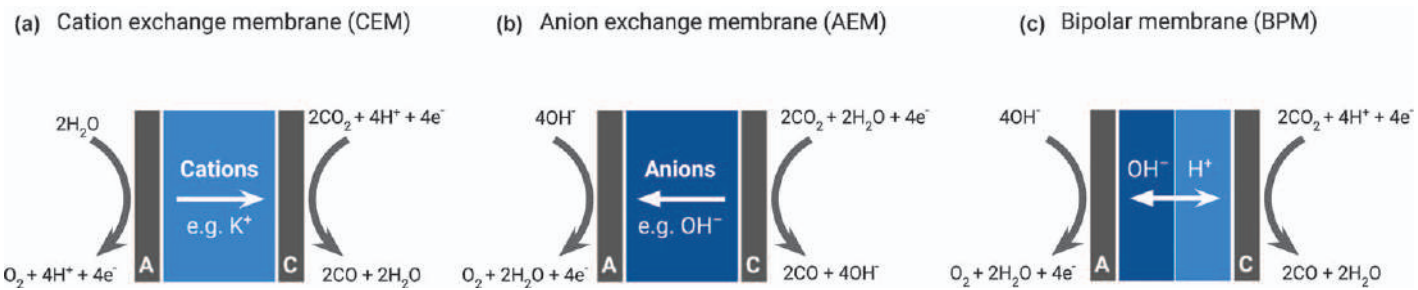

Figure 10.9 An overview of the anode (labelled ''A'') and cathode (labelled ''C'') half reactions that occur within a CO_2 to CO conversion flow cell as governed by (a) a cation exchange membrane, (b) an anion exchange membrane, and (c) a bipolar membrane. Reproduced from ref. 4 with permission from American Chemical Society, Copyright 2018.

crossover and exhibits high anion conductivity and stability is therefore needed for a practical CO_2 electrolyzer containing an AEM.

10.5.2 Cation Exchange Membranes

CEMs, such as Nafion®, contain negatively-charged functional groups that mediate the conduction of positive ions, such as H^+, from the anode to the cathode (Figure 10.9b). A Nafion®-based CO_2RR flow reactor operating at ambient temperature and pressure was first demonstrated in 2008 by Newman and co-workers.[88] Modifying the Nafion® membrane and cathode interface with a solid-supported aqueous buffer layer (1 M $KHCO_3$) was shown to suppress H_2 formation. This modified cell configuration enabled CO production with a FE_{CO} of 20% at a current density of 100 mA cm^{-2}. However, the reactor suffered from poor stability and the FE_{CO} degraded quickly over 5 h of electrolysis.

10.5.3 Bipolar Membranes

There is also a growing body of literature regarding zero-gap membrane reactors utilizing a BPM for the CO_2RR. A BPM is a membrane that consists of an anion exchange layer (AEL) adjacent to a cation exchange layer (CEL). BPMs induce H_2O dissociation at the CEL-AEL interface under an applied potential, and maintain a constant pH at both sides of the cell as H^+ ions migrate towards the cathode and OH^- ions move to the anode (Figure 10.9c).[98] As with a CEM, H^+ is driven towards the cathode; however, the added benefit of a BPM is that the basic anolyte enables inexpensive anode catalyst materials (*e.g.*, Ni foam) to be used instead of rare-earth metal catalysts.[99,100] BPMs have also been shown to inhibit product crossover, a parasitic process in AEM-based CO_2 flow reactors.[101] Indeed, the suppression of product crossover enables BPM-containing electrolyzers to achieve industrially relevant performance metrics. We performed gas-fed CO_2 electrolysis in a BPM-based zero-gap reactor and found that incorporating a solid supported layer between the BPM and the cathode was instrumental to reaching high CO selectivities.[102] These results track the findings made by Newman and co-workers with a CEM-based reactor.[88] We also demonstrated that humidifying the gaseous CO_2 is key to maintaining reactor longevity: the BPM configuration utilizing humidified CO_2 is capable of reaching a ~65% FE_{CO} at 100 mA cm^{-2} and 3.4 V over a period of 24 h.[16] Another report by us showed that the H^+ flux delivered to the cathode from BPMs can be used to convert HCO_3^- to electrochemically active CO_2 *in situ* to supply the reactant for the CO_2RR.[103] Managing the H^+ flux to the cathode to reduce HER, and minimizing the voltage consumption (>0.83 V) required to induce water splitting at the CEL-AEL interface, are the most significant challenges associated with the scale-up of BPM containing CO_2 electrolyzers.[104] These results warrant further research on designing membranes

specific for CO_2 reduction, along with an increased focus on the engineering of the membrane/GDE interface.

10.6 Gas Diffusion Electrodes

10.6.1 Gas Diffusion Layers

Conventional GDLs for CO_2RR are composed of an array of carbon-based fibers that form a carbon cloth or paper.[105] The network of carbon fibers creates a highly porous medium containing tortuous paths through which gaseous CO_2 travels. A second denser carbon fiber microporous layer (MPL) component can be situated on top of the carbon cloth or paper. MPLs contain carbon powder or nanofibres bound by polytetrafluoroethylene (PTFE), which are spread evenly in a thin layer on top of the carbon fiber backing layer of the GDL. The MPL provides a smoother interfacial layer that minimizes the contact resistance in zero-gap membrane reactors and also enables a more uniform distribution of catalyst.

10.6.2 Gas Diffusion Electrode Structure and Function

When catalysts are applied to GDLs, the combined materials are referred to as gas diffusion electrodes (GDEs). Supported catalysts on carbon-based GDLs are the most common type of GDE, although non-carbon-based GDEs have also been reported to be used at the anode.[16] For CO_2 reduction in zero-gap reactors and hybrid reactors, the inclusion of a GDE at the cathode is essential for achieving high current densities. Catalysts can be incorporated onto the GDL through multiple deposition methods, including: drop-casting; airbrushing; electrodeposition; compression; or by incorporating a catalyst into the material of the GDL itself.[14,78,79] The immobilization of catalysts onto these conductive, high surface area layers has the effect of creating high catalytic surface areas with long residence times for CO_2 within the electrode. This combination allows for heterogeneous catalysts to achieve high current densities for electrochemical reactions. The addition of a catalyst layer onto a GDL provides an opportunity to modulate the properties of the GDE by changing the composition of the catalyst ink and the application method.

During CO_2 reduction, the cathode GDE facilitates an electron transfer process when CO_2 and H_2O react on a solid catalyst surface to produce desirable carbon products. The effectiveness of a GDE in selectively mediating the CO_2RR at high current densities is influenced by the properties of both the GDL and the catalyst coating. GDE properties that affect the nature of the interface include conductivity, porosity, permeability, hydrophobicity, and chemical stability, and can be controlled through the meticulous selection of materials and fabrication methods.[106] Manipulating the carbon fiber component of GDLs is challenging because the fabrication methods are arduous and complex.[106] Manipulating the MPL and catalyst layer, however, is

relatively easier. Kenis and co-workers have examined microfluidic reactors using GDLs coated with Ag nanoparticle catalysts.[14,78,79] Altering the PTFE content of MPLs was observed to affect the H_2O transport properties of the GDEs.[79] Changes in the composition, deposition method, and morphology of the catalyst layer similarly influence the responding performance metrics.[14,78] The aqueous chemistry at the catalyst surface in the membrane-free microfluidic reactor used in these studies is different from that of a zero-gap membrane reactor because the GDE is in direct contact with a free-flowing electrolyte. Nonetheless, the findings from the microfluidic studies provide useful insight into the influence of GDE properties on electrochemical CO_2 reduction performance for zero-gap membrane reactors and hybrid reactors. The mass transport and catalytic performance of GDEs are also affected by properties including porosity, permeability, and conductivity, factors that were not considered in this series of studies. In contrast to fuel cells, catalyst layer deposition methodologies for CO_2 reduction have not yet been optimized. Modulating the properties of catalyst layers and GDLs therefore provides an opportunity for performance improvements using existing technologies and reactor architectures.

The required characteristics of a GDL and catalyst layer for CO_2 reduction are generally understood qualitatively, but the rational design and fabrication of GDEs are non-trivial. Beyond the variations on existing GDE configurations mentioned above, more direct changes to the catalyst ink composition and deposition methodologies may yield more pronounced improvements in performance.[14,78,79] The primary functions of the binding polymer in catalyst inks are to create a suitable hydrophobic surface and to immobilize catalyst particles. PTFE is commonly used in this role for its excellent hydrophobic properties and chemical stability, but adding ion-exchange polymers such as Nafion® or Sustainion® imparts a supporting catalytic function to the binder. Replacing PTFE with other suitable polymers also enables control over the relative hydrophobicity of the interface, which is especially useful for CO_2 reduction because different reactor architectures have unique electrode/electrolyte interfacial properties that must be maintained. Improvements on the current metal nanoparticle catalysts can be expected to come from catalyst engineering; however, the most active portion of the catalyst is embedded beneath the surface of the deposited layer, facing away from the membrane when in an assembled reactor. Traditional nanostructuring approaches must therefore be reassessed because the primary active surface area is not easily accessible to surface characterization techniques.[11] This reversed geometry presents a unique challenge in catalyst layer engineering because GDEs must be designed not only with high active surface areas but also with porosity and permeability to enable efficient mass transport to and from the active catalytic sites. Methodologies such as air-brushing with precise control over deposition parameters can influence the morphology and promote the formation of these highly porous layers with suitable permeability.[14] Implementing electrode fabrication methods comparable with existing

state-of-the-art methods used in analogous fuel cell systems, and addressing these design challenges, is paramount if commercially relevant performance metrics are to be met for CO_2RR.[107] Engineering the catalyst–aqueous interface to optimize the number of active sites and the amount of H_2O supplied to the cathode (without flooding the cell) is necessary to achieve stable, high-selectivity conversion of CO_2 at appreciable current densities.

10.6.3 Water Management

Water management is critical for CO_2RR in zero-gap membrane reactors. Strategies for managing H_2O supply and consumption is complicated because H_2O is present in multiple phases and locations within the flow reactor. For most CO_2RR chemistry, H_2O is a reactant; thus, a constant supply of H_2O to the cathode is needed. However, H_2O can also block CO_2 from reaching the active catalytic sites, thereby promoting the HER and reducing the CO_2RR selectivity. Finding the conditions that provide the ideal amount of H_2O to the catalyst is paramount to CO_2RR in a flow reactor.

In gas-fed zero-gap reactors, H_2O is needed to hydrate the membrane. Hydration of the membrane is needed to enhance ion conductivity and prevent mechanical failure of the membrane. We have demonstrated substantial improvements in stability in BPM-based zero-gap membrane systems by simply managing the relative humidity of the gaseous CO_2 feed (Figure 10.10).[16] This finding corroborated our earlier experiments in which a similar improvement in performance was achieved by adding a solid-supported electrolyte layer adjacent to the bipolar membrane, highlighting the influence of membrane hydration on CO_2RR performance.[16] While the membrane can be hydrated by incorporating a solid-supported electrolyte layer or adjacent catholyte compartment, the cell potential is driven up due to high ohmic losses. Bell, Weber, and Weng highlighted the

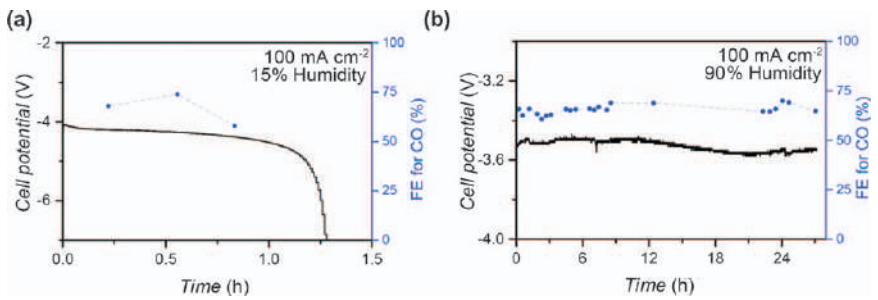

Figure 10.10 Comparison of the stabilities (as measured by the required cell potential at $J = 100$ mA cm^{-2}) of two analogous BPM-based flow cells containing a solid electrolyte support layer fed with either (a) 15% humidity CO_2 gas, or (b) 90% humidity CO_2 gas.
Reproduced from ref. 4 with permission from American Chemical Society, Copyright 2018.

effects of operating conditions on H_2O transport processes of diffusion and electro-osmotic drag.[92] Their work shows that thinner membranes can mitigate membrane dehydration in zero-gap reactors with humidified gaseous feeds at both the cathode and anode, but this may increase the risk of flooding in reactors with a liquid electrolyte at the anode. The PTFE content of the GDE cathode can modulate hydrophobicity to achieve an optimal H_2O balance.[79] Addressing H_2O management in CO_2RR zero-gap reactors is in the early stages of development, and solutions must be tailored for specific cell configurations.

While the mass transport of CO_2, H_2O, and CO_2RR products is largely influenced by the GDL, the macroscale geometry of chemically-benign electrolyzer components manipulates the fluid dynamics of gas and liquid flow within the reactor and therefore must also be considered. The flow plates govern how species are transported to and from the catalytically active regions of the reactor. The flow field channel thickness, path lengths, and patterns will affect the distribution of CO_2 and H_2O delivered to the cathode.[108–110] The rich literature on fuel cells and H_2O electrolyzers teach that distribution of these reactants needs to be uniform in continuous flow reactors to avoid non-uniform local current densities, conversion efficiencies, and interface chemistry.[111–113] Defining the relationships between reactor geometry and performance is only starting to be addressed in the CO_2RR community.[112]

10.7 Conclusions

Research in the CO_2RR field has largely focused on batch type H-cell experiments, which do not account for the significant influence of non-catalytic components and feedstock characteristics on overall cell performance. Electrochemical flow reactors provide a more commercially relevant testing platform than H-cells because flow reactors enable the systematic manipulation of non-catalytic components that affect the industrial viability of CO_2 electrolyzers. This chapter emphasized the importance of testing catalysts at higher current densities, and highlighted promising strategies to optimize the GDL, PEM, flow field, feedstock type, and electrolyte supply to drive CO_2 electroreduction towards the higher current densities required for commercialization. We hope this chapter will encourage researchers to consider system-integrated testing of CO_2RR materials to accelerate the translation of this important technology from the lab into practice.

References

1. T. R. Cook, D. K. Dogutan, S. Y. Reece, Y. Surendranath, T. S. Teets and D. G. Nocera, *Chem. Rev.*, 2010, **110**, 6474–6502.
2. M. R. Shaner, H. A. Atwater, N. S. Lewis and E. W. McFarland, *Energy Environ. Sci.*, 2016, **9**, 2354–2371.

3. N. Z. Muradov and T. N. Vezirolu, *Int. J. Hydrogen Energy*, 2005, **30**, 225–237.
4. D. M. Weekes, D. A. Salvatore, A. Reyes, A. Huang and C. P. Berlinguette, *Acc. Chem. Res.*, 2018, **51**, 910–918.
5. R. Masel, Z. Liu, D. Zhao, Q. Chen, D. Lutz and L. Nereng, in *Commercializing Biobased Products*, 2015, pp. 215–257.
6. S. Verma, B. Kim, H.-R. M. Jhong, S. Ma and P. J. A. Kenis, *ChemSusChem*, 2016, **9**, 1972–1979.
7. J. M. Spurgeon and B. Kumar, *Energy Environ. Sci.*, 2018, **11**, 1536–1551.
8. P. De Luna, C. Hahn, D. Higgins, S. A. Jaffer, T. F. Jaramillo and E. H. Sargent, *Science*, 2019, **364**, eaav3506.
9. C. M. Gabardo, A. Seifitokaldani, J. P. Edwards, C.-T. Dinh, T. Burdyny, M. G. Kibria, C. P. O'Brien, E. H. Sargent and D. Sinton, *Energy Environ. Sci.*, 2018, **11**, 2531–2539.
10. S. Verma, X. Lu, S. Ma, R. I. Masel and P. J. A. Kenis, *Phys. Chem. Chem. Phys.*, 2016, **18**, 7075–7084.
11. C.-T. Dinh, T. Burdyny, M. G. Kibria, A. Seifitokaldani, C. M. Gabardo, F. P. García de Arquer, A. Kiani, J. P. Edwards, P. De Luna, O. S. Bushuyev, C. Zou, R. Quintero-Bermudez, Y. Pang, D. Sinton and E. H. Sargent, *Science*, 2018, **360**, 783–787.
12. Z. Yin, H. Peng, X. Wei, H. Zhou, J. Gong, M. Huai, L. Xiao, G. Wang, J. Lu and L. Zhuang, *Energy Environ. Sci.*, 2019, **12**, 2455–2462.
13. Y. C. Li, D. Zhou, Z. Yan, R. H. Gonçalves, D. A. Salvatore, C. P. Berlinguette and T. E. Mallouk, *ACS Energy Lett.*, 2016, **1**, 1149–1153.
14. H.-R. Jhong, F. R. Brushett and P. J. A. Kenis, *Adv. Energy Mater.*, 2013, **3**, 589–599.
15. T. Li, Y. Cao, J. He and C. P. Berlinguette, *ACS Cent. Sci.*, 2017, **3**, 778–783.
16. D. A. Salvatore, D. M. Weekes, J. He, K. E. Dettelbach, Y. C. Li, T. E. Mallouk and C. P. Berlinguette, *ACS Energy Lett.*, 2017, 149–154.
17. B. Endrődi, E. Kecsenovity, A. Samu, F. Darvas, R. V. Jones, V. Török, A. Danyi and C. Janáky, *ACS Energy Lett.*, 2019, **4**, 1770–1777.
18. J. He, N. J. J. Johnson, A. Huang and C. P. Berlinguette, *ChemSusChem*, 2017, **11**, 48–57.
19. J. Qiao, Y. Liu, F. Hong and J. Zhang, *Chem. Soc. Rev.*, 2014, **43**, 631–675.
20. C. Costentin, M. Robert and J.-M. Savéant, *Chem. Soc. Rev.*, 2013, **42**, 2423–2436.
21. H. Yang, J. J. Kaczur, S. D. Sajjad and R. I. Masel, *J. CO_2 Util.*, 2017, **20**, 208–217.
22. E. J. Dufek, T. E. Lister, S. G. Stone and M. E. McIlwain, *J. Electrochem. Soc.*, 2012, **159**, F514–F517.
23. M. Jouny, W. Luc and F. Jiao, *Ind. Eng. Chem. Res.*, 2018, **57**, 2165–2177.
24. D. Kim, J. Resasco, Y. Yu, A. M. Asiri and P. Yang, *Nat. Commun.*, 2014, **5**, 4948.

25. X. Liu, J. Xiao, H. Peng, X. Hong, K. Chan and J. K. Nørskov, *Nat. Commun.*, 2017, **8**, 15438.
26. S. Nitopi, E. Bertheussen, S. B. Scott, X. Liu, A. K. Engstfeld, S. Horch, B. Seger, I. E. L. Stephens, K. Chan, C. Hahn, J. K. Nørskov, T. F. Jaramillo and I. Chorkendorff, *Chem. Rev.*, 2019, **119**, 7610–7672.
27. H. Mistry, R. Reske, Z. Zeng, Z.-J. Zhao, J. Greeley, P. Strasser and B. R. Cuenya, *J. Am. Chem. Soc.*, 2014, **136**, 16473–16476.
28. R. Reske, H. Mistry, F. Behafarid, B. R. Cuenya and P. Strasser, *J. Am. Chem. Soc.*, 2014, **136**, 6978–6986.
29. W. Zhu, Y.-J. Zhang, H. Zhang, H. Lv, Q. Li, R. Michalsky, A. A. Peterson and S. Sun, *J. Am. Chem. Soc.*, 2014, **136**, 16132–16135.
30. W. Zhu, R. Michalsky, Ö. Metin, H. Lv, S. Guo, C. J. Wright, X. Sun, A. A. Peterson and S. Sun, *J. Am. Chem. Soc.*, 2013, **135**, 16833–16836.
31. S. Liu, X.-Z. Wang, H. Tao, T. Li, Q. Liu, Z. Xu, X.-Z. Fu and J.-L. Luo, *Nano Energy*, 2018, **45**, 456–462.
32. S. Sen, D. Liu and G. T. R. Palmore, *ACS Catal.*, 2014, **4**, 3091–3095.
33. A. Loiudice, P. Lobaccaro, E. A. Kamali, T. Thao, B. H. Huang, J. W. Ager and R. Buonsanti, *Angew. Chem., Int. Ed.*, 2016, **55**, 5789–5792.
34. A. S. Hall, Y. Yoon, A. Wuttig and Y. Surendranath, *J. Am. Chem. Soc.*, 2015, **137**, 14834–14837.
35. X. Min and M. W. Kanan, *J. Am. Chem. Soc.*, 2015, **137**, 4701–4708.
36. E. R. Cave, C. Shi, K. P. Kuhl, T. Hatsukade, D. N. Abram, C. Hahn, K. Chan and T. F. Jaramillo, *ACS Catal.*, 2018, **8**, 3035–3040.
37. K. J. P. Schouten, E. P. Gallent and M. T. M. Koper, *J. Electroanal. Chem.*, 2014, **716**, 53–57.
38. Y. Pang, T. Burdyny, C.-T. Dinh, M. G. Kibria, J. Z. Fan, M. Liu, E. H. Sargent and D. Sinton, *Green Chem.*, 2017, **19**, 4023–4030.
39. J. E. Pander, D. Ren, Y. Huang, N. W. X. Loo, S. H. L. Hong and B. S. Yeo, *ChemElectroChem*, 2018, **5**, 219–237.
40. Y. Zhang, W. Wu, K. Zhang, C. Liu, A. Yu, M. Peng and J. Zhai, *Phys. Chem. Chem. Phys.*, 2016, **18**, 32178–32184.
41. C. F. C. Lim, D. A. Harrington and A. T. Marshall, *Electrochim. Acta*, 2017, **238**, 56–63.
42. R. Kas, R. Kortlever, H. Yılmaz, M. T. M. Koper and G. Mul, *ChemElectroChem*, 2015, **2**, 354–358.
43. A. S. Varela, M. Kroschel, T. Reier and P. Strasser, *Catal. Today*, 2016, **260**, 8–13.
44. M. R. Singh, Y. Kwon, Y. Lum, J. W. Ager 3rd and A. T. Bell, *J. Am. Chem. Soc.*, 2016, **138**, 13006–13012.
45. E. Pérez-Gallent, G. Marcandalli, M. C. Figueiredo, F. Calle-Vallejo and M. T. M. Koper, *J. Am. Chem. Soc.*, 2017, **139**, 16412–16419.
46. O. Ayemoba and A. Cuesta, *ACS Appl. Mater. Interfaces*, 2017, **9**, 27377–27382.
47. J. Resasco, L. D. Chen, E. Clark, C. Tsai, C. Hahn, T. F. Jaramillo, K. Chan and A. T. Bell, *J. Am. Chem. Soc.*, 2017, **139**, 11277–11287.

48. J. He, K. E. Dettelbach, D. A. Salvatore, T. Li and C. P. Berlinguette, *Angew. Chem., Int. Ed.*, 2017, **56**, 6068–6072.
49. Y. Y. Birdja, E. Pérez-Gallent, M. C. Figueiredo, A. J. Göttle, F. Calle-Vallejo and M. T. M. Koper, *Nat. Energy*, 2019, **4**, 732–745.
50. S. Ren, D. Joulié, D. Salvatore, K. Torbensen, M. Wang, M. Robert and C. P. Berlinguette, *Science*, 2019, **365**, 367–369.
51. P. Millet, R. Ngameni, S. A. Grigoriev, N. Mbemba, F. Brisset, A. Ranjbari and C. Etiévant, *Int. J. Hydrog. Energy*, 2010, **35**, 5043–5052.
52. T. Burdyny and W. A. Smith, *Energy Environ. Sci.*, 2019, **12**, 1442–1453.
53. L.-C. Weng, A. T. Bell and A. Z. Weber, *Phys. Chem. Chem. Phys.*, 2018, **20**, 16973–16984.
54. R. L. Cook, R. C. MacDuff and A. F. Sammells, *J. Electrochem. Soc.*, 1990, **137**, 607–608.
55. D. W. Dewulf and A. J. Bard, *Catal. Lett.*, 1988, **1**, 73–79.
56. N. Gupta, M. Gattrell and B. MacDougall, *J. Appl. Electrochem.*, 2006, **36**, 161–172.
57. M. R. Singh, E. L. Clark and A. T. Bell, *Phys. Chem. Chem. Phys.*, 2015, **17**, 18924–18936.
58. T. Burdyny, P. J. Graham, Y. Pang, C.-T. Dinh, M. Liu, E. H. Sargent and D. Sinton, *ACS Sustain. Chem. Eng.*, 2017, **5**, 4031–4040.
59. A. Seifitokaldani, C. M. Gabardo, T. Burdyny, C.-T. Dinh, J. P. Edwards, M. G. Kibria, O. S. Bushuyev, S. O. Kelley, D. Sinton and E. H. Sargent, *J. Am. Chem. Soc.*, 2018, **140**, 3833–3837.
60. H. Ooka, M. C. Figueiredo and M. T. M. Koper, *Langmuir*, 2017, **33**, 9307–9313.
61. J. D. Goodpaster, A. T. Bell and M. Head-Gordon, *J. Phys. Chem. Lett.*, 2016, **7**, 1471–1477.
62. M. R. Singh, J. D. Goodpaster, A. Z. Weber, M. Head-Gordon and A. T. Bell, *Proc. Natl. Acad. Sci. U. S. A.*, 2017, **114**, E8812–E8821.
63. B. A. Zhang, T. Ozel, J. S. Elias, C. Costentin and D. G. Nocera, *ACS Cent. Sci.*, 2019, **5**, 1097–1105.
64. T. Cheng, H. Xiao and W. A. Goddard, *Proc. Natl. Acad. Sci. U. S. A.*, 2017, **114**, 1795–1800.
65. J. H. Montoya, C. Shi, K. Chan and J. K. Nørskov, *J. Phys. Chem. Lett.*, 2015, **6**, 2032–2037.
66. W. Sheng, A. P. Bivens, M. Myint, Z. Zhuang, R. V. Forest, Q. Fang, J. G. Chen and Y. Yan, *Energy Environ. Sci.*, 2014, **7**, 1719–1724.
67. J. K. Norskov, T. Bligaard, A. Logadottir, J. R. Kitchin, J. G. Chen, S. Pandelov and U. Stimming, *J. Electrochem. Soc.*, 2006, **153**, L33.
68. E. Skúlason, V. Tripkovic, M. E. Björketun, S. Gudmundsdóttir, J. Rossmeisl, T. Bligaard, H. Jónsson and J. K. Nørskov, *J. Phys. Chem. C*, 2010, **114**, 18182–18197.
69. Z. W. Seh, J. Kibsgaard, C. F. Dickens, I. Chorkendorff, J. K. Nørskov and T. F. Jaramillo, *Science*, 2017, **355**, eaad4998.
70. E. R. Cave, J. H. Montoya, K. P. Kuhl, D. N. Abram, T. Hatsukade, C. Shi, C. Hahn, J. K. Nørskov and T. F. Jaramillo, *Phys. Chem. Chem. Phys.*, 2017, **19**, 15856–15863.

71. Y.-J. Zhang, V. Sethuraman, R. Michalsky and A. A. Peterson, *ACS Catal.*, 2014, **4**, 3742–3748.
72. H. Yano, F. Shirai, M. Nakayama and K. Ogura, *J. Electroanal. Chem.*, 2002, **533**, 113–118.
73. T. T. H. Hoang, S. Ma, J. I. Gold, P. J. A. Kenis and A. A. Gewirth, *ACS Catal.*, 2017, **7**, 3313–3321.
74. E. J. Dufek, T. E. Lister and M. E. McIlwain, *Electrochem. Solid-State Lett.*, 2012, **15**, B48–B50.
75. J.-J. Lv, M. Jouny, W. Luc, W. Zhu, J.-J. Zhu and F. Jiao, *Adv. Mater.*, 2018, **30**, 1803111.
76. B. Endrődi, G. Bencsik, F. Darvas, R. Jones, K. Rajeshwar and C. Janáky, *Prog. Energy Combust. Sci.*, 2017, **62**, 133–154.
77. A. D. Castillo, A. Del Castillo, M. Alvarez-Guerra, J. Solla-Gullón, A. Sáez, V. Montiel and A. Irabien, *Appl. Energy*, 2015, **157**, 165–173.
78. S. Ma, R. Luo, J. I. Gold, A. Z. Yu, B. Kim and P. J. A. Kenis, *J. Mater. Chem. A*, 2016, **4**, 8573–8578.
79. B. Kim, F. Hillman, M. Ariyoshi, S. Fujikawa and P. J. A. Kenis, *J. Power Sources*, 2016, **312**, 192–198.
80. T.-T. Zhuang, Z.-Q. Liang, A. Seifitokaldani, Y. Li, P. De Luna, T. Burdyny, F. Che, F. Meng, Y. Min, R. Quintero-Bermudez, C. T. Dinh, Y. Pang, M. Zhong, B. Zhang, J. Li, P.-N. Chen, X.-L. Zheng, H. Liang, W.-N. Ge, B.-J. Ye, D. Sinton, S.-H. Yu and E. H. Sargent, *Nat. Catal.*, 2018, **1**, 421–428.
81. S. Ma, R. Luo, S. Moniri, Y. Lan and P. J. A. Kenis, *J. Electrochem. Soc.*, 2014, **161**, F1124–F1131.
82. C.-T. Dinh, F. P. G. de Arquer, D. Sinton and E. H. Sargent, *ACS Energy Lett.*, 2018, **3**, 2835–2840.
83. S. Ma, M. Sadakiyo, R. Luo, M. Heima, M. Yamauchi and P. J. A. Kenis, *J. Power Sources*, 2016, **301**, 219–228.
84. Electrochemical Dictionary, ed. A. J. Bard, G. Inzelt and F. Scholz, Springer-Verlag, Berlin Heidelberg, **vol. 2**.
85. B. A. Rosen, A. Salehi-Khojin, M. R. Thorson, W. Zhu, D. T. Whipple, P. J. A. Kenis and R. I. Masel, *Science*, 2011, **334**, 643–644.
86. E. Irtem, T. Andreu, A. Parra, M. D. Hernández-Alonso, S. García-Rodríguez, J. M. Riesco-García, G. Penelas-Pérez and J. R. Morante, *J. Mater. Chem. A*, 2016, **4**, 13582–13588.
87. D. Higgins, C. Hahn, C. Xiang, T. F. Jaramillo and A. Z. Weber, *ACS Energy Lett.*, 2019, **4**, 317–324.
88. C. Delacourt, P. L. Ridgway, J. B. Kerr and J. Newman, *J. Electrochem. Soc.*, 2008, **155**, B42–B49.
89. P. Jeanty, C. Scherer, E. Magori, K. Wiesner-Fleischer, O. Hinrichsen and M. Fleischer, *J. CO_2 Util.*, 2018, **24**, 454–462.
90. R. S. Jayashree, S. K. Yoon, F. R. Brushett, P. O. Lopez-Montesinos, D. Natarajan, L. J. Markoski and P. J. A. Kenis, *J. Power Sources*, 2010, **195**, 3569–3578.
91. D. T. Whipple, E. C. Finke and P. J. A. Kenis, *Electrochem. Solid-State Lett.*, 2010, **13**, B109–B111.

92. L.-C. Weng, A. T. Bell and A. Z. Weber, *Energy Environ. Sci.*, 2019, **12**, 1950–1968.
93. A. Pătru, T. Binninger, B. Pribyl and T. J. Schmidt, *J. Electrochem. Soc.*, 2019, **166**, F34–F43.
94. D. Ren, J. Fong and B. S. Yeo, *Nat. Commun.*, 2018, **9**, 925.
95. L. Paltrinieri, E. Huerta, T. Puts, W. van Baak, A. B. Verver, E. J. R. Sudhölter and L. C. P. M. de Smet, *Environ. Sci. Technol.*, 2019, **53**, 2396–2404.
96. F. Li, L. Chen, G. P. Knowles, D. R. MacFarlane and J. Zhang, *Angew. Chem., Int. Ed. Engl.*, 2017, **129**, 520–524.
97. K. Jiang, R. B. Sandberg, A. J. Akey, X. Liu, D. C. Bell, J. K. Nørskov, K. Chan and H. Wang, *Nat. Catal.*, 2018, **1**, 111–119.
98. N. M. Vargas-Barbosa, G. M. Geise, M. A. Hickner and T. E. Mallouk, *ChemSusChem*, 2014, **7**, 3017–3020.
99. R. S. Reiter, W. White and S. Ardo, *J. Electrochem. Soc.*, 2016, **163**, H3132–H3134.
100. M. B. McDonald, S. Ardo, N. S. Lewis and M. S. Freund, *ChemSusChem*, 2014, **7**, 3021–3027.
101. Y. C. Li, Z. Yan, J. Hitt, R. Wycisk, P. N. Pintauro and T. E. Mallouk, *Adv. Sustainable Syst.*, 2018, **2**, 1700187.
102. Y. C. Li, D. Zhou, Z. Yan, R. H. Gonçalves, D. A. Salvatore, C. P. Berlinguette and T. E. Mallouk, *ACS Energy Lett.*, 2016, **1**, 1149–1153.
103. T. Li, E. W. Lees, M. Goldman, D. A. Salvatore, D. M. Weekes and C. P. Berlinguette, *Joule*, 2019, **3**, 1487–1497.
104. K. N. Grew, J. P. McClure, D. Chu, P. A. Kohl and J. M. Ahlfield, *J. Electrochem. Soc.*, 2016, **163**, F1572–F1587.
105. S. Verma, U. O. Nwabara and P. J. A. Kenis, in *Nanocarbons for Energy Conversion: Supramolecular Approaches*, ed. N. Nakashima, Springer International Publishing, Cham, 2019, pp. 219–251.
106. S. Park, J.-W. Lee and B. N. Popov, *Int. J. Hydrog. Energy*, 2012, **37**, 5850–5865.
107. E. H. Majlan, D. Rohendi, W. R. W. Daud, T. Husaini and M. A. Haque, *Renewable Sustain. Energy Rev.*, 2018, **89**, 117–134.
108. J. Lobato, P. Cañizares, M. A. Rodrigo, F. J. Pinar, E. Mena and D. Úbeda, *Int. J. Hydrog. Energy*, 2010, **35**, 5510–5520.
109. A. Kumar and R. G. Reddy, *J. Power Sources*, 2003, **113**, 11–18.
110. J. Nie and Y. Chen, *Int. J. Hydrog. Energy*, 2010, **35**, 3183–3197.
111. X. Li and I. Sabir, *Int. J. Hydrog. Energy*, 2005, **30**, 359–371.
112. S. Shimpalee, S. Greenway and J. W. Van Zee, *J. Power Sources*, 2006, **160**, 398–406.
113. J. R. Hudkins, D. G. Wheeler, B. Peña and C. P. Berlinguette, *Energy Environ. Sci.*, 2016, **9**, 3417–3423.

Subject Index